University of Southampton

Faculty of Medicine

Clinical and Experimental Sciences

# Characterization of microglial heterogeneity in the CNS by single-cell RNA sequencing

by

**Tim Arno Othni Muntslag**

ORCID ID https://orcid.org/0000-0001-5624-0300

Thesis for the degree of Doctor of Philosophy

October 2022

**University of Southampton**

# Abstract

Faculty of Medicine

Clinical and Experimental Sciences

Thesis for the degree of Doctor of Philosophy

## Characterization of microglial heterogeneity in the CNS by single-cell RNA sequencing

by

Tim Arno Othni Muntslag

Microglia are parenchymal macrophages that find their origin in the early embryonic yolk sac. These myeloid cells migrate to and take residency in the central nervous system (CNS), in which they are transcriptionally heterogenous in a context-dependent manner. Many microglial states and subtypes have been described by single-cell RNA sequencing (scRNA-seq), vastly accelerating knowledge of microglial biology; yet it is currently unknown how adult microglial heterogeneity emerges, or what regulons drive differentiation.

Here, an atlas of transcriptional heterogeneity across the murine lifespan was developed, identifying 7 major myeloid subtypes in the CNS, one of which features an equivalent in human gestation. The occurrence of *ex vivo*-activated microglia (*ex*AM) was also confirmed, a microglial state affected by cell isolation. In the present study it has been observed that standard scRNA-seq procedures introduce these effects, and that transcriptional inhibition is an effective means to their mitigation. This adaptation was implemented in a novel scRNA-seq protocol, generating a dataset in sexually immature microglia (SIM), a key developmental age for the acquisition of a mature microglial identity.

Age was the main driver of microglial heterogeneity, albeit some evidence of sex-specific effects was also noted. Consequentially, male and female microglia display differential population dynamics, whereby age-associated subtypes emerge earlier in female mice. Furthermore, subtype-specific regulons in the female cortex were identified, offering novels ways to target and modify age-associated disease. To my knowledge, this study is the first that details microglial heterogeneity in health in a large-scale atlas, and the population dynamics that give rise to age-associated microglial heterogeneity.

# Table of Contents

# Table of figures

# Table of tables

# Contributions to the thesis

Herewith, I would like to acknowledge and thank those who made a scientific contribution to this body of work.

**Chapter 3**: Lyla Rowe, MSc, who performed the quality control and integration of the large-scale atlas, and the associated Monocle analysis.

**Chapter 4**: Rachel Green and Matthew J. Rose-Zerilli, PhD, for their assistance with Dropseq and mixed-species experiments.

**Chapter 5**: Lucy Kimbley, Joshua Grant, and Matthew J. Rose-Zerilli, PhD, for their assistance with the Drop-seq experiment.

# Declaration of authorship

Print name: Tim Arno Othni Muntslag

Title of thesis: Characterization of microglial heterogeneity in the CNS by single-cell RNA sequencing

I declare that this thesis and the work presented in it is my own and has been generated by me as the result of my own original research.

In confirm that:

1. This work was done wholly or mainly while in candidature for a research degree at this University;
2. Where any part of this thesis has previously been submitted for a degree or any other qualification at this University or any other institution, this has been clearly stated;
3. Where I have consulted the published work of others, this is always clearly attributed;
4. Where I have quoted from the work of others, the source is always given. With the exception of such quotations, this thesis is entirely my own work;
5. I have acknowledged all main sources of help;
6. Where the thesis is based on work done by myself jointly with others, I have made clear exactly what was done by others and what I have contributed myself;
7. Parts of this work have been published as:

Hu, Yanling, Gemma L. Fryatt, Mohammadmersad Ghorbani, Juliane Obst, David A. Menassa, Maria Martin-Estebane, Tim A. O. Muntslag, et al. 'Replicative Senescence Dictates the Emergence of Disease-Associated Microglia and Contributes to Aβ Pathology'. *Cell Reports* 35, no. 10 (8 June 2021): 109228. https://doi.org/10.1016/j.celrep.2021.109228.

Menassa, David A., Tim A. O. Muntslag, Maria Martin-Estebané, Liam Barry-Carroll, Mark A. Chapman, Istvan Adorjan, Teadora Tyler, et al. 'The Spatiotemporal Dynamics of Microglia across the Human Lifespan'. *Developmental Cell* 57, no. 17 (12 September 2022): 2127-2139.e6. https://doi.org/10.1016/j.devcel.2022.07.015.

Signature: Date: 03/10/2022

# Acknowledgements

A PhD Is never completed in isolation, it is the culmination of the shared efforts of a community. Over the past years I have had the pleasure to meet people across England, each willing and able to lend a hand. I learned a lot about myself over the course of the PhD: I have come to know and trust my eye for science; appreciate the importance of consistency; and have learned to better cope with my own shortcomings. Only now do I understand why a PhD is a Doctor of Philosophy.

To Diego, my main supervisor. I am grateful for the opportunity to have joined the lab. We did not always align when we started on this project together; two people with a strong opinion and a passion for science. However, in time, I learned to open to criticism from you, to accept your teachings. I have become a better scientist and person for it, and I am fortunate to have had you to guide me. To Mat and Jonathan, my other supervisors. Thank you for your expertise, without which this project would not have been developed. Thank you for keeping me on my toes, for your insight and kindness.

To the MRC, IfLS and MDC, and all the people at the university to have helped me over the years. Thank you for all your hard work and attention, I have had many opportunities I never expected to be privy to. To Jessica, my unofficial mentor, thank you for your entrepreneurship, and the cups of coffee. I value the bond that grew from that.

To the people in the lab that I shared most of my time with: Joe, Gemma, David. You each brought a genuine connection that I sometimes missed while away from the Netherlands. You have become family to me. Joe, for your humour, confidence and vulnerability, and for all the shared memories. You have become like a brother. Gemma, for your openness and care, and for being a great mom to Lucas. Not many of us has the care of a child alone, but you are mighty. David, for your commitment to the field and your laughter. You have set a benchmark for what it means to be a good scientist, and always knew how to bring light into a dark room.

To Monica, Georgie, and all the other team members and friends, past and present, thank you for your ear when I needed it, and for coming to find me when you needed mine. Thank you for the birthdays, cakes, and getaways. To Saskia and Michael, and Nico, thank you for all the friendship and shared experiences we had these past years; here is to many more adventures.

To my partner, Serena, thank you for being there for me in the highs and lows, for making a home with me where I feel safe, valued and needed. For the willingness to share your culture and family, and for being part of mine. If a PhD gives me wisdom, you give me joy. To my family back home, thank you for the support for as long as I can reminder. This degree is for all of us.

Thank you all for bringing such richness to my life.

# Definitions and abbreviations

| | |
|---|---|
| ActD | actinomycin D |
| AD | Alzheimer's disease |
| ADHD | attention deficit hyperactivity disorder |
| AE | ArrayExpress |
| Aif1 | Allograft inflammatory factor 1 |
| AIM | aged inflammatory microglia |
| ALS | amyotrophic lateral sclerosis |
| Aniso | anisomycin |
| ARM | activated response microglia |
| Aß | amyloid-ß |
| ATM | axon tract-associated microglia |
| BAM | border-associated macrophages, Binary Alignment Map |
| BM | bone marrow |
| BP | BioProject |
| Ca | calcium |
| CAM | CNS-associated macropages |
| CB | cerebellum |
| CBM | cerebellum |
| CC | corpus callosum |
| CCA | Canonical Correlation Analysis |
| CH | cerebrum |
| CNS | central nervous system |
| CP | choroid plexus |
| CPM | cycling and proliferating microglia |
| CRB | cerebrum |
| Csf1r | colony stimulating factor 1 receptor |
| CTX | cortex |
| Cx3cl1 | C-X3-C motif ligand 1 (fractalkine) |
| Cx3cr1 | C-X3-C Motif Chemokine Receptor 1 |
| DAM | disease-associated microglia |
| DC | dendritic cell |
| DEG | differentially expressed genes |
| DGE | digital gene expression |
| DMEM | Dulbecco's Modified Eagle's Medium |
| DRS | debris removal solution |
| E | embryonic day |
| EDM | early developmental microglia |
| EM1 | enzyme mix 1 |
| EM2 | enzyme mix 2 |
| EMP | erythromyeloid progenitors |
| *ex*AM | *ex vivo*-activated microglia |
| F | female |
| FACS | fluorescence-activated cell sorting |
| FB | forebrain |
| FBS | fetal bovine serum |
| FSC | forward scatter |
| GEO | Gene Expression Omnibus |

| | |
|---|---|
| GM | grey matter |
| GM-CSF | granulocyte macrophage-colony stimulating factor |
| GO | gene ontology |
| Gpr56 | G protein-coupled receptor 56 |
| HDAC | histone deacetylase |
| HIP | hippocampus |
| HOM | homeostatic microglia |
| Hoxb8 | Homeobox B8 |
| HPC | high performance computing |
| HPF | hippocampal formation |
| Iba1 | ionized calcium-binding adaptor molecule 1 |
| IDE | integrated development environment |
| IFN | interferon |
| IRM | interferon response microglia |
| KNN | K-nearest neighbours |
| LAM | lipid-associated macrophages |
| LPM | lysosome pathway-associated microglia |
| M | months old, male |
| MACS | magnetic-activated cell sorting |
| MAD | median absolute deviation |
| MafB | Transcription Factor B |
| MB | midbrain |
| MdC | monocyte-derived cells |
| MDI | microglial developmental index |
| Mg | magnesium |
| MGnd | neurodegeneration-associated microglia |
| MRBII | myelin removal beads II |
| MS | multiple sclerosis |
| MTDR | Mitotracker Deep Red FM |
| MΦ | early microglia |
| N | no |
| N.A. | not available |
| N/A | not applicable |
| ND | neurodegeneration |
| NGS | next generation sequencing |
| NLDR | non-linear dimensionality reduction |
| OCD | obsessive-compulsive disorder |
| OLF | olfactory bulb |
| OPC | oligodendrocyte progenitor cells |
| P | postnatal day |
| PAM | proliferative region-associated microglia |
| PC | principal component |
| PCA | principal component analysis |
| PCR | polymerase chain reaction |
| PCW | postconceptual week |
| PD | Parkinson's disease |
| pMac | macrophage precursors |
| Pparg | peroxisome proliferator-activated receptor gamma |
| QC | quality control |
| RT | room temperature |

| | |
|---|---|
| Runx1 | runt-related transcription factor 1 |
| Sall1 | Spalt-like transcription factor 1 |
| SC | spinal cord |
| scRNA-seq | single-cell RNA sequencing |
| SD | standard deviation |
| SIM | sexually immature microglia |
| SIP | Stock Isotonic Percoll |
| snRNA-seq | single-nuclei RNA sequencing |
| SSC | side scatter |
| STAMP | single-cell transcriptome attached to microparticles |
| STR | striatum |
| SVZ | subventricular zone |
| sxRNA-seq | single-cell and single-nucleus RNA-sequencing |
| TF | transcription factor |
| Tgf-β | Transforming growth factor-β |
| Tmem119 | Transmembrane protein 119 |
| Tripto | triptolide |
| TRM | transiting response microglia |
| TSM | tissue-specific macrophage |
| *t*SNE | *t*-distributed stochastic neighbour embedding |
| UMAP | uniform manifold approximation and projection |
| UMI | unique molecular identifiers |
| WAM | white matter-associated microglia |
| WB | whole brain |
| WM | white matter |
| WT | wild type |
| Y | yes |
| YS | yolk sac |

# Chapter 1 Introduction

The homeostatic, central nervous system (CNS) immune environment is composed of a diverse array of cells, among which CNS-associated macrophages (CAM) (10%), and microglia (~75%) (Mrdjen et al., 2018). As the largest immune population, microglia are integral to CNS development, homeostasis, and disease, due to their roles in neurogenesis, synaptic pruning and immune surveillance, (Wolf et al., 2017).

Interestingly, microglia are a heterogeneous population in which select microglial subtypes respond to various cues in different manners (Gertig and Hanisch, 2014). Since their first characterization in 1919 by Pio del Rio-Hortega, 'the father of microglia', single-cell technologies are rapidly detailing this diversity and are revolutionizing the understanding and interpretation of microglial identity.

In this chapter I aim to introduce core concepts in microglial biology, from the yolk sac (YS) progenitors and developmental ontogeny of microglia; to context-dependent heterogeneity; single-cell technologies; and the hypothesis and aims, in which adult microglial diversity derives from the maturation of and selection against early developmental subtypes.

## 1.1 Yolk sac-derived myeloid progenitors and *in vivo* lineage tracing

Between embryonic day (E)7.0 and E9.0, early haematopoiesis is localised to the extra-embryonic YS (Ginhoux et al., 2010; Hoeffel et al., 2015). By E10.5, hematopoietic progenitors start to migrate to the fetal liver, which will become the main hematopoietic organ after E11.5, before adult haematopoiesis is localized to the spleen and bone marrow (BM) (Lichanska and Hume, 2000; Orkin and Zon, 2008; Ginhoux et al., 2010; Hoeffel et al., 2015). The microglial population was thought to derive from embryonic and postnatal hematopoietic cells. However, the blood-brain barrier closes in early development and circulating monocytes do not make a lasting contribution to the population (Ginhoux et al., 2010; Hashimoto et al., 2013; Bruttger et al., 2015; Askew et al., 2017; Huang et al., 2018; Goldmann et al., 2016). In fact, microglial progenitors arise from primitive myeloid progenitors in the YS, a cell type known as erythromyeloid progenitors (EMP) (Ginhoux et al., 2010).

EMP generate all myeloid cells, with macrophages and microglia sharing developmental origins. *In vivo* lineage tracing (*i.e.* fate-mapping studies) specified the origin of myeloid cells during early haematopoiesis (E6.5 - E8), in which differentiation is typified by the expression of runt-related transcription factor 1 (*Runx1*) (Ginhoux et al., 2010). Several key studies have since made use of the Cre-lox system. The Cre-lox system relies on the introduction of Cre recombinase and loxP sequences, to modify gene expression in a site-specific manner. In this way, the system has allowed researchers to delineate the myeloid lineage, each localising progenitors to the YS (Ginhoux et al.,

2010; Kierdorf et al., 2013; Hoeffel et al., 2015; Buttgereit et al., 2016; Sheng et al., 2015; Mass et al., 2016). However, the developmental pathways causal to myeloid lineage differentiation have been a source of debate.

## 1.2 Developmental differentiation of myeloid cells

Macrophages and microglia share an early developmental lineage and, consequentially, a core macrophage transcriptional profile (Goldmann et al., 2016; Mass et al., 2016). Detailed profiling marks a gradual transition from EMP to macrophages, with a profile that includes *Csf1r*, *Cx3cr1* and *Iba1* (Mass et al., 2016).

Csf1r, or colony stimulating factor 1 receptor, mediates self-renewal and survival of macrophages and microglia (Elmore et al., 2014; Hoeffel et al., 2015; Obst et al., 2017) - Csf1r is encoded by the *c-fms* proto-oncogene and is a widely accepted myeloid marker (Sasmono and Williams, 2012; Elmore et al., 2014; Hoeffel et al., 2015). Cx3cr1, or C-X3-C Motif Chemokine Receptor 1, is a protein that is widely expressed in immune and non-immune cells, which mediates chemotaxis towards its ligand fractalkine (*i.e.* C-X3-C motif ligand 1) (Cx3cl1) in a concentration gradient-dependent manner (M. Lee et al., 2018). In turn, ionized calcium-binding adaptor molecule 1 (Iba1) is encoded by Allograft inflammatory factor 1 (*Aif1*) and is a microglial and macrophage protein that interacts with the actin cytoskeleton and mediates phagocytosis (Lituma et al., 2021; Schwabenland et al., 2021) .

Two main myeloid developmental models have been put forth that address the origin of the microglial population and their diversification from macrophages in mice. Hoeffel *et al.* (2015) made a case for two parallel pathways of divergence for microglia and macrophages. In their model, microglia derive from C-Kit$^{+}$ EMP at E7 and (peripheral) macrophages from C-Myb$^{+}$ EMP at E8.5 (Hoeffel et al., 2015). In contrast, Mass *et al.* (2016) argue that microglia and macrophages leave the YS in a single developmental pathway (Mass et al., 2016). Here, at E8.5, YS EMP characterized by Kit$^{+}$ Gata1/2$^{+}$ Cd45$^{low}$ differentiate into macrophage precursors (pMac) (Kit$^{-}$ Cd45$^{+}$ Cx3cr1$^{+}$) (Mass et al., 2016). pMac first appear in the YS at E9.5, in which expression of Cx3cr1 mediates subsequent tissue colonization throughout the embryo. Once in the parenchyma, pMac mature into (early) macrophages from E10.25 onwards, giving rise to tissue-specific macrophages (TSM), including CAM and microglia.

Of note, tissue-specific signatures were detected as early as E12.5, a developmental time-window with widespread macrophage tissue colonisation (Mass et al., 2016). This has led Mass *et al.* (2016) to propose that myeloid maturation parallels organogenesis, and concurrent with the expression of tissue-dependent lineage-determining transcription factors (TF). Indeed, the TF Sall1 is specific to parenchymal microglia, whereas Pparg and Id3 are critical for the differentiation of alveolar and

Kupffer cells, respectively (Mass et al., 2016a). Sall1, or Spalt-like transcription factor 1, regulates microglial identity and physiological functions (Buttgereit et al., 2016). Given their transcriptional commonalities, the distinct identity of each cell type is proposed to be the culmination of environmentally and developmentally programmed TF; extrinsic and intrinsic factors, respectively (Gosselin et al., 2017). That is, the core transcriptional gene profile is subject to environmental factors that drive epigenetic modification and differentiation.

### 1.2.1 Hoxb8 and non-Hoxb8 lineage microglia

The group of Mario R. Capecchi recently brought forth a third theory that proposes a hybrid of both myeloid developmental models. In their model of microglial ontogeny, two distinct lineages leave the YS and give rise to murine brain microglia in a *Hoxb8*-dependent and -independent manner (De et al., 2018). *Hoxb8*-expressing microglia share a developmental origin with non-Hoxb8 microglia in the YS, but the former undergo a migratory path through the fetal liver prior to CNS localization from E12.5 onwards, in parallel with widespread organogenesis (De et al., 2018).

Hoxb8, or Homeobox B8, is a TF with a role in the regulation of behaviour. Genetic disruption of *Hoxb8* causes defects in nociception and excessive grooming in mice models, the latter of which is interpreted as a symptom of trichotillomania , an obsessive-compulsive disorder (OCD) (Chen et al., 2010). Mice with mutations to Hoxb8 display corticostrial circuit defects, a neural circuit that has previously been associated with OCD pathogenesis (Ahmari et al., 2013; Shepherd, 2013). Interestingly, coat loss in *Hoxb8*-KO was aggravated by female sex hormones; coat loss starts at 3 weeks of age (at the start of sexual maturation), with a larger loss coinciding with sexual maturity (at 6-8 weeks old) (Tränkner et al., 2019).

*In vivo* lineage tracing played a central role in identifying Hoxb8$^{+}$ cells as microglia. However, *Hoxb8* expression is restricted to primitive haematopoiesis in the embryonic YS (without expression beyond E12); therefore, lineage tracing of Hoxb8$^{+}$ cells is technically challenging. To circumvent this limitation, De *et al.* (2018) developed a novel two-colour model of Cx3cr1$^{GFP/+}$ Hoxb8$^{IRES\text{-}Cre/+}$ Rosa26$^{CAG\text{-}LSL\text{-}tdTomato/+}$ mice that constitutively express the tdTomato-reporter in myeloid cells. Colocalization of tdTomato$^{+}$ cells with Tmem119 confirmed that these early hematopoietic cells are in fact microglial progenitors; Tmem119, or Transmembrane protein 119, is a microglial cell-surface protein of unknown function (Bennett et al., 2016).

Furthermore, Hoxb8$^{+}$ and Hoxb8$^{-}$ microglial subtypes display a differential non-overlapping function, density, and distribution. Indeed, both subtypes display similar levels of synaptic pruning capacity, even though Hoxb8$^{+}$ microglia were more readily able to proliferate in response to neuronal injury (De et al., 2018). A greater ability to respond to injury is expected to be associated with lineage specific differentially expressed genes (DEG). Moreover, conceptually, the co-

occurrence of two routes of migration into the CNS and the subsequent diversification of microglia illustrate how cellular biology is informed by the environment.

The work by De *et al.* (2018) corroborates earlier findings by Swinnen *et al.* (2013), which showed an increase of microglial density beyond what can be achieved by proliferation alone, arguing for a second set of microglial progenitors infiltrating the CNS parenchyma in development (Swinnen et al., 2013). In addition, the existence of two developmental microglial lineages suggests that microglial progenitor sub-populations could drive adult heterogeneity. In this way, the adult microglial population is hypothesized to derive from YS EMP that follow distinct developmental pathways (Figure 1).

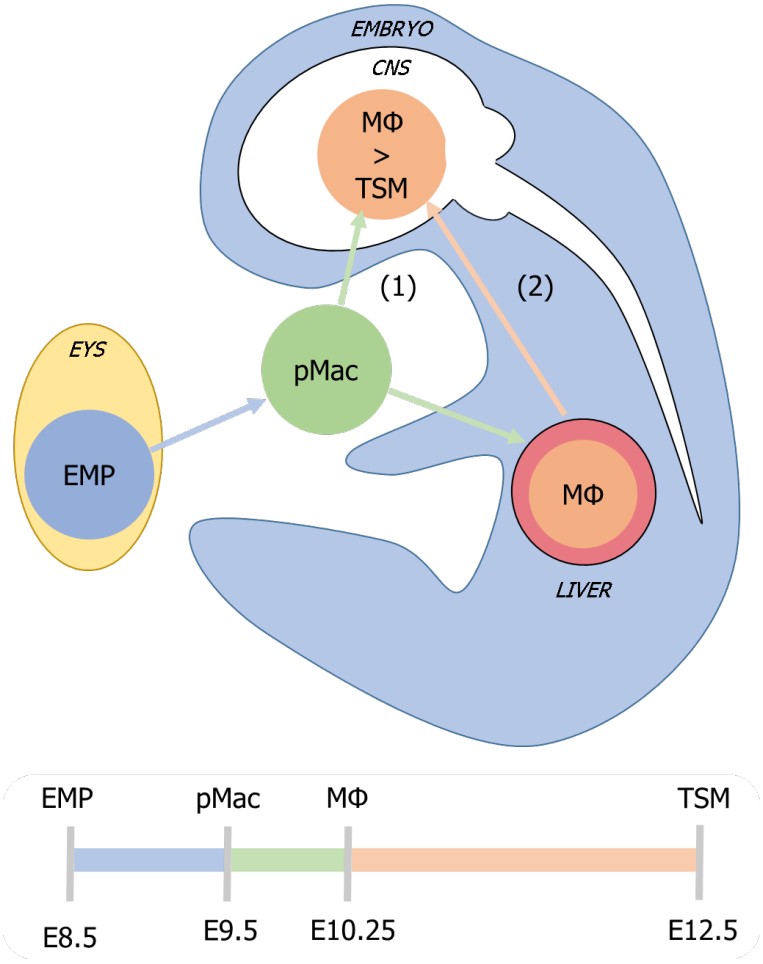


*Figure 1: Developmental colonization of the CNS by microglia. Erythromyeloid progenitors (EMP) in the embryonic yolk sac (YS) start to emerge at embryonic day (E) 8.5. By E9.5, EMP have acquired a core macrophage profile that includes Cx3cr1, thereby mediating tissue infiltration in the central nervous system (CNS) and liver. Macrophage precursors (pMac) differentiate into early microglia (MΦ), prior to differentiation into tissue-specific macrophages (TSM) (i.e. microglia). Two developmental pathways have been proposed to drive CNS colonization: Hoxb8-independent (1) and –dependent (2). The Hoxb8-dependent pathway is featured by a staged migration through the embryonic liver to the developing brain from E12.5 onwards.*

By extension, lineage tracing in zebrafish similarly identified distinct developmental pathways of myeloid cells. Two distinct waves of progenitors are thought to play a role, with links back to primitive and definitive haematopoiesis (Ferrero et al., 2018). However, unlike in mice, early microglia in zebrafish are not believed to derive from EMP (Ferrero et al., 2018; Xu et al., 2015). In

fact, it was argued that EMP have been misclassified as a homogenous population in mice, where these are in fact distinct from other potential progenitor sources(Ferrero et al., 2018). Hoxb8$^{+}$ progenitors and their developmental pathway are examples of such a possibility in mice and other species(Chen et al., 2010; Ferrero et al., 2018). Future studies will need to address and refine the developmental ontogeny in humans, as it has become clear that modelling of such biological processes might be specific to the species of interest.

### 1.2.2 Transplantation studies and lineage commitment

Transplantation of donor cells to a host complements insights of lineage tracing, as constructs of (trans)genes can be traced in a host, and allow for the differentiation between intrinsic and extrinsic features of a lineage (Kretzschmar and Watt, 2012) .

Transplantation of YS macrophages, and fetal liver and adult monocytes can regenerate alveolar macrophages, to establish a tissue-specific signature and self-renew (van de Laar et al., 2016). However, fetal monocytes were most efficient at repopulating the lung, suggestive of nuances in macrophage colonization potential, as was evidenced by their greater expression of granulocyte macrophage-colony stimulating factor (GM-CSF) and proliferation capacity. In contrast, adult tissue macrophages from the liver, peritoneum and colon failed to differentiate into self-renewing alveolar macrophages (van de Laar et al., 2016). This highlights a loss of differentiation plasticity, and is reminiscent of Waddington's landscape, a model that conceptualizes a progressive differentiation towards developmental and cellular end-states (Waddington and Kacser, 1957).

Intracerebral transplantation of cultured and primary microglia into the postnatal, murine, Csf1r$^{-/-}$ brain parenchyma – a model that lacks microglia in the CNS – proliferate and establish a microglial population that express typical markers such as *Tmem119*, *Sall1*, *Gpr56* (Bennett et al., 2018). Gpr56, also known as Adgrg1, is an adhesion G protein-coupled receptor that is enriched in microglia relative to other (choroid plexus) macrophages, where it functions to regulate immune responses and inflammation (Van der Poel et al. 2019, Lin et al. 2017).

Similarly, transplantion of C-Kit$^{high}$, Hoxb8$^{+}$ hematopoietic progenitors from the fetal liver (E12.5) into the CNS proliferate and differentiate in Cx3cr1$^{+}$ Tmem119$^{+}$ microglia (De et al., 2018). However, even though transplantation of fetal haematopoietic cells or BM-derived cells allows for parenchymal engraftment in the CNS; the transcriptional, epigenetic, and response to inflammatory challenge of these cells differs (De et al., 2018; Shemer et al., 2018). Only YS progenitors fully recapitulate adult microglial signatures (Bennett et al., 2018), supporting microglial ontogeny in early development.

Taken together, myeloid differentiation and lineage commitment differ by subtype, displaying variations in survival, transcriptional plasticity, and repopulating potential by maturation state.

### 1.2.3 Microglial specification and transforming growth factor-β

Microglial progenitors in the brain mature according to a two-step model of phenotypical differentiation; early microglia (<E14) develop into pre-microglia (E14 – postnatal day (P)9) prior to becoming adult microglia (>P9) (Matcovitch-Natan et al., 2016) (Figure 2).

In support of the rapid developmental expansion of the microglial population, early microglia are enriched by cell cycle and differentiation genes (*e.g. Mcm5*, *Dab2)* (Alliot et al., 1999; Matcovitch-Natan et al., 2016). In turn, pre-microglia express genes linked to migration, neurogenesis and cytokine secretion at a time when they are actively involved with neural maturation and synaptogenesis, whereas homeostatic functions in adult microglia are accompanied by the expression of *Cd14*, *Csf1r* and *Pmepa1* (Sierra et al., 2010; Paolicelli et al., 2011; Matcovitch-Natan et al., 2016). Microgliogenesis and differentiation is dependent on the TF Pu.1 (Spi1) and Irf8, respectively. Irf8 acts downstream of Pu.1 mediating differentiation to pMac, whereas Pu.1 is a target for Runx1 – Runx1, Pu.1 and Irf8 function to drive a lineage commitment cascade (Huang et al., 2008; Kierdorf et al., 2013a). Interestingly, stage-specific enhancers of transcription have been identified in YS macrophages, and early and adult microglia (Lara-Astiaso et al., 2014; Matcovitch-Natan et al., 2016). However, no equivalent TF has been identified in pre-microglia (Matcovitch-Natan et al., 2016). In the absence of intrinsic transcriptional regulators at this developmental time, extrinsic factors might mediate continued specification.

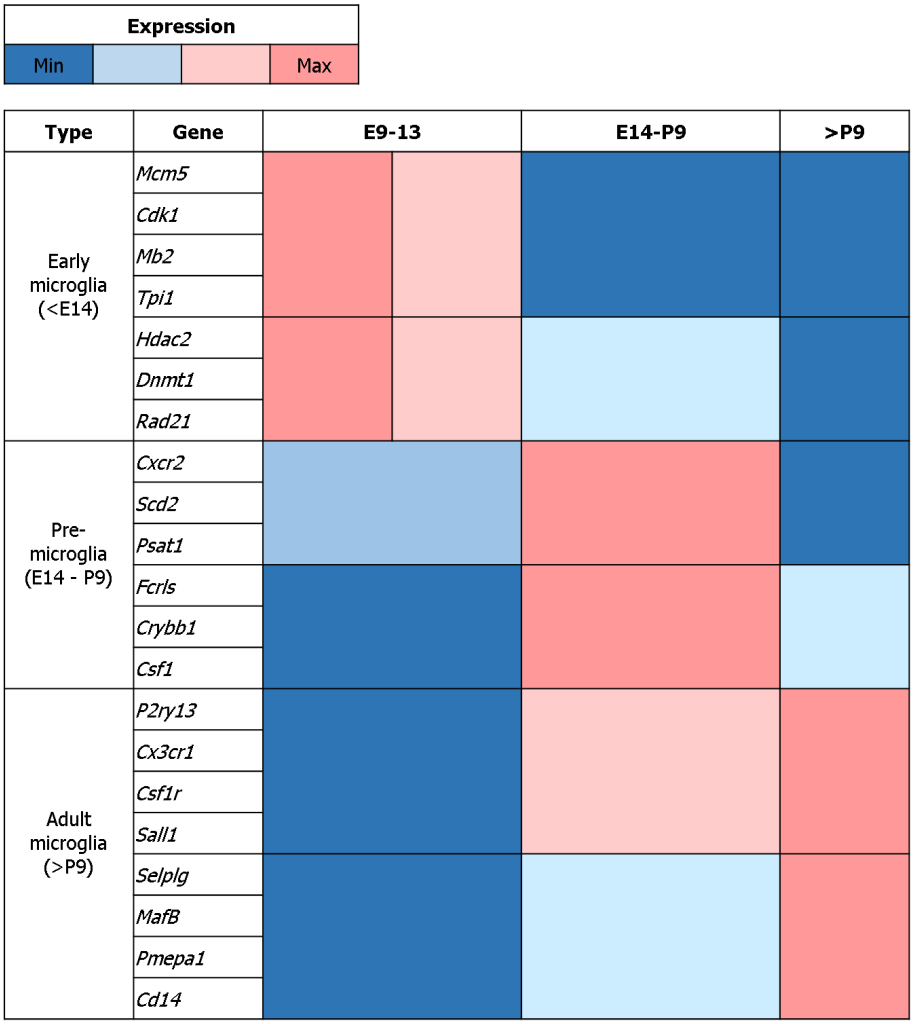


*Figure 2: Microglial specification in the developing CNS. Microglial specification as a stepwise process, in which early microglia (<E14), mature into pre-microglia (E14 – P9), prior to taking on an adult microglial signature (>P9). Key genes and their expression patterns in development are depicted. Adapted from (Matcovitch-Natan et al., 2016)*

Transforming growth factor (Tgf)-β functions as such an environmental factor and drives myeloid lineage differentiation and specification (Butovsky et al., 2014; Utz et al., 2020). Tgf-β has been found to regulate the expression of several microglial TF, including Sall1 and MafB (Gosselin et al., 2017). Transcription Factor B (MafB) functions to maintain steady-state microglia and limits interferon and inflammation pathway activation (Buttgereit et al., 2016; Kierdorf et al., 2013; Matcovitch-Natan et al., 2016). Interestingly, the absence of Tgf-β affects microglial development only after E14.5, reducing microglial density, and features a loss of microglial identity and a more amoeboid morphology (Butovsky et al., 2014; Matcovitch-Natan et al., 2016). The temporal relevance of this molecule suggests a role in the developmental transition from early to pre-microglia (E14 – P9); this is further typified by the expression of Sall1 in pre-microglia onwards. Therefore, Tgf-β provides a critical environmental cue that drives microglial identity and immunophenotype early in development. In this manner, the spatial and temporal dynamics of extrinsic and intrinsic TF are critical for microglial phenotypic differentiation and CNS function (Figure 3). It is currently unknown if and to which extend the two-step specification affects $Hoxb^{+}$ and $Hoxb^{-}$ microglia differentially. Given that microglial identity derives from developmentally-

and environmentally regulated TF, and these subtypes are linked to distinct functional responses, it is highly likely that differences will soon be identified.

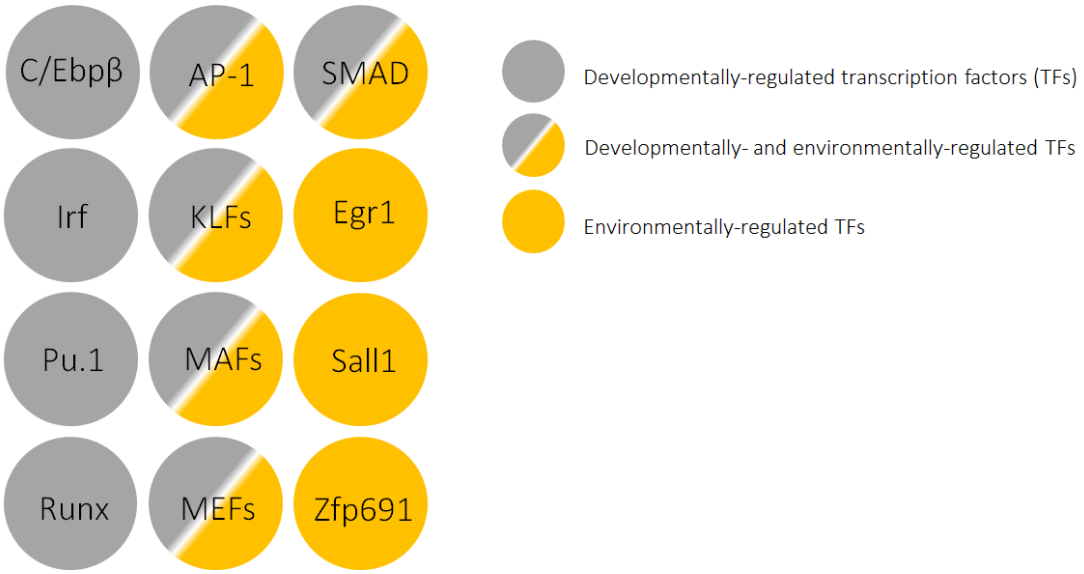


*Figure 3: Core macrophage profile and transforming growth factor-β -induced gene expression. The core macrophage profile includes several transcription factors (TF) that are modulated by environmental factors like transforming growth factor (Tgf)-β (gold); solely influenced by developmentally regulated T (grey); or modulated by both developmental and environmental factors. In fact, expression of genes like Sall1 that are solely induced by Tgf-β are indicative of progressive, environmentally dependent differentiation from a core macrophage profile*

## 1.3 Microglial heterogeneity: context-dependent regulation

The microglial population expands rapidly from a very limited number of progenitor cells at E8.5 to an estimated 3 million in adulthood (Lawson et al., 1990; Alliot et al., 1999; Haimon et al., 2018). As discussed, this population progresses from a core macrophage signature to a specialized microglial subtype, believed to originate from 2 distinct microglial lineages and their interaction with environmentally regulated TF (Figure 1).

Adult microglial heterogeneity has long been considered bimodal, where the classical paradigm of functional polarisation categorises cells as either active or resting; M1 or M2, respectively. However, in recent years researchers have redefined microglial activity, arguing that microglia occupy a spectrum of heterogeneity (Ransohoff, 2016). Indeed, with technological innovation and accumulating biological understanding, diverse and dynamic microglial subtypes and states are recognized in a context-dependent manner (Grabert et al., 2016; Hammond et al., 2019; Martinez and Gordon, 2014; Safaiyan et al., 2021; Sala Frigerio et al., 2019). In this section I will address known effectors of cellular heterogeneity in detail, elucidating how cell cycle, age, region, and sex each contribute to form the identity of the microglial population.

### 1.3.1 Cycling and proliferating microglia

Cell cycle is generally described by mitosis and interphase, which can be further subdivided into G0-, G1-, S- and G2-phase; cells in G0 are non-cycling, quiescent/resting cells. Cellular quiescence corresponds to changes in the ratio of G1- to S-phase, where inhibition of cyclin-dependent kinase activity increased G1-phase length and loss of pluripotency (Soufi and Dalton, 2016). G1-phase is a 'commitment window' where differentiation signals (*e.g.* Tgf-β) induce cell fate decisions through factors like cyclin D and SMADs (Soufi and Dalton, 2016). DNA is synthesized in the S-phase, prior to cell growth in G2-phase, and the generation of two daughter cells during mitosis. By extension, cell cycle status in hematopoietic stem cells (HSC) is linked to transcriptional activity (Lauridsen et al., 2018); quiescent and proliferating HSC are characterized by low and high transcriptional activity, respectively. In this way, cell cycle phase influences sensitivity to developmental cues and subsequent cellular heterogeneity.

Microglial proliferation is most pronounced during development and plateaus in adulthood (Alliot et al., 1999; Askew et al., 2017; Nikodemova et al., 2015). Of note, Askew *et al.* have determined that microglial density in steady-state is maintained through coupling of apoptosis to local proliferation; 1.4% of adult microglia are thought to be proliferating at any given time (Askew et al., 2017). At this rate, the complete microglial population in mice renews every ~100 days. It is currently unknown to which extend microglial population dynamics are shared between mice and humans, albeit several studies support that microglia are long-lived cells in both species (Askew et al., 2017; Füger et al., 2017; Réu et al., 2017).

Cycling and proliferating microglia, also known as CPM, are actively cycling microglia (Li et al., 2019). CPM express canonical cell cycle-associated markers (Supplementary Table 5). However, recent work has shown that CPM also have a module of cell cycle-associated genes unique to microglia, distinct from canonical cell cycle genes shared with other cells (Li et al., 2019). Considering that microglia are heterogeneous and display an array of phenotypes throughout life, it is important to delineate cell cycle effects from subtype-specific microglial transcriptional signatures.

### 1.3.2 Microglial sensome and age-specific heterogeneity

The CNS is subject to extensive microglia-mediated modifications in development and age-associated degeneration, including neuronal maturation, synaptic pruning and immunomodulatory and phenotypical differentiation (Matcovitch-Natan et al., 2016). In correspondence, microglial heterogeneity peaks in development, and with age and injury (Hammond et al. 2019, Li et al. 2019).

The microglial sensome, defined by Hickman *et al.* (2013), features a prominent role in the age-specific transcriptional heterogeneity. The microglial sensome is a distinct cluster of protein coding transcripts for sensing endogenous ligands, microbe recognition and host defence, excluding

secreted proteins and organelle-specific proteins – the sensome tethers microglial subtype to its local environment (Hickman et al., 2013). The sensome contains several key microglial genes, including *Hexb*, *P2ry12*, *Tmem119*, *Trem2* and *Cx3cr1* (Hickman et al., 2013; Butovsky et al., 2014; Grabert et al., 2016). As stated, *Cx3cr1* encodes a chemokine receptor that mediates pMac migration; $Cx3cr1^{+}$ progenitors migrate towards neuronal fractalkine (Cx3cl1) (Mass et al., 2016; Mecca et al., 2018). Expression of *Cx3cl1* is upregulated during the developmental expansion of microglia, after which its expression is reduced and stabilised during homeostasis; coupling neural and microglial maturation in development (Nikodemova et al., 2015). With age, although *Cx3cr1* expression remains relatively stable in health, *Cx3cl1* is reduced further and coincides with increased neuro-inflammatory markers, chronic elevations of Il-1β , and dystrophic microglia in the hippocampus (HIP) (Streit et al., 2004; Hickman et al., 2013; Mecca et al., 2018).

In total, 31% of the sensome genes are downregulated with age, 80% of which encode for endogenous ligand-associated genes (Hickman et al., 2013). *Trem2*, *P2ry12*, *Dap12* and *Tmem119* are but a few of the genes affected. Of note, 44 out of 100 genes are directly or indirectly interacting with Dap12 (*i.e.* Tyrobp) (Hickman et al., 2013; Mecca et al., 2018). In fact, Trem2 is known to Dap12 forms a signalling cascade with Trem2, which is known to stimulate Dap12-signaling and ERK-mediated actin polymerization and cytoskeletal reorganization for chemokine-dependent chemotaxis and phagocytosis; associated with elevated levels of Apoe; and a loss of Tgf-β signalling (Mecca et al., 2018). Indeed, age correlates negatively with Tgf-β signalling and corresponds to a loss of microglial identity (Hickman et al., 2013; Butovsky et al., 2014; Grabert et al., 2016; Galatro et al., 2017; Olah et al., 2018). In essence, age and the microglial sensome underlie microglial phenotypical differentiation and changes to microglial identity, converging on the Trem2-Dap12 and Cx3cl1-Cx3cr1 axes (Figure 4).

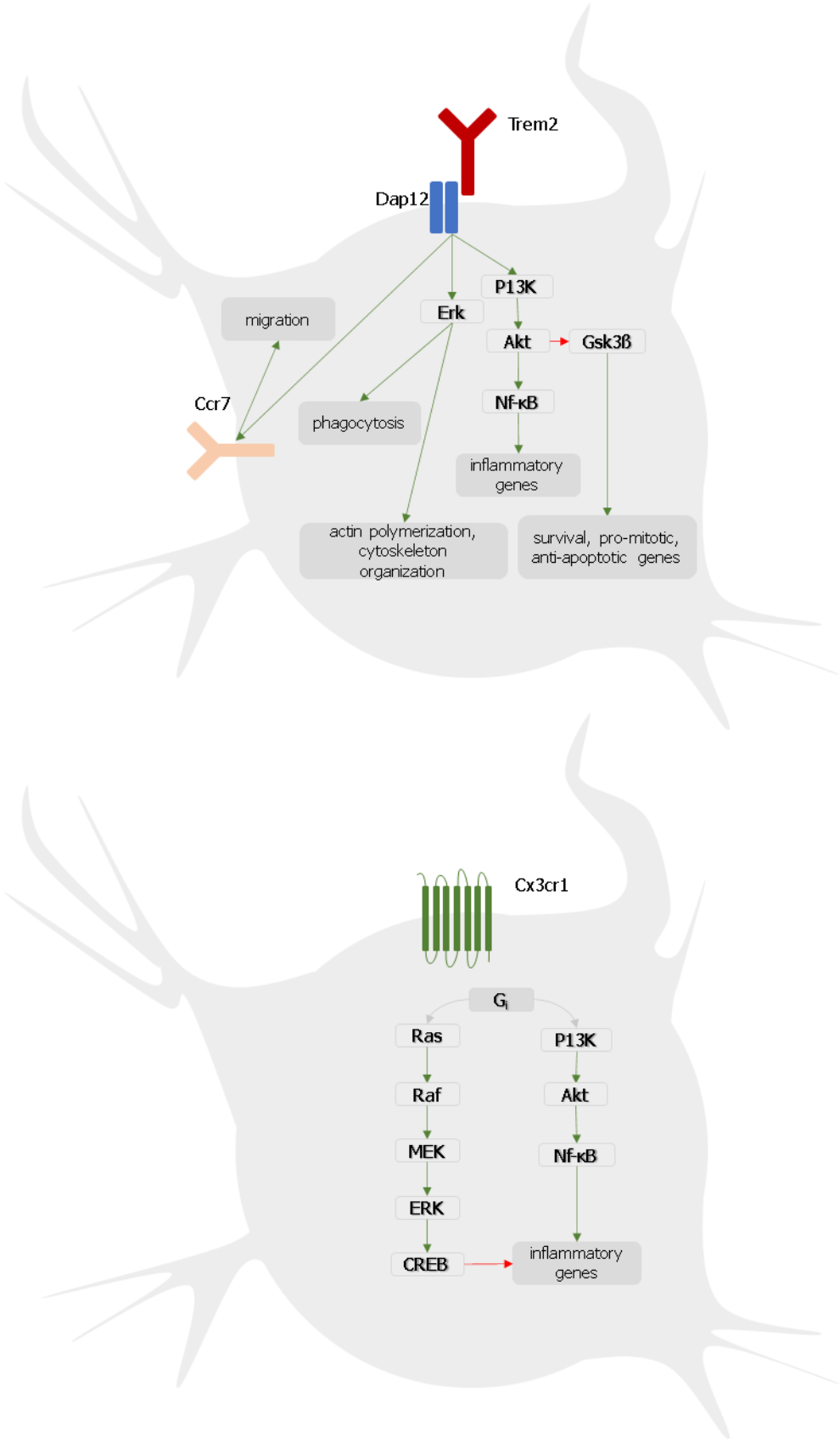


*Figure 4: Age-dependent molecular mechanisms of microglia. Schematic of Trem2-Dap12and Cx3cl1-Cx3cr1 signalling. Both membrane bound and soluble Trem2 and Cx3cl1 can bind their respective receptor. Adapted from (Mecca et al., 2018).*

#### 1.3.2.1 Disease-associated microglia: Trem2-Apoe signalling and phenotypical differentiation

First described by Keren-Shaul *et al.* (2017), disease-associated microglia (DAM) are a microglial subtype that emerges with age and age-associated disease. The transition from homeostatic to DAM is a mechanistically coupled two-step event through Trem2-independent and –dependent pathways (Keren-Shaul et al., 2017). During activation, microglia lose canonical marker gene expression (*e.g. P2ry12*, *Cx3cr1*, *Tmem119*) and show stage-specific identities; stage 1 DAM are featured by the expression of *Tyrobp*, *Apoe* and *Lyz2*, whereas stage 2 DAM are coupled to *Trem2*, *Cd11c* (*i.e. Itgax*), *Csf1*, *Lpl* and *Cst7*. Strikingly, *Trem2* mutations are a known risk factor for Alzheimer's disease (AD), suggesting that the appearance of this microglial subtype is neuroprotective, and corresponds to the proposed function of $Cd11c^{+}$ plaque-associated microglia; Itgax is believed to increase amyloid clearance and inflammatory response limitation (Kamphuis et al., 2016). In turn, Trem2 functions to maintain the metabolic fitness of microglia through regulation of autophagy (Krasemann et al., 2017). Similarly, facial nerve axotomy induces acute neurodegeneration and is coupled to the emerge of this phenotype (Tay et al., 2018a).

DAM bear resemblance to other phenotypes, known as neurodegeneration disease-associated microglia (MGnD) and activated response microglia (ARM) (Keren-Shaul et al., 2017; Krasemann et al., 2017; Sala Frigerio et al., 2019). These subtypes are present in health and numbers increase with disease, illustrating a role for these microglial cells in healthy aging (Sala Frigerio et al., 2019). For each of these studies, *Apoe* is central to subtype emergence; Apoe interacts with Trem2 and drives the generation of this subtype by inhibiting the function of Tgf-β (Krasemann et al., 2017). In effect, age- and age-associated disease impairs microglia to sense their environment, while concurrently undergoing a functional adaptation to combat pathology.

### 1.3.3 Region-dependent heterogeneity and maturation

Studies have shown that the adult brain varies in microglial morphology, density and function in a region-dependent manner (Lawson et al., 1990; Yang et al., 2013; Grabert et al., 2016; De Biase et al., 2017). Tissue colonisation of microglial progenitors in the brain parenchyma enables the population to expand rapidly (Lawson et al., 1990; Alliot et al., 1999; Haimon et al., 2018). The population continues to proliferate until it stabilises in adulthood after a selection phase removes roughly 50% of the population between postnatal week 3 and 6 (Lawson et al., 1990; Nikodemova et al., 2015; Askew et al., 2017; Haimon et al., 2018). Interestingly, it is currently unknown why this overshoot of the population occurs. Furthermore, the selection of microglia is region-specific, with the cerebellum (CB) and hippocampal formation (HPF) undergoing selection at an early time-point relative to the cortex (CTX) (Askew et al., 2017).

As stated, microglial density in steady-state is maintained through coupling of apoptosis to local proliferation (Askew et al., 2017). Notably, region-dependent differences are pronounced. *e.g.*, The dentate gyrus is featured by a particular high rate of proliferation that slows with age, unlike other regions that display a more stable rate throughout life (Askew et al., 2017). By extension, microglial density varies in a region-dependent manner, as density in murine grey matter-enriched regions is greater than in white matter-enriched areas (Lawson et al., 1990; Askew et al., 2017).

Metabolic and immune-associated clusters of genes are particularly important for regional microglial heterogeneity. Indeed, distinct microglial immunophenotypes were discovered in the CB, CTX, HIP and striatum (STR) (Grabert et al., 2016). Region-dependent enrichment of metabolic processes and immune response in the CB and HIP discriminate them from their striatal and cortical counterparts, with transcriptional regulators of cellular metabolism like peroxisome proliferator-activated receptor gamma (*Pparg*), and immune and defence responses coupled to interferon pathway activation (Grabert et al., 2016a). Of note, *Pparg* has been described earlier as a key TF for the development of alveolar macrophages. The relative enrichment of *Pparg* in macrophage subtypes, and other genes like it, marks the serpentine nature of cellular identity and lineage differentiation.

Differences in myeloid metabolism are coupled to immunophenotype, where the CB and HIP microglia are more inflammatory than their cortical and striatal counterparts (Jin et al., 2014; Orihuela et al., 2016). With age, both metabolism and immune-associated gene clusters had an overall reduction, with the majority of metabolic genes age-stable (±75%) and most immune-related genes age-altered (>80%) (Grabert et al., 2016). *e.g.* Expression of *Tmem119*, *P2ry12*, *Fcrls* and *Hexb* is reduced in the aging CB, as are several genes involved with Tgfβ-signalling (*e.g. Tgfbr1*) (Grabert et al., 2016). Each of these genes are key canonical markers for microglial identity and are intertwined with the effects of aging (Butovsky et al., 2014; Hickman et al., 2013; Mecca et al., 2018). Recent work shows that these canonical markers convey immune checkpoints that modulate microglial phenotype and its subsequent response (Deczkowska et al., 2018). Inherent region-dependent variations in microglial sensome genes might therefore underlie age-specific phenotypical divergence. *e.g.*, *Trem2*, *Csf1r* and *Cx3cr1* are all expressed at lower levels in the HIP and CB than the CTX and STR (Grabert et al., 2016).

Importantly, a landmark study by Li *et al.* (2019) offered a different perspective than Grabert *et al.* (2016) (Li et al., 2019). Li *et al.* (2019) used scRNA-seq. Microglia of distinct CNS regions were isolated and sequenced, and corroborated with RNA-seq. In this study, no regional heterogeneity in gene expression was detected (Li et al., 2019).This discrepancy remains an unresolved paradox and requires further investigation. However, scRNA-seq studies have reliably found distinct signatures between white and grey matter microglia.

#### 1.3.3.1 Functional emergence of white matter microglia

Myelination of the murine CNS starts at birth and is mostly complete by P60 (Snaidero and Simons, 2014). White matter, postnatal microglia regulate the number and maturation of oligodendrocyte progenitor cells (OPC)in myelinated regions, and are supportive of the proposed role of microglia in normal myelinogenesis (Hagemeyer et al., 2017; Wlodarczyk et al., 2017). Three studies have recently characterised white matter microglia in the corpus callosum, optic tract, medial lemniscus and/or CB in the murine CNS, this subtype is defined as proliferative region-associated microglia (PAM) or axon tract-associated microglia (ATM) in early development, or white matter-associated microglia (WAM) with ageing (Hammond et al., 2019; Li et al., 2019; Safaiyan et al., 2021). The transcriptional profile of these microglia is characterised by *Lpl*, *Spp1*, *Apoe* and *Itgax* (*Cd11c*), genes commonly linked to amyloid plaque-associated microglia, and suggestive of a transcriptional overlap. Remarkably, how microglial subtype heterogeneity arises is currently unknown; however, given that microglial specification is subject to intrinsic and extrinsic factors, changing conditions are expected to create an opportunity for the emergence of such heterogeneity.

#### 1.3.3.2 Interferon-response microglia

Interferon response microglia (IRM), also referred to as injury-responsive microglia, have been reported in health and disease and upregulate interferon (IFN) signalling pathway genes (Hammond et al., 2019; Sala Frigerio et al., 2019). IRM typically express genes like IFN-induced transmembrane protein 3 (*Ifitm3*), ubiquitin-specific protease 18 (*Usp18*), and 2'-5' oligoadenylate synthetase-like 2 (*Oasl2*).

Type I IFN (IFN-I) are the main CNS effectors (in response to viral and bacterial infection), acting as immunomodulators for inflammasome activation (González-Navajas et al., 2012). Interestingly, IFN-I gene *IFN-ß* plays a beneficial role in developmental synaptic pruning and myelin debris removal with multiple sclerosis (MS) (Goldmann et al., 2016; Kocur et al., 2015). Conversely, IFN-ß aggravates neuroinflammation and synapse loss in AD (Roy et al., 2020).

Dysregulation of IFN-I in the CNS, also known as interferonopathy, is associated with white matter diseases like Aicardi-Goutières syndrome and Cree encephalitis (Crow and Stetson, 2021). *e.g.* Loss of Usp18 in white matter microglia, a negative regulator of IFN, leads to microgliosis, constitutive expression of IFN-pathway genes, and white matter structural deficits (Goldmann et al., 2016, 2015; Schwabenland et al., 2019).

Of note, an artificial trajectory of differentiation (*i.e.* pseudotime analysis) of murine microglia found that IRM and DAM-like cells attain a 'mutually exclusive response state'; cells either differentiate into IRM or DAM cells (Sala Frigerio et al., 2019). Indeed, IRM are postulated to have a distinct functional role from DAM, with AD genes showing a particular enrichment in DAM-like

cells without an equivalent in IRM (Sala Frigerio et al., 2019). Such transcriptional heterogeneity in disease illustrates a role for environmentally regulated factors in the divergence of microglia. It is currently unknown what TF drive microglial subtype emergence and specification.

### 1.3.4 Sex-specific microglial heterogeneity and disease susceptibility

The CNS displays sexual dimorphism during development (Lenz et al., 2013; Thion et al., 2018). Studies have shown that the male and female brains display differential neuronal morphology and astrocyte complexity, mediated by gonadal steroids and culminating in behavioural differentiation (Lenz et al., 2013; Schwarz and McCarthy, 2008). Interestingly, recent work has started to show that microglia have a sex-specific profile in maturation that is associated with distinct phenotypes (Guneykaya et al., 2018; Hanamsagar et al., 2017; Thion et al., 2018; Villa et al., 2018). Microglia, as mediators in neuropathology, are therefore critical for brain homeostasis, and may do so in a sex-specific manner.

Inflammatory insults can induce long-term effects in microglial function in postnatal development, effects which are absent if occurring in adolescence (Bilbo et al., 2006, 2005). However, it are perturbations of male microglia that are coupled to schizophrenia- and autism-like symptoms (Estes and McAllister, 2016; Haida et al., 2019). The vulnerability of microglia to inflammatory insults suggests the existence of 'sensitivity windows', critical developmental time-points where microglial phenotypic plasticity is high, concurrent with ample lineage-specifying cues and an responsiveness to these cues (Fawcett and Frankenhuis, 2015). Therefore, male and female microglia appear to mature differently. Indeed, Hanamsagar *et al.* (2017) have shown that microglia follow a distinct maturation pathway in a sex-specific manner. More specifically, the authors describe a microglial developmental index (MDI), a measure of developmental maturity and immune reactive state, with adult male microglia (P60) scoring lower on the MDI. However, immune activation increases MDI in males to levels similar to females (Hanamsagar et al., 2017). Similarly, amyloidosis accelerates the emergence of DAM-like states in female microglia (Sala Frigerio et al., 2019), suggestive of age- and sex-dependent microglial maturation and heterogeneity.

Cellular heterogeneity is dependent on sex, with differential microglial densities and function. At 13 weeks (P91), male microglial densities are greater across a range of regions, including the CTX, HIP and amygdala (Guneykaya et al., 2018). Although in the HIP these differences are already present at 3 weeks (P21), the amygdala has an inverse relation, with a smaller density in males than females. These spatial differences are accompanied by differences in membrane properties, signalling pathways, microglial identity and immunophenotype. Indeed, Villa *et al.* (2018) transplanted 12 week old (P84), female murine microglia into the male CNS, after which males were more resilient to ischemic stroke, indicating that female microglia have a neuroprotective phenotype (Villa et al., 2018a). This study suggests that a higher MDI is neuroprotective, and by

extension, accelerated MDI with AD might therefore ameliorate disease, corresponding to the suggested protective role of DAM. Sex-, region- and age-related effects are therefore intimately connected.

## 1.4 Single-cell technologies

Many new microglial subtypes and phenotypes have been described with single-cell technologies, a new branch of research techniques that allow characterization of a single-cell genome, epigenome, transcriptome, proteome, metabolome and receptor repertoire, or combinations thereof (Gohil et al., 2021; Lee et al., 2020; Lent et al., 2021; Sankowski et al., 2021; Seydel, 2021; Shapiro et al., 2013) (Table 1).

Of these technologies, 10X is a commercially, industry leading, platform that has become the standard for scRNA-seq. It outperforms most alternatives on performance in accuracy and sensitivity (Svensson et al., 2017; Ziegenhain et al., 2017). Despite these benefits, instrument and assay costs are high and beyond the scope of this project.

*Table 1: Single-cell categories and technologies.*

| Category | Technologies |
|---|---|
| Genome | SCI-seq[1], DLP+[2], 10X[3] |
| Epigenome | scATAC-seq[4], snmC-seq[5], 10X[6] |
| Transcriptome | MARS-seq2[7], SMART-seq2[8], CEL-seq2[9], Drop-seq[10], 10X[11] |
| Proteome | MELC[12], CyTOF[13] |
| Metabolome | SpaceM[14], MALDI MS[15], SLMS[16], GCIB-SIMS[17] |
| Receptor repertoire | TetTCR-seq[18] |
| Multi | G&T-seq[19], scMT-seq[20], CITE-seq[21], scTrio-seq[22], 10X[23] |

*Note: Recent single-cell technologies across the modalities. The table provides a brief overview of some of the methods currently available; however, this is not meant to be inclusive of all variants. [1], (Vitak et al., 2017); [2], (Laks et al., 2019); [3], ("Single Cell CNV," n.d.); [4], (Buenrostro et al., 2015); [5], (Luo et al., 2017); [6], ("Single Cell ATAC," n.d.); [7], (Keren-Shaul et al., 2019, p. 2); [8], (Picelli et al., 2013); [9], (Hashimshony et al., 2016, p. 2); [10], (Macosko et al., 2015); [11], ("Single Cell Gene Expression," n.d.); [12], (Schubert et al., 2006); [13], ("| Fluidigm," n.d.); [14], (Rappez et al., 2021); [15], (Li et al., 2000); [16], (Zhu et al., 2021); [17], (Pareek et al., 2020); [18], (Zhang et al., 2018); [19], (Macaulay et al., 2015); [20], (Hu et al., 2016); [21], (Stoeckius et al., 2017); [22], (Hou et al., 2016); [23], ("Single Cell Multiome ATAC + Gene Expression," n.d.)*

### 1.4.1 Single-cell (and single-nuclei) RNA-sequencing

Of the technologies, single-cell RNA-sequencing, or scRNA-seq, has found the most widespread use and number of applications. scRNA-seq is the conceptual progression of bulk RNA-sequencing. Both are part of the umbrella of next-generation sequencing (NGS), a staple in cellular biology and medicine (Sandberg, 2014). The approaches have been widely adopted and have gained preference over microarray, as it is featured by a greater accuracy over a wider dynamic range, enabling the detection of more differentially expressed genes (DEG) and over a larger range of expressions (Pandey and Williams, 2014). However, despite RNA-seq being the most accurate approach to date, RNA-Seq can be inefficient in its ability to detect rare transcripts, as it reports on an average

transcriptome of all samples and cells in its analysis, thereby limiting the identification of cellular heterogeneity (Chen et al., 2019; Shapiro et al., 2013; Svensson et al., 2017; Tan et al., 2016). In contrast, scRNA-seq platforms have been reported to be sensitive up to single mRNA molecules and can partition individual cell transcriptomes, thereby accelerating the discovery of novel single-cell subtypes and phenotypes; single- cell atlases and states, respectively (Janes, 2016).

Cell phenotypes describe an expression profile that informs on the microenvironment and the effects of time, including circadian rhythms and transcriptional bursts. In contrast, subtype characterization assigns cells to a lineage (*e.g.* neuronal, oligodendrocyte, myeloid) (Janes, 2016). Both are valuable in the exploration of microglial heterogeneity, although they differ in the quantity of cells tested, and their respective number of reads per cell (*i.e.* read depth). In short, identifying single-cell subtype classes requires a lower average read depth of more cells and informs on lineage heterogeneity, whereas a greater read depth of fewer cells informs on cell state. However, distinctions between cell atlases and cell states are not binary, especially if nomenclature and semantics are not agreed upon or consistently reported in literature (Janes, 2016).

scRNA-seq has two main variants, that is, single-cell and single-nuclei sequencing (snRNA-seq). scRNA-seq outperforms snRNA-seq on cellular viability and RNA yield; yet there are considerable weaknesses in relation to frozen or hard-to-dissociate tissue, as well as the preservation of *in vivo* transcriptional signatures and occurrence of *ex vivo*-activated microglia (*ex*AM) with scRNA-seq (Machado et al., 2021; Slyper et al., 2020); an effect that will be addressed in Chapter 5, where I will address technical artefacts in scRNA-seq. In addition, distinct isolation protocols have been shown to result in distinct capture efficiencies (Slyper et al., 2020). *e.g.*, snRNA-seq has aided the characterization of multi-nucleated skeletal myofibers (Dos Santos et al., 2020; Kim et al., 2020; Petrany et al., 2020); whereas microglial activation genes are not detected with snRNA-seq (Thrupp et al., 2020). The availability of tissue, the target cell and desired output all restrict experimental design freedoms and require specific adaptations in experimental procedures. Furthermore, since its invention, researchers in the field of scRNA-seq (and snRNA-seq) have quickly engineered a wide range of approaches (Figure 5).

Taken together, scRNA-seq is particularly well-suited for the detailed characterization of the myeloid lineage with its states and subtypes. Indeed, there are over 250 examples utilizing this technology for microglia since its inception in 2015 (Hammond et al., 2019; Keren-Shaul et al., 2017; Li et al., 2019; Van Hove et al., 2019).

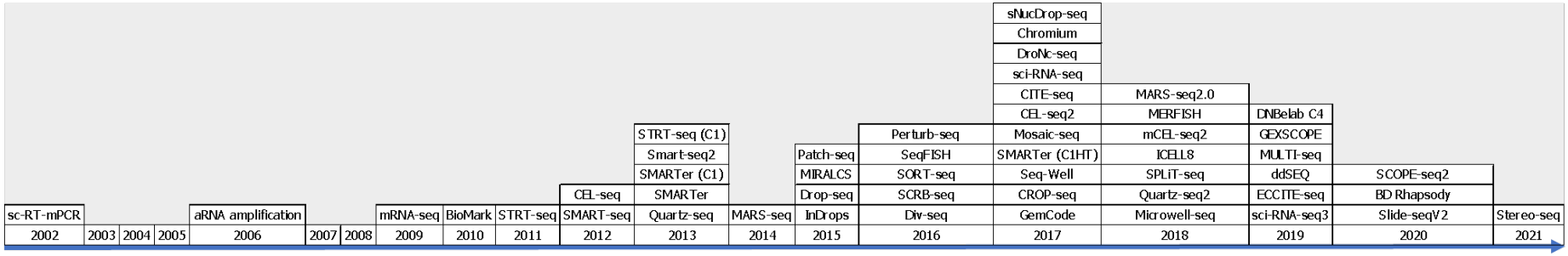


*Figure 5 Timeline of novel single-cell technologies. Single-cell, single-nuclei, and spatial transcriptomics approaches were included, with at least two reports of its use in literature. Timeline is from left to right, and from bottom to top. Created from (Svensson et al., 2020).*

## 1.5 Hypothesis and aims

In this chapter, microglial ontogeny, heterogeneity, and scRNA-seq were discussed. Microglia find their origin in the embryonic YS and migrate and colonize the CNS early in development. Intrinsic and extrinsic factors act synergistically to establish the adult population, which is a rich population that varies by age, region, and sex. Much work has gone into the description of early and late life microglial subtypes like PAM, ATM, DAM and IRM. However, it is currently unknown how microglial heterogeneity gives rise to adult heterogeneity, as is it unknown how age-associated subtypes emerge from adult homeostatic microglia. It was hypothesized that distinct microglial subtypes drive adult heterogeneity, in which male and female microglia display differential trajectories of maturation and population dynamics. Moreover, age-associated microglial subtypes are expected to be driven by distinct gene regulatory networks.

**Aim 1: Generation of a microglial single-cell atlas in murine development**

- Objective 1: To establish a framework of current knowledge
- Objective 2: To explore context-dependent microglial heterogeneity
- Objective 3: To translate murine early developmental effects to human gestation
- Objective 4: To perform a trajectory analysis of microglial differentiation

**Aim 2. Drop-seq platform performance and pilot of cortical microglia**

- Objective 5: To measure Drop-seq platform performance
- Objective 6: To develop an in-house scRNA-seq dataset of cortical microglia
- Objective 7: To explore data quality and transcriptional heterogeneity in cortical microglia.

**Aim 3: Establish a microglial scRNA-seq protocol.**

- Objective 8: To test the utility of chemical fixation with MetOH and DSP.
- Objective 9: To explore the characteristics of FACS and MACS for scRNA-seq.
- Objective 10: To assess cellular activation and yield in purification methods.
- Objective 11: To determine the effect of dissociation condition on ex vivo signatures.
- Objective 12: To implement a novel microglial isolation protocol for Drop-seq.

**Aim 4: Study of female gene regulatory networks in health and disease**

- Objective 13: To establish a female-specific atlas in the murine cortex.
- Objective 14: To explore the transition to an adult microglial phenotype.
- Objective 15: To determine the effects of amyloidosis on transcriptional heterogeneity and population dynamics.
- Objective 16: To identify transcription factors central to age-associated microglial subtypes.

# Chapter 2 General methodologies

## 2.1 Animals

C57BL/6- and Macgreen-mice were used in this study. Macgreen mice have an intracellular reporter of *c-fms* (*Csf1r*) gene expression by an enhanced green fluorescent protein construct (EGFP) (*Csf1r*-EGFP) (Sasmono and Williams, 2012). Both models were bred and maintained in the animal facilities of the University of Southampton (UK), according to local standards. These include standard chow (RM-1) (SDS, 801010) and water *ad libitum*, temperatures between 21 to 24°C, and a 12:12 light-dark cycle; light period from 07:00 to 19:00. All experimental procedures were conducted under ethical approval and according to personal and project licenses under the UK Animals (Scientific Procedures) Act (1986).

## 2.2 Anaesthesia and perfusion

Animals were subjected to a lethal intraperitoneal dose of sodium pentobarbitone (Pentoject, Animalcare, VM10347/4014) (200 mg/mL) between 08:00 and 11: 00AM.Mice were injected with 150 µL of Pentoject. The animal's toe-pinch- and corneal reflex were tested prior to proceeding with transcardial perfusion. After anaesthetic depth was confirmed (*i.e.* the absence of reflex), each animal was perfused with 20 millilitre (mL) phosphate-buffered saline (PBS) (1X) (Thermo Fisher, 70011044) (pH 7.2 ± 0.1), supplemented with heparin sodium (5 I.U. / mL) (Figure 6). Cessation of circulation and/or heartbeat were used as secondary measures to confirm death.

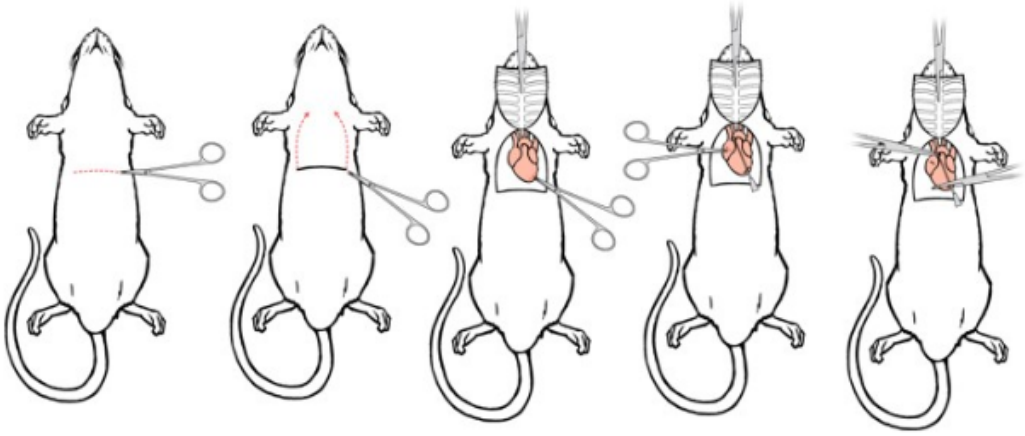

*Figure 6: Transcardial perfusion. First, a lateral incision of the integument and abdominal wall exposed the diaphragm. The ribcage was then cut bilaterally, opening the pleural cavity for access to the heart. With the sternum overhead, any excess fat was carefully removed from the pericardium, after which a butterfly-winged needle was inserted into the left ventricle and clamped into place. Finally, an incision to the right atrium created an outlet and the animal was perfused.*

## 2.3 Tissue harvesting and dissection

Tissue harvesting started with the removal of the head of a perfused animal (Figure 7). The skin was removed from the skull and any remaining neck muscles were trimmed down with surgical scissors (ToughCut) (F.S.T., 14054-13) to free the skull. A fine scissors (Martensitic Stainless Steel) (F.S.T., 14094-11) was then inserted into the foramen magnum and a sagittal cut from the base of the skull to the nose bones was made. With a rongeurs (F.S.T., 16021-14), the frontal bones and meninges were removed to free the brain from the skull.

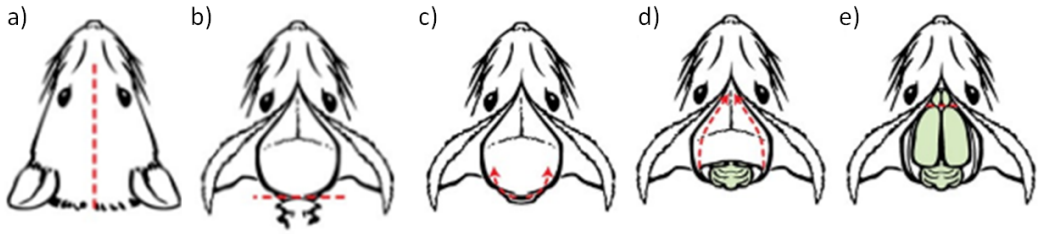


*Figure 7: Tissue harvesting and dissection. The head is removed after perfusion, after which the skin and remaining neck muscles are removed to clear the skull (a, b). Entering through the foramen magnum, a scissors split the skull bones across the sagittal suture up-to-and-including the nasal bone (c, d). Rongeurs were used to remove the skull bilaterally from the brain. With the brain exposed, a rounded spatula was inserted posterior from the olfactory bulbs and aided the removal of the brain from the skull (e).*

Once the brain was free from the skull, the CB and cerebrum (CH) were separated from each other in an ice-cooled 10-cm petri-dish with PBS (1X), without (w/o) calcium (Ca), magnesium (Mg) and phenol); the brainstem (BS) was cut coronally through the midbrain. When dissecting for the CTX, the cerebral hemispheres were separated along the longitudinal fissure and the HPF dissected from the inside of the CTX. Independent of the tissue-of-interest, and as soon as the tissue was dissected out, the tissue was stored in 2 mL PBS (1X) (w/o Ca, Mg, phenol) or in 2 mL 'Enzyme mix 1' (EM1) (Miltenyi, 130-092-628, 130-107-677) on ice, until all tissue was collected.

## 2.4 Microglial isolation

Microglia can be isolated in a plethora of ways and protocols need to be adjusted to the desired outcome measure. In short, tissue was dissociated, myelin was removed, and microglia enriched for, so these steps are described in detail in the following sections.

### 2.4.1 Tissue dissociation

Dissociation of brain tissue was performed in three distinct manners: Dounce homogenizer-mediated mechanical dissociation; actinomycin D (ActD)-supplemented (papain-mediated) enzymatic dissociation; or enzymatic dissociation alone.

The approaches vary in dissociation temperature; ice-cold (4°C), room temperature (RT; 21-23°C), or heated (37°C), respectively. RT conditions were simulated with a water bath (set to 22°C), whereas standard dissociation was performed in a heated oven. The approaches were distilled into 3 protocol variations that span the broad range of experimental procedures currently available in literature (Figure 72).

After collection, 30 µL 'Enzyme Mix 2' (EM2) (Miltenyi, 130-092-628, 130-107-677) was added to EM1, according to the guidelines of the producer. Prior to dissociation, independent of approach, the collected tissue was cut into small pieces using fine scissors (Martensitic Stainless Steel) (F.S.T., 14094-11). Mechanical dissociation was performed with a loose pestle of a 7 mL Dounce homogenizer (D9063, Sigma), followed by dissociation with a tight pestle, to liberate cells from tissue with 15 strokes each (adapted from (Hammond et al., 2019). Both ActD and standard dissociation approaches made use of pre-cut pipette tips, where tissue was progressively dissociated from large-, through medium-, to small-clearance pipette, a trituration series (Figure 8).

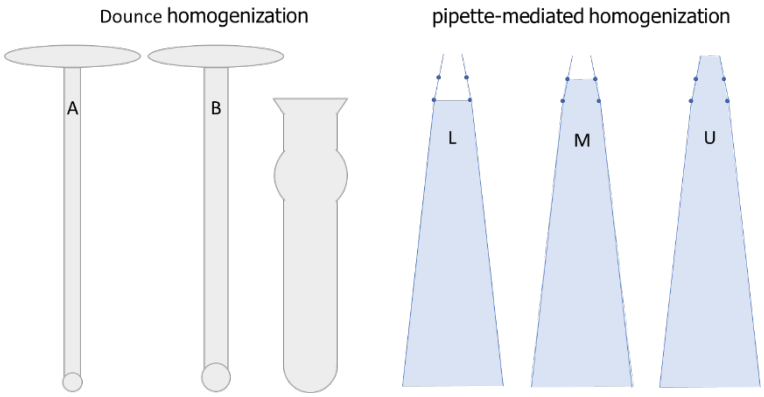


*Figure 8: Trituration series for tissue dissociation. Dounce homogenization utilized a 7 mL container, a small pestle (with large clearance) (A), and a large pestle (B). Each sample (and for each pestle size) was dissociated with 15 strokes. Pipette-mediated homogenization was done in progressively smaller apertures from large (L), to medium (M) to uncut (U) 1 mL pipets. Each step, and for each sample, was done for 1 minute at R.T. to mediate dissociation. Regardless of homogenization method, prior to dissociation, each sample was cut into small pieces with a fine scissors (Martensitic Stainless Steel) (F.S.T., 14094-11).*

For ActD dissociation, ActD (Sigma, A1410) was added to the collection solution (*i.e.* EM1) for working concentration of 30 µM. ActD is a light-sensitive, hygroscopic substance and was diluted (in DMSO) to stock concentration (8 mM) and stored at -20°C for up to a month. To ensure ActD was protected from light, stock solutions were stored in black Eppendorfs. Similarly, (micro-)dissected tissue samples were collected in bijous with EM1 covered with aluminium foil to minimize light exposure. To further minimize batch-specific effects, experimental series using ActD were performed using the same stock preparations, and no aliquots were reused after thawing.

### 2.4.2 Purification of single-cell suspensions: removal of myelin and cell debris

CNS-derived single cells were subjected to a round of purification, to remove any myelin and/or cell debris. Three distinct approaches were utilized, which fall in two broad categories: gradient centrifugation, and bead-dependent purification.

Gradient centrifugation was done with Percoll PLUS (Fischer Scientific, 10166144) or Debris Removal Solution (Miltenyi, 130-109-398). Bead-dependent removal was performed with Myelin Removal Beads II (Miltenyi, 130-096-733).

#### 2.4.2.1 Percoll-mediated gradient centrifugation

Percoll-mediated gradient centrifugation effectively removes myelin from the cell suspension and captures/enriches myeloid cells in the pellet. Normally, gradient centrifugation is performed with multiple density layers (Lee and Tansey, 2013). However, a single Percoll layer (~37%) effectively captures microglia in the lower pellet, improving on the handling speed (Grabert et al., 2016; Grabert and McColl, 2018).

For each sample, 5 mL of stock of isotonic Percoll (SIP) was prepared; 9 parts Percoll, 1 part PBS (10X) (w/o Ca, Mg, phenol). SIP was added to a 7 mL cell suspension in FACS-buffer for a 37% Percoll layer. Suspension was mixed and centrifuged at 500 x g for 30 minutes at 4°C without break (Eppendorf, 5810 R). Recommended centrifugal temperature is 18°C, yet in communication with the manufacturer and in observation this has not led to differences in purification efficiency (data not shown).

#### 2.4.2.2 Debris Removal solution

Cell pellets were supplemented with 3100 µL of ice-cold HBSS-buffer, to a total volume of approximately 3.5 mL, and added with 1050 µL of Debris Removal Solution (DRS) (Miltenyi, 130-109-398). 4 mL of HBSS-buffer was overlayed gently (*i.e.* dropwise) with a P1000 pipette (Gilson, F167370). The preparation was centrifuged at 1000 x g for 30 minutes at 4°C. Three phases formed and the top two were aspirated, supplemented to 14 mL with HBSS-buffer, and invert mixed. Then, cells were centrifuged again at 1000 x g for 10 minutes at 4°C.

The recommended protocol was deviated from recommended protocol on three aspects (Miltenyi, 130-109-398). First, resuspended cell pellets approximate 3500 µL, reflective of the relatively large size of cortical tissue. Consequentially, the volume of DRS from 900 to 1050 µL, to maintain the proportion of DRS to cells. Second, centrifugal forces were reduced from 3000 to 1000 x g (and increased centrifugal time) to accommodate speed limitations of the centrifuge (Eppendorf, 5810 R). Third, PBS was exchanged with HBSS-buffer. Both buffers include calcium and magnesium (and

exclude phenol); HBSS-buffer was selected for experimental simplicity in combination with other steps.

#### 2.4.2.3 Myelin Removal Beads

Myelin Removal Beads II (MRBII) (Miltenyi, 130-096-733) are a bead-dependent alternative to gradient centrifugation purification. MRBII purification is achieved by magnetic-activated cell sorting (MACS), a proprietary design of Miltenyi Biotec. Magnetic microparticles are bound to a myelin targeted antibody for the (negative) selection and removal of myelin debris from cell suspensions. I have used MRBII in combination with large selection (LS) (Miltenyi, 130-042-401) or large depletion (LD) columns (Miltenyi, 130-042-901). These columns vary in capacity and throughput for myelin depletion.

Cells were resuspended in 600 µL of HBE-buffer (for a total volume of ~ 900 µL) and supplemented with 100 µL of MRBII. Cells were incubated on ice for 15 minutes at 4°C, after which incubation was stopped by diluting the reaction mixture with HBE-buffer (to a total volume of 15 mL). Columns were prepared and myelin debris removed as recommended, collected in 3 mL of HBE-buffer.

### 2.4.3 Characterisation and enrichment of microglia: magnetic- and fluorescence-activated cell sorting

Both magnetic- (MACS) and fluorescence-activated cell sorting (FACS) were used for the characterization and enrichment of microglia (Figure 9).

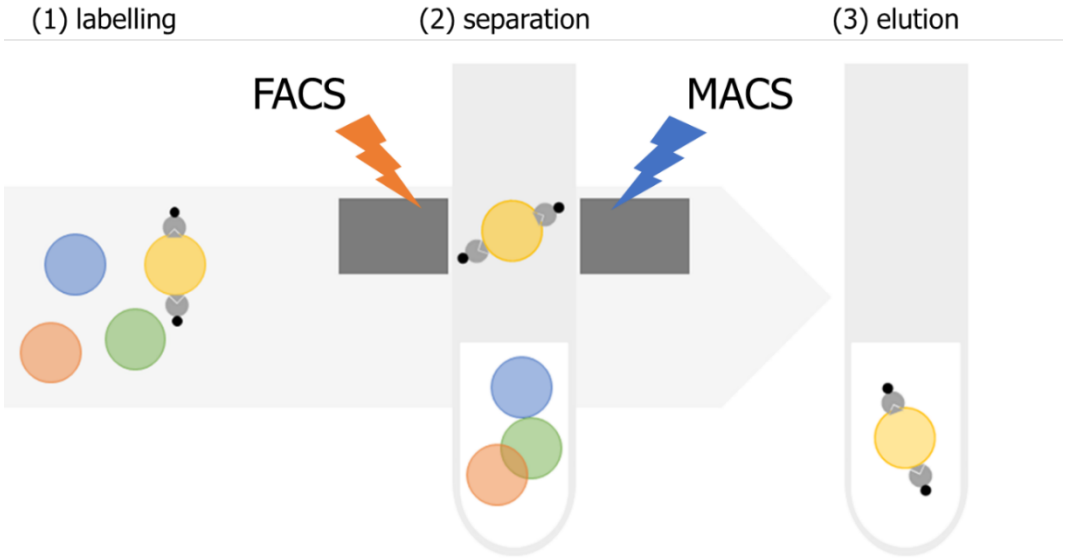


*Figure 9: Schematic of fluorescence and magnetic-activated cell sorting workflow. Cells were labelled with antibodies conjugated with fluorescent reporters or magnetic nanoparticles (1). Once in contact with their respective effector, light, and magnetism, respectively, cells bound by the antibodies separate from the mixed cell suspension (2). Positive selection enables the subsequent elution and enrichment of cells identified by those antibodies (3).*

#### 2.4.3.1 Magnetic-activated cell sorting and the isolation of Cd11b$^{+}$ cells

MACS enables the enrichment of microglia through magnetic microbeads conjugated to monoclonal rat anti-mouse/human Cd11b (Mac-1a) antibodies (M1/70.15.11.5, IgG2b) (Miltenyi Biotec, 130-049-601). Single cell suspensions were resuspended in 90 – 270 µL of HBE-buffer; and supplemented with 10 – 30 µL of microbeads. Cells were incubated with the microbeads for 15 minutes on (wet-)ice.

Positive selection with LS columns (130-042-401), coupled to a QuadroMACS (Miltenyi Biotec, 130-090-976) separator, effectively isolates CNS-derived monocytes/macrophages, and to some extend granulocytes, NK cells, CD5$^{+}$ B1-cells and dendritic cells (Miltenyi Biotec). In my experience, I found that the use of varying microbeads (in large cell pellets) did not lead to unspecific binding, yet it simplified resuspension and preserved a 1:10-ratio of HBE-buffer to microbeads (data not shown).

#### 2.4.3.2 RNA extraction and gene expression analysis by polymerase chain reaction

RNA of microglial cell pellets was extracted with the RNeasy Plus micro kit (74036, Qiagen), according to the manufacturer's guidelines. Cells were lysed in RLT lysis buffer with 143 mM β-mercaptoethanol, genomic DNA removed with gDNA Eliminator columns, and RNA bound onto a RNeasy MinElute spin column. RNA was washed and eluted; elution of RNA in 12 – 14 uL of nuclease-free water (129114, Qiagen). For a positive control, whole brain RNA was isolated from adult mice using the Trizol method (15596018, Thermo Fisher). 500 ng RNA was converted to cDNA with the iScript cDNA Synthesis Kit (1708891, BioRad), once more, following manufacturer's instructions.

I designed a panel of custom primers (Sigma Aldrich) for polymerase chain reaction (PCR): Csf1r, Cx3cr1, Egr1, Fos, Gapdh, Hexb, Ier2, Jun, P2ry12, Tmem119. Primer qualities were assessed with electrophoresis in a 1.6% agarose gel. Primer sequences are supplied in the Appendix (Supplementary Table 20). Data were analyses with the 2-ΔΔCt method with Primer Opticon 3 software, using Gapdh and/or Hexb as housekeeping genes; Gapdh was used as a loading control of RNA, whereas Hexb was a control for microglial load, thereby accounting for potential impurities in the isolated cell pellets.

#### 2.4.3.3 Flow cytometry and fluorescence-activated cell sorting (FACS) of microglia

Fluorescence-activated cell sorting (FACS) (*i.e.* flow cytometry) was utilized to characterize and/or enrich for microglial cells. Microglia express several markers that, when combined with fluorescence reporter-conjugated antibodies will function to identify microglia in mixed cell suspension (Askew et al., 2017). A table of all used antibodies, reagents and materials is supplied in the Appendix (Supplementary Table 19).

Identification of microglia has been achieved by the following gating schematic (Figure 10). In short, the expected population was selected for its size features across the forward (FSC) and side-scatter (SSC), size and complexity respectively, after which I selected for single- and viable cells (Viability-eFluor450$^{-}$, Viability-eFluor780$^{-}$, or Viability-7AAD$^{-}$), prior to microglial identification (*i.e.* Cd11b-BV421$^{+}$ Cd45-APC$^{+}$, Csf1r-EGFP$^{+}$, P2ry12-PE$^{+}$). To prevent clumping of cells, the suspension buffer (*i.e.* PBE-buffer) was devoid of Mg and Ca, and the addition of EDTA chelated any remaining ions.

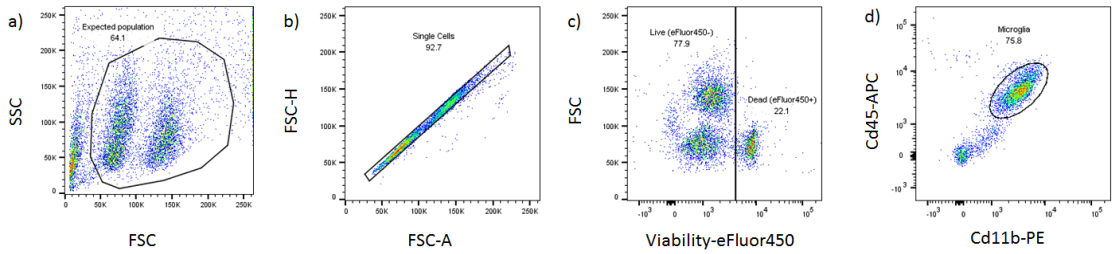


*Figure 10: Gating scheme for the identification of microglia. a) Cells of the appropriate size were selected in a plot of forward-scatter (FSC) and side-scatter (SSC). Next, single-cells (FSC-A and FSC-H) (b) and live cells (eFluor450-) (c) were selected, prior to identifying microglia by their expression of Cd11b and Cd45 (Cd11b+ Cd45low).*

Single-cell gating can be achieved in a range of manners, I choose to trial two, one with a single plot for FSC-A and FSC-H, and another for FSC-A and FSC-H followed by SSC-A and SSC-W. No obvert differences were detected and I diverted to singlet selection by plotting FSC-A and FSC-W (Figure 11).

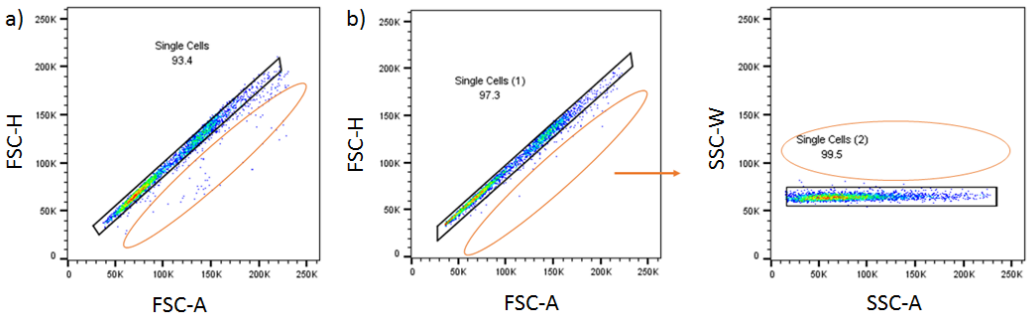


*Figure 11: Direct comparison of single-cell gating approaches. Gating for single-cells can be achieved by an FSC-A and FSC-H plot (a), or a serial gating for FSC-A and FSC-H to SSC-A and SSC-W (b). No obvious differences were detected between approaches. Oval markers indicate the relative localization of doublets.*

To further the identification of microglia and simplify gating, Csf1r and P2ry12 were used. P2ry12 reliably detected Cd11b$^{+}$ Cd45$^{+}$ microglia. However, only a proportion of those cells display cellular activity of EGFP (Figure 12).

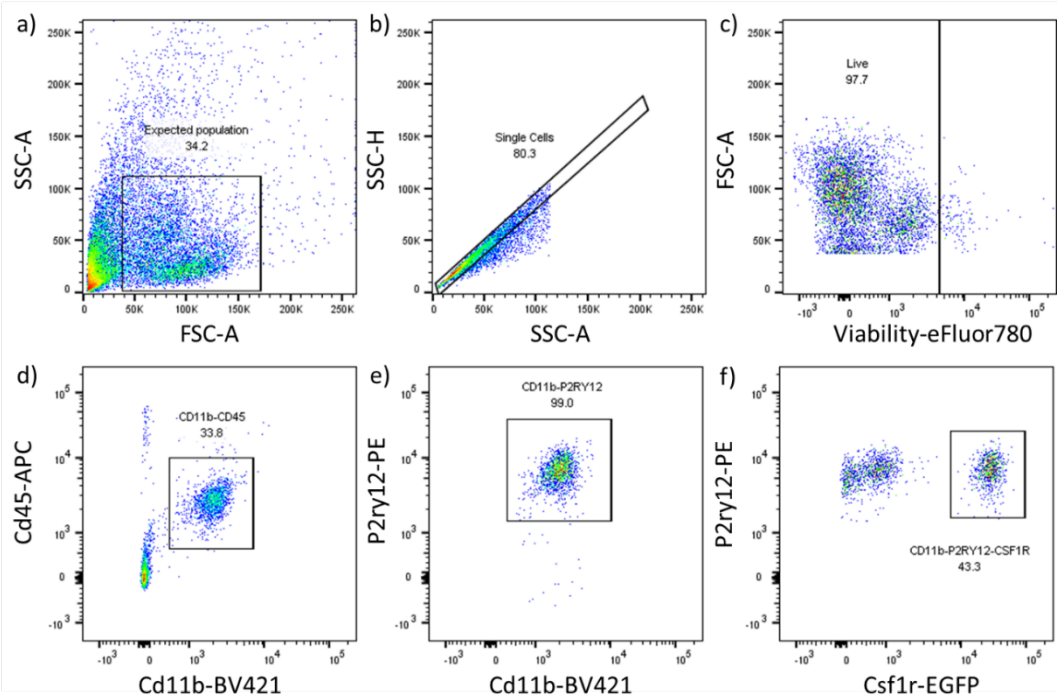


*Figure 12: Flow cytometric identification of microglia with canonical markers. The expected population is gated for with forward- (FSC-A) and side-scatter area (SSC-A) (a), after which singlets (b) and viable (c) cells are selected. eFluor780 was used for viability. Microglia were gated as Cd11b⁺ Cd45⁺. All (99%) identified microglia express P2ry12, albeit only ~43% of those cells are EGFP⁺. Macgreen mice were used with a reporter construct of Csf1r-EGFP.*

To detail this discrepancy, EGFP⁺ cells were backgated for Cd11b and Cd45 (Figure 13). Of note, of those cells identified as microglia, not all were EGFP⁺. Cd11b⁺ Cd45⁺ cells display a heterogeneity in size, where only the largest reliably express EGFP.

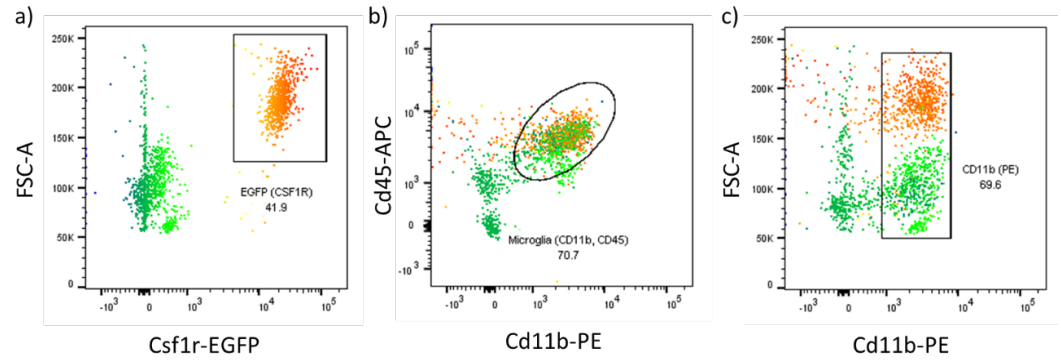


*Figure 13: Back gating of EGFP-positive cells highlights limitations to Macgreen mice. Fluorescent expression of Csf1r-EGFP does not identify all microglia (Cd11b⁺ Cd45⁺) (b). Larger cells reliably express EGFP, smaller cells do not.*

## 2.5 Drop-seq – Experimental pipeline

Microfluidic devices were generated and provided by the group of Jonathan J. West. The experimental pipeline of Drop-seq consist of 11 steps, including the reverse transcription of single-cell transcriptome attached to microparticles (STAMP), tagmentation, polymerase chain (PCR) reactions, and purification and quality control (QC) steps (Macosko et al., 2015).

The experimental protocol for Drop-seq is readily available and detailed online (Macosko and Goldman, 2018). However, I will detail some of the characteristics of the Drop-seq runs here (Figure 14).

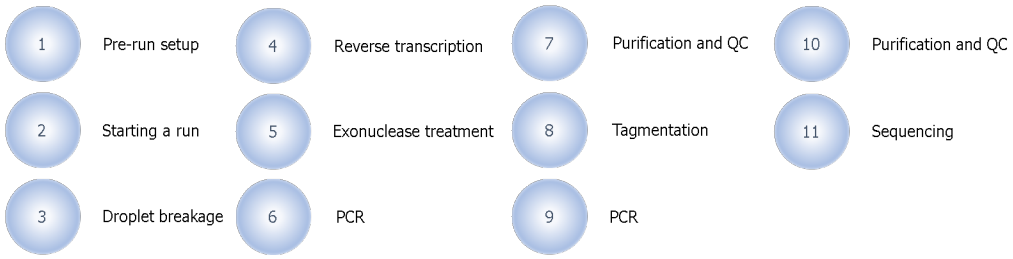


*Figure 14: Drop-seq experimental pipeline. The experimental process can be grossly divided in 11 steps, flowing from the pre-run setup, through several rounds of polymerase chain reaction (PCR), purification and quality control (QC), and completed with sequencing of the samples.*

Isolated single cells were suspended in PBS-BSA (0.01%) (100 cells/µl) and barcoded beads (Chemgenes, 'Barcoded Bead SeqB') in lysis buffer (120 beads/µl), each loaded into syringes and onto the microfluidic device. A magnetic stirrer (VP Scientific, 710D2) combined with a mixing disc were (VP Scientific, 772DP-N42-5-2) used to keep the microparticles in suspension, not exceeding 30 rounds-per-minute.

Droplets were generated in the system with standard flow rates; oil (BioRad, 370533) at 15,000 µl/hour, cells and beads at 4,000 µl/hour. Droplets co-encapsulated cells with barcoded beads and lysis buffer at final concentration of 50 cells and 60 beads/µl (in ~1 nl droplets with ~124 µm diameter). After completion of the run, droplets were broken with perfluoro-octanol (Sigma, 370533), oil removed, and beads resuspended in 6X SSC-buffer.

STAMP were reverse transcribed and excess bead primers of stored beads were removed by an exonuclease I treatment, after which beads were washed, and then resuspend in $H_2O$ for quantification. Depending on the bead recovery, multiples of 100 cells (*i.e.* 2,000 beads) of each sample were allocated to microcentrifuge tubes. Beads were subjected to 16 cycles of polymerase chain reaction (PCR); the number of cycles is microglia specific, other cells might require more of less amplification (Macosko and Goldman, 2018). PCR products were purified with AMPure XP beads (Beckman Coulter Life Sciences, A63880) according to the recommend instructions, eluted in 10 µL of $H_2O$, and PCR product pools were made for each sample. cDNA yield and quality were determined with the Bioanalyzer High-Sensitivity DNA kit (Agilent, 5067-4626). PCR products had an average size of 1734 ± 28 base pairs (bp) and a yield of 173 ± 90 pg/µL. Normal concentrations from 50 cells/µl vary between 400 – 1000 pg/µl; however, variations in concentration are expected due to variations in cell concentration and the number of beads, as well as PCR inefficiencies or RNA degradation (Macosko et al., 2015).

400 or 500 pg of purified cDNA was prepared for tagmentation. The mixture was incubated in a thermocycler at 55 °C for 5 minutes, neutralized and incubated for 5' at R.T. Each cDNA sample

was supplemented with a tagmentation PCR mix, including a N701 or N702 index for multiplexing. For the pilot, I used N701 and N702 for male and female cells, respectively. For the female-specific age-dependent libraries, I used N701 and N702 for P21 and P60, respectively. After which another PCR program was run (12 cycles), followed by AMPure XP-bead purification and analysis with the Bioanalyzer High-Sensitivity DNA kit (Agilent, 5067-4626). Tagmented libraries had an average size of 503 ±2 bp, a yield of 5.1 ± 0.3 nM, and over 95% purity.

An equimolar library pool (3 nM) was used as input for denaturation with 0.2 M NaOH. The denatured libraries were diluted to 30 pM and diluted once more to a loading concentration of 1.3 pM in hybridization-buffer (HT1, Illumina, 15009740). A 0.3 µM custom primer was prepared. Microglial libraries were sequenced (paired end) on a NextSeq 500 platform, utilizing NextSeq 500/550 Mid Output Kits (TG-160-2001, 150 cycles, V2; 20024904, V2.5), each with a maximum of 130,000,000 reads per cell. Sequencing runs parameters were as follows: read 1 (20 bp), read 1 index (8 bp), read 2 (50 bp), Custom Read 1 primer.

## 2.6 High-performance computing

I would like to acknowledge the use of the IRIDIS HPC Facility and associated support services in the completion of this work. The high-performance computing (HPC) was used for computationally demanding analyses. This includes the Drop-seq computational pipeline (2.7), as well as the integration of the large-scale atlas and their respective analyses (Chapter 3). Sequencing specifications were as follows: read 1 (20 base pair (bp)), read 2 (50 bp) and Read 1 Index (8 bp), to accommodate multiplexing. Drop-seq - Computational Pipeline

Raw (FastQ) sequencing reads were converted to a sorted, unmapped Binary Alignment Map (BAM) (FastqToSam, Picard bundled in Dropseq-tools v1.0) and filtered to remove all read-pairs with a barcode base quality of <10 (Figure 15). The second read was trimmed at the 5’ end to remove any TSO-adapter sequence and at the 3’ end to remove polyA tails. Reads were aligned against mouse reference genome (mm10) using STAR aligner (v2.5.0a), then sorted/converted/merged to a BAM with a tag “GE” onto reads for data extraction. The DigitalExpression program (Dropseq-tools v1.0) extracted digital gene expression (DGE) information of the mRNA transcripts (*i.e.* unique molecular identifiers (UMI)) and created a DGE matrix where rows contain genes and cell (barcodes) in columns.

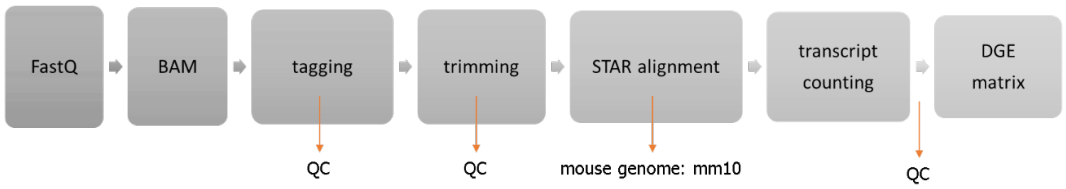


*Figure 15: Drop-seq computational pipeline. Raw sequencing reads were converted into Binary Alignment Map (BAM)-files, tagged, and trimmed. Reads that passed quality control (QC) were aligned to the mouse genome with STAR aligner, transcripts counted and converted into a digital gene expression (DGE) matrix.*

The Drop-seq computational pipeline (from FastQ to DGE-matrix) requires considerable computational power, which were found at the IRIDIS High Performance Computing Facility of the University of Southampton.

## 2.7 R and RStudio

DGE matrices were loaded and processed in R and RStudio. RStudio is an Integrated Development Environment (IDE) for R, itself a programming language suitable for statistical computing and graphics. For the analyses, R version 4.0.3 was combined with RStudio 1.3.1093. To utilize R and RStudio for scRNA-seq, Seurat was selected, a stand-alone bioinformatic tools for bespoke analyses.

### 2.7.1 Seurat

With the advent of scRNA-seq, many bioinformatic tools for clustering have been developed including RaceID, scran, SC3 and Seurat. Seurat is a tool that effectively encapsulates each analysis step, from quality control (QC), data normalisation and scaling, to dimensionality reduction, clustering and DGE analysis (Butler et al., 2018; Hao et al., 2021; Satija et al., 2015; Stuart et al., 2019).

Seurat was consistently found to outperform other scRNA-seq tools on matters of accuracy, robustness and running time, making it a good candidate for the exploration of microglial heterogeneity (Duò et al., 2018; Freytag et al., 2018). Seurat is an R toolkit for single cell genomics. Moreover, Seurat is user-friendly and benefits from a large user base, designed for droplet-based data, scalable to hundreds of thousands of transcriptomes across conditions, and performs unsupervised analysis by utilizing a machine-learning driven-approach to identify cell types (Butler et al., 2018). For these reasons, Seurat has become a popular tool in recent years, with numerous examples that utilized Seurat across single-cell platforms and fields of study that include haematology, neuroscience, and pharmacology (Avey et al., 2018; Chen et al., 2017; Gierahn et al., 2017; Villani et al., 2017)

The first inception of Seurat was in 2015, since then, the tool has recently taken on its 4$^{th}$ version (Butler et al., 2018; Hao et al., 2021; Satija et al., 2015; Stuart et al., 2019). Seurat V2, V3 and V4 were used in the analyses. Seurat follows a typical bioinformatic pipeline that allow for consistency

while offering a plethora of variations to specify the analysis (Figure 16). Generally, a count matrix and metadata are joined into a Seurat object for quality control (QC), normalization, scaling, and variable feature detection. Linear dimensionality reduction resolves statistically significant gene sets for cluster identification and non-linear dimensional reduction. Non-linear reduction projects the effects of these gene sets onto a 2-dimensional plane. Differential gene expression analysis of the identified clusters allows for subsequent cluster annotation.

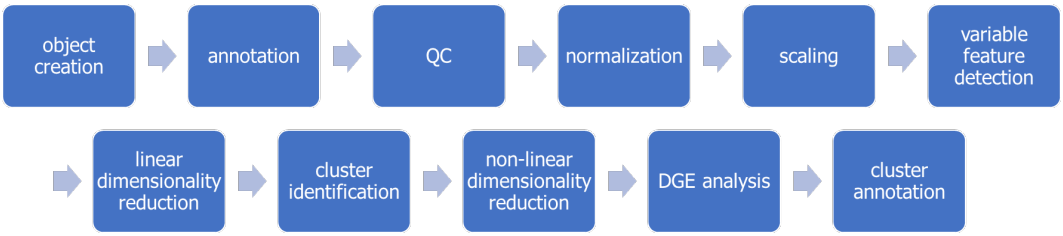


*Figure 16: Standard Seurat pipeline for scRNA-seq analysis. Count and metadata are joined into a Seurat object, annotated, and subjected to a quality control (QC). The object undergoes normalization, scaling, and variable feature detection. Linear dimensionality reduction of the variable features, cluster identification and non-linear dimensionality reduction precede subsequent differential gene expression (DGE) analysis, and cluster annotation.*

#### 2.7.1.1 Object creation and annotation

DGE matrices (and metadata) were loaded into Seurat for object creation. Object creation was restricted to cells expression a minimum of 200 genes, of which genes are shared with at least 3 cells. In the object, a pattern search for mitochondrial (and ribosomal) genes was performed, and their relative contribution to transcriptome stored in the metadata with the "AddModuleScore"-function. "AddModuleSCore" was also utilized to annotate among others the signatures of core microglial genes (Galatro et al., 2017). If needed, annotations functioned to aid QC with the "subset"-function, ensuring only cells of interest were kept for analysis. In such cases, all cells with a positive score were considered (> 0).

#### 2.7.1.2 Quality control and Median Absolute Deviation

QC is a critical step in scRNA-seq analysis and aims to remove outlier cells across a range of factors. Most commonly, Seurat utilizes parameters encompassing library size, library complexity, and mitochondrial and ribosomal content by setting subjective limits to these variables (*Chapter 1 Quality Control | Basics of Single-Cell Analysis with Bioconductor*, n.d.; "Quality Control," n.d.). Here, I will provide an argument for the use of the Median Absolute Deviation (MAD) as an alternative QC metric.

The number of detected transcripts in single-cells (*i.e.* library size), and the number of unique genes in the library (*i.e.* library complexity), are the earliest markers of quality in single-cell and single-nucleus RNA-sequencing (sxRNA-seq). Users commonly implement cut-off values; however, these requires expertise and fine-tuning, as these often vary greatly between sample conditions, cell types, single-cell platforms and read depth.

Similarly, mitochondrial and ribosomal transcript content in sxRNA-seq are proxies of cell quality. Cell membrane rupture and damage is associated with a loss of cytoplasmic transcripts, whereas transcripts associated with intracellular complexes like ribosomes and mitochondria are largely unaffected by these effects, effectively enriching for these transcripts with cell damage. Generally, transcript capture and amplification in droplet-based systems are limited by the finite resources provided for it. That is, capture of higher ribosomal and mitochondrial transcripts will deplete resources for other transcripts, in which even small changes in mapping to these genes will reduce overall library complexity (Osorio and Cai, 2020). Unfortunately, like library size and complexity, mitochondrial and ribosomal content also vary with context, obfuscating standardization.

For example, cell types vary in their cellular metabolism and relative gene expression, with cardiomyocytes known to be highly metabolically active with large numbers of mitochondria, and variations in library complexity between tissues (Almanzar et al., 2020; Osorio and Cai, 2020). Moreover, species-specific cut-off values might be needed; high-quality mouse cells have less than 5% mitochondrial transcripts, whereas human cells would be better served with a threshold for 10% (Osorio and Cai, 2020). This is complicated further, as human (monocyte-derived) macrophages and other cell types have been reported to have an interquartile range above 10%, making the threshold highly variable depending on the context.

This variability (across parameters and biological diversity) has led recent studies to adopt a 3 × MAD range for outlier cut-off (Daniszewski et al., 2018; Kracht et al., 2020; Tung et al., 2017; Waise et al., 2019). MAD is a measure of statistical dispersion and a 'consistent estimator of the population standard deviation'. One might consider the use of the standard deviation (SD) itself for QC, however, SD is rooted in the square of data and outliers have a large effect on the SD. MAD does not require data to be squared and MAD is therefore more robust to outliers, providing a better estimation of the quality parameters of sxRNA-seq data and aid QC. By using MAD, outlier removal can be standardized in sxRNA-seq QC, independent of context-dependent variables like cell type. Moreover, I belief that this standardization is particularly salient for integrated objects, as it is aids large-scale data integration across a wide range of conditions as is common to a single-cell atlas. Notably, setting thresholds remains the preferred way of performing QC; in fact, setting thresholds for a single data source is faster and generally performs well.

Traditionally, QC is done with user-defined upper thresholds. These thresholds work well for single source data; however, to reduce bias and accommodate variability in experimental procedure, the Mean Absolute Deviation (MAD) was used to filter out low quality cells for integrated objects. MAD allowed for the selective removal of outliers across several QC parameters (*e.g.* nCount_RNA; nFeature_RNA; percent.rb; percent.mt). To identify outliers in library size and library complexity, both metrics were represented on a log-scale, to accurately identify outliers before normalization

was performed. Any cells outside of the lower and upper threshold were removed (3X MAD) (Figure 17).

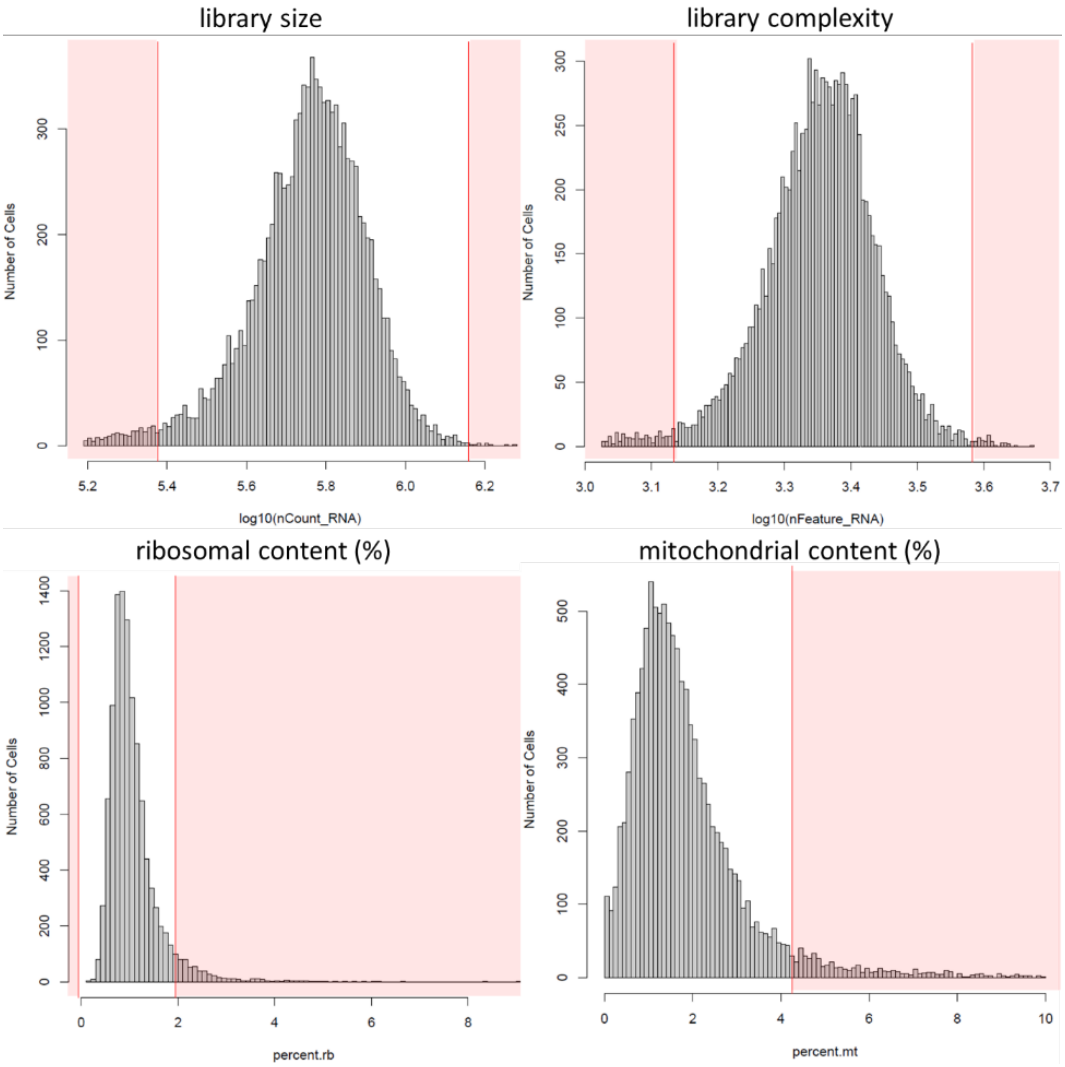


*Figure 17: Representative application of MAD across QC parameters. Displayed are lower and upper thresholds of library size (nCount_RNA), library complexity (nFeature_RNA), ribosomal content (percent.rb), and mitochondrial content (percent.mt) of Sala Frigerio et al. 2019. Outliers below or above determined thresholds (red) were removed. Note the absence of a lower limit with mitochondrial content.*

#### 2.7.1.3 Normalization, scaling and variable feature selection

"SCTransform" and "NormalizeData" was utilized for the log-normalisation of data. "SCTransform" naturally holds arguments for scaling and regression, whereas "NormalizeData" was used in combination with "ScaleData". Library size and complexity, and mitochondrial and ribosomal content were readily regressed for; however, other variables like cell cycle scoring were considered. "CellCycleScoring", a function with similarities to "AddModuleScore", scored cells on their expression of cell cycle phase-specific genes, assigning these to G1-, G2/M- or S-phase. Lists of cell cycle genes are included in Supplementary Table 5. The most variable 3000 genes were selected for feature selection with "FindVariableFeatures".

#### 2.7.1.4 Linear dimensionality reduction

Principal component analysis (PCA) was performed with the "RunPCA" function; RunPCA generates sets of genes that are correlated statistically. Of those 3000 variable features that were selected, the 50 strongest predictors of that variability (*i.e.* principal components, PC) were calculated. "ElbowPlot", "JackStraw" and "ScoreJackStraw" informed on the statistical significance of those PC, selecting only those factors with a $P < 0.05$.

#### 2.7.1.5 Clustering

Seurat utilizes the K-Nearest Neighbours (KNN) algorithm for non-linear dimensionality reduction. The KNN is a non-parametric, learning algorithm, that is, KNN is a fast algorithm, capable of testing feature similarities. KNN was initiated with "FindNeighbours", after the clustering resolution of cells was varied with "FindClusters", a Louvain-based function, in a range of 0.1 – 2.0.

Clustering is subjective measure in scRNA-seq data analysis. To aid the selection of the appropriate clustering resolution, a clustering hierarchy was build with "clustree" from the Clustree package (0.4.3). For a first-pass analysis, the resolution that failed to increase the number of clusters from its lower tiered predecessor was selected, a commonly used heuristic prior to a review of the biological significance of the identified clusters.

#### 2.7.1.6 Non-linear dimensionality reduction

To project the clusters (and their corresponding transcriptome) onto a graph, non-linear dimensionality reduction (NLDR) was perfo. There many different methods to reduce dimensionality, t-distributed stochastic neighbour embedding (*t*-SNE) and uniform manifold approximation and projection (UMAP) amongst them (Xiang et al., 2021).

*t*-SNE was found to be the best accurate and with good computational speed, whereas UMAP better preserves the global structure of the underlying cluster relations better and has a larger stability. t-SNE- and UMAP-plots were constructed with the "RunTSNE" and "RunUMAP" functions, and graphs requiring a reduction parameter (like "DimPlot") with the reduction parameter set to "tsne" or "umap", respectively.

#### 2.7.1.7 Differential gene expression analysis and statistical analyses

Differential gene expression of single cells was done with "FindAllMarkers". Statistical significance was achieved with a P-value < 0.05, based on Bonferroni correction using all dataset genes. A minimum of 25% of all cells in a cluster needed to express the gene for it to be considered; "min.pct" set at 0.25. Cluster markers were visualized with "DoHeatmap", "VlnPlot", and "FeaturePlot". To support my analyses, I confirmed cluster results with Metascape, an annotation

tool that integrates 40 independent knowledge databases, including DAVID (Zhou et al., 2019). Unless stated otherwise, p values are represented as follows, *p<0.05, **p<0.01, ***p<0.001 and ****p<0.0001).

### 2.7.2 Data and code accessibility

All data and scripts can be made available upon request. Please contact the corresponding author: Diego Gomez-Nicola at D.Gomez-Nicola@soton.ac.uk.

# Chapter 3 Single-cell atlas of microglial heterogeneity in the healthy CNS

## 3.1 Introduction

Single-cell technologies have redefined microglial biology, adding to an ever-growing repertoire of microglial subtypes and phenotypes (Hammond et al. 2019; Keren-Shaul et al. 2017; Krasemann et al. 2017; Li et al. 2019; Marsh et al. 2021; Matcovitch-Natan et al. 2016; Safaiyan et al. 2021). To understand the respective relationship of individual studies to one another, a single-cell atlas aims to provide a curated compendium of available knowledge in various contexts. In effect, a single-cell atlas illustrates subtypes that are reliably reported between sources (Chen et al. 2021; Geirsdottir et al. 2017; Lavin et al. 2014).

Several atlases have been developed since the adoption of single-cell technologies and 'Big Data' biology. This includes examples like the 'Mouse Cell Atlas', 'Human Cell Atlas', 'Single Cell Expression Atlas', and 'Single-Cell Portal', as well as efforts like The Tabula Muris Consortium (Almanzar et al., 2020; Han et al., 2018; Schaum et al., 2018; Svensson et al., 2020). Each of these resources covers a broad range of organs, cell types and contexts. However, to my knowledge, no such atlas has been specifically developed for microglia. Consequentially, single-cell studies report on a range of microglial subtypes, each with a distinct nomenclature, obfuscating underlying transcriptional similarities and conceptual understanding.

Hammond *et al.* (2019) is currently the largest dataset on microglial biology, a seminal piece of work that includes approximately 76,000 cells across the murine lifespan (Hammond et al., 2019). This work was used and expanded upon to provide in-depth knowledge of microglial transcriptional heterogeneity across data sources. In this chapter, I detail the generation and analysis of a microglial single-cell atlas of 113,689 cells; to study context-dependent microglial heterogeneity; translate murine early developmental findings into human gestation; identify their pseudotemporal order and population dynamics.

### 3.1.1 Microglial heterogeneity – representation across the lifespan

Established microglial subtypes were discussed in section 1.3. Here, I will briefly review these subtypes before delving into the single-cell atlas, by summarizing their transcriptional signature and age of occurrence.

scRNA-seq studies have identified distinct developmental, adult, and age- or disease-associated microglial subtypes, as well as CAM, CPM and *ex*AM (Table 2) (Hammond et al. 2019; Keren-Shaul

et al. 2017; Krasemann et al. 2017; Li et al. 2019; Marsh et al. 2021; Matcovitch-Natan et al. 2016; Safaiyan et al. 2021). Notably, transcriptional similarities and distinctions exist between subtypes and states, supportive of their shared ontogeny and the subsequent divergence in a context-dependent manner.

*Table 2: Transcriptional signatures of known microglial subtypes.*

| Age | Subtype/state | Source | Transcriptional signature |
|---|---|---|---|
| Development | ATM | Hammond *et al.* 2019 | Spp1, Gpnmb, Igf1, Lgals3, Fabp5, Cd9, Lpl, Ctsl, Lgals1, Apoe |
| | PAM | Li *et al.* 2019 | Spp1, Gpnmb, Lpl, Pld3, Ctsl, Csf1, Igf1, Ctsb, Slc23a2, Gpx3 |
| Adult | HOM | Matcovitch-Natan *et al.* 2016 | Cts3, Ctsd, Laptm5, Csf1r, C1qa, Selplg, C1qc, Tmem119, Sparc, Serinc3 |
| Age/disease | ARM | Sala Frigerio *et al.* 2019 | Cst7, Clec7a, Itgax, Cd74, H2-Ab1, H2Aa, Ctsb, Ctsd, Spp1, Gpnmb |
| | DAM | Keren-Shaul *et al.* 2017 | Itgax, Mamdc3, Cst7, Fam20c, Ccl4, Lmbrd2, Egr2, Csf1, 5430435G22Rik, Ccl3 |
| | IRM | Hammond *et al.* 2019 | Ifitm3. Ifi27l2a, Ccl12, Lgals3bp, Ifit3, Rtp4, H2-K1, Isg15, Cst7, Bst2 |
| | MGnd | Krasemann *et al.* 2017 | Cxxc5, Tgfbr2, Golm1, Sall1, Slco2b1, Cst3, P2ry12, P2ry12, St3gal6, Pde3b |
| | WAM | Safaiyan *et al.* 2019 | Apoe, C1qb, Fth1, Lyz2, H2-D1, Ctsb, Ctss, Ctsz, H2-K1, Ftl1, B2m |
| General | CAM | Hammond *et al.* 2019 | Pf4, F13a1, Ifitm2, Dab2, Fcna, Lyz2, Ms4a7, Lgals1, Ifitm3, Ms4a6c |
| | CPM | Li *et al.* 2019 | **Nuf2**, **Pscrc1**, **Ncapd2**, **Ccnb2**, **Smc4**, *Mcm4*, *Exo1*, *Slbp*, *Gmnn*, *Cdc45* |
| | *ex*AM | Marsh *et al*. 2022 | Hist1h1c, Hist1h2bc, Ubc, Jund, Rgs1, Hspa1a, Hsp90aa1, Ccl4, Dusp1, Hspa1b |

*Note: Top 10 differentially expressed genes of known microglial subtypes. The age and source in which these subtypes were identified are detailed. G2M-phase genes in CPM are highlighted in bold, whereas S-phase genes are in Italic. ATM, axon tract-associated microglia; ARM, activated response microglia; CAM, CNS-associated macrophage; CPM, cycling and proliferating microglia; DAM disease-associated microglia; exAM, ex vivo-activated microglia; HOM, homeostatic microglia; IRM, interferon response microglia; MGnd, neurodegeneration-associated microglia; PAM, proliferative region-associated microglia; WAM, white matter-associated microglia.*

### 3.1.2 Trajectory inference and pseudotiming

Cell and lineage divergence is a highly complex and temporally ordered process. Several bioinformatic tools have been developed to reconstruct differentiation trajectories in scRNA-seq data. Broadly speaking, these include methods based on transcriptional entropy, RNA velocity and trajectory inference (*i.e.* pseudotemporal ordering) (Grün et al., 2016; Guo et al., 2017; Manno et al., 2017; Teschendorff and Enver, 2017; Trapnell et al., 2014).

Transcriptional entropy, or signalling promiscuity, approximates cellular potency and differentiation potential of a cell – cells lower on the Waddington landscape have reduced entropy. That is, transcriptional profiles associated with more diverse biological processes are indicative of an immature phenotype, whereas less processes are associated with a differentiated cell (Grün et

al., 2016; Guo et al., 2017). Similarly, RNA velocity uses the relative prevalence of un-spliced and spliced mRNA, or nascent and mature mRNA, respectively, to inform on the transcriptional kinetics at any given developmental stage (Manno et al., 2017). With RNA velocity, more un-spliced transcripts equal an immature phenotype and function to predict differentiation dynamics. In turn, trajectory inference projects transcriptionally similar cells onto a lower dimensional space and identifies branch and converging points between them, to construct a lineage structure (Cao et al., 2019). Each method allows for an unbiased and transcriptome-based method to order cells along an artificial (differentiation) trajectory. However, of the three, trajectory inference has rapidly become the preferred method, with over 70 distinct tools developed to date (Saelens et al., 2019).

Trajectory inference allows for an unsupervised identification of cellular subtypes, delineation of a differentiation tree, and inference of regulatory interactions. Furthermore, most of the tools are developed in R programming language, facilitating integration with Seurat, the analysis tool of choice. Trajectory inference methods can be subdivided in cyclic-, linear-, bi- and multifurcation-, tree-, and graph-based methods; descriptive of their unique ability to detect underlying trajectory structures (Figure 18).

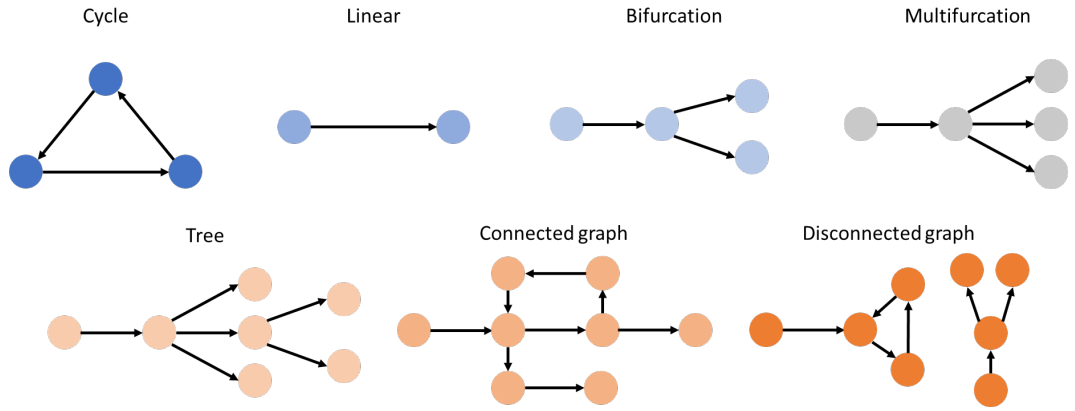


*Figure 18: Trajectory inference types. Trajectory inference methods are categorized in 7 archetypes, ranging from low complexity cycle and linear, to high complexity connected and disconnected graph-based methods. Monocle3 utilizes a Tree-based structure, allowing users to define a moderately complex differentiation trajectory. Adapted from Saelens et a. (2019).*

However, the tools vary considerably in their performance to the point that there is no 'one-size-fits-all'. To that end, a decision diagram developed by Saelens *et al.* (2019) was used to aid the selection of the tool for trajectory inference (Saelens et al., 2019). No *a priori* assumptions of the underlying topology were made of the microglial lineage. Following the decision diagram for tool selection, the tree-based approach was favoured (Saelens et al., 2019). Of the four tree-based approaches considered (*i.e.* Slingshot, PAGA, Monocle, and MST), only Monocle has publicly available vignettes for use in combination with Seurat, driving my choice for it.

Monocle 3, the latest version of the package, has shown good overall performance, scoring well on accuracy, stability, and usability (Saelens, Cao 2019). Unfortunately, Monocle 3 performance declines over 100,000 cells; methods like PAGA and Slingshot outperformed Monocle on this.

However, PAGA is a Python-based tool, Slingshot lacks Seurat integration, and the atlas does not greatly exceed beyond 100,000 cells.

Unlike its predecessors, Monocle 3 has built-in functions to construct a framework of cellular coordinates that can be used for trajectory inference (Cao et al., 2019). However, the framework can be completed in Seurat, using the cellular coordinates from that tool to inform on the lineage structure, offering a means to improve integration and interpretation of the two bioinformatic tools.

## 3.2 Aims and objectives

In this chapter, I set out to detail a microglial single-cell atlas across the murine lifespan. This is to establish a framework of current microglial transcriptomic heterogeneity, as well as to explore context-dependent microglial diversity. Furthermore, I wish to illustrate how murine developmental insights of cellular processes can be meaningful for human gestation. Similarly, I aim to determine the pseudotemporal order of microglia, to identify the differentiation trajectories that give rise to adult and late life heterogeneity.

**Aim 1: Generation of a microglial single-cell atlas in murine development.**

- Objective 1: To establish a framework of current knowledge
- Objective 2: To explore context-dependent microglial heterogeneity
- Objective 3: To translate murine early developmental effects to human gestation
- Objective 4: To perform a trajectory analysis of microglial differentiation

## 3.3 Materials and methods

12 representative scRNA-seq datasets were selected - see section 1.3.1 - of current biological and technical trends in the microglial field. To standardize data pre-processing and downstream integration, I developed a bioinformatic pipeline capable of being utilized sequentially (Figure 19). In short, count matrices were collected and Seurat objects were generated that underwent QC; were normalized and scaled; and regressed for 'nFeature_RNA', 'percent.rb', 'G2M.Score', and 'S.Score' (Step1). 3000 integration features were selected with "SelectIntegrationFeatures" and anchors identified with "FindIntegrationAnchors" (Step2). Linear and non-linear dimensionality reduction, PCA and UMAP, respectively (Step3), were followed by DGE- and gene ontology (GO)-analyses, and trajectory inference (Step4).

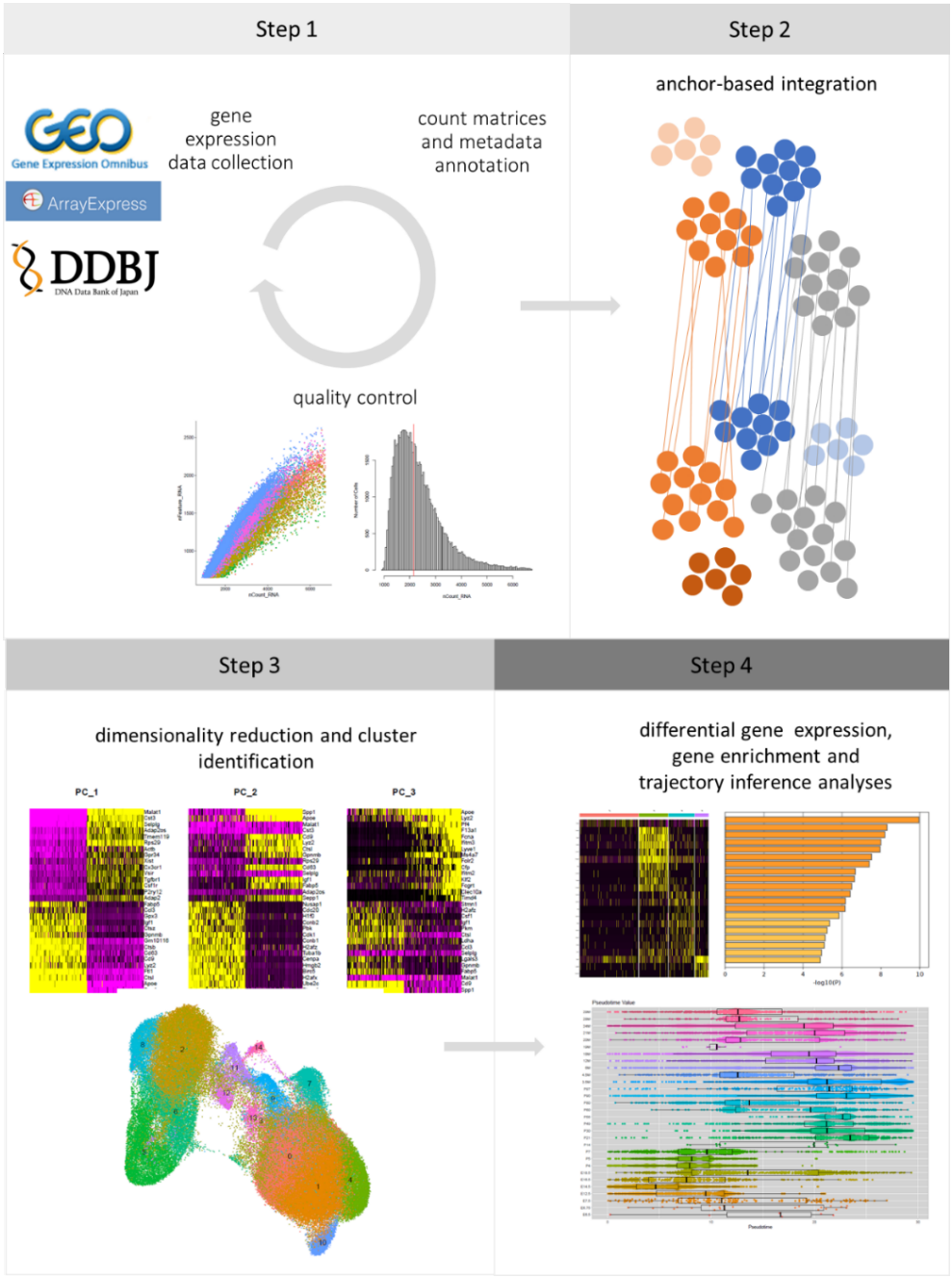


*Figure 19: Overview of bioinformatic pipeline for analysis of microglial scRNA-seq datasets. Selected datasets are acquired from open-access databases and pre-processed using QC metrics. Seurat anchor-based integration is carried out, resulting in a combined dataset encompassing a vast scope of biological variables. Data analysis methods involve dimensional reduction techniques and graphical clustering of cells. Finally, biological interpretation of clusters is achieved by differential gene expression, gene enrichment, and trajectory analyses.*

### 3.3.1 Dataset Acquisition

Count matrices and metadata were obtained from open access depositories of genomic data: Gene Expression Omnibus (GEO), BioProject (BP) and ArrayExpress (AE) (Table 3, Table 4). To supplement the publicly available data where needed, additional data was provided by the original authors. Both murine and human datasets were collected.

For the mouse lifespan, 12 datasets were combined for 113,689 (wild-type) microglia spanning between embryonic day 6.5 (E6.5) to 29-months old (29M) (*i.e.* ~880 postnatal days, or P880); each varying in their distribution of age- region- and sex-derived single-cells.

*Table 3: Features of scRNA-seq datasets in the murine single-cell atlas.*

| Source | Year | Accession # | Cell # | Age | Region | Sex |
|---|---|---|---|---|---|---|
| Dulken *et al.* | 2019 | BP: PRJNA450425 | 2732 | P90, 28M, 29M | SVZ | M |
| Sala Frigerio *et al.* | 2019 | GEO: GSE127893 | 5124 | P90, 6M, 12M, 21M | CTX, HIP | F, M |
| Hammond *et al.* | 2019 | GEO: GSE121654 | 68660 | E14.5, P4, P5, P30, 3.5M, 18M | WB | F, M |
| Keren-Shaul *et al.* | 2017 | GEO: GSE98969 | 7602 | P49, P80, P90, 4.5M, 6M, 20M | WB, SC, CB, CTX | N.A. |
| Li *et al.* | 2019 | GEO: GSE123025 | 1649 | E14.5, P7, P60 | WB, CB, CP, CTX, HP, OLF, STR | M |
| Masuda *et al.* | 2019 | GEO: GSE120745 | 1814 | E16.5, P21, 3.5M | CB, CC, CTX, FB, MB, HIP, SC | F, N.A. |
| Matcovich-Natan *et al.* | 2016 | GEO: GSE79819 | 3038 | E12.5, E18.5, P56 | WB, YS | N.A. |
| Mathys *et al.* | 2017 | GEO: GSE103334 | 984 | P90, P97, 3.5M, 4.5M | HIP | N.A. |
| Pijuan-Sala *et al.* | 2019 | AE: E-MTAB-6967 | 200 | E6.5, E6.75, E7.5 | WB | N.A. |
| Safaiyan *et al.* | 2021 | GEO: GSE166548 | 9777 | P14, 18M, 19M, 24M | CTX, WM | F, M |
| The Tabula Muris Consortium | 2020 | GEO: GSE109774 | 12002 | P90, 18M, 24M | CB, CTX, HIP | F, M |
| Utz *et al.* | 2020 | GEO: GSE146926 | 108 | E16.5 | WB | N.A. |

*Note: Details of the respective source data is tabled, including cell and data accession numbers, age, CNS region, and sex. All data are post quality control. AE, AssayExpress; BP, BioProject; CB, cerebellum; CC, corpus callosum; CP, choroid plexus; CTX, cortex; E, embryonic day; F, female; GEO, Gene Expression Omnibus; HIP, hippocampus; M, month, male; N.A., not available; ND, neurodegeneration; P, postnatal day; SC, spinal cord; SVZ, subventricular zone; YS, yolk sac; WB, whole brain; WM, white matter; WT, wild type.*

For the human single-cell atlas, 4 datasets were integrated for a total size of 22,138 single-cell and single-nuclei (Table 4). Like the mouse atlas, I combined cells and nuclei from a variety of gestational ages, CNS regions and sexes.

*Table 4: Features of scRNA-seq datasets in the human single-cell atlas.*

| Source | Year | Accession # | Cell/nuclei # | Age (PCW) | Region | Sex |
|---|---|---|---|---|---|---|
| Cao *et al.* | 2020 | GSE156793 | 6072 | 13, 16 – 18 | CRB, CB | F, M |
| Kracht *et al.* | 2020 | GSE141862 | 14573 | 7 -11, 13 – 16 | WB | F, M |
| Fan *et al.* | 2020 | GSE120046 | 1358 | 5 – 12, 14 - 15, 18 - 20, 22, 24 | PONS | N.A. |
| Bian *et al.* | 2020 | GSE133345 | 135 | 3 – 6, 8 | WB | N.A. |

*Note: Details of the respective source data is tabled, including cell, nuclei and data accession numbers, age, CNS region, and sex. All data are post quality control. AE, AssayExpress; BP, BioProject; CB, cerebellum; CRB, cerebrum; F, female; GEO, Gene Expression Omnibus; M, male; N.A., not available; PCW, post conceptual week; WB, whole brain; WM.*

### 3.3.2 Trajectory analysis

Monocle 3 was utilized from the group of Cole Trapnell (Cao et al., 2019). To integrate Monocle 3 with Seurat, the object was converted the atlas to a 'CellDataSet' object with the "SeuratWrappers" packing function 'as.cell_data_set'. The UMAP locations, as defined by Seurat, were used and projected onto a UMAP space with the 'cluster_cells' function, after which 'learn_graph' to identify branch points and convergences. A supervised analysis was performed with E6.5 as the root for the graph, with the 'order_cells' function.

## 3.4 Results

### 3.4.1 Murine single-cell atlas quality and cluster stability

The murine cell atlas is composed of 12 distinct data sources that contribute differentially: varying in cell number, age, region, and sex (Table 3). As a result, some differences were expected between clusters. However, overt source-specific clustering and enrichment is indicative of low-quality data integration that could necessitate subsequent batch corrections, beyond that which is achieved by Canonical Correlation Analysis (CCA). I found that CCA performed well, with overall features of a high-quality integration (Figure 20, Supplementary Figure 1). That is, each identified cluster is composed of several sources and no overt variability was detected in QC parameters (*i.e.* nCount_RNA, nFeature_RNA, percent.rb, percent.mt) (Figure 20).

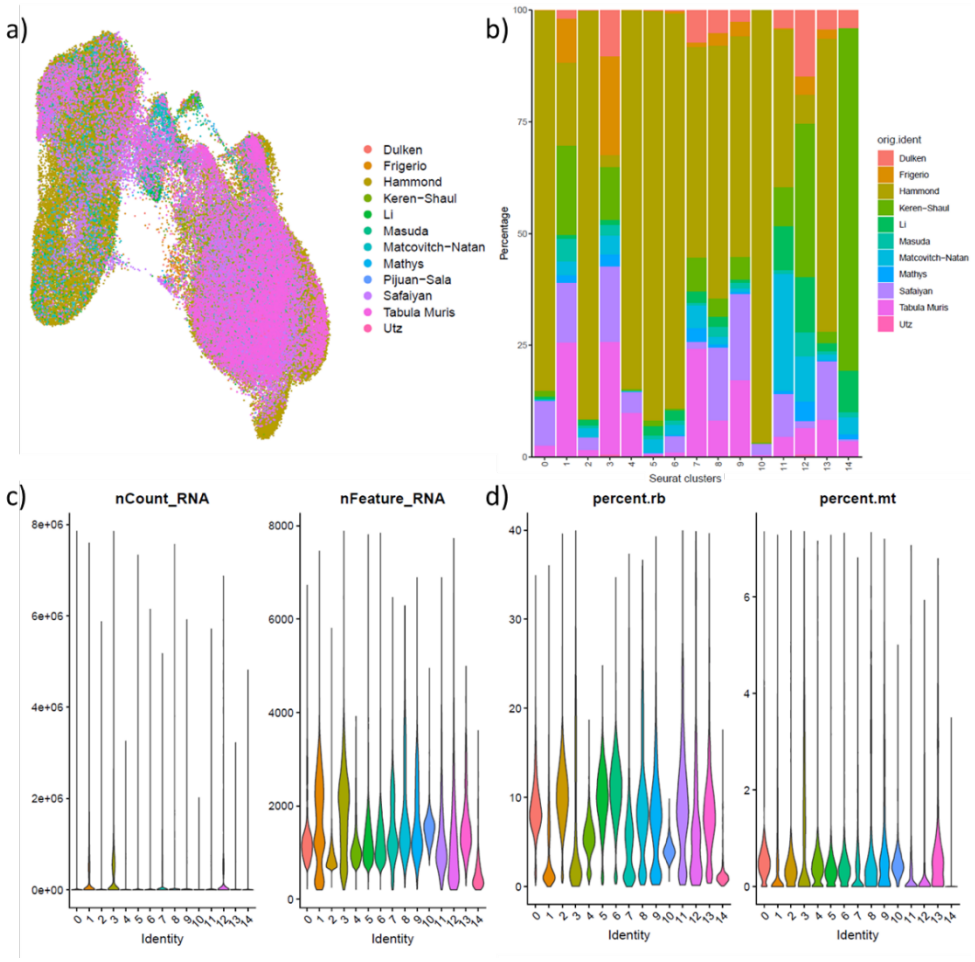


*Figure 20: QC of integration single-cell atlas. a) Large-scale transcriptional similarities are found within the source data. b) Each of 16 clusters is driven by cells from distinct data sources. c/d) Quality Control (QC) metrics in cluster identities. c) Number of transcripts (i.e. library size) (nCount_RNA) and the number of genes (i.e. library complexity) (nFeature_RNA). d) Percentage of ribosomal (percent.rb) and mitochondrial transcripts (percent.mt) are displayed.*

Clustering of cells with a UMAP-plot, and most other forms of (non-)linear dimensionality reduction, are subjective measures. The algorithm requires input from the user, who decides what the number of dimensions and resolution is that will be used for the projection. In that, it is important to strike a balance between statistical and biological significance, and in my view, lower (and more conservative) dimensions and resolution are often preferred, as it will provide a more robust biological result.

To determine dimensionality, as stated previously (in section 2.8.1.4), the heuristic of 'ElbowPlot' was combined with statistical testing by "JackStraw" and 'JackStrawPlot' (Figure 21). Each principal component (PC) in the integrated dataset is scored and ranked on its variability (as measured by the SD). The 'elbow' of dimensionality defines a subjective threshold of variability, in which the variability drops considerably (*i.e.* PC10) (Figure 21). In contrast, statistical inference of each PC with JackStraw found that most of the first 50 PC are statistically significant. Therefore, I chose to review the top 20 dimensions for this dataset, excluding PC that offer little to the transcriptional heterogeneity in the dataset.

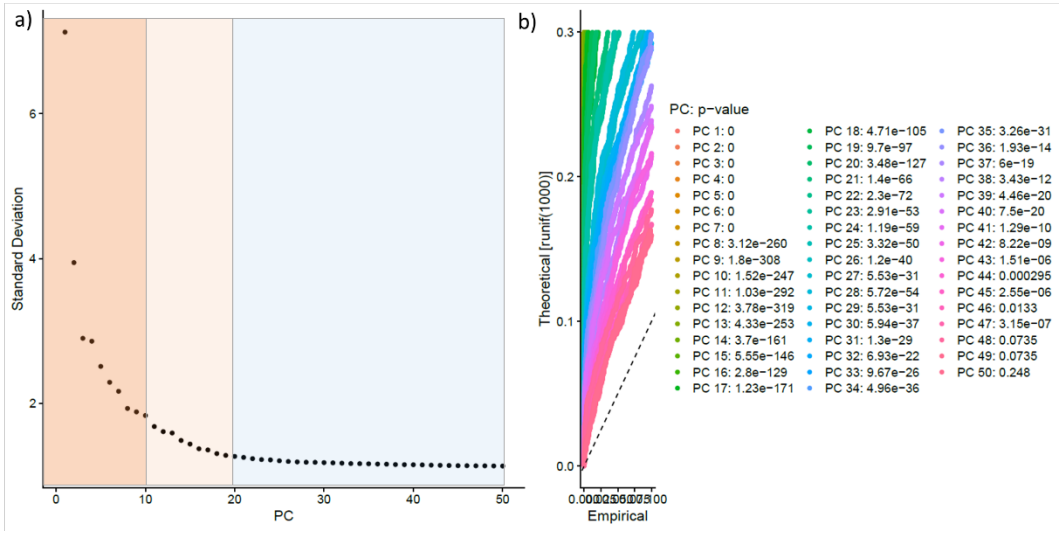


*Figure 21: Determination of dimensionality. a) An ElbowPlot is commonly used to determine the 'elbow' of a dataset, ranking the dimensions of a dataset that describe the underlying variability (i.e. transcriptional heterogeneity). The standard deviation of the top 50 principal components (PC) are displayed. b) A JackStraw analysis infers statistical significance of the PC, results which are displayed by a JackStrawPlot.*

Principal component analysis (PCA) identified the gene sets that drive each PC (Figure 22, Supplementary Figure 2, Supplementary Figure 3,Supplementary Figure 4). Genes in PC1 and PC2 include canonical microglial genes like *Cx3cr1*, *Hexb* and *Tmem119*, as well as cell cycle-associated genes like *Mki67* and *Top2a* (Hammond et al., 2019; Li et al., 2019) (Figure 22). In turn, PC8 is featured by interferon-linked genes, which imply the presence of IRM (Hammond et al., 2019; Sala Frigerio et al., 2019) (Supplementary Figure 2). Lastly, genes in PC20 contained genes that are biologically relevant in early development- and age-associated lysosomal pathway and anti-oxidative genes (*e.g. Prdx1*, *Tmsb4x*, *Ctsb*) (Supplementary Figure 4) (Cermak et al., 2016; Jeong et al., 2018; Masuda et al., 2019). Taken together, these show that statistically correlated gene sets (i.e. PC) are biologically relevant for clustering.

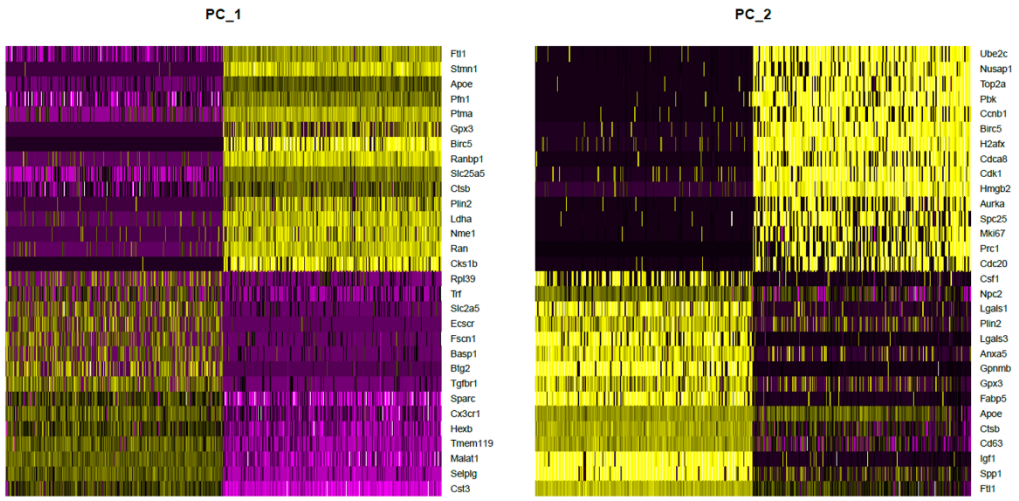


*Figure 22: Principal component analysis. Principal component (PC) 1 and 2 are visualized, illustrating their respective gene sets.*

Unlike dimensionality, the resolution parameter is not typically tested statistically. Here, the resolution where the number of clusters level off is typically used for a preliminary analysis. 'Clustree' identified the number of clusters with varying resolutions. In the analysis, all resolutions between 0.1 and 2.0 were tested (Figure 23).

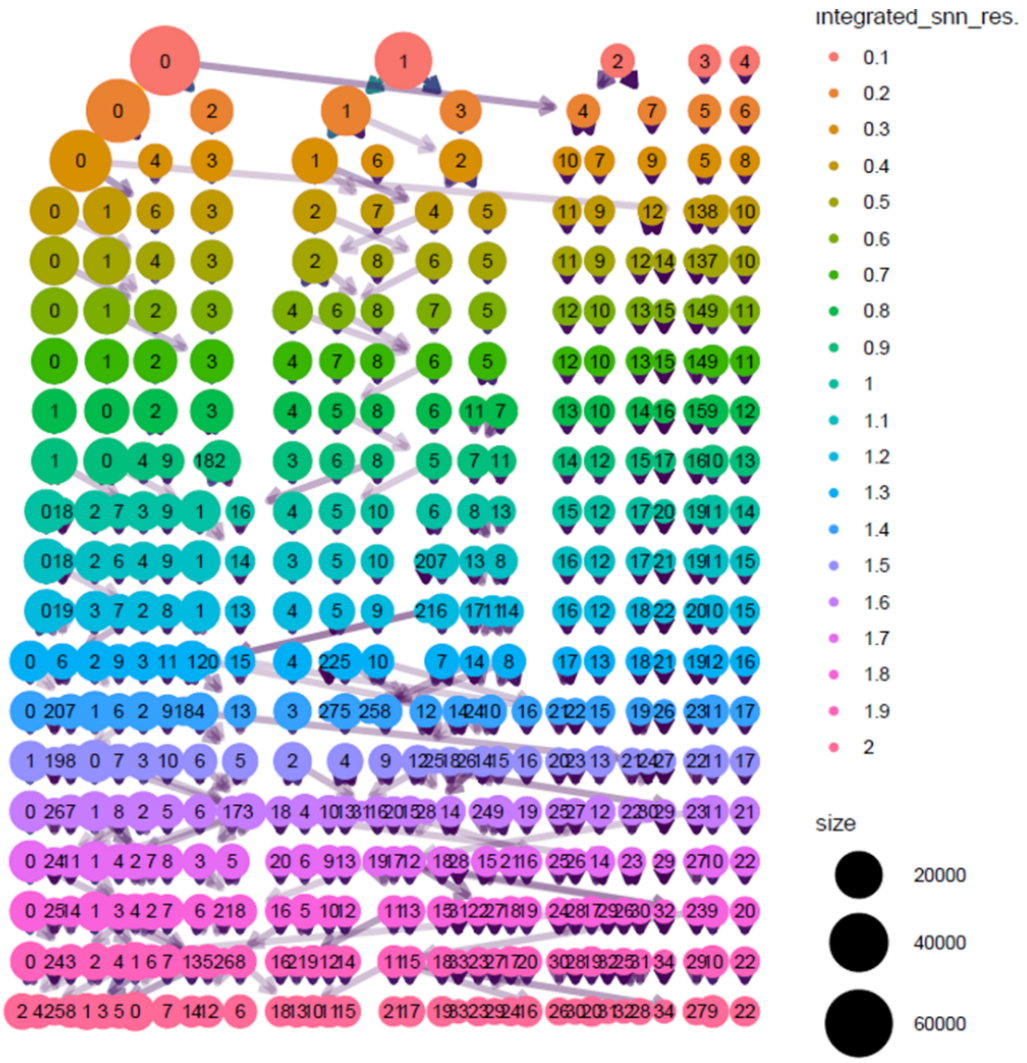


*Figure 23: Determination of cluster resolution. Clustree visualises the number identified clusters with resolutions between 0.1 and 2. Higher resolutions splits larger groups of cells into an ever more expanding repertoire of clusters.*

In the dataset, clusters first stabilize at resolution 0.7. However, I set resolution to 0.5, a more conservative option that manages to preserve the major clusters, without over clustering (Figure 24). To that end, 20 dimensions and a resolution of 0.5 were selected.

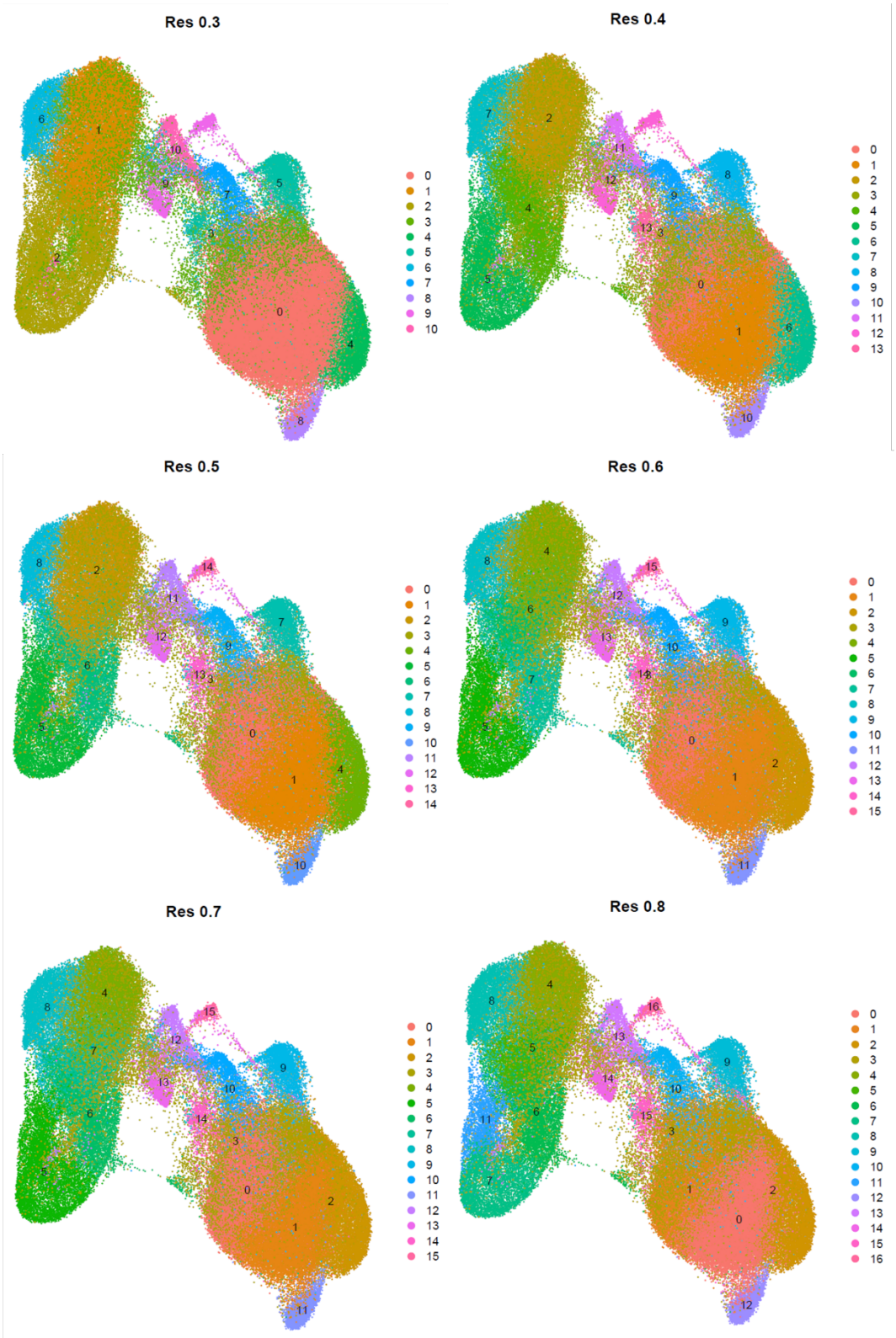


*Figure 24: Linear dimensionality and cluster identification parameters. Cluster identification (with 20 dimensions) was tested on a range of resolutions; 0.3 to 0.8 were considered for the integrated object, and 0.5 selected.*

### 3.4.2 Transcriptomic heterogeneity of microglia in the murine lifespan

Broadly, 15 clusters of cells with distinct transcriptional profiles were identified (Figure 25). In this section, I will detail the annotation of well-known myeloid profiles such as CAM, *ex*AM, CPM, HOM, and several others across a variety of biological factors (*e.g*. age, region, sex).

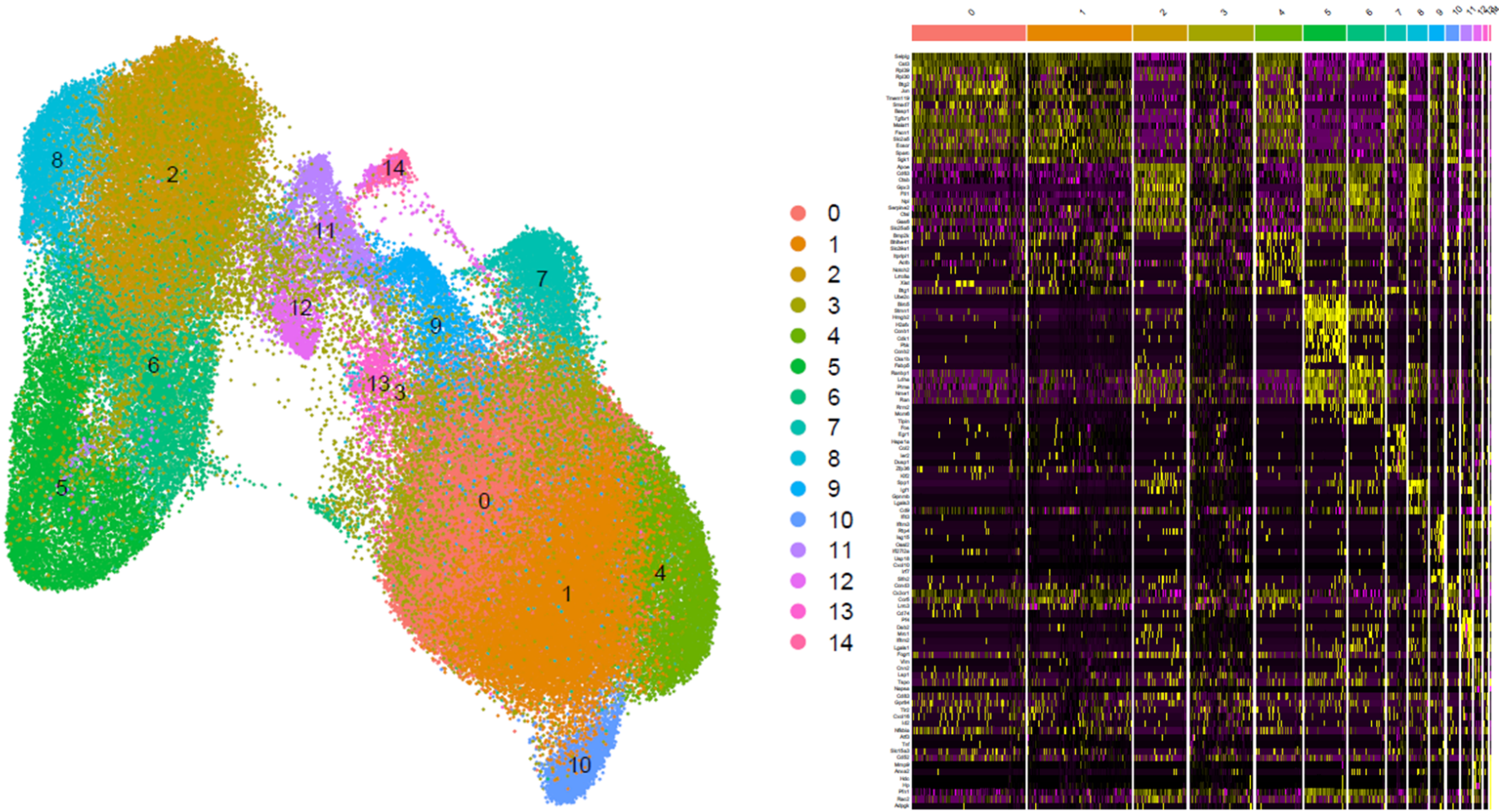


*Figure 25: General microglial heterogeneity during the murine lifespan. A total of 113,689 cells in the integrated were assigned to15 transcriptionally distinct clusters. A Uniform Manifold Approximation and Projection (UMAP)-plot is displayed, as well as the cluster-specific heatmap of the top 10 genes in each. Clusters are colour coded and shared between the UMAP-plot and heatmap. Gene expression levels in the heatmap range from low (purple) to high (gold). UMAP-plot of PC1-20 and resolution 0.5. FindAllMarkers with 'only.pos = TRUE', 'min.pct = 0.25',' logfc.threshold = 0.25', 'test.use = "wilcox"'*

#### 3.4.2.1 Non-microglial cells, the minimum fraction, and technical artefacts

3 non-microglial clusters were identified in the single-cell atlas, which include neutrophils, monocytes, CNS-associated macrophages (CAM; also known as border-associated macrophages, BAM) (Li et al., 2019; Mrdjen et al., 2018). In addition, *ex vivo*-activated microglia (*ex*AM) were resolved, a microglial state that features a dissociation-induced, artefactual gene signature (Marsh et al., 2022). These 4 populations function to informed on the quality of the scRNA-seq data, and on the minimum fraction of the dataset.

##### 3.4.2.1.1 Neutrophils

Cluster 14 is the smallest cluster (*i.e.* 385 cells or ~0.3%) and the rarest cell type in the atlas (*i.e.* minimum fraction). Several established microglial gene lists were tested with 'AddModuleScore', however, no correspondence with known microglial subtypes was detected (data not shown; see Supplementary Table 3 for a table of established microglial markers). To explore the identity of cluster 14 further, differential gene expression (DGE) analysis identified 37 genes (with an avg_log2FC over 1.5), which were subsequently tested with *Metascape (*Figure 26) (Zhou et al., 2019).

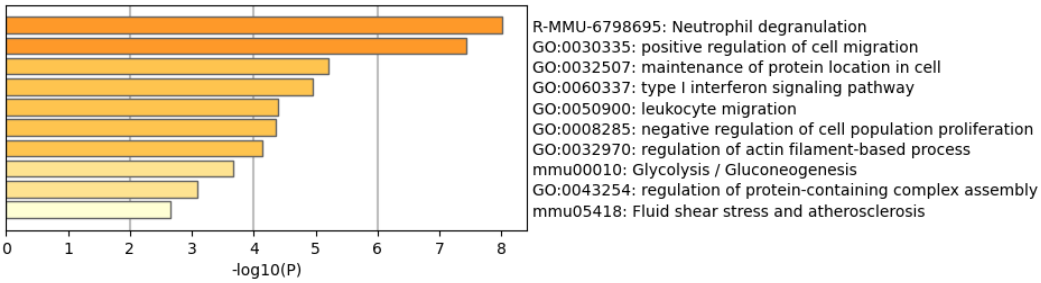


*Figure 26: Neutrophil marker expression in the atlas. Cluster 14 express genes commonly associated with neutrophil degranulation, cell migration and the type I interferon signalling pathway.*

10 of 37 genes were involved with neutrophil degranulation and include *Cxcr2*, *Mmp9*, *S100a11*. Although this suggests these cells are neutrophils, this by itself does not confirm an origin; genes can have multiple associations beyond what is currently annotated by GO. To this end, I used a neutrophil gene list, as described by Xie *et al.* (2020) (Supplementary Table 4) (Xie et al., 2020). The module score (*i.e.* gene list enrichment score) of the genes effectively localized to cluster 14 (Figure 27).

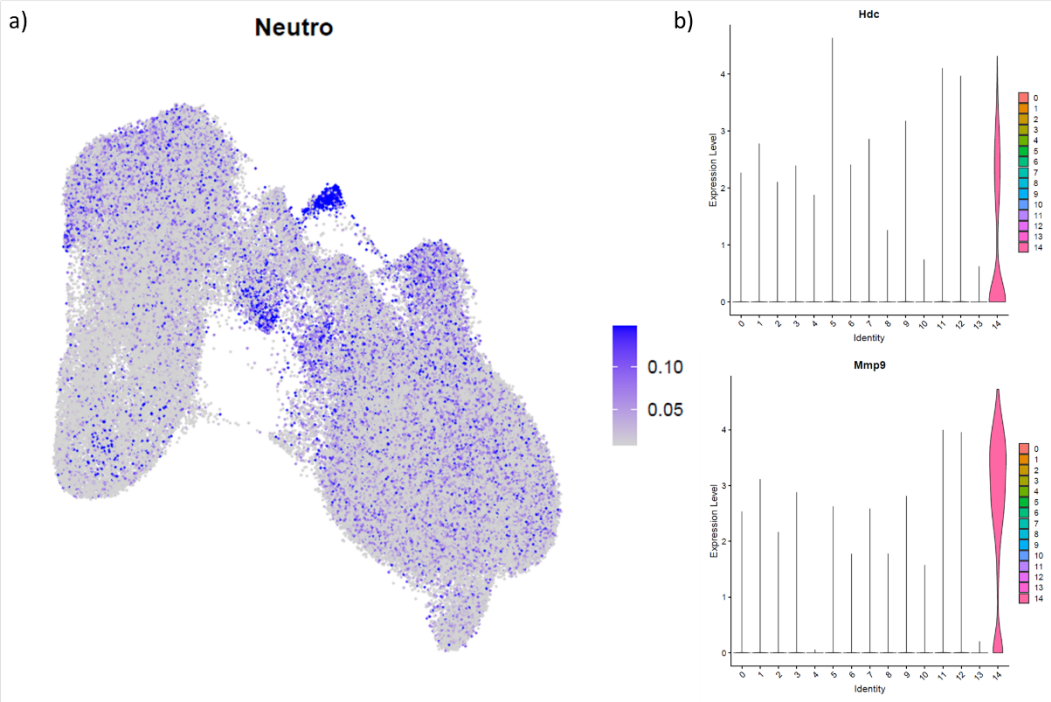


*Figure 27: Neutrophil gene markers are enriched in cluster 14. b) VlnPlot of selected neutrophil markers (i.e. Hdc, Mmp9).*

Remarkably, most cells in cluster 14 derive from Keren-Shaul *et al.* (2017) (Figure 20). This study used a $Cd45^{+}$ enrichment strategy and reported isolation of other immune cells like neutrophils, NK cells, etc (Keren-Shaul et al., 2017). It is possible that the annotation and enrichment of core microglial genes did not effectively minimize the retention of these cells, impacting downstream data quality negatively. Furthermore, in my exploration of cluster markers, it was noted that neutrophils share several genes with dendritic cells (DC) (e.g. *Hdc*, *S100a11*), suggesting that further sub clustering of cluster 14 might delineate these two cell subtypes.

#### 3.4.2.1.2 Monocytes

Unlike cluster 14, cluster 12 does not show a large transcriptional distinction from other clusters and is only featured by the expression of *Lgal3*, *Cnn2*, *Cd74* and *Lsp1* (over an avg_log2FC of 1.5) (Figure 28, Supplementary Table 4). None of these genes are unique to the cluster and can also be found in clusters 2, 5, 11, and 14. Cluster 12 might in fact derive from several immune cells, *e.g.* $Ly6C^{low}$ or $Ly6C^{hi}$ monocytes, monocyte-derived cells (MdC). Each of these are featured by the expression of *Csf1r* and *Cx3cr1* (Mrdjen et al., 2018; Percin et al., 2018), and supports the absence of cluster-specific markers. As for the neutrophil cluster, further sub clustering is expected to address this.

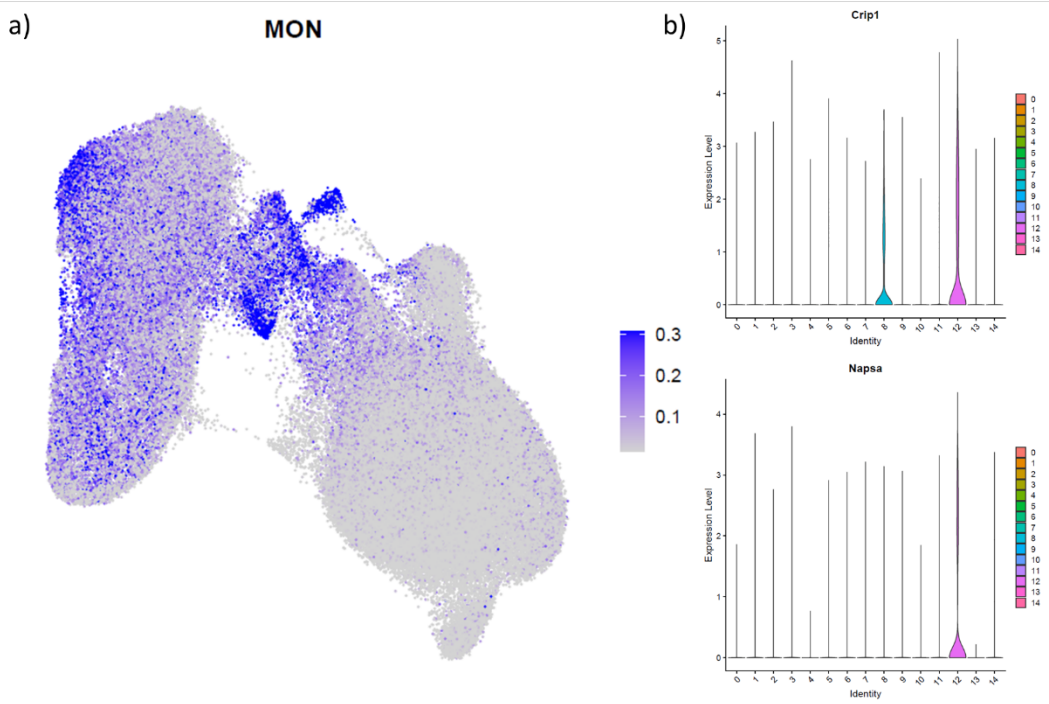


*Figure 28: Monocyte-like signatures are non-selective. a) A relative enrichment of monocyte-associated genes are enriched in cluster 12, albeit non-selectively with widespread expression of genes in cluster 8, 12 and 14. b) VlnPlot of selected monocyte genes (i.e. Crip1, Napsa).*

#### 3.4.2.1.3 CNS-associated macrophages

CAM are the second largest immune cell population in the CNS (Mrdjen et al., 2018). Enrichment method selection and the shared developmental ontogeny of CAM and microglia often see both subtypes retained by dimensionality reduction and analysis of transcriptional (Jordão et al., 2019; Li et al., 2019; Van Hove et al., 2019). Indeed, CAM are often deliberately kept as an internal reference in scRNA-seq microglial studies (Hammond et al., 2019).

To identify CAM in the dataset, I used 'AddModuleScore' in combination with 10 canonical markers of CAM: *Clec12a*, *Mrc1*, *Ms4a8*, *Ms4a4a*, *Pf4*, *F13a1*, *Dab2*, *Lyve1*, *Stab1*, *Siglec1* (Kierdorf et al., 2019; Van Hove et al., 2019). Cluster 11 was identified as CAM (Figure 29).

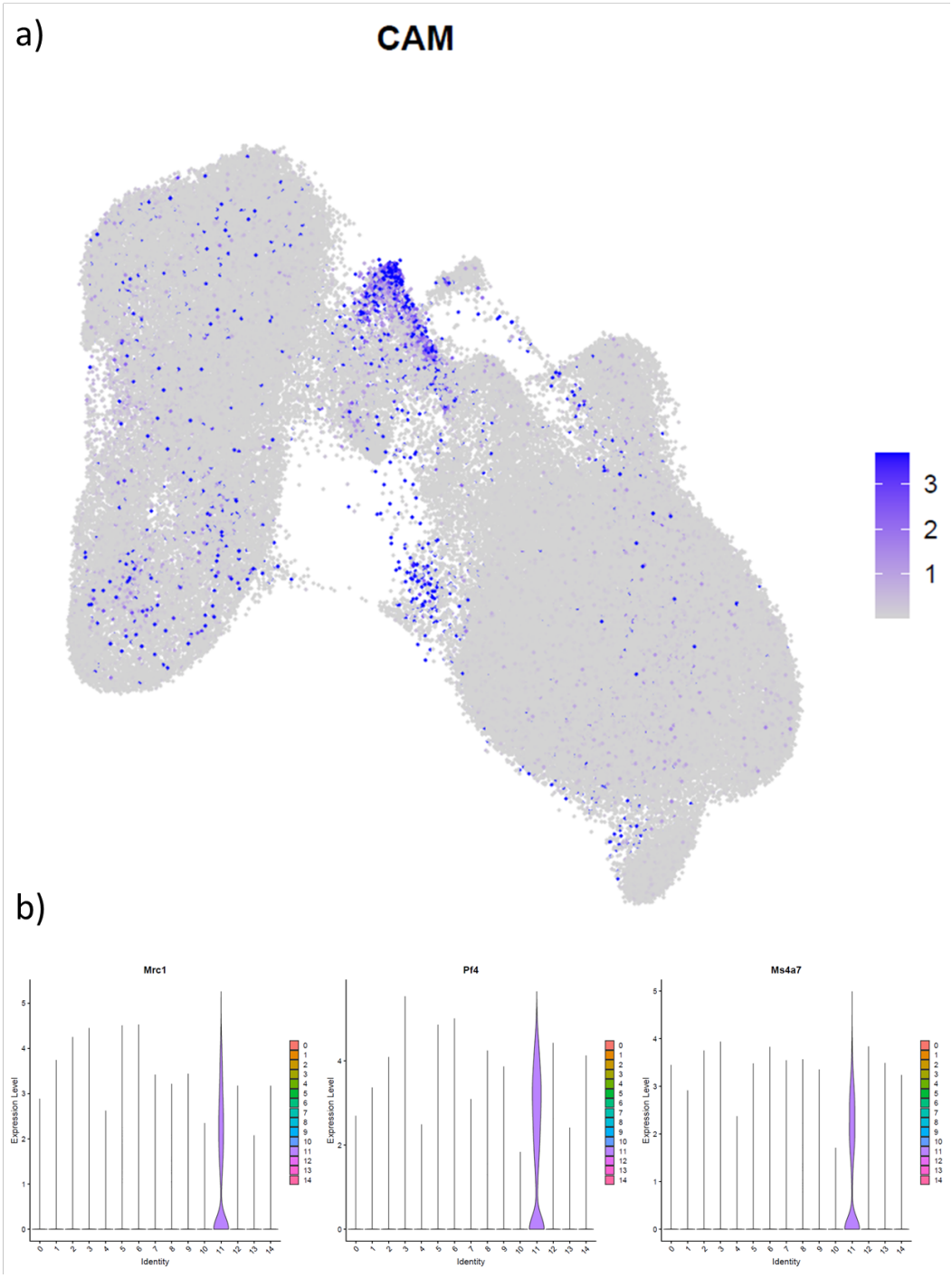


*Figure 29:CNS-associated macrophages are present in the single-cell atlas. a) CNS-associated macrophages (CAM) are identified in cluster 11 by canonical markers of such cells. b) VlnPlot of Mrc1, Pf4 and Ms4a7 are displayed.*

#### 3.4.2.1.4 Technical artefacts and *ex vivo* activated microglia

scRNA-seq data (in particular when derived from microglia) is known to be susceptible to technical artefacts (Adam et al., 2017; Marsh et al., 2022; Wu et al., 2017). Microglia that have acquired an artefactual signature are commonly known as *ex*AM (Marsh et al., 2022). I utilized 3 gene list that are enriched in *ex*AM, to aid the identification of such microglia in the single-cell atlas. Each gene list could identify those cells most affected by technical artefacts, yet distinct differences in their accuracy to do so were noted (Supplementary Figure 5). A gene list first described by Marsh *et al.* (2022) best captured the *ex vivo* signature (Figure 30). The list derives from standard-dissociated

microglia relative to those isolated in the presence of transcriptional and translational inhibitors and clearly defines dissociation-induced technical artefacts (Supplementary Table 5).

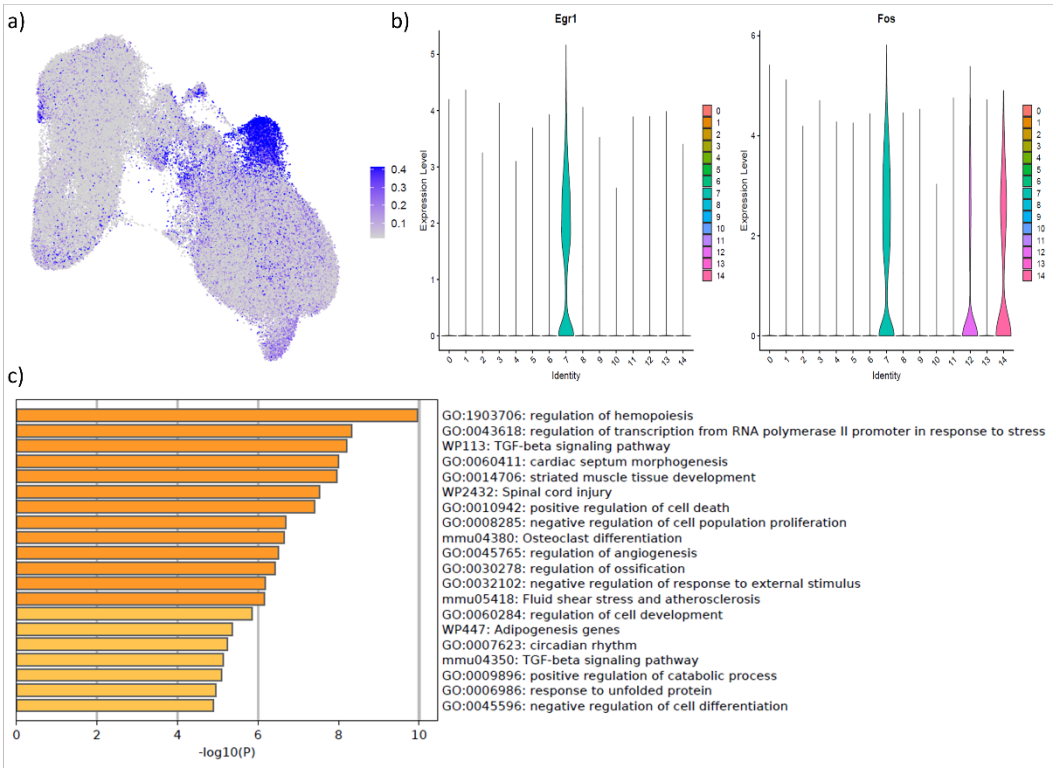


*Figure 30: Identification of exAM. a) A gene list from Marsh et al. (2022) was used in combination with 'AddModuleScore'. b) VlnPlot ex vivo-activated microglia (exAM) genes. c) Functional gene annotation (with Metascape) identified a.o. an association with response to stress and TGF-beta signalling pathway.*

In correspondence to the gene lists and other sources on technical artefacts in scRNA-seq, cluster 7 markers include genes like *Fos*, *Jun*, *Egr1*, *Ier2* and *Zfp36* (Adam et al., 2017; Brink et al., 2017; Li et al., 2019; Marsh et al., 2022; Van Hove et al., 2019; Wu et al., 2017) (Figure 30). Broadly, genes in cluster 7 were associated with the regulation of hemopoiesis (GO:1903706), regulation of transcription from RNA polymerase II promoter in response to stress (GO:0043618) and TGF-ß signalling pathway (WP113), as determined with *Metascape* (Zhou et al., 2019) (Figure 30). The associated with the TGF-ß signalling pathway hint towards the interconnected nature of *ex vivo* signatures with microglial identity and might need mitigation to improve microglial scRNA-seq data quality. Given that 4023 of 113690 cells (~3.5%) in the atlas are localized to this cluster, the question remains to which extend this holds true.

#### 3.4.2.2 Age functions as the main driver of microglial heterogeneity in health

Ageing alters the epigenetic marks of DNA and drives differentiation, a process commonly known as the epigenetic clock theory of aging (Horvath and Raj, 2018; Reik, 2007). DNA methylation-base age typically increases as pluripotent cells differentiate, leading to a loss of stem and progenitor cells and an increase of senescent cells (Horvath and Raj, 2018). Therefore, it is anticipated that aging affects microglial heterogeneity. Microglial heterogeneity is typically highly transcriptionally diverse in early development, reduced in adulthood, and increased once more with aging (Masuda

et al., 2020). Given that the microglial population in health is locally maintained (without contributions of circulating monocytes) (Askew et al., 2017), all cells in the CNS are part of the same differentiation trajectory and allows for the temporal organization of such phenotypes.

To test the temporal order of microglial subtypes, a trajectory inference was performed on the single-cell atlas gene profiles with Monocle 3. Embryonic day 6.5 (E6.5) was set as the root of the analysis, and cells were projected onto the associated UMAP co-ordinates (Figure 31). Several branch points and convergences were identified (Figure 31). Broadly, early developmental microglia are featured by a low pseudotime score that is mostly stable until postnatal day 7 (P7) (Figure 31). From P7 onwards, the score rapidly increases and reaches adult levels by P21. Adult levels remain relatively stable until continued aging progressively reverts microglial scores to developmental levels.

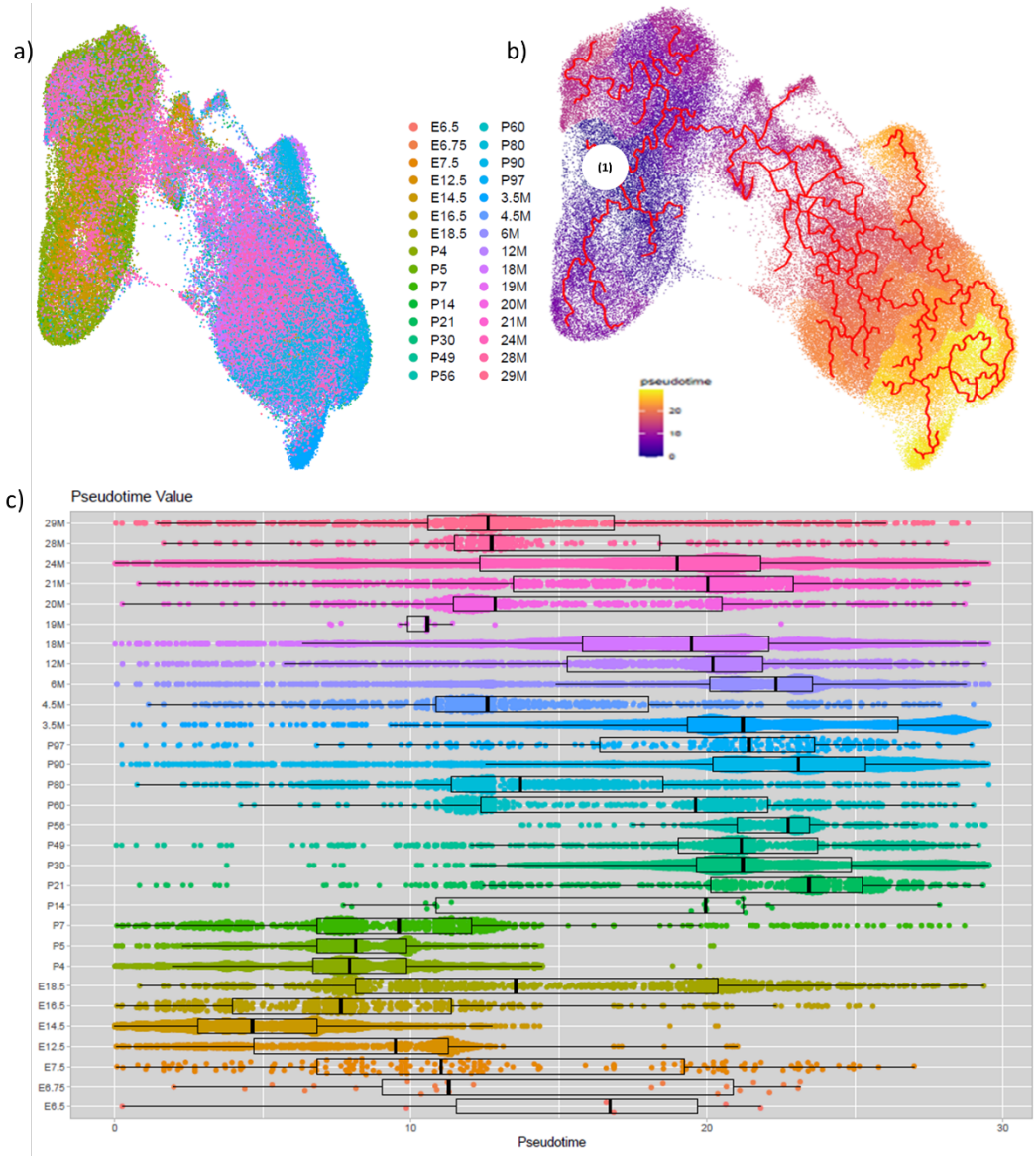


*Figure 31: Age as a driver of microglial heterogeneity. a) Illustration of age groupings in the single-cell atlas, ranging from E6.5 to 29M old cells. Root cells are marked by (1) b) Trajectory inference of the atlas on the UMAP co-ordinates, with low pseudotiming values in blue, and high values in yellow. c) Boxplots of pseudotime values (and their median) in the age groupings. E, embryonic day; P, postnatal day; M, month.*

To delve into the age-dependent transcriptional dynamics, microglia were grouped in seven maturation stages: early microglia (E10.5 – E14.5), pre-microglia (E14.5 – P9), sexually immature microglia (SIM) (P9-P28), adolescent microglia (P28 – P60), adult microglia (P60 – 6M), middle age microglia (6M- 18M), and old age microglia (>18M). In correspondence with Matcovitch-Natan *et al.* (2016), early development displays a distinct transcriptional signature in line with disease- (DAM) and proliferative region-associated microglia (PAM), and axon tract microglia (ATM) (*e.g. Spp1*, *Apoe*, *Igf1*) (Figure 32) (Hammond et al., 2019; Keren-Shaul et al., 2017; Li et al., 2019; Matcovitch-Natan et al., 2016). Similarly, expression of *Hmgb2*, *Mki67* and *Mcm5* is featured and typically associated with cellular proliferation. However, once adolescence is reached (between P28 and P60), a more typical microglial signature is acquired that includes the expression of *Tmem119* and *Selplg (*Figure 32*)*. Of note, the transition to a mature microglial signature in SIM (P9-P28) is shrouded due to the lack of studies that have investigated this stage of maturation *(*Figure 32*)*.

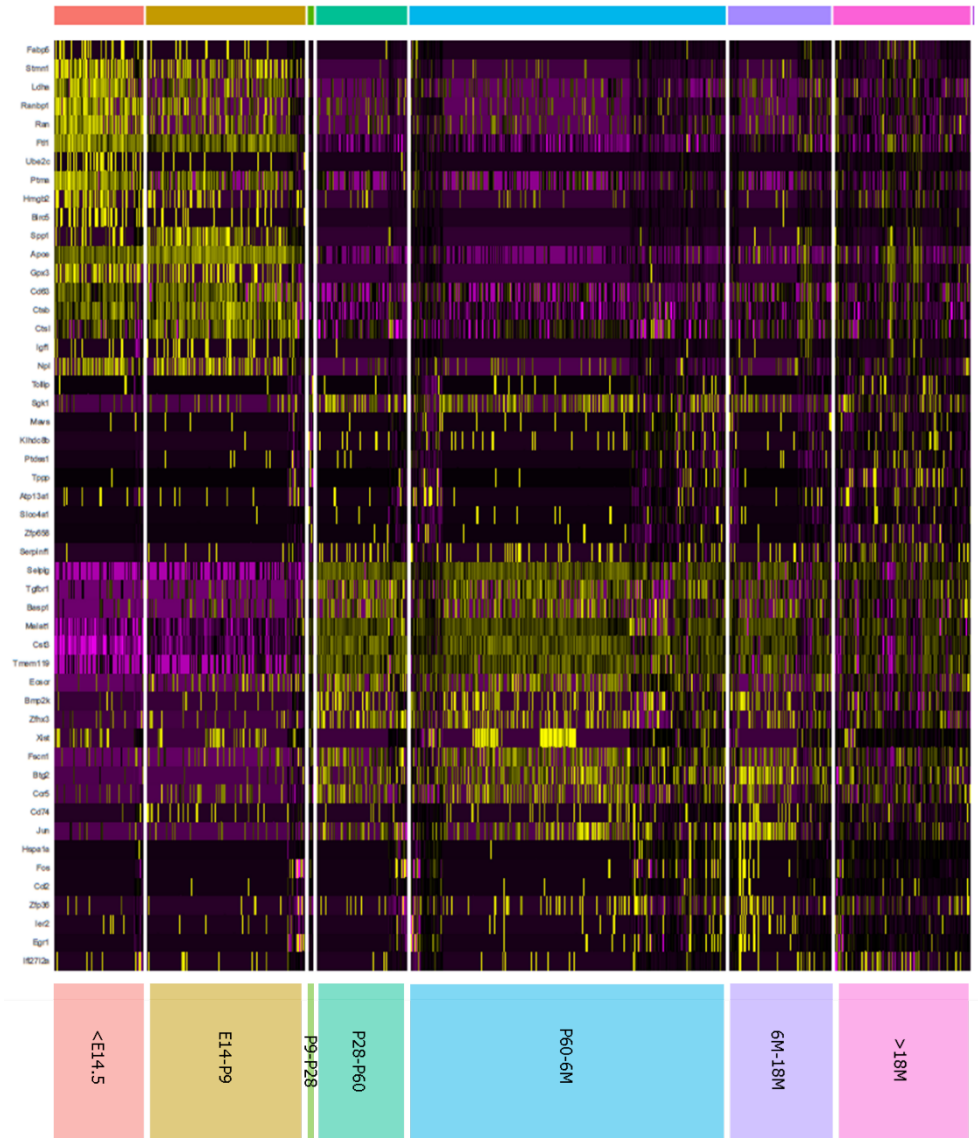


*Figure 32: Transcriptional distinction between early developmental microglia and postnatal mature microglia. Age group-dependent transcriptional signatures transition between pre-microglia (E14.5 – P9) and sexually immature microglia (SIM) (P9-P28). The top 10 genes (ordered by 'avg_log2FC') of each age group are displayed. FindAllMarkers with 'only.pos = TRUE', 'min.pct = 0.25',' logfc.threshold = 0.25', 'test.use = "wilcox"'.*

### 3.4.2.3 Early developmental microglia

The results show that early and pre-microglia have a distinct gene signature, which transitions into an adult homeostatic signature from SIM onwards (Figure 32). In fact, cluster 5, 6 and 8 (in early development) share a core signature with cluster 2 that includes the expression of *Apoe*, *Cd63*, *Ctsb*, *Gpx3*, *Ftl1*, *Npl*, *Serpine2*, *Ctsl* and *Gas6* (Figure 33). The predominant occurrence in early life has led me to term cluster 2, as 'early developmental microglia' (EDM).

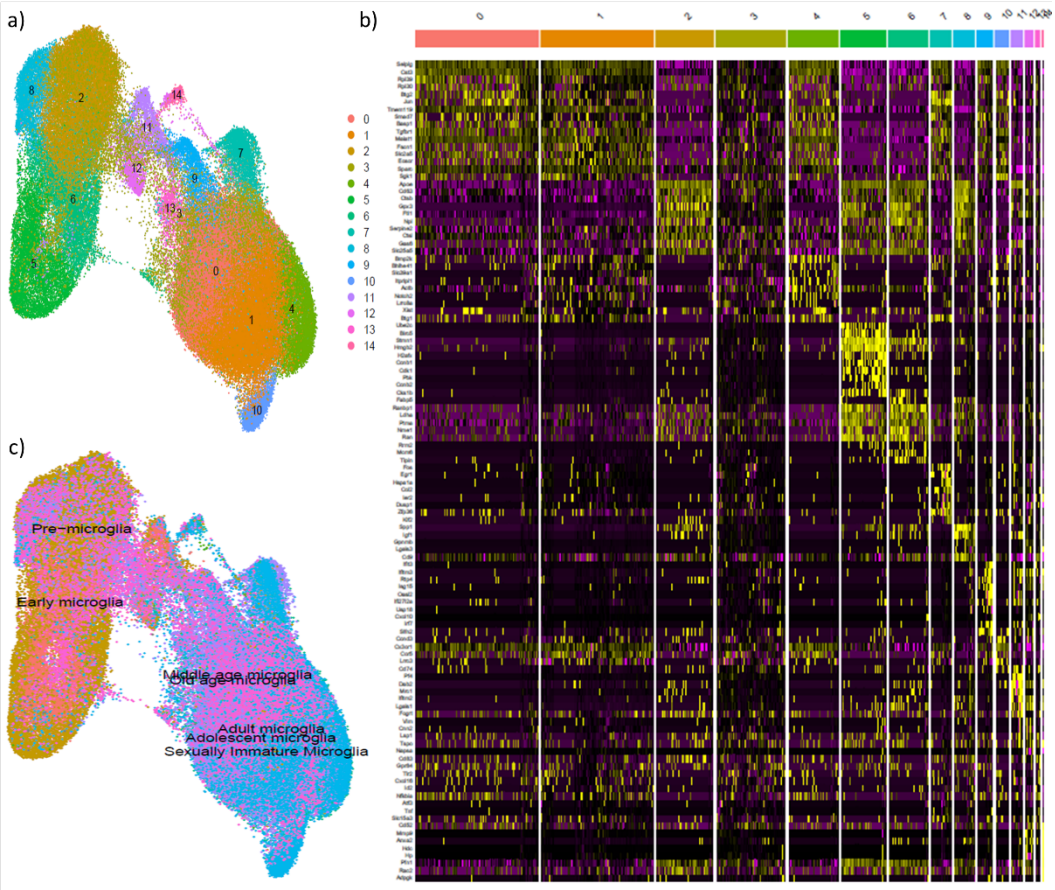


*Figure 33: Cluster-specific gene expression and age group distribution in the single-cell atlas. a) DimPlot of Seurat clsuters. b) A heatmap of the top 10 genes (ordered by 'avg_log2FC') of each cluster are displayed. FindAllMarkers with 'only.pos = TRUE', 'min.pct = 0.25',' logfc.threshold = 0.25', 'test.use = "wilcox"'. c) DimPlot of age group annotations.*

*Apoe* plays a role in lipid and cholesterol maintenance. Interestingly, *Cd63* has recently been identified as a marker in lipid-associated macrophages (LAM). Roles of *Apoe*, *Ctsb*, *Cd63* in lipid metabolism and protein degradation, suggest that these are typical features of myeloid cells shared across the lifespan.

### 3.4.2.4 Lysosome pathway-associated microglia and the convergence of phenotypes

Disease-associated microglia (DAM), as well as MGnd and ARM, are best known for their occurrence in (models of) age-associated disease (*e.g.* AD, MS, ALS) (Keren-Shaul et al., 2017; Krasemann et al., 2017; Sala Frigerio et al., 2019). Of note, there have been reports about the transcriptional similarities of DAM with PAM and ATM (Hammond et al., 2019; Keren-Shaul et al., 2017; Li et al., 2019). Module score annotations with the top 50 genes of these subtypes support such similarities

(Figure 34). Indeed, 6 out of the top 50 DAM, PAM and ATM signature genes are shared between them (*i.e. Csf1*, *Lpl*, *Spp1*, *Igf1*, *Gpnmb*, *Apoe)*. All 6 were enriched in cluster 8, albeit *Apoe* is a remarkable exception to that, which broadly extends into early developmental clusters and CAM. Clusters 2, 5-6, 8 and 12 each express *Apoe* highly, suggestive of a broad role of *Apoe* in CNS myeloid cells (Figure 34).

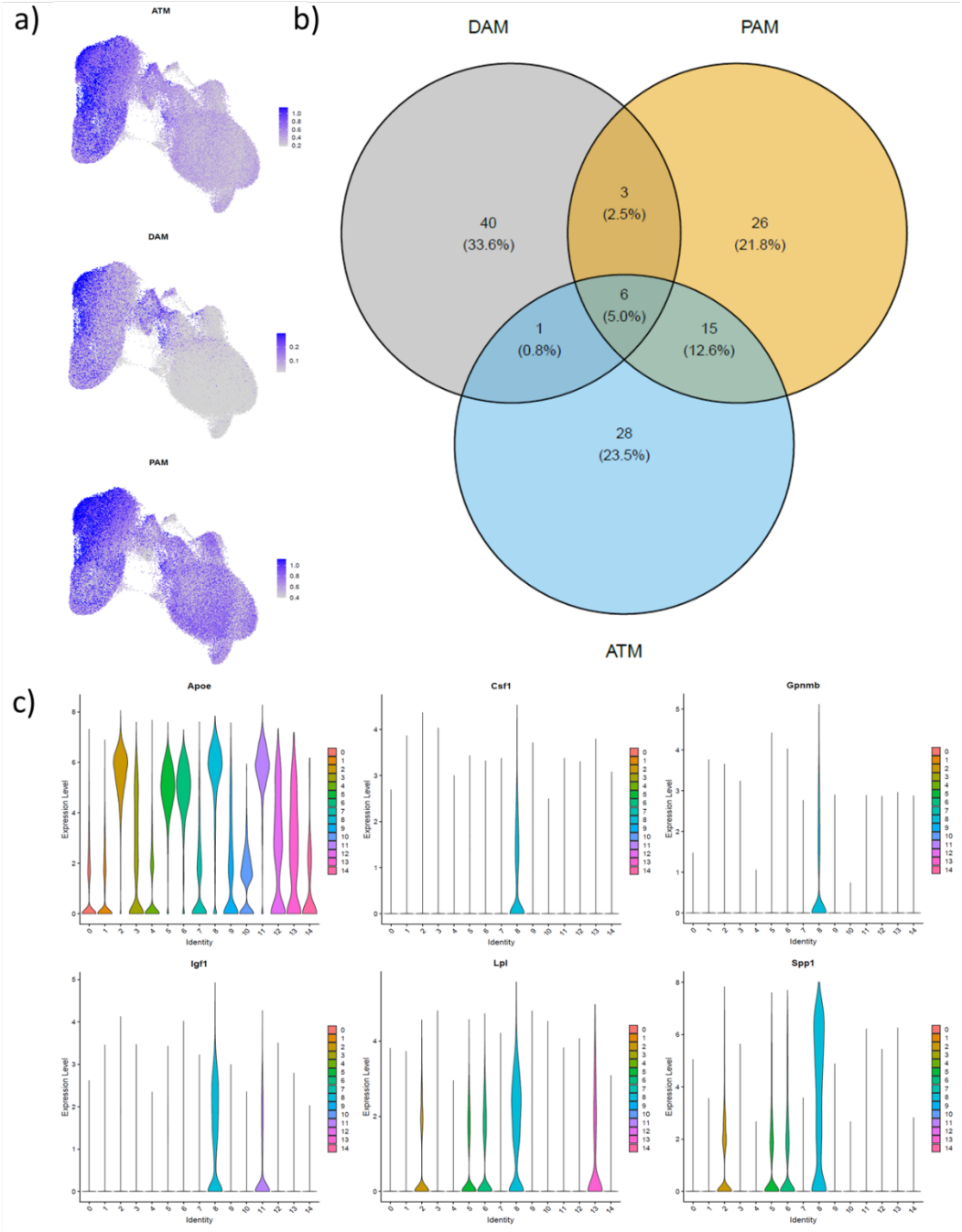


*Figure 34: Transcriptional overlap between disease-, proliferative region- and axon tract-associated microglia. a) Gene list annotations of disease- (DAM), proliferative region- (PAM) and axon tract-associated microglia (PAM) b) The top 50 genes ofeach were compared, in order to discriminate between early developmental and age-associated microglial subtypes. c) 6 genes (i.e. Csf1, Lpl, Spp1, Igf1, Gpnmb, Apoe) were shared amongst all 3 subtypes.*

PAM and ATM selectively share 15 genes of their top 50 signature genes, 14 of which were significantly expressed in cluster 8, thereby discriminating them from DAM (Figure 35). Interestingly, I noticed the expression of *Itgax* and *Ank* in cluster 8, two genes commonly associated

with DAM (Kamphuis et al., 2016; Keren-Shaul et al., 2017). Of those two genes, only *Ank* was a (statistically significant) cluster marker. Immunohistochemistry has previously identified Cd11c$^{+}$ microglia in the white matter during myelinogenesis, as well as with aging and disease (Benmamar-Badel et al., 2020), further highlighting the similarities between PAM, ATM and DAM phenotypes.

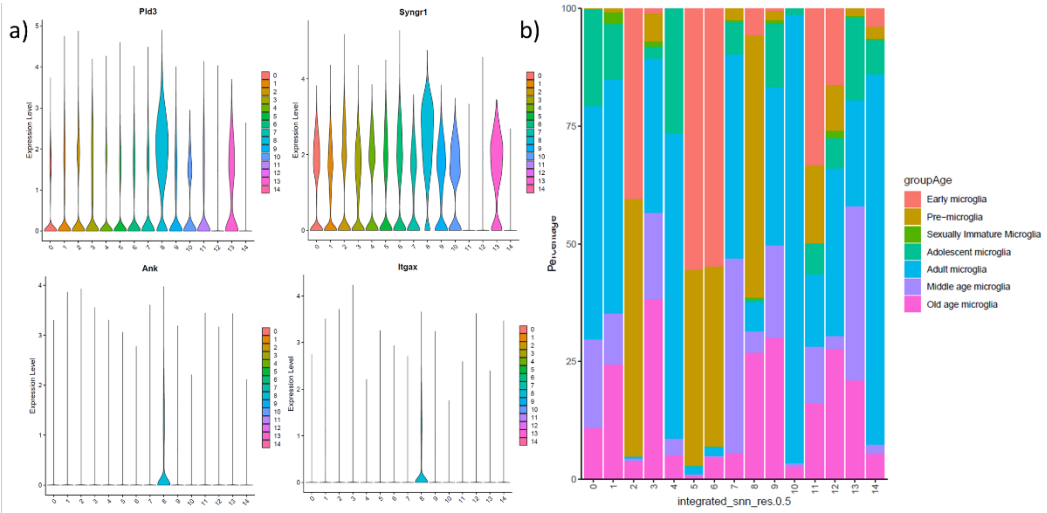


*Figure 35: Phagocytic microglia display a mixed transcriptional signature and are evident throughout life. a) VlnPlot of genes typically associated with axon tract- and proliferative region-associated microglia (Pld3, Syngr1), as well as disease-associated microglia genes like Ank and Itgax. b) Barplot of age group and cluster identity illustrates that pre-microglia are the largest contributors to cluster 8, although middle age and old age microglia are also evident.*

In concurrence, looking into their relative distribution across the lifespan, cluster 8 cells are predominantly pre-microglia, albeit a significant number of cells were also evident with age (Figure 35). In fact, I cannot exclude that some age-associated DAM are present, as a subgroup of middle and old age microglia are localized to cluster 8. Of note, other clusters feature old age microglia too and allocation to old age alone does not imply a DAM-like state. Subsequentially, the phenotypical convergence of ATM, PAM and DAM have led me to describe cluster 8 as lysosomal pathway-associated macrophage (LPM), corresponding to and reflective of their phagocytic function independent of age. Moreover, LPM show an enrichment for AD-associated risk factors (*e.g. Apoe*, *Ctsb*, *Pld3*) and warrant further study in early developmental heterogeneity as a therapeutic target (Figure 36).

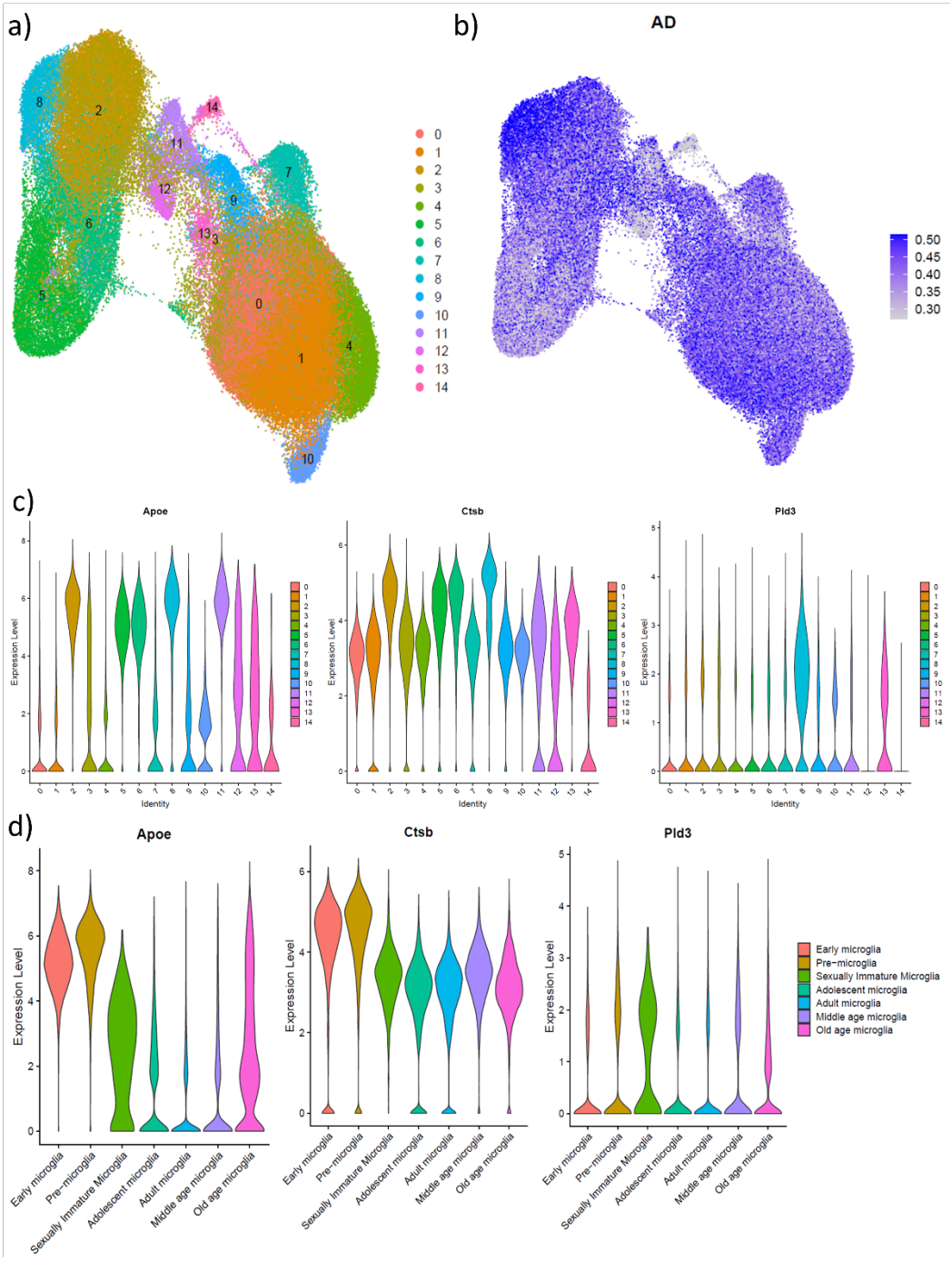


*Figure 36: Enrichment of AD risk factors in early development. a) Dimplot of identified clusters in the murine cell atlas. b) Cluster 8 (i.e. LPM) are enriched for late onset Alzheimer's disease (AD) risk factors, as reported by Sala Frigerio et al. (2019). c/d) 3 examples are shown (i.e. Apoe, Ctsb, Pld3) in a cluster- and age group-specific manner.*

### 3.4.2.5 Microglial proliferation follows a wave-like pattern throughout life

Microglial proliferation is a critical cellular process that underlies population dynamics. As discussed, CPM are most typically associated with early development and the expansion of the microglial population (Alliot et al., 1999; Askew et al., 2017; Nikodemova et al., 2015). The developmental expansion is concurrent with *Sall1*- and *Tgfb1*- activated gene cascades to adult microglial identity (Butovsky et al., 2014; Buttgereit et al., 2016). CPM prevalence occurs in 3 waves during the murine lifespan, the most predominant one of which between E7.5 and P21 (Figure 37). However, middle age and old age increases of microglial proliferation are biologically interesting. It

showcases ongoing population dynamics in old age that correspond to microglial dynamics in age-associated disease, while simultaneously highlighting middle age as a potential target for modulation of the microglial population (Krasemann et al. 2017; Nikodemova et al. 2016).

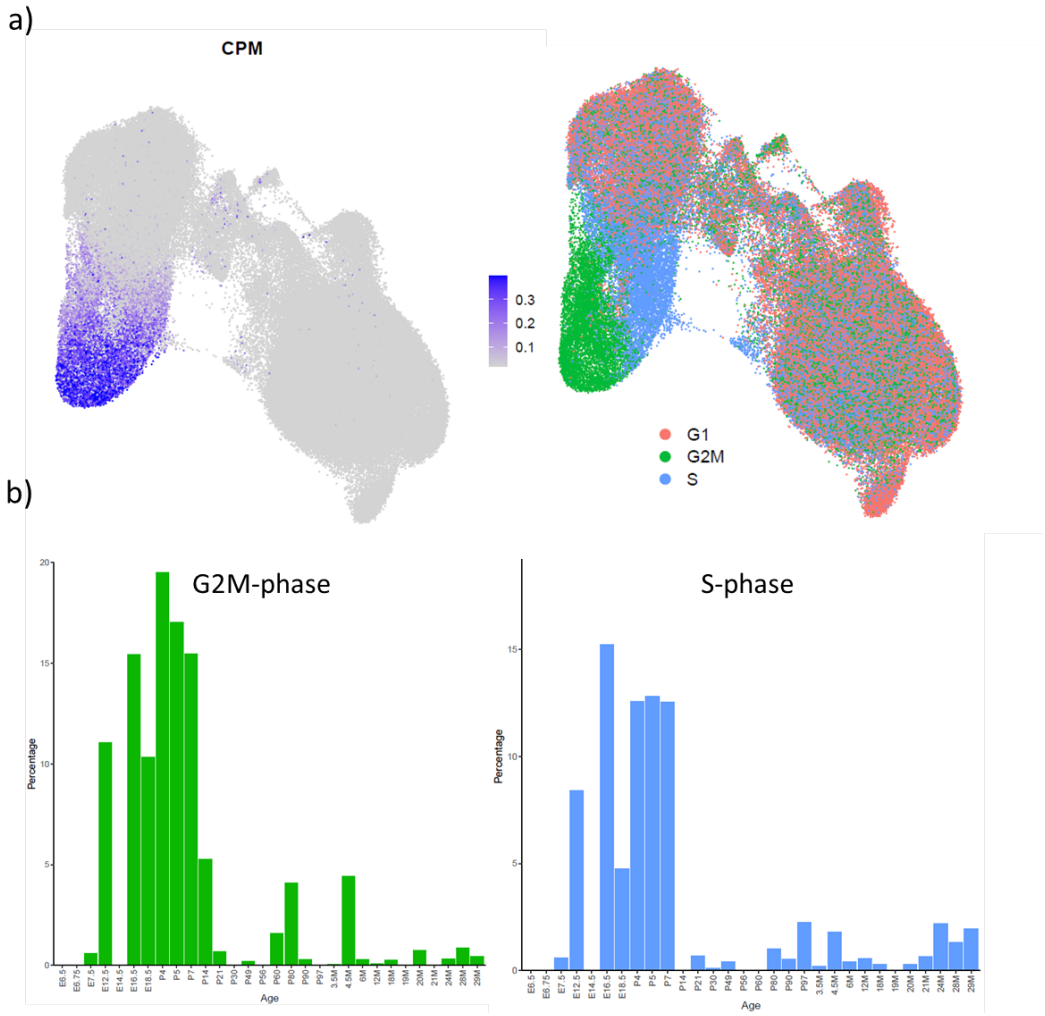


*Figure 37: Microglial proliferation in the murine lifespan. a) Annotation of cell phase resolves distinct clusters of cells in G2M- and S-phase. b) Actively cycling and proliferating microglia (CPM) are most evident in early development, independent of phase.*

#### 3.4.2.5.1 Wave-like patterns of human gestational, microglial proliferation

With such widespread processes in murine early development, it is scientifically and biologically relevant to study if such processes are present in human gestation. To that end, I gathered count matrices and metadata of 4 human single-cell and single-nuclei studies in gestation including embryonic, early fetal, and mid-late fetal age (Bian et al., 2020; Cao et al., 2019; Fan et al., 2020; Kracht et al., 2020); together these span a broad range from post conceptual week (PCW) 7 to 24 (Table 4).

Indeed, a similar wave-like pattern of microglial proliferation in gestation became evident, the largest of which in early gestation (Figure 38) (Menassa et al., 2022).

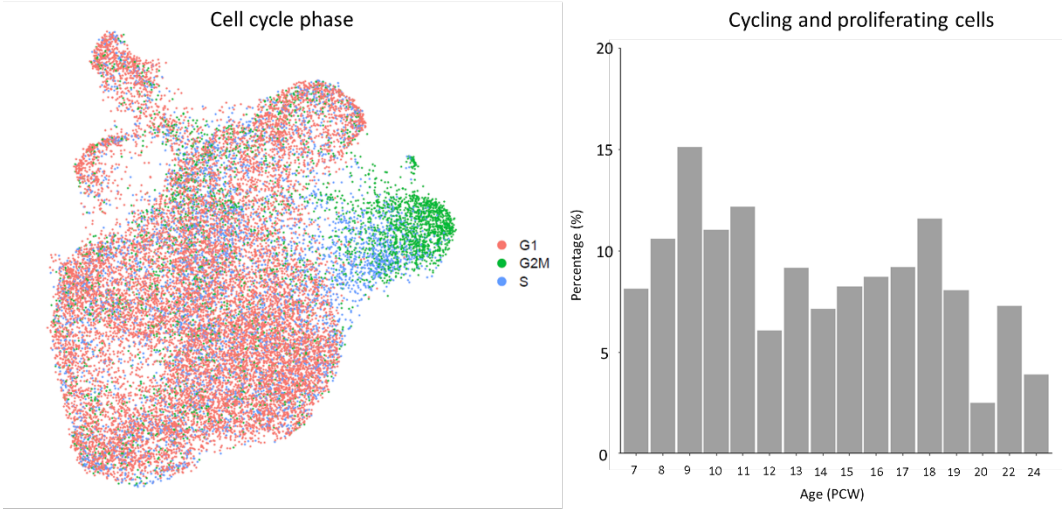


*Figure 38: Cycling and proliferating myeloid cells in human gestation. a) Actively cycling and proliferating microglia (CPM) in the scRNAseq dataset were identified across gestational age. b) Barplot of CPM across human gestation; only ages with a minimum of 50 cells were selected (7 – 24 PCW). PCW, post conceptual week.*

In the integrated object, 8 clusters were identified that express typical myeloid markers, among which CPM (Figure 38, Supplementary Figure 6, ). This proliferation cluster also displayed a wave-like distribution across gestation, first peaking at 9 PCW and then peaking again at 18 PCW, tracking the pattern observed at the histological level (Menassa et al., 2021).

Like in the large-scale murine atlas, the UMAP-plot was split by data source (*i.e.* original identity). All sources align well spatially suggestive of a high-quality integration (Supplementary Figure 7). To ensure these cells are transcriptional similar across assays, a necessary additional precaution was taken. I tested the alignment of CPM cells between source data and identified forty conserved markers by utilizing the 'FindConservedMarkers' function of the Seurat package. Gene ontology and protein-protein interaction enrichment analyses of this gene set with *Metascape* underscored their association with cell cycle processes (Figure 39).

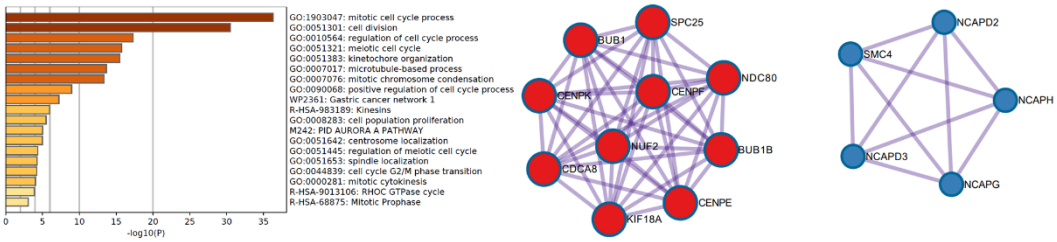


*Figure 39: Metascape analysis of conserved CPM markers. Gene ontology (GO) and protein-protein interaction (PPI) enrichment analysis mark key mitotic cell cycle processes. PPI enrichment analysis identified mitotic spindle checkpoint and amplification of signal from the kinetochores (in red), as well as mitotic chromosome condensation and condensing I complex (in blue)*

Unfortunately, human scRNA-seq data remains rare and it makes a similar extension throughout life more complex. More research in human microglial heterogeneity is needed to detail this

further, as early developmental waves of proliferation and selection give rise to adult homeostatic and non-homeostatic phenotypes.

#### 3.4.2.6 Homeostatic microglia are heterogeneous in the healthy murine CNS

Homeostatic microglia (HOM) have long been thought to be a single population, however, much like other microglial subtypes, HOM are recognized to be a heterogeneous population composed of various subgroups (Hammond et al., 2019; Li et al., 2019). A homeostatic gene list first published by Matcovitch-Natan et al. (2016) was used to identify the clusters; the list includes microglial markers that are expressed from P28 onwards (Matcovitch-Natan et al., 2016) (Supplementary Table 3). 5 distinct HOM clusters were identified (*i.e.* cluster 0,1,3, 4 and 10) with relatively stable and selective levels of homeostatic and sensome gene expression (Figure 40) (Supplementary Table 3).

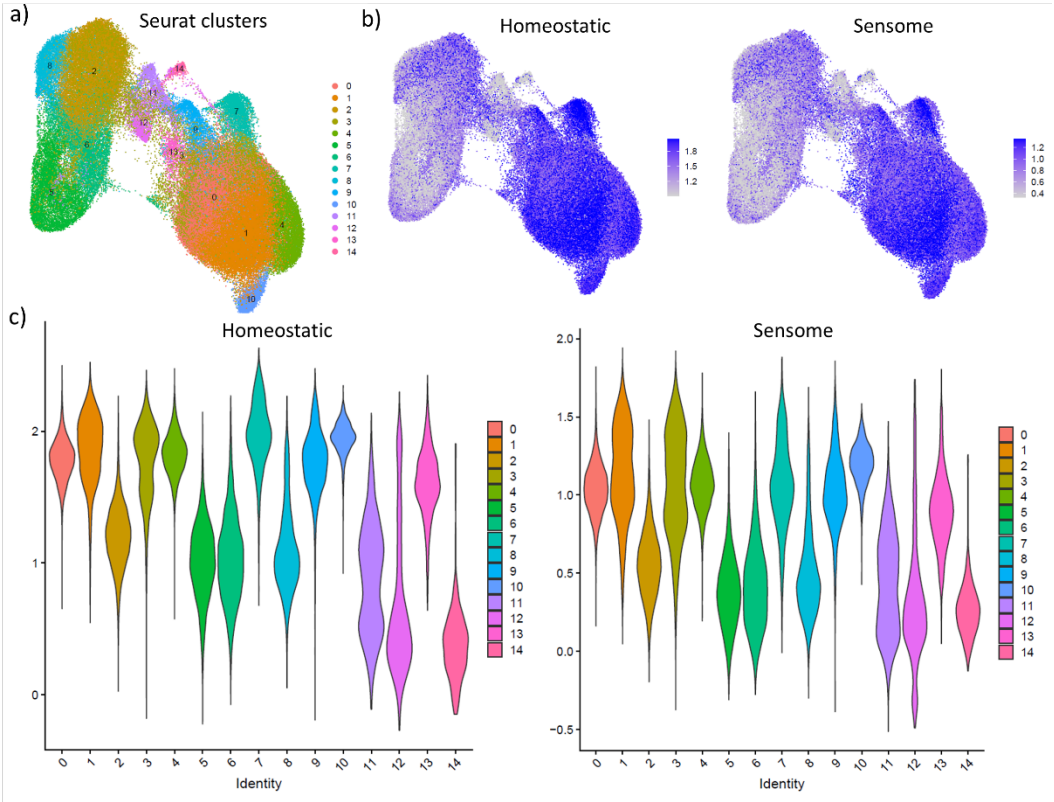


*Figure 40: Homeostatic microglial identity corresponds to the sensome signature. a) DimPlot of identified murine clusters across the lifespan. b) FeaturePlot of homeostatic (Matcovitch-Natan et al., 2016) and sensome markers (Hickman et al., 2013)feature similar annotations. c) VlnPlot of cluster-specific expression levels of both annotations.*

It was argued that such age-specific trajectory inference results would be reflected by changes in homeostatic microglial genes. Therefore, the homeostatic gene score expression was tested throughout the lifespan. Indeed, homeostatic signatures were stably expressed throughout most of adult life, with lower levels in early development and old age, and a high correlation between homeostatic and sensome gene signatures (Figure 41).

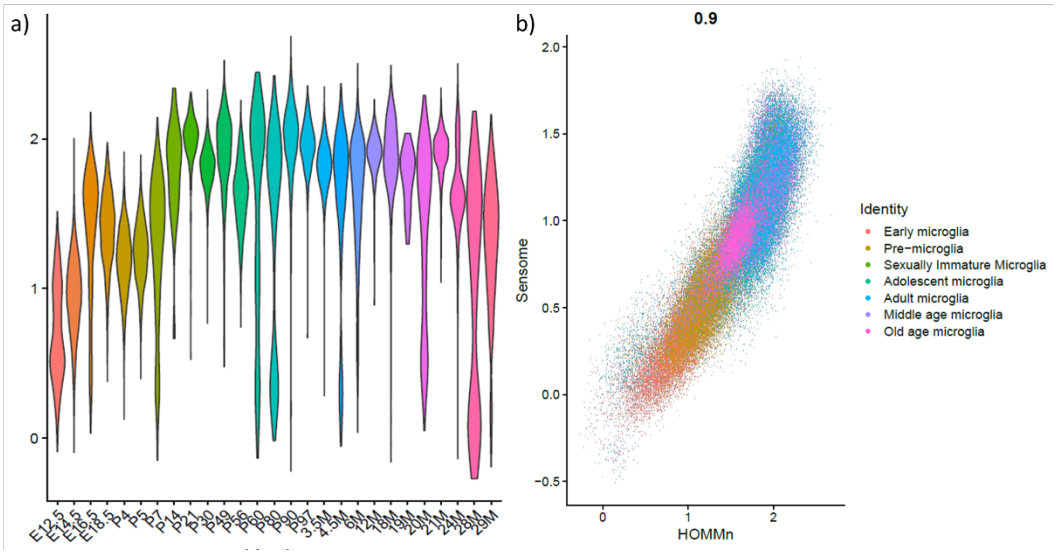


*Figure 41: Homeostatic gene expression throughout life. a) Homeostatic gene expression increases in early development to attain a stable level throughout adulthood. Old age (>18M) is featured by a loss of said homeostatic genes. b) Homeostatic and sensome gene expression correlate highly.*

Next, a panel of microglial genes (*Csf1r*, *Cx3cr1*, *Hexb, P2ry12, Tgfbr1*, *Tmem119*) were selected and displayed individually (Figure 42). 3 key points were noted. First, *Hexb* was expressed highly and stable in all developmental and homeostatic clusters, as well as in several others (*e.g. ex*AM); indirect proof of the validity of Hexb to reliably identify microglia (Masuda et al., 2020) (Figure 42). Second, in contrast, *Csf1r*, *Cx3cr1*, *P2ry12*, *Tgfbr1* and *Tmem119 s*howed considerable variability in the clusters, highlighting their transcriptional dynamics throughout life (Figure 42). Notably, *P2ry12* and *Tmem119* levels were both lowered in cluster 8, that is, LPM (Figure 42).

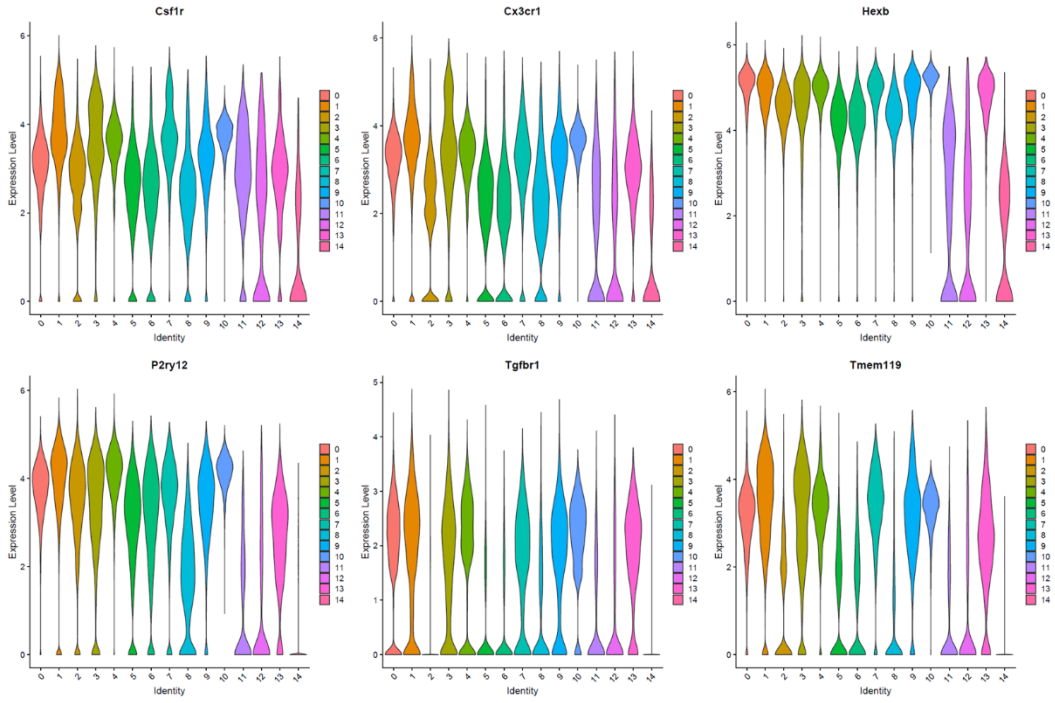


*Figure 42: Homeostatic gene expression in the single-cell atlas. VlnPlot of 6 homeostatic genes in a cluster-specific manner.*

Regarding *Tgfbr1* and *Tmem119*, expression of these genes was overtly lower in early development, in line with their developmentally regulated expression; *Tmem119*, and *Tgfbr1* expression increases

with age, reaching stable adult levels from P14 onwards (Figure 43) (Bennett et al., 2016; Butovsky et al., 2014).

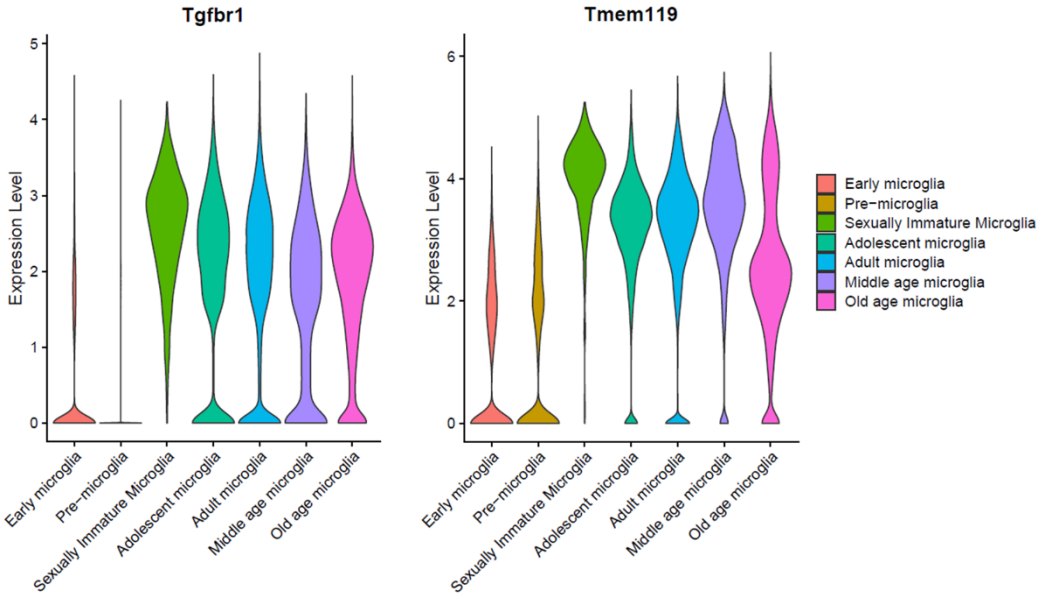


*Figure 43: Microglial maturation and canonical marker expression. VlnPlot of Tgfbr1 and Tmem119 expression levels by age group.*

#### 3.4.2.7 Interferon response microglia – a distinct age-associated microglial subtype

Interferon response microglia (IRM) are enriched for genes in the interferon (IFN) response pathway. The canonical type I IFN signalling pathway is featured by mediators of antiviral and inflammatory responses, as well as repressors of inflammatory pathways (Ivashkiv and Donlin, 2014). Although some IFN genes have also been reported in other age-associated cell types like DAM or white matter-associated microglia (WAM), IRM cells are believed to be mutually exclusive (Sala Frigerio et al., 2019). Sala Frigerio *et al.* (2019) performed a trajectory inference and found that microglia with age differentiate into either IRM or ARM (*i.e.* DAM) (Sala Frigerio et al., 2019).

Although some IRM cells can be seen throughout the single-cell atlas, most are localized to cluster 10 and are transcriptionally distinct from LPM (Figure 44). Furthermore, markers of cluster 10 display minimal overlap with typical markers of age-associated DAM or WAM, and none of which are shared between all three (Figure 45). As shown previously, *Apoe* expression is elevated in early development (cluster 2, 5, 6 and 8) and in CAM (Figure 36). In contrast, HOM and IRM expression of *Apoe* is relatively low (Figure 36), supportive of a distinct trajectory.

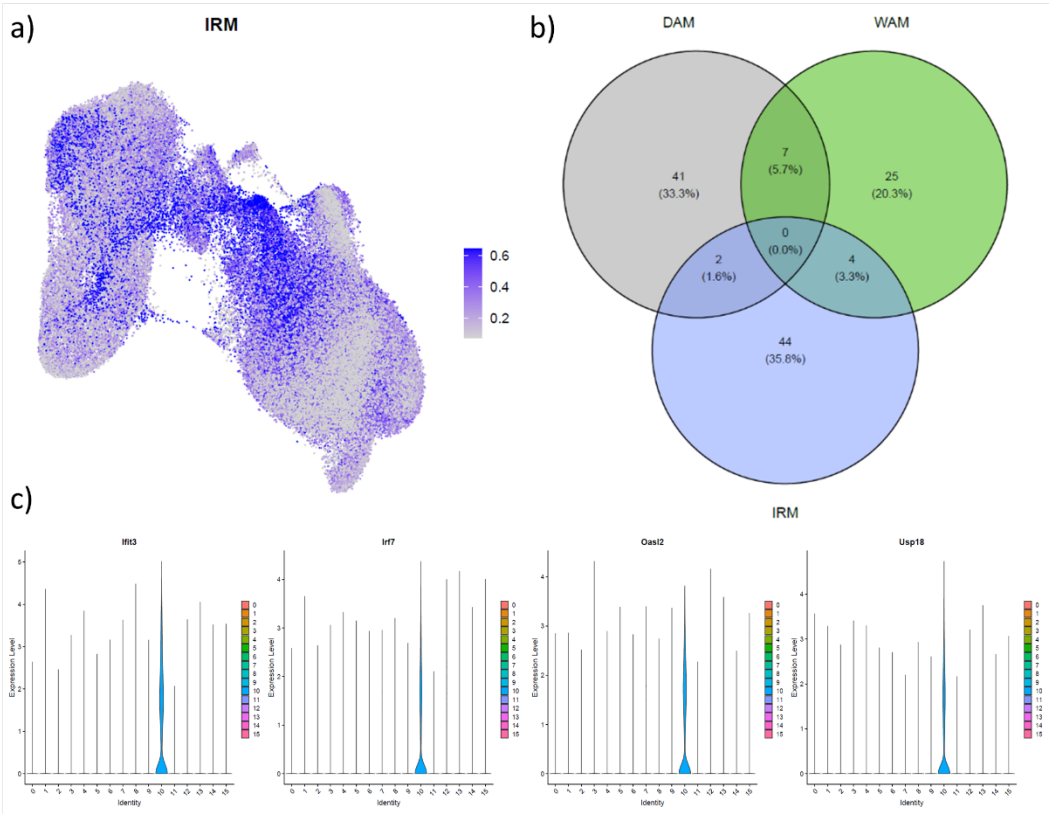


*Figure 44: Interferon response microglia in the single-cell atlas. a) FeaturePlot of IRM gene annotation. b) Transcriptional overlap between age-associated microglial subtypes is minimal. Disease- (DAM) and white matter-associated microglia (WAM) and interferon response microglia (IRM) do not display large transcriptional similarities, with the greatest overlap between DAM and WAM signatures. c) Cluster 10 cells express interferon response genes (e.g. Ifit3, Irf7, Oasl2, Usp18) and are identified as interferon response microglia (IRM).*

#### 3.4.2.8 Aged Inflammatory Microglia

Cluster 13 is marked by genes like *Cd83*, *Gpr84*, *Tlr2*, *Cxcl16*, *Id2* and *Nfkbia*. *Cd83* is best described for as a mature dendritic cell (DC) marker, as well as an immune checkpoint molecule in B- and T-cell differentiation (Grosche et al., 2020; Z. Li et al., 2019). Although there have been reports of DC populations that express Iba1 and could therefore be confused with myeloid cells (Köhler, 2007); cluster 13 reliably expressed typical microglial markers like *Tmem119*, *Hexb*, *P2ry12* and *Tgfbr1*, as well as *Csf1r* and *Cx3cr1* to comparable levels as seen in CAM (*i.e.* cluster 11) (Figure 42). In microglia, *Cd83* has been linked to inflammatory microglia in murine and human tissue that increases with age (Jin et al., 2021; Olah et al., 2020; Zheng et al., 2021). Indeed, cluster 13 increases with age, an effect that I will address in the next section on microglial population dynamics. The inclusion of genes involved with the microglial activation cascade (*i.e. Tlr2*, *Nfkbia*) further highlighted their inflammatory state. For that reason, this cluster was termed Aged Inflammatory Microglia (AIM).

### 3.4.3 Age-specific effects on microglial population dynamics

Age is the major driver of microglial heterogeneity in health. Early development and age-associated clusters identified and explored, including AIM, CAM, CPM, EDM, HOM, IRM and LPM. The data

shows that these 7 major subtypes are the drivers of microglial heterogeneity in the murine lifespan; 5 distinct HOM-clusters bring the total to eleven. However, the underlying population dynamics are so far unexplored. That is, how the emergence and decline of microglial subtypes varies in an age-dependent manner. To this end, I illustrated their respective occurrence across the age groups; from early microglia up to and including old age microglia (Figure 45).

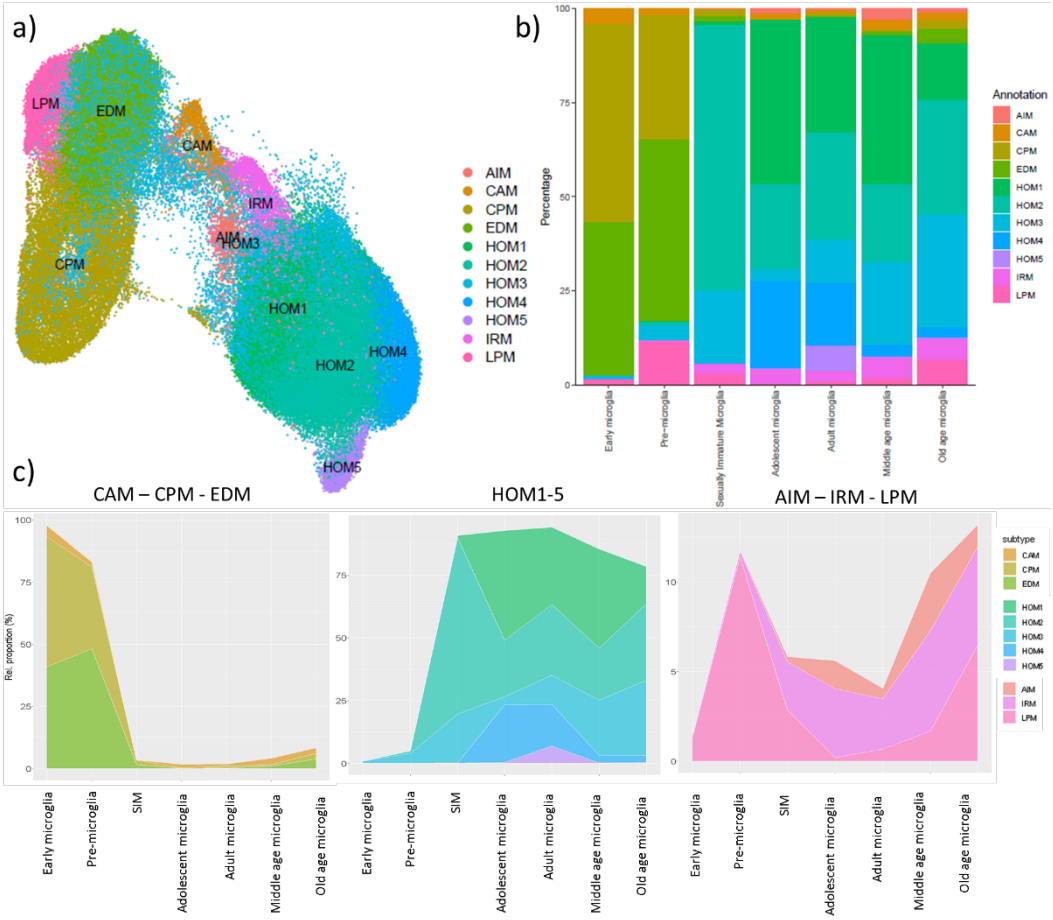


*Figure 45: Age group-dependent cluster distribution and annotation. a) DimPlot of microglial and CAM clusters. 15 cluster were identified, 11 of which include microglial clusters and CAM, excluding cluster 7, 12 and 14. b) BarPlot of age group specific population dynamics. c) StackedBarPlot of the 11 clusters, to display predominant clusters by developmental age. AIM, Aged Inflammatory Microglia, CAM, CNS-associated macrophages; CPM, cycling and proliferating microglia; EDM, early developmental microglia; HOM, homeostatic microglia; IRM, interferon response microglia; LPM, lysosome pathway-associated microglia. Early microglia (<E14), pre-microglia (E14-P9), SIM, sexually immature microglia (P9-P28), adolescent microglia (P28-P60), adult microglia (P60-6M), middle age microglia (6M-18M), old age microglia (>18M). P, postnatal day; M, months old.*

Most microglia in early development are CPM and EDM; 80 – 95% of all microglia belong to these subtypes. In old age, CPM and EDM occur as a minority population. In turn, CAM do not have an overt age-specific prevalence and can stably be identified across the lifespan.

Unlike CPM and EDM, HOM-clusters gradually increase in early development, followed by an exponential growth in SIM (P9-P28) (Figure 45). By adulthood, HOM-clusters reach a maximum, after which the populations decrease to approximately 80% of all microglia in old age. Interestingly, the HOM-clusters display a differential maturation profile. HOM2 reach their maximum early in development, concurrent with the rapid expansion of the homeostatic population. In contrast,

HOM3 gradually increases with age, increasing its relative proportion in a declining homeostatic population.

In turn, the loss of HOM-clusters with old age are concurrent with the gains of other phenotypes (Figure 45). AIM form a small yet stable microglial population with aging, whereas IRM and LPM each increase to ~6% in old age. LPM display a bi-modal pattern of occurrence, in which early developmental and late life prevalence suggests biological relevance in each.

Interestingly, on average, AIM, IRM and LPM have lower pseudotime scores than HOM-clusters (Figure 46). Furthermore, HOM3 has the largest variability in pseudotime score, a finding that is supported by the relatively large proportion of middle age microglia and old age microglia in this subtype. Sala Frigerio *et al.* (2019) had previously described TRM, also known as 'transiting response microglia' (Sala Frigerio et al., 2019). It is possible HOM3 describes a similar intermediary microglial subtype, central to maturation and age-associated loss of microglial identity.

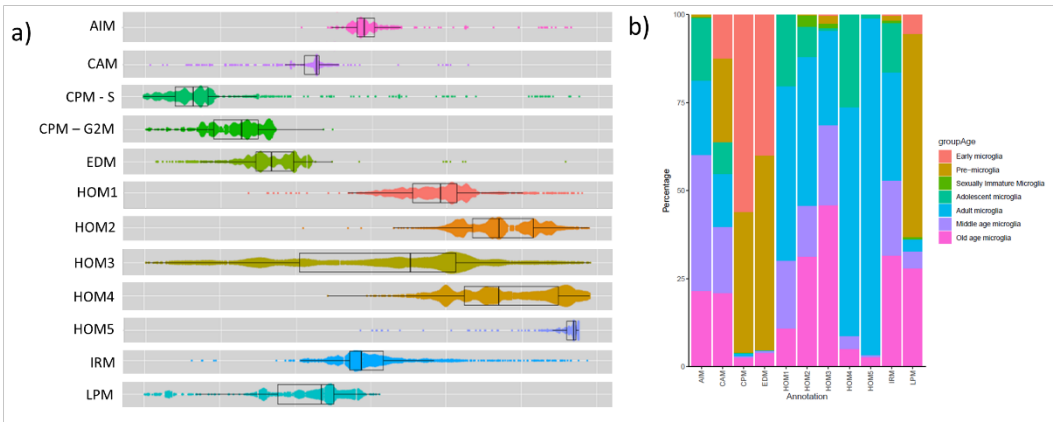


*Figure 46: Homeostatic clusters display a higher pseudotime score. a) Boxplots of the major 11 microglial and CAM clusters for their pseudotime scores. Variations in score are evident. b) Barplot of cluster distribution by age group. AIM, Aged Inflammatory Microglia, CAM, CNS-associated macrophages; CPM, cycling and proliferating microglia; EDM, early developmental microglia; HOM, homeostatic microglia; IRM, interferon response microglia; LPM, lysosome pathway-associated microglia. Early microglia (<E14), pre-microglia (E14-P9), sexually immature microglia (P9-P28), adolescent microglia (P28-P60), adult microglia (P60-6M), middle age microglia (6M-18M), old age microglia (>18M). P, postnatal day; M, months old*

Taken together, acquisition of a mature microglial identity finds its origin in early developmental clusters like CPM, EDM and LPM (Figure 45). The maturation of microglia is concurrent with an increased pseudotime score, which is reduced with the emergence of age-associated subtypes like AIM, IRM and LPM (Figure 46). Strikingly, the occurrence of LPM in early development and late life implies that this phagocytic microglial subtype is a marker of dysbiosis; in which LPM functions to establish homeostasis. Moreover, the transcriptional similarities of PAM, ATM and DAM, elude that such microglia are each states within the umbrella of the LPM subtype (Figure 34, Figure 35, Figure 36).

### 3.4.4 No overt region-specific signatures were detected

Microglial region-specific signatures have been a debated concept in the single-cell literature. Here, no region-specific enrichment was evident in the clusters (Figure 47). Most cells derive from whole brain (WB) samples, possibly introducing a source data bias against the identification of such effects. Moreover, simple differences in population dynamics might explain bulk RNA-seq transcriptional heterogeneity, where scRNA-seq might be lacking. In short, the analyses were not designed to resolve this debate. Albeit a moderate enrichment of yolk sac (YS)-derived microglia in cluster 11 (*i.e.* CAM) was noted, as well as an enrichment of neutrophils in the spinal cord (Figure 47, Supplementary Figure 8).

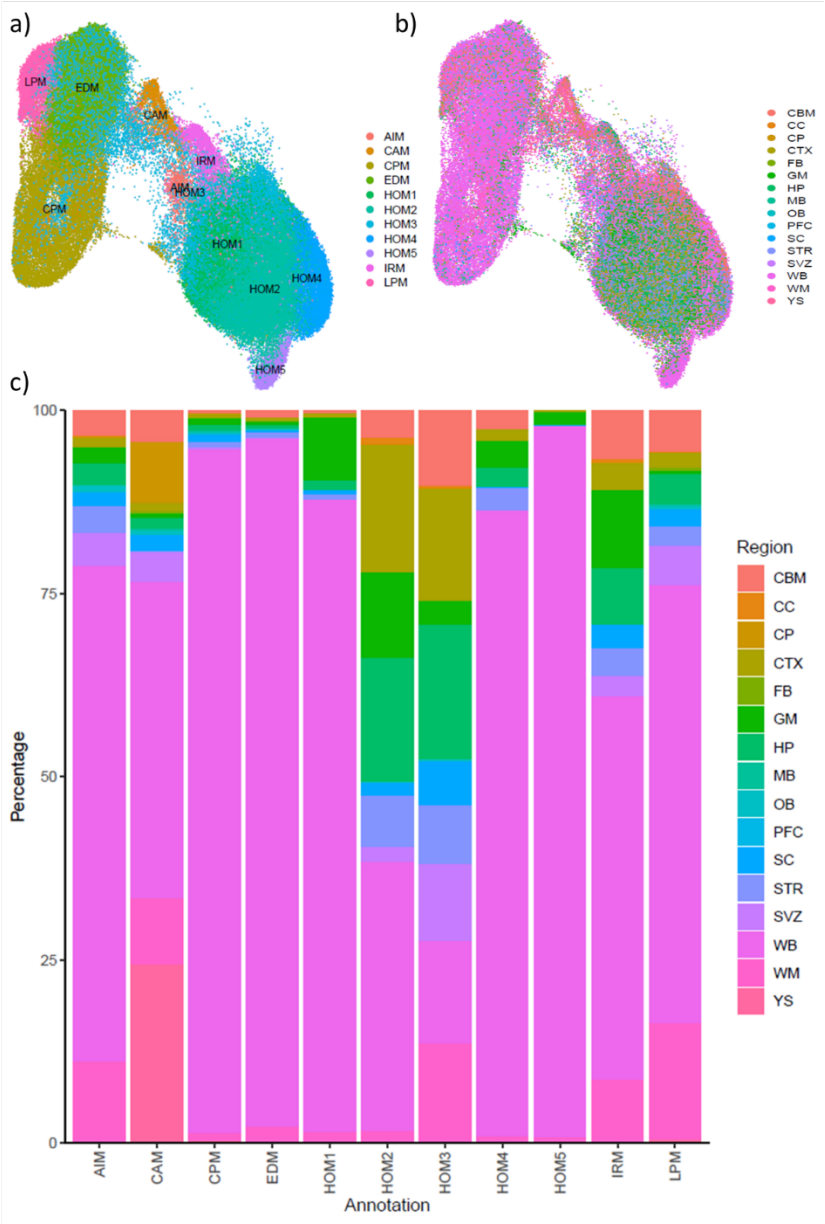


*Figure 47: Regional cluster identities. Cluster identities derive from a diverse range of regions and do not illustrate any region-specific clusters, albeit a relative enrichment of yolk sac (YS) microglia can be seen in cluster 11. AIM, Aged Inflammatory Microglia, CAM, CNS-associated macrophages; CPM, cycling and proliferating microglia; EDM, early developmental microglia; HOM, homeostatic microglia; IRM, interferon response microglia; LPM, lysosome pathway-associated microglia. CBM, cerebellum; CC, corpus callosum; CP, choroid plexus; CTX, cortex; FB, forebrain; GM, grey matter; HP, hippocampus; MB, midbrain; OB, olfactory bulb; PFC, prefrontal cortex; SC, spinal cord; STR, striatum; SVZ, subventricular zone; WB, whole brain; WM, white matter; YS, yolk sac.*

CAM, a macrophage population featured by the expression of a.o. *Cd74*, *Pf4*, *Dab2*, *Apoe and Mrc1*, were discussed previously *(*Figure 29*,* Supplementary Table 2*).* In fact, markers (with an avg_log2FC over 1.5) in cluster 11 greatly overlapped with YS markers *(*Supplementary Table 11*)*. Moreover, the absence of *P2ry12*, *Tgfbr1* and *Tmem119* expression in CAM was noted (Figure 42). Such findings further support their shared ontogeny and subsequent divergent differentiation. Moreover, it provides an argument against regional specific signatures, where microglial subtypes are distributed across the CNS.

### 3.4.5 Microglial maturation and sex-specific heterogeneity

Several studies have reported sex-specific effects in microglia, including those supporting distinct transcriptional signatures, functions and maturation trajectories (Guneykaya et al., 2018; Hanamsagar et al., 2017; Villa et al., 2018). However, most studies report on male mice and prevent such comparisons, or fail to report on sex all together, a feature that was causal to an unequal distribution of sexes in the dataset; a total of 28,740 cells were annotated as female, 66,569 as male. This uneven distribution is best visualized in cluster 10 (*i.e.* HOM5), where most cells derive from male cells (Figure 48). Of note, HOM5 (*i.e.* cluster 10) is disproportionally enriched for male 3.5M old cells (~95%), more than what the sex distribution at this age would predict (13,680 of 22,031 cell are male at this age; ~62%) (Figure 48, Supplementary Table 12). Interestingly, most of these cells derive from Hammond *et al.* (2019). Cluster 10 is featured by typical homeostatic microglial markers, perhaps to a more defined level, and corresponds to a higher pseudotime score (Figure 40, Figure 46). Sample collection, tissue processing, as well as cluster parameters can each play a role in the cluster identification.

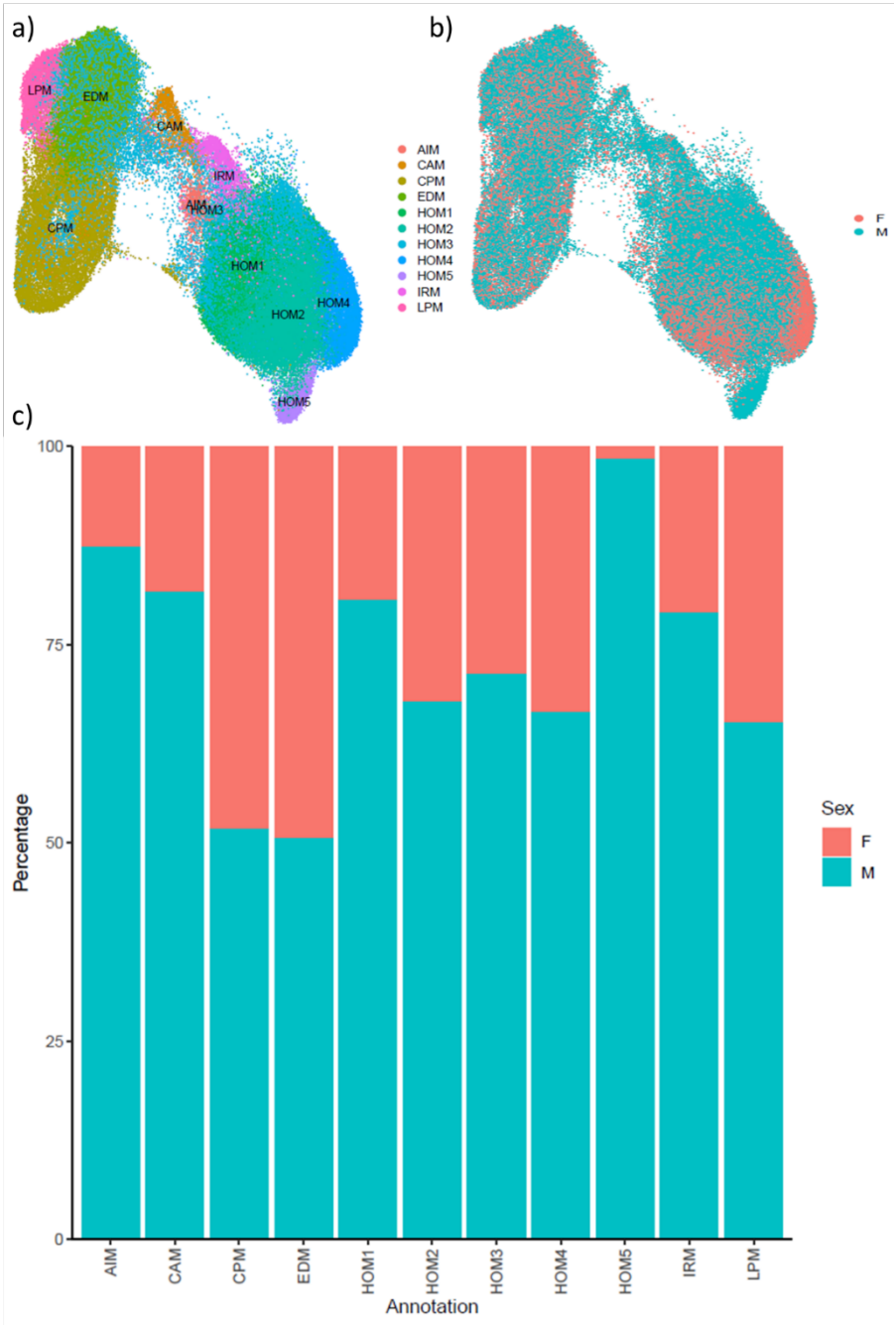


*Figure 48: Sex is distributed unevenly across the cluster identities. Female- and male-specific microglia percentages differ in the single-cell atlas, with greater numbers of male microglia. Uneven distributions are most pronounced HOM5.*

To move beyond this limitation, a trajectory inference was performed of sex-specific cells in an age-dependent manner (Figure 49). As it became evident in previous analyses, there is a lack of available data in SIM, in the transition of pre-microglia (E14.5 – P9) to adolescent microglia (P28 – P60). However, a unique convergent and divergent maturation pattern was found between male and female cells across the lifespan (Figure 49). From a shared developmental pseudotime score, female microglia mature faster to P90, scores converge at 3.5M, to diverge once more in old age (21M) (Figure 49).

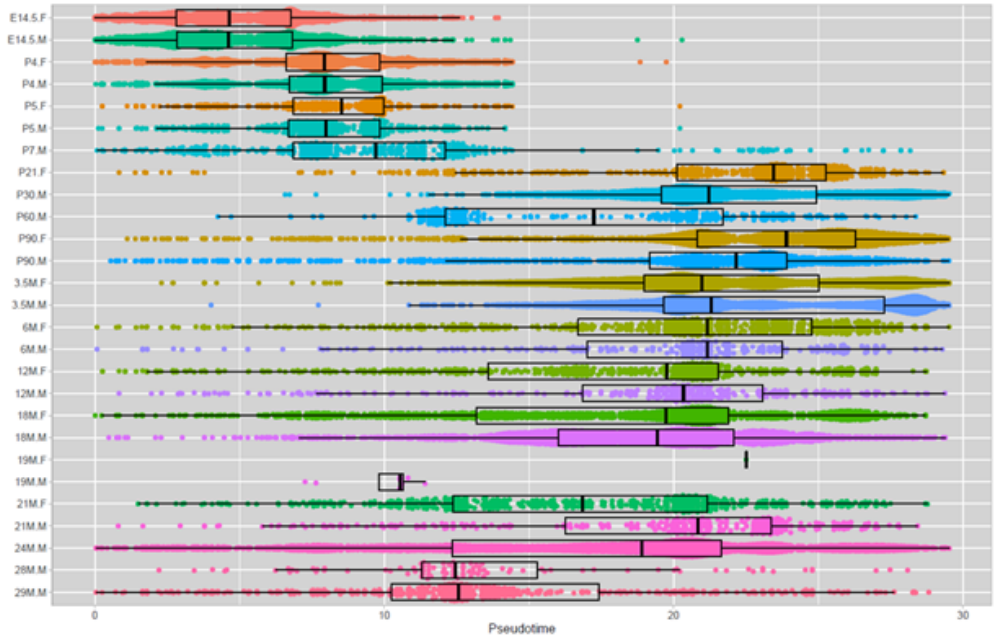


*Figure 49: Microglial maturation varies in a sex-specific manner. Female and male microglia display distinct maturation trajectories, where female microglia start to display a greater degree of maturation from P5, to equilibrate around at 3.5M old.*

To further the understanding of sex-specific maturation, I created a subset of key age groups (excl. cluster 7, 11, 12 and 14). E14.5, P4, P90, 3.5M, 6M, 18M and 21M were selected, as these capture the convergent and divergent behaviour described previously. These ages naturally have a more balanced sex-distribution than in the complete atlas, although more male cells were evident in both 3.5 and 18M and cluster-specific enrichment is noted. See Supplementary Table 12 for a 3-way contingency table of cell number based on age, sex, and cluster.

DGE-analysis of the age groups in a sex-specific manner identified key genes that varied along the lifespan (Figure 50). Interestingly, apart from the expression of *Xist* –an X-chromosome inactivation genes specific to females - no pan-sex differential genes were detected. That is, gene expression signatures vary by age group, sex, and cluster (Figure 50).

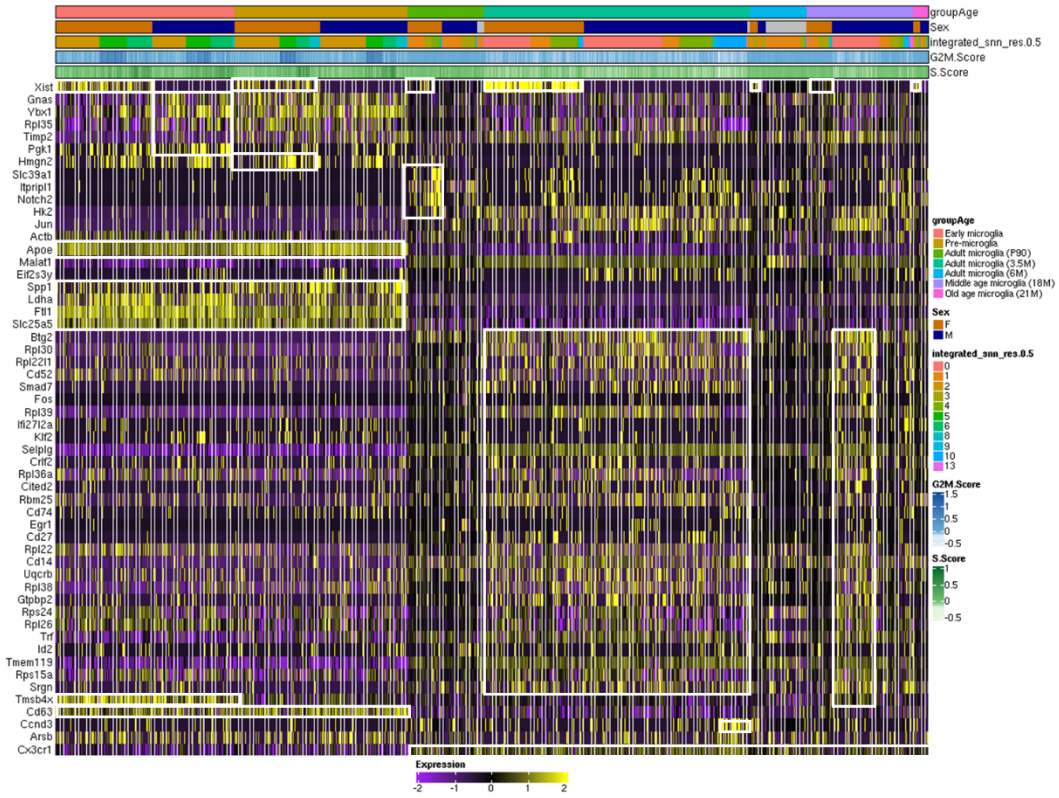


*Figure 50: Sex-specific differentially expressed genes in group ages. Heatmap of age group specific genes differentially expressed between sexes. Key genes are annotated with a white rectangle, to illustrate the sex, age, and cluster in which they are expressed.*

Early on in development, a typical gene signatures was identified that includes the expression of *Apoe*, *Spp1* and *Cd63*, consistent with findings in the large-scale atlas (Figure 33). Interestingly, early microglia also express *Tmsb4x*. This gene has previously been discussed as a lysosomal pathway-associated gene in the principal component analysis (PC20) (Supplementary Figure 4).*Tmsb4x* has also been described as a typical gene enriched in single-cell relative to single-nuclei RNA-sequencing (Gerrits et al., 2020).

Once mice have reached 3.5M old, both male and female microglia take on a broad gene signature. At first glance this includes microglial markers like *Tmem119* and *Selplg*, and a variety of ribosomal genes such as *Rpl30*, *Rpl22l1*, *Rpl39*, *Rpl36a*, *Rpl22*, *Rpl38*, *Rps24*, *Rpl26* and *Rps15a*. *Metascape* analysis shows that these genes encode proteins that enable SRP-dependent co-translational protein targeting to the cell membrane (Figure 51).

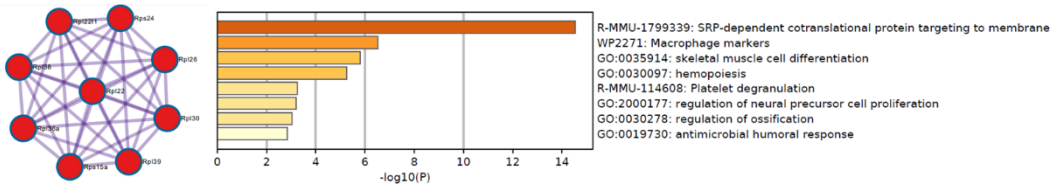


*Figure 51: Protein-protein interaction network and gene enrichment of adult microglia.*

This finding is not directly of importance; however, this same gene signature is upregulated once more in middle age, male microglia, without an equivalent in female microglia. Moreover, it is specifically enriched in cluster 0 (*i.e.* HOM1), and extended by the expression of *Tmsb4x*, hinting at

a male-specific transcriptional program. Similarly, cluster 10 (*i.e.* HOM5) showed an expression of *Ccnd3*, a gene typically associated with cell cycle, but one that has previously been ascribed to sex-specific microglial maturation and immune function (and the role of microbiota) (Erny et al., 2015; Thion et al., 2018).

What became evident is that differences in male and female maturation corresponds to distinct population dynamics throughout life (Figure 52). Indeed, AIM, and IRM in middle age (18M) male mice are elevated, as are LPM in old age (21M) females. Furthermore, female HOM-clusters gradually reduce in prevalence with age, whereas males remain broadly stable.

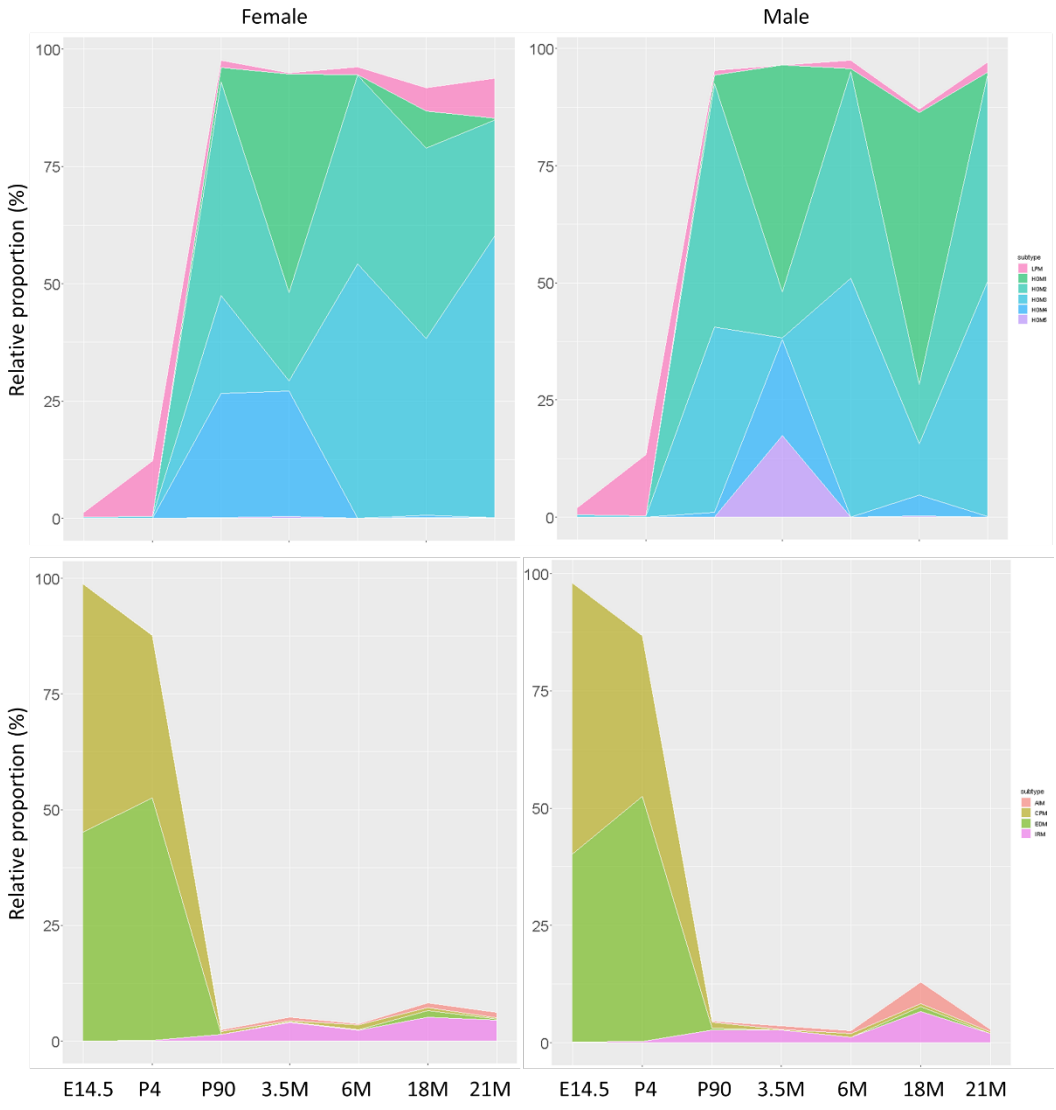


*Figure 52: Sex-specific population dynamics across the lifespan. Relative proportions of female and male microglial subtypes differ, where female have a greater increase of LPM in old age, male display greater proportions of AIM and IRM by middle age. AIM, Activated Inflammatory Microglia; CPM, cycling and proliferating microglia; EDM, early developmental microglia; HOM, homeostatic microglia; IRM, interferon response microglia; LPM, lysosome pathway-associated macrophage.*

Furthermore, the prevalence of HOM-clusters varies in a sex-specific manner (Figure 53). Over the course of the lifespan, both sexes take on a HOM3 subtype at E14.5 and P4. However, from P90 onwards the first differences emerge; albeit HOM1 and HOM2 have similar proportions in both sexes, approximately 30% of female microglia take on a HOM4 state. In contrast, male microglial

development is protracted, acquiring HOM4 (and HOM5) at 3.5M. Similarly, by middle age (18M) male microglia have a larger diversity of HOM-clusters than female cells and are featured by a relative increase in HOM1. Moreover, HOM3 increases with age in both sexes, although male microglial increases are tempered by the concurrent increases of HOM1 and HOM4. Follow up research is needed to ascertain if HOM3 is indeed as an intermediary or transitory microglial state, and how and if these cells can be targeted for therapeutic intervention.

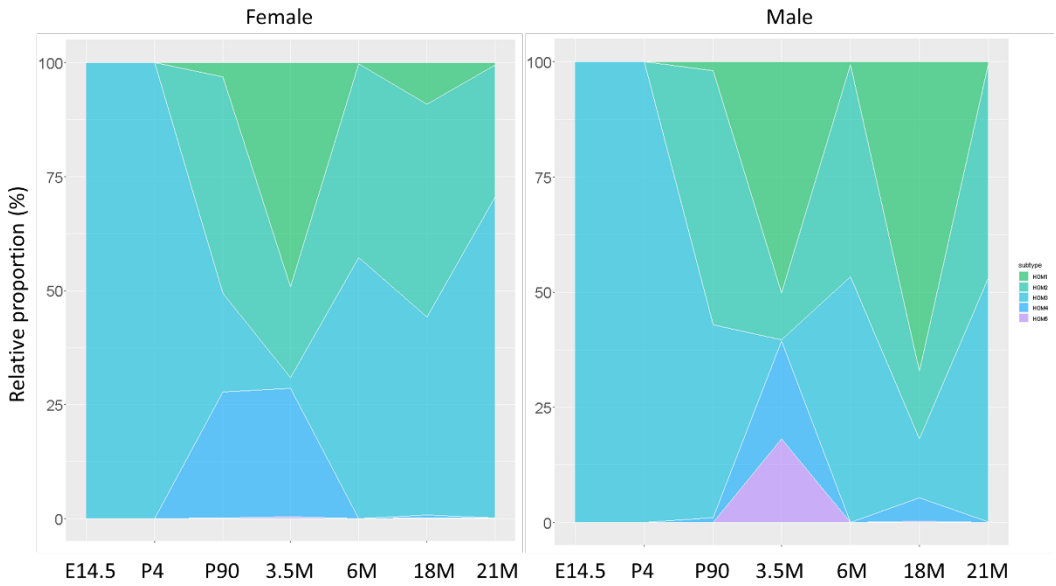


*Figure 53: Population dynamics of HOM-clusters in a sex-specific manner. Female and male homeostatic (HOM)-clusters have different proportions across life. Greater diversity is typically seen in male cells, concurrent with a protracted development to a high pseudotemporal score (HOM4, HOM5).*

Taken together, the analyses indicate that male and female transition through the different clusters using different temporal trajectories, but they do not have unique microglial subtypes. The male microglial population displays a protracted development and greater homeostatic heterogeneity. This in fact suggests that there is a male-specific cluster in the atlas. Such effects could aid the understanding of age-associated disease susceptibility in females; however, it should be noted that these effects are small and require reproduction *in situ*.

## 3.5 Discussion

Here, an atlas of microglial heterogeneity in health was generated that includes cycling and proliferating microglia (CPM), early developmental microglia (EDM), interferon response microglia (IRM), lysosome pathway-associated macrophage (LPM), age inflammatory microglia (AIM), and *ex vivo* activated microglia (*ex*AM). Moreover, it was found that age is the largest driver of microglial heterogeneity in health, without overt transcriptional dynamics driven by CNS region. Age and sex intersect to drive sex-specific maturation, microglial heterogeneity, and population dynamics. Before addressing the microglial clusters in detail, I will bring to light some of the intrinsic limitations and caveats-associated with these analyses.

### 3.5.1 Technical limitations on biological heterogeneity

Technical variables can impose limitations in the discrimination of biologically relevant transcriptional heterogeneity. In the analyses, several bioinformatic tools were utilized that each have features that could restrain discovery. 3 considerations are made, not to diminish the value of the results, but to provide a context in which these results were acquired.

First, Monocle 3 is a tree-based approach; that is, it does well with tree-like lineage structures (Cao et al., 2019; Saelens et al., 2019). Monocle 3 lacks the ability to reconstruct more complex graph-based structures. I do not anticipate this to affect the findings, albeit it is important to recognize the potential limitations of such a choice. A trajectory was identified that allowed for the identification of an age-dependent microglial maturation profile in old age that features a loss of microglial identity, sex-specific divergence of maturation, and cluster-specific pseudotime scores. In light of that, a connected graph-based method like PAGA would be the most appropriate method for trajectory inference (Saelens et al., 2019). Not having done so could have restricted the ability to detect further complex interactions.

Second, *ex*AM were present in the integrated dataset, the effects of which I choose not to remove from the dataset (by regression or gene exclusion), to provide a fair representation of transcriptional heterogeneity in scRNA-seq data. Cluster 9 in the data was enriched for *ex vivo*-activated gene signatures, corresponding to established gene lists describing such features. The association of these signatures with Tgf-ß signalling in *ex*AM, and early developmental Tgf-ß signalling for the acquisition of an adult microglial identity, suggests that such effects are intrinsic to microglia. In fact, identification of *ex*AM with a gene list provided by Li et al. (2019) underlines this, reaching far beyond cluster 9 and into homeostatic clusters. Removal of such effects by regression might therefore affect true biological heterogeneity. It would be interesting to explore the causal factors behind artefactual gene signatures (if these become a prohibitive factor).

Third, Svensson *et al.* (2020) find that the number of identified subtypes in an atlas is proportional to the number of cells in it (Svensson et al., 2020). In the dataset, the minimum fraction were neutrophils (cluster 14). However, looking at the myeloid clusters alone, the argument can be made that the rarest fraction is AIM (cluster 13); 907 AIM cells were identified amongst 113,689 cells in the atlas, which equates to <1% of the total. Furthermore, 5 distinct clusters of homeostatic microglia were identified. Together, the identification of AIM and the presence of HOM heterogeneity provides an argument for the relative stability of the atlas. That is, if such states can be reliability detected with known markers, smaller populations that might have been missed are not expected to have a large biological role in healthy aging.

In fairness, selecting a resolution of 0.5 (or 20 dimensions) in an atlas of this size is remarkable. Many other studies using less cells have used a higher resolution (Hammond et al., 2019; Kracht et

al., 2020). This would extract more information out of the atlas. This would increased the number of cluster in the atlas defined here too, yet by not doing that, I was able to define clusters reliably. In fact, it strengthens the claim pertaining to the transcriptional similarities of DAM, PAM and ATM.

### 3.5.2 DAM, PAM and ATM are collectively described by a common gene signature

Cluster 8 is enriched with genes commonly ascribed to DAM, PAM and ATM, including *Csf1*, *Lpl*, *Spp1*, *Igf1*, *Gpnmb*, and *Apoe.* This core set of genes is found in all three cell types and are typical markers for *in situ* hybridization of such cells, in parallel to probes for Cd11c (Itgax) and Clec7a (Hammond et al., 2019; Keren-Shaul et al., 2017; Li et al., 2019; Safaiyan et al., 2021). This has led me (and others before me) to argue for a more integrative nomenclature in the field of scRNA-seq (Benmamar-Badel et al., 2020).

Benmamar-Badel *et al.* (2020) annotate DAM, PAM ATM collectively as $Cd11c^{+}$ microglia, effectively forming a bridge between their previous work and others (Benmamar-Badel et al., 2020; Kamphuis et al., 2016; Keren-Shaul et al., 2017; Wlodarczyk et al., 2017). However, for nomenclature to be reflective of function, as well as the multi-dimensional nature of microglial identity, I would like to argue that these phagocytic cells are collectively best described as 'lysosome pathway-associated macrophage' or LPM.

DAM, PAM and ATM are each ascribed a protective role and occur throughout development, aging and disease. In addition, recent work identified white matter-associated microglia (WAM) in the aging brain; and lipid-associated macrophages (LAM) in adipose tissue (Jaitin et al., 2019; Safaiyan et al., 2016). Each subtype (in the CNS or periphery) is thought to be phagocytic and essential for lipid metabolism. Taken together, it is highly likely that LPM describe a family of closely related myeloid states, taking on a distinct (nuanced) signature depending on the context (*e.g.* age, disease, sex). Indeed, despite their transcriptional similarities, there have been reports of varying dependencies on *Trem2* and *Apoe,* key regulators of age-associated disease as well as early development (Butovsky et al., 2014; Jaitin et al., 2019; Keren-Shaul et al., 2017; Safaiyan et al., 2021).

*e.g.*, PAM in early development are independent of *Trem2* and *Apoe*, whereas WAM with aging are independent of *Apoe* alone (Li et al., 2019; Safaiyan et al., 2021). In contrast, to acquire an LMP signature, microglia and macrophages rely on *Trem2* and *Apoe* depending on which state these cells are in (Jaitin et al., 2019; Keren-Shaul et al., 2017). Regardless, the TREM2-APOE signalling pathway is central to LMP signature acquisition.

Interestingly, there have been reports that dysfunction of DAM-like cells was associated with lipid droplet accumulations (Baik et al., 2019; Krasemann et al., 2017; Marschallinger et al., 2020; Ulland et al., 2017). Furthermore, some (but not all) DAM undergo replicative senescence in AD in humans

and mouse models (Hu et al., 2021). Together, these studies outline a context-specific diversification of the LPM family not evident in healthy aging. As always, microglia appear to be a population of cells with distinct responses and responders (Gertig and Hanisch, 2014).

### 3.5.3 Age-dependent microglial heterogeneity and population dynamics

Age is the main driver of microglial heterogeneity. Early in CNS development, three typical subtypes can be identified: EDM, CPM, LPM. Each of these subtypes have their largest prevalence in early development, albeit LPM is an exception to that rule, where age increases their prevalence once more. Of note, the increase of LPM, as well as IRM and AIM, is concurrent with a proportional decline of homeostatic signatures with age. The loss of HOM clusters might underlie a biologically and clinically relevant finding.

Age brings about neuroinflammation and susceptibility to diseases like AD, Parkinson's disease (PD) and MS (Von Bernhardi et al., 2015). Microglia are central to changes to the CNS immune environment and are known mediators in each of these diseases. Changes to the microglial population are therefore indirectly linked to healthy aging. A loss of microglial identity towards a more inflammatory subtype (*e.g.* AIM, IRM, LPM) might be functionally necessary; however, as discussed, transcriptional diversification, cell lipid stress and replicative senescence could abrogate effective cellular responses to tissue damage accrued with disease (Baik et al., 2019; Hu et al., 2021; Krasemann et al., 2017; Marschallinger et al., 2020). In fact, LPM might be of particular importance.

The family of LPM consists of a plethora of distinct microglial and macrophage subtypes, including LAM, DAM, WAM, ATM, PAM, MGnd and ARM. As a family, LPM interact broadly (and to different degrees) with the TREM2-APOE pathway and are associated with late-onset AD risk factors. In the atlas, LPM are enriched for AD-risk factors in early life, as well as in old age. In fact, early developmental and old age expression of *Apoe* appear to have an inverse relationship with homeostatic signatures.

Interestingly, the CNS immune environment in early development is relatively quiescent compared to old age (Mogilenko et al., 2022). That is, the environment in which *Apoe* functions differs between age groups, potentially affecting its subsequent transcriptional diversity. Microglia are known to be regulated by autocrine and paracrine signalling, among which in communication with neurons and astrocytes (Matejuk and Ransohoff, 2020; Szepesi et al., 2018). Furthermore, microglial LRRC33 is a TGF-ß1 -associated molecule that establishes a milieu in which microglial homeostasis is acquired and maintained only after interactions with integrin aVb8-bearing cells (*e.g.* astrocytes, OPC, oligodendrocytes), for a highly localized and self-propagating cascade of microglial identity (Qin et al., 2018). Absence of such interactions increased microglial reactivity and myelopathy, clearly outlining the importance of microglia to be in interaction with their

environment. By extension, it would be interesting to explore if there are substantial interactions between microglia in healthy aging, *e.g.* between IRM and LPM. scRNA-seq tools like Cell Chat are well within this functionality (Jin et al., 2021). Regardless, if cell-cell interactions are critical to microglial identity, loss of sensome genes with age would impinge on microglial homeostasis. Furthermore, variations in such environment- or region-specific support signals could instil regional heterogeneity.

### 3.5.4 No regional heterogeneity was detected in the atlas

Region-specific microglial heterogeneity has long been an established factor in humans and mice, with reports of epigenetic, transcriptional, translational and metabolic diversity throughout the CNS (Askew et al., 2017; Ayata et al., 2018; Böttcher et al., 2019; De Biase et al., 2017; Grabert et al., 2016; Hart et al., 2012; Lawson et al., 1990; Lopes et al., 2022). However, Li *et al.* (2019) argues against the presence of such diversity. Here, the authors failed to detect regional transcriptional heterogeneity with scRNA-seq and RNA-seq. At first glance, no regional heterogeneity in healthy aging was detected, as there are no clusters specific to the CTX, CB, HIP, or any of the other regions included in the dataset. However, given the wide-spread evidence of regional heterogeneity (across modalities), it is important to understand why no such effects were identified with scRNA-seq.

First, inroads have been made to increase the understanding how transcriptional heterogeneity gives rise to the microglial population. Of note, distinct population dynamics in male and female cells were shown. Considering that, and reflecting on the bulk RNA-seq study by Grabert *et al.* (2016), it is highly likely the reported divergence of regional transcriptional heterogeneity with age was driven by distinct microglial populations. This then begs to question, why did Li *et al.* (2019) not find such heterogeneity in their bulk RNA-seq work? To start, the age of the animals used differed between the studies; P60 mice for Li *et al.* (2016), where Grabert *et al.* (2016) make use of animals that are 4, 12 and 22 months old (Grabert et al., 2016; Li et al., 2019). I have shown that age is the main driver of heterogeneity, and such experimental differences are expected to play a role. To continue, Li *et al.* (2019) isolate and sequence a relatively small population of cells, which effectively informs on microglial states like CPM, but might fall short in identifying large-scale population dynamics and microglial subtypes. To truly address transcriptomic, regional heterogeneity, it will be important to employ spatial transcriptomics and histology of well-established microglial markers in a targeted manner.

Second, some form of regional heterogeneity in the healthy CNS is evident. LPM and IRM cells were identified in the atlas, each of which has been reported to be enriched in white matter tissues (Hammond et al., 2019; Li et al., 2019; Sala Frigerio et al., 2019). *Csf1*, *Spp1* and *Gpnmb* are commonly used to identify LPM in early development, whereas IRM express *Usp18*, a gene which encodes a protein in white matter microglia (Goldmann et al., 2015; Hammond et al., 2019; Li et

al., 2019). Although there have been reports that these cell types could in fact be transcriptionally similar, the data reported here suggests that LPM and IRM are transcriptionally distinct populations in correspondence with Sala Frigerio *et al.* (2019) (Hammond et al., 2019; Sala Frigerio et al., 2019). Indeed, LPM and IRM feature different levels of *Apoe* expression; high and low *Apoe* expression, respectively. Currently there is not answer how *Apoe* in LPM corresponds to an independence of *Apoe* in PAM and WAM.

Looking at regional heterogeneity beyond the grey- and white- matter, no further tissue-specific heterogeneity was identified apart from a minor enrichment of YS-derived cells in CAM (*i.e.* cluster 11). As stated, it is likely that this enrichment is due to the transcriptional similarities within the myeloid lineage (Mass et al., 2016). The absence of any further findings might originate due to bioinformatic limitations.

In the generation of the single-cell atlas 3000 variables were selected and retained. This is a default parameter in the 'SelectIntegrationFeatures' function. Furthermore, prior to that, 2000 genes variable genes are selected with 'FindVariableFeatures' in each individual dataset. Albeit these settings reduce computational requirements and increase the identification of major sources affecting heterogeneity, it could confound the detection of smaller factors like region and sex.

In the dataset, a large-scale age-specific effect on microglial heterogeneity was identified. The size of this effect might simply mean that there is no 'resources' left to identify other context-specific effects. That is, if most of the transcriptional signatures are driven by age, a minority effect will be less evident. To circumvent such limitations, researchers need to ensure such effects are not selected against in their bioinformatic pipeline. Similarly, although a large range of tissues was included in the atlas, none have the same prevalence as WB-derived cells. This imbalance is expected to introduce biases in the subtype and state identification.

A point of interest, recent work by Seeker *et al.* (2022) identified regional glial heterogeneity in the normal human white matter of the CNS. Using snRNA-seq, the authors find distinct microglial transcriptional signatures in the CTX, CB, and cervical SC (Seeker et al., 2022). Relative to the CB and CTX, the cervical SC has an increased expression of HIF1A, and a higher expression of histocompatibility-associated genes, reminiscent of the findings by Grabert *et al.* (2016) (Grabert et al., 2016a; Seeker et al., 2022). In fact, it matches to and underscores the potential role of population dynamics in the identification of such region-specific signatures. Moreover, upregulation of HIF1A in microglia has been shown to increase AD-associated neuropathology, and in turn, associates with an origin of such pathology in the white matter (Hahn et al., 2022; March-Diaz et al., 2021; Safaiyan et al., 2021).

### 3.5.5 Microglial heterogeneity during sexual maturation is understudied

Regarding sex-specific heterogeneity, similar arguments apply as those use for region specificity, where bioinformatic parameters, methods and cellular distribution are expected to influence the outcome. Although literature has started to explore sex-specific heterogeneity, scRNA-seq data that includes both male and female remains sparse, often only male tissues are used. In the atlas, the sex imbalance is clearly visible and across all annotated subtypes. On average, male and female cells are at a ratio of 2:1. Fortunately, the failure to sex-match research is a recognized problem in biomedical science and drug development, one which is increasingly addressed (Ravindran et al., 2020; Zucker and Beery, 2010). However, in contrast to regional effects, the size of the atlas and the bimodal nature of sex allowed furher study of the effects of sex on microglial maturation. Indeed, preliminary analyses of sex-specific heterogeneity have shown that male and female microglia age differentially.

Distinct pseudotemporal trajectories were identified between male and female microglia, with female cells progressing faster to a mature microglial identity; consistent with male and female cells having a different microglial developmental index (MDI), terminology first introduced by the group of Staci Bilbo, and in correspondence with other studies reporting on sex-specific microglial heterogeneity (Guneykaya et al., 2018; Hanamsagar et al., 2017; Thion et al., 2018; Villa et al., 2018).

Interestingly, microglial age group-specific differentially expressed genes (DEG) were detected. Most strikingly, adult (3.5M) male and female microglia express a gene signature that is enriched for typical microglial markers like *Tmem119* and *Selplg*, as well as several ribosomal-associated transcripts. GO analysis with *Metascape* showed that the ribosomal transcripts form a protein-protein interaction network, a network of transcripts that could stimulate cell membrane protein targeting. Of importance, the expression of this signature is concurrent with the sensome signature and by extension MDI. Pseudotemporal scores and DEG follow a similar pattern. Remarkably, once microglia reach middle age, male microglia retain this signature enriched for ribosomal markers in a cluster-specific manner, whereas female cells lose it. Furthermore, the signature in middle age microglia is restricted to cluster 0 (*i.e.* HOM1), outlining the differences in population dynamics between the sexes. Moreover, the absence of the ribosomal signature in female cells precedes the loss of HOM-clusters and the proportional increase of LMP in old age microglia.

Taken together, female microglia mature faster towards an adult microglial signature; however, female cells also lose this identity at an earlier age and display a greater predisposition to age-associated disease (Pinares-Garcia et al., 2018). In contrast, males undergo a protracted development and are more susceptible to early developmental diseases like autism and schizophrenia (Pinares-Garcia et al., 2018). Such findings imply that there is a biological trade-off

between fast and slow maturation, where microglial health is a finite resource throughout the lifespan (Figure 54).

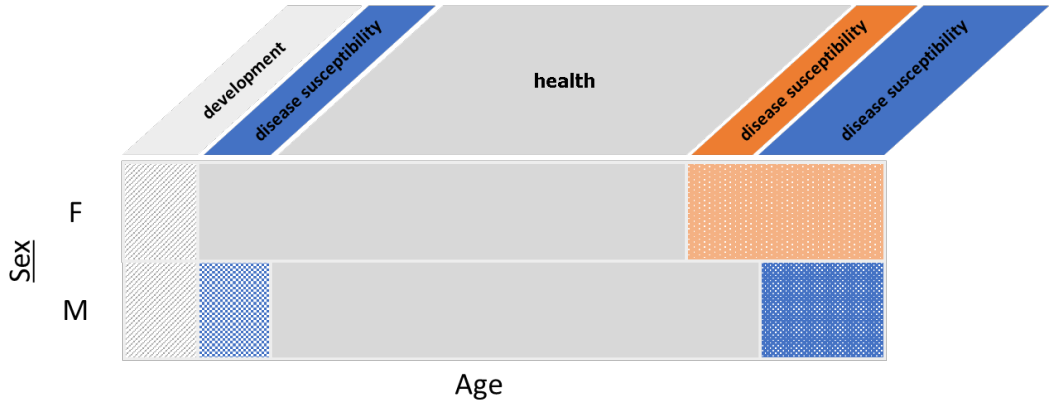


*Figure 54: Hypothetical model of sex-specific early and late life disease susceptibility. Female microglia mature faster than male microglia, leaving males prone to early developmental disease, whereas females display a greater propensity to age-associated disease. In this model, microglial fitness is finite in both sexes.*

### 3.5.6 Summary

In summary, the single-cell atlas was particularly well-suited for the identification of age-specific effects on microglial heterogeneity. Age is the largest driver of microglial heterogeneity during the lifespan, with smaller sex-specific effects, and without region-specific effects.

In this compendium, a conservative approach to subtype identification was taken, consequentially, key microglial subtypes from literature were reliably identified, as well as provided sorely needed simplifications in nomenclature.

The microglial population consists of several transcriptionally unique microglial subtypes, among which AIM, CPM, EDM, HOM, IRM and LPM. Throughout life the prevalence of these six microglial subtypes varies, from what appears to be functional adaptations to biological events like developmental expansion, myelination, and age-associated neuroinflammation. LPM, as a family of microglial subtypes, is postulated to display greater variability with expanding context-dependent drivers of heterogeneity; diversification which is absent in healthy aging.

Lastly, for effects of region and sex on microglial heterogeneity, bioinformatic and experimental workflows need to target such effects to allow for their identification from larger age-specific effects. A study of sex-specific microglial selection in a region-specific manner would help provide a valuable answer currently missing in literature. How does sex-specific disease susceptibility emerge and does microglial selection play a role in that?

## 3.6 Supplementary Figures

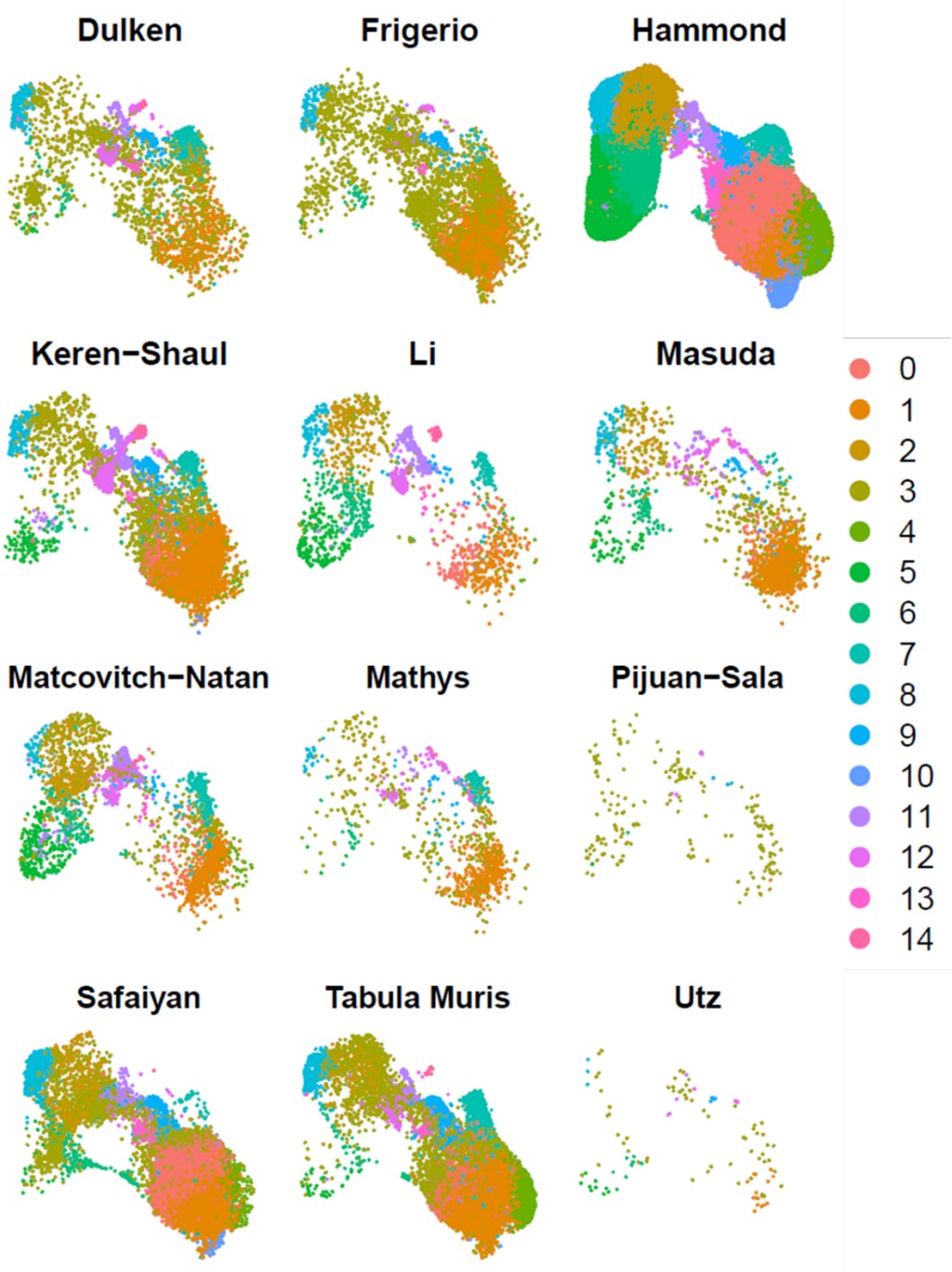


*Supplementary Figure 1: DimPlot of identified clusters and the anchors identified between datasets. 15 distinct clusters (of 113,690 cells) were identified in the integrated single-cell atlas, each with corresponding anchors between clusters across datasets. Clusters in the integrated object were identified with 20 dimensions and a resolution of 0.5.*

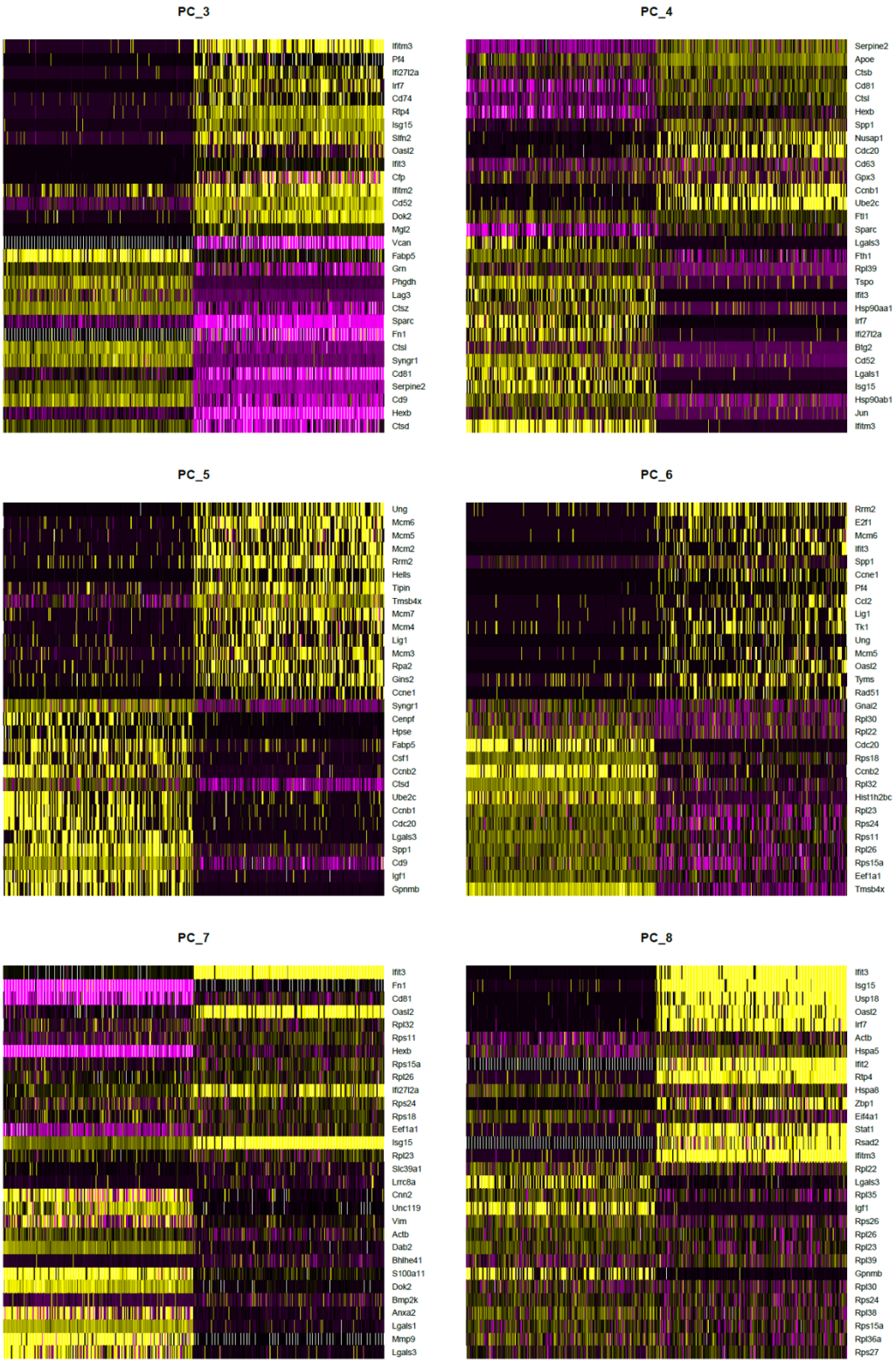


*Supplementary Figure 2: Principal component analysis (2). Principal component (PC) 3 to 8 are visualized, illustrating their respective gene sets.*

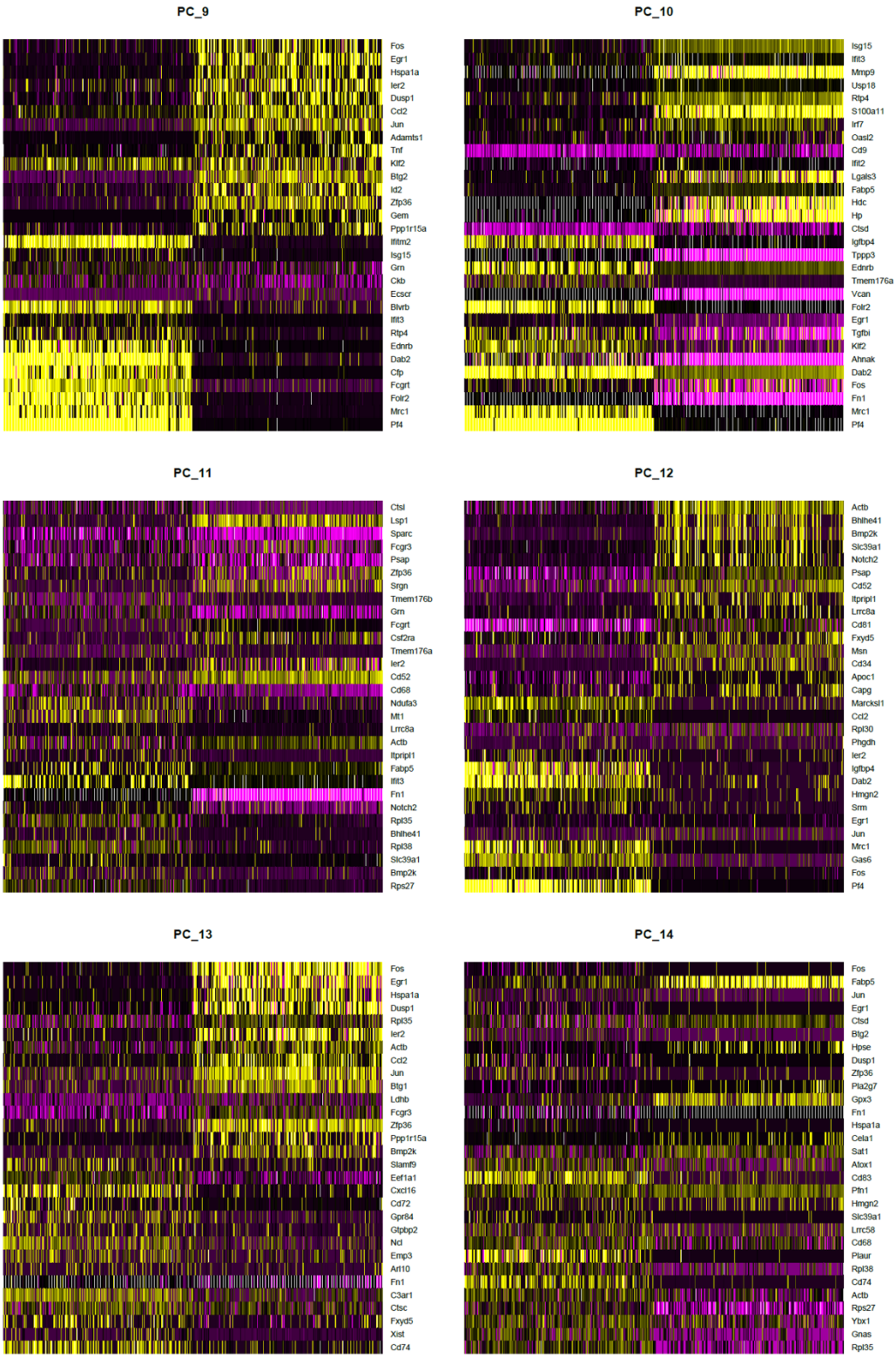


*Supplementary Figure 3: Principal component analysis (3). Principal component (PC) 9 to 14 are visualized, illustrating their respective gene sets.*

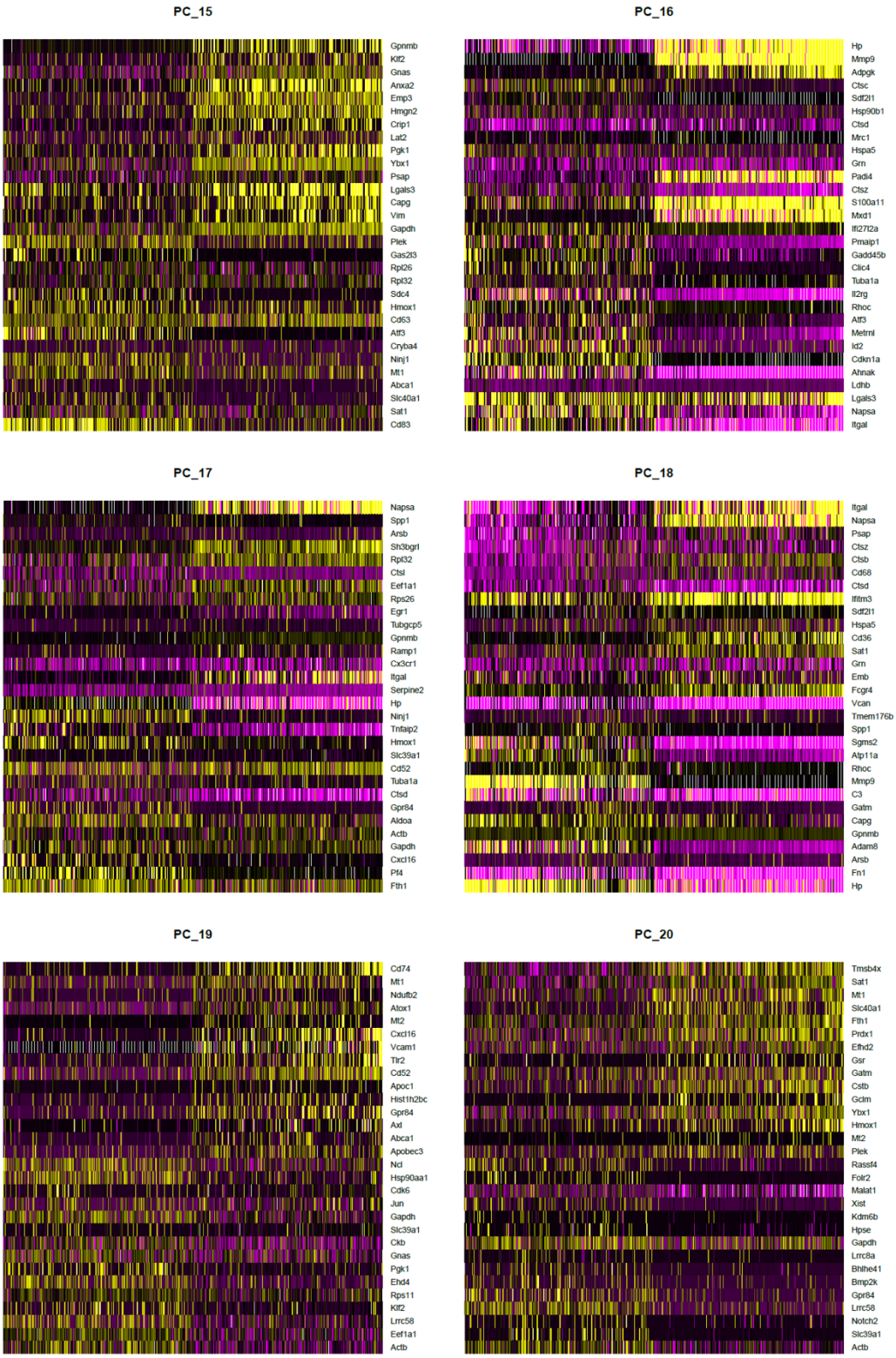


*Supplementary Figure 4: Principal component analysis (4). Principal component (PC) 15 to 20 are visualized, illustrating their respective gene sets.*

*Supplementary Table 1: Top 50 cluster markers of the single-cell atlas (1).*

| # | **Seurat cluster (*i.e.* integrated_snn_res.0.5)** | | | | | | |
|---|---|---|---|---|---|---|---|
| | *0* | *1* | *2* | *3* | *4* | *5* | *6* |
| 1 | Selplg | Malat1 | Apoe | NONE AVAILABLE | Bmp2k | Ube2c | Fabp5 |
| 2 | Cst3 | Tmem119 | Cd63 | | Bhlhe41 | Birc5 | Ranbp1 |
| 3 | Rpl39 | Fscn1 | Ctsb | | Slc39a1 | Stmn1 | Ldha |
| 4 | Rpl30 | Selplg | Gpx3 | | Itpripl1 | Hmgb2 | Stmn1 |
| 5 | Btg2 | Slc2a5 | Ftl1 | | Actb | H2afx | Ptma |
| 6 | Jun | Ecscr | Npl | | Notch2 | Ccnb1 | Nme1 |
| 7 | Tmem119 | Sparc | Serpine2 | | Lrrc8a | Cdk1 | Ran |
| 8 | Smad7 | Tgfbr1 | Ctsl | | Selplg | Pbk | Rrm2 |
| 9 | Basp1 | Basp1 | Gas6 | | Xist | Ccnb2 | Mcm6 |
| 10 | Tgfbr1 | Sgk1 | Slc25a5 | | Btg1 | Cks1b | Tipin |
| 11 | Hk2 | Cx3cr1 | Cryba4 | | Tgfbr1 | Top2a | Ftl1 |
| 12 | Rpl36a | Pmepa1 | Fcgrt | | Fscn1 | Cdca8 | Eif5a |
| 13 | Pmp22 | Cst3 | Apoc1 | | Hk2 | Cdc20 | Fen1 |
| 14 | Rpl22l1 | Ptgs1 | Plin2 | | Tmf1 | Nusap1 | Tpi1 |
| 15 | Rps27 | Eng | Npc2 | | Tmem119 | Tuba1b | Npl |
| 16 | Slc2a5 | Ccr5 | Ybx1 | | Adrb2 | Cdca3 | Npm1 |
| 17 | Ecscr | Zfhx3 | Clta | | Malat1 | Cdkn2c | Eef1g |
| 18 | Uqcrb | Nrip1 | Rac2 | | Cst3 | Ran | Mcm3 |
| 19 | Rps15a | Lair1 | Mt1 | | Cdk6 | Spc24 | Spp1 |
| 20 | Cd14 | Slc1a3 | Rps19 | | Dhrs3 | Tubb5 | Cdk4 |
| 21 | Malat1 | Lrrc3 | Pfn1 | | Ccr5 | Rrm2 | Slc25a5 |
| 22 | Fam46a | Thrsp | Gatm | | Zbtb38 | Hmgn2 | Gins2 |
| 23 | Klk8 | Trf | Ctsz | | Cx3cr1 | Tuba1c | Aldoa |
| 24 | Rps24 | Pmp22 | Cd68 | | Tnpo3 | Mki67 | Mcm5 |
| 25 | Zfhx3 | Bmp2k | Igf1 | | Zfhx3 | Ranbp1 | Hspa8 |
| 26 | Trf | Fgd2 | Gnas | | Dusp6 | Spc25 | Eif4a1 |
| 27 | Sparc | Klhdc8b | Gltp | | Atf7ip | Aurka | Ung |
| 28 | Hexb | Plod1 | Arpc1b | | Nrip1 | Ptma | Mcm2 |
| 29 | Slc1a3 | Usp2 | Arpc5 | | Mgat4a | Tacc3 | Tyms |
| 30 | Sox4 | Dusp6 | Gpx1 | | Pmepa1 | Asf1b | Cryba4 |
| 31 | Thrsp | Hexb | Pqlc2 | | Sox4 | Smc2 | Gpx3 |
| 32 | Rpl22 | Sqstm1 | Nme1 | | Slc1a3 | Cdkn3 | Plin2 |
| 33 | Ptgs1 | Herpud1 | Rpl35 | | Mbnl2 | Cenpf | Rfc2 |
| 34 | Rpl38 | Frmd4b | Pld3 | | Sgk1 | Aurkb | Mcm7 |
| 35 | Xist | Mgat4a | Capns1 | | Cysltr1 | Tk1 | Prdx1 |
| 36 | Lair1 | Prkab1 | Snx2 | | Pmp22 | Ccna2 | Tubb5 |
| 37 | Cx3cr1 | Mfap3 | Renbp | | Lair1 | Arl6ip1 | Hspd1 |
| 38 | Serpinf1 | Chsy1 | Anxa5 | | Basp1 | Hmgn1 | Gmnn |
| 39 | Calhm2 | Sesn1 | Commd4 | | Dnmt3a | Cenpe | Rpa2 |
| 40 | Susd3 | Tmem86a | Igfbp4 | | Slc40a1 | Racgap1 | Gapdh |
| 41 | Taz | Itpripl1 | Myl6 | | Rps27 | Tpx2 | Pfn1 |
| 42 | Nrip1 | Spint1 | Ckb | | Fkbp5 | Ldha | Rpsa |
| 43 | Tmem86a | Slc46a1 | Lag3 | | Rgl2 | Prc1 | Hmgn1 |
| 44 | Srgn | Spsb1 | Eef1g | | Cd14 | Ddx39 | Marcksl1 |
| 45 | Rpl23 | Nfkbia | Eif5a | | Rpl39 | Kif22 | Lig1 |

| | | | | | | | |
|---|---|---|---|---|---|---|---|
| 46 | Thap3 | Hk2 | Rps5 | | Fgd2 | Tyms | Tuba1b |
| 47 | Ppcdc | Adrb2 | Gipc1 | | Frmd4b | Nme1 | Rfc4 |
| 48 | Garnl3 | Fcgr3 | Hmgn2 | | Tubgcp5 | Eif5a | Lgals1 |
| 49 | Mgll | Mbnl2 | Gmpr | | Sesn1 | Bub3 | Ybx1 |
| 50 | Cd27 | Tpst2 | Uqcrc1 | | Trf | Gpx1 | Ctsb |

*Note: Cluster-specific markers were identified with the 'FindAllMarkers' function of Seurat. FindAllMarkers with 'only.pos = TRUE', 'min.pct = 0.25',' logfc.threshold = 0.25', 'test.use = "wilcox"'.*

*Supplementary Table 2: Top 50 cluster markers of the single-cell atlas (2).*

| # | **Seurat cluster (*i.e.* integrated_snn_res.0.5)** | | | | | | | |
|---|---|---|---|---|---|---|---|---|
| | *7* | *8* | *9* | *10* | *11* | *12* | *13* | *14* |
| 1 | Fos | Spp1 | Ifit3 | Ccnd3 | Cd74 | Ifitm3 | Cd83 | Mmp9 |
| 2 | Jun | Igf1 | Ifitm3 | Zfp36 | Pf4 | Lgals1 | Gpr84 | Ifitm2 |
| 3 | Egr1 | Gpnmb | Rtp4 | Cx3cr1 | Dab2 | Ifitm2 | Tlr2 | Anxa2 |
| 4 | Hspa1a | Lgals3 | Isg15 | Selplg | Apoe | Vim | Cxcl16 | Lgals3 |
| 5 | Btg2 | Apoe | Oasl2 | Ccr5 | Mrc1 | Lgals3 | Id2 | Hdc |
| 6 | Ccl2 | Fabp5 | Ifi27l2a | Lrrc3 | Ifitm3 | Cnn2 | Nfkbia | Hp |
| 7 | Ier2 | Cd63 | Usp18 | Fscn1 | Ifitm2 | Cd74 | Atf3 | Pfn1 |
| 8 | Dusp1 | Ftl1 | Cxcl10 | Tmem119 | Lgals1 | Lsp1 | Tnf | Tspo |
| 9 | Zfp36 | Cd9 | Irf7 | Sgk1 | Ifi27l2a | Tspo | Slc15a3 | Rac2 |
| 10 | Klf2 | Ctsb | Slfn2 | Tgfbr1 | Fcgrt | Napsa | Cd52 | Adpgk |
| 11 | Adamts1 | Ctsl | Stat1 | Pmp22 | Folr2 | Anxa2 | Cxcl10 | S100a11 |
| 12 | Btg1 | Anxa5 | Bst2 | Frmd4b | Snx2 | Emb | Lgals3 | Cnn2 |
| 13 | Ppp1r15a | Plin2 | Lgals3bp | Gpr165 | Mgl2 | Calm1 | Herpud1 | Glipr2 |
| 14 | Klf6 | Gpx3 | Xaf1 | Nrip1 | Blvrb | Arhgdib | Marcksl1 | Mxd1 |
| 15 | Socs3 | Csf1 | Ifit2 | Mgat4a | Cfp | Rps19 | C3ar1 | Adam8 |
| 16 | Dusp6 | Lgals1 | Parp14 | Plxnb2 | Igfbp4 | Arpc5 | Cd14 | Arpc5 |
| 17 | Sgk1 | Cstb | Ly6e | Iffo1 | Bst2 | Rac2 | Arl5c | Syne1 |
| 18 | Bhlhe41 | Pld3 | Tor3a | Arl10 | Ctsc | Cd52 | Cd74 | Pygl |
| 19 | Tnpo3 | Plaur | Stat2 | Adrb2 | Tmem106a | Pfn1 | Ier3 | Padi4 |
| 20 | Id2 | Syngr1 | Rsad2 | Calhm2 | Anxa5 | Crip1 | Cd9 | Ifitm3 |
| 21 | Malat1 | Ldha | Oas1a | Slc1a3 | Marcksl1 | Fxyd5 | Ccl2 | Cd24a |
| 22 | Nfkbia | Hmox1 | Herc6 | Lair1 | Tmem176a | Rpl14 | Ccrl2 | Lsp1 |
| 23 | Otud1 | Tpi1 | Zbp1 | Fgd2 | Fxyd5 | Tmsb10 | Capg | Capg |
| 24 | Cited2 | Aldoa | Slfn5 | Tns3 | Klf2 | Rpsa | Cdkn1a | Txn1 |
| 25 | Smad7 | Anxa2 | Irgm1 | Atf7ip | Slfn2 | Ptma | Sdc4 | Ifitm1 |
| 26 | Gem | Npl | Ccl2 | Cst3 | Rtp4 | Anxa5 | Cstb | Aldh2 |
| 27 | Adrb2 | Ctsz | Samhd1 | Cdk6 | Tgfbi | Gpx1 | Adamts1 | Gpi1 |
| 28 | Slc15a3 | Ybx1 | Irf9 | Jun | Ednrb | Itgal | Pdgfa | Rtp4 |
| 29 | Bmp2k | Nme1 | Cd52 | Cd34 | Dok2 | Rps5 | Relb | Cd52 |
| 30 | Trib1 | Clta | Fgl2 | Msn | Hgsnat | Tpm4 | Srgn | Pilra |
| 31 | Fosb | Gng12 | Epsti1 | Hexb | Irf7 | Sh3bgrl | Cd72 | Arhgdib |
| 32 | Ier3 | S100a1 | Irf1 | Abca1 | Pltp | Rps18 | Rab20 | Slfn2 |
| 33 | Hsp90aa1 | Psmb6 | Isg20 | Zfhx3 | Crip1 | Arpc1b | Pmp22 | Cxcr2 |

| | | | | | | | | |
|---|---|---|---|---|---|---|---|---|
| 34 | Dnajb1 | Npc2 | Gbp2 | Slc2a5 | Ftl1 | Myl6 | Plaur | Tmem154 |
| 35 | Gadd45g | Apoc1 | Fam46a | Sparc | Serpinb6a | Capg | Vcam1 | Thbs1 |
| 36 | Tmem119 | Folr2 | Ddx58 | Tubgcp5 | Emp3 | Ftl1 | Tnfaip2 | Rnf144a |
| 37 | Ccr5 | Vat1 | Sdc3 | Ptgs1 | Fth1 | Serp1 | Cd63 | Myl6 |
| 38 | Tnf | Aplp2 | Ifih1 | Ecscr | Cd36 | Iqgap1 | Rhoc | Myh9 |
| 39 | Plk3 | Gatm | Parp12 | Btg2 | Hmox1 | Rpl32 | Gem | Rab3d |
| 40 | Dhrs3 | Lag3 | Parp9 | Usp2 | Tspo | Ifi27l2a | Sgk1 | Gpx1 |
| 41 | Selplg | Gpr137b | Znfx1 | Mat2a | Aldh2 | Emp3 | Ifrd1 | Pstpip1 |
| 42 | Hist1h1c | Hpse | Rnf114 | Itpripl1 | Pla2g7 | Plin2 | Crlf2 | Plp2 |
| 43 | Hk2 | Uap1l1 | Fcgr4 | Sqstm1 | Isg15 | S100a10 | Tgif1 | Calm1 |
| 44 | Nfkbid | Bnip3 | Hk2 | Klhdc8b | Rps5 | Rpl4 | Ier2 | Fth1 |
| 45 | Tmx4 | Mt1 | Lgals9 | Taf10 | Gas6 | Slfn2 | Glipr1 | G6pdx |
| 46 | Itpripl1 | Pgk1 | Apobec3 | Stard5 | Plin2 | Hspa8 | Plek | Serp1 |
| 47 | Lair1 | Emp3 | Cxcl16 | Rgl2 | Tmem176b | Fcgr4 | Mat2a | Rasgrp4 |
| 48 | Cd14 | Gapdh | Ddx60 | Plek | Oasl2 | Cfp | Slc3a2 | Glipr1 |
| 49 | Slc2a5 | Slc25a5 | Gpr84 | Npc1 | Calm1 | Ccnd3 | Zfp36 | Emb |
| 50 | Kdm6b | Cd83 | Tspo | Atp8a2 | Mpp1 | Gsn | Tubb6 | Iqgap1 |

*Note: Cluster-specific markers were identified with the 'FindAllMarkers' function of Seurat. FindAllMarkers with 'only.pos = TRUE', 'min.pct = 0.25',' logfc.threshold = 0.25', 'test.use = "wilcox"'.*

*Supplementary Table 3: Microglial gene lists.*

| # | **Hammond *et al.* 2019** | | **Hickman *et al.* 2013** | **Keren-Shaul *et al.* 2017** | **Li *et al.* 2019** | **Matcovitch-Natan *et al.* 2016** | **Safaiyan *et al.* 2021** |
|---|---|---|---|---|---|---|---|
| | *ATM* | *IRM* | *Sensome* | *DAM* | *PAM* | *Adult microglia* | *WAM* |
| 1 | Spp1 | Ifitm3 | P2ry12 | Itgax | Spp1 | Cst3 | Apoe |
| 2 | Gpnmb | Ifi27l2a | Tmem119 | Mamdc2 | Gpnmb | Ctsd | C1qb |
| 3 | Igf1 | Ccl12 | Gpr34 | Cst7 | Lpl | Laptm5 | Fth1 |
| 4 | Lgals3 | Lgals3bp | Csf1r | Fam20c | Pld3 | Csf1r | Lyz2 |
| 5 | Fabp5 | Ifit3 | Cd53 | Ccl4 | Ctsl | C1qa | H2-D1 |
| 6 | Cd9 | Rtp4 | Siglech | Lmbrd2 | Csf1 | Selplg | Ctsb |
| 7 | Lpl | H2-K1 | Cx3cr1 | Egr2 | Igf1 | C1qc | Ctss |
| 8 | Ctsl | Isg15 | Selplg | Csf1 | Ctsb | Tmem119 | Ctsz |
| 9 | Lgals1 | Cst7 | Ly86 | 5430435G22Rik | Slc23a2 | Sparc | H2-K1 |
| 10 | Apoe | Bst2 | Fcgr3 | Ccl3 | Gpx3 | Serinc3 | Ftl1 |
| 11 | Anxa5 | Ifi204 | Fcer1g | Clec7a | Sgpl1 | Ctss | B2m |
| 12 | Gm10116 | Oasl2 | Dap12 | Baiap2l2 | Sepp1 | Olfml3 | Cd63 |
| 13 | Syngr1 | Cd52 | Slco2b1 | Tmem154 | Cd9 | Cx3cr1 | Capg |
| 14 | Gpx3 | Irf7 | Itgam | Lpl | Abca1 | Jun | Cd52 |
| 15 | Cd63 | H2-D1 | Tgfbr1 | Ank | Plin2 | Ly6e | Spp1 |
| 16 | Pld3 | Rpl39 | Slc2a5 | Zfp692 | Syngr1 | 4632428N05Rik | Anxa5 |
| 17 | Gm1673 | Cxcl10 | P2ry13 | Siglec1 | Cd63 | Junb | Cd74 |

| | | | | | | | |
|---|---|---|---|---|---|---|---|
| 18 | Ctsb | B2m | Ifngr1 | Itga5 | Hpse | Trem2 | Lgals3 |
| 19 | Ftl1 | Ccl5 | Itgr1 | Tcf19 | Plek | Hexb | Tspo |
| 20 | Plin2 | Stat1 | Itgb5 | Cox6a2 | Lag3 | P2ry12 | Cst7 |
| 21 | Lyz2 | Slfn2 | Ccr5 | Spp1 | Slc37a2 | Ly86 | Atp6v0c |
| 22 | Ccl9 | Trim30a | Cd74 | Axl | Hif1a | Cd81 | Fam20c |
| 23 | Anxa2 | Ly6e | Emr1 | Igf1 | Fam20c | Mafb | Vim |
| 24 | Lilrb4a | Usp18 | Cmtm6 | Gpnmb | Serpine2 | Rhob | Cybb |
| 25 | Csf1 | Rpl27a | Cd68 | Ildr2 | Ctsd | Siglech | Ifitm3 |
| 26 | Pkm | Rps21 | Trem2 | Fxyd6 | Apoe | Rnase4 | Clec7a |
| 27 | Ccl6 | Phf11b | Fcgr2b | Psat1 | Ctsz | Bin1 | Crip1 |
| 28 | Mif | Gm9843 | Cd52 | Il1b | Ctsa | Pld4 | Anxa2 |
| 29 | S100a1 | Rps29 | Itgb2 | St14 | Tpp1 | Abhd12 | Lgals1 |
| 30 | Ldha | Rps12 | Gi24 | Arhgap26 | Lamp1 | Fos | Cd63-ps |
| 31 | Folr2 | Wdr89 | Entpd1 | 4632427E13Rik | Myo1e | Marcks | Ftl1-ps1 |
| 32 | Cstb | Tor3a | Cd180 | Birc5 | Abcd2 | Sirpa | Mir692-1 |
| 33 | Fabp3 | Gm4951 | Cmtm7 | Mettl15 | Aplp2 | Basp1 | Gm7541 |
| 34 | Gng12 | H2-Q7 | Lgals9 | Gpr65 | Gas6 | Slco2b1 | Ftl1-ps2 |
| 35 | Lag3 | Parp14 | Tgfbr2 | Cdca8 | Soat1 | Cyth4 | Gm12164 |
| 36 | Sepw1 | Ly6a | Ecscr | H2-Q7 | Lipa | Itgb5 | |
| 37 | Apoc1 | Rpl38 | Tmem173 | Etl4 | Grn | Tgfbr1 | |
| 38 | Tpi1 | Sp100 | Tlr2 | Ifit2 | Timp2 | Zfp36 | |
| 39 | Plaur | Uba52 | Lag3 | Capg | Psat1 | Phyhd1 | |
| 40 | Ifitm2 | Gm10076 | Ltf | Tmem8 | Gpr137b | Egr1 | |
| 41 | Ybx1 | Zfos1 | P2ry6 | Lyz2 | C3ar1 | Ctsz | |
| 42 | Npl | Ifit1 | Il10ra | Apoe | Pnpla7 | Fgd2 | |
| 43 | Hpse | Xaf1 | Lair1 | Slc1a2 | Gusb | Adap2 | |
| 44 | Vat1 | Rps20 | Gpr183 | Pycrl | Gpr137b-ps | Unc93b1 | |
| 45 | Sepp1 | Rpl22l1 | Tmem37 | Ifi27l2a | Gba | Itm2c | |
| 46 | Ctsz | Cd72 | Cd37 | Lgi2 | Ttyh2 | P2ry13 | |
| 47 | Aplp2 | Ch25h | Cd86 | Ero1lb | Anxa5 | Ptgs1 | |
| 48 | Gatm | Gm10073 | Slamf9 | Nceh1 | Cd68 | Irf8 | |
| 49 | Npc2 | Rplp2 | Tlr7 | Ch25h | Ccl3 | Arrb2 | |
| 50 | Gpr137b | Rps28 | Cd14 | Zfp189 | Hexa | Pmepa1 | |

*Note: Microglial gene lists of axon tract-associated microglia (ATM), interferon response microglia (IRM), disease-associated microglia (DAM, proliferative region-associated microglia (PAM), white matter-associated microglia (WAM), adult (homeostatic) microglia, and the sensome. Gene lists find their origins across the microglial field, most notably and respectively: Hammond et al. (2019); Keren-Shaul et al. (2017); Li et al (2019); Safaiyan et al. (2021); Matcovitch-Natan et al. (2016), and Hickman et al. (2013).*

*Supplementary Table 4: Non-microglial gene lists.*

| # | **Ochacka *et al.* 2021** | | **Xie *et al.* (2020)** | |
|---|---|---|---|---|
| | *DC* | *NK-cell* | *Monocyte* | *Neutrophil* |
| 1 | S100a8 | Ttr | S100a4 | Retnlg |
| 2 | S100a9 | Ptgds | Ms4a6c | S100a8 |
| 3 | Il1b | Enpp2 | Crip1 | S100a9 |
| 4 | Ngp | Clu | Ctss | Ngp |
| 5 | Retnlg | Mt3 | Ccl9 | Lcn2 |
| 6 | Camp | Aldoc | F13a1 | Wfdc21 |
| 7 | S100a11 | Ptn | Plac8 | Ltf |
| 8 | Slpi | Sparcl1 | Fn1 | Slpi |
| 9 | G0s2 | Chchd10 | Ccr2 | Il1b |
| 10 | Hp | Dbi | Psap | S100a11 |
| 11 | Wfdc21 | Cpe | Ms4a4c | Pglyrp1 |
| 12 | Lcn2 | Cryab | Npc2 | Mmp9 |
| 13 | Msrb1 | Car2 | Ifi30 | Gm5483 |
| 14 | Ifitm2 | Tsc22d1 | Lyz2 | Mmp8 |
| 15 | Hdc | Bsg | Pld4 | Cxcr2 |
| 16 | Ltf | Igfbp7 | Lamp1 | Msrb1 |
| 17 | Pglyrp1 | Vtn | Ifitm3 | Stfa2l1 |
| 18 | Anxa1 | Mt2 | Smpdl3a | Hdc |
| 19 | S100a6 | 1500015O10Rik | Ly86 | Ccl6 |
| 20 | Ifitm1 | Mt1 | Ctsc | Dusp1 |
| 21 | Wfdc17 | Plpp3 | Vim | Clec4d |
| 22 | Srgn | Gpm6b | Lgals1 | Ifitm1 |
| 23 | Fxyd5 | Flt1 | Clec4a3 | S100a6 |
| 24 | Anxa2 | Gstm1 | S100a10 | Lrg1 |
| 25 | Lrg1 | Prnp | Prdx1 | Csf3r |
| 26 | Gsr | Ndrg2 | Anxa5 | Anxa1 |
| 27 | Ccl6 | Crip2 | Ctsb | Mxd1 |
| 28 | Ifitm6 | Pltp | Dbi | Grina |
| 29 | Cd52 | S100a1 | Napsa | C5ar1 |
| 30 | Cxcl2 | Car4 | Apoe | Camp |

*Note: Non-microglial gene lists of dendritic cells (DC), natural killer (NK)-cells, monocyte and neutrophil markers. Gene lists derive from Ochaka et al. (2021) and Xie et al. (2020), each single-cell RNA-sequencing studies.*

*Supplementary Table 5: Supplementary gene lists.*

| # | **Marsh *et al.* 2022** | **Regev *et al.* 2016** | | **Sala Frigerio *et al.* 2019** |
|---|---|---|---|---|
| | *exAM* | *S-phase* | *G2M-phase* | *AD risk factors* |
| 1 | Hist1h1c | Mcm4 | Nuf2 | Apoe |
| 2 | Hist1h2bc | Exo1 | Psrc1 | Trem2 |
| 3 | Ubc | Slbp | Ncapd2 | Tyrobp |
| 4 | Jund | Gmnn | Ccnb2 | Cr2 |
| 5 | Rgs1 | Cdc45 | Smc4 | Bin1 |
| 6 | Hspa1a | Msh2 | Lbr | Cd2ap |
| 7 | Hsp90aa1 | Mcm6 | Tacc3 | Epha1 |
| 8 | Ccl4 | Rrm2 | Cenpa | Clu |
| 9 | Dusp1 | Pold3 | Kif23 | Ms4a6d |
| 10 | Hspa1b | Blm | Cdca2 | Picalm |
| 11 | Ccl3 | Ubr7 | Anp32E | Abca7 |
| 12 | Rhob | Mcm5 | G2E3 | Cd33 |
| 13 | Jun | Clspn | Cdca3 | H2-Eb1 |
| 14 | Zfp36 | Hells | Anln | Sorl1 |
| 15 | Klf2 | Nasp | Cenpe | Slc24a4 |
| 16 | Junb | Rpa2 | Gas2L3 | Dsg2 |
| 17 | Fos | Rad51Ap1 | Tubb4B | Inpp5d |
| 18 | Txnip | Tyms | Cenpf | Mef2c |
| 19 | Egr1 | Rrm1 | Dlgap5 | Zcwpw1 |
| 20 | Adamts1 | Rfc2 | Hjurp | Fermt2 |
| 21 | Btg2 | Prim1 | Cks1Brt | Cass4 |
| 22 | Wfdc21 | Brip1 | Gtse1 | Ptk2b |
| 23 | Ier5 | Usp1 | Bub1 | Ctsf |
| 24 | Atf3 | Ung | Birc5 | Ccl11 |
| 25 | Hist1h4i | Pola1 | Ube2C | Plcg2 |
| 26 | Gem | Mcm2 | Rangap1 | Abi3 |
| 27 | Ier2 | Fen1 | Hmmr | Pld3 |
| 28 | Ier3 | Tipin | Ect2 | Mme |
| 29 | Hist1h2br | Pcna | Tpx2 | Mmel1 |
| 30 | Hist1h1e | Cdca7 | Ckap5 | Ece1 |
| 31 | Il1b | Uhrf1 | Cbx5 | Ece2 |
| 32 | Serpine1 | Casp8Ap2 | Nek2 | Ace |
| 33 | Nfkbid | Cdc6 | Ttk | Mmp2 |
| 34 | Fosb | Dscc1 | Cdca8 | Mmp9 |
| 35 | Egr2 | Wdr76 | Nusap1 | Mmp14 |
| 36 | Cited2 | E2F8 | Ctcf | Bsg |
| 37 | Klf6 | Dtl | Cdc20 | Ide |
| 38 | Nfkbiz | Ccne2 | Cks2 | Serpinf2 |
| 39 | Hist2h2aa1 | Atad2 | Mki67 | Apeh |
| 40 | Hist1h4d | Gins2 | Tmpo | Mobp |
| 41 | Gm26532 | Chaf1B | Ckap2L | Ctsd |
| 42 | | Pcna-Ps2 | Aurkb | Ctsb |
| 43 | | | Kif2C | Bace1 |

| | | | | |
|---|---|---|---|---|
| 44 | | | Cdk1 | Bace2 |
| 45 | | | Kif20B | Mapt |
| 46 | | | Top2A | Aplp1 |
| 47 | | | Aurka | Aplp2 |
| 48 | | | Ckap2 | App |
| 49 | | | Hmgb2 | Psen1 |
| 50 | | | Cdc25C | Psen2 |
| 51 | | | Ndc80 | Adam10 |
| 52 | | | Kif11 | Adamts4 |
| 53 | | | | Vkorc1 |
| 54 | | | | Tspoap1 |
| 55 | | | | Pvr |

*Note: Supplementary gene lists of ex vivo activated microglia (exAM), S- and G2M-phase specific genes, and Alzheimer's disease (AD)-associated risk factors, as reported by Marsh et al. (2022), Aviv Regev, and Sala Frigerio et al. (2019), respectively.*

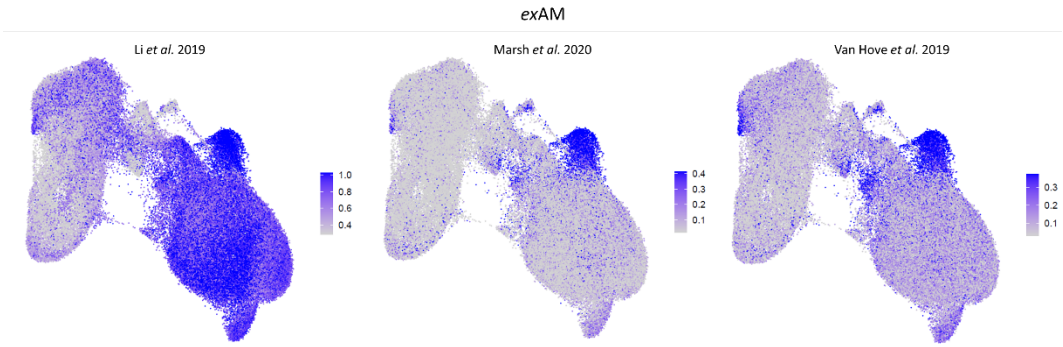


*Supplementary Figure 5: Identification of ex vivo-activated microglia.*

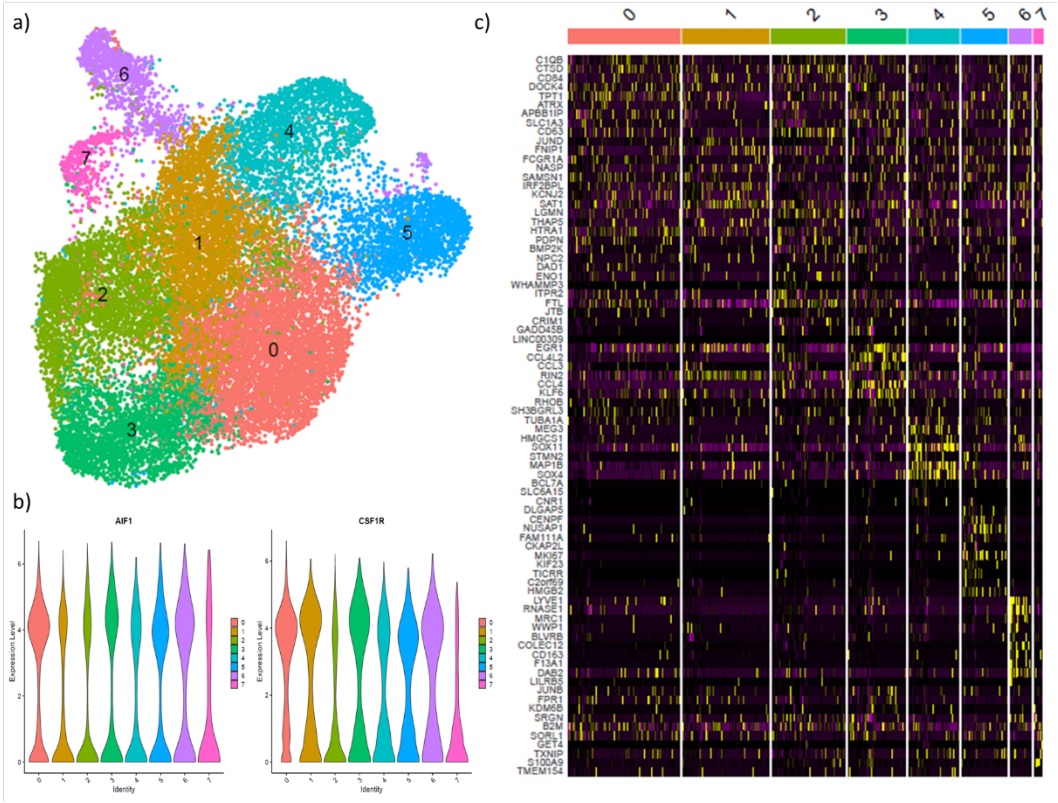


*Supplementary Figure 6: Human gestational myeloid heterogeneity. a) Dimplot of identified Seurat clusters. b) Each cluster features typical myeloid markers. c) Heatmap of cluster-specific genes; top 10 genes (ordered by 'avg_log2FC'), as determined with 'FindAllMarkers' with 'only.pos = TRUE', 'min.pct = 0.25',' logfc.threshold = 0.25', 'test.use = "wilcox"'.*

*Supplementary Table 6: Cluster markers of human gestational myeloid cells.*

| 0 | 1 | 2 | 3 | 4 | 5 | 6 | 7 |
|---|---|---|---|---|---|---|---|
| C1QB | FNIP1 | PDPN | GADD45B | TUBA1A | DLGAP5 | RNASE1 | JUNB |
| CTSD | FCGR1A | BMP2K | LINC00309 | MEG3 | CENPF | MRC1 | FPR1 |
| CD84 | NASP | NPC2 | EGR1 | HMGCS1 | NUSAP1 | WWP1 | KDM6B |
| DOCK4 | SAMSN1 | DAD1 | CCL4L2 | SOX11 | FAM111A | BLVRB | SRGN |
| TPT1 | IRF2BPL | ENO1 | CCL3 | STMN2 | CKAP2L | COLEC12 | B2M |
| ATRX | KCNJ2 | WHAMMP3 | RIN2 | MAP1B | MKI67 | CD163 | SORL1 |
| APBB1IP | SAT1 | ITPR2 | CCL4 | SOX4 | KIF23 | F13A1 | GET4 |
| SLC1A3 | LGMN | FTL | KLF6 | BCL7A | TICRR | DAB2 | TXNIP |
| CD63 | THAP5 | JTB | RHOB | SLC6A15 | C2orf69 | LILRB5 | S100A9 |
| JUND | HTRA1 | CRIM1 | SH3BGRL3 | CNR1 | HMGB2 | CD28 | TMEM154 |
| CYBA | PLXDC2 | HCCS | CD36 | NRXN1 | TK1 | TGFBI | DUSP1 |
| SPP1 | TREM2 | GPNMB | CCL2 | SLC4A10 | CDC20 | USP36 | IFITM2 |
| OLFML3 | RNF122 | LAGE3 | CH25H | SMAD9 | CCNB2 | IQGAP2 | S100A8 |
| C6orf62 | ARRDC3 | FOLR2 | CX3CR1 | GAP43 | CKAP2 | TLN1 | SP110 |
| FSCN1 | PRKCA | SLC25A45 | HERPUD1 | KIF21A | ARL6IP1 | DOCK5 | NFKBIA |

*Note: Cluster marker genes of in the integrated object. The top 15 genes are displayed. "FindAllMarkers" was used with default settings, e.g. 'only.pos = TRUE', 'min.pct = 0.25', 'logfc.threshold = 0.25', 'test.use = "wilcox"'.*

*Supplementary Table 7: Conserved CPM markers (1) – Bian et al. 2020.*

| Gene | Bian_p_val | Bian_avg_log2FC | Bian_pct.1 | Bian_pct.2 | Bian_p_val_adj |
|---|---|---|---|---|---|
| *CENPF* | 3.66E-14 | Inf | 1 | 0.626 | 2.29E-09 |
| *GTSE1* | 5.16E-14 | 122.2347465 | 0.955 | 0.451 | 3.23E-09 |
| *MKI67* | 1.69E-13 | Inf | 1 | 0.659 | 1.05E-08 |
| *NUSAP1* | 3.11E-13 | 363.1648182 | 1 | 0.626 | 1.95E-08 |
| *ASPM* | 2.43E-12 | 451.1595691 | 0.909 | 0.462 | 1.52E-07 |
| *TACC3* | 3.76E-12 | 344.4097827 | 0.932 | 0.549 | 2.35E-07 |
| *TPX2* | 5.66E-12 | 109.2505152 | 0.909 | 0.44 | 3.54E-07 |
| *TOP2A* | 1.04E-11 | Inf | 1 | 0.824 | 6.54E-07 |
| *NDC80* | 2.66E-11 | 200.1402787 | 0.705 | 0.176 | 1.67E-06 |
| *CENPE* | 3.83E-11 | 787.3171603 | 0.818 | 0.363 | 2.40E-06 |
| *SMC4* | 2.01E-10 | 319.8839671 | 1 | 0.78 | 1.26E-05 |
| *CDCA8* | 1.00E-09 | 15.47531343 | 0.818 | 0.385 | 6.29E-05 |
| *KIF14* | 3.67E-09 | 65.96963986 | 0.75 | 0.319 | 0.000229921 |
| *ANLN* | 3.71E-09 | 244.8638249 | 0.818 | 0.462 | 0.00023191 |
| *DIAPH3* | 1.04E-08 | 3.933753103 | 0.614 | 0.165 | 0.000650144 |
| *CKAP2L* | 4.41E-11 | 84.72467539 | 0.795 | 0.286 | 2.76E-06 |
| *PRR11* | 2.08E-11 | 246.30652 | 0.909 | 0.418 | 1.30E-06 |
| *NUF2* | 8.31E-11 | 109.4336097 | 0.841 | 0.341 | 5.20E-06 |
| *SPC25* | 1.39E-06 | 272.2750307 | 0.636 | 0.286 | 0.086833709 |
| *NCAPH* | 5.65E-09 | 113.5785762 | 0.795 | 0.385 | 0.00035379 |
| *CKAP2* | 8.75E-08 | 606.8428335 | 0.886 | 0.571 | 0.005476731 |
| *NCAPG* | 2.29E-10 | 1.044791363 | 0.773 | 0.253 | 1.43E-05 |
| *CDC25C* | 4.20E-05 | 73.63338822 | 0.455 | 0.165 | 1 |
| *KIF18A* | 0.001486961 | 81.79035097 | 0.318 | 0.121 | 1 |
| *NCAPD2* | 9.26E-11 | 188.5987183 | 0.955 | 0.505 | 5.80E-06 |
| *MELK* | 2.44E-08 | 366.0502084 | 0.795 | 0.341 | 0.001526293 |

| | | | | | |
|---|---|---|---|---|---|
| *BUB1B* | 2.68E-06 | 475.6950315 | 0.682 | 0.352 | 0.167512058 |
| *DLGAP5* | 3.93E-10 | 14.03261839 | 0.818 | 0.407 | 2.46E-05 |
| *HELLS* | 0.001640773 | 366.0502084 | 0.705 | 0.462 | 1 |
| *BUB1* | 3.66E-11 | 81.83928531 | 0.864 | 0.418 | 2.29E-06 |
| *STIL* | 3.63E-10 | 181.3852431 | 0.705 | 0.209 | 2.27E-05 |
| *ATAD2* | 5.48E-05 | 543.5016984 | 0.795 | 0.582 | 1 |
| *TMPO* | 1.28E-06 | 11.14722831 | 0.909 | 0.758 | 0.08039923 |
| *KIF20B* | 2.66E-08 | 316.9985765 | 0.955 | 0.659 | 0.001664038 |
| *RAD51AP1* | 9.17E-07 | 130.8909167 | 0.705 | 0.385 | 0.05736202 |
| *CENPK* | 1.95E-05 | 291.0287513 | 0.75 | 0.516 | 1 |
| *C21orf58* | 6.26E-06 | 344.4084678 | 0.682 | 0.363 | 0.391824312 |
| *SCLT1* | 0.230716092 | 96.26623572 | 0.5 | 0.473 | 1 |
| *NCAPD3* | 0.003978318 | 145.3178671 | 0.591 | 0.33 | 1 |
| *KIF5B* | 0.040929522 | 123.4938392 | 0.955 | 0.857 | 1 |

*Note: Conserved marker genes of cycling and proliferating microglia (CPM) (cluster 5). 40 conserved CPM markers were identified, independent of data source. "FindConservedMarkers" was used with default settings, e.g. 'only.pos = TRUE', 'logfc.threshold = 0.25'.*

*Supplementary Table 8: Conserved CPM markers (2) – Fan et al. 2020.*

| Gene | Fan_p_val | Fan_avg_log2FC | Fan_pct.1 | Fan_pct.2 | Fan_p_val_adj |
|---|---|---|---|---|---|
| *CENPF* | 2.25E-67 | Inf | 0.848 | 0.27 | 1.41E-62 |
| *GTSE1* | 9.39E-107 | 279.3610464 | 0.803 | 0.102 | 5.88E-102 |
| *MKI67* | 2.96E-96 | 473.5339325 | 0.826 | 0.139 | 1.85E-91 |
| *NUSAP1* | 1.33E-66 | Inf | 0.894 | 0.343 | 8.31E-62 |
| *ASPM* | 1.49E-78 | 565.8664058 | 0.705 | 0.109 | 9.30E-74 |
| *TACC3* | 5.37E-83 | 182.1095342 | 0.78 | 0.13 | 3.36E-78 |
| *TPX2* | 9.62E-71 | 309.0662083 | 0.742 | 0.152 | 6.02E-66 |
| *TOP2A* | 6.73E-71 | Inf | 0.886 | 0.286 | 4.21E-66 |
| *NDC80* | 1.33E-67 | 153.2294248 | 0.591 | 0.083 | 8.31E-63 |
| *CENPE* | 2.27E-48 | 192.2083995 | 0.629 | 0.144 | 1.42E-43 |
| *SMC4* | 1.18E-57 | 225.3903855 | 0.932 | 0.419 | 7.37E-53 |
| *CDCA8* | 8.05E-88 | 255.6833856 | 0.659 | 0.075 | 5.04E-83 |
| *KIF14* | 4.89E-39 | 16.26970239 | 0.371 | 0.052 | 3.06E-34 |
| *ANLN* | 7.45E-89 | 132.8746246 | 0.636 | 0.065 | 4.66E-84 |
| *DIAPH3* | 7.47E-50 | 45.05352943 | 0.455 | 0.063 | 4.67E-45 |
| *CKAP2L* | 6.47E-95 | 349.462159 | 0.659 | 0.066 | 4.05E-90 |
| *PRR11* | 3.29E-29 | 180.6667081 | 0.659 | 0.272 | 2.06E-24 |
| *NUF2* | 1.88E-63 | 137.3850909 | 0.667 | 0.13 | 1.18E-58 |
| *SPC25* | 9.53E-24 | 91.21974664 | 0.621 | 0.303 | 5.97E-19 |
| *NCAPH* | 7.34E-70 | 89.77706046 | 0.583 | 0.075 | 4.59E-65 |
| *CKAP2* | 2.95E-36 | 444.6800317 | 0.773 | 0.332 | 1.85E-31 |
| *NCAPG* | 4.22E-106 | 45.50544641 | 0.659 | 0.05 | 2.64E-101 |
| *CDC25C* | 6.29E-41 | 3.020424689 | 0.341 | 0.039 | 3.94E-36 |
| *KIF18A* | 5.45E-30 | 85.44439423 | 0.295 | 0.042 | 3.41E-25 |
| *NCAPD2* | 1.24E-61 | 23.41259649 | 0.705 | 0.144 | 7.76E-57 |
| *MELK* | 3.36E-27 | 29.59594709 | 0.712 | 0.35 | 2.11E-22 |
| *BUB1B* | 2.33E-53 | 134.5005979 | 0.523 | 0.085 | 1.46E-48 |
| *DLGAP5* | 1.05E-47 | 109.9747828 | 0.5 | 0.087 | 6.56E-43 |
| *HELLS* | 1.04E-31 | 34.95464004 | 0.598 | 0.197 | 6.48E-27 |
| *BUB1* | 3.07E-57 | 114.2762072 | 0.561 | 0.091 | 1.92E-52 |
| *STIL* | 3.71E-46 | 62.36584568 | 0.424 | 0.057 | 2.32E-41 |
| *ATAD2* | 6.41E-46 | 32.06924996 | 0.75 | 0.247 | 4.01E-41 |
| *TMPO* | 1.93E-33 | 76.60845902 | 0.864 | 0.496 | 1.21E-28 |
| *KIF20B* | 1.81E-21 | 39.09777535 | 0.727 | 0.361 | 1.13E-16 |
| *RAD51AP1* | 2.35E-50 | 105.6466311 | 0.568 | 0.11 | 1.47E-45 |
| *CENPK* | 1.49E-42 | 146.0421581 | 0.545 | 0.117 | 9.30E-38 |
| *C21orf58* | 2.36E-42 | 101.3181346 | 0.614 | 0.159 | 1.48E-37 |
| *SCLT1* | 2.30E-10 | 30.62655492 | 0.553 | 0.322 | 1.44E-05 |
| *NCAPD3* | 1.09E-23 | 20.52411678 | 0.523 | 0.181 | 6.82E-19 |
| *KIF5B* | 1.89E-11 | 162.9025576 | 0.902 | 0.807 | 1.19E-06 |

*Note: Conserved marker genes of cycling and proliferating microglia (CPM) (cluster 5). 40 conserved CPM markers were identified, independent of data source. "FindConservedMarkers" was used with default settings, e.g. 'only.pos = TRUE', 'logfc.threshold = 0.25'.*

*Supplementary Table 9: Conserved CPM markers (3) – Cao et al. 2020.*

| Gene | Cao_p_val | Cao_avg_log2FC | Cao_pct.1 | Cao_pct.2 | Cao_p_val_adj |
|---|---|---|---|---|---|
| *CENPF* | 4.67E-228 | 2.120825035 | 0.258 | 0.009 | 2.92E-223 |
| *GTSE1* | 3.86E-195 | 1.309892423 | 0.183 | 0.002 | 2.42E-190 |
| *MKI67* | 0 | 3.222783591 | 0.355 | 0.008 | 0 |
| *NUSAP1* | 3.58E-276 | 1.183391101 | 0.292 | 0.008 | 2.24E-271 |
| *ASPM* | 0 | 3.394374792 | 0.333 | 0.007 | 0 |
| *TACC3* | 6.94E-99 | 0.472884617 | 0.145 | 0.01 | 4.35E-94 |
| *TPX2* | 5.76E-219 | 0.83076071 | 0.22 | 0.005 | 3.60E-214 |
| *TOP2A* | 0 | 2.400820572 | 0.349 | 0.012 | 0 |
| *NDC80* | 4.60E-182 | 0.610878547 | 0.179 | 0.003 | 2.88E-177 |
| *CENPE* | 5.48E-220 | 1.670801642 | 0.242 | 0.008 | 3.43E-215 |
| *SMC4* | 4.20E-196 | 1.881014153 | 0.294 | 0.021 | 2.63E-191 |
| *CDCA8* | 2.49E-98 | 0.284788986 | 0.1 | 0.002 | 1.56E-93 |
| *KIF14* | 2.55E-166 | 0.643211995 | 0.163 | 0.003 | 1.60E-161 |
| *ANLN* | 1.37E-194 | 0.906103398 | 0.194 | 0.004 | 8.54E-190 |
| *DIAPH3* | 0 | 3.116139187 | 0.456 | 0.021 | 0 |
| *CKAP2L* | 2.73E-148 | 0.592587058 | 0.142 | 0.002 | 1.71E-143 |
| *PRR11* | 1.81E-124 | 0.700269154 | 0.197 | 0.015 | 1.13E-119 |
| *NUF2* | 7.20E-120 | 0.467461123 | 0.144 | 0.006 | 4.51E-115 |
| *SPC25* | 2.14E-154 | 2.649985953 | 0.15 | 0.003 | 1.34E-149 |
| *NCAPH* | 1.95E-92 | 0.343247989 | 0.107 | 0.004 | 1.22E-87 |
| *CKAP2* | 2.89E-107 | 0.95945264 | 0.186 | 0.017 | 1.81E-102 |
| *NCAPG* | 2.54E-133 | 0.536991746 | 0.142 | 0.004 | 1.59E-128 |
| *CDC25C* | 4.37E-155 | 1.002401561 | 0.157 | 0.003 | 2.73E-150 |
| *KIF18A* | 8.04E-120 | 0.605974935 | 0.121 | 0.003 | 5.03E-115 |
| *NCAPD2* | 1.01E-79 | 0.355504423 | 0.144 | 0.014 | 6.35E-75 |
| *MELK* | 3.88E-183 | 0.919373129 | 0.244 | 0.013 | 2.43E-178 |
| *BUB1B* | 1.57E-184 | 0.870803034 | 0.199 | 0.006 | 9.80E-180 |
| *DLGAP5* | 8.86E-102 | 0.279240482 | 0.1 | 0.002 | 5.55E-97 |
| *HELLS* | 4.73E-91 | 0.528479839 | 0.168 | 0.017 | 2.96E-86 |
| *BUB1* | 3.19E-147 | 0.725620736 | 0.157 | 0.004 | 2.00E-142 |
| *STIL* | 3.63E-185 | 1.060892294 | 0.236 | 0.012 | 2.27E-180 |
| *ATAD2* | 1.11E-182 | 2.58699309 | 0.305 | 0.027 | 6.97E-178 |
| *TMPO* | 3.31E-149 | 0.999157324 | 0.247 | 0.021 | 2.07E-144 |
| *KIF20B* | 1.30E-87 | 0.668993649 | 0.176 | 0.02 | 8.16E-83 |
| *RAD51AP1* | 1.62E-60 | 0.287487333 | 0.11 | 0.011 | 1.02E-55 |
| *CENPK* | 2.26E-138 | 0.937581184 | 0.236 | 0.021 | 1.42E-133 |
| *C21orf58* | 9.51E-123 | 0.37949591 | 0.129 | 0.003 | 5.95E-118 |
| *SCLT1* | 7.40E-91 | 8.283047002 | 0.517 | 0.193 | 4.63E-86 |
| *NCAPD3* | 5.01E-73 | 0.611291607 | 0.16 | 0.02 | 3.14E-68 |
| *KIF5B* | 1.45E-21 | 0.586363209 | 0.166 | 0.062 | 9.06E-17 |

*Note: Conserved marker genes of cycling and proliferating microglia (CPM) (cluster 5). 40 conserved CPM markers were identified, independent of data source. "FindConservedMarkers" was used with default settings, e.g. 'only.pos = TRUE', 'logfc.threshold = 0.25'.*

*Supplementary Table 10: Conserved CPM markers (4) – Kracht et al. 2020.*

| Gene | Kracht_p_val | Kracht_avg_log2FC | Kracht_pct.1 | Kracht_pct.2 | Kracht_p_val_adj | max_pval | minimump_p_val |
|---|---|---|---|---|---|---|---|
| *CENPF* | 0 | 293.1976406 | 0.525 | 0.047 | 0 | 3.66E-14 | 0 |
| *GTSE1* | 0 | 24.85636421 | 0.206 | 0.009 | 0 | 5.16E-14 | 0 |
| *MKI67* | 0 | 108.5326754 | 0.527 | 0.032 | 0 | 1.69E-13 | 0 |
| *NUSAP1* | 0 | 424.4828615 | 0.506 | 0.032 | 0 | 3.11E-13 | 0 |
| *ASPM* | 0 | 324.9369315 | 0.416 | 0.021 | 0 | 2.43E-12 | 0 |
| *TACC3* | 0 | 32.06983822 | 0.251 | 0.02 | 0 | 3.76E-12 | 0 |
| *TPX2* | 0 | 75.42078633 | 0.237 | 0.012 | 0 | 5.66E-12 | 0 |
| *TOP2A* | 0 | 36.39792334 | 0.669 | 0.06 | 0 | 1.04E-11 | 0 |
| *NDC80* | 0 | 202.1004497 | 0.238 | 0.016 | 0 | 2.66E-11 | 0 |
| *CENPE* | 0 | 327.8222963 | 0.335 | 0.022 | 0 | 3.83E-11 | 0 |
| *SMC4* | 0 | 7.544013658 | 0.393 | 0.054 | 0 | 2.01E-10 | 0 |
| *CDCA8* | 0 | 76.79338448 | 0.206 | 0.011 | 0 | 1.00E-09 | 0 |
| *KIF14* | 0 | 258.5632714 | 0.187 | 0.009 | 0 | 3.67E-09 | 0 |
| *ANLN* | 0 | 39.2965477 | 0.204 | 0.009 | 0 | 3.71E-09 | 0 |
| *DIAPH3* | 5.61E-216 | 45.05280723 | 0.133 | 0.009 | 3.51E-211 | 1.04E-08 | 0 |
| *CKAP2L* | 3.16E-289 | 138.8287873 | 0.158 | 0.008 | 1.98E-284 | 4.41E-11 | 1.26E-288 |
| *PRR11* | 7.93E-277 | 135.9438812 | 0.302 | 0.048 | 4.96E-272 | 2.08E-11 | 3.17E-276 |
| *NUF2* | 2.86E-276 | 150.3708316 | 0.162 | 0.01 | 1.79E-271 | 8.31E-11 | 1.14E-275 |
| *SPC25* | 3.66E-274 | 160.4696728 | 0.131 | 0.004 | 2.29E-269 | 1.39E-06 | 1.47E-273 |
| *NCAPH* | 1.17E-265 | 52.26769743 | 0.14 | 0.006 | 7.33E-261 | 5.65E-09 | 4.69E-265 |
| *CKAP2* | 2.79E-264 | 210.937773 | 0.333 | 0.064 | 1.75E-259 | 8.75E-08 | 1.12E-263 |
| *NCAPG* | 8.77E-249 | 66.69452056 | 0.129 | 0.005 | 5.49E-244 | 2.29E-10 | 3.51E-248 |
| *CDC25C* | 4.02E-232 | 150.3708557 | 0.118 | 0.005 | 2.52E-227 | 4.20E-05 | 1.61E-231 |
| *KIF18A* | 3.56E-222 | 95.59233194 | 0.131 | 0.008 | 2.23E-217 | 0.001486961 | 1.42E-221 |
| *NCAPD2* | 1.08E-215 | 122.9547424 | 0.213 | 0.029 | 6.73E-211 | 9.26E-11 | 4.30E-215 |
| *MELK* | 3.49E-204 | 242.6956981 | 0.138 | 0.011 | 2.18E-199 | 2.44E-08 | 1.40E-203 |
| *BUB1B* | 6.60E-199 | 13.4979211 | 0.125 | 0.008 | 4.13E-194 | 2.68E-06 | 2.64E-198 |
| *DLGAP5* | 3.76E-193 | 232.1525054 | 0.152 | 0.015 | 2.35E-188 | 3.93E-10 | 1.50E-192 |
| *HELLS* | 2.32E-189 | 16.20019277 | 0.351 | 0.094 | 1.45E-184 | 0.001640773 | 9.30E-189 |
| *BUB1* | 2.35E-188 | 95.54842002 | 0.184 | 0.025 | 1.47E-183 | 3.66E-11 | 9.42E-188 |
| *STIL* | 9.76E-104 | 65.32185539 | 0.112 | 0.017 | 6.11E-99 | 3.63E-10 | 1.45E-184 |

| | | | | | | | |
|---|---|---|---|---|---|---|---|
| *ATAD2* | 3.10E-163 | 156.1416113 | 0.202 | 0.036 | 1.94E-158 | 5.48E-05 | 4.46E-182 |
| *TMPO* | 8.46E-174 | 55.14327066 | 0.266 | 0.058 | 5.29E-169 | 1.28E-06 | 3.38E-173 |
| *KIF20B* | 2.73E-170 | 134.5011861 | 0.315 | 0.083 | 1.71E-165 | 2.66E-08 | 1.09E-169 |
| *RAD51AP1* | 1.81E-149 | 148.4761954 | 0.127 | 0.014 | 1.13E-144 | 9.17E-07 | 7.22E-149 |
| *CENPK* | 2.23E-109 | 30.62354754 | 0.138 | 0.024 | 1.40E-104 | 1.95E-05 | 9.06E-138 |
| *C21orf58* | 3.59E-72 | 223.7650904 | 0.151 | 0.042 | 2.25E-67 | 6.26E-06 | 3.80E-122 |
| *SCLT1* | 1.83E-23 | 108.5326754 | 0.123 | 0.056 | 1.15E-18 | 0.230716092 | 2.96E-90 |
| *NCAPD3* | 6.50E-80 | 27.67165947 | 0.113 | 0.022 | 4.07E-75 | 0.003978318 | 2.60E-79 |
| *KIF5B* | 1.40E-24 | 26.29905789 | 0.295 | 0.19 | 8.77E-20 | 0.040929522 | 5.60E-24 |

*Note: Conserved marker genes of cycling and proliferating microglia (CPM) (cluster 5). 40 conserved CPM markers were identified, independent of data source. "FindConservedMarkers" was used with default settings, e.g. 'only.pos = TRUE', 'logfc.threshold = 0.25'.*

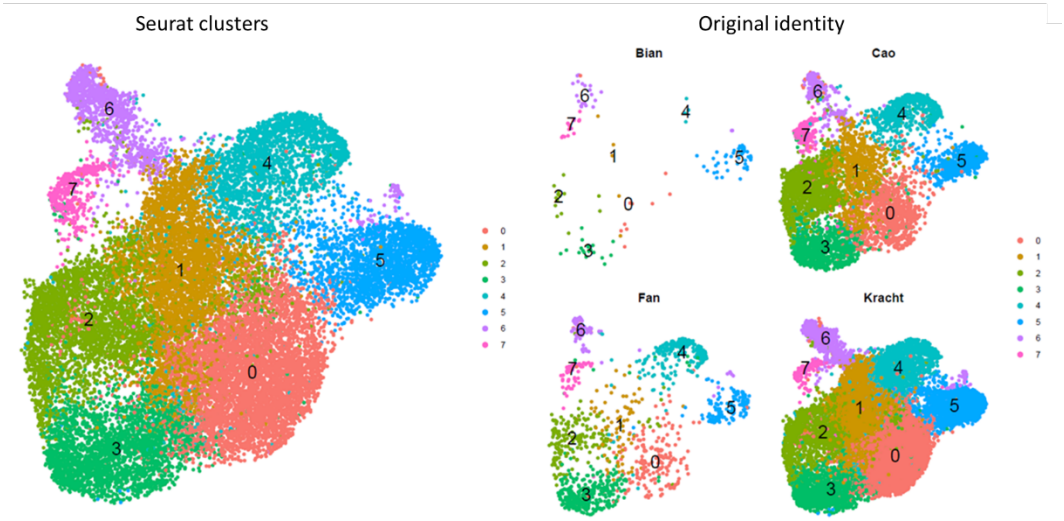


*Supplementary Figure 7: Spatial distribution of human gestational myeloid cells by original identity. 7 distinct clusters were identified, each of which are composed of cells from all 4 data sources (i.e. original identity).*

*Supplementary Table 11: Transcriptional similarities of YS and CAM.*

| | Region and subtype - YS vs CAM | | | | | |
|---|---|---|---|---|---|---|
| gene | p_val | avg_log2FC | pct.1 | pct.2 | p_val_adj | cluster |
| Pf4 | 2.86E-239 | 3.659262487 | 0.859 | 0.35 | 8.58E-236 | YS |
| Dab2 | 1.09E-107 | 2.616545929 | 0.778 | 0.415 | 3.28E-104 | YS |
| Lgals1 | 2.40E-249 | 2.487708008 | 0.905 | 0.416 | 7.19E-246 | YS |
| Ifitm2 | 2.30E-91 | 2.29505368 | 0.747 | 0.391 | 6.90E-88 | YS |
| Mrc1 | 1.50E-129 | 2.03016306 | 0.808 | 0.366 | 4.51E-126 | YS |
| Fcgrt | 3.39E-141 | 1.966760491 | 0.876 | 0.571 | 1.02E-137 | YS |
| Snx2 | 1.81E-147 | 1.965805891 | 0.998 | 0.583 | 5.44E-144 | YS |
| Ifitm3 | 2.62E-145 | 1.955917009 | 0.84 | 0.339 | 7.85E-142 | YS |
| Igfbp4 | 8.16E-71 | 1.801216738 | 0.75 | 0.41 | 2.45E-67 | YS |
| Apoe | 1.51E-198 | 1.790467165 | 0.997 | 0.777 | 4.54E-195 | YS |
| Blvrb | 5.42E-21 | 1.712248217 | 0.655 | 0.464 | 1.63E-17 | YS |
| Anxa5 | 5.22E-31 | 1.686567876 | 0.693 | 0.434 | 1.57E-27 | YS |
| Tmem106a | 1.09E-42 | 1.621431035 | 0.715 | 0.347 | 3.27E-39 | YS |

| | | | | | | |
|---|---|---|---|---|---|---|
| Irf7 | 0.00199911 | 1.601016379 | 0.548 | 0.29 | 1 | YS |
| Isg15 | 2.15E-06 | 1.592475842 | 0.474 | 0.343 | 0.006454338 | YS |
| Rtp4 | 4.89E-89 | 1.57226286 | 0.788 | 0.358 | 1.47E-85 | YS |
| Slfn2 | 0.000306213 | 1.472435128 | 0.582 | 0.384 | 0.918639786 | YS |
| Ftl1 | 7.21E-213 | 1.438700491 | 1 | 0.994 | 2.16E-209 | YS |
| Cnn2 | 9.04E-05 | 1.412194131 | 0.47 | 0.292 | 0.271259426 | YS |
| Tspo | 3.34E-47 | 1.403636539 | 0.761 | 0.508 | 1.00E-43 | YS |
| Cd74 | 0 | 5.311680693 | 0.82 | 0.377 | 0 | CAM |
| Pf4 | 0 | 3.891583663 | 0.887 | 0.325 | 0 | CAM |
| Dab2 | 0 | 2.595638798 | 0.818 | 0.399 | 0 | CAM |
| Ifitm3 | 0 | 2.266263673 | 0.796 | 0.318 | 0 | CAM |
| Mrc1 | 0 | 2.161065975 | 0.781 | 0.346 | 0 | CAM |
| Ifitm2 | 0 | 2.126423728 | 0.776 | 0.374 | 0 | CAM |
| Apoe | 0 | 2.104944765 | 0.996 | 0.786 | 0 | CAM |
| Lgals1 | 0 | 2.02422236 | 0.821 | 0.403 | 0 | CAM |
| Ifi27l2a | 5.17E-244 | 1.983734996 | 0.66 | 0.358 | 1.55E-240 | CAM |
| Folr2 | 1.24E-155 | 1.685719824 | 0.588 | 0.349 | 3.72E-152 | CAM |
| Fcgrt | 1.05E-275 | 1.665749465 | 0.81 | 0.562 | 3.14E-272 | CAM |
| Snx2 | 1.62E-231 | 1.441120987 | 0.843 | 0.581 | 4.87E-228 | CAM |
| Mgl2 | 0 | 1.392708058 | 0.644 | 0.223 | 0 | CAM |
| Blvrb | 1.43E-231 | 1.365494424 | 0.732 | 0.448 | 4.30E-228 | CAM |
| Cfp | 0 | 1.362794748 | 0.623 | 0.253 | 0 | CAM |
| Igfbp4 | 4.73E-276 | 1.311542852 | 0.715 | 0.394 | 1.42E-272 | CAM |
| Bst2 | 2.23E-260 | 1.280317123 | 0.828 | 0.561 | 6.70E-257 | CAM |
| Ctsc | 0 | 1.255242632 | 0.985 | 0.841 | 0 | CAM |
| Tmem106a | 0 | 1.245944267 | 0.686 | 0.329 | 0 | CAM |
| Anxa5 | 3.04E-196 | 1.222704348 | 0.715 | 0.426 | 9.12E-193 | CAM |

*Note: Top 20 yolk sac (YS) progenitors and CNS-associated macrophage (CAM) markers support transcriptional similarities between both subtypes. "FindConservedMarkers" was used with default settings, e.g. 'only.pos = TRUE', 'logfc.threshold = 0.25'.*

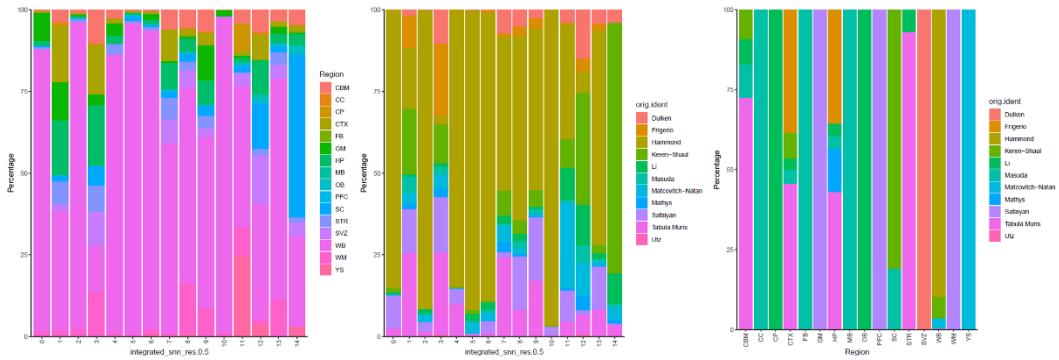


*Supplementary Figure 8: Two-dimensional bar plots on region, original and cluster identity. Cluster 11 and 14 display some degree of region-specific enrichment, with enrichments for YS- and SC-isolated cells, respectively. Cluster 11 does not relate to a specific source, albeit cluster 14 appears to be mostly driven by cells from Keren-Shaul et al. (2016). Without a subsequent similar enrichment of cells by Masuda, cells appear to derive from the former source.*

*Supplementary Table 12: Sex-specific contingency table of cell annotations across the lifespan.*

| | Early microglia | | Pre-microglia | | Adult microglia (P90) | | Adult microglia (3.5M) | | Adult microglia (6M) | | Middle age microglia (18M) | | Old age microglia (21M) | | |
|---|---|---|---|---|---|---|---|---|---|---|---|---|---|---|---|
| ***Cluster*** | ***F*** | ***M*** | ***F*** | ***M*** | ***F*** | ***M*** | ***F*** | ***M*** | ***F*** | ***M*** | ***F*** | ***M*** | ***F*** | ***M*** | ***#*** |
| *AIM* | 0 | 0 | 1 | 1 | 9 | 8 | 65 | 96 | 2 | 4 | 24 | 311 | 6 | 3 | 530 |
| *CPM - G2M* | 2320 | 2083 | 1385 | 1385 | 4 | 16 | 6 | 3 | 1 | 1 | 2 | 25 | 0 | 0 | 7231 |
| *CPM - S* | 2026 | 1856 | 1132 | 1130 | 15 | 22 | 17 | 20 | 6 | 4 | 10 | 19 | 2 | 3 | 6262 |
| *EDM* | 3674 | 2747 | 3753 | 3838 | 1 | 12 | 2 | 1 | 1 | 0 | 33 | 67 | 1 | 0 | 14130 |
| *HOM1* | 0 | 0 | 0 | 0 | 86 | 52 | 3888 | 6615 | 1 | 4 | 172 | 3945 | 2 | 3 | 14768 |
| *HOM2* | 0 | 0 | 0 | 0 | 1302 | 1551 | 1573 | 1341 | 264 | 296 | 879 | 865 | 136 | 282 | 8489 |
| *HOM3* | 17 | 33 | 29 | 24 | 594 | 1177 | 185 | 44 | 356 | 343 | 817 | 747 | 330 | 321 | 5017 |
| *HOM4* | 0 | 0 | 0 | 0 | 756 | 29 | 2226 | 2804 | 0 | 0 | 12 | 304 | 0 | 1 | 6132 |
| *HOM5* | 0 | 0 | 0 | 0 | 5 | 2 | 33 | 2388 | 0 | 0 | 3 | 15 | 1 | 0 | 2447 |
| *IRM* | 6 | 7 | 8 | 21 | 41 | 79 | 339 | 365 | 15 | 8 | 111 | 456 | 25 | 12 | 1493 |
| *LPM* | 90 | 109 | 849 | 955 | 42 | 31 | 17 | 3 | 11 | 12 | 106 | 56 | 47 | 14 | 2342 |
| ***#*** | 8133 | 6835 | 7157 | 7354 | 2855 | 2979 | 8351 | 13680 | 657 | 672 | 2169 | 6810 | 550 | 639 | **68841** |

*Note: A subset of 7 ages was created: E14.5, P4, P90, 3.5M, 6M, 18M and 21M for a total of 68841 cells. Cell numbers are displayed by age group, sex and subtype (i.e. cluster). AIM, Activated Inflammatory Microglia; CPM, cycling and proliferating microglia; EDM, early developmental microglia; HOM, homeostatic microglia; IRM, interferon response microglia; LPM, lysosome pathway-associated macrophage. F, female; M, male; M, months old; P, postnatal day.*

# Chapter 4 Drop-seq platform performance and pilot of cortical microglia

In the previous chapter, a compendium was developed of murine microglial heterogeneity across the lifespan. Broadly, seven major subtypes were identified that differ in their maturation speed in a sex-specific manner, culminating in distinct population dynamic profiles, and the identification of *exAM*. Biological and technical noise are endemic to any experiment, yet these are important to identify prior to developing a targeted experimental setup (Wagner et al., 2016). Here, Drop-seq was tested and generated a pilot dataset to measure the extend of such noise.

#### 4.1.1.1 Drop-seq: droplet microfluidics and cellular diversity

All scRNA-seq platforms have microfluidic systems at its core, that is, systems which manipulate micrometre-sized liquids through channels and into chambers (Pan et al., 2022). In contrast, scRNA-seq platforms vary in costs, method of quantitation and performance (Figure 55). CEL-seq2, SMART-seq2, MARS-seq and Drop-seq are all popular variants of such scRNA-seq platforms that are well-, chip- or droplet-based, offering simplicity, control, and high throughput, respectively. Of these methods, Drop-seq appears to be the preferred platform for several reasons.

| | CEL-seq2 | SMART-Seq2 | MARS-Seq | Drop-Seq |
|---|---|---|---|---|
| Publication | Hashimshony *et al.* 2016 | Picelli *et al.* 2014 | Jaitin *et al.* 2014 | Macosko *et al.* 2015 |
| Type | Well | Chip | Droplet | Droplet |
| MoQ | UMI | Transcript | UMI | UMI |
| Accuracy (R=) | 0.94 | 0.85 | 0.8 | 0.92 |
| Sensitivity (#M) | 13 | 45 | 130 | 10 |
| Costs ($) * | 2,250 | 1,090 | 820 | 690 |

*Figure 55: scRNA-seq platform comparisons. Direct comparison of well-known and utilized single-cell RNA-sequencing (scRNA-seq) platforms on type (i.e. well, chip, droplet), method of quantitation, accuracy, sensitivity and costs. Costs are relative costs in United States dollar ($) for sequencing 254 cells to an average read depth of 250,000. Information collated from the works of Ziegenhain et al. (2017 and Svensson et al. (2017). MoQ, method of quantitation; #M, number of molecules; R=, correlation; UMI, unique molecular identifier.*

Drop-seq has been successfully utilized in a plethora of studies, including work on the developmental maturation of retinal progenitors and thymus, cell type-specific responsiveness to

energy status, the identification of disease-associated subtypes, and cross-region analysis of the mammalian brain (Campbell et al., 2017; Fang et al., 2019; Kernfeld et al., 2018; Yuzwa et al., 2017).

Drop-seq is the most cost-effective technique and shows excellent accuracy and sensitivity (Figure 55). Drop-seq was developed in the lab of Steven McCarroll and enables the profiling of thousands of single-cells in a high-throughput and cost-effective manner (Macosko et al., 2015).

As a droplet-based microfluidics approach, Drop-seq captures 3'-end poly-adenylated RNA (*e.g.* mRNA) from individual cells. When controlling for read depth, RNA-based scRNA-seq techniques like Drop-seq have a relative increase in sensitivity and accuracy in comparison to whole-transcript scRNA-seq (*e.g.* SMART-seq-2) (Figure 55) (Svensson et al., 2017). Accuracy describes the fidelity in which the transcripts can be measured, whereas the sensitivity describes the lower detection limit.

The detection limit for Drop-seq is ~10 molecules and, importantly, accuracy correlates with bulk RNA-Seq measures (R = 0.92) (Figure 55). Of note, read depth per cell is a key factor for sensitivity, although accuracy is mostly independent of it. Accuracy is a measure of the technique, marking the limitations of the chosen platform and independent of the number of reads per cell, as is the case for sensitivity. Indeed, study shows that accuracy saturates around 250,000 sequenced reads per cell, whereas sensitivity does so from 1 million reads (Svensson et al., 2017).

### 4.1.2 Characteristics of Drop-seq microfluidics and cellular diversity

Single-cell transcriptomes in Drop-seq are generated by the co-encapsulation of barcoded beads and cells in ~1 nL-sized water-in-oil droplets. In short, single-cells from complex tissue are co-encapsulated with beads after which 3'-end poly-adenylated RNA is captured by bead primers for the generation of single-cell transcriptomes attached to microparticles (STAMP) (Figure 56).

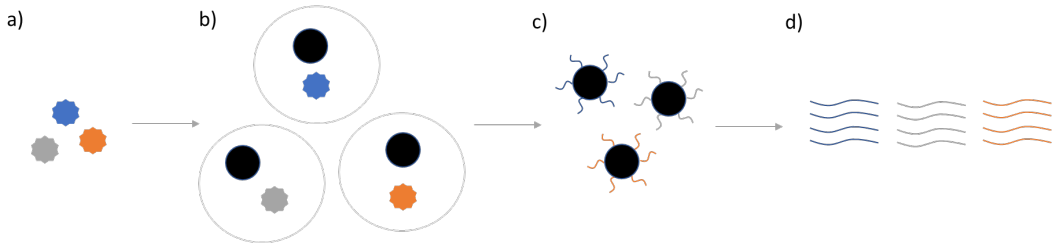


*Figure 56: Drop-seq barcoding schematic for single-cell microglial transcriptomes. a) Complex tissue is dissociated to isolate individual microglia. b) Co-encapsulation of isolated cells with barcoded beads (circles). c) Once cells and beads come in contact, cells lyse, allowing for the capture of cell-specific poly-adenylated RNA and the generation of 'single-cell transcriptomes attached to microparticles' (STAMP). d) STAMP are utilized for single-cell library preparation and sequencing.*

Droplet formation and co-encapsulation of cells and beads is mediated by the co-flow of beads in lysis buffer, cells in suspension, and oil; oil functions to join cells and beads in monodisperse droplets. The probability of finding both particles in a droplet is approximated by the Poisson distribution (Mazutis et al., 2013) (Equation 1). In this manner, with the probability of finding a

certain number of particles (x) at a given average number of particles in a droplet (λ), droplet occupancy is described in Figure 57.

$$P(X_1 = x_1, X_2 = x_2) = \frac{e^{-\lambda 1}\,\lambda_1^{x1}}{x_1!} * \frac{e^{-\lambda 2}\,\lambda_1^{x1}}{x_2!}$$

*Figure 57: Poisson distribution and droplet occupancy. Predicting the number of particles (i.e. cells or beads) in droplets can be calculated with the Poisson distribution. λ represents the average number of particles in the droplet volume, and x the number of particles found in the droplet. In effect, changing the cell and bead concentrations will drive their changes of co-encapsulation. e.g., preparing cells and beads to 100 cells and 120 beads/µL, the chances to co-encapsulate 1 cell and 1 bead will approximate: 0.091 * 0.106 = 0.01 (1%). By extension, beads that encounter cells at 50 cells/µL is roughly 5%.*

The barcoded beads are composed of PCR handles, a cell barcode, and unique molecular identifiers (UMI) (Figure 58) (Macosko et al., 2015). The PCR handle offers a scaffold for PCR amplification, whereas the UMI and cell barcodes aid the identification of specific transcripts or cells, respectively. Each primer bead contains over $10^8$ primer beads, each with an identical cell barcode and up to ~65,000 distinct UMI (to control of amplification biases), enabling the profiling of thousands of cells, and the accurate enumeration of transcripts in a single experiment.

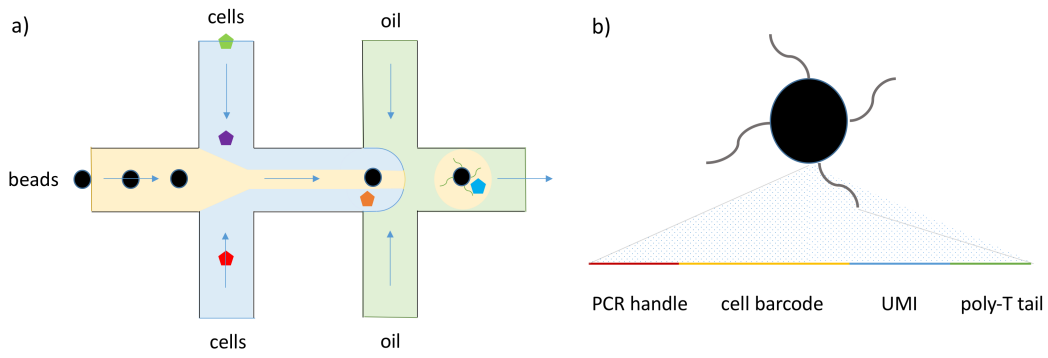


*Figure 58: Schematic of particle co-encapsulation. a) Co-encapsulation of particles is mediated by the serial co-flow of beads (circles), cells (pentagons) and oil; the oil enables droplet formation and captures cells and beads together. The Poisson distribution approximates the likelihood of capturing single-cells and primer beads. b) The barcoded primer beads are composed of a PCR handle, a cell barcode, a unique molecular identifier (UMI) and a poly-T tail for the capture of cell-specific polyadenylated RNA. Each bead contains the same cell barcode and up to 48 (~65,000) distinct UMI.*

### 4.1.3 Limitations of Drop-seq: technical and biological noise

Drop-seq has limitations users need to be aware of, as measures of accuracy are intertwined with biological and technical noise. Like most scRNA-seq protocols, Drop-seq captures 3'-end poly-adenylated RNA only, excluding small RNAs (*e.g.* mature miRNA) and non-coding RNAs without poly-A tails. Butovsky *et al.* (2014) have previously shown that microglial identity is under the transcriptional control of miRNAs in a region-dependent manner (Butovsky et al., 2014). This inherent feature of Drop-seq provides an a priori limit to the transcriptional read out.

#### 4.1.3.1 Technical noise of scRNA-seq

Typical technical factors known to impair the ability to detect true heterogeneity are batch effects, transcriptome library quality, and cell specific capture efficiency and amplification bias (Wagner et al., 2016). Batch effects signify variability in data due to a technical factor. Generally, randomization of all conditions in experimental design will minimize such effects. However, with large-scale and complex designs, these effects could remain and need to be mitigated bioinformatically. Fortunately, Harmony, LIGER and Seurat are all effective tools to integrate disparate samples (Tran et al., 2020). Seurat utilizes canonical correlation analysis (CCA) to mitigate batch effects (Butler et al., 2018; Tran et al., 2020). Furthermore, captured RNA quantity and composition differ and experimental protocol (Huarte et al. 2021; Thrupp et al. 2020). Consequentially, library qualities will differ between cell types. Moreover, quantification bias signifies an error in which weights are unevenly assigned to individual components. In the context of scRNA-seq, such a bias describes differences in sequencing read allocation based on cell- or transcript-specific characteristics. Fortunately, the use of UMI allow for digital quantification of the transcripts, greatly reducing quantitative imprecision, a major source of technical noise with scRNA-seq (Islam et al., 2014).

#### 4.1.3.2 Biological factors influencing transcriptional heterogeneity in microglia

Biological noise and cellular identity can be defined by the biological contexts and factors with which it interacts (*e.g.* environmental stimuli, cell development, cell cycle and spatial context) (Wagner et al., 2016).

In the large-scale atlas (Chapter 3), I discussed the importance of cell cycle for transcriptional heterogeneity. As show, murine and human microglia display wave-like patterns in early development, concurrent with the developmental expansion of these cells (Figure 37, Figure 38) (Askew et al., 2017; Menassa et al., 2021). Moreover, cell cycle phase affects sensitivity to environmental cues and cellular heterogeneity (Lauridsen et al., 2018). In fact, the environment is known to play a large role in the emergence of microglial identity. Environmental cues like those by Tgf-ß are examples of such effects. However, as discussed, microglia can also take on an *ex vivo*-activated signature (*i.e. ex*AM) during cell isolation, obfuscating their native transcriptional read out (Figure 30) (Brink et al., 2017; Marsh et al., 2022; Wu et al., 2017).

### 4.1.4 Single-cell isolation – a review of methods

To take inventory of current scRNA-seq procedures, I reviewed many studies for their methodological approach (Table 5). This includes and extends beyond the scope of those discussed in the atlas. A typical scRNA-seq protocol consist of 6 distinct steps: anaesthesia, perfusion and tissue dissection, dissociation, purification, enrichment, and scRNA-seq; 7 when including chemical fixation. Of note, most studies utilize enzymatic dissociation, Percoll gradient centrifugation and fluorescence-activated cell sorting (FACS) (Figure 58); the standard of scRNA-seq.

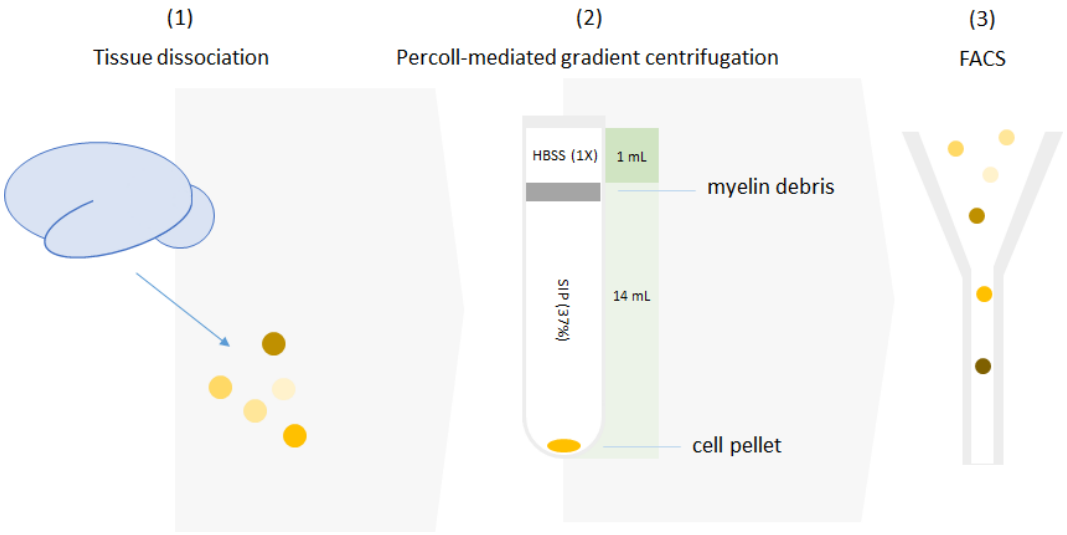


*Figure 59: Diagrammatic representation of microglial isolation. (1) Tissue is dissociated to isolate single-cells. (2) Percoll-mediated gradient centrifugation removes myelin debris on top of the Stock Isotonic Percoll (SIP)-solution (37%), purifying myelin debris from the cell suspension. (3) The cell pellet is labelled with identifying antibodies for fluorescence-activated cell sorting (FACS) for the enrichment of cells from a heterogeneous cell suspension.*

*Table 5: Review of scRNA-seq procedures.*

| Publication Details | | | | Experimental Procedure | | | | | | | | | |
|---|---|---|---|---|---|---|---|---|---|---|---|---|---|
| **First Author** | **Last Author** | **Publication Year** | **Journal/Book** | **Anaesthesia** | **Exsanguination** | **CNS Region** | **Dissociation** | | | | **Purification** | | **Enrichment** |
| | | | | | | | *Enzymatic Dissociation* | *Tool* | *Temperature (°C)* | *Duration (minutes)* | *Inhibitors* | *Purification* | *Method* | *MACS/ FACS* |
| Zeisel, Amit | Linnarsson, Sten | 2015 | Science | ketamine-xylazine | Y | N.A. | Y | Papain-based (Worthington) | N.A. | N.A. | N/A | N | N/A | FACS |
| Matcovitch-Natan, Orit | Amit, Ido | 2016 | Science | N.A. | Y and N | CTX, HIP, SC | N | Homogenizer (Dispomix) | N.A. | N.A. | N/A | Y | Gradient centrifugation (Percoll) | FACS |
| Tasi, Bosiljka | Zeng, Hongkui | 2016 | Nature | isoflurane | Y | CTX | Y | Pronase-based | RT | 70 | N/A | N | N/A | FACS |
| Mathys, Hansruedi | Tsai, Li-Huei | 2017 | Cell Reports | N.A. | Y | HIP | Y | Papain-based (Neural Tissue Dissociation Kit (P) (Miltenyi Biotec)) | 37 | 15 | N/A | N | N/A | FACS |
| Keren-Shaul, Hadas | Amit, Ido | 2017 | Cell | N.A. | Y | CB, CTX, SC, WB | N | Homogenizer (Dispomix) | N.A. | N/A | N/A | Y | Gradient centrifugation (Percoll) | FACS |
| Sousa, Carole | Micheluci, Alessandro | 2018 | EMBO Reports | ketamine-dorbene | Y | WB | N | Homogenizer (Potter) | N.A. | N/A | N/A | Y | Myelin Removal Kit (Miltenyi Biotec)[3] | FACS |
| Kalish, Brian T. | Greenberg, Michael E. | 2018 | PNAS | isoflurane | N | LG | Y | Papain-based (papain, pronase and proteinase XXIII) | 37 | 60 | N/A | Y | Gradient centrifugation | N/A |
| Schaum, Nicholas | The Tabula Muris Consortium | 2018 | Nature | Avertin | Y | CTX, CB, HIP, STR | N | Homogenizer (Dounce) | N.A. | N/A | N/A | Y | Myelin Removal Beads II (Miltenyi Biotec) | FACS |
| Huang, Yubin | Peng, Bo | 2018 | Nature Neuroscience | chloral hydrate | Y | WB | Y | AccμMax (Sigma) | RT | 30 | N/A | Y | Gradient centrifugation (Percoll) | FACS |
| Hrvatin, Sinisa | Michael E. Greenberg | 2018 | Nature Neuroscience | isoflurane | Y | CTX | Y | Papain-based (Worthington) | 37 | 60 | TTX (1 μM), AP-V (100 μM), actinomycin D (5 μg /mL), triptolide (10 μM), anisomycin (10 μg) | Y | Gradient centrifugation | N/A |
| Tuan Tay | Marco Prinz | 2018 | Acta Neuropathologica Communications | N.A. | Y | P | N.A. | N.A. | N.A. | N.A. | N/A | Y | Gradient centrifugation (Percoll) | FACS |
| Blanca Pijuan-Sala | Göttgens, Berthold | 2019 | Nature | N.A. | N | WB | Y | Trypsin-based | 37 | 7 | N/A | N | N/A | N/A |
| Dulken, Ben | Brunet, Anne | 2019 | Nature | N.A. | Y | SVZ | Y | Papain-based[4] | 37 | 10 | N/A | Y | Gradient centrifugation (Percoll) | FACS |
| Gunner, Georgia | Schafer, Dorothy | 2019 | Nature Neuroscience | $CO_2$ | Y | CTX | Y | Papain-based | 37 | 60 | tetrodotoxin (1 μM), 2-amino-5-phosphonopentanoic acid (100 μM), actinomycin D (5 μg / mL), and triptolide (10 μM) | N | N/A | N/A |
| Van Hove, Hannah | Movahedi, Kiavash | 2019 | Nature Neuroscience | N.A. | Y | CP, D | Y | Collagenase-based (collagenase type I and collagenase type IV) | 37 | 20 | actinomycin D (30 μM) | Y | Gradient centrifugation (Percoll) | FACS |
| Geirsdottir, Laufey | Marco Prinz | 2019 | Cell | N.A. | Y | WB | N | Homogenization | N.A. | N/A | N/A | Y | Gradient centrifugation (Percoll) | FACS |
| Sebastian Utz | Greter, Melanie | 2020 | Cell | $CO_2$ | Y | WB, YS | Y | Collagenase-based | 37 | 20 | N/A | N | N/A | FACS |
| Schaum, Nicholas | The Tabula Muris Consortium | 2020 | Nature | Avertin | Y | CTX, CB, HIP, STR | N | Homogenizer (Dounce) | N.A. | N/A | N/A | Y | Myelin Removal Beads II (Miltenyi Biotec) | FACS |
| Sala Frigerio, Carlo | De Strooper, Bart | 2019 | Cell Reports | $CO_2$ | Y | CTX, HIP | Y | Papain-based (Adult Brain Dissociation Kit) (Miltenyi Biotec) | 4 | 30 | N/A | Y | Gradient centrifugation (Debris Removal Solution, Miltenyi Biotec) | FACS |
| Li, Qingyun | Barres, Ben A. | 2019 | Neuron | CO2 or N.A. | Y and N | CB, CP, CTX, HIP, OB, STR | N | Homogenizer (Dounce) | 4 | N/A | N/A | Y (≥ P7) | Myelin Removal Beads II (Miltenyi Biotec) | FACS |
| Hammond, Timothy | Stevens, Beth | 2019 | Immunity | N.A. | Y | WB | N | Homogenizer (Dounce) | 4 | N/A | N/A | Y (≥P30) | Gradient centrifugation (Percoll) | FACS |
| Masuda, Takahiro | Prinz, Marco | 2020 | Nature Immunology | N.A. | Y | CB, CTX, HIP | N | Homogenizer (Potter) | N/A | N/A | N/A | Y | Gradient centrifugation (Percoll) | FACS |
| Lau, Shun-Fat | Ip, Nancy | 2020 | Cell Reports | isoflurane | Y | WB | Y | Papain-based | 37 | 30 | N/A | Y | Gradient centrifugation (Percoll) | FACS |
| Mangale, Vrushali | Lane, Thomas | 2020 | Glia | N.A. | Y | SC, WB | N | Homogenization | N.A. | N/A | N/A | Y | Gradient centrifugation (Percoll) | FACS |
| Wang, Shoutang | Colonna, Marco | 2020 | Journal of Experimental Medicine | ketamine-xylazine | Y | WB | Y | Trypsin-based (Neural Tissue Dissociation (T) (Miltenyi Biotec) | 37 | 30 | N/A | Y | Gradient centrifugation (Percoll) | FACS |
| Safaiyan, Shima | Simons, Mikael | 2021 | Neuron | N.A. | Y | CC, CTX, OT, WM | Y | Papain-based (Neural Tissue Dissociation Kit (P) (Miltenyi Biotec)) | 37 | 15 | actinomycin D (45 μM) | Y | Gradient centrifugation (Debris Removal Solution and Myelin Removal Beads) [6] | FACS |

*Note: Publication details and matching experimental procedures were collected.A variety of regions were studied: CB, cerebellum; CC, corpus callosum; CTX, cortex; CP, choroid plexus; D, dura; OT, HIP, hippocampus; LG, lateral geniculate; OB, olfactory bulb; OT, optic tract; P, pons; SC, spinal cord; STR, striatum; SVZ, subventricular zone; WM, white matter; YS, yolk sac. Two enrichment methods were common: MACS, magnetic-activated cell sorting; FACS, fluorescence-activated cell sorting. Some data points were not 'available' (N.A.), whereas others are 'not applicable' (N/A).*

## 4.2 Aims and objectives

Drop-seq is a cost-effective tool capable of delivering high-quality scRNA-seq data. Therefore, I have chosen to do a Drop-seq experiment with adult male and female microglia in standard experimental procedures, which includes enzymatic tissue dissociation, myelin debris removal, and fluorescence-activated cell sorting (FACS). Unfortunately, Drop-seq has a relatively low co-encapsulation efficiency in comparison to other platforms, necessitating many cells as input, and could show signs of technical artefacts; all which limitations that need to be explored prior to developing a context-specific study.

In this chapter I aim to test Drop-seq platform performance and develop a pilot dataset of cortical sex-specific microglia. This dataset is devised to help answer several questions regarding the implementation of scRNA-seq, assess data quality and bioinformatic pipelines for a context-dependent study of microglial transcriptional heterogeneity.

**Aim 2. Drop-seq platform performance and pilot of cortical microglia**

- Objective 5: To measure Drop-seq platform performance
- Objective 6: To develop an in-house scRNA-seq dataset of cortical microglia
- Objective 7: To explore data quality and transcriptional heterogeneity in cortical sex-specific microglia.

## 4.3 Methods

### 4.3.1 Animals and single-cell isolation

Cortical microglia were isolated from female and male MacGreen mice (n=2, each), as described in Figure 58; a more detailed description can be found in Chapter 2. In short, tissue dissection was followed by the enzymatic and mechanical dissociation of tissue with the Neural Tissue Dissociation Kit (P). Myelin was depleted from the cell suspension through Percoll-mediated gradient centrifugation, prior to the enrichment of microglia by FACS.

### 4.3.2 Flow cytometry – microglial enrichment

Single-cells from MacGreen mice were sorted with the Aria II (BD Biosciences, San Jose, USA) fitted with the 100 µm nozzle to reduce shear-stress, and a cooled collection chamber (4°C). The Aria II was fitted with 3 lasers: violet (407), blue (488) and red (633). MacGreen cells were incubated with 7AAD (7-Aminoactinomycin D) (Fisher Scientific, 559925) (1/200) to exclude dead cells. Cells were excited with the 488-laser to detect viable cells (PerCP-Cy5.5) positive for EGFP (FITC) (Figure 60);

activity of Csf1r in MacGreen mice is reported by EGFP. Approximately 150,000 cells for each sex were sorted in Yield modus to maximize recovery at the expense of purity.

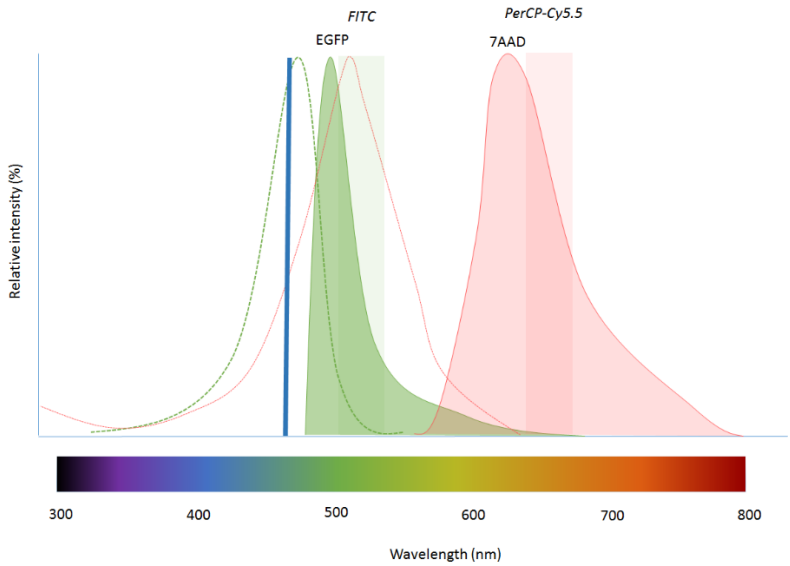


*Figure 60: Spectral view of Macgreen sorting. Viable (7AAD-), Csf1r-positive (EGFP⁺) microglia were sorted from female and male cortices. EGFP and 7AAD were detected with the FITC- and PerCP-Cy5.5 emission filters, respectively. Both fluorescent reporters were excited by the Blue (488) laser.*

### 4.3.3 Drop-seq – droplet microfluidics and single-cell library generation

Single-cells (100 cells/µl) and barcoded microparticles (120 beads/µl) were co-encapsulated in droplets with cell lysis buffer (~1 nl, ~124 µm; 60 beads/µl, final concentration). The system was run with flow rates for oil at 15,000 µl/hour; cells and beads at 4,000 µl/hour.

The stochastic nature of co-encapsulation stipulates that most droplets do not contain a cell. At the 120 beads/uL, the theoretical prevalence of a single beads is 5.7%; empirically this was ~6% for both samples, with minimal presence of doublets (<0.5%; measures of good run efficiencies.

Droplets were broken and collected by centrifugation, and captured RNA subjected to cDNA synthesis (Maxima-H RTase), generating single-cell transcriptomes attached to microparticles (STAMP) (Figure 56). 1100 STAMP from each sample were selected for PCR amplification, library preparation and Illumina sequencing.

### 4.3.4 PCR and Library Preparation

Exonuclease treatment removed bead primers that did not capture an RNA. The library was amplified by polymerase chain reaction (PCR) (16 cycles), purified with AMPure XP beads (Agencourt, A63880) and assessed with a BioAnalyzer High Sensitivity Chip (Agilent, 5067-4626) according to the manufacturer's instructions. Library sizes were 1,750 – 1,850, with concentrations between 240 – 265 pg/µl and a minimal coverage of 93%, signifying an absence of impurities and overall good library qualities. Normal concentrations from 50 cells/µl vary between 400 – 1000

pg/µl; however, variations in concentration are expected due to variations in cell concentration and the number of beads (Macosko et al., 2015). The purified and amplified cDNA was subjected to Nextera XT tagmentation, purified once more and prepared for NextSeq 500 sequencing. A 10 µl library pool at 3 nM was used as input for denaturation; 100 µL of sample was combined with 1200 µl of HT1 buffer.

### 4.3.5 Next Generation Sequencing

Single-cell libraries of sex-specific cortical microglia were sequenced on a NextSeq 500 platform (Version 2 chemistry). A Mid Output (TG-160-2001, 150 cycles) flow-cell with a maximum of 130,000,000 reads per cell was used. This was a shared sequencing run and libraries averaged 15,637 reads per cell.

### 4.3.6 High-performance computing - IRIDIS and raw data processing

Raw sequencing reads were converted to a sorted unmapped BAM file (FastqToSam, Picard bundled in Dropseq-tools v1.0) and filtered to remove all read-pairs with a barcode base quality of <10. The second read was trimmed at the 5' end to remove any TSO-adapter sequence and at the 3' end to remove polyA tails. Reads were aligned against mouse reference genome (mm10) using STAR aligner (v2.5.0a), then sorted/converted/merged to a BAM with a tag "GE" onto reads for data extraction. The DigitalExpression program (Dropseq-tools v1.0) extracted digital gene expression (DGE) information of the mRNA transcripts (UMI) and created a DGE matrix where rows contain genes and cell (barcodes) in columns.

### 4.3.7 Seurat and quality control

Seurat (2.3.4) (Butler et al., 2018), an R toolkit for single cell genomics was utilized. Creation of the Seurat object was restricted to cells with a minimum of 200 genes that are shared among at least 3 cells. Mitochondrial genes were identified and tagged, prior to further quality control by saturation analysis and the visualisation of the number of genes (nFeature_RNA) (*i.e.* library complexity), number of transcripts (nCount_RNA) (*i.e.* library size) and mitochondrial content (percent.mt). Thresholds were set for quality control (QC), to include cells with less than 2500 unique genes and a mitochondrial content of 8%. To remove noise from the dataset using a negative binomial approach, the object was regressed for library complexity and size, and mitochondrial load.

## 4.4 Results

This chapter functions to detail the performance of Drop-seq and the bioinformatic pipeline necessary to generate a pilot dataset. Isolated sex-specific, cortical microglial were captured with

the Drop-seq platform and libraries of each sex were prepared. I set out to sequence 1100 STAMP of each sex and estimated to detect ~125 CNS-associated macrophages (CAM); CAM were used as the minority fraction. Here, I will address Drop-seq platform performance, standard pre-processing, principal component analysis and dimensionality reduction, and cluster identification.

### 4.4.1 Mixed species experiments and Drop-seq platform performance

To ensure the Drop-seq platform performs as expected, that is, cellular distributions can be approximately accurately by the Poisson distribution, species mixed experiments are performed. In short, a mixed species experiments co-flows human and mouse cells to identify impurities at a given bead and cell concentration. Libraries are generated of the captured cells, after which mapping identifies mouse- and human-derived transcripts; species specificity illustrates if single cells can be effectively identified. This and other species mixing experiment are performed by the group of Matthew J. Rose-Zerilli, an example of which confirmed robust single-cell encapsulation and high species specificity (95%) (Figure 61).

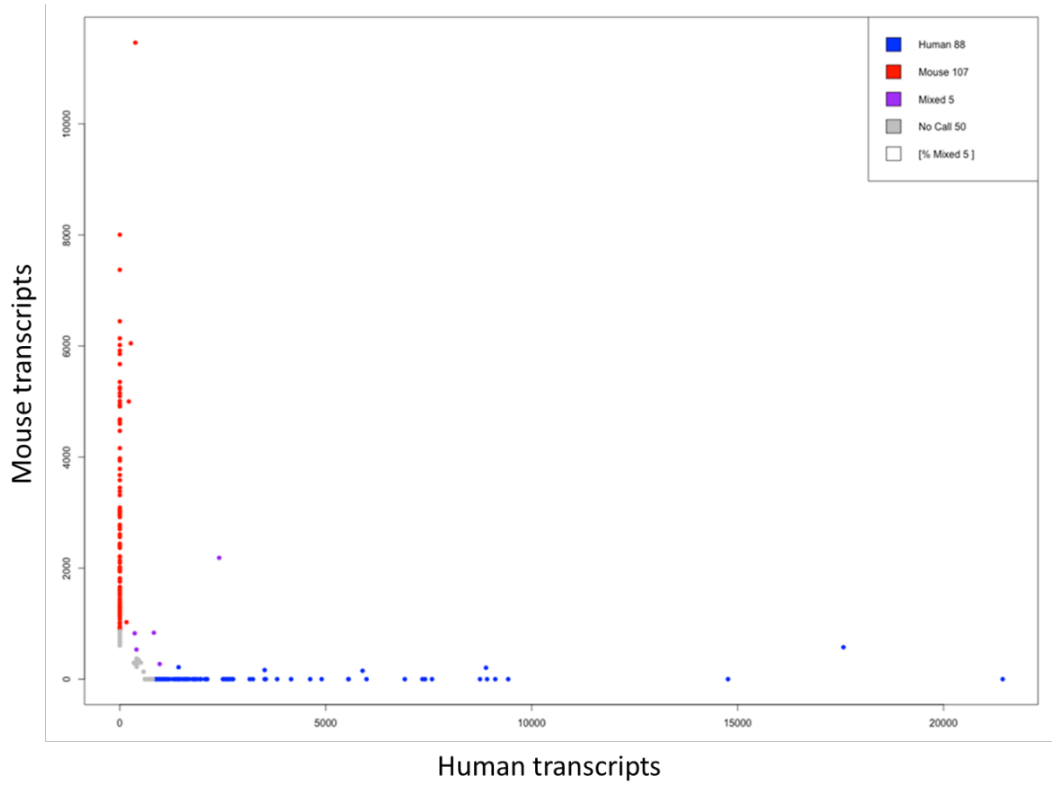


*Figure 61: Typical mixed-species experiment characteristics. Human and mouse single-cells (100 cells/µl) and barcoded microparticles (120 beads/µl) were co-encapsulated in droplets with cell lysis buffer. Alignment to the human and mouse transcriptome illustrate high species specificity, with 5% of all cells featured by a mixed, non-specific, transcript signature.*

### 4.4.2 scRNA-seq and ambient RNA

Droplets that have not encountered a cell house ambient RNA. Ambient RNA is actively secreted by live cells and/or released by cell lysis, resulting in droplets without a cell (Lun et al., 2019). Removal of these empty droplets is important for downstream analysis. How much of the detected

transcripts are cellular can be approached by the cumulative fraction of mapped reads plot - the inflection point in the curve marks the separation between ambient and cellular transcripts (Figure 62). For both sexes, approximately 750 out of 1100 cells have a cumulative fraction of approximately 0.5; that is, 68% of all cells provide meaningful data (Figure 62). Cumulative distributions like these are typical for Drop-seq, where the distribution of reads per cell are unevenly distribution.

I aimed to sequence 1100 cells of each sex; however, the cumulative fraction of mapped reads suggests that I fell short of this goal, with 1,327 cells (686 female, 641 male) remaining after removal of empty droplets (Figure 62). To further increase the ability to distinguish ambient and cellular RNA, it will be important to reduce cell stress during isolation.

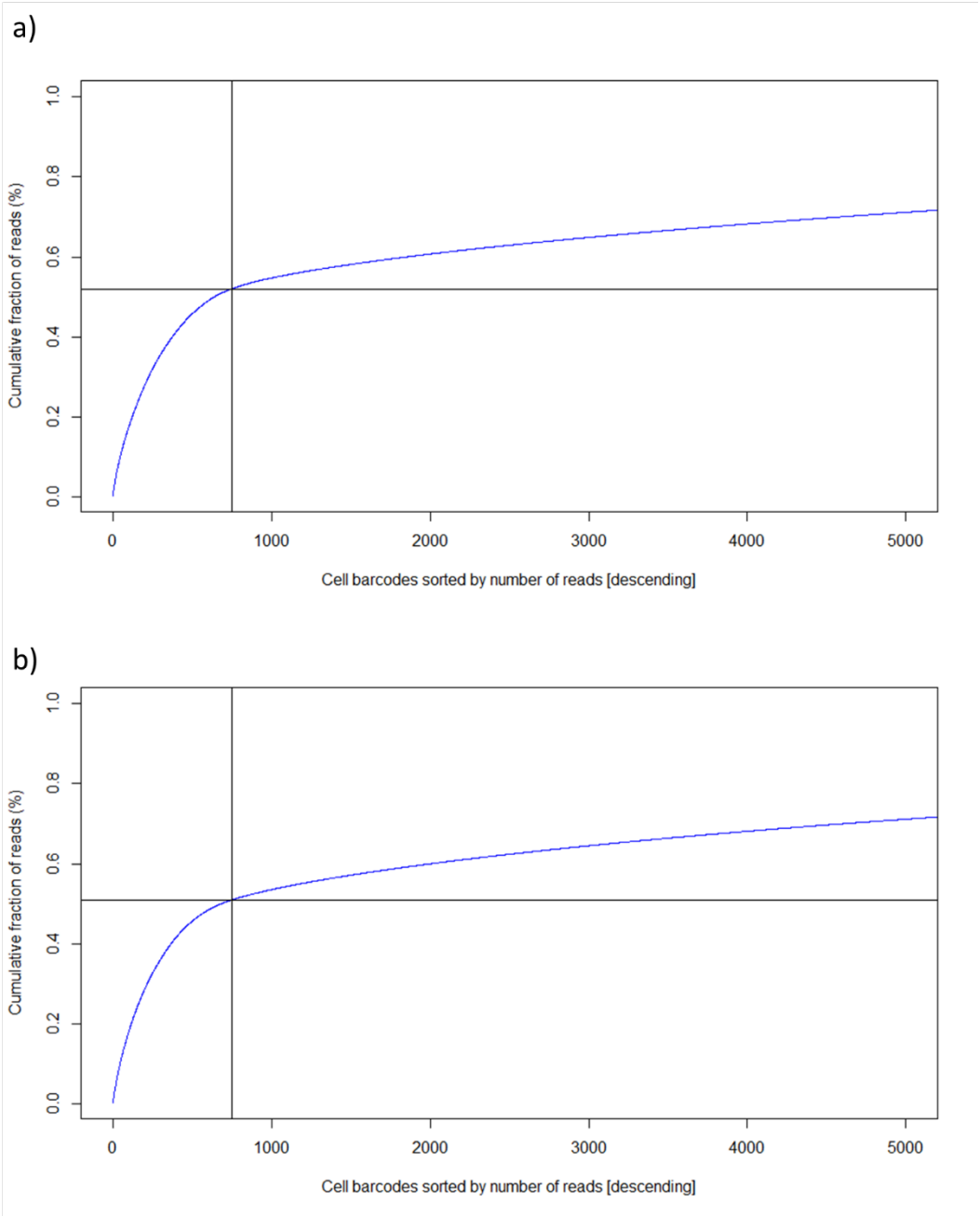

*Figure 62: Cumulative fraction of mapped reads a) Female and b) male cumulative fraction plots of mapped reads. Each featured an inflection point, as marked by the cross-sections at 750 (x-axis) and 0.52 or 0.51 (y-axis), female and male, respectively.*

### 4.4.3 Sequencing saturation is not reached

Sequencing saturation analysis reveals that most cells do not reach saturation (Figure 63). The number of transcripts ($\log^{10}$) is starting to plateau, or saturate, around 125,000 reads per cell; sequencing more at this point will only result in marginal increases in detected transcripts. In the dataset, 1 out of 1,327 identified cells (0.1%) reached 125,000 reads, with an average read depth of 15,637 reads per cell (Figure 63).

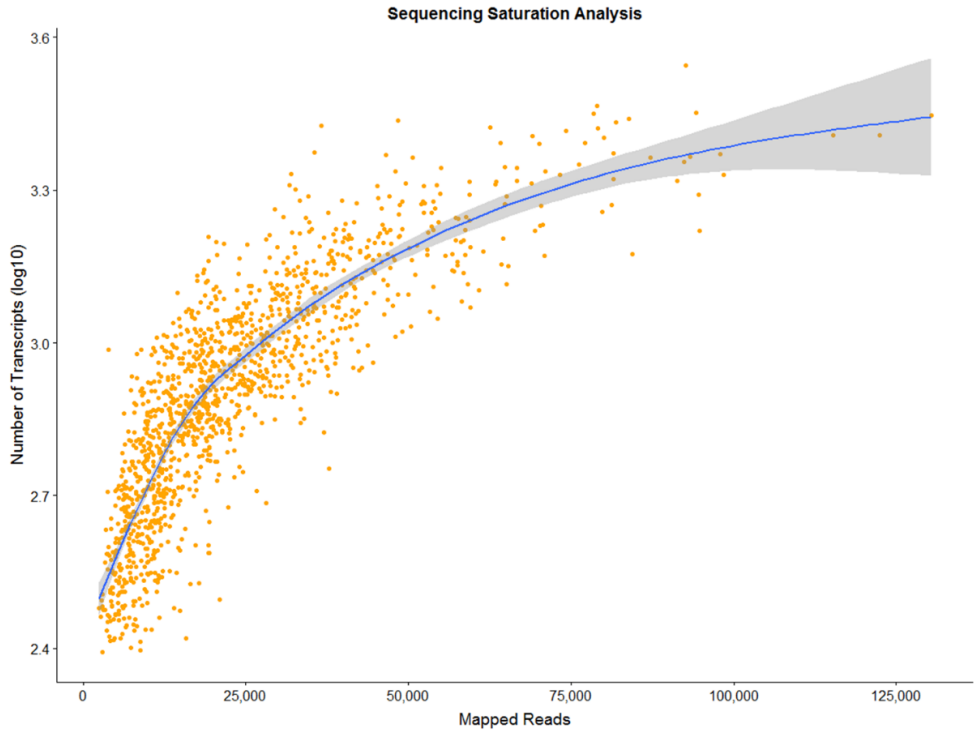


*Figure 63: Sequencing saturation analysis. The plot depicts the number of detected transcripts (log10) over the number of mapped reads for all cortical microglia passing primary processing (n= 1,327). Over 99% of cells do not reach saturation, set to occur around 125,000 reads per cell. Locally estimated scatterplot smoothing (LOESS) regression was used to approximate the trend in the dataset and supplemented with confidence intervals.*

### 4.4.4 Cell quality parameters and quality control

Cell quality in the pilot was assessed with library complexity and size and mitochondrial content (Figure 64). Bell-shaped curves for each parameter are indicative of good quality cells and allow for lower- and upper-limits to be set where needed. In this dataset, an upper limit of 2500 genes was set, and complemented with a lower threshold of 300 for library complexity and size, and an upper limit to mitochondrial content of 0.08% (Figure 64)

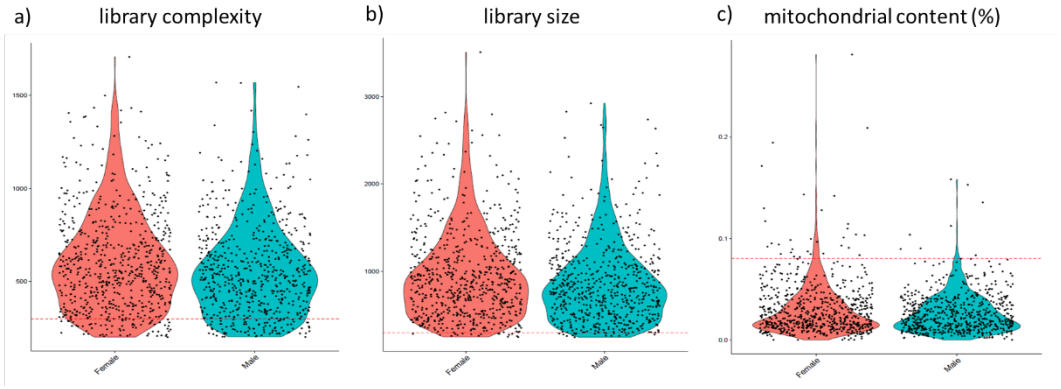


*Figure 64: Cell quality metrics of the microglial pilot data. Female and male microglia and their corresponding a) library complexity (nFeature_RNA) (i.e. nGene), b) library size (nCount_RNA) (i.e. nUMI), and the c) mitochondrial content (percent.mt). Lines are displayed to indicate upper and lower limits; nFeature_RNA .> 300, nCount_RNA > 300 , percent.mt < 0.08.*

The median library complexity and size of the male and female cells approximates 600 and 900, respectively (Figure 64). In contrast, previous scRNA-Seq work by Gokce *et al.* (2016) report that striatal microglia reach saturation around 500,000 reads and express roughly 2,000 genes (Gokce et al., 2016). Albeit region-dependent heterogeneity could affect library complexity and saturation, it suggests that the cortical microglial transcriptome was not fully interrogated at 15,637 reads per cell, leaving potential novel transcripts undetected.

### 4.4.5 Linear dimension reduction and principal component determination

As discussed previously, principal component analysis (PCA) is a central step in scRNA-seq to reduce dimensionality – see Section 2.8.1.4. Once more, ElbowPlot and JackStrawPlot were used to explore transcriptional heterogeneity before clustering. The ElbowPlot showed that the first 13 principal components (PC) describe most of the variability, of which JackStraw and JackStrawPlot analysis found that PC 1 through 8 and 12.are statistically significant (Figure 65).

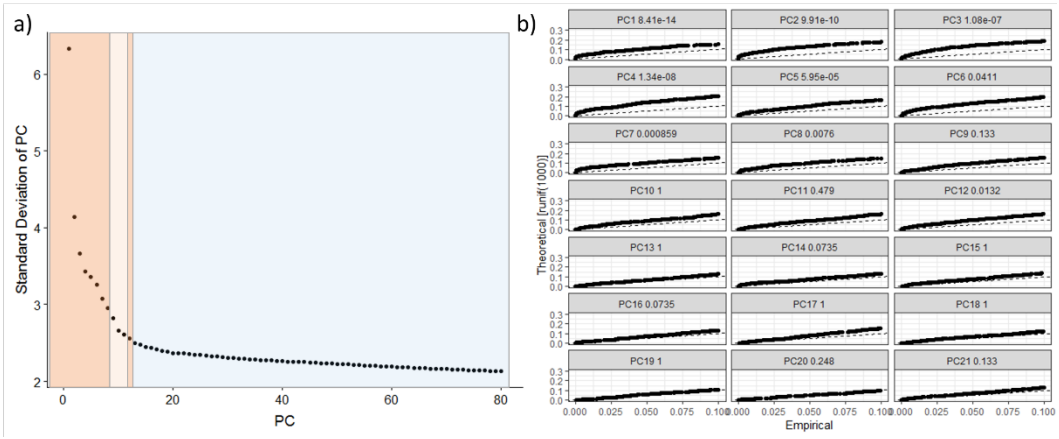


*Figure 65: Dimensionality in the pilot data. The standard deviation of the first 80 PC were depicted. The 'elbow' was found at PC 13. b) JackStrawPlot for cortical microglia. Several PC are statistically significant (P<0.05) (i.e. PC1:8, 12). Each of these sets are consistently above threshold (1e-05). The P-value for each PC is based on a proportion test of 200 genes compared to the proportion of genes expected below the threshold.*

### 4.4.6 Cluster identification of myeloid cells: microglia, CNS-associated macrophages and *ex*AM

Most of the cells have transcriptional profiles that correspond to microglia, with wide-spread expression of *Csf1r*, *Hexb*, *Tmem119* and *P2ry12* in cluster 0 to 3 (Figure 66). Interestingly, cluster 4 does not match a microglial signature, with a reduced or absent expression of *Hexb*, *Tmem119* and *P2ry12*. In fact, this cluster shows a signature reminiscent of CAM, a population that show modest levels of *Csf1r* but lacks *Tmem119* (Satoh et al. 2015).

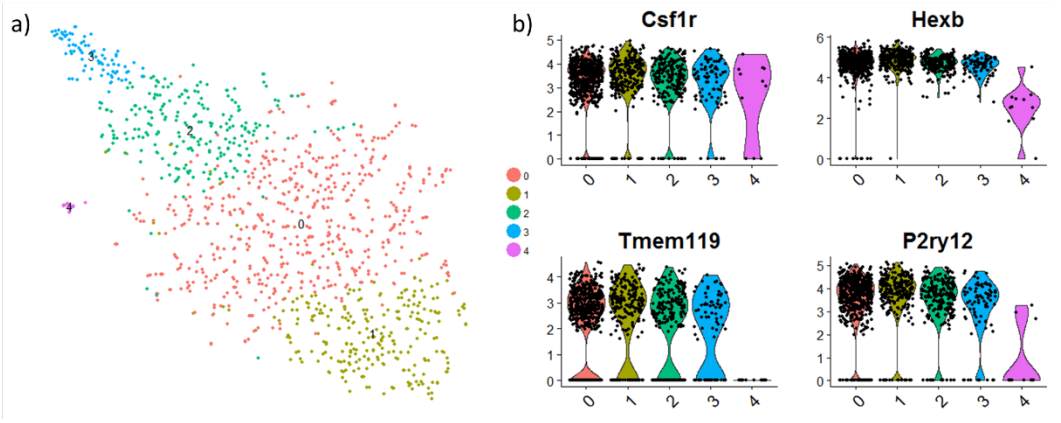


*Figure 66: Canonical microglial marker expression in cortical microglia clusters. a) t-SNEplot of cortical microglia. b) VlnPlot of Csf1r, Hexb, Tmem119 and P2ry12.The tSNE-plot is generated with a resolution of 0.4 and 9 dimensions (i.e. 1:8, 12).*

As stated, EGFP$^{+}$ cells (Macgreen mice, Csf1r-EGFP) were sorted from cortical tissue from male and female mice (4.3.2). Although commonly used as a marker for microglia in the CNS, *Csf1r* is a broadly expressed myeloid marker and can also be expressed by other macrophages; *Csf1r* is a key gene in their core profile (Mass et al., 2016). However, as seen previously, several other genes distinguish CAM from microglia and are selectively enriched in cluster 4 (Figure 29, Supplementary Table 2,Figure 67).

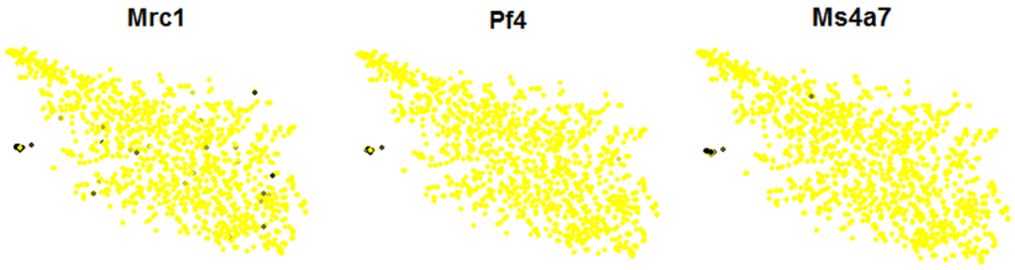


*Figure 67: CAM in Csf1r-EGFP+ sorted cells. FeaturePlot of CNS-associated microglia (CAM) markers (i.e. Mrc1, Pf4, Ms4a7). Gene module expression levels in the plot range from low (gold) to high (black).*

As anticipated, CAM are the minimum fraction in the pilot dataset. In correspondence, no cell actively cycling and proliferating microglia (CPM) were identified, a minority cell not exceeding 1.4% of the adult microglial population and less than the prevalence of CAM (Askew et al., 2017; Mrjden et al. 2018). Unfortunately, a large proportion of microglial cells were affected by *ex*AM-like IEG signatures, most of which in cluster 2 and 3 (Figure 68).

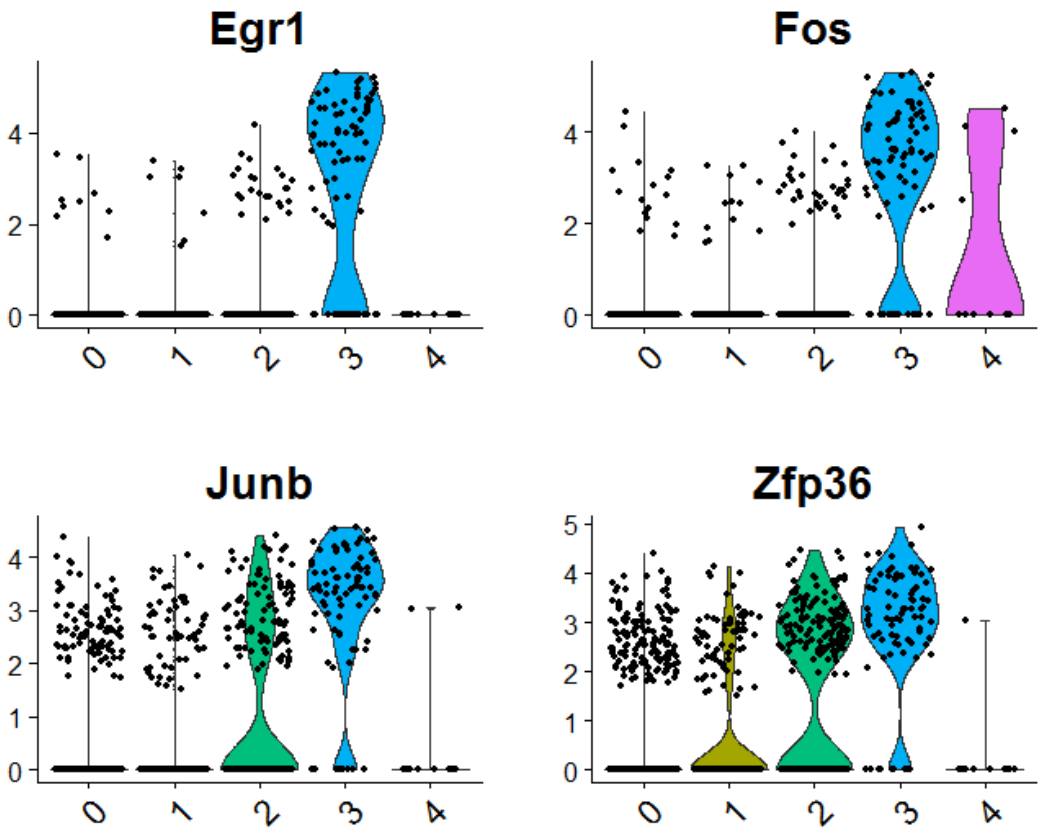


*Figure 68: Detection of exAM-like signatures with standard experimental procedures. VlnPlot of exAM-like immediate early gene (IEG) Egr1, Fos, Junb and Zfp36 in a cluster-specific manner.*

A DGE analysis was performed with "FindAllMarkers", a Heatmap of these results can be found in Supplementary Figure 10. Of note, Van den Brink *et al.* (2017) identified a gene list associated with dissociation of mouse stem cells; Fos- and Jun-expressing subpopulations were also identified in mouse acinar cells and zebrafish osteoblasts (Brink et al., 2017). Similarly, cluster 4-specific genes were enriched by genes from this list, suggesting that this is a conserved cellular response to dissociation. The list of genes shared between cell types was named the IEG module (Table 6); a complete list of activated muscle stem cells genes can be found in Supplementary Table 13.

*Table 6: Immediate early gene module characterization.*

| Gene: | Full name: |
|---|---|
| Atf3 | Activating transcription factor 3 |
| Btg2 | BTG Anti-Proliferation Factor 2 |
| Dnajb1 | DnaJ Heat Shock Protein Family (Hsp40) Member B1 |
| Dusp1 | Dual Specificity Phosphatase 1 |
| Egr1 | Early Growth Response 1 |
| Fos | Fos Proto-Oncogene, AP-1 Transcription Factor Subunit |
| Hspa8 | Heat Shock Protein Family A (Hsp70) Member 8 |
| Ier2 | Immediate Early Response 2 |
| Jun | Jun Proto-Oncogene, AP-1 Transcription Factor Subunit |
| Junb | JunB Proto-Oncogene, AP-1 Transcription Factor Subunit |
| Jund | JunD Proto-Oncogene, AP-1 Transcription Factor Subunit |
| Mt1 | Metallothionein 1A (MT1A) |
| Nfkbia | NF-Kappa-B Inhibitor Alpha |
| Ppp1r15a | Protein Phosphatase 1 Regulatory Subunit 15a |
| Socs3 | Suppressor of Cytokine Signalling 3 |
| Ubc | Ubiquitin C |
| Zfp36 | Zfp36 Ring Finger Protein |

***Note**: Cluster 4-specific genes were compared to an activated cell signature of FACS-sorted, immediate early gene (IEG)-enriched muscle stem cells, as described by Van den Brink et al. (2017). 17 of 32 were shared between both suggestive of a broadly conserved IEG gene module in response to dissociation.*

In fact, using the IEG module in the dataset (corroborating the trend observed for the *ex*AM genes), a progressive increase of expression from cluster 0, to 2 to 3 was noted (Figure 69). A trend like this hints towards a dynamic and global effect of *ex*AM-like signatures on all microglia in this pilot. Moreover, cluster 3 also features the lowest levels of *Tmem119* and *P2ry12* (Figure 66), suggesting that the emergence of such *ex*AM-like signatures is paired with a loss of microglial identity, and doubly confounding the transcriptional read-out. These findings correspond to aged and diseased conditions (Dubbelaar et al., 2018); homeostatic microglial genes are downregulated in these conditions. The loss of P2ry12 by dissociation corresponds to findings by Li *et al.* (2019), and is reminiscent of a loss of immune-checkpoints causal to DAM emergence (Deczkowska et al., 2018; Li et al., 2019). Thereby, emergence of such signatures requires mitigation, experimentally and/or bioinformatically.

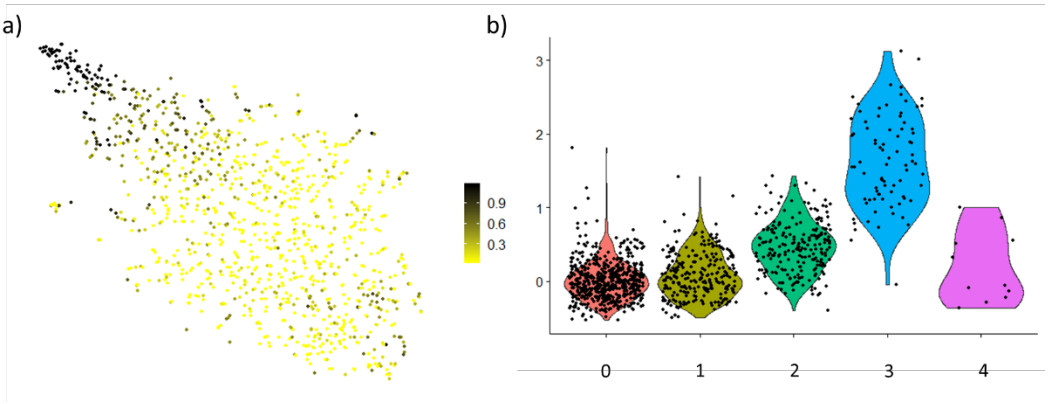


*Figure 69: Progressive enrichment of the IEG gene module in the pilot data. a) FeaturePlot of the immediate early gene (IEG) module expression. b) VlnPlot of the IEG module in a cluster-specific manner.*

### 4.4.7 Principal component selection and clustering

The interdependence of *a priori* knowledge and novel discovery is most salient with the identification of clusters. To maximize the exploration of microglial transcriptional heterogeneity, I explored if genes associated CAM or exAM-like signatures could be removed from the data; PC selection is the first starting point. Strikingly, of the 9 significant clusters, 3 feature genes associated with CAM and exAM (Supplementary Figure 9). PC2 is enriched for CAM genes (*e.g. Mrc1*, *Pf4*,), whereas PC 7 and 8 are enriched for IEG (*e.g. Egr1, Fos*) (Figure 70) (Brink et al., 2017; Kierdorf et al., 2019; Wu et al., 2017).

The inclusion of all significant PCs (1:8, 12) results in the most heterogeneous mapping of diversity, whereas the exclusion of PC2, or PC7 and PC8 effectively removes cells characterized by the expression of IEG and CAM, respectively (Figure 70). Removal of such PC might therefore offer a means to the removal of CAM and exAM signatures might therefore be achieved by the exclusion of PC affected by these effects. However, as, discussed, *ex*AM genes and microglial identity are intertwined.

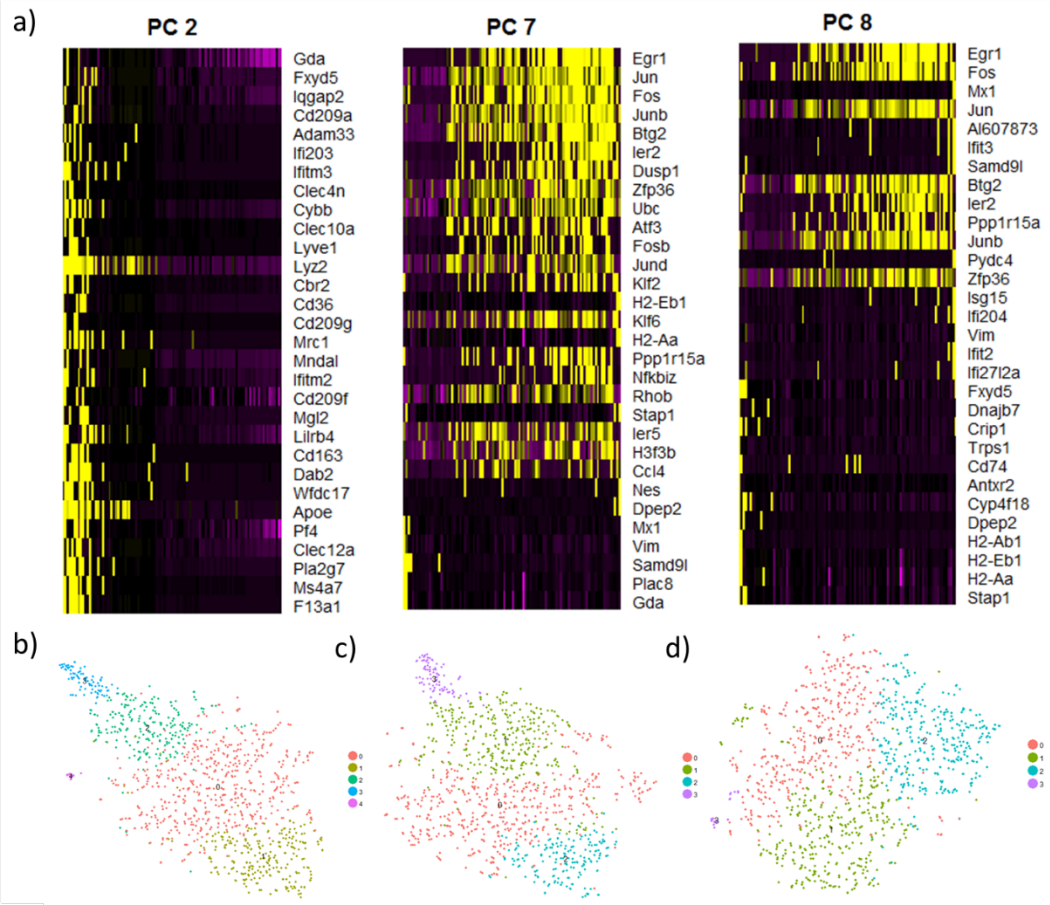


*Figure 70: Biological markers and PC-dependent clustering. a) Principal component (PC) heatmap for PC2, 7 and 8. PC2 is featured by CAM genes, whereas PC 7 and 8 are associated with IEG, respectively. b-d) The selective removal of either set is causal to differential clustering characteristics. b) Clustering with all significant PC (PC1:8, 12) retains CAM and IEG, c) whereas the selective removal of PC2, d) or PC7 and PC8exclude CAM and exAM, respectively. CAM, CNS-associated macrophage; exAM, ex vivo-activated microglia; IEG, immediate early gene.*

*e.g. Zfp36* is a marker for both homeostatic (HOM) and aged inflammatory microglia (AIM), whereas *Ifit3* is enriched in interferon response microglia (IRM) (Supplementary Table 1, Supplementary Table 2). Indeed, *Zfp36* is a marker and transcription factor for microglial identity (Grabert et al., 2016; Hanamsagar et al., 2017; Wehrspaun et al., 2015). Here, both *Zfp36* and *Ifit3* are correlated with PC rich with IEG (Figure 70). The interlaced nature of such gene signatures greatly reduces the efficiency of PC exclusion, urging for alternative approaches to be considered.

An alternative might be offered by the regression and/or removal of exAM genes from the variable gene list (Van Hove et al., 2019). However, like the removal of PC, this will affect microglial gene signatures and is not preferred. Experimental approaches might be need to truly mitigate such technical artefacts, of which several implementations have started to emerge (Hammond et al., 2019; Marsh et al., 2022; Safaiyan et al., 2021; Sala Frigerio et al., 2019; Wu et al., 2017).

## 4.5 Discussion

Here, I set out to assess Drop-seq platform performance and generate an in-house scRNA-seq dataset. As a platform, Drop-seq offers a cost-effective means to study microglial heterogeneity,

albeit some limitations have been discussed. That is, capture efficiency is low and resource allocation is unevenly distributed. These are accepted limitations, understanding that this platform has the benefit of using UMI for quantification, and does so with great accuracy and sensitivity (in comparison to other platforms).

With Drop-seq, I was able to generate a pilot dataset of adult cortical microglia of both sexes, which was used to explore data quality and transcriptional heterogeneity. Notably, despite the loss of cells due to some of the inherent limitations (or a failure to detect cells by a lowered sequencing depth), the data was broadly of good quality. *e.g.* Less than 5% of cells displayed transcripts of mixed species, and mitochondrial content of cells was low. CAM were also identified, *a priori* set to be minimum fraction, confirming that the platform behaves predictably. Unfortunately, as previously discussed in the atlas, the occurrence of exAM-like signatures in the data suggests that standard experimental procedures affect microglia negatively, as has been the case for other cell types (Brink et al., 2017).

The identification of such findings urged me to explore bioinformatic methods to mitigate the inclusion of exAM-like signatures. To that end, the focus was on the PC that include IEG (and CAM) signatures. Exclusion of such effects is possible through these means; however, as discussed, the exAM signatures are intimately tied to native microglial identity and activation, which would undermine the ability to identify such processes in scRNA-seq data (Figure 30).

Regression and/or removal of these genes from the variable gene list would similarly affect this capacity. The most viable alternative is to mitigate such effects experimentally. As stated, scRNA-seq consist of six broad steps, each of which change the environment of microglia. In the next chapter, I will detail the experimental procedures that could affect the prevalence of exAM-like signatures.

### 4.5.1 Supplementary figures

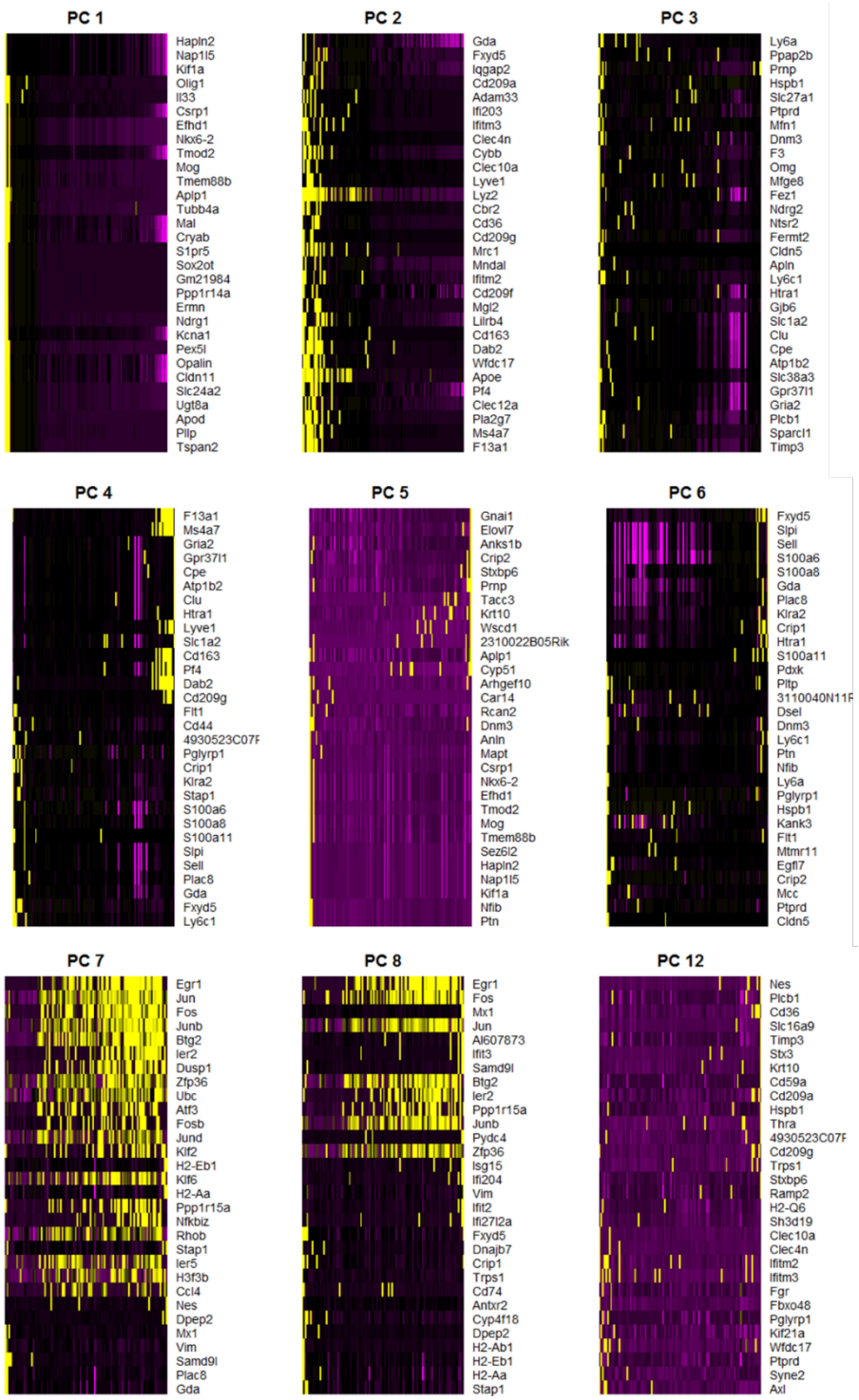


*Supplementary Figure 9: Significant principal components of the pilot data. Principal component (PC) 1 to 8 and 12 are displayed. Markers for canonical microglia, exAM and CAM are present.*

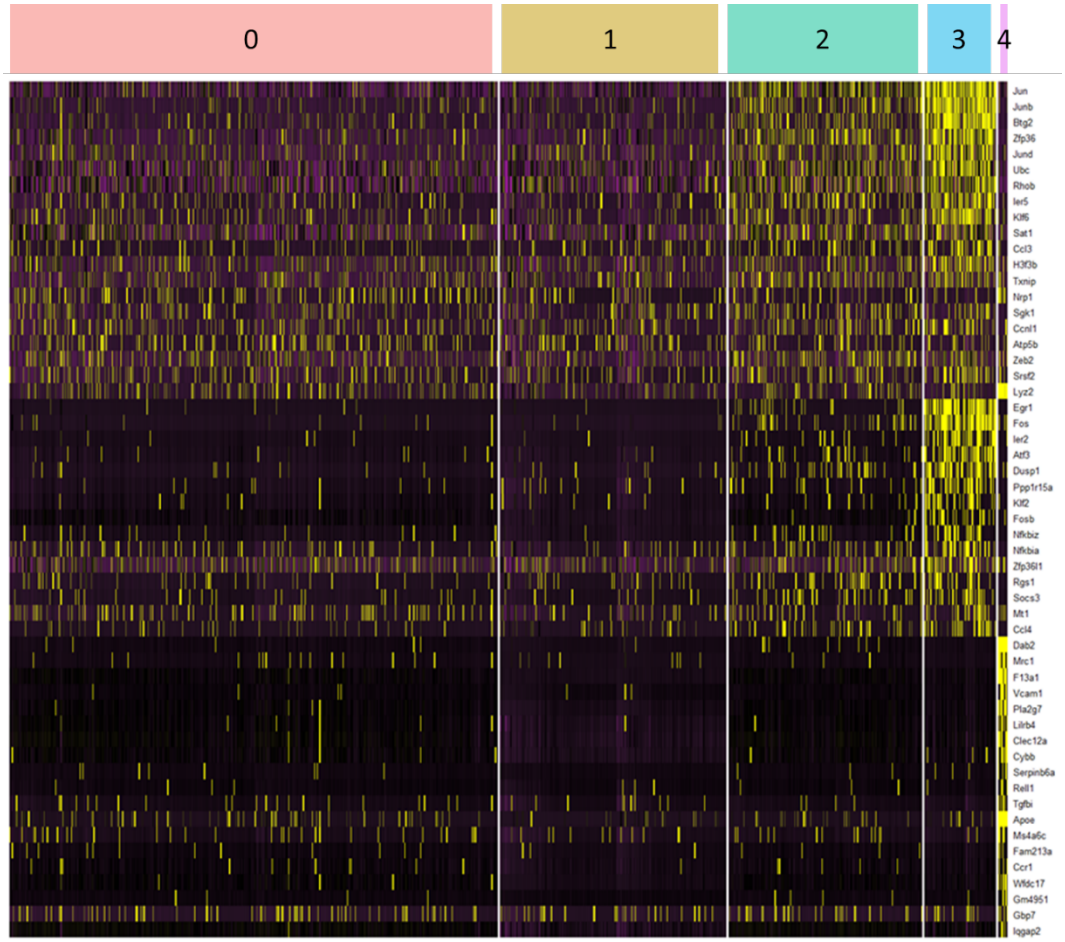


*Supplementary Figure 10: Standard experimental procedures instil exAM-like signatures. Heatmap of cluster-specific markers include ex vivo-activated microglia (exAM) signatures like immediate early gene expression. "FindAllMarkers" was used 'only.pos = FALSE', 'min.pct = 0.2',' logfc.threshold = 0.25', 'test.use = "negbinom"'.*

*Supplementary Table 13: Activated muscle stem cell module.*

| | | | |
|---|---|---|---|
| 1 | **Atf3** | 17 | Hspb1 |
| 2 | **Btg2** | 18 | Hspe1 |
| 3 | Cebpb | 19 | Hsph1 |
| 4 | Cebpd | 20 | Id3 |
| 5 | Cxcl1 | 21 | **Ier2** |
| 6 | Dnaja1 | 22 | **Jun** |
| 7 | **Dnajb1** | 23 | **Junb** |
| 8 | **Dusp1** | 24 | **Jund** |
| 9 | **Egr1** | 25 | **Mt1** |
| 10 | **Fos** | 26 | Mt2 |
| 11 | Fosb | 27 | **Nfkbia** |
| 12 | Hsp90aa1 | 28 | Nr4a1 |
| 13 | Hsp90ab1 | 29 | **Pp1r15a** |
| 14 | Hspa1a | 30 | **Socs3** |
| 15 | Hspa1b | 31 | **Ubc** |
| 16 | **Hspa8** | 32 | **Zfp36** |

*Note: Complete gene module of activated muscle stem cells. Genes in bold are shared with cluster 4 markers.*

# Chapter 5 Technical artefacts and scRNA-seq: cell isolation and *ex vivo* gene signatures

## 5.1 Single cell isolation and single-cell RNA-sequencing

Single-cell RNA-sequencing (scRNA-seq) has enabled the generation of large-scale, whole-genome cell atlases, rapidly increasing cell type marker identification in multicellular tissues (Han et al., 2018; Regev et al., 2017; Schaum et al., 2020, 2018). However, as seen before, standard experimental procedures are linked to the occurrence of *ex*AM (Figure 30,Figure 68). Broadly, *ex vivo* gene signatures are induced when single cells are isolated from their native environment (Adam et al., 2017; Brink et al., 2017; Lacar et al., 2016; Machado et al., 2017; van Velthoven et al., 2017).

Tissue dissociation and cell isolation is a combination of mechanical disruption and/or enzymatic cleavage methods. Commonly used enzymes include papain and collagenase (Marsh et al., 2022; Slyper et al., 2020). The selection for each enzyme varies, as it will affect epitope availability on the cellular membrane, a key consideration for fluorescence-activated cell sorting (FACS) and cytometry by time-of-flight (CyTOF) (Marsh et al., 2022; Mattei et al., 2020). However, both enzymes function most efficiently at physiological temperatures and many protocols therefore opt to dissociate tissue at 37°C (Dulken et al., 2019; Hrvatin et al., 2018; Lau et al., 2020; Mathys et al., 2017; Safaiyan et al., 2021; Utz et al., 2020; Van Hove et al., 2019; Wang et al., 2020). Notably, transcription and translation are reduced at lower temperatures.

Here, I review the most relevant current methods to minimize the *ex vivo* activation in scRNA-seq, to preserve *in vivo* microglial identity.

### 5.1.1 *Ex vivo* cellular activation and scRNA-seq

Complex tissues like the central nervous system hosts are wide range of cells, including astrocytes, oligodendrocytes, neurons, endothelial and mural cells, and microglia (Wu et al., 2017). Each environment, with its relative proportion of grey- and white-matter and cellular heterogeneity, has been shown to have distinct mechanical properties (Budday et al., 2015; MacManus et al., 2017). In this way, each region will have its own characteristics in relation to single cell isolation.

One of the first studies that reported on the effects of sample preparation on transcriptomic data derives from human peripheral blood mononuclear cells (PBMC). A microarray study demonstrated an *ex vivo* induction of over 2,000 genes by overnight storage (Baechler et al., 2004). Dysregulated genes typically belonged to pathways involving stress, such as heat shock proteins (HSP),

immediate-early genes (IEG) and early response genes (ERG); typical dissociation-induced artefacts. Since then, several other studies in skeletal muscle satellite cells (SC), kidney, and brain cells have found similar effects (Adam et al., 2017; Brink et al., 2017; Machado et al., 2017; van Velthoven et al., 2017; Wu et al., 2017).

All cells will eventually display an activated signature given sufficient time, however, there are distinct differences in response time (Machado et al., 2021a; Marsh et al., 2022; Wu et al., 2017). Microglia, endothelial cells, and mural cells are first-responders and found to be particularly sensitive to standard dissociation (Adam et al., 2017; Wu et al., 2017). It is unknown why such cell-specific sensitivities are found; however, it stands to reason these effects are due to intrinsic predispositions to stimuli associated with their biological roles. Cells in a multicellular organism are in constant communication to establish homeostasis or return to it, by sending and receiving autocrine, paracrine, and endocrine signals, as well as signals through gap junctions and mechanosenzing. Microglial signals are mediated by the 'sensome', a cluster of protein-encoding transcripts for sensing endogenous ligands and microbes (Hickman et al., 2013). The sensome facilitates microglia to survey the brain parenchyma *in vivo*, a central function of the immune cell (Nimmerjahn et al., 2005). However, the same sensome (*i.e.* cellular machinery) actives microglia during cell isolation protocols and masks the native transcriptome. Similarly, endothelial and mural cells are key effectors in blood-brain barrier homeostasis and immune signalling (Daneman and Prat, 2015).

*Ex vivo* activation has become a recognized caveat of scRNA-seq, a confounding variable which has fostered novel ways of mitigating such disruptions to the native transcriptome.

### 5.1.2 Enzymatic cell isolation and digestion temperature

Digestion temperature is a key feature of cell isolation. As stated, typical enzymes like papain and collagenase are most active at physiological temperatures. However, cold-activated enzymes (CAP) like the Himalayan, glacier-born *Bacillus Licheniformis* protease enable digestion at lower temperatures (Adam et al., 2017; Hertzano et al., 2021; O'Flanagan et al., 2019).

Studies that use CAP for digestion have reported on a lower level of technical artefacts in comparison to standard heated digestion, featured by lower gene expression levels of IEG like *Fos*, *Egr1*, *Zfp36*, *Ier2*, *Jun* and *Dusp1* (Adam et al., 2017; Hertzano et al., 2021; O'Flanagan et al., 2019). Furthermore, heated dissociation displayed a considerable transcriptional variability depending on the digestion time (Adam et al., 2017).

However, other features of enzymatic digestion are less desirable. Like more commonly used enzymes, enzymatic cleavage of epitopes could confound downstream flow cytometric analyses and remains a consideration for or against the use of any digestion enzyme (Hertzano et al., 2021).

Attempts to adapt these cold-activated proteins to brain tissue are expected to be confounded further by DNAse activity. DNAse is an essential component in single cell isolation protocols, to degrade cell-free DNA and reduce cell clumping; however, there is currently no cold-active DNase (Marsh et al., 2022). Furthermore, cells could undergo a cold-shock response, which is also expected to alter the transcriptome (Machado et al., 2021). Lastly, cell recoveries vary depending on the digestion temperature (Denisenko et al., 2020). *e.g.*, renal macrophages were found to be less abundant with heated digestion (Denisenko et al., 2020).

Taken together, higher levels of cellular activation during heated digestion favour CAP-mediated digestion. Remarkably, despite this effect, CAP have not found more wide-spread use in scRNA-seq since their first discovery, even if these appear to offer superior sample quality. I postulate that their underrepresentation in the single-cell field is due to cost considerations; cold-activated enzymes are generally more expensive than their heat-activated counterparts and could limit large-scale studies.

### 5.1.3 Mechanical dissociation protocols

Now, if (heated) enzymatic dissociation introduces technical artefacts, can users select against using enzymes? The literature indicates that enzyme-free processing is possible, limiting dissociation to the mechanical disruption of tissue. Most commonly, studies report on the use of Dounce homogenizers (Almanzar et al., 2020; Hammond et al., 2019a; Q. Li et al., 2019a; Schaum et al., 2018) or Potter pestles (Masuda et al., 2020; Sousa, 2018) (Table 5). Mechanical dissociation utilizes shearing and/or grinding forces to isolating cells ("Guide to the Disruption of Biological Samples - 2012," n.d.).

Mechanical dissociation can be performed at lower temperatures and comes at a reduced cost relative to enzymatic protocols. However, without the aid of enzymatic cleavage, yield in such methods vary across experimental conditions and will therefore not meet all experimental design needs (Marsh et al., 2022; Slyper et al., 2020). Droplet-based platforms require more cells than plate-based approaches, potentially limiting its adaptation for high-throughput scRNA-seq. Furthermore, by recovering less cells from tissue, mechanical dissociation may underestimate true cellular heterogeneity, introducing a bias towards more numerous and accessible cells over rare subtypes.

Interestingly, some protocols of mechanical dissociation still make use of DNase in cold conditions, even if DNase is not functional at lower temperatures (Almanzar et al., 2020; Li et al., 2019; Marsh et al., 2022; Schaum et al., 2018).

Of note, Marsh *et al.* (2022) reported on the presence an *ex vivo* gene signature in studies that utilize Dounce homogenization (Marsh et al., 2022). The authors argue that the effect is minimal

and Dounce is an effective tool in minimizing artefactual genes, as enzymatic dissociation induces a stronger signature. However, the *ex vivo* signature remained elevated when compared to protocols that use transcriptional and translation inhibitors (Marsh et al., 2022). The question then arises, what are the characteristics of such inhibition and how could these benefit microglial studies?

## 5.2 Transcriptional and translation inhibition and scRNA-seq

Recent scRNA-seq literature illustrates a trend to enzymatic dissociation in the presence of inhibitors, that is, transcriptional and translation inhibitors.

Transcription in eukaryotes is dependent on 3 RNA polymerases, large complexes that bind to and initiate DNA transcription (Rosenberg and Rosenberg, 2012). Inhibiting transcription in eukaryotes can be achieved by a broad range of products, including amanitin, actinomycin, DRB, flavopiridol, and triptolide (Bensaude, 2011). Translational inhibition can be achieved by, among others, cycloheximide, emetine and anisomycin (Abbas et al., 2011; Chan et al., 2004). Each offers a means to reduce the cellular response to dissociation, preserving biological microglial signatures and improving data quality.

Three inhibitors are commonly used in scRNA-seq studies: actinomycin (ActD), triptolide (Tripto) and anisomycin (Aniso). I will review ActD and its use in isolation, or in combination with Tripto and Aniso, for microglial scRNA-seq.

### 5.2.1 Combinatorial inhibition of ex vivo artefacts in the CNS

A seminal study by Hrvatin *et al.* (2018) implemented a combination of factors to abrogate technical artefacts in neurons. To study cortical, transcriptional responses to light exposure in mice, the authors developed a heated, isolation protocol for scRNA-seq that included the use of ActD, Tripto, Aniso, TTX and AP-5 (Hrvatin et al., 2018). TTX and AP-5 block voltage-gated sodium and NMDAR-channels, respectively. Therefore, the combination of inhibitors is expected to effectively block transcriptional, translation, and activity-dependent alterations to the *in vivo* signature.

The lab of Beth Stevens has since adapted and introduced this protocol for microglial biology (Marsh et al., 2022). The protocol inhibits *ex vivo* gene expression by combining ActD, Tripto and/or Aniso during the phases of exsanguination, collection, and digestion, excluding TTX and AP-5. Of note, transcriptional inhibition with ActD and Trip are generally well-accepted throughout isolation; however, translational inhibition with Aniso has not been used during exsanguination, suggestive of contra-indications at this stage (Hrvatin et al., 2018; Marsh et al., 2022).

Two studies have utilized the developed protocol (Hasselmann et al., 2019; McQuade et al., 2020). The protocol is touted for its flexibility, capable of generating high quality scRNA-seq data across a range of CNS cells (Marsh et al., 2022). However, for the isolation and sequencing of microglia, ActD alone is a sufficient for the mitigation of *ex vivo* signatures in scRNA-seq (Marsh et al., 2022; Wu et al., 2017).

### 5.2.2 Transcriptional inhibition with actinomycin D

The longest-standing and most used transcriptional inhibitor in scRNA-seq studies is ActD. ActD is an antibiotic and antineoplastic molecule that derives from the *Streptomyces* genus, and contains two cyclic peptides interlinked with a phenoxazine(Lai et al., 2019; Liu et al., 2016) (Figure 71). ActD is postulated to bind DNA, which, in turn, inhibits RNA polymerases and transcription (Lai et al., 2019; Wu et al., 2017).

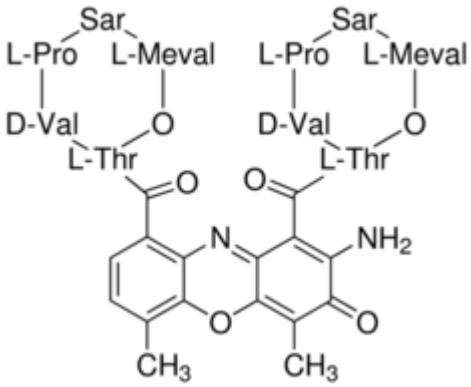


*Figure 71: Molecular structure of Actinomycin D. Actinomycin D (C62H86N12O16) (1255.42 Da) is a polypeptide with antibiotic and antineoplastic features. Two cyclic peptides are coupled by a phenoxazine. Sourced image from Sigma("Actinomycin D from Streptomyces sp., ~98% (HPLC) | Sigma-Aldrich," n.d.).*

scRNA-seq studies of CNS tissue have used ActD across a distinct number of phases during single-cell isolation (Gunner et al., 2019; Hasselmann et al., 2019; Hrvatin et al., 2018; Marsh et al., 2022; McQuade et al., 2020; Pavel et al., 2019; Safaiyan et al., 2021; Van Hove et al., 2019; Wu et al., 2017) (Table 7). ActD is commonly used during collection and digestion of tissue; additionally, several studies extend its use to during exsanguination and downstream cell handling. Concentrations generally vary between 4 and 45 µM, although higher concentrations are often restricted to ActD used in isolation. In isolation, the concentration varies from 15 to 45 µM, depending on the temperature and duration of the digestion. When combined with a second transcriptional inhibitor (*i.e.* triptolide) and a translational inhibitor (*i.e.* anisomycin), ActD has been used at 4 µM.

At these concentrations, all three classes of eukaryotic RNA polymerases are inhibited by ActD: Class 1, 40 nM; Class 2, 400 nM; and Class 3, 4 µM (5 ug/mL), respectively (Bensaude, 2011). Moreover, ActD displays low reversibility; albeit transcription displays a modest recovery after removal of ActD, more than 24-hours was needed for a return to a priori full-length transcript

synthesis (Bensaude, 2011; Hadjiolova et al., 1995; Schluederberg et al., 1971). Furthermore, ActD has a relatively large safety window, without genotoxic stress until a concentration of 100 µM (Mussil et al., 2019). In short, ActD offers wide-spectrum, long-lasting and well-tolerated transcriptional inhibition.

To minimize *ex vivo* cellular activation in cell isolation, Wu *et al.* (2017) were the first to trial transcriptional inhibition with ActD in a scRNA-seq study. Without ActD, up to 100% of microglial cells displayed an activated profile, whereas ActD limited the induction *of* an *ex vivo* profile to less than 5% (Wu et al., 2017). Similarly, the use of ActD prevented cellular activation of CNS-associated macrophages (Van Hove et al., 2019). Furthermore, reducing temperatures to 22 or 11°C further diminished the percentage of activated microglial cells, and aided the removal of dissociation-induced artefacts in endothelial and mural cells (Wu et al., 2017).

The most current implementation of ActD is featured by Safaiyan *et al.* (2021). The authors include 45 µM of ActD in cell isolation during collection and (heated) digestion, and effectively isolate microglia from the CNS without signs of dissociation-induced artefacts, as expression of genes like *Fos*, *Egr1*, *Atf2*, and *Zfp36* is lacking (Safaiyan et al., 2021a).

### 5.2.3 Weighted benefits: transcriptional inhibition, microglial enrichment, and RNA decay

Safaiyan *et al.* (2021) identify astrocytes, ependymal cilia and secretory cells, erythroid-like and vascular cells, macrophages, and neuroblasts and NPCs (Safaiyan et al., 2021). However, disproportionally, the isolation recovers microglia at the expense of neurons; up to 50% of all cells are microglia (Safaiyan et al., 2021). *In situ*, microglia compose 5 to 12% of all CNS-cells. It will be important to define the target population of any scRNA-seq study, as it might not effectively capture all cells equally.

Furthermore, any reagent will have potential limitations in its use. Prior to its adoption in scRNA-seq, ActD had been used to study mRNA decay rates in cultured cells (Lai et al., 2019). mRNA decay is a biological phenomenon that describes the natural decline and breakdown of mature RNA transcripts and is significantly heterogeneous; mRNA transcript stabilities vary. Indeed, genes like *Dusp1*, *Ier3* and *Nfkb1a* are particularly sensitive to degradation, whereas others like *Gapdh* and *Rpl14* are more stable, albeit also subject to change (Lai et al., 2019). A microarray study of human fibroblasts identified that 4,992 (9.1%) of 54,613 probe-set transcripts decayed more than 25% by 4 hours in the presence ActD (Lai et al., 2019; Qiu et al., 2015).

Recent work in microglial cells – using ActD in isolation or in combination - have not shown any detrimental effects of transcriptional inhibition (Marsh et al., 2022; Safaiyan et al., 2021). However, two downstream effects on data quality will need to be taken into consideration. First, prolonged incubation with ActD and/or differences in sample processing time can affect library complexity

and might introduce technical variations between samples (*i.e.* baseline drifting); batch correction would therefore be critical when using ActD. Second, susceptible (and rare) transcripts are expected to be selected against during processing, reducing native library complexity. Droplet-based scRNA-seq platforms are inherently less suitable for the detection of rare transcripts and an addition of ActD is expected to further reduce library complexity.

## 5.3 Chemical fixation and single-cell (library) metrics

Fixation is an established procedure in histology. Aldehydes like paraformaldehyde (PFA) are routinely used *in situ* for the preservation of biological tissues and cells. Although implementations of it have been devised for RNA-seq and plate-based scRNA-seq (Machado et al., 2017; Thomsen et al., 2016; van Velthoven et al., 2017), PFA fixed cells are not compatible with high-throughput platforms like 10X Genomics (Machado et al., 2021). However, methanol (MetOH) or dithio-bis (succinimidyl propionate) (DSP) have been tested for droplet-based platforms and are reported to retain RNA quality well (Alles et al., 2017; Attar et al., 2018).

Long-term MetOH fixation effectively retains transcriptional profiles up to several months (Alles et al., 2017a). However, after weeks, recovery of murine hindbrain cells was down to 12-19% of total cells at the start of the time course (Alles et al., 2017). Since CNS immune cells are naturally susceptible to the detrimental effects of fixation (Alles et al., 2017), this could lower microglial recovery further. Furthermore, MetOH fixation permeabilizes the cellular membrane, causal to ~10% loss of cytoplasmic transcripts, potentially increasing ambient RNA. Transcript loss did not result in a loss of phenotypical characterization of mouse hindbrain cells or human PBMCs (Alles et al., 2017; Chen et al., 2018). However, finer classifications of cells (reliant on rare transcripts) are anticipated to be negatively affected. In turn, despite reports of good RNA quality, DSP fixation has been shown to gently fragment transcripts, diminishing cDNA yield with prolonged fixation, and introducing a 3'-end bias with sequencing (Attar et al., 2018).

Both chemicals have been shown to aid scRNA-Seq by minimizing technical artefacts and enable expansions of experimental design (Alles et al., 2017; Attar et al., 2018). Short-term fixation with MetOH or DSP might therefore proof useful for the preservation of microglial *in vivo* states. However, no such studies have been performed currently. If possible, chemical fixation of cells offers a means to reduce technical noise and simplify batching, thereby improving library quality and cell quantity.

## 5.4 Summary

Taken together, isolation of single cells for scRNA-seq needs an account of tissue and cell-specific responses to isolation. Heated and enzymatic dissociation is commonly used; albeit marred by *ex*

*vivo* gene inductions in microglia. ActD alone is sufficient to block the induction of *ex vivo* signatures, and the use of inhibitors to block *ex vivo* signatures are central to good quality microglial scRNA-seq data. In turn, cell fixation could increase flexibility in experimental design. A multi-modal approach to dissociation-induced signature mitigation will eventually yield the best results.

## 5.5 Aims and objectives

In the previous chapters I have detailed a single-cell atlas of microglial heterogeneity in health, and I have completed a Drop-seq platform performance review and pilot study of cortical microglia. In these chapters *ex vivo* signatures were identified. In this chapter, I aim to establish a microglial scRNA-seq procedure that mitigates such effects.

**Aim 3: Establish a microglial scRNA-seq protocol.**

- Objective 8: To test the utility of chemical fixation with MetOH and DSP.
- Objective 9: To explore the characteristics of FACS and MACS for scRNA-seq.
- Objective 10: To assess cellular activation and yield in purification methods.
- Objective 11: To determine the effect of dissociation condition on ex vivo signatures.
- Objective 12: To implement a novel microglial isolation protocol for Drop-seq.

*Table 7: scRNA-seq studies utilizing transcriptional inhibition.*

| Author Details | | | | Experimental Procedure | | | | | | | | | | | | | | | |
|---|---|---|---|---|---|---|---|---|---|---|---|---|---|---|---|---|---|---|---|
| First | Last | Year | Publication | Exsanguination | | | Collection | | | Digestion | | | | | | Processing | | |
| | | | | ActD | Tripto | Aniso | ActD | Tripto | Aniso | ActD | Tripto | Aniso | Enzymatic | TEMP (°C) | T (minutes) | ActD | Tripto | Aniso |
| Wu, Ye Emily | Hong, Weizhe | 2017 | Neuron | | | | 30 | | | 15 | | | Y | 11 | 30 | 3 | | |
| | | | | | | | 30 | | | 15 | | | Y | 22 | 30 | 3 | | |
| | | | | | | | 45 | | | 45 | | | Y | 34 | 20 | 3 | | |
| Hrvatin, Sinisa | Greenberg, Michael | 2018 | Nature Neuroscience | 4 | 10 | | | | | 4 | 10 | 38 | Y | 37 | 60 | | | |
| Gunner, Georgia | Schafer, Dorothy | 2019 | Nature Neuroscience | 4 | 10 | | | | | | | | Y | | | | | |
| Harris, Rayna | Fenton, Andre | 2019 | Hippocampus | | | | | | | | | | Y | | | | | |
| Hasselmann, Jonathan | Blurton-Jones, Mathew | 2019 | Neuron | 4 | | | 4 | 10 | 102 | 4 | 10 | 102 | Y | 37 | 30 | | | |
| Pavel, Abaffy | Sindelka, Radek | 2019 | bioRxiv | | | | | | | 20* | | | Y | 4 | 60 | 2 | | |
| | | | | | | | | | | 20* | | | Y | 37 | 60 | 2 | | |
| Van Hove, Hannah | Movahedi, Kiavash | 2019 | Nature Neuroscience | | | | 30 | | | 15 | | | Y | 11 | 50 | 3 | | |
| Marsh, Samuel | Stevens, Beth | 2020 | bioRxiv | 4 | 10 | | 4 | 10 | 102 | 4 | 10 | 102 | N | *N/A* | *N.A* | | | |
| McQuade, Amanda | Blurton-Jones, Mathew | 2020 | Nature Communications | 4 | | | 4 | 10 | 102 | 4 | 10 | 102 | Y | 37 | 30 | | | |
| Safaiyan, Shima | Simons, Mikael | 2021 | Neuron | | | | 45 | | | 45 | | | Y | 37 | 15 | | | |

*Note: inhibitor concentrations are reported as µM for consistency. If reported in µg/mL, the concentrations were calculated with molecular weights of 1255.42, 360.41 and 265.30 g/mol, for Actinomycin D (ActD), Triptolide (Tripto) and Anisomycin (Aniso), respectively. Pavel et al. (2019) had erroneously reported their used concentrations (i.e. 25 ug/mL, 2 nM), which has been adjusted in the table.*

## 5.6 Methods

Several Drop-seq protocols for primary microglia were tested (Figure 72). The experimental comparison included seven distinct steps: anaesthesia, perfusion and tissue dissection, dissociation, purification, enrichment, chemical fixation, and scRNA-seq. I choose to vary four key steps, targeting chemical fixation, enrichment, purification, and dissociation. Varying these factors, a total of 72 unique experimental procedures can be developed. Not all are within the scope of this body of work. To that end, I prioritized variations within each step, reasoning that these will best detail the effect of each; variations between steps were not accounted for experimentally.

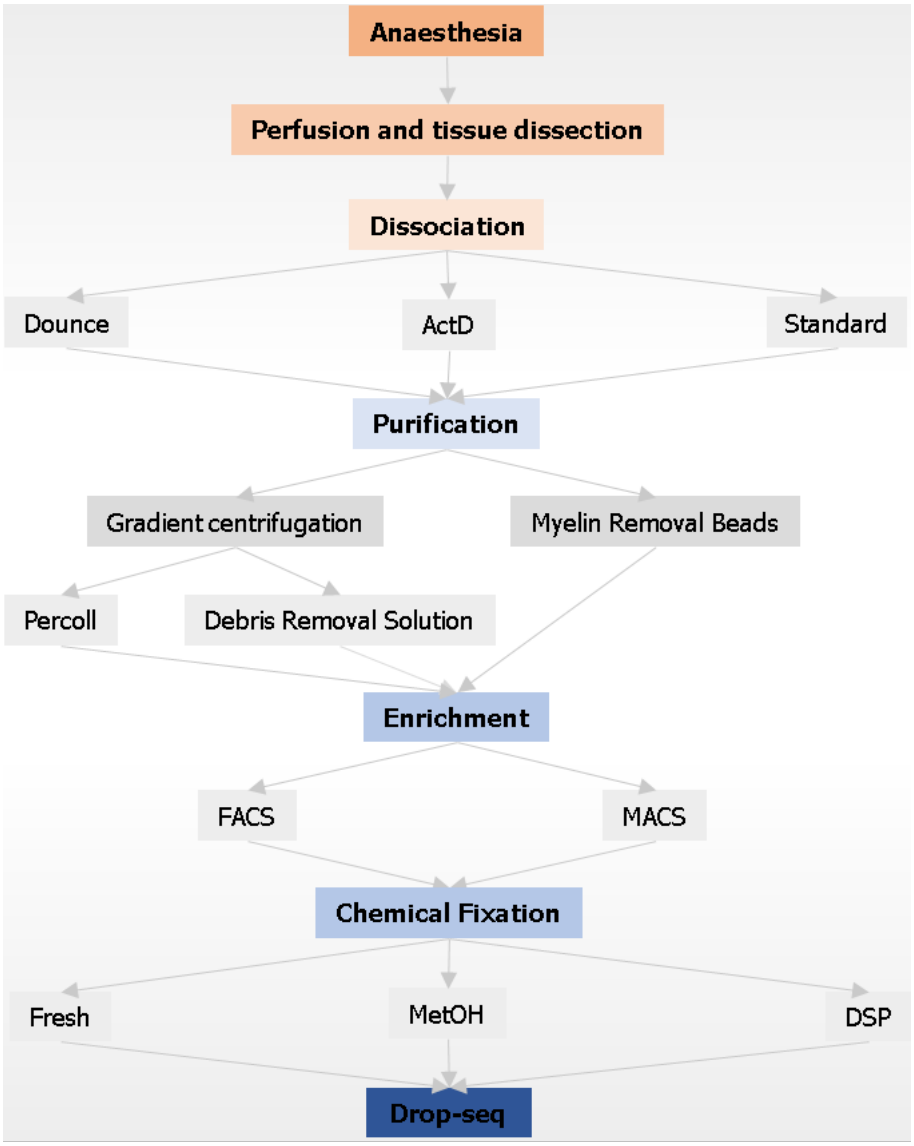


*Figure 72: Drop-seq workflow for murine microglia. Graphical summary of protocol variations for single-cell isolation and scRNA-seq.*

### 5.6.1 Direct comparison of MACS and FACS

Adult mice were anaesthetized, perfused, and tissue dissected and dissociated (*i.e.* standard), followed by bead-dependent purification (Chapter 2). Cells were stained for Cd11b with a magnetic

*micro*particle- or fluorescent reporter-conjugated antibody. $Cd11b^+$-cells were enriched with MACS or FACS, after which cells were subjected to a second round of staining, including a viability dye (eFluor520), a canonical microglial marker (P2ry12) and mitochondrial activity dye (Mitotracker Deep Red). Single, viable $P2ry12^+$-cells were assessed

### 5.6.2 Culture of a microglial cell line

Microglial cells (*i.e.* N13) were seeded into and maintained in a T75 cell culture flask with pre-warmed culture medium; Dulbecco's Modified Eagle's Medium (DMEM) (61965-059, Thermo Fisher) with 10% fetal bovine serum (FBS), and 100 U/mL of Penicillin-Streptomycin. Cells were incubated at 37°C in 5% $CO_2$, changing the media every 3 days. To passage the cells, cells were spun down (at 900x RPM) and resuspend in 5 mL of culture media, after which 500 uL was added to a new T75 flask with 14.5 mL of pre-warmed media.

To collect cells, media was removed, cells washed with distilled water and trypsinized with 5 mL trypsinization solution (HBSS (1X) and Trypsin-EDTA (0.5%) (1X). Trypsinization was stopped with culture medium, cells spun down and resuspended in culture medium. A C-chip or haemocytometer was used to apportion 1,000,000 cells for each test.

### 5.6.3 Chemical fixation

Chemical fixation was tested with two reagents: DSP and MetOH (Alles et al., 2017a; Attar et al., 2018a). Cells were fixed for 1 to 3 days. Flow cytometry enabled an assessment of their respective cell number and viability.

Aliquots of 10 µL DSP (Thermo Scientific, 22586) were prepared in anhydrous DMSO, to a stock concentration of 50 mg/mL (*i.e.* 50X) and stored at -80°C until use. 50X DSP was diluted to 1X working stock concentration with PBS. Working stock was filtered using a 30 µm filter and stored on ice prior to cell fixation. General lab stock of ice-cold methanol was used. DSP and methanol were added dropwise under gentle agitation, to ensure minimal precipitation

## 5.7 Results

### 5.7.1 Chemical fixation reduces recovery and alters population characteristics

Chemical fixation could improve experimental flexibility and library quality. As stated, long-term fixation was expected to significantly reduce recovery, thereby minimizing the capacity to pool tissue (Alles et al., 2017). Indeed, MetOH fixation for up to 2 months resulted in significant cellular debris and clumping in the sample and inefficient recovery (<5%) for both microglial culture cells and *ex vivo* isolated murine microglia (data not shown). Cellular morphology and recovery were compared in MetOH and DSP, to accurately assess their respective value for short-term fixation (Figure 73).

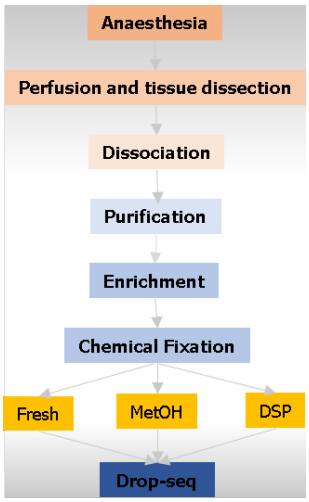


*Figure 73: Chemical fixation and scRNA-seq. Fresh, methanol (MetOH) and dithio-bis (succinimidyl propionate) (DSP) were compared.*

Cellular morphology is differentially affected by DSP and MetOH fixation. In situ cellular morphology is an indirect measure of microglial function; amoeboid and ramified microglia have distinct features, characterized by round and arborized cells (Davis et al., 2017). By extension, flow cytometric measures of cellular morphology are descriptive of the cell quality. DSP, or Lomant's reagent, was suggested to preserve normal cellular morphology, whereas MetOH acts as a permeabilizing agent that dissolve lipids of the cell membrane and disrupts cellular integrity (Alles et al., 2017; Attar et al., 2018; Jamur and Oliver, 2010). Indeed, distinct morphologies for fresh and DSP- and MetOH-fixed cells were found, best illustrated by a shift in the size and granularity of the population (Figure 74).

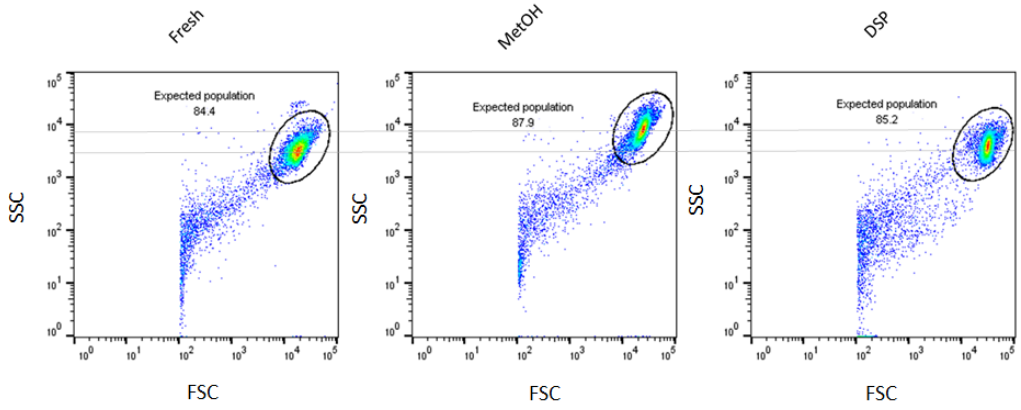


*Figure 74: Flow cytometry of cultured microglia in fresh and fixed conditions. Fresh, methanol (MetOH) and dithio-bis (succinimidyl propionate (DSP)-fixed N13 cells and their respective size (FSC) and granularity (SSC). 'Expected populations' mark the N13 cells, and the grey (horizontal) lines detail granularity across conditions.*

Cells undergo a morphological change with MetOH-fixation that bears similarities to heat-treatment. Cells display an increase in granularity with fixation that is suggestive of a loss in cell integrity (Figure 75). Maintaining cellular integrity might be of particular importance for

subsequent single-cell analysis, as increases in ambient RNA is expected to confound detection of true cellular transcripts. favouring DSP over MetOH fixation.

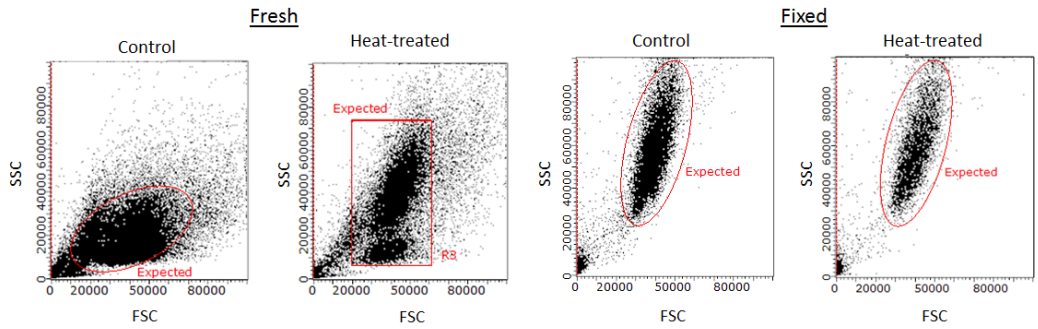


*Figure 75: Comparison of morphological features in fresh and fixed microglial cells. Fresh and methanol (MetOH)-fixed N13-cells were subjected to heat-induced cell death (90 seconds at 68°C) or control conditions. 'Expected populations' mark the N13 cells.*

Cell recovery gradually decreases over time for both DSP and MetOH, where DSP consistently featured a greater relative recovery than MetOH. For both reagents, recovery drops to approximately 60% after 1 day of fixation and continues to get decline to 50 and 45% at 3 days for DSP and MetOH, respectively (Figure 76). These numbers suggest a limited utility for cell pooling.

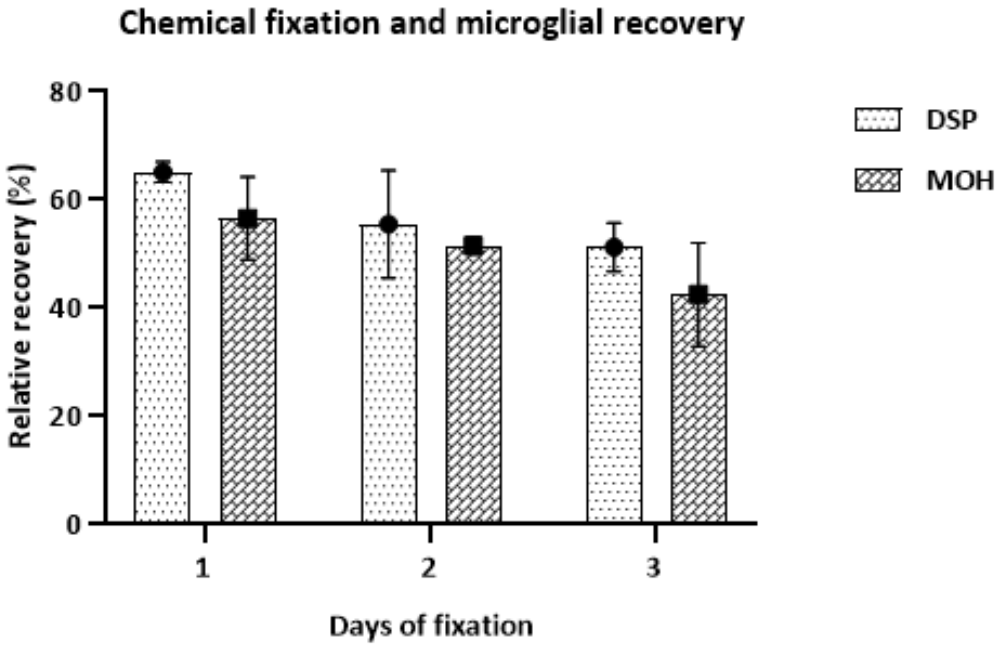


*Figure 76: Chemical fixation and cell recovery. Short-term fixation of dithio-bis (succinimidyl propionate (DSP) and methanol (MetOH) reduces cell recovery with time of fixation for both DSP (n=2, all time-points) and MetOH (n=2, all time-points). DSP performed better than MetOH on all three durations measured. No statistically significant effects were found (2-way ANOVA with Tukey's multiple comparison). Bars are standard deviations.*

### 5.7.2 MACS-mediated enrichment is fast and mitigates *ex vivo* signatures

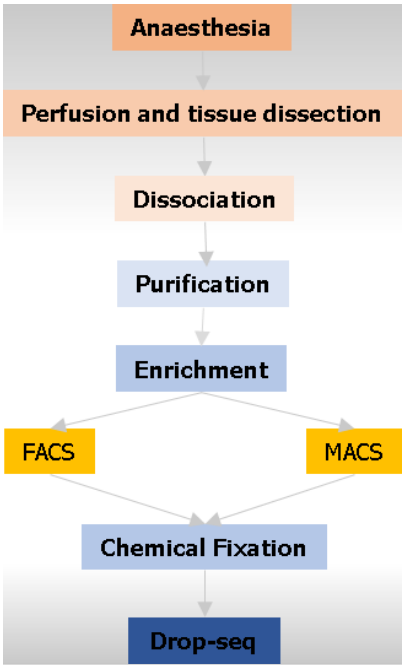


*Figure 77: Enrichment strategy and scRNA-seq. Fluorescence- (FACS) and magnetic-activated cell sorting (MACS) are the most used approaches for single-cell enrichment.*

Enrichment of cells for scRNA-seq is typically done with FACS or MACS (Figure 77). Flow cytometry can rapidly sort cells with great purity. Flow rates can be varied between 1 and 11 that correspond to ~10-80 µL / min; however, it is not recommended to exceed flow rates that increase the number of detected events per second above 2,000. In this manner, sorting of cells from regions that have a lower prevalence like the SC and CB will take a longer time, having a direct influence on cell viability and protocol feasibility. Indeed, with these considerations accounted for, only the CH and ISO readily allow enough cells to be sorted cells within an hour (Table 8); Macosko *et al.* (2015) recommend 150,000 for a typical experiment. In this manner, the limiting factors for the protocol are the relative cell concentrations and prevalence of microglia.

*Table 8: Region-dependent FACS-mediated recovery times.*

| *ROI* | *Events (#)* | *Acquisition time (s)* | *#/second* | *Estimated recovery time (minutes) (~150,000)* |
|---|---|---|---|---|
| CH | 43,568 | 570 | 76 | 33 |
| CB | 10,439 | 320 | 33 | 77 |
| ISO | 36,152 | 322 | 112 | 22 |
| HPF | 6,669 | 203 | 33 | 76 |
| SC | 3,816 | 300 | 13 | 197 |

*Note: Estimated recovery time of (~150,000) microglia with FACS varies by region of interest (ROI). Commonly accepted sorting times are times less than 30 minutes. Only the cerebrum (CH) and isocortex (ISO) can readily lend itself to these limitations. CB, cerebellum; HPF, hippocampal formation; SC, spinal cord.*

Moreover, distinct variations in cellular activation are evident between fluorescence- and magnetic-activated cell sorting. Cellular activation and *ex vivo* signature induction have been shown to associate with elevated levels of mitochondrial activity in muscle stem cells (Brink et al., 2017). To this end, I tested mitochondrial activity with Mitotracker Deep Red FM (MTDR) in FACS and MACS-enriched P2ry12$^{+}$-cells. P2ry12 has excellent correspondence with Cd11b$^{+}$Cd45+ cells (99%), the standard gating strategy for microglia (Figure 10). MTDR fluorescence varied between

approaches, best illustrated by the relative fluorescence of Pry12$^{+}$ subtypes, albeit an increase of MTDR was noted in FACS- relative to MACS-enriched cells (Figure 78).

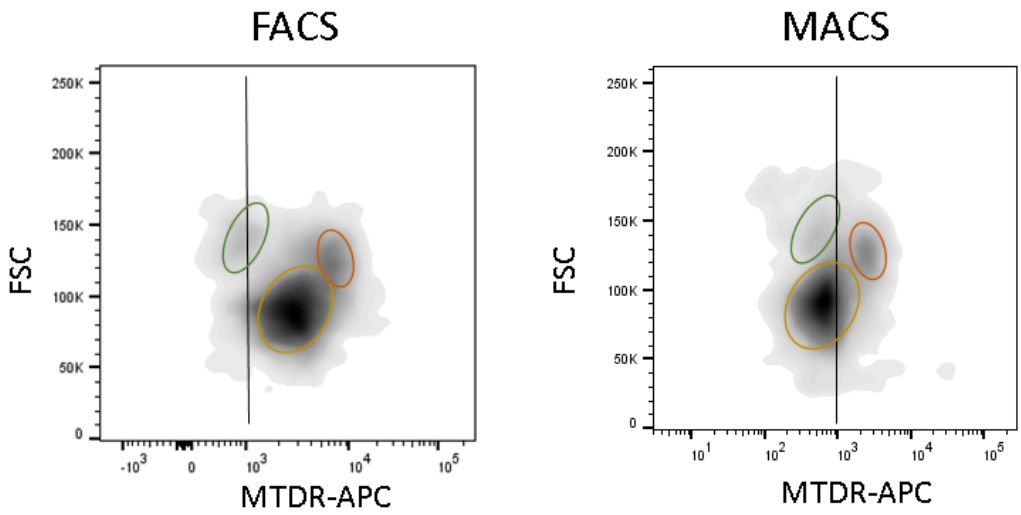


*Figure 78: MACS-isolated cells display reduced mitochondrial activity. P2ry12$^{+}$ cells are enriched, and their respective MTDR-fluorescence is displayed (n=1). The coloured circles capture three distinct cellular populations shared between conditions. The vertical (black) line in each plot functions to illustrate an expression level of 103. FACS, fluorescence-activated cell sorting; MACS, magnetic-activated cell sorting; FSC, forward scatter; MTDR-APC, Mitotracker Deep Red; APC, Allophycocyanin.*

MACS enrichment utilizes selection columns and consists of 3 phases. A typical workflow for the positive selection and enrichment of Cd11b$^{+}$ cells include pre-selection, effluent and post-selection suspensions. However, microglial recovery with MACS has inefficiencies during processing, reducing the total cell yield in processing. Pre-selection, the cell suspension contains the largest quantity of Cd11b$^{+}$ cells (Pre-), whereas recovery of cells after magnetic separation and positive selection is reduced by approximately 35% (Post-) (Figure 78). It is possible that some of the cells were retained in the selection column. However, flushing the column out for a second time did not result in a recovering a larger number of cells (Post- (2)) (Figure 79). Moreover, no cells were detected in the effluent (Effluent) (Figure 79). Some cells might have ruptured in the process of isolation, thereby reducing the overall yield.

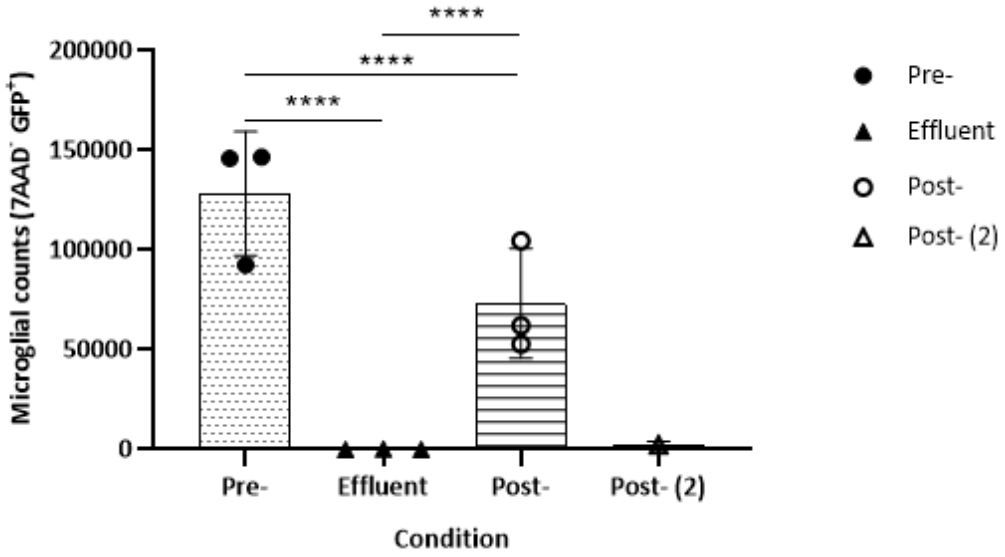


*Figure 79: MACS-mediated microglial recovery. Microglial numbers were measured (7AAD⁻ GFP⁺) across the MACS enrichment process, including the pre-enriched population (Pre-), the effluent, post-enriched population (Post-) and a second flush (Post- (2)) to ensure the effective depletion of cells from the column. Microglial recovery is diminished throughout processing. Statistically significant differences in the steps of isolation were found (Tukey's multiple comparison's test) (****, P<0.001). Post- (2) was excluded from statistical analysis (n=1). Bars are standard deviations.*

As a point of consideration, the anti-Cd11b microbeads that enable the isolation of Cd11b⁺ cells are M1/70 clones. Unfortunately, most antibodies used for flow cytometric analysis of Cd11b are also M1/70 clones and are therefore expected to compete for binding with the microbeads; cells are stained and bound with microbeads prior to binding with Cd11b-PE. Indeed, staining cells with microbeads at a concentration of 1/100, instead of the conventional 1/10 concentration, results in an increase of Cd11b-PE signal, suggestive of competitive binding of the Cd11b protein (Figure 80). However, the detection of Cd11b was not obfuscated by the competitive antagonism between the microbeads and the Cd11b-PE antibody. Future studies might benefit from utilizing alternatives.

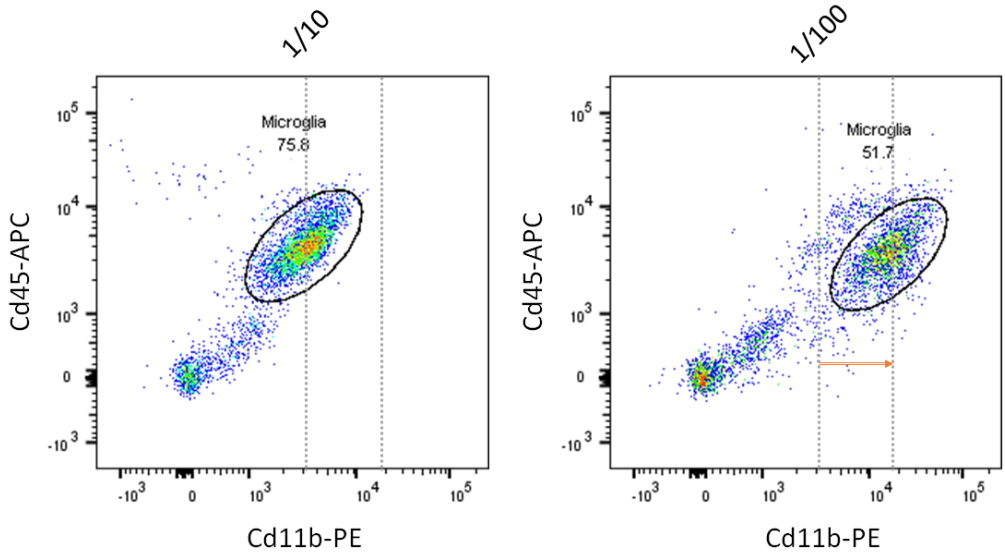


*Figure 80: Competitive antagonism of Cd11b microbeads and the flow cytometric detection of Cd11b. a) Cells were magnetically labelled with Cd11b microbeads (1/10) and followed by the binding of Cd11b conjugated to PE (BioLegend, 101207) (1/500) for the identification of Cd11b. Both microbeads and Cd11-PE are M1/70 clones and are in direct competition for binding sites. b) Lowering microbead concentration to 1/100 reduces the isolation efficiency, although there is an observed shift in PE signal strength. APC, Allophycocyanin; PE, phycoerythrin.*

Taken together, FACS-mediated enrichment can be utilized for scRNA-seq and might be well-suited to plate-based experimental designs. However, MACS is the preferred option for droplet-based platforms. Some inefficiencies in enrichment are evident with MACS isolation, yet these are outweighed by the high-throughput nature and cellular quiescence of MACS-isolated cells.

### 5.7.3 Lowered microglial recovery with increased purity

As stated, purification of single cell suspensions occurs in two broad categories: gradient centrifugation- and bead-dependent myelin and cell debris removal (Figure 81).

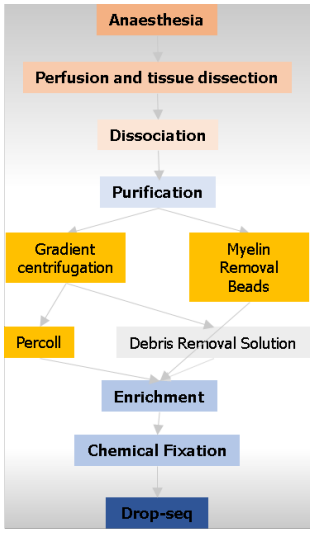


*Figure 81:Purification methods of scRNA-seq. Gradient centrifugation and myelin removal beads-dependent purification are the main strategies used; the latter of which is subdivided in Percoll or debris removal solution.*

The selection of density gradient centrifugation- and bead-dependent purification varies with context. Bead-dependent purification is effective in juvenile, murine tissue; however, it is myelin quantities in the adult murine brain will exceed the capacity of the beads and columns (Miltenyi). Some have opted to use gradient-centrifugation and bead-dependent purification in combination for droplet-based scRNA-seq, finding that each method in isolation fails to effectively remove myelin debris (Safaiyan et al., 2021). However, when enriching for cells, no such additional steps were taken, and gradient centrifugation was found to be an effective means of purification (Geirsdottir et al., 2019; Hammond et al., 2019; Keren-Shaul et al., 2017; Masuda et al., 2019; Tay et al., 2018; Van Hove et al., 2019).

Purity of MACS-enriched P2ry12$^{+}$-cells is greater with gradient centrifugation, 88% for Percoll and 75% for bead-dependent purification, respectively (Figure 82). Moreover, I found an incomplete depletion of myelin from adult isocortical tissue using beads, with visible contamination remaining in the cell suspension (data not shown). The loss of purity when using Myelin Removal Beads II (Miltenyi, 130-096-733) could confound subsequent scRNA-seq. This finding supports the limitations of bead-dependent isolation. To increase purity, when LS- with were exchanged with LD-columns no such myelin debris was observed (data not shown), as has previously been described (Zhou and Li, 2019). However, LD-columns offer a slower flowthrough and a significant increase in handling time, increasing the risk of *ex vivo* signatures and introducing additional experimental limitations (data not shown). Operation of beads-dependent purification might necessitate cold-room usage and/or inclusion of inhibitors during processing.

Interestingly, no differences were detected in mitochondrial activity between bead-dependent and gradient centrifugation, as measured with Mitotracker Deep Red (Figure 82). This suggests that the purification method is not a key driver for the induction of *ex vivo* signatures in microglia.

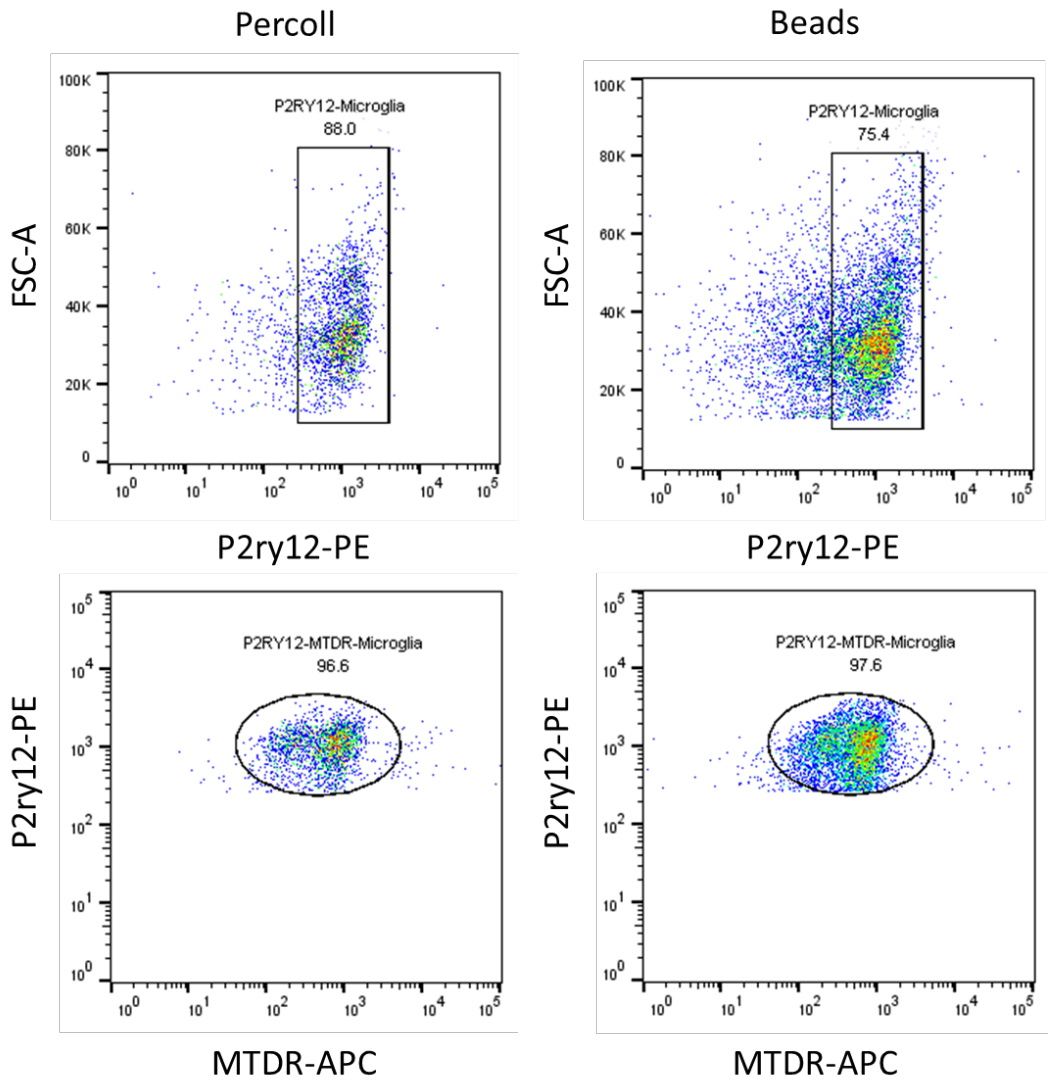


*Figure 82: Purification method-dependent microglial population characteristics. a-b) Percoll-gradient centrifugation displays a higher purity of MACS-enriched (P2ry12+-) microglia (88%) than the beads equivalent (75%). c-d) No differences in mitochondrial activity are remarked. APC, Allophycocyanin; FSC-A, forward scatter, area; MTDR, Mitotracker Deep Red; PE, phycoerythrin.*

Cellular viability and yield are interconnected. Larger centrifugal forces would increase recovery at the cost of a reduced viability and *vice versa*. Bead-dependent purification greatly outperforms Percoll purification, recovering up to 2-fold larger number of microglia (**Error! Reference source not found.**). However, I did not find large differences in cell viability between both approaches (data not shown), suggesting that other factors might influence recovery.

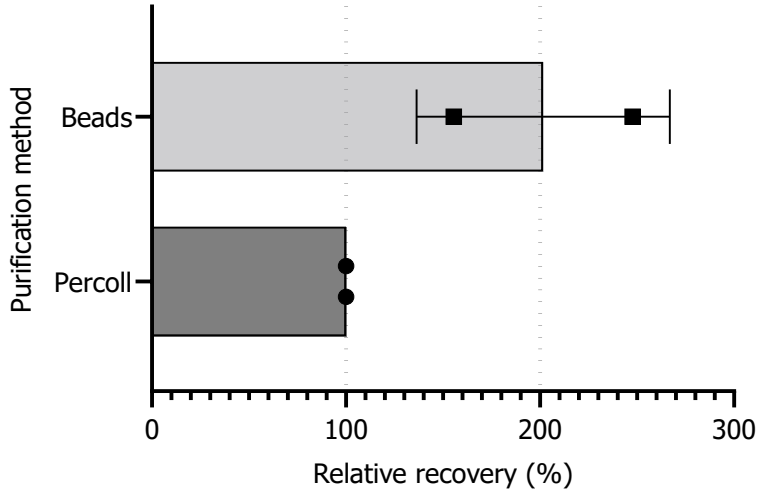


*Figure 83: Beads-dependent purification doubles microglial recovery. Bead-dependent purification maximizes recovery of P2ry12+ microglia. Stringency of Percoll (and other gradient centrifugation methods) restrict recovery. Each dot represents a sample. Tick lines at 100 and 200%. Scatterplot with bar, mean with standard deviation (n=2).*

Taken together, there is a distinct trade-off between purity and microglial yield in MACS isolated cells. **I** chose to opt for greater purity, to ensure high quality scRNA-seq libraries. However, yield and viability will need to be assessed across dissociation methods.

### 5.7.4 Microglial recovery is largest in standard dissociation conditions

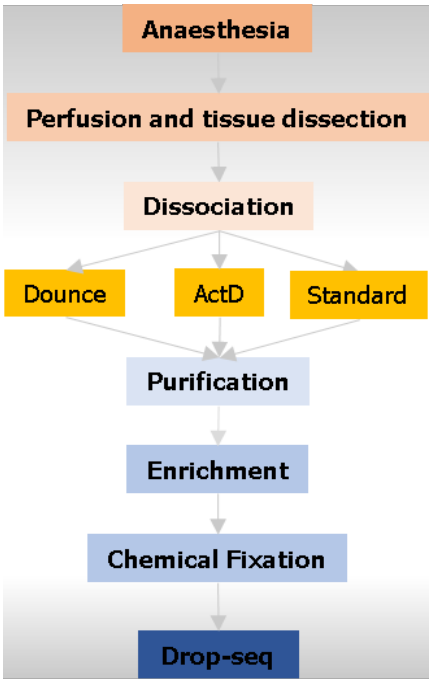


Microglial recovery is expected to vary between cell isolation methods, and I set out to do a direct comparison on cell yield and viability (Figure 84). ActD and standard dissociation protocols generally vary in digestion method (*i.e.* mechanical or automatic), digestion temperature, and varying on the presence or absence of ActD (Table 5). Similarly, mechanical dissociation protocols can vary substantially (Hammond et al., 2019; Li et al., 2019; Schaum et al., 2020, 2018).

A Dounce homogenization protocol was implemented, as was established by Hammond *et al.* (2019). Whole brain dissociation was achieved by using the loose (A) and tight (B) pestles sequentially, each 15 times in EM1 while rotating the pestle.

*Figure 84: Dissociation strategies in scRNA-seq. Dissociation methods vary on its use of mechanical and/or enzymatic digestion, and dissociation temperature. 'Dounce' features a cold, mechanical dissociation, whereas 'Standard' features a heated (37°C) enzymatic digestion. 'ActD' is a modified protocol in which digestion (at room temperature) occurs in the presence of actinomycin D, a transcriptional inhibitor.*

Although papain is not (fully) active at 4°C at which mechanical dissociation was tested, the (proprietary) formulation might contain other factors supportive of cell viability and effectively enables comparison with the other dissociation protocols. Other in-house

formulations (incl. DNAse I) were tested but these were not deemed be a satisfactory comparison without details regarding the formulation.

Single cell suspensions were generated with the 3 dissociation protocols; that is, standard, ActD, and Dounce. Cell suspensions were purified with Debris Removal Solution, a density-gradient approach. This condition ensured that I retained microglia with high purity, even if this comes at a cost of recovery. The number of viable cells that were recovered from each were quantified. As expected, dissociation in the presence of ActD at room temperature (21-23 °C) decreased microglial recovery relative to standard dissociation (38%), an effect that was more pronounced at 4°C with Dounce homogenization (26%) (Figure 85). Of note, viability did not display large variability, with all procedures routinely recovering ≥95% live cells (Figure 86).

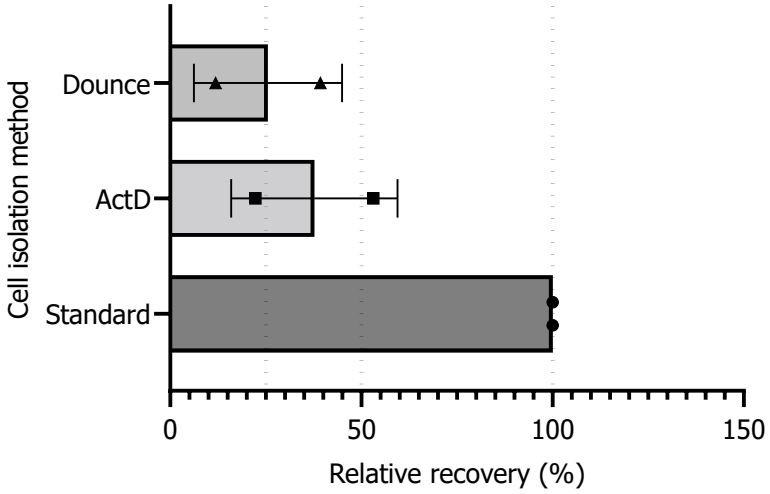


*Figure 85: Standard dissociation recovers microglia most effectively. Relative recovery of P2ry12+ microglia from isocortical tissue in Dounce- and ActD- to standard-isolation protocols. Standard dissociation at 37°C is most effective in recovery of microglia, whereas both ActD- and Dounce-isolation reduce recovery to 26 and 38%, respectively. Each dot represents a sample. Tick lines at 25, 50 and 100%. Scatterplot with bar, mean with standard deviation (n=2).*

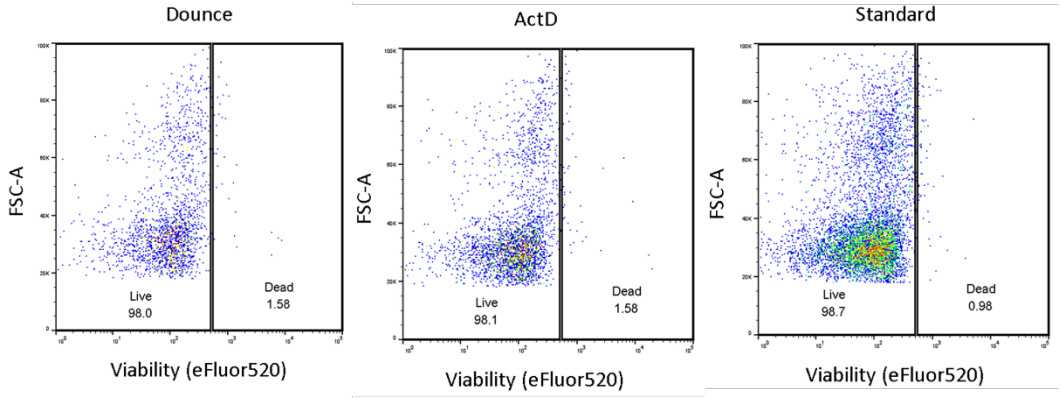


*Figure 86: Viability of cells in distinct cell isolation protocols. Representative plots of viability (eFluor520) in standard-, ActD-, and Dounce-isolated cells. FSC-A, forward scatter, area; ActD, actinomycin D.*

### 5.7.5 Mechanical dissociation and transcriptional inhibition reduce *ex vivo* signatures

*Ex vivo* signatures do not vary with purification method, yet mitochondrial activity was lower in MACS when compared to FACS. However, the effect of the different dissociation methods on the microglial gene expression was still to be determined.

To that end, microglia were isolated from the adult cortex and profile gene expression with qPCR. Cells were purified with gradient centrifugation (*i.e.* 'debris removal solution'), enriched microglia with MACS, and compared Dounce-, ActD-, standard-isolated microglia. I developed a panel of genes that includes canonical microglial markers (*Csf1r*, *Cx3cr1*, *Hexb*, *P2ry12*, *Tmem119*) and artefact-associated markers (*Egr1*, *Fos*, *Ier2*, *Jun*). All designed primers displayed good parameters, with excellent melting curves and size. However, Csf1r, Ier2 and Tmem119 did not pass quality control, as PCR products of Csf1r, Ier2 and Tmem119 were either lacking or multiple (Supplementary Figure 11). Gapdh was used as an internal loading control, and Hexb as a secondary microglial load control. Hexb is a stable, canonical marker of microglia in health and disease (Masuda et al., 2020). Of note, cells display considerable variability by dissociation protocol, and some by collection method (Figure 87); in the series, cells were collected and stored as a pellet, or cells were collected and stored in lysis buffer.

*Jun* (and *Fos* to a lesser degree) are expressed significantly less in Dounce- and ActD-isolated cells (Figure 87). The lower expression associates with a lower dissociation temperature; lower levels are detected for mechanically dissociated tissue. *Jun* and *Fos* are genes involved in the cell stress response, and critical genes in the formation of activation protein-1 (AP-1), a protein complex associated with multifaceted roles that include cell growth and apoptosis (Leppä and Bohmann, 1999). However, as such, a reduction of both genes with Dounce- and ActD-isolated cells supports the effectiveness of these protocols in preventing the induction of *ex vivo* dissociation-induced signatures. Similarly, *Egr1* is reduced in ActD-isolated cells, however, unlike *Fos* and *Jun*, it does so more than Dounce-isolated cells, suggestive of a superior effect of ActD (Figure 87).

Looking at the canonical marker panel, *Cx3cr1* is significantly downregulated in Dounce-isolated cells, whereas no statistically significant difference in *P2ry12* expression was noted (Figure 87). *P2ry12* expression does show a downward and upward trend for Dounce- and ActD-isolated cells, respectively. Combined with a statistically significant reduction of *Egr1* and *Jun*, these results suggest that ActD-isolated cells best preserves *in vivo* microglial identity. Using *Gapdh* with a combination of *Cx3cr1*, *Hexb* and *P2ry12* as internal controls gave similar findings (Supplementary Figure 12).

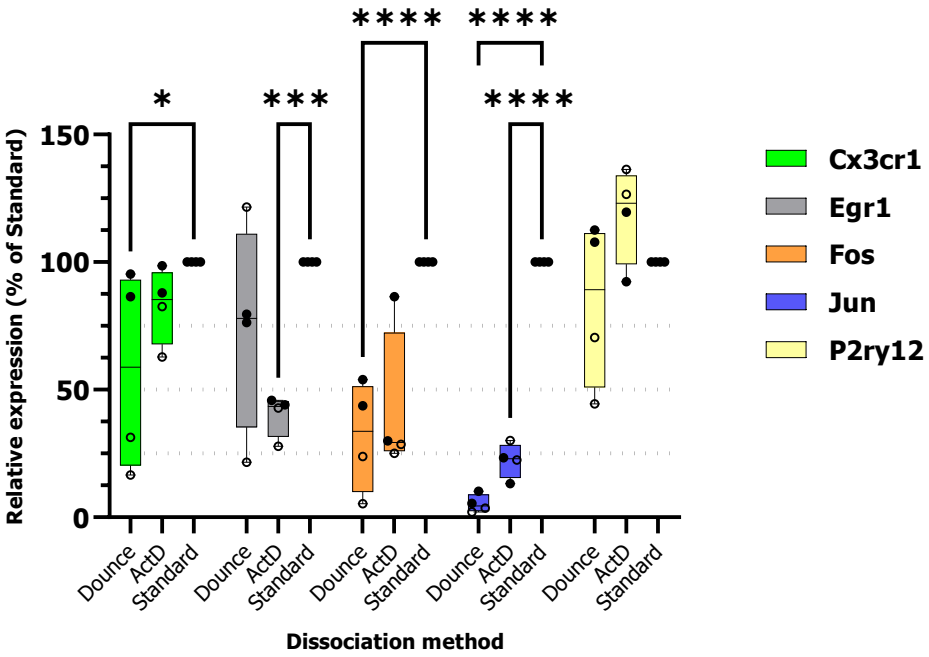


*Figure 87: Early-response genes and dissociation method. Expression of early-response genes and canonical microglial markers in cell isolation protocols vary. Gene expression levels are relative to standard dissociation. Sequentially, gene levels were corrected for Gapdh and Hexb. Box-and-whisker plot with standard deviation. Each dot represents a sample composed of 2 isocortices from male or female tissue (n=4). Cells collected in a pellet (○) and in lysis buffer (●) Two-way ANOVA (Dunnett's) was used for the statistical analysis of genes and cell isolation protocol (**, P<0.01; ***, P<0.001; ****, P<0.0001).*

## 5.8 Removal of exAM with ActD in scRNA-seq

To finally test the efficacy of my protocol, a scRNA-seq dataset was generated it: dissociation with ActD at RT, purification with debris removal solution, and enrichment with Cd11b$^{+}$ magnetic microbeads. Cells from female mice aged P21 and P60 were used, complementing male and female P90 cells from the pilot in an integrated Seurat object. As described previously, I made use of the MAD for QC prior to standard integration (Section 2.8.1.2, Figure 17).

### 5.8.1 Cell quality is lower in *ex*AM-treated cells

Cell quality is affected by the experimental procedures. Albeit evidence of *exAM* was evident in the pilot dataset, the overall quality of the cell suspension in the study was good (Figure 64, Figure 66,Figure 69). Now, relative to the pilot, ActD-treated cells have increased library complexity and size, as well as mitochondrial and ribosomal content (Figure 88). No differences in quality were found between P21 and P60-derived ActD-treated cells (Supplementary Figure 13).

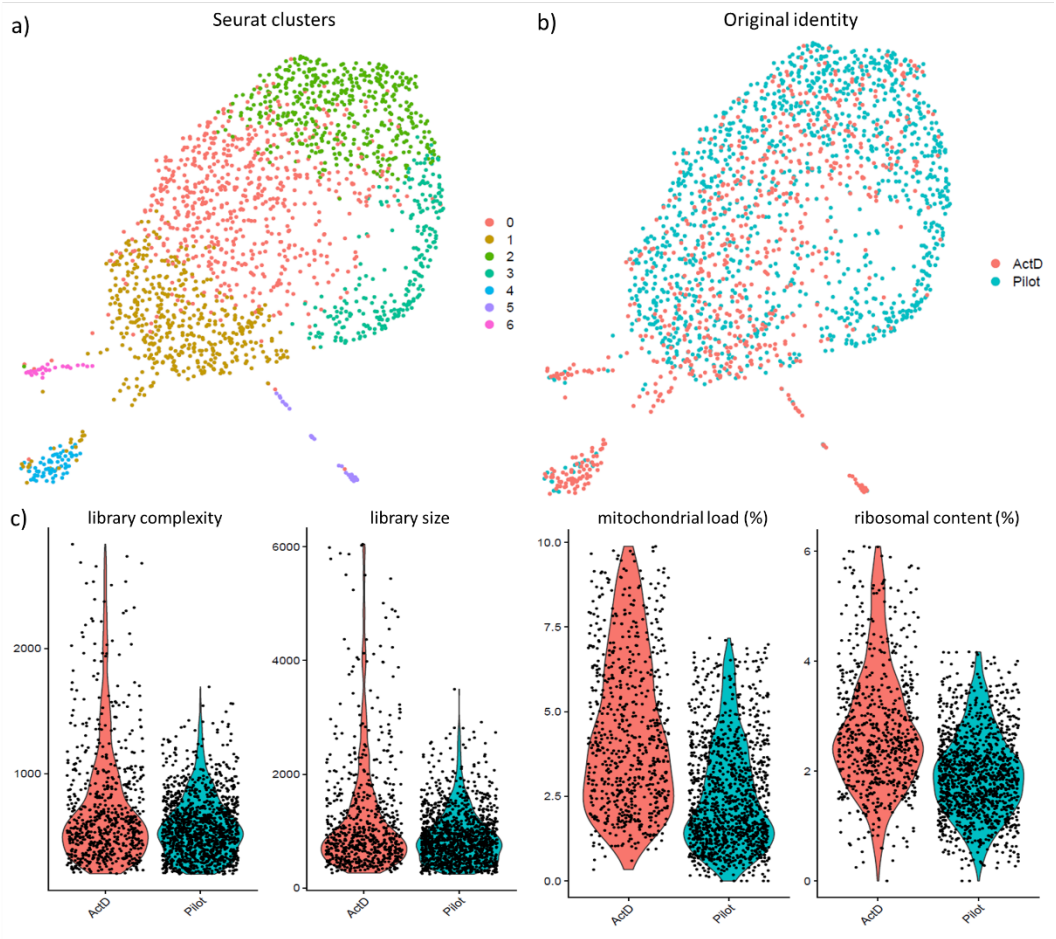


*Figure 88: Single-cell suspension qualities differ between standard- and ActD-isolated microglia. 7 Seurat clusters are identified (a) that vary in distribution by isolation method (b), and by general QC-parameters. ActD, actinomycin D; QC, quality control.*

Differences in library size and complexity are expected to derive from differences in read depth. In fact, read depth of ActD-treated cells was lower on average. Cells in the pilot were sequenced to an average depth of 15,637 and ActD-treated cells to 12,218 reads/cell. This was unexpected, as I set out to increase read depth relative to the pilot data. Furthermore, ActD-treated cells showed a relative increase of mitochondrial and ribosomal content, indicative of lower cell qualities (Osorio and Cai, 2020; Subramanian et al., 2021). Indeed, 687 of 1020 (~67%) ActD-treated cells in the object pass MAD QC, compared to 1245 of 1329 (~94%) in the pilot. It is possible that elevated levels of mitochondrial and ribosomal genes could be reflective of the younger age of the samples treated with ActD. Although some evidence of diversity in ribosomal content was found (Figure 50), it is unlikely an increase in mitochondrial content is an indicator of quality. Commonly, these effects are suggestive of a loss of cytoplasmic transcripts by membrane disruption and a reduction of sample quality. A more likely explanation is that a lower read depth of cytoplasmic RNA is due to RNA decay. As stated previously, ActD is readily used to study RNA decay and it is something which would need to be considered in future studies (Lai et al., 2019). Regardless, the integrated data allows for a direct comparison of *ex*AM signatures between the isolation methods.

### 5.8.2 ActD treatment mitigates the introduction of an exAM signature

7 transcriptionally distinct clusters were identified in the object. The identified clusters featured homeostatic (HOM)-clusters, CNS-associated macrophages (CAM) and exAM, as well as aged inflammatory microglia (AIM) and OPC (Figure 89). The presence of OPC is surprising, the occurrence of which could indicate an impurity in the isolation. This is something that can be improved upon by using gradient-centrifugation and bead-dependent purification in combination, as was done by Safaiyan *et al*. (2021); however, the impurity is a relatively small cluster and does not detract from the interpretation of the results.

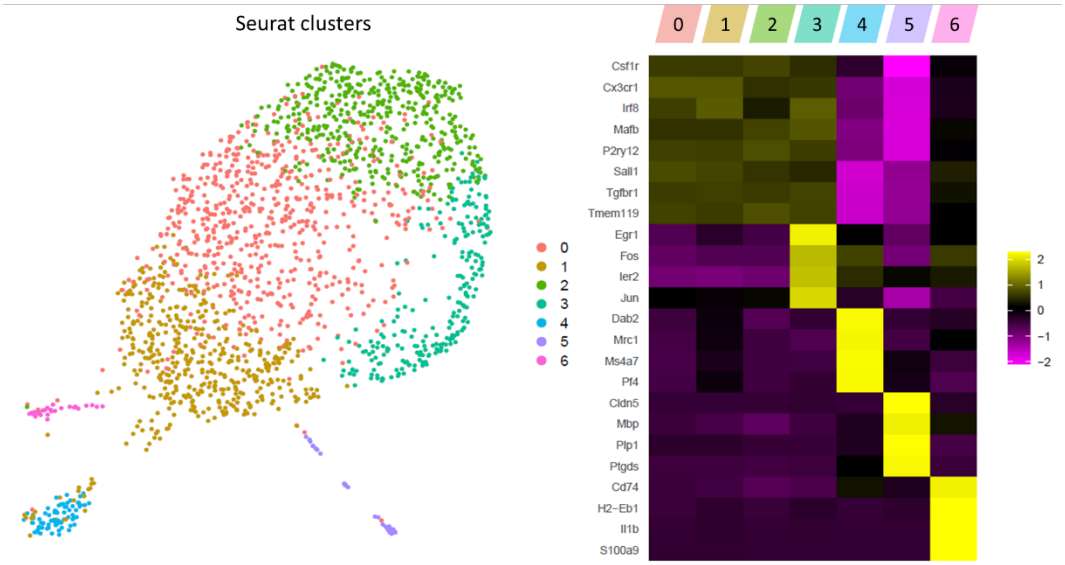


*Figure 89: Transcriptional heterogeneity of identified clusters.*

However, most clusters are microglia, 3 of which are HOM-clusters (cluster 0, 1, 2). Canonical microglial markers are highly expressed in these clusters, with only moderate variations in expression. Of note, cluster 3 features similar levels of such markers, albeit supplemented with a module for *ex*AM-associated genes like *Egr1*, *Fos*, *Ier2* and *Jun* (Figure 90).

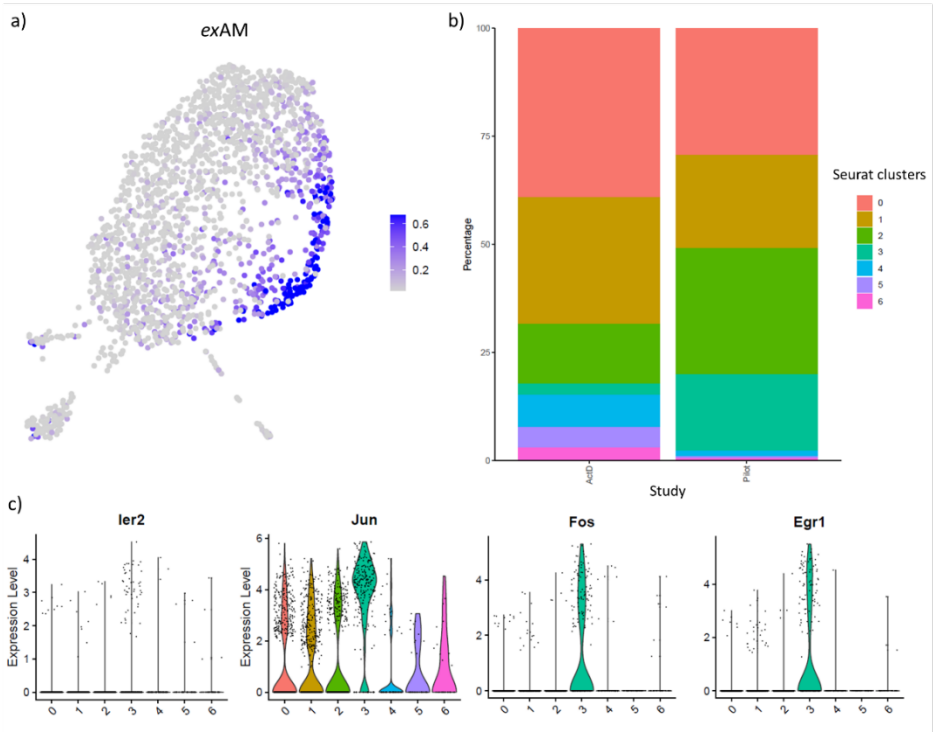


*Figure 90: exAM are enriched in standard-isolated cells. a) Enrichment of exAM signatures are enriched in cluster 3, as shown in a FeaturePlot (a) and in a barplot detailing their distribution by isolation method (b). Gene expression scale is from low to high, grey to blue, respectively. c) ViolinPlots of 4 exAM signature genes are depicted by cluster. ActD, actinomycin D; exAM, ex vivo-activated microglia.*

Furthermore, the skewed distribution of cluster 3 towards cells from the pilot suggest transcriptional inhibition is an effective means of mitigating such effects in microglial scRNA-seq. Importantly, accounting for differences in cell number, 2.6% of all ActD-treated cells take on an exAM signature, compared to 17.6% of all standard isolated cells, approximately a 7-fold reduction of such signatures relative to pilot data (Figure 89, Supplementary Table 14).

## 5.9 Discussion

scRNA-seq studies of microglia can account for *ex vivo* signatures in a plethora of ways, some of which are addressed in this chapter. As stated, modifying the central four variables on the available approaches culminates in 72 distinct protocols. I aimed to make stepwise progress through this variability to reduce the number technical conditions to test. Therefore, the study does not aim to be a full account of the currently available options; however, it does serve to inform on key characteristics of microglial scRNA-seq to mitigate *ex vivo* signatures and improve data quality. Several key determinations were made:

1. Chemical fixation with DSP and MetOH reduced cell yield, limiting its application for scRNA-seq.
2. MACS displayed higher throughput and reduced mitochondrial activity than FACS.
3. Gradient centrifugation has greater purification efficiency than a bead-dependent alternative.
4. *Ex vivo* signatures are reduced by using ActD and/or lowering dissociation temperature.
5. Implementation of ActD-treatment for scRNA-seq raised concerns of cell quality.

### 5.9.1 Loss of cells with chemical fixation and future implementations

It was observed that chemical fixation is associated with an incremental loss of cells and disruption of cellular morphology with prolonged incubation, in line with previous studies (Alles et al., 2017a; Attar et al., 2018a; Chen et al., 2018). Although fixation was initially thought as a promising step for the reduction of technical noise and sample pooling, recovery reduced to 65% with DSP to 55% with MetOH after just one day of fixation, an effect that continued to worsen for both over the course of 3 days. These limitations halted efforts with MetOH and DSP and neither was tested for their effect on *ex viv*o signatures.

MetOH-fixed is associated with a loss of membrane integrity and a loss of cytoplasmic transcripts (Alles et al., 2017). These were not concomitant with an increase in mitochondrial transcripts, classically a marker of good cellular health, which led the authors to conclude that cell quality is preserved. However, Denisenko et al. (2020) recently discovered that MetOH-fixed (kidney) cells are enriched for genes common to tubular cells and erythrocytes (*e.g.* haemoglobins) (Denisenko et al., 2020). Like the dissociation-induced signature described previously, these transcripts correspond to an *ex vivo* profile. When speaking of *ex vivo* signatures, technical artefacts are not limited to dissociation-induced and need to be placed into a larger framework, to recognize the specific limitations of any experimental choice.

Regardless, chemical fixation might still offer a benefit to scRNA-seq, and progress has been made since these first implementations. Adaptations in rehydration of MetOH-fixed cells improved RNA integrity and membrane integrity (Chen et al., 2018). Furthermore, DSP and MetOH have found use in spatial transcriptomics (Lee et al., 2021; Machado et al., 2021), as well as in multimodal single-cell studies combining intracellular phospho-protein staining and transcriptomics (Gerlach et al., 2019; Nesterenko et al., 2021). Similarly, glyoxal, an aldehyde fixative, does not cross-link RNA like PFA and might offer value for scRNA-seq (Channathodiyil and Houseley, 2021), although this is yet to be tested.

### 5.9.2 MACS is favoured for droplet-based scRNA-seq

The speed and gentle nature of MACS enrichment favour this method for droplet-based scRNA-seq. However, FACS might still be the preferred choice in other formats. Plate-based platforms like SMART-seq2 and MARS-seq are not expected to suffer from similar limitations. Single cells in plate-based platforms are commonly sorted into lysis buffer, capturing transcriptomes prior to a cellular response to shear stress. In this way, FACS enrichment of rare cells that express specific combinations of proteins can be achieved. Indeed, seminal papers utilizing FACS for cell enrichment have opted for plate-based platforms (Mathys et al., 2017; Safaiyan et al., 2021).

In addition, MACS has displayed some inefficiencies of recovery that could necessitate experimental designs that maximize technical repeats. Recoveries from tissue with a lower total microglial quantity like the HPF, CB and SC could benefit from such adaptations. A paradox, as these same regions would benefit from the speed in which MACS can enrich for microglia, independent of the relative quantity and proportion of cells present in the tissue. Combinations of MACS-mediated positive (or negative) selection followed by FACS are examples of this (Travaglini et al., 2020).

Some further considerations remain. First, I have not performed a repeat experiment in the comparison of FACS and MACS and care must be taken not to generalize results from a single experiment. Second, the correlation of mitochondrial activity with cellular activation was not tested and *ex vivo* signatures, as was done by Van den Brink *et al.* (2017). Mitochondrial activity can also be a marker of good cellular health, or a marker of distinct metabolic functions, and this cannot be excluded as an alternative interpretation.

Analysis of scRNA-seq datasets could help to resolve this further, to correlate *ex vivo* signatures with cell isolation methods. *e.g.*, typical stress-induced signatures were identified in Dounce-isolated microglia of the dataset of Hammond *et al.* (2019) (Supplementary Figure 7). In this work, tissue was dissociated mechanically and enriched for with FACS. This corresponds to recent findings by Marsh *et al.* (2022), in which mechanical dissociation displayed elevated *ex vivo* signatures (*i.e.* '*ex*AM') with FACS, relative to cold (and heated) dissociation with inhibitors (Marsh et al., 2022).This strengthens my argument against the use of FACS in droplet-based scRNA-seq. Further work is needed to characterize the specific sorting conditions that will induce *ex vivo* signatures in microglia.

### 5.9.3 Gradient centrifugation displays elevated purity and lowered yield

The results showed that gradient centrifugation increased sample purity relative to bead-dependent purification; 88 and 78%, respectively. Myelin debris removal with LS-columns was incomplete, with debris remaining in the cell suspension. LD-columns might offer an alternative solution but working in a cold-room will become a necessity due to the low flowthrough of the column type. I chose not to pursue this avenue, aiming to keep experimental complexities low and processing time at a minimum. Furthermore, gradient centrifugation and bead-dependent removal of myelin did not affect mitochondrial activity differentially, suggesting that purification method is not a key driver of *ex vivo* signatures. Indeed, research has shown that varying centrifugal forces during purification does not greatly affect gene expression, although some differences in cellular viability were remarked (Pavel et al., 2019).

Cellular viability might be an explanation of the differences in microglial recovery between purification methods, with bead-dependent purification outperforming gradient centrifugation. Of

note, no differences in cell viability was found between methods; $Cd11b^+$ enrichment or any subsequent wash might aid the removal of dead cells. Alternatively, white matter-associated microglia are recovered more effectively with bead-dependent approaches. The use of antibodies with a designated target is expected to be more selective than gradient centrifugation; non-specificity in gradient centrifugation might select against microglia in white matter. As discussed previously, tensile properties of white- and grey-matter tissues differ. Although regional and age variability is reported, white matter is on average stiffer than grey matter (Budday et al., 2015; MacManus et al., 2017). These tensile properties could underlie distinct purification efficiencies. Further research is needed to detail these method-specific characteristics. By extension, bead-dependent purification might be better suited for the isolation of white-matter associated microglia like WAM, ATM and PAM.

### 5.9.4 Dissociation method, recovery, viability, and *ex vivo* signatures

The assessment of dissociation method is twofold by addressing cell yield and viability, and *ex vivo* signatures.

#### 5.9.4.1 Standard isolation maximizes microglial recovery

Standard (heated) enzymatic dissociation recovers the most microglia, without any overt differences in viability. This is in-line with previous work comparing cold, mechanical and heated, enzymatic digestion (Denisenko et al., 2020; Marsh et al., 2022). Interestingly, microglial recovery with mechanical dissociation is impaired further in aged mouse tissue, possibly reflective of the mechanical properties of said tissue. Together, these results highlight some concerns for studies isolating cells in cold conditions, in particular when dealing with (micro-)dissected tissues with a relatively small number of microglia (*e.g.* SC, HPF, CEB).

#### 5.9.4.2 ActD reduces *ex vivo* signatures and preserves microglial identity

However, despite the promise of microglial recovery, isolation of cells in heated digestion is known to induce *ex vivo* signatures. *Ex vivo* signatures varied between the dissociation methods. On average, and relative to standard dissociation, mechanical and ActD protocols reduced the expression levels of *Fos*, *Jun* and *Egr1*, suggesting that both isolation protocols could reduce the induction of technical artefacts.

In addition, a cell isolation-specific effect was noted, where the expression of Egr1 in Dounce-homogenized cells fails to be reduced, compared to an effective reduction when ActD is used. I have previously addressed that Dounce-isolated cells display a higher level of *ex vivo* signatures than those isolated in the presence of inhibitors. The elevated levels of Egr1 in Dounce-isolated cells are supportive of this finding.

Regarding canonical gene expressions, a significant reduction of *Cx3cr1* expression was found with Dounce homogenization. Other studies have reported on a loss of canonical markers (*e.g.* Cx3cr1, P2ry12, Sall1) with age, neurological disease, and *in vitro* (Dubbelaar et al., 2018; Gosselin et al., 2017). In correspondence, a loss of P2ry12 expression was also evident in *ex vivo*-activated microglia (*i.e. ex*AM) of the scRNA-seq pilot (Figure 65). This suggests that a loss of canonical marker genes is a typical response of microglia outside of homeostasis, one that is reproduced by *ex vivo* activation.

To my knowledge, this is the first study to suggest that *P2ry12* is reduced with *ex vivo* activation. Marsh et al. (2022) investigated the association of microglial identity and activation score, which includes P2ry12, Tmem119, Hexb and Cx3cr1, yet they did not report on a similar loss due to the composite nature of said module scores. By extension, it would be interesting to disentangle the *ex vivo*-induced loss of microglial identity and the acquisition of a disease-like signature (*e.g.* DAM), a signature commonly associated with a loss in canonical marker gene expression.

Of note, no significant loss of Cx3cr1 or P2ry12 was found in ActD-isolated cells; in fact, an upward trend of P2ry12 expression was detected. These results could indicate that microglial identity is preserved in the presence of ActD, counteracting some of the detrimental effects of cell isolation. Furthermore, it would support the use of ActD in mechanical isolation. However, it is possible that ActD affects the transcriptome in a so far unknown manner, even in the absence of genotoxic stress (with a concentration below 100).

#### 5.9.4.3 Implementation of ActD in scRNA-seq

ActD was used at a concentration of 30 µM, well within the accepted range to prevent genotoxic stress (Mussil et al., 2019). However, evidence of RNA decay was found, mitochondrial and ribosomal content increased in the presence of ActD. Consequentially, a large proportion of cells did not pass the MAD filter during QC; 33% of ActD-treated cells were excluded, compared to 6% in the pilot. *A priori* this was a consideration, however, the absence of such effects with 45 µM ActD, as those described by Sala Frigerio et al. (2019) raised questions about the implementation of the drug, or at least raised some caution regarding the use of this approach. No gross differences in protocol length or procedure were evident, albeit dissociation temperature was lowered from 37°C to R.T.

In concurrence, cell clumps in the final suspension were identified (data not shown). To circumvent this issue, the suspension was filtered prior to the Drop-seq run. Although this reduced the total number of cells and single-cell transcriptomes-attached to microparticles (STAMP), the run completed without errors (data not shown). The troubleshooting of this issue on the day took time and put them in the run media for longer than was needed, each contributing to a lower cell quality.

In retrospect, cold-activated enzymes might proof particularly beneficial for microglial isolations. It would efficiently dissociate tissue into a single-cell suspension at a colder temperature and keep ActD concentrations low; ActD concentration has been lowered effectively with colder temperatures (Wu et al. 2017). In addition, cold-activated enzymes would increase cell number, and library size and complexity, relative to dissociation at room temperature in the presence of ActD. This is less economical but will have positive downstream effects on the data quality. In addition, platform selection might have played a role in the read-out. Drop-seq is a high-throughput and cost-effective platform that offers good overall performance. However, in comparison to 10X, a commercially available platform, sensitivity of reads is approximately 2-fold lower. At a given read depth and independent of cell input number, a benchmark study identified 17,000 transcripts and 3000 genes with 10X, compared to 8000 transcripts from 2500 genes with Drop-seq .(Zhang et al., 2019). In parallel, read distribution across the barcodes is skewed with Drop-seq, with 10X allocating sequencing resources more evenly. Library size and complexity are expected to increase drastically by implementing this system, to the benefit of the scRNA-seq data quality. For reference, Sala Frigerio *et al.* (2019) and Marsh *et al.* (2022) both utilize the 10X platform in their implementation of ActD with microglia without any obvious signs of lowered cell quality.

Moreover, in contrast to the qPCR data, no differences in homeostatic genes were found between the pilot data (utilizing a standard dissociation) and ActD-treated microglia. Critically, the pilot and ActD study differ in the ages that were used; P90, and P21 and P60, respectively. Age is the main driver of microglial heterogeneity, and thomeostatic gene expression levels vary between early development and adulthood. Interactions of age- and isolation-specific effects might therefore occlude a clear read-out, one which need to be addressed in a more targeted study.

### 5.9.5 Summary

This chapter was to test distinct experimental procedures for scRNA-seq, that is, chemical fixation, enrichment, purification, and dissociation. Chemical fixation by itself was not found to be beneficial for microglial recovery, nor was FACS-mediated enrichment preferred. At its core, the selection of a protocol for droplet-based scRNA-seq of microglia distilled into a ‘maximalist’ or ‘minimalist’ choice. The maximalist includes beads-dependent purification and standard dissociation, whereas the minimalist veers into the use of gradient density centrifugation and ActD.

The maximalist allows for the largest recovery of microglia, however, issues of purity and *ex vivo* signatures could affect native transcriptional signatures. The minimalist ensures microglial purity, and preservation of microglial identity at the expense of yield. Combinations of both could be possible, when using bead-dependent purification with ActD-treatment. However, throughput and experimental complexity might decrease and increase, respectively, some of which are not always

practical in molecular labs and could introduce baseline drifting. Similarly, adult tissue might not be effectively purified with beads, introducing further considerations for downstream processing.

However, transcriptional inhibition alone is sufficient to preserve microglial identity and to minimize the introduction of *ex*AM-like signatures. Moreover, this data of sexually immature microglia (SIM) in an otherwise sparsely studied developmental age will help detail microglial maturation and subtype emergence in health and disease.

## 5.10 Supplementary figures and tables

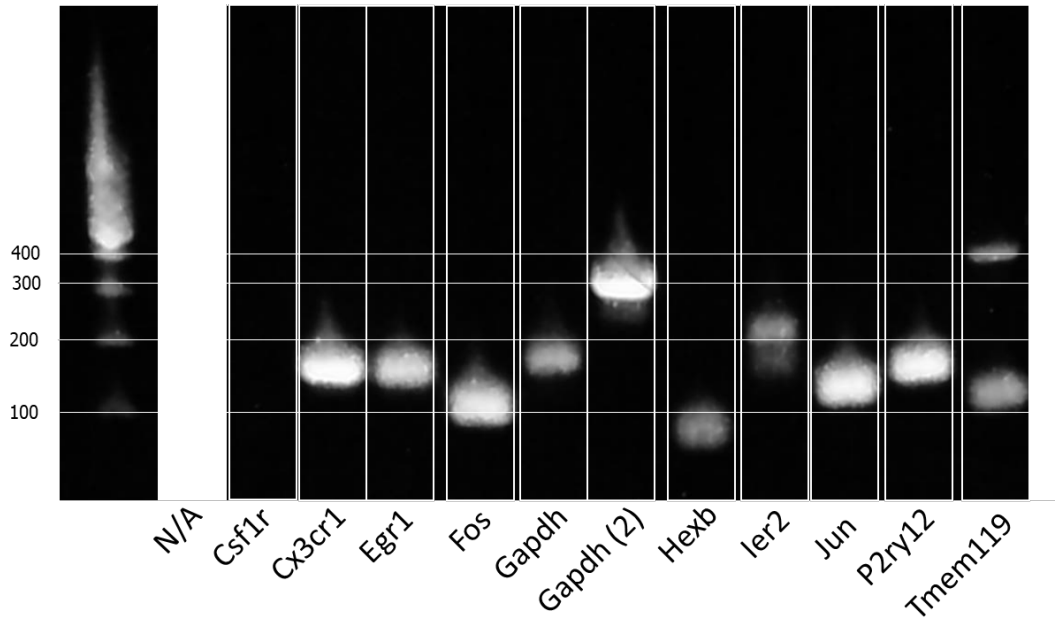


*Supplementary Figure 11: Quality control of designed primers. All primers display good quality parameters, apart from Csf1r, Ier2 and Tmem119, which were either not detected (Csf1r) or display double bands (Ier2, Tmem119).*

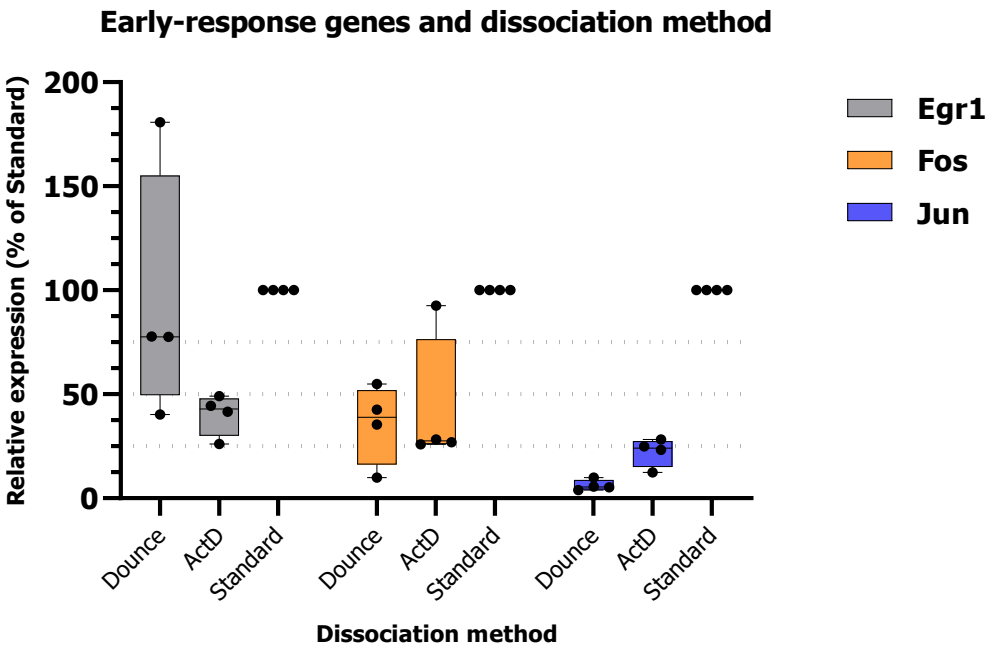

*Supplementary Figure 12: Early-response genes in cell isolation protocols. Distinct patterns of ERG can be noted in response to varying dissociation methods. Relative gene expression in relation to standard dissociation. Values are corrected for Gapdh; and Hexb, Cx3cr1 and P2ry12 sequentially.*

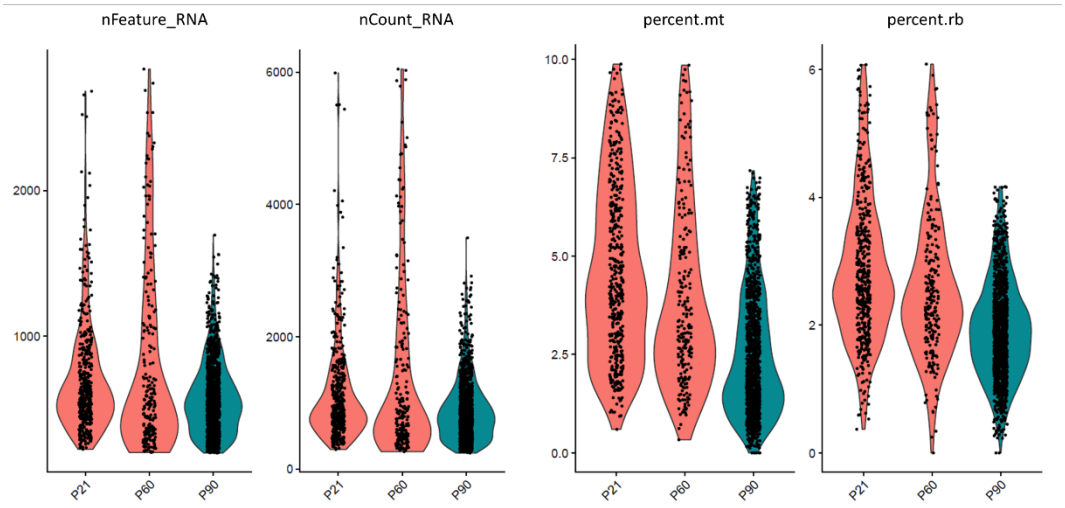


*Supplementary Figure 13: Parameters of cell quality by original identity and age.*

*Supplementary Table 14: Cluster cell allocation by study.*

| | **Seurat clusters** | | | | | | | |
|---|---|---|---|---|---|---|---|---|
| **Study** | *0* | *1* | *2* | *3* | *4* | *5* | *6* | **Total** |
| ActD | 269 | 201 | 95 | 18 | 51 | 32 | 21 | 687 |
| Pilot | 365 | 269 | 363 | 219 | 17 | 5 | 7 | 1245 |

*Note: Number of cells in each Seurat cluster (after quality control). The pilot study was performed with a standard isolation protocol that utilizes enzymatic dissociation, gradient centrifugation, and FACS; whereas ActD-treated cells are dissociated in the presence of 30 µM ActD, gradient centrifugation and MACS.*

# Chapter 6 Female gene regulatory networks in health and disease

## 6.1 Introduction

Sex is an established risk factor for neurodevelopmental and neurodegenerative disorders (Loomes et al., 2017; Podcasy and Epperson, 2016; Wooten et al., 2004). Although males and females are biased towards neurodevelopmental and neurodegenerative disease, respectively, the effects of sex on disease susceptibility are more nuanced. Men are typically more susceptible to autism, attention deficit hyperactivity disorder (ADHD), and motor neuron and PD, whereas females suffer more from anxiety, depression, MS and AD (Pinares-Garcia et al., 2018). Effects of which are thought to be partly mediated by microglia. In AD, microglia are critical mediators of the CNS immune environment and enriched for AD-associated risk genes like *Apoe*, *Ctsb*, *Pld3*, *Trem2* (Bellenguez et al., 2022; Cruchaga et al., 2014; Sala Frigerio et al., 2019).

Remarkably, as discussed previously, most biomedical studies do not consistently include females and there is a considerable knowledge gap in the molecular understanding why females are more susceptible to AD. In this final chapter, I will delve into sex-specific microglial specification, and address female, cortical microglial maturation in the context of disease by transcriptional and gene regulatory network analysis (Aibar et al., 2017).

### 6.1.1 Sex-specific microglial heterogeneity

As discussed, male and female microglial maturation follow a distinct trajectory of maturation (Figure 49). The question then emerges, why do female microglia mature faster? There have been reports that sex hormones play a role in providing female microglia an early neuroprotective function (Schwarz and Bilbo, 2012). Indeed, oestrogen has been shown to reduce microglial activation by Kir2.1 inward-rectifier $K^+$ channel (Wu et al., 2016). In fact, female microglia transplanted into male microglia are more capable of mitigating the sequalae of ischemia in the male brain (Villa et al., 2018). Lasting protective effects outside of the female brain imply epigenetic imprinting of environmental cues absent in males. Epigenetics has been shown to play a role in both masculinization and feminization (Nugent et al., 2015; VanRyzin et al., 2020). Strikingly, only male microglia are influenced by gonadal hormones at birth, hormones which downregulate *Dnmt* expression at a critical period for sexual differentiation (VanRyzin et al., 2020). The absence of gonadal hormones in this critical window maintains *Dnm*t and protects females from masculinization.

The first exposure of female microglia to endogenous gonadal hormones is at puberty. Of note, the emergence of gonadal hormones in females is concurrent with the selection phase of microglia (Askew et al., 2017; Nikodemova et al., 2015). As discussed previously, microglial expansion is predominantly driven by CPM in early development of mice and humans, a finding that is in line with established literature (Figure 37, Figure 38)) (Askew et al., 2017; Menassa et al., 2022; Nikodemova et al., 2015). In turn, microglial numbers in the brain start to decline from P14 until adult homeostasis is reached (Nikodemova et al., 2015). Sexual maturation and sex hormones increase shortly after weaning (~P21) to stabilize at P60, concurrent with microglial selection windows. In addition, the selection of microglia is regionally distinct; CB and HIP display an early increase in number and selection, where cortical microglia undergo a protracted development (Askew et al., 2017). Taken together, these results suggest that microglial population dynamics are associated to gonadal hormone exposure, an effect which could be regionally heterogenous (Figure 91).

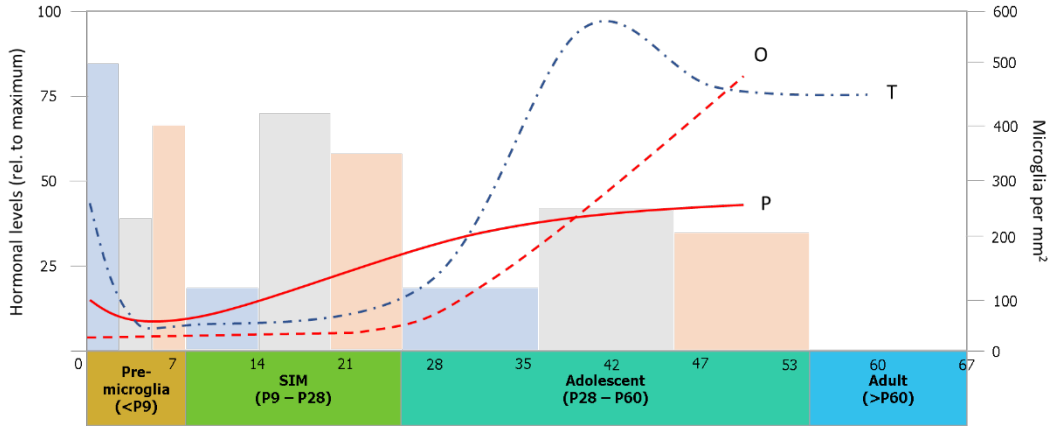


*Figure 91: Hormonal levels and microglial selection. Male and female levels of progesterone and oestrogen in the CNS start to increase in Sexually Immature Microglia (SIM), to stabilize at P60. Inversely, microglial densities in cerebellar (blue), cortical (grey), and hippocampal (orange) densities are highest in pre-microglia, SIM and pre-microglia, respectively. Adapted from (Askew et al., 2017; Bell, 2018). O, oestrogen; T, testosterone; P, progesterone.*

Given that age-associated diseases like Alzheimer's are more prevalent in females, that microglial expansion and selection underlie the adult population, that microglia have a central role in neuroinflammation, and that distinct sex-specific MDI trajectories have been identified, exploring Sexually Immature Microglia (SIM) (P9-28) could be interesting to understand how such disease susceptibility emerges. However, biomedical research has long forgotten about females, best exemplified by the number of female cells in the atlas relative to male, and this developmental time is not commonly studied (Ravindran et al., 2020; Zucker and Beery, 2010) (Table 3). Crucially, transcriptional regulation by transcription factors (TF), also known as regulons, is not typically considered in scRNA-seq data of microglia.

### 6.1.2 Gene regulatory networks inference and clustering

Regulons typically associated with microglial identity are Irf8, Mafb, Sall1, and Spi1 (Pu.1) (Buttgereit et al., 2016; Kierdorf et al., 2013b; Masuda et al., 2012; Matcovitch-Natan et al., 2016; Rustenhoven et al., 2018). Irf8, Mafb, Sall1 and Spi1 were reviewed in Chapter 1. In short, *Irf8* and *Spi1* expression initiates early in development, where they have been found to play a role in microgliogenesis and differentiation in the microglial lineage commitment cascade in early microglia (<E14) (Huang et al., 2008; Kierdorf et al., 2013a). In turn, Mafb and Sall1 are under the influence of Tgf-ß, mediating an environment-dependent driver for microglial maturation from pre-microglia onwards (E14-P9) (Buttgereit et al., 2016; Kierdorf et al., 2013; Matcovitch-Natan et al., 2016). Identification of such regulons in a small-scale study would further delineate microglial identity at a higher-order level, potentially ameliorating study-specific artefacts akin to a large-scale atlas.

Gene regulatory network identification is a novel approach in scRNA-seq. Like trajectory inference, it has quickly become a popular tool that is under active development (Aibar et al., 2017; Chan et al., 2017; Dijk et al., 2018; Jackson et al., 2020). Of the methods that are publicly available, SCENIC, or 'single-cell regulatory network inference and clustering', is the most used form.

#### 6.1.2.1 Single-cell regulatory network inference and clustering

SCENIC is an R- and Python-based computational tool that combines the identification of gene regulatory networks with clustering of cellular heterogeneity (Aibar et al., 2017) (Figure 92). SCENIC uses "GENIE3" to construct a co-expression module of genes regulated by the same TF; it performs a TF-enrichment analysis of regulons by "RcisTarget", thereby improving accuracy of subtype and state identification; and scores regulon expression in single-cells with "AUCell". The result is a binary matrix of regulon activity that can be projected onto a *t*-SNE- or UMAP-plot.

Interestingly, SCENIC has already been utilized to identify microglia in distinct lineages, as well as within gestational microglia (Aibar et al., 2017; Kracht et al., 2020). However, to my knowledge, it has not been applied to a single-cell atlas of microglia across the lifespan. Identifying key regulons in such a compendium will further aid the understanding of microglial biology and establish novel therapeutic targets age-associated disease.

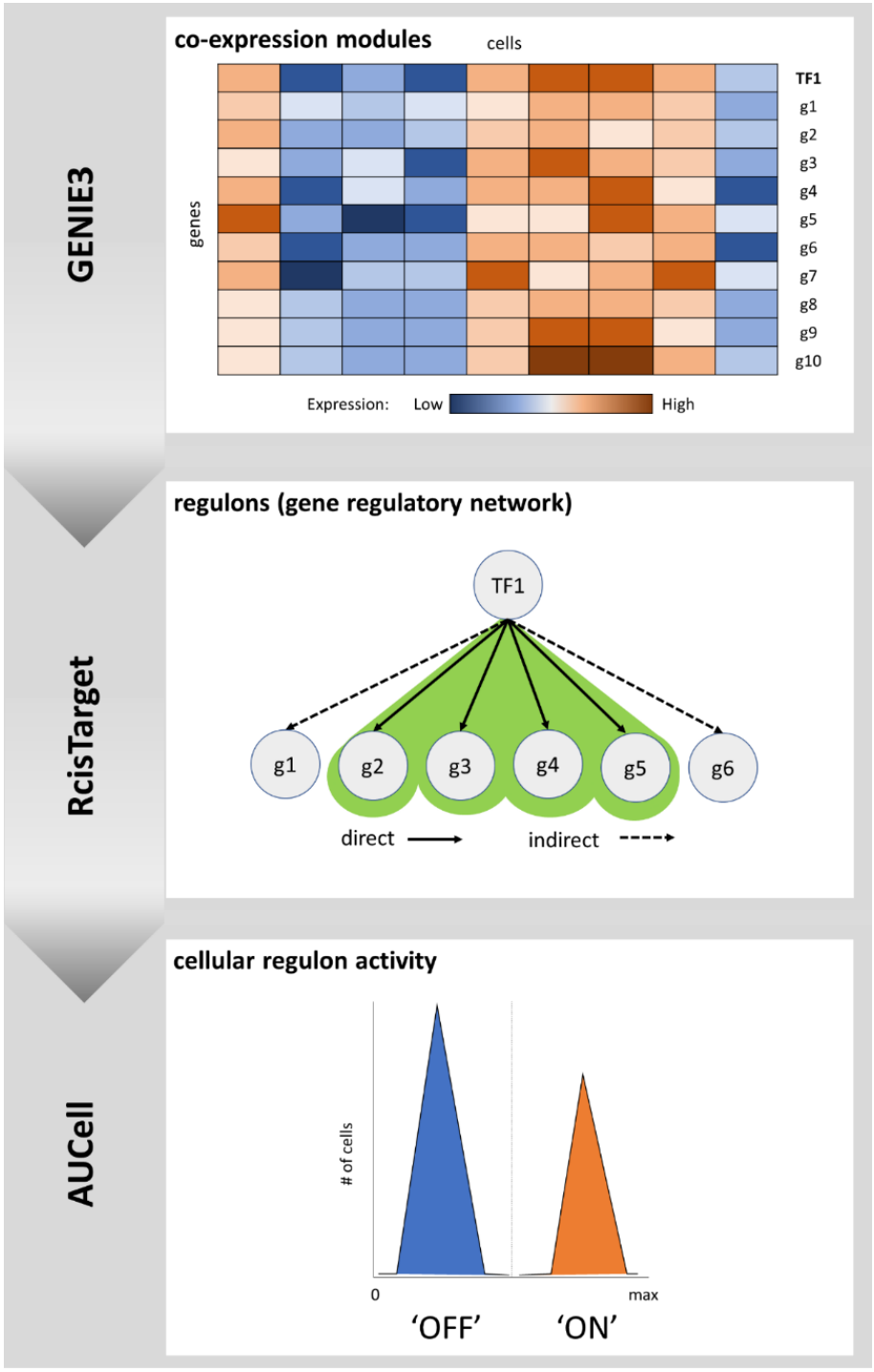


*Figure 92: SCENIC workflow. SCENIC utilizes "GENIE3" (or "GRNBoost2") for the identification of co-expression modules. Regulons of the expression modules are tested with "RcisTarget" for the determination of a gene regulatory network, thereby identifying direct and indirect targets. After which cellular regulon activity is binarized and tested with "AUCell", to assign the absence of or expression on the regulons; 'OFF' and 'ON', respectively.*

## 6.2 Aims and objectives

In this final chapter, I aim to establish an atlas of female, microglial heterogeneity in the cortex, from Sexually Immature Microglia (SIM) to old age. This will enable me to consolidate previously established gene lists and microglial subtypes, investigate a critical developmental window of microglial maturation, and ascertain the effects on genotype on transcriptional heterogeneity and population dynamics. Similarly, I aim to determine gene regulatory networks in microglia that drive heterogeneity, to aid biomarker discovery and therapeutic intervention strategies for healthy aging.

**Aim 4: Study of female gene regulatory networks in health and disease.**

- Objective 13: To establish a female-specific atlas in the murine cortex.
- Objective 14: To explore the transition to an adult microglial phenotype.
- Objective 15: To determine the effects of amyloidosis on transcriptional heterogeneity and population dynamics.
- Objective 16: To identify transcription factors central to age-associated microglial subtypes.

## 6.3 Materials and methods

### 6.3.1 Dataset Acquisition

3 datasets were gathered that include wild type and AD model-derived cells ($APP^{NL-G-F}$). These include data from Sala Frigerio *et al.* (2020), and Tabula Muris Consortium (2020), datasets that were used in the large-scale atlas previously, as well as in the in-house generated data of SIM. To minimize confounding variables, I chose to select only female-derived cells in the cortex (Table 9).

*Table 9: Features of scRNA-seq datasets in the small-scale female atlas.*

| | | | Age | | | | | |
|---|---|---|---|---|---|---|---|---|
| **Source** | **Year** | **Accession** | *P21* | *3M* | *6M* | *12M* | *21M* | **Genotype** |
| Muntslag *et al.* | 2022 | N/A | 450 | | | | | WT |
| Sala Frigerio *et al.* | 2019 | GEO: GSE127893 | | 357 | 341 | 312 | 302 | WT |
| | | | | 351 | 282 | 210 | 250 | $APP^{NL-G-F}$ |
| Tabula Muris Consortium | 2020 | GEO: GSE109774 | | 436 | | | | WT |

*Note: Details of the respective source data is tabled, including year, accession number (if applicable), the number of cells at the given ages, and genotype. All data are post quality control. APP, AD-model genotype; P, postnatal day; M, months old, WT, wild type genotype.*

A total of 3291 cells were included, including 450 SIM (P9 – P28), 1767 adult microglia (P60-6M), 522 middle age microglia (6M – 18M), and 552 old age microglia (>18M). As stated, SIM are a sparse commodity when it comes to scRNA-seq data (Table 3). This is particularly salient as the transition

from early developmental to old age subtypes can be localized to this developmental window (Figure 32).

The $APP^{NL-G-F}$ mice harbour disease relevant 'Swedish and Beyreuther/Iberian mutations with and without Artic mutation in the APP gene' (Saito et al., 2014). This prevents the use of artificial transgenic overexpression and better captures the AD phenotype. Broadly, these mice are featured by an invasive amyloid-ß (Aß) pathology, neuroinflammation and memory impairment by 6 months old.

### 6.3.2 Seurat and Metascape

Seurat and Metascape were utilized as described previously (Butler et al., 2018; Zhou et al., 2019). In short, a quality control (QC) of each dataset was performed individually, after which the objects were normalized, scaled and regressed for 'nFeature_RNA', 'percent.rb', 'G2M.Score', and 'S.Score'. Canonical Correlation Analysis, anchor-based integration was performed, followed by dimensionality reduction and cluster identification (Butler et al., 2018). I chose to use 10 dimensions at a resolution of 0.6. Differential gene expression analyses were performed with 'FindAllMarkers' with Wilcoxon test for statistical significance. Cluster-specific markers are reported in. Cluster markers or gene regulatory network-derived - see– were tested in *Metascape* utilizing with 'Express Analysis' (Zhou et al., 2019).

### 6.3.3 SCENIC

A default SCENIC bioinformatic pipeline of SCENIC was applied, as first described by Aibar *et al.* (2017). To add functionality for subsequent visualization, I made adaptations to the pipeline to include modifications made by Kracht *et al.* (2020). In short, this script uses a log-normalized count matrix as input; adds an additional QC step; and enables the projection of identified regulons onto a Heatmap, and onto a UMAP-plot pertaining to their analysis in Seurat.

## 6.4 Results

### 6.4.1 Transcriptomic heterogeneity of microglia in the murine lifespan

Albeit female microglial studies are starting to increase, SIM are understudied (Hanamsagar et al., 2017; Masuda et al., 2019; Sala Frigerio et al., 2019; Villa et al., 2018). To ameliorate this absence, a single-cell dataset was generated of cortical microglia in healthy, female mice at P21. This dataset was detailed in the previous chapter – see section 5.8. Here, I used this dataset (and two publicly available datasets) to establish an integrated object that spans from SIM to old age microglia,

including both wild type (WT) and APP$^{NL\text{-}G\text{-}F}$ (APP) cells. No APP-derived microglia were available at P21. 5 distinct clusters were identified (Figure 93, Supplementary Table 15).

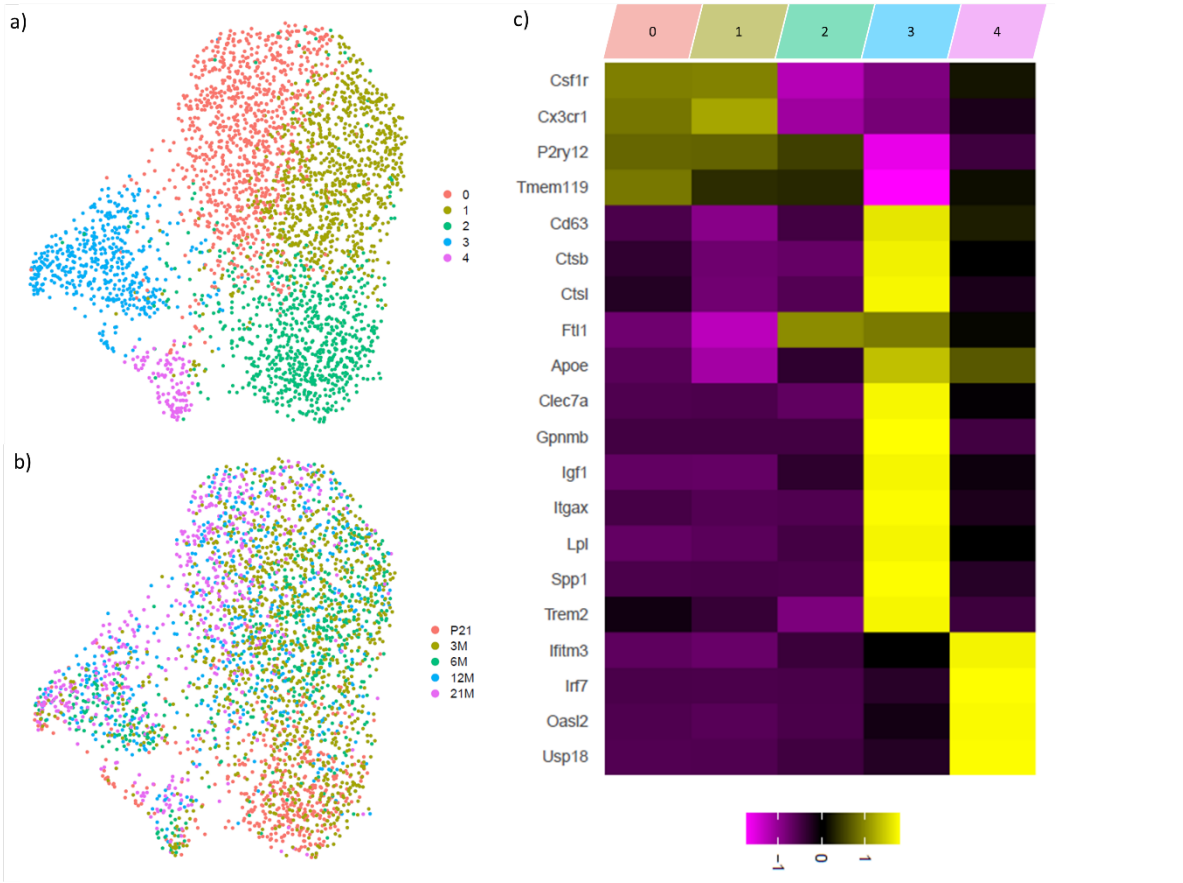


*Figure 93: Cluster identification in female, cortical microglia in health and disease. a) 5 clusters were identified in a small-scale atlas of wild type- and APP$^{NL\text{-}G\text{-}F}$-derived cells. b) Microglial age distributions vary and show similarities with cluster identity distributions. c) Typical homeostatic genes are enriched in cluster 0,1 and 2. Lysosome pathway-associated macrophages (LPM) and interferon response microglia (IRM) genes are enriched in cluster 3 and 4, respectively.*

To detail which microglial subtypes are present in this integrated dataset, the expression of genes known from the large-scale single-cell atlas were tested, aiming to capture broad microglial heterogeneity in this way (Supplementary Table 16). This list includes homeostatic clusters genes, previously described as HOM-clusters, as well as *sensome*, early developmental microglia (EDM), interferon response microglia (IRM) and lysosome pathway-associated macrophage (LPM) genes. Most of the cells in female cortical maturation express typical microglial markers. Based on their homeostatic gene expression (and the absence of LPM or IRM markers), cluster 0, 1 and 2 were identified as homeostatic; cluster 3 were identified as LPM and cluster 4 as IRM (Figure 93).

### 6.4.2 SIM and the dynamic acquisition of a homeostatic microglial signature

In the large-scale atlas, there lacked a significant contribution of SIM (Table 3). Here, I have effectively bridged this gap by including the single-cell dataset. The rapid maturation of microglia from pre-microglia to adolescent microglia can in fact be captured at the SIM stage (*i.e.* P9 – P28) (Figure 94). At this stage, homeostatic genes continue to increase to adult levels. This acquisition can be noted in *Csf1r* and *Cx3cr1*, although this is most evident for *Cx3cr1* at 3 months old, indicative

of the protracted nature of cortical maturation. Interestingly, P21 also lose genes typically associated with early development (*e.g. Ftl1*, *Tmsb4x*, *Rps14*), confirming that SIM are a highly dynamic developmental time-window in microglial heterogeneity (Supplementary Figure 14).

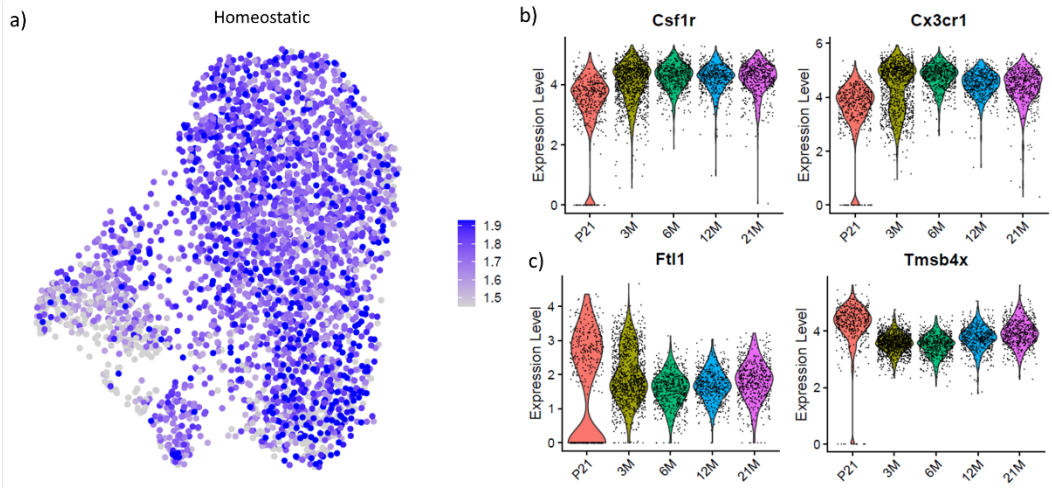


*Figure 94: Homeostatic gene acquisition in SIM. a) FeaturePlot of homeostatic markers, as defined by (Matcovitch-Natan et al., 2016). Sexually Immature Microglia (SIM) are featured by b) adult homeostatic and c) early developmental microglial markers, marking a transitional age in the acquisition of microglial identity.*

To further explore this developmental age, DGE analysis was done on the Seurat clusters with 'FindAllMarkers'. Cells from P21 mostly clustered to cluster 2 (Supplementary Figure 15), which led me to think clusters might better respect general transcriptional similarities and could mitigate any source specific artefactual gene introductions. 17 statistically significant genes were enriched in cluster 2, most of which were associated with regulation of actin cytoskeleton organization (GO:0032956), cell chemotaxis (GO:0060326) or regulation of calcium ion transport (GO:0051924) (Figure 95). These biological processes correspond to an acquisition of microglial identity; however, effects were small (Supplementary Table 15), as they have been for HOM-clusters in the large-scale atlas (Supplementary Table 1, Supplementary Table 2).

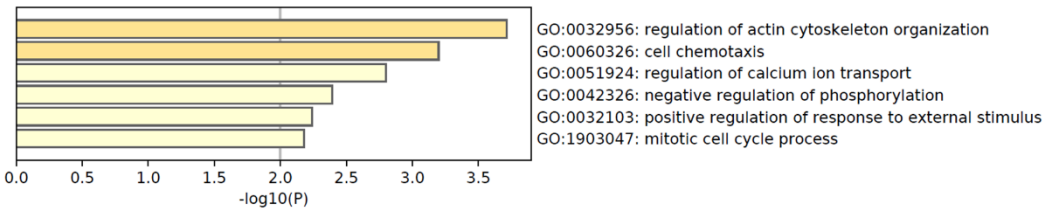


*Figure 95: SIM are featured by morphological and migratory genes. Enrichment of Gene Ontology (GO) categories in Sexually Immature Microglia (SIM).*

### 6.4.3 Age-associated microglia and genotype

Two age-associated microglial clusters were identified that correspond to LPM and IRM; cluster 3 and 4, respectively. These minority clusters display typical markers associated with them, including genes like *Csf1*, *Igf1* and *Lpl*, and *Ifit3*, *Oasl2*, *Usp18* (Figure 96).

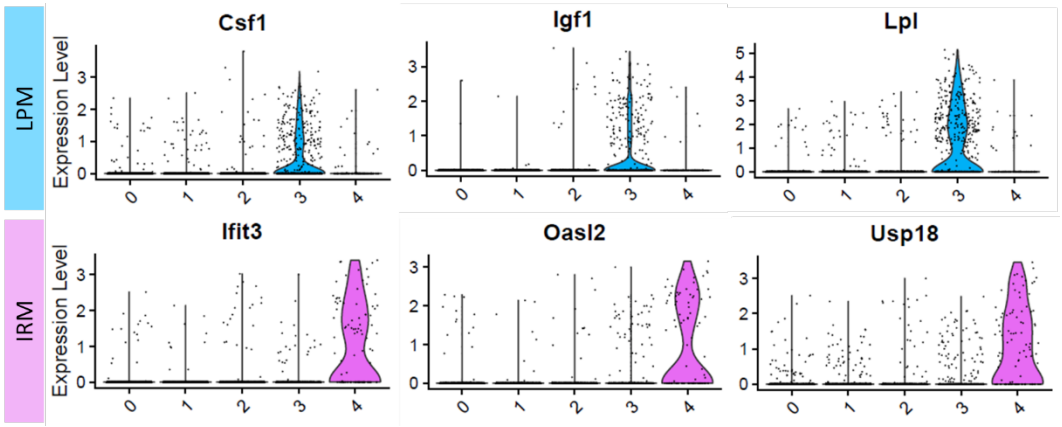


*Figure 96: Age-associated microglial subtypes in health and disease. Lysosome pathway-associated macrophages (LPM) and interferon response microglia (IRM) were identified in the small-scale cortical atlas. 3 canonical markers (and their expression levels) are displayed by Seurat cluster identity.*

As age-associated disease is linked to microglial heterogeneity, WT and AD models affect transcriptional signatures differentially. A distinct age distribution of C57BL/6 and APP model-derived cells was observed, where average age is higher for clusters enriched for LPM and IRM, suggestive of an accelerated microglial phenotype by APP (Figure 97).

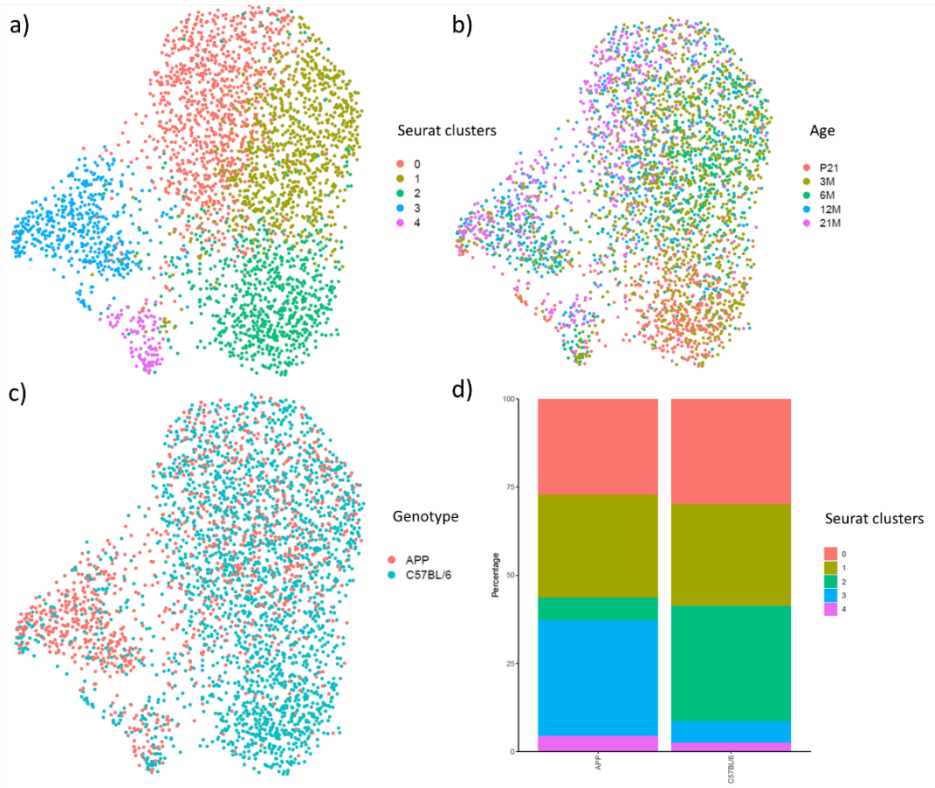


*Figure 97: Female cortical microglial maturation and genotype. a/b) 5 clusters were identified that broadly track distinct age groups spanning from Sexually Immature Microglia (SIM) (P21) to old age microglia (21M). c/d) Uneven distribution of genotype can be observed in the object. P, postnatal day; M, month.*

To explore this further, the gene signatures were split by genotype and grouped by age. In this way, it became obvious that albeit LPM displayed an age- and genotype-specific expression level, IRM-associated genes were equally expressed, independent of age or genotype (Figure 98). This has previously been addressed in the large-scale atlas by referencing Sala Frigerio *et al.* (2019), the current source under review. Interestingly, LPM were suggested to be a converging point of age,

sex, and genetics; a microglial subtype that is enriched for AD-associated risk factors like *Apoe*, *H2-Ab1*, and *H2-Eb1* (Sala Frigerio et al., 2019).

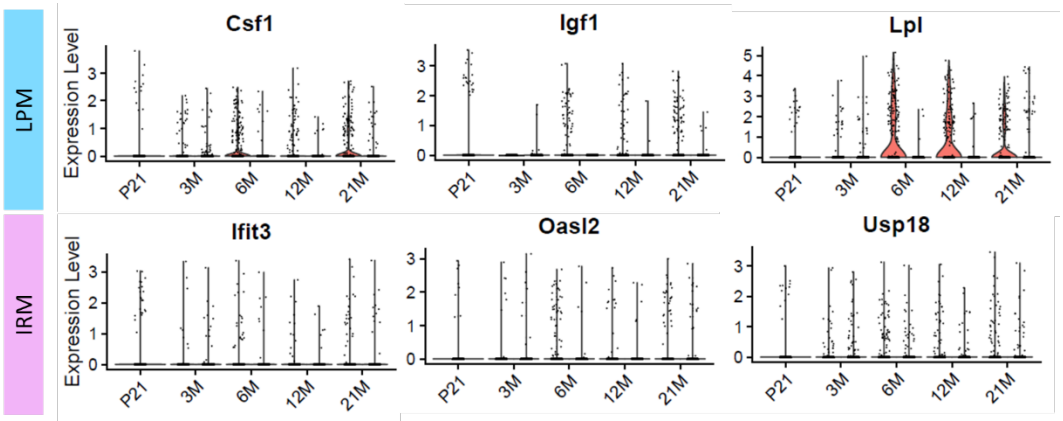


*Figure 98: Not all age-associated microglial subtypes display an age- and genotype-specific variability in expression level. Lysosome pathway-associated macrophages (LPM)-associated genes are differentially affected by age and genotype, whereas IRM have no such enrichment. Typical LPM and IRM genes were selected. Cells are split by genotype ($APP^{NL\text{-}G\text{-}F}$, C57BL/6) and grouped by age; C57BL/6 in blue, APP in red*

An enrichment of *Apoe*, *Ctsb*, and *Pld3* was seen in early development and old age LPM (Figure 36). Trem2 is a fourth genetic factor that is associated with the emergence of disease-associated microglia (DAM) (*i.e.* LPM) (Keren-Shaul et al., 2017b; Mecca et al., 2018). Interestingly, all four AD-associated genes are enriched in LPM with age (Figure 98). Early development is featured by an increase of *Apoe* levels, after which expression abates, to increase once more in old age (Figure 36) (Butovsky et al., 2014). Remarkably, *Ctsb*, *Pld3* and *Trem2* expression levels do not show any overt changes with healthy aging, albeit a moderate increase can be observed in old age microglia (21M).

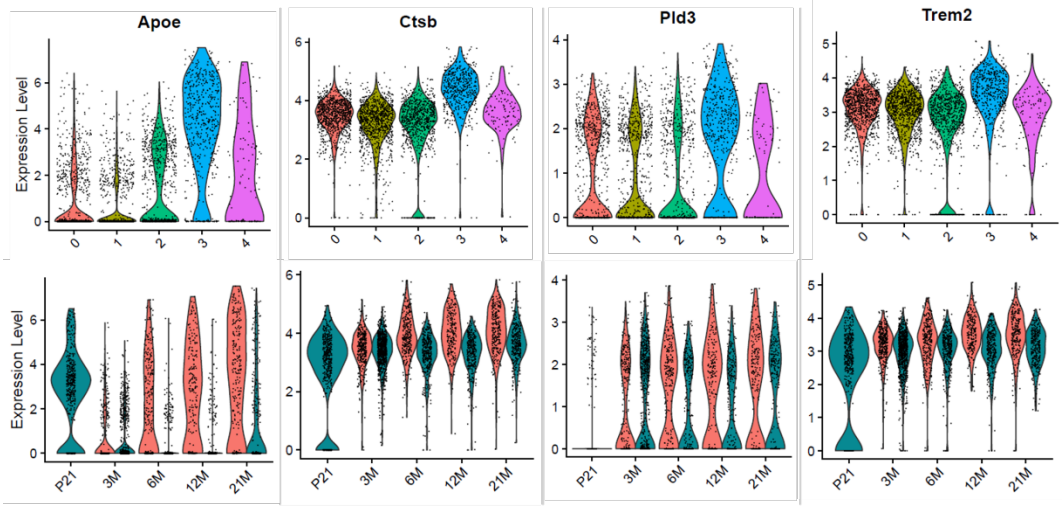


*Figure 99: LPM, AD-associated risk factors, age, and genotype. Lysosome pathway-associated macrophages (LPM) are enriched for Alzheimer's disease (AD) risk factor genes that display age- and genotype-specific variations in expression level. Each AD gene is organized by column and displayed by cluster, and by age split by genotype; C57BL/6 in blue, APP in red. P, postnatal day; M, months old.*

In contrast, amyloidosis in $APP^{NL\text{-}G\text{-}F}$ mice increases the expression of all 4 selected AD risk genes (Figure 99). At 3 months old, $APP^{NL\text{-}G\text{-}F}$ and WT maintain a similar expression profile of these genes. However, as early as 6 months old, expression of *Apoe*, *Ctsb*, *Pld3* and *Trem2* in $APP^{NL\text{-}G\text{-}F}$-derived microglia is increased to levels beyond which are attained in health well into old age. Combined,

the upregulation of these genes implies the acquisition of a microglial signature primed to interact and mitigate amyloidosis in AD.

Interestingly, Hickman *et al.* (2013), the authors who first coined the microglial sensome, reported on a loss of *Trem2* expression with old age (-1.24 logFC) (Hickman et al., 2013). At first glance this appears to be at odds with the findings here. However, looking into the ages used for their analysis, young and old were represented by 5- and 24-month-old mice, adult and old age microglia, respectively. This goes on to suggest that microglial *Trem2* expression is well-maintained into old age before a rapid drop of expression. Alternatively, it is possible these are study-specific factors, possibly hinting towards dysfunctional microglia. *Trem2* would make for an interesting target in the large-scale atlas.

### 6.4.4 Microglial population dynamics and amyloidosis

With amyloidosis to influence AD risk gene expression, microglial population dynamics are expected to differ between WT and $APP^{NL\text{-}G\text{-}F}$. As seen in the large-scale atlas, healthy aging is featured by a loss of early developmental signatures like those in cluster 2, to the benefit of typical homeostatic signature (cluster 0 and 1), prior to emergence of age-associated clusters (*i.e.* cluster 3, 4) (Supplementary Figure 14, Figure 32, Figure 100). In health, maturation appears to complete by 6 months of age. In contrast, with amyloidosis, there's an earlier emergence of age-associated clusters like LPM and IRM, and a decline of HOM-clusters as early as 3 months old (Figure 100). With microglia rapidly maturing to age-associated subtypes during amyloidosis, it begs to question what transcription factors are driving such phenotypical diversification.

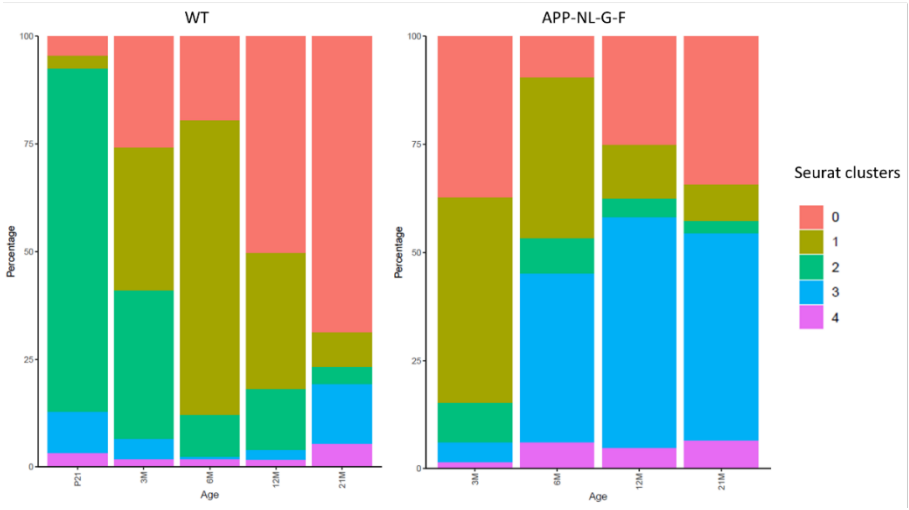


*Figure 100: Temporal population dynamics of WT- and $APP^{NL\text{-}G\text{-}F}$-derived microglia. Wild type (WT) and $APP^{NL\text{-}G\text{-}F}$ microglial population dynamics differ, with AD-derived microglia featured by an accelerated emergence of age-associated microglia (LPM, IRM), as early as 6M. M, months old.*

### 6.4.5 Gene regulatory networks identify disease-like microglia regulons

Well-established regulons of microglial identity include Irf8, Mafb, Sall1 and Spi1 (Pu.1). These regulons are expressed to similar levels from SIM onwards, independent of age or genotype (Figure 101). Their relative stability in expression levels underlines their respective importance to microglia identity, yet this does aid the understanding of microglial heterogeneity in these conditions.

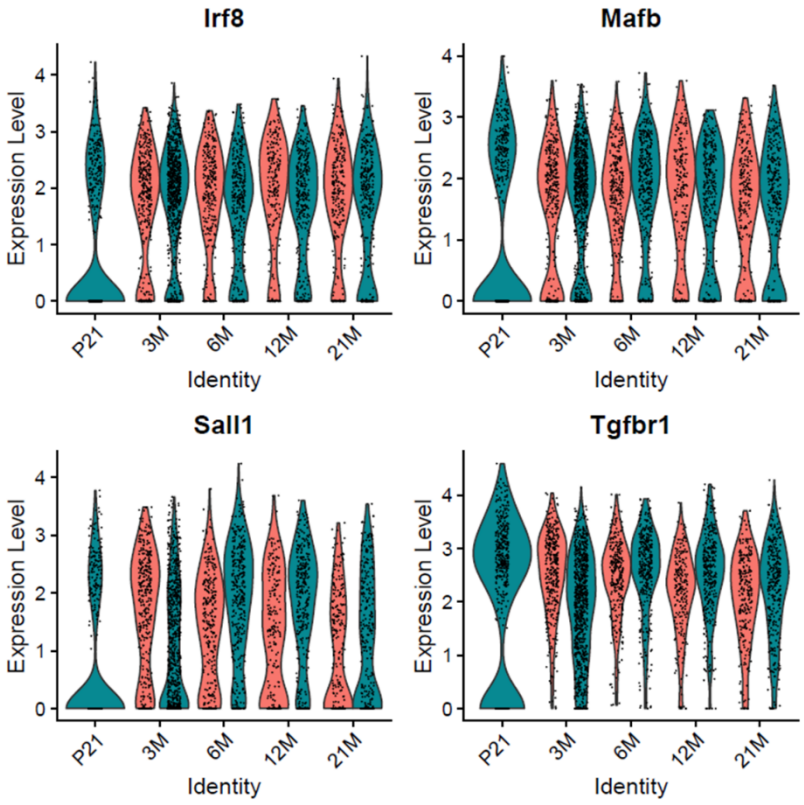


*Figure 101: Canonical microglial regulons lack age- or genotype-specific heterogeneity. 4 well-established microglial transcription factors (TF) are displayed: Irf8, Mafb, Sall1, Tgfbr1. No age- or genotype-specific differences in expression levels can be remarked.*

To identify regulons that drive microglial transcriptional diversification, I utilized SCENIC. With it, a plethora of TF were identified that vary their expression in an age- and cluster-specific manner (Figure 102, Supplementary Table 17, Supplementary Table 18). Homeostatic signatures (cluster 0, 1 and 2) are enriched for regulons like Gmeb1 and Sin3aS, whereas clusters enriched for immature and disease-like microglia have a relative low expression of each (Figure 102). Instead, cells are enriched for factors like Atf3, Bhlhe40 and Irf7 (Figure 102). Moreover, I would like to point out that P21 and 21M cells cluster together hierarchically, consistent with their expression of an EDM-signature, and in support of findings in the large-scale atlas (Figure 31, Figure 93,Figure 102).

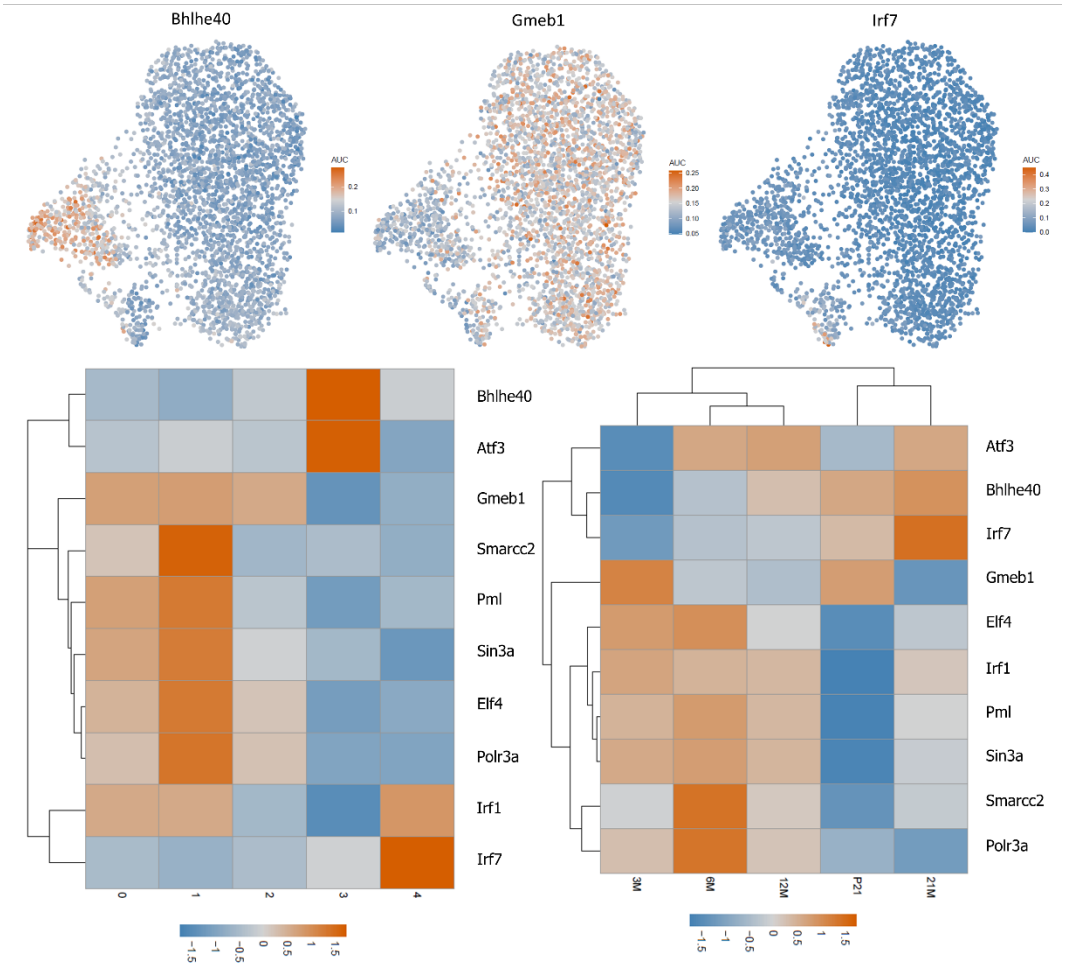


*Figure 102: Transcription factor enrichment in an age- and cluster-specific manner. 3 major transcription factors (TF) drive transcriptional diversification of homeostatic microglia (cluster 0, 1, 2) to disease-like subtypes (cluster 3, 4) are displayed in FeaturePlots. Area under the curve (AUC) (i.e. enrichment) is scaled by row, where blue and orange are low and high expression, respectively. TF enrichment of all major (and minor) TF further details their hierarchical similarities by cluster (bottom left) and age (bottom right). Both wild type and $^{APPNL-G-F}$ cells are included in all figures. g, genes, p, postnatal day; M, months old.*

HOM-cluster-associated regulons include Gmeb1, Smarcc2, Pml, Sin3a, Elf4 and Polr3a (Figure 102). Of these regulons, Gmeb1 is reliably enriched in all three HOM-clusters and reduced in activity in LPM and IRM (Figure 102). Gmeb1, also known as glucocorticoid modulatory element binding protein 1, loss of which confers a stress-related genetic susceptibility for AD (de Quervain et al., 2004; Lemche, 2018). A loss of Gmeb1 activity in age-associated microglial subtypes might therefore provide an explanation why such cells are typically linked to pathology. In contrast, age-associated microglial subtypes like LPM and IRM are driven by Bhlhe40 and Irf7, respectively (Figure 102). Bhlhe40 was found to regulate 72 genes in female cortical microglia, among which *Apoe*, *Ctsb* and *Lpl* (Friedman et al., 2018; Krasemann et al., 2017; Yung, 2019). In turn, Irf7 regulates 52 genes, including *Cxcl10*, *Ifitm3* and *Usp18* (Rubino et al., 2018; Xu et al., 2021).

Interestingly, there is a widespread transcriptional redundancy between the top 10 most variable regulons (Figure 103). Moreover, these regulon interactions include self-reinforcing networks of microglial identity (Chew and Petretto, 2019; Fagnocchi et al., 2016; Grubman et al., 2019).

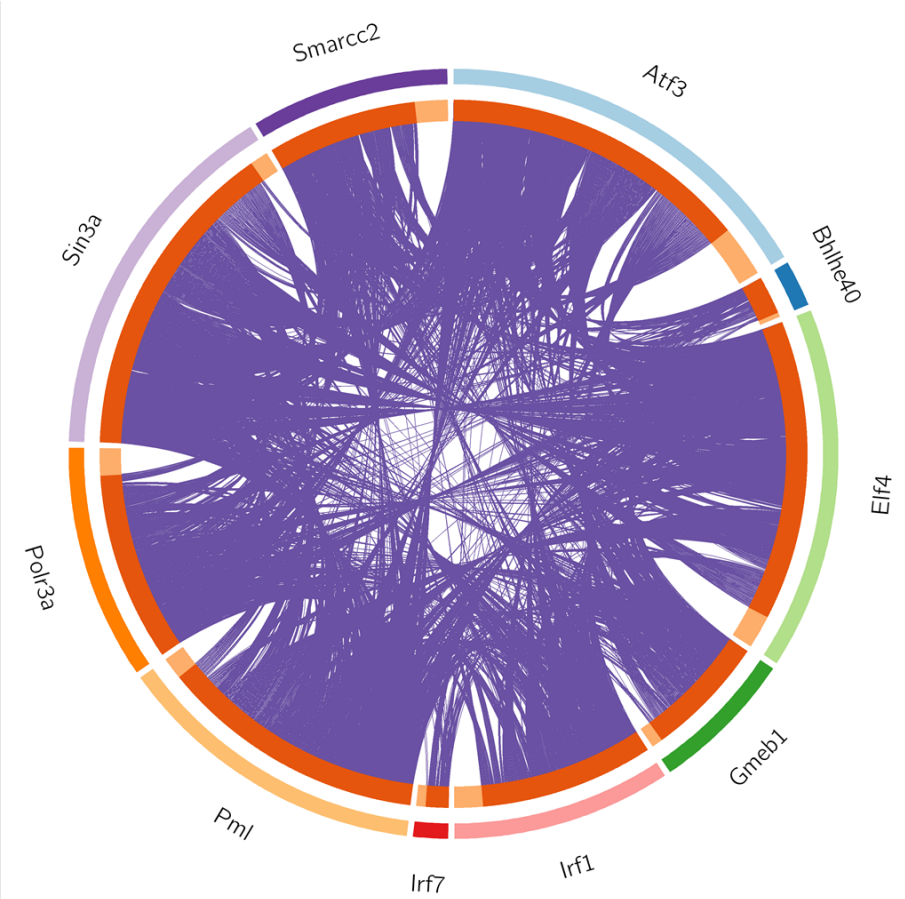


| TF | Stimulated by: | Stimulates: |
|---|---|---|
| **Atf3** | Atf3, Irf1, Pml, Smarcc2 | Atf3, Bhlhe40, Irf1, Polr3a, Sin3a, Smarcc2 |
| **Bhlhe40** | Atf3, Bhlhe40, Sin3a, Smarcc2 | Bhlhe40, Smarcc2 |
| **Elf4** | Elf4, Irf1, Pml, Polr3a, Sin3a | Elf4, Gmeb1, Irf1, Polr3a, Sin3a |
| Gmeb1 | Elf4, Sin3a | Sin3a |
| **Irf1** | Atf3, Elf4, Irf1, Pml, Sin3a | Atf3, Elf4, Irf1, Irf7, Sin3a |
| **Irf7** | Irf1, Irf7 | Irf7, Pml |
| Pml | Irf7, Polr3a | Atf3, Elf4, Irf1, Sin3a |
| Polr3a | Atf3, Elf4, Sin3a | Elf4, Pml |
| **Sin3a** | Elf4, Gmeb1, Irf1, Pml, Sin3a, Smarcc2 | Bhlhe40, Elf4, Gmeb1, Irf1, Polr3a, Pml, Sin3a, Smarcc2 |
| Smarcc2 | Atf3, Bhlhe40, Sin3a | Atf3, Bhlhe40, Sin3a |

*Figure 103: Transcriptional overlap of microglial regulons in cortical microglia. A 'Circos' plot from a Metascape analysis illustrates the input gene lists overlap; only verified targets in female cortical microglia are reported. Regulatory network interactions of the top 10 most variable regulons. Self-reinforcing regulons are highlighted in bold.*

Looking at the sheer number of regulon interactions, Sin3a is the strongest driver of microglial heterogeneity in female cortical microglia (Figure 103, Supplementary Table 17, Supplementary Table 18). Sin3a is known to form a co-repressor complex with histone deacetylase (HDAC) for MeCP2 (Jin et al., 2017). Low activity of Sin3a in microglia in early development and old age hint towards a loss of transcriptional repression and microglial diversification, whereas upregulation of Sin3a with adulthood is reflective of the progressive fine-tuning of microglial identity towards a defined homeostatic signature.

Similarly, Atf3 is a broad-spectrum TF that targets 613 genes in the small-scale cortical atlas, among which, *Bhlhe40*, *Ccl4*, *Cd74*, *Cst7*, *Ctsb*, *Dusp1*, *Egr1*, *Irf1*, *Lpl* and *Spp1*. In contrast, both Bhlhe40 and Irf7 are self-reinforcing regulons that only affect Smarcc2 and Pml, respectively. Such specificity suggests that these regulons are end-stage lineage determining factors. It is the apparent specificity of Bhlhe40 and Irf7 that could make these regulons valuable therapeutic targets.

## 6.5 Discussion

In this chapter I delved into female, cortical microglial heterogeneity in a small-scale atlas. 5 distinct clusters were identified, including HOM- and age-associated clusters. Four objectives were set out *a priori*, some of which were achieved while others were marred by challenges.

### 6.5.1 Generation of a small-scale female-specific microglial atlas

3 data sources were integrated for a total of 3,219 cells in health and disease. Two of these sources, Sala Frigerio *et al.* (2019) and the Tabula Muris Consortium, have previously been utilized for the generation of the large-scale atlas. Here, these functioned to reliably anchor adult microglial signatures into the dataset, thereby ensuring any age- or genotype-specific effects were put into context. To extend upon these signatures, a single-cell dataset of cortical, female microglia from P21 C57BL/6 mice was generated (Chapter 5). A gap was identified in literature, which this dataset was set out to mitigate.

Unfortunately, the number of cells that were sequenced (and their quality) imposed limitations to the scope of the results. The aim was to clearly outline microglial selection in the female cortex. Albeit this study provides a first glimpse into this developmental time window, to truly capture the selection phase (and all the microglial subtypes at such a time), the age range, cell number and read depth need to be increased. Ideally, collecting 5,000 cells from wild type and AD disease model-derived mice of P7, P14, P21, P28, P42, P56, at a depth of ~50,000 reads/cell would provide this answer. This would equate to approximately 30,000 total cells, enough to collect at least 50 cycling and proliferating microglia (CPM) for each age, with CPM as the minimum fraction. This range would allow researchers to capture early developmental microglia and age-associated microglial subtypes concurrently, to address microglial selection in health and disease, and explore if and how LPM differ in such contexts. More specifically, microglial population dynamics already display a differential maturation trajectory as early as 3-months old in APP mice. Given that microglia in early development also increase AD risk factor genes (Chapter 3), it would be interesting to see how AD risk factor genes in development drive subsequent LPM emergence. However, despite not being able to detail the selection phase to the desired level, the integration of approximately 500 cells

from P21 to 21M allowed for the identification an age-specific effect on microglial heterogeneity like that described in the large-scale atlas.

### 6.5.2 Transition to a mature microglial phenotype

Microglia undergo a dramatic change in gene expression signature between pre-microglia (E14.5 – P9) and adolescent microglia (P28 – P60) (Figure 32). Here, this transition was localized to SIM (P9 – P28), in parallel with the onset of microglial selection in the cortex (Askew et al., 2017; Nikodemova et al., 2015). P21 cells display a transitional signature, enriched for both early developmental and homeostatic genes such as *Ftl1* and *Tmsb4x*, and *Csf1r* and *Cx3cr1*. *Tmsb4x*, *Ftl1* and *Rps14* have previously been described by Li *et al.* (2019) and Hammond *et al.* (2019) in pre-microglia. *Ftl1*, *Tmsb4x* and *Rps14* were associated with the regulation of metal homeostasis, actin cytoskeleton dynamics and ribosomal components, respectively (Hammond et al., 2019; Li et al., 2019). Genes associated with the actin skeleton were identified here too and underline the developmental origin of these signatures.

Interestingly, *Tmsbx4* has previously been described in disease-associated choroid plexus macrophages and in experimental autoimmune encephalomyelitis, a model of MS (Jordão et al., 2019; Mendiola et al., 2020). This goes on to show that non-homeostatic conditions obscure defined lineage signatures; transcriptional distinctions are non-binary and early and late life signatures share similarities. Furthermore, *Tmsb4x* does not appear to be restricted to C57BL/6 murine cells. Embryonic, CD1 mouse cells are enriched for, among others, *Tmsbx4* and cell cycle-related *Eef1a1* (Masuda et al., 2019). Similarly, *TMSB4X* and *EEF1A1* are expressed in human tissue-resident macrophages (Bian et al., 2020). As shown previously, there are commonalities in cellular proliferation between mouse and human development (Figure 37, Figure 38); however, these commonalities do not appear to stop there.

### 6.5.3 Early emergence of age-associated microglial subtypes with amyloidosis

The effects of amyloidosis on transcriptional heterogeneity and population dynamics were studied. 5 distinct clusters were identified in the small-scale atlas, including HOM-, LPM- and IRM-clusters. These subtypes broadly follow the large-scall atlas findings; HOM-clusters increase with maturation and decline with the emergence of LPM and IRM.

It was previously determined that IRM in health do not display an increase in *Apoe*. In fact, IRM have levels of Apoe expression akin to HOM-clusters (Figure 42). However, in this dataset an increase of *Apoe* in IRM relative to HOM-clusters was noted (Sala Frigerio et al., 2019). Given the age- and genotype-specific effects on *Apoe* expression levels, it is likely that the increase of *Apoe* in cluster 4 is mostly driven by aged, APP-derived cells. Moreover, 'transiting response microglia'

(TRM) were not captured in the analyses. The original publication describes TRM as an intermediary state to 'activated response microglia' (ARM) (*i.e.* LPM). TRM display elevated levels of Apoe without typical LPM genes. It is possible these cells have contaminated the cluster 4, increasing the average expression *Apoe* in IRM. By extension, CNS-associated macrophages (CAM) were not identified, another subtype which has a higher expression of *Apoe*. Both this and the study by Sala Frigerio *et al.* (2019) made use of $Cd11b^{+}$ enrichment, a strategy which is known to enrich for CAM. These cells have not been excluded from the analysis and could highlight an impurity; however, the interaction of age and genotype is expected to reduce the relative proportion of CAM, minimizing their effect on transcriptional heterogeneity.

The strongest age- and genotype-specific effects pertain to LPM (in line with previous work by Sala Frigerio *et al.* (2019). Amyloidosis, as modelled by $APP^{NL\text{-}G\text{-}F}$ mice, significantly accelerates, and increases the expression of AD risk factors like *Apoe*, *Ctsb*, *Pld3* and *Trem2*. This effect is absent in IRM, further outlining the divergence of microglial subtypes with age. Of note, these age-associated microglial subtypes are linked to unique regulons.

### 6.5.4 Bhlhe40 and Irf7 as potential therapeutic targets for Alzheimer's disease

Transcriptional regulation is mediated by a host of factors, including regulons. 10 TF were described that vary in an age- and cluster-specific manner. Regarding $APP^{NL\text{-}G\text{-}F}$, amyloidosis accelerates the emergence of age-associated microglial subtypes, reducing the size of the homeostatic population at a younger age. It is unclear which regulons drive the emergence of such subtypes. Instead, regulons specific to IRM and LPM independent of genotype were identified.

IRM are featured by an increase in activity of Irf1 and Irf7, whereas LPM have higher activity levels of Atf3 and Bhlhe40. All four display some degree of self-reinforcing signalling, however, Bhlhe40 and Irf7 appear to be an end-stage TF; no broad-spectrum gene targets are identified. Such specificity is valuable for therapeutic intervention strategies.

#### 6.5.4.1 Bhlhe40 and LPM

*Bhlh40* is characterized is a range of immune cells. In T cells, it is known to regulate cytokine production, whereas *Bhlhe40* in peritoneal and alveolar macrophages is central to self-renewal and maintenance (Cook et al., 2020; Jarjour et al., 2019; Lin et al., 2014; Rauschmeier et al., 2019). In turn, KO of *Bhlhe40* impaired hippocampal neuronal excitability and synaptic plasticity (Hamilton et al., 2018). This work did not report on microglia or macrophages; however, the absence of *Bhlhe40* is expected alter CNS myeloid function.

*Bhlhe40* is part of the core neurodegeneration gene set, a list of 134 genes including genes like *Apoe*, *Ctsb*, *Gpnmb*, *Igf1*, *Itgax* and others (Friedman et al., 2018). Interestingly, Krasemann *et al.*

(2018) showed that *Apoe* KO diminished Bhlhe40 (and Atf3) expression and ameliorates the loss of canonical homeostatic microglial genes (*e.g.* Tmem119, Csf1r, Sall1), suggesting that *Apoe*, a downstream target of *Bhlhe40* feeds into the self-reinforcing cascade of LPM. Since then, the group of Oleg Butovsky has seen that *Bhlhe40* expression is increased in humanized APOE4 relative to APOE3-mice (in both neurodegeneration and early-life stress) (Yung, 2019). In parallel, humanized APOE4-mice reduced the *Spi1* expression in early development, which could affecting cell number. Taken together, *Bhlhe40* and *Apoe* are critical regulators of microglial subtype, implying that such interactions in LPM in early development could predispose to late-onset AD. Moreover, targeting *Bhlhe40* might offer a means to ameliorate pathology.

#### 6.5.4.2 Irf7 and IRM

In contrast, IRM presence and function are not found to be affected by amyloidosis. Although IRM occurrence is at an earlier developmental time and increases with age, amyloidosis does not increase prevalence beyond what is achieved in healthy aging. It is currently unknown what the main driver is for IRM emergence. As discussed, the expression of *Apoe* is not commonly associated with IRM. In fact, *Apoe* KO does not affect its presence (as is the case for LPM), supportive of an *Apoe*-independent phenotypical specialization (Sala Frigerio et al., 2019). Here, Irf7 activity was identified, as well as activity of its upstream regulator Irf1, to be responsible for the acquisition of an IRM signature. Irf7 activity enables the expression of genes like *Cxcl10*, *Ifitm3* and *Usp18* (Rubino et al., 2018; Xu et al., 2021). However, the function of IRM is. IRM cells are believed to be anti-inflammatory cells, reminiscent of the classical M2-phenotype, where Irf7 downregulates pro-inflammatory genes (Cohen et al., 2014). Ifn-β1 mediates the expression of *Irf7*, whereas *Irf7* is downregulated by chronic exposure to Tgf-ß, effectively establishing an axis of Tgf-b -Irf7 in microglial activation (Cohen et al., 2014; Hagemeyer and Prinz, 2014). The importance of Tgf-ß in microglial identity has been discussed; Tgf-ß mediates the expression of Mafb and Sall1 from pre-microglia onwards (Butovsky et al., 2014; Buttgereit et al., 2016). Furthermore, the importance of environmental cues like Tgf-ß for the microglial state of activation was discussed in Chapter 3; interactions of microglial LRRC33 with integrin aVb8-bearing cells reduces microglial activation; without which myelopathy is a common occurrence (Qin et al., 2018). These studies point towards a role for the sensome in IRM, in which loss of this signature (and its proteins for microglial sensing) instils a pro-inflammatory state. Altogether, targeting Irf7 is expected to boost anti-inflammatory functions of IRM, ensuring that age- and disease-associated neuroinflammation is ameliorated.

### 6.5.5 Summary

The prompt emergence of LPM and IRM with amyloidosis goes on to show the unique context of female microglial heterogeneity with age. Accelerated maturation in early development, is compounded by an accelerated maturation by amyloidosis. Although such adaptations can be

beneficial in the short-term, long-term microglial fitness is diminished as fitness is finite. Key regulons of the LPM and IRM subtypes were identified, providing novel therapeutic targets at the heart of microglial biology.

## 6.6 Supplementary Figures and Tables

*Supplementary Table 15: Cluster-specific markers.*

| # | Seurat cluster (i.e. integrated_snn_res.0.6) | | | | | | |
|---|---|---|---|---|---|---|---|
| | p_val | avg_log2FC | pct.1 | pct.2 | p_val_adj | cluster | gene |
| 1 | 3.88E-06 | 0.306 | 0.677 | 0.708 | 0.007765 | 0 | Tpst2 |
| 2 | 5.39E-14 | 0.290 | 0.854 | 0.859 | 1.08E-10 | 0 | Coro1a |
| 3 | 2.56E-37 | 0.288 | 1.000 | 0.999 | 5.13E-34 | 0 | Tmsb4x |
| 4 | 0.002002 | 0.258 | 0.238 | 0.359 | 1 | 0 | Tgfbi |
| 5 | 0.003837 | 0.593 | 0.402 | 0.425 | 1 | 1 | Bank1 |
| 6 | 0.000301 | 0.585 | 0.558 | 0.590 | 0.601532 | 1 | Kif21b |
| 7 | 1.73E-10 | 0.533 | 0.253 | 0.426 | 3.45E-07 | 1 | Zfp758 |
| 8 | 4.13E-12 | 0.508 | 0.236 | 0.418 | 8.25E-09 | 1 | AI987944 |
| 9 | 1.76E-38 | 0.450 | 0.926 | 0.830 | 3.53E-35 | 1 | Stab1 |
| 10 | 1.00E-21 | 0.427 | 0.792 | 0.754 | 2.01E-18 | 1 | Zfp69 |
| 11 | 2.84E-47 | 0.575 | 0.255 | 0.082 | 5.67E-44 | 2 | Plp1 |
| 12 | 9.83E-33 | 0.552 | 0.255 | 0.044 | 1.97E-29 | 2 | Ccr1 |
| 13 | 2.54E-07 | 0.511 | 0.970 | 0.889 | 0.000508 | 2 | Bin1 |
| 14 | 2.49E-09 | 0.463 | 0.952 | 0.813 | 4.98E-06 | 2 | Mlxipl |
| 15 | 8.78E-06 | 0.401 | 0.432 | 0.240 | 0.01756 | 2 | Camk2n1 |
| 16 | 1.72E-15 | 0.389 | 0.636 | 0.304 | 3.43E-12 | 2 | Slc12a2 |
| 17 | 1.69E-16 | 0.361 | 0.850 | 0.531 | 3.37E-13 | 2 | Akap8l |
| 18 | 2.10E-14 | 0.348 | 0.309 | 0.064 | 4.19E-11 | 2 | Coro1b |
| 19 | 6.40E-08 | 0.332 | 0.525 | 0.181 | 0.000128 | 2 | Ccdc88a |
| 20 | 7.05E-13 | 0.309 | 0.572 | 0.218 | 1.41E-09 | 2 | Ccnd1 |
| 21 | 1.11E-183 | 4.586 | 0.935 | 0.552 | 2.21E-180 | 3 | Apoe |
| 22 | 2.62E-13 | 3.935 | 0.365 | 0.288 | 5.23E-10 | 3 | Spp1 |
| 23 | 1.31E-167 | 3.905 | 0.802 | 0.353 | 2.61E-164 | 3 | Cst7 |
| 24 | 4.16E-98 | 3.237 | 0.682 | 0.325 | 8.33E-95 | 3 | Cd74 |
| 25 | 3.51E-122 | 3.045 | 0.698 | 0.306 | 7.01E-119 | 3 | Lpl |
| 26 | 6.50E-65 | 2.662 | 0.539 | 0.259 | 1.30E-61 | 3 | H2-Ab1 |
| 27 | 4.89E-15 | 2.519 | 0.369 | 0.287 | 9.78E-12 | 3 | H2-Aa |
| 28 | 5.35E-151 | 2.366 | 0.967 | 0.714 | 1.07E-147 | 3 | Lyz2 |
| 29 | 5.08E-38 | 2.281 | 0.506 | 0.315 | 1.02E-34 | 3 | Ccl4 |
| 30 | 1.02E-80 | 2.158 | 0.661 | 0.356 | 2.04E-77 | 3 | Ank |
| 31 | 7.83E-22 | 2.524 | 0.549 | 0.194 | 1.57E-18 | 4 | Ifit2 |
| 32 | 2.96E-39 | 2.479 | 0.686 | 0.223 | 5.93E-36 | 4 | Ifit3 |
| 33 | 1.69E-19 | 2.412 | 0.647 | 0.350 | 3.38E-16 | 4 | Ccl12 |
| 34 | 1.06E-52 | 2.347 | 0.843 | 0.265 | 2.12E-49 | 4 | Ifitm3 |
| 35 | 4.82E-45 | 2.323 | 0.794 | 0.292 | 9.63E-42 | 4 | Usp18 |
| 36 | 2.42E-31 | 2.187 | 0.706 | 0.294 | 4.84E-28 | 4 | Ifi204 |
| 37 | 3.17E-47 | 2.184 | 0.745 | 0.263 | 6.35E-44 | 4 | Irf7 |

| | | | | | | | |
|---|---|---|---|---|---|---|---|
| 38 | 5.47E-33 | 2.125 | 0.686 | 0.282 | 1.09E-29 | 4 | Oasl2 |
| 39 | 5.13E-21 | 1.997 | 0.500 | 0.191 | 1.03E-17 | 4 | Mx1 |
| 40 | 2.76E-16 | 1.806 | 0.422 | 0.169 | 5.53E-13 | 4 | Ifit1 |

*Note: A table of all the top 10 cluster markers, sorted by 'cluster' and 'avglog_2FC'. Activity of each is displayed based on the proportion (of 1) each contributes to the gene signature of their respective identities.*

*Supplementary Table 16: Selected gene list for the identification of female microglial subtypes.*

| Subtype | Gene |
|---|---|
| HOM/sensome | Csf1r |
| | Cx3cr1 |
| | P2ry12 |
| | Tmem119 |
| EDM | Apoe |
| | Cd63 |
| | Ctsb |
| | Ctsl |
| | Ftl1 |
| LPM | Apoe |
| | Clec7a |
| | Gpnmb |
| | Igf1 |
| | Itgax |
| | Lpl |
| | Spp1 |
| | Trem2 |
| IRM | Ifitm3 |
| | Irf7 |
| | Oasl2 |
| | Usp18 |

*Note: A genelist was generated that brought together signatures of homeostatic (HOM) and sensome markers, early developmental microglia (EDM), lysosome pathway-associated microglia (LPM), and interferon response microglia (IRM).*

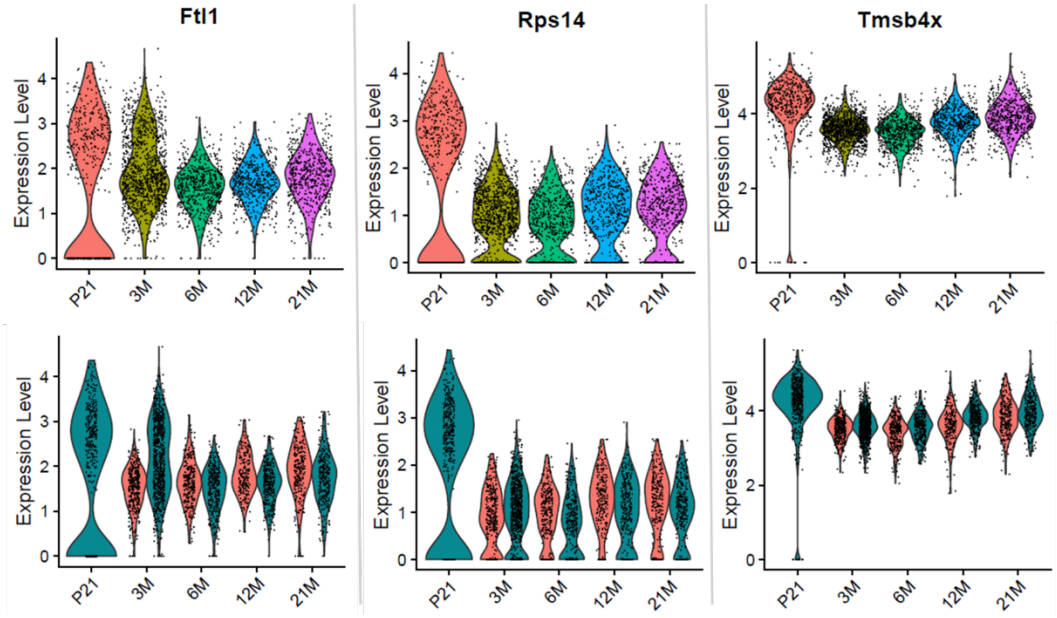


*Supplementary Figure 14: Loss of early developmental genes during maturation. Expression levels of early development-associated genes decline with maturation. Maturation and loss of such genes differ by age and genotype.*

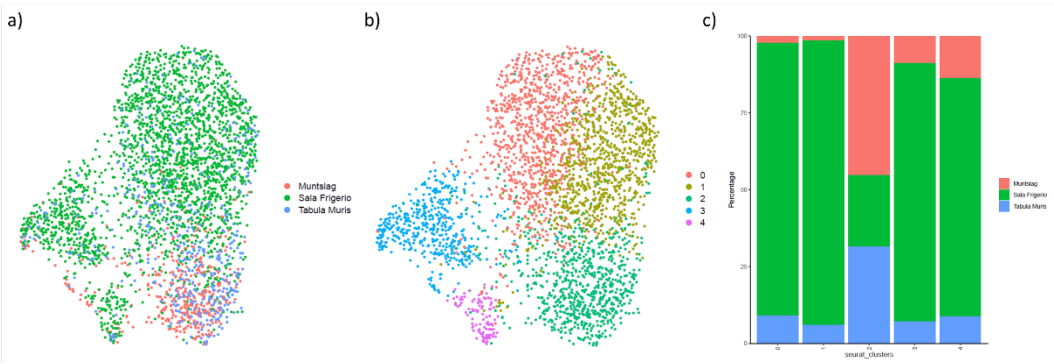


*Supplementary Figure 15: Atlas characteristics of female, cortical microglial heterogeneity. a) 3 sources were integrated, one self-generated and two publicly available sources. b) 5 distinct Seurat clusters were identified. c) Sources differed in their relative distribution across clusters.*

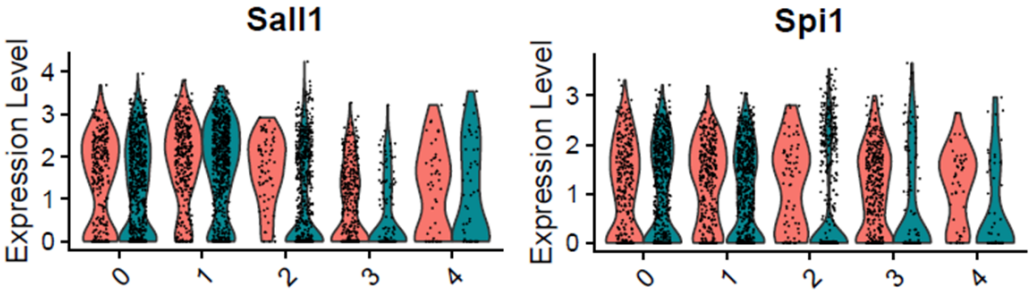


*Supplementary Figure 16: Canonical microglial regulons (2). Two well-established microglial transcription factors (TF) are displayed: Sall1, Spi1 (Pu.1). No age- or genotype-specific differences in expression levels can be remarked.*

*Supplementary Table 17: Regulon activity in a cluster-specific manner.*

| | **Seurat clusters** | | | | |
|---|---|---|---|---|---|
| *TF* | *0* | *1* | *2* | *3* | *4* |
| Sin3a_582g | 0.329 | 0.342 | 0.313 | 0.302 | 0.286 |
| Atf3_613g | 0.319 | 0.323 | 0.319 | 0.365 | 0.305 |
| Elf4_569g | 0.292 | 0.304 | 0.288 | 0.269 | 0.272 |
| Pml_493g | 0.225 | 0.236 | 0.206 | 0.190 | 0.200 |
| Irf1_343g | 0.187 | 0.187 | 0.173 | 0.163 | 0.190 |
| Polr3a_368g | 0.172 | 0.185 | 0.172 | 0.156 | 0.157 |
| Gmeb1_228g | 0.152 | 0.153 | 0.150 | 0.124 | 0.131 |
| Smarcc2_311g | 0.120 | 0.136 | 0.111 | 0.112 | 0.108 |
| Setdb1_273g | 0.117 | 0.130 | 0.116 | 0.111 | 0.111 |
| Foxo3_156g | 0.089 | 0.095 | 0.092 | 0.085 | 0.082 |
| Bhlhe40_72g | 0.080 | 0.071 | 0.091 | 0.154 | 0.094 |
| Zfp523_129g | 0.063 | 0.068 | 0.059 | 0.052 | 0.055 |
| Egr1_131g | 0.050 | 0.053 | 0.043 | 0.042 | 0.042 |
| Zfp69_63g | 0.045 | 0.046 | 0.045 | 0.036 | 0.039 |
| E4f1_60g | 0.038 | 0.044 | 0.035 | 0.034 | 0.033 |
| Irf2_34g | 0.033 | 0.039 | 0.037 | 0.022 | 0.036 |
| Nfatc2_22g | 0.028 | 0.034 | 0.026 | 0.018 | 0.024 |
| Creb5_31g | 0.028 | 0.033 | 0.033 | 0.039 | 0.031 |
| Zbtb37_16g | 0.023 | 0.032 | 0.024 | 0.017 | 0.022 |
| Zeb1_29g | 0.027 | 0.030 | 0.027 | 0.029 | 0.038 |
| Zfp105_25g | 0.022 | 0.024 | 0.016 | 0.017 | 0.023 |
| Zfp97_18g | 0.020 | 0.023 | 0.020 | 0.018 | 0.018 |
| Zfp760_33g | 0.021 | 0.023 | 0.020 | 0.020 | 0.017 |
| Irf7_54g | 0.031 | 0.022 | 0.034 | 0.057 | 0.153 |
| Foxj2_22g | 0.018 | 0.022 | 0.015 | 0.012 | 0.014 |
| Zfp442_20g | 0.010 | 0.013 | 0.008 | 0.007 | 0.011 |
| Zfp11_11g | 0.010 | 0.013 | 0.007 | 0.011 | 0.009 |
| Tef_37g | 0.011 | 0.013 | 0.011 | 0.010 | 0.013 |
| Snapc4_12g | 0.012 | 0.011 | 0.011 | 0.009 | 0.009 |
| Zfp623_13g | 0.012 | 0.011 | 0.009 | 0.008 | 0.011 |
| Thra_20g | 0.006 | 0.008 | 0.008 | 0.008 | 0.009 |
| Stat2_38g | 0.007 | 0.005 | 0.007 | 0.011 | 0.110 |
| Cux2_11g | 0.004 | 0.004 | 0.004 | 0.005 | 0.002 |
| Foxo4_20g | 0.003 | 0.003 | 0.006 | 0.011 | 0.006 |
| Klf2_11g | 0.002 | 0.003 | 0.004 | 0.006 | 0.004 |
| Fos_17g | 0.003 | 0.002 | 0.003 | 0.006 | 0.006 |

*Note: A table of all transcription factors (TF) (i.e. regulons) in a cluster-specific-manner. Activity of each is displayed based on the proportion (of 1) each contributes to the gene signature of their respective identities.*

*Supplementary Table 18: Regulon activity in an age-specific manner.*

| | **Age** | | | | |
|---|---|---|---|---|---|
| *TF* | *P21* | *3M* | *6M* | *12M* | *21M* |
| Atf3_613g | 0.325 | 0.318 | 0.333 | 0.333 | 0.333 |
| Sin3a_582g | 0.296 | 0.330 | 0.333 | 0.328 | 0.319 |
| Elf4_569g | 0.280 | 0.294 | 0.295 | 0.289 | 0.287 |
| Pml_493g | 0.193 | 0.222 | 0.226 | 0.221 | 0.215 |
| Irf1_343g | 0.160 | 0.185 | 0.183 | 0.183 | 0.180 |
| Polr3a_368g | 0.170 | 0.174 | 0.179 | 0.174 | 0.168 |
| Gmeb1_228g | 0.149 | 0.151 | 0.145 | 0.145 | 0.142 |
| Smarcc2_311g | 0.105 | 0.120 | 0.136 | 0.122 | 0.118 |
| Setdb1_273g | 0.115 | 0.120 | 0.128 | 0.119 | 0.115 |
| Foxo3_156g | 0.095 | 0.089 | 0.095 | 0.091 | 0.086 |
| Bhlhe40_72g | 0.100 | 0.080 | 0.091 | 0.097 | 0.103 |
| Zfp523_129g | 0.053 | 0.064 | 0.065 | 0.061 | 0.059 |
| Egr1_131g | 0.034 | 0.051 | 0.052 | 0.048 | 0.048 |
| Zfp69_63g | 0.042 | 0.046 | 0.043 | 0.042 | 0.042 |
| E4f1_60g | 0.036 | 0.037 | 0.042 | 0.037 | 0.039 |
| Irf7_54g | 0.042 | 0.028 | 0.036 | 0.037 | 0.052 |
| Irf2_34g | 0.042 | 0.034 | 0.036 | 0.030 | 0.031 |
| Creb5_31g | 0.036 | 0.031 | 0.035 | 0.030 | 0.032 |
| Nfatc2_22g | 0.030 | 0.026 | 0.033 | 0.028 | 0.023 |
| Zeb1_29g | 0.031 | 0.026 | 0.033 | 0.026 | 0.029 |
| Zbtb37_16g | 0.025 | 0.024 | 0.031 | 0.022 | 0.022 |
| Zfp105_25g | 0.012 | 0.021 | 0.024 | 0.021 | 0.021 |
| Zfp760_33g | 0.020 | 0.021 | 0.023 | 0.020 | 0.021 |
| Zfp97_18g | 0.017 | 0.021 | 0.022 | 0.020 | 0.022 |
| Foxj2_22g | 0.015 | 0.018 | 0.021 | 0.017 | 0.014 |
| Zfp11_11g | 0.006 | 0.010 | 0.013 | 0.010 | 0.011 |
| Tef_37g | 0.012 | 0.011 | 0.013 | 0.011 | 0.012 |
| Zfp623_13g | 0.006 | 0.010 | 0.012 | 0.012 | 0.010 |
| Zfp442_20g | 0.008 | 0.011 | 0.011 | 0.009 | 0.010 |
| Stat2_38g | 0.013 | 0.007 | 0.011 | 0.009 | 0.015 |
| Snapc4_12g | 0.010 | 0.011 | 0.010 | 0.011 | 0.011 |
| Thra_20g | 0.014 | 0.007 | 0.007 | 0.007 | 0.005 |
| Cux2_11g | 0.003 | 0.004 | 0.004 | 0.005 | 0.004 |
| Foxo4_20g | 0.013 | 0.003 | 0.004 | 0.004 | 0.006 |
| Klf2_11g | 0.008 | 0.002 | 0.004 | 0.002 | 0.002 |
| Fos_17g | 0.009 | 0.002 | 0.003 | 0.002 | 0.003 |

*Note: A table of all transcription factors (TF) (i.e. regulons) in an age-specific-manner. Activity of each is displayed based on the proportion (of 1) each contributes to the gene signature of their respective identities.*

# Chapter 7 General discussion

## 7.1 Review of main findings

It was hypothesized that distinct microglial subtypes drive adult heterogeneity and are featured by sex-specific trajectories of differentiation. Moreover, age-associated microglia were expected to have distinct gene regulatory networks. Several key observations were made during this thesis:

1. Seven major myeloid subtypes occur in the CNS across the murine lifespan.
2. Biological aging is the main catalyst for microglial heterogeneity.
3. Female microglia mature faster and feature a greater prevalence of age-associated subtypes at a younger age.
4. Distinct regulons drive the emergence of age-associated microglial subtypes.
5. Microglia are prone to *ex vivo*-activated signatures with scRNA-seq.

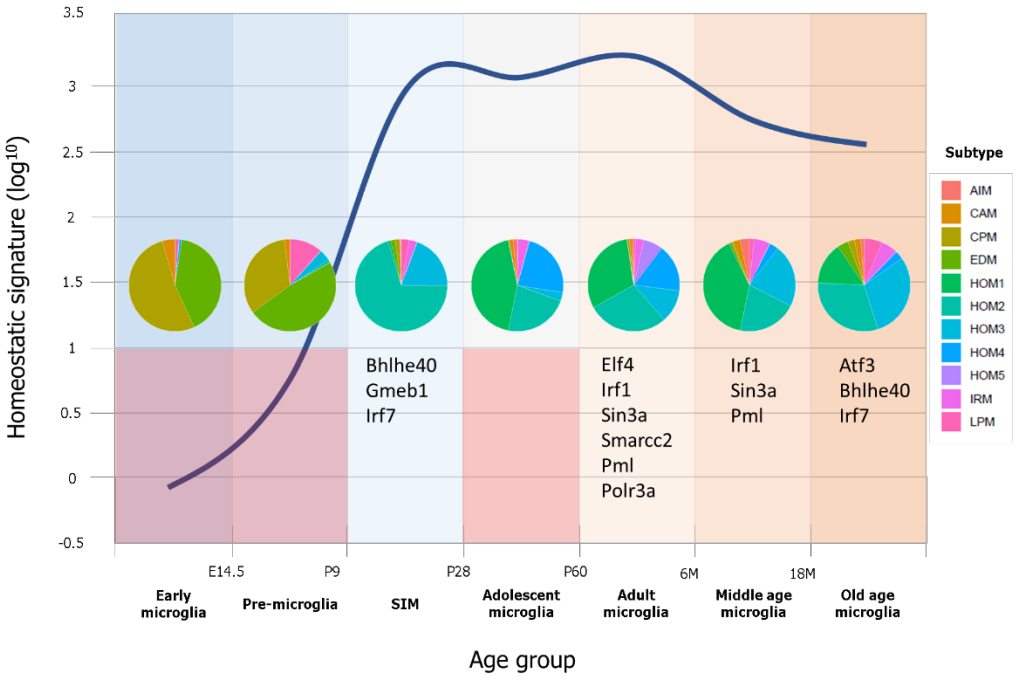


*Figure 104: Graphical abstract of microglial heterogeneity in the murine lifespan. Homeostatic gene signatures increase with age, to stabilize between postnatal day 9 (P9) and 6-months old (6M). The blue line is a $log^{10}$ of the ratio of homeostatic (HOM) over all other clusters. e.g. The gradual loss of a homeostatic signature becomes evident from middle age onwards, concurrent with an increased prevalence of age-associated microglial subtypes (i.e. AIM, IRM, LPM). Pie charts display the relative contribution of each subtype at the given age groups. The increase of age-associated subtypes (in females) is paralleled by the loss and acquisition of regulons (e.g. Sin3a, Atf3, Bhlhe40, Irf7). AIM, aged inflammatory microglia; CAM, CNS-associated macrophage; CPM, cycling and proliferating microglia; E, embryonic day; EDM, early developmental microglia; IRM, interferon response microglia; LPM, lysosome pathway-associated microglia; SIM, sexually immature microglia.*

### 7.1.1 Seven major myeloid subtypes are observed in the CNS during the murine lifespan.

Seven major CNS myeloid subtypes were identified in the murine lifespan, six of which are microglial subtypes: AIM, CPM, EDM, HOM, IRM and LPM. In turn, the HOM subtype can be subdivided into

five minor states: HOM1, 2, 3, 4 and 5. These subtypes display distinct age-specific distributions, as age was found to be the largest driver of microglial heterogeneity. Seven age groups detail the aging process, which can be reduced further to three broad stages: early development (<P9), adulthood (P9 – 6M), and late life (>6M) (Figure 104).

Early development is dominated by CPM, EDM and LPM subtypes. At this stage, homeostatic signatures are still increasing to adult levels. In adulthood, HOM signatures are mostly stable, albeit concurrent with increased HOM heterogeneity. Throughout adulthood, the microglial population is relatively stable and there is low prevalence of age-associated subtypes. This stability is gradually lost in later life, where AIM, IRM and LPM increase in prevalence at the expense of HOM signatures and heterogeneity.

#### 7.1.1.1 CPM, selection and repopulation

CPM feature a wave-like pattern that is most evident in early development, albeit adult and old age microglia see relative increases of actively proliferating cells too. CPM have previously been well-described, adding to findings related to the concept of microglial selection phase (Askew et al., 2017; Nikodemova et al., 2015). Interestingly, human gestational microglia display similar wave-like patterns (Menassa et al., 2021), suggesting that cycles of proliferation and apoptosis are naturally occuring biological processes shared between species. Notably, it is currently unknown if each proliferation wave is coupled to a selection phase, and how these function to drive microglial heterogeneity.

Several signalling cascades are central to microglial proliferation, among which the Csf1r-Csf1-Il34 pathway. In fact, this pathway plays a role in health and CNS disease like prion and AD (Ginhoux et al., 2010; Obst et al., 2020; Olmos-Alonso et al., 2016). Interestingly, Il34 and Csf1 have also been shown to be differentially expressed between white and grey-matter, thereby establishing a region-specific effect on microglial proliferation and heterogeneity (Easley-Neal et al., 2019; Kana et al., 2019). Consequentially, the Csf1r-pathway is frequently studied in repopulation studies and a current clinical target.

Huang *et al.* (2018) recently published a repopulation study that reproduced that the microglial population solely derives from microglial progenitors, a finding previously described (Askew et al., 2017; Bruttger et al., 2015; Ginhoux et al., 2010; Goldmann et al., 2016; Hashimoto et al., 2013; Huang et al., 2018). However, the novelty in this work lies in their report on the temporal transcriptional signature of repopulating microglia with RNA-seq. The authors find that shortly after depletion, the microglial population is enriched for proliferation-associated genes, after which the population re-established homeostasis 60 days after repopulation had started (Huang et al., 2018). The initial response is most likely mediated by CPM, however, to my knowledge, no scRNA-seq data is currently available that describes this process in detail. The single-cell atlas and subtype-specific

marker genes could help resolve this, utilizing this data to deconvolve the RNA-seq data produced by the authors (Wang et al., 2018). Detailing the population dynamics of such a study could help refine clinical trials, providing novel microglial targets for CNS disease.

#### 7.1.1.2 EDM – a novel subtype in early development

In this study, EDM are the most numerous subtype in early and pre-microglia. Typical markers of this subtype include *Apoe*, *Cd63*, *Ctsb*, *Gpx3*, *Ftl1* and *Npl*. Other studies have previously reported on the signatures in early development (Hammond et al., 2019; Li et al., 2019). However, this study is the the first to describe their role in the emergence of the adult microglial population. In fact, the data suggests that EDM are the main source of the adult population. This argument is two-fold. Firstly, the core signature of EDM is shared with (and extended upon by) CPM and LPM. Secondly, EDM have a low pseudotemporal score, and a differentiation trajectory that tracks from EDM to LPM, CPM and HOM; a junction of maturation with EDM at the centre. Secondly, female and male microglia mature differentially, to stabilize in adulthood and diverge once more in middle-age. EDM-like signatures might therefore be of particular importance in sex-specific microglial heterogeneity.

#### 7.1.1.3 LPM – early development and late life prevalence

In this work, I made the argument that lysosome pathway-associated microglia, or LPM, are an umbrella term for a family of phagocytic microglia. This family includes (but is not limited to) DAM, ARM, MGnd, ATM, PAM and LAM, and can broadly be described as a family of microglia that is prevalent in the CNS. Each of these myeloid cells have been described centrally or peripherally, in early development or late life, all of which are phagocytic cells capable of the removal of myelin, lipid-rich debris (Hammond et al., 2019; Jaitin et al., 2019; Keren-Shaul et al., 2017; Krasemann et al., 2017; Li et al., 2019; Sala Frigerio et al., 2019). Unlike other studies reporting on specific contexts, in the large-scale atlas, LPM as a cluster did not show a transcriptional distinction between early and late life; neither did the cluster show signs of fragmentation at higher cluster resolutions. Indeed, LPM are transcriptionally similar in healthy aging, independent of age. Given that multiple HOM-clusters were identified, most likely indicative of distinct microglial states, LPM effectively capture a signature that does not diversify in healthy aging, but otherwise describe a family of microglial states. Others have argued for such transcriptional similarity and I hope the shared push for simplification aids the conceptual understanding of this subtype (Benmamar-Badel et al., 2020).

As stated, the LPM signature is highly dependent on Trem2-Apoe signalling, albeit variations in dependency have been reported, both of which are key regulators of age-associated disease as well as early development (Butovsky et al., 2014; Jaitin et al., 2019; Keren-Shaul et al., 2017; Safaiyan et al., 2021).

Trem2 maintains metabolic fitness in LPM (Krasemann et al., 2017; Ulland et al., 2017). However, when clearance capacity of microglia is exceeded (by the loss of *Trem2*), microglial dysfunction ensues and canonical markers are lost (*e.g. Tmem119*, *Tgfbr1*) (Krasemann et al., 2017; Nugent et al., 2020). Moreover, the human ε4 allele of APOE (APOE4) is an established late-onset Alzheimer's disease (LOAD) risk factor. How APOE contributes to cognitive development is currently unknown, however, elevated levels of APOE in early development are critically associated with white matter development. Carriers of the *APOE*4 variant displayed lower myelin levels at 2.5 years of age (Dean et al., 2014; Malkki, 2014). Of note, like *Apoe*, *Ctsb* is enriched in LPM and is associated with AD risk, and encodes for cathepsin B, a lysosomal cysteine peptidase. Loss of which is causal to lysosomal dysfunction and accumulation of amyloid-ß and cholesterol (Mueller-Steiner et al., 2006). The relative enrichment of such AD-risk factors and the involvement of Trem2-Apoe signalling outlines their importance to CNS disease.

Beyond the scope of this work but of critical importance is to establish the function of LPM. As a whole, microglia have been assigned both detrimental and beneficial roles (Aguzzi et al., 2013; Deczkowska et al., 2018; Lee et al., 2010; Wolf et al., 2013). As discussed, LPM can become dysfunctional when clearance capacity is exceeded, and LPM are enriched for AD-associated risk factors (Krasemann et al., 2017; Sala Frigerio et al., 2019). It is therefore reasonable to argue that whether LPM aid or aggravate pathology is dependent on the interplay of age, sex, and genes. This may be a bimodal oversimplification of function, reminiscent of classical M1 and M2 categorization, which fails to fully capture the *in vivo* function of these subtypes. That is, transcription does not inform on function. However, transcriptional heterogeneity can aid the further delineation of function.

### 7.1.2 Transcriptional and regulon heterogeneity

Transcription factors are key mediators of transcriptional heterogeneity. Several age- and cluster-specific enrichments of such regulons were identified in the small-scale atlas, an atlas of microglial maturation in health and disease.

*Atf3* and *Bhlhe40*, and *Irf7* are selectively enriched in LPM and IRM, respectively. These regulons are attractive therapeutic targets to modulate the expression of *Bhlhe40* and *Ir7*, to alter the population dynamics and response to pathology. Alternatively, the selective depletion of *Bhlhe40* or *Irf7*, or any other genes that describe LPM and IRM, might offer a means to detail if these subtypes are beneficial or detrimental to CNS health.

Although research has started to explore the functions of LPM, less is known about the function of IRM. However, looking at the transcriptome of this subtype, IRM emergence might be a biological consequence of increased IFN-signalling with age; or a sign of CNS injury like those encountered

with stroke; white matter lesions typically seen with MS, traumatic brain injury (TBI) or AD (Deczkowska et al., 2017; McDonough et al., 2017; Xu et al., 2021). The molecular mechanisms of all these diseases have been coupled to ischemic injury, and pathology is commonly associated with white matter (De Keyser et al., 2008; Ramos-Cejudo et al., 2018; Wirth et al., 2017). Of note, Safaiyan *et al* (2019) describes WAM in AD, a white-matter enriched subtype that features both LPM and IRM signatures concurrently. It is possible WAM are IRM. It appears that expression of *Apoe* in IRM, or lack thereof, is linked to widespread amyloidosis and healthy aging, respectively. *Apoe* is a critical mediator of LPM and it is reasonable to assume that although IRM emergence does not rely on *Apoe*, *Apoe* expression could affect the IRM signature and its function.

Each regulon is coupled to the expression of a wide range of genes that define each subtype. LPM are enriched for Bhlhe40, a transcription factor known to stimulate *Apoe*, *Ctsb* and *Lpl* (Friedman et al., 2018; Krasemann et al., 2017b; Yung, 2019), whereas Irf7 activity enables the expression of genes like *Cxcl10*, *Ifitm3* and *Usp18* (Rubino et al., 2018; Xu et al., 2021). Interestingly, *Atf3* regulates among others *Bhlhe40*, *Cd74*, *Ctsb*, *Dusp1*, *Egr1*, *Irf1*, *Lpl* and *Spp1.* Therefore, these interactions firmly place *Atf3* within microglial identity acquisition, and hints towards a role in the emergence of *exAM* by its regulation of *Dusp1* and *Egr1*. *Atf3* is a core gene of the integrated stress response and could make LPM more susceptible to *ex*AM-like signatures than other microglial subtypes (Jiang et al., 2004; Pakos-Zebrucka et al., 2016). Once more, it becomes obvious that the microglial population is a lineage with distinct responses and responders (Gertig and Hanisch, 2014).

### 7.1.3 scRNA-seq and technical artefacts

Technical artefacts are a common problem in scRNA-seq data (Brink et al., 2017; Marsh et al., 2022; Wu et al., 2017). *ex*AM were identified in the large-scale atlas and with standard isolation procedures. However, mitigation of such effects was possible with Dounce homogenization, and with transcriptional inhibition. Other methods are available, these include cold-activated proteases, and combinatorial inhibition of transcription and translation (Adam et al., 2017; Hrvatin et al., 2018; Marsh et al., 2022). Not discussed previously, 'Ribotag' might offer a bulk RNA-seq approach to the mitigation of *ex*AM signatures in scRNA-seq data.

First introduced by Sanz *et al.* (2014), Ribotag isolates ribosome-associated mRNA by the immunoprecipitation (IP) of large ribosomal subunit 22 (Rpl22) (Sanz et al., 2009); the combination with Cre recombinase allows this approach to be cell-specific. Haimon *et al.* (2018) applied this approach with Cx3cr1$^{CreER}$, establishing an inducible mouse model that enables the isolation of myeloid mRNA (Haimon et al., 2018). A direct comparison with a standard isolation protocol, including enzymatic digestion and FACS, showed that IP of mRNA better preserves the coding mRNA. Specifically, IP of myeloid cells retains microglial quiescence, reduces IEG signatures, and excludes nuclear long non-coding RNA like metastasis-associated lung adenocarcinoma transcript

1 (Malat1) (Derrien et al., 2012; Haimon et al., 2018). Of note, Malat1 was identified in the large-scale atlas, as a marker of HOM-clusters. Such enrichment goes on to show that even clusters without any typical *ex*AM signatures are affected by the choice of isolation method; the downstream effects of which need to be acknowledged in every experimental paradigm. Strikingly, Malat1 is a known epigenetic factor associated with M1 polarization, suggesting that RiboTag too has inherent limitations (Qiu et al., 2021). However, in spite of that, IP of mRNA increased the number and variety of transcripts, thereby increasing library size and complexity (Haimon et al., 2018). This feature might help mitigate cell quality loss with ActD. However, since Ribotag is a bulk approach, how could such an approach be implemented in a scRNA-seq design?

Deconvolution is a bioinformatic approach that utilizes scRNA-seq data to determine the cell composition of bulk RNA-seq data. MuSiC is a highly cited variant of such an implementation, albeit a wide variety of methods has been developed (Avila Cobos et al., 2020; Wang et al., 2019). It is a goal to make the large-scale atlas available for deconvolution, acting as a resource of the field. However, as discussed, isolation methods affect scRNA-seq data, even in the absence of typical exAM-like signatures. Ribotag could function as a complementary approach to refine cluster-specific markers.

Microglial studies heavily rely on transgenic mice models coupled to canonical marker genes. Commonly used reporter mice make use of *Cx3cr1* and *Csf1r*, or *Tmem119*, *P2ry12*, *Sall1* and *Hexb* (Eme-Scolan and Dando, 2020; Jung et al., 2000; Sasmono and Williams, 2012). As discussed, stability of *Hexb* expression, independent of subtype and context could make $Hexb^{tdTomato}$ an attractive target for a RiboTag adaptation (Eme-Scolan and Dando, 2020; Masuda et al., 2020).

Moreover, it is worth considering that *in situ* hybridization or spatial transcriptomics approaches would allow for a more detailed confirmation of signatures. Satija et al. (2015) were the first to corroborate single-cell expression data with a spatial location (Satija et al., 2015), a solid approach that since has been adopted in the microglial field (Favuzzi et al., 2021; Gunner et al., 2019; Hammond et al., 2019; Silva et al., 2021). Alternatively, despite of reports highlighting the lack of correlation between transcriptional and translational measures, novel microglial subtypes can be identified with histology (Hammond et al., 2019; Li et al., 2019; Masuda et al., 2019; Safaiyan et al., 2021), which could function as a surrogate approach for the identification of technical artefacts in microglia.

## 7.2 Future perspectives

### 7.2.1 Spatial transcriptomics and *in situ* hybridization

*In situ* hybridization utilizes DNA probes to identify RNA in a spatial context at a single-cell resolution. Like scRNA-seq, *in situ* hybridization has many distinct variants, of which smFISH, or single-molecule RNA fluorescence *in situ* hybridization, is considered the "gold standard" (Nagle et al., 2021; Raj et al., 2008). However, famed for its accuracy and capture rate, it lacks in throughput. To address this limitation, combinatorial FISH methods have been developed, including MERFISH, seqFISH+, and split-FISH (Chen et al., 2015; Eng et al., 2019; Goh et al., 2020). Experiments can readily be scaled up to include 200 to 500 genes, or up to ~10,000 at considerable costs; however, similar to smFISH, DNA probes used to identify the RNA are designed *a priori*, negating an unbiased characterization of the cellular transcriptome (Nagle et al., 2021).

A more high-throughput and unbiased approach can be found in spatial transcriptomics. Spatial transcriptomics was named the 'Method of the Year' by Nature in 2020'; single-cell multimodal omics was in 2019, and single-cell RNA and DNA sequencing in 2013. Spatial transcriptomics allows the preservation of the spatial context in which RNA transcripts are transcribed; tissue is stored and fixed, and permeabilized for the *in situ* capture of local transcripts.

Two main competing commercial products are currently available for use: 10X Visium and Nanostring. Neither is capable of the single-cell resolution seen with *in situ* hybridization methods; however, Visium does not necessitate the generation and selection of a probe panel for gene detection, making it an unbiased approach. Spatial transcriptomic data, scRNA-seq and deconvolution are currently used in combination to maximize the information in these studies (Dong and Yuan, 2021; Song and Su, 2021). It is expected that the continued research and rapid developments of this field will allow for a single-cell resolution in spatial transcriptomics soon. Regardless, smFISH, combinatorial FISH and spatial transcriptomics all offer ways to complement scRNA-seq findings.

### 7.2.2 Multi-omics

Mono-modal technologies like scRNA-seq and the alternatives that were discussed are complementary, each contributing a distinct facet of microglial heterogeneity. With their occurrence, novel bioinformatic approaches continue to be developed to integrate these distinct datasets (Butler et al., 2018; Forcato et al., 2020; Hao et al., 2021; Korsunsky et al., 2019). However, correlations between modalities remains an indirect, computational approximation. The advance of multi-modal assays increases experimental consistency, reproducibility and stability, acting synergistically to further expand biological understanding (Hao et al., 2021).

As stated before, many multi-modal technologies have been developed, including G&T-seq, scMT-seq, CITE-seq, scTrio-seq and 10X (Hou et al., 2016; Hu et al., 2016; Macaulay et al., 2015; Stoeckius et al., 2017; Zhang et al., 2018). Multi-modal assays vary in their combination of modalities. However, the transcriptome and epigenome are most readily studied, to characterize chromatin accessibility and RNA expression concurrently (Cao et al., 2018; Chen et al., 2019; Liu et al., 2019; Ma et al., 2020; Zhu et al., 2019). Broadly, cells and/or nuclei are isolated, processed in bespoke single-cell platforms, and followed by serial library preparations of the epigenetic and gene expression libraries. Of note, Ma *et al.* (2020) describe and use SHARE-seq and showed that chromatin accessibility changes precede transcriptional heterogeneity in mouse skin, implying that lineage commitment studies would benefit from such a multi-modal analysis. However, to my knowledge no such multi-omics study has been performed in microglia, while epigenetics is increasingly recognized to play a role in their heterogeneity (Ayata et al., 2018; Datta et al., 2018; Gosselin et al., 2017; Kracht et al., 2020; Lavin et al., 2014; Nott et al., 2019; Wendeln et al., 2018).

### 7.2.3 Epigenetics and microglial heterogeneity

Epigenetic regulation of gene expression is typically done by two mechanisms: DNA methylation and histone modification. In fact, these mechanisms are functionally linked and each contribute to transcriptional heterogeneity (H.-T. Lee et al., 2020). Several key studies have reported on the roles of epigenetics in microglia in health and disease, most of which concerning methylation and acetylation of histones (Ayata et al., 2018; Datta et al., 2018; Lavin et al., 2014; Matcovitch-Natan et al., 2016; Wendeln et al., 2018).

Lavin et al. (2014) combined RNA-seq, ATAC-seq and ChiP-seq to delineate the myeloid lineage by their the enhancer landscapes; distinct subtypes are coupled to unique environment-dependent enhancers (Lavin et al., 2014). *i.e.* The intergenic region of *Pu.1* is enriched for mono-methylation of Histone H3 at lysine 4 (H3K4me1), a feature which is shared across the myeloid lineage, and a mark of an active or primed enhancer for the transcriptional regulation of *Pu.1*. In turn, macrophages are selectively enriched for H3Kme1 enhancers in the *Mafb* region, whereas the Sall1 motif is in microglia. Such histone modifications characterize the regulatory state of a cell and corroborate their respective roles in microglial ontogeny (Buttgereit et al., 2016; Kierdorf et al., 2013; Lavin et al., 2014; Matcovitch-Natan et al., 2016). In fact, microglia (and lung macrophages) are epigenetically most removed from other macrophages (Lavin et al., 2014). These findings go on to show that the CNS environment provides a significant environmental cue for microglial identity, one which CAM fail to achieve.

As stated, epigenetic (and transcriptional) heterogeneity underlies cellular regulatory state, which in turn drives functional specialization. Ayata *et al.* (2018) identified polycomb repressive complex 2, or PRC2, as a critical regulator of the inhibitory histone H3 lysine 27 trimethylation

(H3K27me3). It was found that PRC2 controls phagocytic function in striatal and cortical microglia, deletion of which induces rampant phagocytosis (Ayata et al., 2018). Normally, microglia phagocytosis is used for synaptic pruning and the removal of apoptotic cells, thereby maintaining CNS homeostasis; however, deletion of PRC2 was causal to the emergence of motor dysfunction, reduced learning and memory, anxiety and seizures. Of note, deletion did not affect cerebellar microglia , a regional subtype that featured elevated phagocytic function natively (that could be affected by distinct population dynamics) (Ayata et al., 2018).

Secondary to histone methylation, acetylation is controlled by histone acetyltransferases (HAT) and deacetylases (HDAC); acetylation by HAT increases chromatin accessibility, whereas HDAC restricts (Qiu et al., 2021; Wang et al., 2015). Datta *et al.* (2018) performed an interesting study in which they identified HDAC1 and HDAC2 as critical regulators in early development. Ablation of both at this stage increases apoptosis and reduced microglial population size (Datta et al., 2018). Of note, albeit microglial numbers increased gradually, matching control conditions by 16 weeks old, dendrite length remained affected. Moreover, deletion of these HDAC reduced proliferation and would have affected the microglial expansion and selection phase, with so far unknown functional consequences (Askew et al., 2017; Datta et al., 2018; Nikodemova et al., 2015). HDAC depletion might in fact be an interesting model to study the early developmental importance of microglial population dynamics on age-associated subtype emergence.

Strikingly, HDAC1 and HDAC2 are redundant in 6 week old, healthy, adolescent mice, whereas it enhanced phagocytosis of amyloid, and mitigate spatial learning and memory deficits in 5XFAD mice, a familial AD model (Datta et al., 2018; Oakley et al., 2006). Like PRC2 deletion, epigenetic modification of HDAC1 and HDAC2 alter phagocytic capacities of microglia (Ayata et al., 2018; Datta et al., 2018). It then begs to question, how are LPM regulated by epigenetics, and are such effects on phagocytosis sex-specific?

As discussed previously, epigenetics have been shown to play a role in the masculinization and femininization of the CNS (Nugent et al., 2015; VanRyzin et al., 2020). Notably, a recent study of spinal cord microglia in an assay for neuropathic pain found that only male microglial responses are featured by an increased expression of ribosomal genes (*e.g Rpl*, *Rps*) (Tansley et al., 2022). EDM have elevated levels of ribosomes, suggesting that male (spinal) microglia have a greater transcriptional similarity to early development subtypes (Hammond et al., 2019; Li et al., 2019). By extension, the protracted development of male microglia (in the absence of oestrogen) during sexual maturation could influence the epigenetic landscape of male microglia, providing them with a greater ability to respond to injury. Such a study would greatly benefit from a multi-modal approach.

### 7.2.4 Animal modelling and translational medicine

Most of the work in this thesis concerns data and literature from murine microglial studies. As stated, human microglial scRNA-seq remains sparse in comparison, and such a focus is a natural consequence of this sparsity. However, an increasing number of studies have started to address the translational gap between murine and human biology, and are offering new ways to mitigate such limitations (Friedman et al., 2018; Galatro et al., 2017; Gosselin et al., 2017; Hirbec et al., 2020).

Broadly, murine and human microglial cells share a large group of orthologous genes (Galatro et al., 2017; Gosselin et al., 2017). In correspondence, a scRNA-seq study of microglia across 10 species spanning 450 million years of evolution identified a core gene signature (Geirsdottir et al., 2019). *e.g.* Spi1 (Pu.1), Irf8 and Sall1 are all highly conserved. On face value, the large overlap of genes is promising and hints towards a high predictive value of animal modelling. In fact, human and mouse epigenetic landscapes are broadly similar, offering novel ways of guiding human disease modelling (Gosselin et al., 2017).However, as is now commonly known, pre-clinical experiments have a poor conversion to clinical trials; treatments are 'lost in translation' (Mak et al., 2014). Notably, species-specific gene modules and differences in biological aging (and the immune challenges that occur in that time) greatly affects organismal and cellular aging (Galatro et al., 2017; Geirsdottir et al., 2019; Gosselin et al., 2017; Grabert et al., 2016). Direct translation of results in human biology are therefore unwarranted. However, new cellular and animal models have started to reduce the translation gap.

Key advances in tissue cell culture methods have given rise to the use of embryonic stem cells (ESC) and induced pluripotent stem cells (iPSC) (Hirbec et al., 2020). ESC and iPSC are increasingly used to more reliably create *in vitro* and *ex vivo* cultures of *in vivo*-like subtypes in 3D-cocultures, organoids, and slice cultures (Bennett et al., 2021; Delbridge et al., 2020; Heider et al., 2021; Ormel et al., 2018). Moreover, chimeric *in vivo* models, or transplantation of human-derived microglia, are fast developing (Abud et al., 2017; Bennett et al., 2018; Hasselmann et al., 2019; Mancuso et al., 2019; Svoboda et al., 2019). Paradoxically, it was insights from animal models, and the understanding of microglial ontogeny and heterogeneity that is the main driver of such advancements (Bennett et al., 2018; Gosselin et al., 2017; Hirbec et al., 2020; Lee et al., 2018). Methodological innovation and biological understanding are therefore intertwined. In time, such adoptions, concurrent with the generation of large-scale atlases like the atlas described here, will continue to drive technological advancements and the reduction of animal use to the benefit of the animals and the translation of molecular biology to clinical care.

# Chapter 8 Appendix

## 8.1 Antibodies used for flow cytometry

*Supplementary Table 19:* ***FACS and MACS antibodies and reagents***

| Antibody | Catalog number: | Producer | Clone | Isotype | Host | Reactivity | Conjugate | Concentration |
|---|---|---|---|---|---|---|---|---|
| 7AAD | 51-68981E | BD Pharmingen | N/A | N/A | N/A | N/A | N/A | 1/200 |
| Cd11b | 562605 | BD Horizon | M1/70 | IgG2b (κ) | Rat | Mouse | BV421 | 1/300 |
| Cd11b | 101207 | BioLegend | M1/70 | IgG2b (κ) | Rat | Mouse | PE | 1/500 |
| Cd11b | 130-049-601 | Miltenyi Biotec | M1/70.15.11.5 | IgG2b (κ) | Rat | Human, mouse | microbeads | 1/10 |
| Cd16/Cd32 (Fc-block) | 101301 | BioLegend | 93 | IgG2a (λ) | Rat | Mouse | N/A | 1/500 |
| Cd45 | 559864 | BD Pharmingen | 30-F11 | IgG2b (κ) | Rat | Mouse | APC | 1/100 |
| Fixable Viability Dye eFluor450 | 65-0863-14 | eBioscience | N/A | N/A | N/A | N/A | 450 | 1/1000 |
| Fixable Viability Dye eFluor780 | 65-0865-14 | eBioscience | N/A | N/A | N/A | N/A | 780 | 1/1000 |
| Isotype | 562603 | BD Horizon | R35-38 | IgG2b (κ) | Rat | N/A | BV421 | 1/500 |
| Isotype | 553991 | BD Pharmingen | A95-1 | IgG2b (κ) | Rat | N/A | APC | 1/500 |
| Isotype | 400635 | BioLegend | RTK4530 | IgG2b (κ) | Rat | N/A | PE | 1/500 |
| P2ry12 | 848004 | BioLegend | S16007D | IgG2b (κ) | Rat | Mouse | PE | 1/500 |
| Ultracomp eBeads Compensation Beads | 01-2222-41 | Thermo Fisher | N/A/ | N/A | N/A | N/A | N/A/ | 1/10 |
| MitoTracker Deep Red FM | M22426 | Thermo Fisher | N/A/ | N/A | N/A | N/A | N/A/ | 62.5 nM |
| ArC Amine Reactie Kit | A10628 | Thermo Fisher | N/A/ | N/A | N/A | N/A | N/A/ | N/A |

***Footnote****: All FACS and MACS antibodies used in this work are tabulated, providing their general characteristics and optimal concentrations. N/A, not applicable.*

## 8.2 Primer sequences

*Supplementary Table 20: Primer sequences for qPCR*

| Gene | Primer | Sequence |
|---|---|---|
| *Csf1r* | FWD | TGCCTCTTCCTCTGTTCCCT |
| | REV | GCTAGTTCTGTGAGGACGGG |
| *Cx3cr1* | FWD | CCATCTGCTCAGGACCTCAC |
| | REV | CACCAGACCGAACGTGAAGA |
| *Egr1* | FWD | TTACCCGCCATATCCGCATC |
| | REV | CTGGCAAACTTCCTCCCACA |
| *Fos* | FWD | GGGACAGCCTTTCCTACTAC |
| | REV | AAAGTTGGCACTAGAGACGG |
| *Gapdh (old)* | FWD | TGAACGGAAAGTCACTGG |
| | REV | TCCACCACCCTGTTGCTGTA |
| *Gadph* | FWD | GCCCTTGAGCTAGGACTGG |
| | REV | TACGGGACGAGGCTGGC |
| *Hexb* | FWD | CGACCACAGTCCCAATTCCA |
| | REV | TGTAATATCGCCGAAACGCCT |
| *Ier2* | FWD | GTCCCTTCCTTGGCTTGGAG |
| | REV | GTCTGTCCCATGACGCAAACT |
| *Jun* | FWD | GCACATCACCACTACACCGA |
| | REV | GGGAAGCGTGTTCTGGCTAT |
| *P2ry12* | FWD | CAAGGGGTGGCATCTACCTG |
| | REV | AGCCTTGAGTGTTTCTGTAGGG |
| *Tmem119* | FWD | CTTCACCCAGAGCTGGTTCC |
| | REV | GTGACACACAGTAGGCCACC |

## 8.3 Reagents

*Supplementary Table 21: Reagents used in this work.*

| Item | Catalogue number: | Producer |
|---|---|---|
| 1-Bromo-3-Chloropropane | B9673-200ML | Sigma-Aldrich |
| 2-Propanol | I9516-500ML | Sigma-Aldrich |
| Actinomycin D | A1410-2MG | Sigma Aldrich |
| Adult Brain Dissociation Kit, mouse and rat | 130-107-677 | Miltenyi Biotec |
| Agencourt, AMPure XP, 5 mL | A63880 | Beckman Coulter Life Sciences |
| BSA, Molecular Biology Grade | B9000S | New England Biolabs |
| Debris Removal Solution | 130-109-398 | Miltenyi Biotec |
| Distilled water | 15230162 | Thermo Fisher |
| DMEM, high glucose, GlutaMAX™ Supplement | 61965-059 | Thermo Fisher |
| DNAse I | 11284932001 | Sigma Aldrich |
| DSP (Lomant's reagent) | 22586 | Thermo Fisher |
| DTT (1,4-Dithiothreitol) | 10197777001 | Sigma Aldrich |
| EDTA (0.5 M), pH 8.0 - RNase-free | AM9260G | Thermo Fisher |
| Ethanol, BioUltra | 51976-500ML-F | Sigma-Aldrich |
| Gibco HBSS 10X without Calcium, Magnesium, Phenol Red | 1535678 | Fisher Scientific |
| Guava instrument cleaning fluid (ICF) | 4200-0140 | Merck, Luminex |
| HBSS (10X) - calcium, magnesium, no phenol red | 14065056 | Thermo Fisher |
| HBSS (10X) with calcium and magnesium, no phenol red | 12519069 | Fisher Scientific |
| High sensitivity DNA kit | 5067-4626 | Agilent Technologies |
| iScript cDNA Synthesis Kit | 1708891 | BioRad |
| KAPA library quantification kit | 7960140001 | Roche |
| KAPA SYBR® FAST | KK4600 | Sigma Aldrich |
| Maxima H Minus Reverse Transcriptase (200 U/µL) | EP0752 | Thermo Fisher |
| Myelin Removal Beads II, h&m&r, 4 ml | 130-096-733 | Miltenyi Biotec |
| Neural Tissue Dissociation Kit (P) | 130-092-628 | Miltenyi Biotec |
| Nuclease-free water | 129114 | Qiagen |
| OptiPrep™ Density Gradient Medium | D1556-250ML | Sigma Aldrich |
| PBS (10X) without Calcium, Magnesium, Phenol Red (pH 7.4) | 70011044 | Thermo Fisher |
| Primers | Sigma-Aldrich | VC00021 |
| RNeasy Plus Micro Kit (50) | 74034 | Qiagen |
| SSC Buffer 20x Concentrate, Saline-Sodium Citrate buffer, made with ultrapure water | S6639-1L | Scientific Laboratory Supplies |
| TE Buffer 10 mM Tris-HCl (pH 8.0) 0.1 mM EDTA | 12090015 | Thermo Fisher |
| Tris EDTA buffer solution | 93283-500mL | Sigma Aldrich |
| UltraPure™ DNase/RNase-Free Distilled Water | 10977035 | Thermo Fisher |

***Footnote**: Tabulation of reagents in this study, detailing the item identifier, catalogue number and producer.*

## 8.4 General materials

*Supplementary Table 22: General materials used in this study.*

| Item | Catalogue number: | Producer |
|---|---|---|
| BD Plastipak 1 mL Hypodermic Syringe | 303172 | Premier Healthcare and Hygiene, Ltd |
| BRAND counting chamber BLAUBRAND® Neubauer improved | BR717820-1EA | Merck |
| Butterfly Needle Infusion Set 23G Short (Green) | H9P30010014 | Hillside Medical |
| C-Chip disposable Hemocytometer/ Fuchs-Rosenthal-Box of 5 | DHC-F01 | NanoEnTek |
| Corning cell strainer pore size 40 µm, blue, sterile | CLS431750 | Sigma Aldrich |
| Corning cell strainer pore size 70 µm, white, sterile | CLS431751 | Sigma Aldrich |
| Cupped disposable dust mask | EN149:2001+A1:2009 FFP3 (NR) | Thorite Direct |
| DNA LoBind® Tubes, DNA LoBind®, 1.5 mL, PCR clean, colorless, 250 tubes (5 bags × 50 tubes) | 30108051 | Eppendorf |
| DNA LoBind® Tubes, DNA LoBind®, 2.0 mL, PCR clean, colorless, 250 tubes (5 bags × 50 tubes) | 30108078 | Eppendorf |
| Laboratory coat, Howie style | 113-8218 | VWR |
| LD Columns | 130-042-901 | Miltenyi Biotec |
| LS+ Positive Selection Columns | 130-042-031 | Miltenyi Biotec |
| NextSeq 500/550 High Output Kit v2.5 (75 Cycles) | 20024906 | Illumina |
| Pipetman L 4-pipette kit | F167370 | Gilson |
| QuadroMACS separator | 130-090-976 | Miltenyi Biotec |
| Sterile cell strainer 70µM (white) | 22-363-548 | Fisher Scientific |

***Footnote**: Tabulation of reagents in this study, detailing the item identifier, catalogue number and producer.*

# Chapter 9 References


| Fluidigm [WWW Document], n.d. URL https://go.fluidigm.com/Cytof (accessed 1.5.22).

Abbas, A.-K., Huang, F.-S., Li, R., Ekström, J., Wigström, H., 2011. Emetine treatment masks initial LTP without affecting long-term stability. Brain Res. 1426, 18–29. https://doi.org/10.1016/j.brainres.2011.10.010

Abud, E.M., Ramirez, R.N., Martinez, E.S., Healy, L.M., Nguyen, C.H.H., Newman, S.A., Yeromin, A.V., Scarfone, V.M., Marsh, S.E., Fimbres, C., Caraway, C.A., Fote, G.M., Madany, A.M., Agrawal, A., Kayed, R., Gylys, K.H., Cahalan, M.D., Cummings, B.J., Antel, J.P., Mortazavi, A., Carson, M.J., Poon, W.W., Blurton-Jones, M., 2017. iPSC-derived human microglia-like cells to study neurological diseases. Neuron 94, 278-293.e9. https://doi.org/10.1016/j.neuron.2017.03.042

Actinomycin D from Streptomyces sp., ~98% (HPLC) | Sigma-Aldrich [WWW Document], n.d. URL http://www.sigmaaldrich.com/ (accessed 7.1.21).

Adam, M., Potter, A.S., Potter, S.S., 2017. Psychrophilic proteases dramatically reduce single-cell RNA-seq artifacts: a molecular atlas of kidney development. Development 144, 3625–3632. https://doi.org/10.1242/dev.151142

Aguzzi, A., Barres, B.A., Bennett, M.L., 2013. Microglia: Scapegoat, Saboteur, or Something Else? Science 339, 156–161. https://doi.org/10.1126/science.1227901

Ahmari, S.E., Spellman, T., Douglass, N.L., Kheirbek, M.A., Simpson, H.B., Deisseroth, K., Gordon, J.A., Hen, R., 2013. Repeated Cortico-Striatal Stimulation Generates Persistent OCD-Like Behavior. Science 340, 1234–1239. https://doi.org/10.1126/science.1234733

Aibar, S., González-Blas, C.B., Moerman, T., Huynh-Thu, V.A., Imrichova, H., Hulselmans, G., Rambow, F., Marine, J.-C., Geurts, P., Aerts, J., van den Oord, J., Atak, Z.K., Wouters, J., Aerts, S., 2017. SCENIC: single-cell regulatory network inference and clustering. Nat. Methods 14, 1083–1086. https://doi.org/10.1038/nmeth.4463

Alles, J., Karaiskos, N., Praktiknjo, S.D., Grosswendt, S., Wahle, P., Ruffault, P.-L., Ayoub, S., Schreyer, L., Boltengagen, A., Birchmeier, C., Zinzen, R., Kocks, C., Rajewsky, N., 2017a. Cell fixation and preservation for droplet-based single-cell transcriptomics. BMC Biol. 15, 44. https://doi.org/10.1186/s12915-017-0383-5

Alles, J., Karaiskos, N., Praktiknjo, S.D., Grosswendt, S., Wahle, P., Ruffault, P.-L., Ayoub, S., Schreyer, L., Boltengagen, A., Birchmeier, C., Zinzen, R., Kocks, C., Rajewsky, N., 2017b. Cell fixation and preservation for droplet-based single-cell transcriptomics. BMC Biol. 15. https://doi.org/10.1186/s12915-017-0383-5

Alliot, F., Godin, I., Pessac, B., 1999. Microglia derive from progenitors, originating from the yolk sac, and which proliferate in the brain. Dev. Brain Res. 117, 145–152. https://doi.org/10.1016/S0165-3806(99)00113-3

Almanzar, N., Antony, J., Baghel, A.S., Bakerman, I., Bansal, I., Barres, B.A., Beachy, P.A., Berdnik, D., Bilen, B., Brownfield, D., Cain, C., Chan, C.K.F., Chen, M.B., Clarke, M.F., Conley, S.D., Darmanis, S., Demers, A., Demir, K., de Morree, A., Divita, T., du Bois, H., Ebadi, H., Espinoza, F.H., Fish, M., Gan, Q., George, B.M., Gillich, A., Gòmez-Sjöberg, R., Green, F., Genetiano, G., Gu, X., Gulati, G.S., Hahn, O., Haney, M.S., Hang, Y., Harris, L., He, M., Hosseinzadeh, S., Huang, A., Huang, K.C., Iram, T., Isobe, T., Ives, F., Jones, R.C., Kao, K.S., Karkanias, J., Karnam, G., Keller, A., Kershner, A.M., Khoury, N., Kim, S.K., Kiss, B.M., Kong, W., Krasnow, M.A., Kumar, M.E., Kuo, C.S., Lam, J., Lee, D.P., Lee, S.E., Lehallier, B., Leventhal, O., Li, G., Li, Q., Liu, L., Lo, A., Lu, W.-J., Lugo-Fagundo, M.F., Manjunath, A.,

May, A.P., Maynard, A., McGeever, A., McKay, M., McNerney, M.W., Merrill, B., Metzger, R.J., Mignardi, M., Min, D., Nabhan, A.N., Neff, N.F., Ng, K.M., Nguyen, P.K., Noh, J., Nusse, R., Pálovics, R., Patkar, R., Peng, W.C., Penland, L., Pisco, A.O., Pollard, K., Puccinelli, R., Qi, Z., Quake, S.R., Rando, T.A., Rulifson, E.J., Schaum, N., Segal, J.M., Sikandar, S.S., Sinha, R., Sit, R.V., Sonnenburg, J., Staehli, D., Szade, K., Tan, M., Tan, W., Tato, C., Tellez, K., Dulgeroff, L.B.T., Travaglini, K.J., Tropini, C., Tsui, M., Waldburger, L., Wang, B.M., van Weele, L.J., Weinberg, K., Weissman, I.L., Wosczyna, M.N., Wu, S.M., Wyss-Coray, T., Xiang, J., Xue, S., Yamauchi, K.A., Yang, A.C., Yerra, L.P., Youngyunpipatkul, J., Yu, B., Zanini, F., Zardeneta, M.E., Zee, A., Zhao, C., Zhang, F., Zhang, H., Zhang, M.J., Zhou, L., Zou, J., The Tabula Muris Consortium, 2020. A single-cell transcriptomic atlas characterizes ageing tissues in the mouse. Nature 583, 590–595. https://doi.org/10.1038/s41586-020-2496-1

Askew, K., Li, K., Olmos-Alonso, A., Garcia-Moreno, F., Liang, Y., Richardson, P., Tipton, T., Chapman, M.A., Riecken, K., Beccari, S., Sierra, A., Molnár, Z., Cragg, M.S., Garaschuk, O., Perry, V.H., Gomez-Nicola, D., 2017. Coupled Proliferation and Apoptosis Maintain the Rapid Turnover of Microglia in the Adult Brain. Cell Rep. 18, 391–405. https://doi.org/10.1016/j.celrep.2016.12.041

Attar, M., Sharma, E., Li, S., Bryer, C., Cubitt, L., Broxholme, J., Lockstone, H., Kinchen, J., Simmons, A., Piazza, P., Buck, D., Livak, K.J., Bowden, R., 2018a. A practical solution for preserving single cells for RNA sequencing. Sci. Rep. 8, 2151. https://doi.org/10.1038/s41598-018-20372-7

Attar, M., Sharma, E., Li, S., Bryer, C., Cubitt, L., Broxholme, J., Lockstone, H., Kinchen, J., Simmons, A., Piazza, P., Buck, D., Livak, K.J., Bowden, R., 2018b. A practical solution for preserving single cells for RNA sequencing. Sci. Rep. 8, 2151. https://doi.org/10.1038/s41598-018-20372-7

Avey, D., Sankararaman, S., Yim, A.K.Y., Barve, R., Milbrandt, J., Mitra, R.D., 2018. Single-Cell RNA-Seq Uncovers a Robust Transcriptional Response to Morphine by Glia. Cell Rep. 24, 3619-3629.e4. https://doi.org/10.1016/j.celrep.2018.08.080

Avila Cobos, F., Alquicira-Hernandez, J., Powell, J.E., Mestdagh, P., De Preter, K., 2020. Benchmarking of cell type deconvolution pipelines for transcriptomics data. Nat. Commun. 11, 5650. https://doi.org/10.1038/s41467-020-19015-1

Ayata, P., Badimon, A., Strasburger, H.J., Duff, M.K., Montgomery, S.E., Loh, Y.-H.E., Ebert, A., Pimenova, A.A., Ramirez, B.R., Chan, A.T., Sullivan, J.M., Purushothaman, I., Scarpa, J.R., Goate, A.M., Busslinger, M., Shen, L., Losic, B., Schaefer, A., 2018. Epigenetic regulation of brain region-specific microglia clearance activity. Nat. Neurosci. 21, 1049–1060. https://doi.org/10.1038/s41593-018-0192-3

Baechler, E.C., Batliwalla, F.M., Karypis, G., Gaffney, P.M., Moser, K., Ortmann, W.A., Espe, K.J., Balasubramanian, S., Hughes, K.M., Chan, J.P., Begovich, A., Chang, S.-Y., Gregersen, P.K., Behrens, T.W., 2004. Expression levels for many genes in human peripheral blood cells are highly sensitive to ex vivo incubation. Genes Immun. 5, 347–353. https://doi.org/10.1038/sj.gene.6364098

Baik, S.H., Kang, S., Lee, W., Choi, H., Chung, S., Kim, J.-I., Mook-Jung, I., 2019. A Breakdown in Metabolic Reprogramming Causes Microglia Dysfunction in Alzheimer's Disease. Cell Metab. 30, 493-507.e6. https://doi.org/10.1016/j.cmet.2019.06.005

Bell, M.R., 2018. Comparing Postnatal Development of Gonadal Hormones and Associated Social Behaviors in Rats, Mice, and Humans. Endocrinology 159, 2596–2613. https://doi.org/10.1210/en.2018-00220

Bellenguez, C., Küçükali, F., Jansen, I.E., Kleineidam, L., Moreno-Grau, S., Amin, N., Naj, A.C., Campos-Martin, R., Grenier-Boley, B., Andrade, V., Holmans, P.A., Boland, A., Damotte, V., van der Lee, S.J., Costa, M.R., Kuulasmaa, T., Yang, Q., de Rojas, I., Bis, J.C., Yaqub, A., Prokic, I., Chapuis, J., Ahmad, S., Giedraitis, V., Aarsland, D., Garcia-Gonzalez, P., Abdelnour, C., Alarcón-Martín, E., Alcolea, D., Alegret, M., Alvarez, I., Álvarez, V., Armstrong, N.J., Tsolaki, A., Antúnez, C., Appollonio, I., Arcaro, M., Archetti, S., Pastor, A.A., Arosio, B., Athanasiu, L., Bailly, H., Banaj, N., Baquero, M., Barral, S., Beiser, A., Pastor, A.B., Below, J.E., Benchek, P., Benussi, L., Berr, C., Besse, C., Bessi, V., Binetti, G., Bizarro, A., Blesa, R., Boada, M., Boerwinkle, E., Borroni, B., Boschi, S., Bossù, P., Bråthen, G., Bressler, J., Bresner, C., Brodaty, H., Brookes, K.J., Brusco, L.I., Buiza-Rueda, D., Bûrger, K., Burholt, V., Bush, W.S., Calero, M., Cantwell, L.B., Chene, G., Chung, J., Cuccaro, M.L., Carracedo, Á., Cecchetti, R., Cervera-Carles, L., Charbonnier, C., Chen, H.-H., Chillotti, C., Ciccone, S., Claassen, J.A.H.R., Clark, C., Conti, E., Corma-Gómez, A., Costantini, E., Custodero, C., Daian, D., Dalmasso, M.C., Daniele, A., Dardiotis, E., Dartigues, J.-F., de Deyn, P.P., de Paiva Lopes, K., de Witte, L.D., Debette, S., Deckert, J., del Ser, T., Denning, N., DeStefano, A., Dichgans, M., Diehl-Schmid, J., Diez-Fairen, M., Rossi, P.D., Djurovic, S., Duron, E., Düzel, E., Dufouil, C., Eiriksdottir, G., Engelborghs, S., Escott-Price, V., Espinosa, A., Ewers, M., Faber, K.M., Fabrizio, T., Nielsen, S.F., Fardo, D.W., Farotti, L., Fenoglio, C., Fernández-Fuertes, M., Ferrari, R., Ferreira, C.B., Ferri, E., Fin, B., Fischer, P., Fladby, T., Fließbach, K., Fongang, B., Fornage, M., Fortea, J., Foroud, T.M., Fostinelli, S., Fox, N.C., Franco-Macías, E., Bullido, M.J., Frank-García, A., Froelich, L., Fulton-Howard, B., Galimberti, D., García-Alberca, J.M., García-González, P., Garcia-Madrona, S., Garcia-Ribas, G., Ghidoni, R., Giegling, I., Giorgio, G., Goate, A.M., Goldhardt, O., Gomez-Fonseca, D., González-Pérez, A., Graff, C., Grande, G., Green, E., Grimmer, T., Grünblatt, E., Grunin, M., Gudnason, V., Guetta-Baranes, T., Haapasalo, A., Hadjigeorgiou, G., Haines, J.L., Hamilton-Nelson, K.L., Hampel, H., Hanon, O., Hardy, J., Hartmann, A.M., Hausner, L., Harwood, J., Heilmann-Heimbach, S., Helisalmi, S., Heneka, M.T., Hernández, I., Herrmann, M.J., Hoffmann, P., Holmes, C., Holstege, H., Vilas, R.H., Hulsman, M., Humphrey, J., Biessels, G.J., Jian, X., Johansson, C., Jun, G.R., Kastumata, Y., Kauwe, J., Kehoe, P.G., Kilander, L., Ståhlbom, A.K., Kivipelto, M., Koivisto, A., Kornhuber, J., Kosmidis, M.H., Kukull, W.A., Kuksa, P.P., Kunkle, B.W., Kuzma, A.B., Lage, C., Laukka, E.J., Launer, L., Lauria, A., Lee, C.-Y., Lehtisalo, J., Lerch, O., Lleó, A., Longstreth, W., Lopez, O., de Munain, A.L., Love, S., Löwemark, M., Luckcuck, L., Lunetta, K.L., Ma, Y., Macías, J., MacLeod, C.A., Maier, W., Mangialasche, F., Spallazzi, M., Marquié, M., Marshall, R., Martin, E.R., Montes, A.M., Rodríguez, C.M., Masullo, C., Mayeux, R., Mead, S., Mecocci, P., Medina, M., Meggy, A., Mehrabian, S., Mendoza, S., Menéndez-González, M., Mir, P., Moebus, S., Mol, M., Molina-Porcel, L., Montrreal, L., Morelli, L., Moreno, F., Morgan, K., Mosley, T., Nöthen, M.M., Muchnik, C., Mukherjee, S., Nacmias, B., Ngandu, T., Nicolas, G., Nordestgaard, B.G., Olaso, R., Orellana, A., Orsini, M., Ortega, G., Padovani, A., Paolo, C., Papenberg, G., Parnetti, L., Pasquier, F., Pastor, P., Peloso, G., Pérez-Cordón, A., Pérez-Tur, J., Pericard, P., Peters, O., Pijnenburg, Y.A.L., Pineda, J.A., Piñol-Ripoll, G., Pisanu, C., Polak, T., Popp, J., Posthuma, D., Priller, J., Puerta, R., Quenez, O., Quintela, I., Thomassen, J.Q., Rábano, A., Rainero, I., Rajabli, F., Ramakers, I., Real, L.M., Reinders, M.J.T., Reitz, C., Reyes-Dumeyer, D., Ridge, P., Riedel-Heller, S., Riederer, P., Roberto, N., Rodriguez-Rodriguez, E., Rongve, A., Allende, I.R., Rosende-Roca, M., Royo, J.L., Rubino, E., Rujescu, D., Sáez, M.E., Sakka, P., Saltvedt, I., Sanabria, Á., Sánchez-Arjona, M.B., Sanchez-Garcia, F., Juan, P.S., Sánchez-Valle, R., Sando, S.B., Sarnowski, C., Satizabal, C.L., Scamosci, M., Scarmeas, N., Scarpini, E., Scheltens, P., Scherbaum, N., Scherer, M., Schmid, M., Schneider, A., Schott, J.M., Selbæk, G., Seripa, D., Serrano, M., Sha, J., Shadrin, A.A., Skrobot, O., Slifer, S., Snijders, G.J.L., Soininen, H., Solfrizzi, V., Solomon, A., Song, Y., Sorbi, S., Sotolongo-Grau, O., Spalletta, G., Spottke, A., Squassina, A., Stordal, E., Tartan, J.P., Tárraga, L., Tesí, N., Thalamuthu, A., Thomas, T., Tosto, G., Traykov, L., Tremolizzo, L., Tybjærg-Hansen, A., Uitterlinden, A., Ullgren, A., Ulstein, I., Valero, S., Valladares, O., Broeckhoven, C.V., Vance, J., Vardarajan, B.N., van der Lugt, A., Dongen, J.V., van Rooij, J., van Swieten, J., Vandenberghe, R., Verhey, F., Vidal, J.-S., Vogelgsang, J., Vyhnalek, M., Wagner, M.,

Wallon, D., Wang, L.-S., Wang, R., Weinhold, L., Wiltfang, J., Windle, G., Woods, B., Yannakoulia, M., Zare, H., Zhao, Y., Zhang, X., Zhu, C., Zulaica, M., Farrer, L.A., Psaty, B.M., Ghanbari, M., Raj, T., Sachdev, P., Mather, K., Jessen, F., Ikram, M.A., de Mendonça, A., Hort, J., Tsolaki, M., Pericak-Vance, M.A., Amouyel, P., Williams, J., Frikke-Schmidt, R., Clarimon, J., Deleuze, J.-F., Rossi, G., Seshadri, S., Andreassen, O.A., Ingelsson, M., Hiltunen, M., Sleegers, K., Schellenberg, G.D., van Duijn, C.M., Sims, R., van der Flier, W.M., Ruiz, A., Ramirez, A., Lambert, J.-C., 2022. New insights into the genetic etiology of Alzheimer's disease and related dementias. Nat. Genet. 54, 412–436. https://doi.org/10.1038/s41588-022-01024-z

Benmamar-Badel, A., Owens, T., Wlodarczyk, A., 2020. Protective Microglial Subset in Development, Aging, and Disease: Lessons From Transcriptomic Studies. Front. Immunol. 11. https://doi.org/10.3389/fimmu.2020.00430

Bennett, F.C., Bennett, M.L., Yaqoob, F., Mulinyawe, S.B., Grant, G.A., Hayden Gephart, M., Plowey, E.D., Barres, B.A., 2018. A Combination of Ontogeny and CNS Environment Establishes Microglial Identity. Neuron 98, 1170-1183.e8. https://doi.org/10.1016/j.neuron.2018.05.014

Bennett, M.L., Bennett, F.C., Liddelow, S.A., Ajami, B., Zamanian, J.L., Fernhoff, N.B., Mulinyawe, S.B., Bohlen, C.J., Adil, A., Tucker, A., Weissman, I.L., Chang, E.F., Li, G., Grant, G.A., Gephart, M.G.H., Barres, B.A., 2016. New tools for studying microglia in the mouse and human CNS. Proc. Natl. Acad. Sci. 113, E1738–E1746. https://doi.org/10.1073/pnas.1525528113

Bennett, M.L., Song, H., Ming, G., 2021. Microglia modulate neurodevelopment in human neuroimmune organoids. Cell Stem Cell 28, 2035–2036. https://doi.org/10.1016/j.stem.2021.11.005

Bensaude, O., 2011. Inhibiting eukaryotic transcription. Which compound to choose? How to evaluate its activity? Transcription 2, 103–108. https://doi.org/10.4161/trns.2.3.16172

Bian, Z., Gong, Y., Huang, T., Lee, C.Z.W., Bian, L., Bai, Z., Shi, H., Zeng, Y., Liu, C., He, J., Zhou, J., Li, X., Li, Z., Ni, Y., Ma, C., Cui, L., Zhang, R., Chan, J.K.Y., Ng, L.G., Lan, Y., Ginhoux, F., Liu, B., 2020. Deciphering human macrophage development at single-cell resolution. Nature 582, 571–576. https://doi.org/10.1038/s41586-020-2316-7

Bilbo, S.D., Biedenkapp, J.C., Der-Avakian, A., Watkins, L.R., Rudy, J.W., Maier, S.F., 2005. Neonatal Infection-Induced Memory Impairment after Lipopolysaccharide in Adulthood Is Prevented via Caspase-1 Inhibition. J. Neurosci. 25, 8000–8009. https://doi.org/10.1523/JNEUROSCI.1748-05.2005

Bilbo, S.D., Rudy, J.W., Watkins, L.R., Maier, S.F., 2006. A behavioural characterization of neonatal infection-facilitated memory impairment in adult rats. Behav. Brain Res. 169, 39–47. https://doi.org/10.1016/j.bbr.2005.12.002

Böttcher, C., Schlickeiser, S., Sneeboer, M.A.M., Kunkel, D., Knop, A., Paza, E., Fidzinski, P., Kraus, L., Snijders, G.J.L., Kahn, R.S., Schulz, A.R., Mei, H.E., Hol, E.M., Siegmund, B., Glauben, R., Spruth, E.J., Witte, L.D. de, Priller, J., 2019. Human microglia regional heterogeneity and phenotypes determined by multiplexed single-cell mass cytometry. Nat. Neurosci. 22, 78. https://doi.org/10.1038/s41593-018-0290-2

Brink, S.C. van den, Sage, F., Vértesy, Á., Spanjaard, B., Peterson-Maduro, J., Baron, C.S., Robin, C., Oudenaarden, A. van, 2017. Single-cell sequencing reveals dissociation-induced gene expression in tissue subpopulations. Nat. Methods 14, 935–936. https://doi.org/10.1038/nmeth.4437

Bruttger, J., Karram, K., Wörtge, S., Regen, T., Marini, F., Hoppmann, N., Klein, M., Blank, T., Yona, S., Wolf, Y., Mack, M., Pinteaux, E., Müller, W., Zipp, F., Binder, H., Bopp, T., Prinz, M., Jung, S., Waisman, A., 2015. Genetic Cell Ablation Reveals Clusters of Local Self-Renewing Microglia in the Mammalian Central Nervous System. Immunity 43, 92–106. https://doi.org/10.1016/j.immuni.2015.06.012

Budday, S., Nay, R., de Rooij, R., Steinmann, P., Wyrobek, T., Ovaert, T.C., Kuhl, E., 2015. Mechanical properties of gray and white matter brain tissue by indentation. J. Mech. Behav. Biomed. Mater. 46, 318–330. https://doi.org/10.1016/j.jmbbm.2015.02.024

Buenrostro, J.D., Wu, B., Litzenburger, U.M., Ruff, D., Gonzales, M.L., Snyder, M.P., Chang, H.Y., Greenleaf, W.J., 2015. Single-cell chromatin accessibility reveals principles of regulatory variation. Nature 523, 486–490. https://doi.org/10.1038/nature14590

Butler, A., Hoffman, P., Smibert, P., Papalexi, E., Satija, R., 2018. Integrating single-cell transcriptomic data across different conditions, technologies, and species. Nat. Biotechnol. 36, 411–420. https://doi.org/10.1038/nbt.4096

Butovsky, O., Jedrychowski, M.P., Moore, C.S., Cialic, R., Lanser, A.J., Gabriely, G., Koeglsperger, T., Dake, B., Wu, P.M., Doykan, C.E., Fanek, Z., Liu, L., Chen, Z., Rothstein, J.D., Ransohoff, R.M., Gygi, S.P., Antel, J.P., Weiner, H.L., 2014a. Identification of a Unique TGF-β Dependent Molecular and Functional Signature in Microglia. Nat. Neurosci. 17, 131–143. https://doi.org/10.1038/nn.3599

Butovsky, O., Jedrychowski, M.P., Moore, C.S., Cialic, R., Lanser, A.J., Gabriely, G., Koeglsperger, T., Dake, B., Wu, P.M., Doykan, C.E., Fanek, Z., Liu, L., Chen, Z., Rothstein, J.D., Ransohoff, R.M., Gygi, S.P., Antel, J.P., Weiner, H.L., 2014b. Identification of a Unique TGF-β Dependent Molecular and Functional Signature in Microglia. Nat. Neurosci. 17, 131–143. https://doi.org/10.1038/nn.3599

Buttgereit, A., Lelios, I., Yu, X., Vrohlings, M., Krakoski, N.R., Gautier, E.L., Nishinakamura, R., Becher, B., Greter, M., 2016. Sall1 is a transcriptional regulator defining microglia identity and function. Nat. Immunol. 17, 1397–1406. https://doi.org/10.1038/ni.3585

Campbell, J.N., Macosko, E.Z., Fenselau, H., Pers, T.H., Lyubetskaya, A., Tenen, D., Goldman, M., Verstegen, A.M.J., Resch, J.M., McCarroll, S.A., Rosen, E.D., Lowell, B.B., Tsai, L.T., 2017. A molecular census of arcuate hypothalamus and median eminence cell types. Nat. Neurosci. 20, 484–496. https://doi.org/10.1038/nn.4495

Cao, J., Cusanovich, D.A., Ramani, V., Aghamirzaie, D., Pliner, H.A., Hill, A.J., Daza, R.M., McFaline-Figueroa, J.L., Packer, J.S., Christiansen, L., Steemers, F.J., Adey, A.C., Trapnell, C., Shendure, J., 2018. Joint profiling of chromatin accessibility and gene expression in thousands of single cells. Science. https://doi.org/10.1126/science.aau0730

Cao, J., Spielmann, M., Qiu, X., Huang, X., Ibrahim, D.M., Hill, A.J., Zhang, F., Mundlos, S., Christiansen, L., Steemers, F.J., Trapnell, C., Shendure, J., 2019. The single cell transcriptional landscape of mammalian organogenesis. Nature 566, 496–502. https://doi.org/10.1038/s41586-019-0969-x

Cermak, S., Kosicek, M., Mladenovic-Djordjevic, A., Smiljanic, K., Kanazir, S., Hecimovic, S., 2016. Loss of Cathepsin B and L Leads to Lysosomal Dysfunction, NPC-Like Cholesterol Sequestration and Accumulation of the Key Alzheimer's Proteins. PLOS ONE 11, e0167428. https://doi.org/10.1371/journal.pone.0167428

Chan, J., Khan, S.N., Harvey, I., Merrick, W., Pelletier, J., 2004. Eukaryotic protein synthesis inhibitors identified by comparison of cytotoxicity profiles. RNA 10, 528–543. https://doi.org/10.1261/rna.5200204

Chan, T.E., Stumpf, M.P.H., Babtie, A.C., 2017. Gene Regulatory Network Inference from Single-Cell Data Using Multivariate Information Measures. Cell Syst. 5, 251-267.e3. https://doi.org/10.1016/j.cels.2017.08.014

Channathodiyil, P., Houseley, J., 2021. Glyoxal fixation facilitates transcriptome analysis after antigen staining and cell sorting by flow cytometry. PLOS ONE 16, e0240769. https://doi.org/10.1371/journal.pone.0240769

Chapter 1 Quality Control | Basics of Single-Cell Analysis with Bioconductor, n.d.

Chen, G., Ning, B., Shi, T., 2019. Single-Cell RNA-Seq Technologies and Related Computational Data Analysis. Front. Genet. 10. https://doi.org/10.3389/fgene.2019.00317

Chen, J., Cheung, F., Shi, R., Zhou, H., Lu, W., Candia, J., Kotliarov, Y., Stagliano, K.R., Tsang, J.S., CHI Consortium, 2018. PBMC fixation and processing for Chromium single-cell RNA sequencing. J. Transl. Med. 16, 198. https://doi.org/10.1186/s12967-018-1578-4

Chen, K.H., Boettiger, A.N., Moffitt, J.R., Wang, S., Zhuang, X., 2015. Spatially resolved, highly multiplexed RNA profiling in single cells. Science 348, aaa6090. https://doi.org/10.1126/science.aaa6090

Chen, R., Wu, X., Jiang, L., Zhang, Y., 2017. Single-Cell RNA-Seq Reveals Hypothalamic Cell Diversity. Cell Rep. 18, 3227–3241. https://doi.org/10.1016/j.celrep.2017.03.004

Chen, S.-K., Tvrdik, P., Peden, E., Cho, S., Wu, S., Spangrude, G., Capecchi, M.R., 2010. Hematopoietic Origin of Pathological Grooming in Hoxb8 Mutant Mice. Cell 141, 775–785. https://doi.org/10.1016/j.cell.2010.03.055

Chew, G., Petretto, E., 2019. Transcriptional Networks of Microglia in Alzheimer's Disease and Insights into Pathogenesis. Genes 10. https://doi.org/10.3390/genes10100798

Cohen, M., Matcovitch, O., David, E., Barnett-Itzhaki, Z.B.-I., Keren-Shaul, H., Blecher-Gonen, R., Adhemar Jaitin, D., Sica, A., Amit, I., Schwartz, M., 2014. Chronic exposure to TGFβ1 regulates myeloid cell inflammatory response in an IRF7-dependent manner. EMBO J. 33, 2906–2921. https://doi.org/10.15252/embj.201489293

Cook, M.E., Jarjour, N.N., Lin, C.-C., Edelson, B.T., 2020. Transcription Factor Bhlhe40 in Immunity and Autoimmunity. Trends Immunol. 41, 1023–1036. https://doi.org/10.1016/j.it.2020.09.002

Crow, Y.J., Stetson, D.B., 2021. The type I interferonopathies: 10 years on. Nat. Rev. Immunol. 1–13. https://doi.org/10.1038/s41577-021-00633-9

Cruchaga, C., Karch, C.M., Jin, S.C., Benitez, B.A., Cai, Y., Guerreiro, R., Harari, O., Norton, J., Budde, J., Bertelsen, S., Jeng, A.T., Cooper, B., Skorupa, T., Carrell, D., Levitch, D., Hsu, S., Choi, J., Ryten, M., Sassi, C., Bras, J., Gibbs, J.R., Hernandez, D.G., Lupton, M.K., Powell, J., Forabosco, P., Ridge, P.G., Corcoran, C.D., Tschanz, J.T., Norton, M.C., Munger, R.G., Schmutz, C., Leary, M., Demirci, F.Y., Bamne, M.N., Wang, X., Lopez, O.L., Ganguli, M., Medway, C., Turton, J., Lord, J., Braae, A., Barber, I., Brown, K., Pastor, P., Lorenzo-Betancor, O., Brkanac, Z., Scott, E., Topol, E., Morgan, K., Rogaeva, E., Singleton, A.B., Hardy, J., Kamboh, M.I., St George-Hyslop, P., Cairns, N., Morris, J.C., Kauwe, J.S.K., Goate, A.M., 2014. Rare coding variants in the phospholipase D3 gene confer risk for Alzheimer's disease. Nature 505, 550–554. https://doi.org/10.1038/nature12825

Daneman, R., Prat, A., 2015. The Blood–Brain Barrier. Cold Spring Harb. Perspect. Biol. 7, a020412. https://doi.org/10.1101/cshperspect.a020412

Daniszewski, M., Senabouth, A., Nguyen, Q.H., Crombie, D.E., Lukowski, S.W., Kulkarni, T., Sluch, V.M., Jabbari, J.S., Chamling, X., Zack, D.J., Pébay, A., Powell, J.E., Hewitt, A.W., 2018.

Single cell RNA sequencing of stem cell-derived retinal ganglion cells. Sci. Data 5, 180013. https://doi.org/10.1038/sdata.2018.13

Datta, M., Staszewski, O., Raschi, E., Frosch, M., Hagemeyer, N., Tay, T.L., Blank, T., Kreutzfeldt, M., Merkler, D., Ziegler-Waldkirch, S., Matthias, P., Meyer-Luehmann, M., Prinz, M., 2018. Histone Deacetylases 1 and 2 Regulate Microglia Function during Development, Homeostasis, and Neurodegeneration in a Context-Dependent Manner. Immunity 48, 514-529.e6. https://doi.org/10.1016/j.immuni.2018.02.016

Davis, B.M., Salinas-Navarro, M., Cordeiro, M.F., Moons, L., Groef, L.D., 2017. Characterizing microglia activation: a spatial statistics approach to maximize information extraction. Sci. Rep. 7, 1576. https://doi.org/10.1038/s41598-017-01747-8

De Biase, L.M., Schuebel, K.E., Fusfeld, Z.H., Jair, K., Hawes, I.A., Cimbro, R., Zhang, H.-Y., Liu, Q.-R., Shen, H., Xi, Z.-X., Goldman, D., Bonci, A., 2017. Local Cues Establish and Maintain Region-Specific Phenotypes of Basal Ganglia Microglia. Neuron 95, 341-356.e6. https://doi.org/10.1016/j.neuron.2017.06.020

De Keyser, J., Steen, C., Mostert, J.P., Koch, M.W., 2008. Hypoperfusion of the Cerebral White Matter in Multiple Sclerosis: Possible Mechanisms and Pathophysiological Significance. J. Cereb. Blood Flow Metab. 28, 1645–1651. https://doi.org/10.1038/jcbfm.2008.72

de Quervain, D.J.-F., Poirier, R., Wollmer, M.A., Grimaldi, L.M.E., Tsolaki, M., Streffer, J.R., Hock, C., Nitsch, R.M., Mohajeri, M.H., Papassotiropoulos, A., 2004. Glucocorticoid-related genetic susceptibility for Alzheimer's disease. Hum. Mol. Genet. 13, 47–52. https://doi.org/10.1093/hmg/ddg361

De, S., Deren, D.V., Peden, E., Hockin, M., Boulet, A., Titen, S., Capecchi, M.R., 2018. Two distinct ontogenies confer heterogeneity to mouse brain microglia. Development 145, dev152306. https://doi.org/10.1242/dev.152306

Dean, D.C., III, Jerskey, B.A., Chen, K., Protas, H., Thiyyagura, P., Roontiva, A., O'Muircheartaigh, J., Dirks, H., Waskiewicz, N., Lehman, K., Siniard, A.L., Turk, M.N., Hua, X., Madsen, S.K., Thompson, P.M., Fleisher, A.S., Huentelman, M.J., Deoni, S.C.L., Reiman, E.M., 2014. Brain Differences in Infants at Differential Genetic Risk for Late-Onset Alzheimer Disease: A Cross-sectional Imaging Study. JAMA Neurol. 71, 11–22. https://doi.org/10.1001/jamaneurol.2013.4544

Deczkowska, A., Amit, I., Schwartz, M., 2018a. Microglial immune checkpoint mechanisms. Nat. Neurosci. 1. https://doi.org/10.1038/s41593-018-0145-x

Deczkowska, A., Keren-Shaul, H., Weiner, A., Colonna, M., Schwartz, M., Amit, I., 2018b. Disease-Associated Microglia: A Universal Immune Sensor of Neurodegeneration. Cell 173, 1073–1081. https://doi.org/10.1016/j.cell.2018.05.003

Deczkowska, A., Matcovitch-Natan, O., Tsitsou-Kampeli, A., Ben-Hamo, S., Dvir-Szternfeld, R., Spinrad, A., Singer, O., David, E., Winter, D.R., Smith, L.K., Kertser, A., Baruch, K., Rosenzweig, N., Terem, A., Prinz, M., Villeda, S., Citri, A., Amit, I., Schwartz, M., 2017. Mef2C restrains microglial inflammatory response and is lost in brain ageing in an IFN-I-dependent manner. Nat. Commun. 8. https://doi.org/10.1038/s41467-017-00769-0

Delbridge, A.R.D., Huh, D., Brickelmaier, M., Burns, J.C., Roberts, C., Challa, R., Raymond, N., Cullen, P., Carlile, T.M., Ennis, K.A., Liu, M., Sun, C., Allaire, N.E., Foos, M., Tsai, H.-H., Franchimont, N., Ransohoff, R.M., Butts, C., Mingueneau, M., 2020. Organotypic Brain Slice Culture Microglia Exhibit Molecular Similarity to Acutely-Isolated Adult Microglia and Provide a Platform to Study Neuroinflammation. Front. Cell. Neurosci. 14. https://doi.org/10.3389/fncel.2020.592005

Denisenko, E., Guo, B.B., Jones, M., Hou, R., de Kock, L., Lassmann, T., Poppe, D., Clément, O., Simmons, R.K., Lister, R., Forrest, A.R.R., 2020. Systematic assessment of tissue dissociation and storage biases in single-cell and single-nucleus RNA-seq workflows. Genome Biol. 21, 130. https://doi.org/10.1186/s13059-020-02048-6

Derrien, T., Johnson, R., Bussotti, G., Tanzer, A., Djebali, S., Tilgner, H., Guernec, G., Martin, D., Merkel, A., Knowles, D.G., Lagarde, J., Veeravalli, L., Ruan, X., Ruan, Y., Lassmann, T., Carninci, P., Brown, J.B., Lipovich, L., Gonzalez, J.M., Thomas, M., Davis, C.A., Shiekhattar, R., Gingeras, T.R., Hubbard, T.J., Notredame, C., Harrow, J., Guigó, R., 2012. The GENCODE v7 catalog of human long noncoding RNAs: Analysis of their gene structure, evolution, and expression. Genome Res. 22, 1775–1789. https://doi.org/10.1101/gr.132159.111

Dijk, D. van, Sharma, R., Nainys, J., Yim, K., Kathail, P., Carr, A.J., Burdziak, C., Moon, K.R., Chaffer, C.L., Pattabiraman, D., Bierie, B., Mazutis, L., Wolf, G., Krishnaswamy, S., Pe'er, D., 2018. Recovering Gene Interactions from Single-Cell Data Using Data Diffusion. Cell 174, 716-729.e27. https://doi.org/10.1016/j.cell.2018.05.061

Dong, R., Yuan, G.-C., 2021. SpatialDWLS: accurate deconvolution of spatial transcriptomic data. Genome Biol. 22, 145. https://doi.org/10.1186/s13059-021-02362-7

Dos Santos, M., Backer, S., Saintpierre, B., Izac, B., Andrieu, M., Letourneur, F., Relaix, F., Sotiropoulos, A., Maire, P., 2020. Single-nucleus RNA-seq and FISH identify coordinated transcriptional activity in mammalian myofibers. Nat. Commun. 11, 5102. https://doi.org/10.1038/s41467-020-18789-8

Dubbelaar, M.L., Kracht, L., Eggen, B.J.L., Boddeke, E.W.G.M., 2018a. The Kaleidoscope of Microglial Phenotypes. Front. Immunol. 9. https://doi.org/10.3389/fimmu.2018.01753

Dubbelaar, M.L., Kracht, L., Eggen, B.J.L., Boddeke, E.W.G.M., 2018b. The Kaleidoscope of Microglial Phenotypes. Front. Immunol. 9. https://doi.org/10.3389/fimmu.2018.01753

Dulken, B.W., Buckley, M.T., Navarro Negredo, P., Saligrama, N., Cayrol, R., Leeman, D.S., George, B.M., Boutet, S.C., Hebestreit, K., Pluvinage, J.V., Wyss-Coray, T., Weissman, I.L., Vogel, H., Davis, M.M., Brunet, A., 2019. Single-cell analysis reveals T cell infiltration in old neurogenic niches. Nature 571, 205–210. https://doi.org/10.1038/s41586-019-1362-5

Duò, A., Robinson, M.D., Soneson, C., 2018. A systematic performance evaluation of clustering methods for single-cell RNA-seq data. F1000Research 7, 1141. https://doi.org/10.12688/f1000research.15666.2

Easley-Neal, C., Foreman, O., Sharma, N., Zarrin, A.A., Weimer, R.M., 2019. CSF1R Ligands IL-34 and CSF1 Are Differentially Required for Microglia Development and Maintenance in White and Gray Matter Brain Regions. Front. Immunol. 10. https://doi.org/10.3389/fimmu.2019.02199

Elmore, M.R.P., Najafi, A.R., Koike, M.A., Dagher, N.N., Spangenberg, E.E., Rice, R.A., Kitazawa, M., Matusow, B., Nguyen, H., West, B.L., Green, K.N., 2014. CSF1 receptor signaling is necessary for microglia viability, which unmasks a cell that rapidly repopulates the microglia-depleted adult brain. Neuron 82, 380–397. https://doi.org/10.1016/j.neuron.2014.02.040

Eme-Scolan, E., Dando, S.J., 2020. Tools and Approaches for Studying Microglia In vivo. Front. Immunol. 11.

Eng, C.-H.L., Lawson, M., Zhu, Q., Dries, R., Koulena, N., Takei, Y., Yun, J., Cronin, C., Karp, C., Yuan, G.-C., Cai, L., 2019. Transcriptome-scale super-resolved imaging in tissues by RNA seqFISH+. Nature 568, 235–239. https://doi.org/10.1038/s41586-019-1049-y

Erny, D., de Angelis, A.L.H., Jaitin, D., Wieghofer, P., Staszewski, O., David, E., Keren-Shaul, H., Mahlakoiv, T., Jakobshagen, K., Buch, T., Schwierzeck, V., Utermöhlen, O., Chun, E., Garrett, W.S., McCoy, K.D., Diefenbach, A., Staeheli, P., Stecher, B., Amit, I., Prinz, M., 2015. Host microbiota constantly control maturation and function of microglia in the CNS. Nat. Neurosci. 18, 965–977. https://doi.org/10.1038/nn.4030

Estes, M.L., McAllister, A.K., 2016. Maternal immune activation: Implications for neuropsychiatric disorders. Science. https://doi.org/10.1126/science.aag3194

Fagnocchi, L., Cherubini, A., Hatsuda, H., Fasciani, A., Mazzoleni, S., Poli, V., Berno, V., Rossi, R.L., Reinbold, R., Endele, M., Schroeder, T., Rocchigiani, M., Szkarłat, Ż., Oliviero, S., Dalton, S., Zippo, A., 2016. A Myc-driven self-reinforcing regulatory network maintains mouse embryonic stem cell identity. Nat. Commun. 7, 11903. https://doi.org/10.1038/ncomms11903

Fan, X., Fu, Y., Zhou, X., Sun, L., Yang, M., Wang, M., Chen, R., Wu, Q., Yong, J., Dong, J., Wen, L., Qiao, J., Wang, X., Tang, F., 2020. Single-cell transcriptome analysis reveals cell lineage specification in temporal-spatial patterns in human cortical development. Sci. Adv. 6, eaaz2978. https://doi.org/10.1126/sciadv.aaz2978

Fang, Z., Weng, C., Li, H., Tao, R., Mai, W., Liu, X., Lu, L., Lai, S., Duan, Q., Alvarez, C., Arvan, P., Wynshaw-Boris, A., Li, Yun, Pei, Y., Jin, F., Li, Yan, 2019. Single-Cell Heterogeneity Analysis and CRISPR Screen Identify Key β-Cell-Specific Disease Genes. Cell Rep. 26, 3132-3144.e7. https://doi.org/10.1016/j.celrep.2019.02.043

Favuzzi, E., Huang, S., Saldi, G.A., Binan, L., Ibrahim, L.A., Fernández-Otero, M., Cao, Y., Zeine, A., Sefah, A., Zheng, K., Xu, Q., Khlestova, E., Farhi, S.L., Bonneau, R., Datta, S.R., Stevens, B., Fishell, G., 2021. GABA-receptive microglia selectively sculpt developing inhibitory circuits. Cell 184, 4048-4063.e32. https://doi.org/10.1016/j.cell.2021.06.018

Fawcett, T.W., Frankenhuis, W.E., 2015. Adaptive explanations for sensitive windows in development. Front. Zool. 12, S3. https://doi.org/10.1186/1742-9994-12-S1-S3

Ferrero, G., Mahony, C.B., Dupuis, E., Yvernogeau, L., Ruggiero, E.D., Miserocchi, M., Caron, M., Robin, C., Traver, D., Bertrand, J.Y., Wittamer, V., 2018. Embryonic Microglia Derive from Primitive Macrophages and Are Replaced by cmyb-Dependent Definitive Microglia in Zebrafish. Cell Rep. 24, 130–141. https://doi.org/10.1016/j.celrep.2018.05.066

Forcato, M., Romano, O., Bicciato, S., 2020. Computational methods for the integrative analysis of single-cell data. Brief. Bioinform. 22, bbaa042. https://doi.org/10.1093/bib/bbaa042

Freytag, S., Tian, L., Lönnstedt, I., Ng, M., Bahlo, M., 2018. Comparison of clustering tools in R for medium-sized 10x Genomics single-cell RNA-sequencing data. F1000Research 7. https://doi.org/10.12688/f1000research.15809.2

Friedman, B.A., Srinivasan, K., Ayalon, G., Meilandt, W.J., Lin, H., Huntley, M.A., Cao, Y., Lee, S.-H., Haddick, P.C.G., Ngu, H., Modrusan, Z., Larson, J.L., Kaminker, J.S., van der Brug, M.P., Hansen, D.V., 2018. Diverse Brain Myeloid Expression Profiles Reveal Distinct Microglial Activation States and Aspects of Alzheimer's Disease Not Evident in Mouse Models. Cell Rep. 22, 832–847. https://doi.org/10.1016/j.celrep.2017.12.066

Füger, P., Hefendehl, J.K., Veeraraghavalu, K., Wendeln, A.-C., Schlosser, C., Obermüller, U., Wegenast-Braun, B.M., Neher, J.J., Martus, P., Kohsaka, S., Thunemann, M., Feil, R., Sisodia, S.S., Skodras, A., Jucker, M., 2017. Microglia turnover with aging and in an Alzheimer's model via long-term *in vivo* single-cell imaging. Nat. Neurosci. 20, 1371. https://doi.org/10.1038/nn.4631

Galatro, T.F., Holtman, I.R., Lerario, A.M., Vainchtein, I.D., Brouwer, N., Sola, P.R., Veras, M.M., Pereira, T.F., Leite, R.E.P., Möller, T., Wes, P.D., Sogayar, M.C., Laman, J.D., den Dunnen, W., Pasqualucci, C.A., Oba-Shinjo, S.M., Boddeke, E.W.G.M., Marie, S.K.N., Eggen, B.J.L., 2017. Transcriptomic analysis of purified human cortical microglia reveals age-associated changes. Nat. Neurosci. 20, 1162–1171. https://doi.org/10.1038/nn.4597

Geirsdottir, L., David, E., Keren-Shaul, H., Weiner, A., Bohlen, S.C., Neuber, J., Balic, A., Giladi, A., Sheban, F., Dutertre, C.-A., Pfeifle, C., Peri, F., Raffo-Romero, A., Vizioli, J., Matiasek, K., Scheiwe, C., Meckel, S., Mätz-Rensing, K., van der Meer, F., Thormodsson, F.R., Stadelmann, C., Zilkha, N., Kimchi, T., Ginhoux, F., Ulitsky, I., Erny, D., Amit, I., Prinz, M., 2019. Cross-Species Single-Cell Analysis Reveals Divergence of the Primate Microglia Program. Cell 179, 1609-1622.e16. https://doi.org/10.1016/j.cell.2019.11.010

Gerlach, J.P., van Buggenum, J.A.G., Tanis, S.E.J., Hogeweg, M., Heuts, B.M.H., Muraro, M.J., Elze, L., Rivello, F., Rakszewska, A., van Oudenaarden, A., Huck, W.T.S., Stunnenberg, H.G., Mulder, K.W., 2019. Combined quantification of intracellular (phospho-)proteins and transcriptomics from fixed single cells. Sci. Rep. 9, 1469. https://doi.org/10.1038/s41598-018-37977-7

Gerrits, E., Heng, Y., Boddeke, E.W.G.M., Eggen, B.J.L., 2020. Transcriptional profiling of microglia; current state of the art and future perspectives. Glia 68, 740–755. https://doi.org/10.1002/glia.23767

Gertig, U., Hanisch, U.-K., 2014. Microglial diversity by responses and responders. Front. Cell. Neurosci. 8. https://doi.org/10.3389/fncel.2014.00101

Gierahn, T.M., Wadsworth, M.H., Hughes, T.K., Bryson, B.D., Butler, A., Satija, R., Fortune, S., Love, J.C., Shalek, A.K., 2017. Seq-Well: A Portable, Low-Cost Platform for High-Throughput Single-Cell RNA-Seq of Low-Input Samples. Nat. Methods 14, 395–398. https://doi.org/10.1038/nmeth.4179

Ginhoux, F., Greter, M., Leboeuf, M., Nandi, S., See, P., Gokhan, S., Mehler, M.F., Conway, S.J., Ng, L.G., Stanley, E.R., Samokhvalov, I.M., Merad, M., 2010. Fate Mapping Analysis Reveals That Adult Microglia Derive from Primitive Macrophages. Science 330, 841–845. https://doi.org/10.1126/science.1194637

Goh, J.J.L., Chou, N., Seow, W.Y., Ha, N., Cheng, C.P.P., Chang, Y.-C., Zhao, Z.W., Chen, K.H., 2020. Highly specific multiplexed RNA imaging in tissues with split-FISH. Nat. Methods 17, 689–693. https://doi.org/10.1038/s41592-020-0858-0

Gohil, S.H., Iorgulescu, J.B., Braun, D.A., Keskin, D.B., Livak, K.J., 2021. Applying high-dimensional single-cell technologies to the analysis of cancer immunotherapy. Nat. Rev. Clin. Oncol. 18, 244–256. https://doi.org/10.1038/s41571-020-00449-x

Gokce, O., Stanley, G.M., Treutlein, B., Neff, N.F., Camp, J.G., Malenka, R.C., Rothwell, P.E., Fuccillo, M.V., Südhof, T.C., Quake, S.R., 2016. Cellular Taxonomy of the Mouse Striatum as Revealed by Single-Cell RNA-Seq. Cell Rep. 16, 1126–1137. https://doi.org/10.1016/j.celrep.2016.06.059

Goldmann, T., Blank, T., Prinz, M., 2016a. Fine-tuning of type I IFN-signaling in microglia — implications for homeostasis, CNS autoimmunity and interferonopathies. Curr. Opin. Neurobiol., Neurobiology of disease 36, 38–42. https://doi.org/10.1016/j.conb.2015.09.003

Goldmann, T., Jordão, M.J.C., Wieghofer, P., Prutek, F., Hagemeyer, N., Frenzel, K., Staszewski, O., Kierdorf, K., Amann, L., Krueger, M., Locatelli, G., Hochgarner, H., Zeiser, R., Epelman, S., Geissmann, F., Priller, J., Rossi, F., Bechmann, I., Kerschensteiner, M., Linnarsson, S., Jung,

S., Prinz, M., 2016b. Origin, fate and dynamics of macrophages at CNS interfaces. Nat. Immunol. 17, 797–805. https://doi.org/10.1038/ni.3423

Goldmann, T., Zeller, N., Raasch, J., Kierdorf, K., Frenzel, K., Ketscher, L., Basters, A., Staszewski, O., Brendecke, S.M., Spiess, A., Tay, T.L., Kreutz, C., Timmer, J., Mancini, G.M., Blank, T., Fritz, G., Biber, K., Lang, R., Malo, D., Merkler, D., Heikenwälder, M., Knobeloch, K.-P., Prinz, M., 2015. USP18 lack in microglia causes destructive interferonopathy of the mouse brain. EMBO J. 34, 1612–1629. https://doi.org/10.15252/embj.201490791

González-Navajas, J.M., Lee, J., David, M., Raz, E., 2012. Immunomodulatory functions of type I interferons. Nat. Rev. Immunol. 12, 125–135. https://doi.org/10.1038/nri3133

Gosselin, D., Skola, D., Coufal, N.G., Holtman, I.R., Schlachetzki, J.C.M., Sajti, E., Jaeger, B.N., O'Connor, C., Fitzpatrick, C., Pasillas, M.P., Pena, M., Adair, A., Gonda, D.D., Levy, M.L., Ransohoff, R.M., Gage, F.H., Glass, C.K., 2017. An environment-dependent transcriptional network specifies human microglia identity. Science 356, eaal3222. https://doi.org/10.1126/science.aal3222

Grabert, K., McColl, B.W., 2018. Isolation and Phenotyping of Adult Mouse Microglial Cells, in: Rousselet, G. (Ed.), Macrophages: Methods and Protocols, Methods in Molecular Biology. Springer New York, New York, NY, pp. 77–86. https://doi.org/10.1007/978-1-4939-7837-3_7

Grabert, K., Michoel, T., Karavolos, M.H., Clohisey, S., Baillie, J.K., Stevens, M.P., Freeman, T.C., Summers, K.M., McColl, B.W., 2016a. Microglial brain region-dependent diversity and selective regional sensitivities to aging. Nat. Neurosci. 19, 504–516. https://doi.org/10.1038/nn.4222

Grabert, K., Michoel, T., Karavolos, M.H., Clohisey, S., Baillie, J.K., Stevens, M.P., Freeman, T.C., Summers, K.M., McColl, B.W., 2016b. Microglial brain region−dependent diversity and selective regional sensitivities to aging. Nat. Neurosci. 19, 504–516. https://doi.org/10.1038/nn.4222

Grosche, L., Knippertz, I., König, C., Royzman, D., Wild, A.B., Zinser, E., Sticht, H., Muller, Y.A., Steinkasserer, A., Lechmann, M., 2020. The CD83 Molecule – An Important Immune Checkpoint. Front. Immunol. 11.

Grubman, A., Chew, G., Ouyang, J.F., Sun, G., Choo, X.Y., McLean, C., Simmons, R.K., Buckberry, S., Vargas-Landin, D.B., Poppe, D., Pflueger, J., Lister, R., Rackham, O.J.L., Petretto, E., Polo, J.M., 2019. A single-cell atlas of entorhinal cortex from individuals with Alzheimer's disease reveals cell-type-specific gene expression regulation. Nat. Neurosci. 22, 2087–2097. https://doi.org/10.1038/s41593-019-0539-4

Grün, D., Muraro, M.J., Boisset, J.-C., Wiebrands, K., Lyubimova, A., Dharmadhikari, G., van den Born, M., van Es, J., Jansen, E., Clevers, H., de Koning, E.J.P., van Oudenaarden, A., 2016a. De Novo Prediction of Stem Cell Identity using Single-Cell Transcriptome Data. Cell Stem Cell 19, 266–277. https://doi.org/10.1016/j.stem.2016.05.010

Grün, D., Muraro, M.J., Boisset, J.-C., Wiebrands, K., Lyubimova, A., Dharmadhikari, G., van den Born, M., van Es, J., Jansen, E., Clevers, H., de Koning, E.J.P., van Oudenaarden, A., 2016b. De Novo Prediction of Stem Cell Identity using Single-Cell Transcriptome Data. Cell Stem Cell 19, 266–277. https://doi.org/10.1016/j.stem.2016.05.010

Guide to the Disruption of Biological Samples - 2012 [WWW Document], n.d. . OPS Diagn. LLC. URL https://opsdiagnostics.com/applications/samplehomogenization/homogenizationguidepart1.html (accessed 10.25.21).

Guneykaya, D., Ivanov, A., Hernandez, D.P., Haage, V., Wojtas, B., Meyer, N., Maricos, M., Jordan, P., Buonfiglioli, A., Gielniewski, B., Ochocka, N., Cömert, C., Friedrich, C., Artiles, L.S., Kaminska, B., Mertins, P., Beule, D., Kettenmann, H., Wolf, S.A., 2018a. Transcriptional and Translational Differences of Microglia from Male and Female Brains. Cell Rep. 24, 2773-2783.e6. https://doi.org/10.1016/j.celrep.2018.08.001

Guneykaya, D., Ivanov, A., Hernandez, D.P., Haage, V., Wojtas, B., Meyer, N., Maricos, M., Jordan, P., Buonfiglioli, A., Gielniewski, B., Ochocka, N., Cömert, C., Friedrich, C., Artiles, L.S., Kaminska, B., Mertins, P., Beule, D., Kettenmann, H., Wolf, S.A., 2018b. Transcriptional and Translational Differences of Microglia from Male and Female Brains. Cell Rep. 24, 2773-2783.e6. https://doi.org/10.1016/j.celrep.2018.08.001

Gunner, G., Cheadle, L., Johnson, K.M., Ayata, P., Badimon, A., Mondo, E., Nagy, M.A., Liu, L., Bemiller, S.M., Kim, K.-W., Lira, S.A., Lamb, B.T., Tapper, A.R., Ransohoff, R.M., Greenberg, M.E., Schaefer, A., Schafer, D.P., 2019. Sensory lesioning induces microglial synapse elimination via ADAM10 and fractalkine signaling. Nat. Neurosci. 22, 1075–1088. https://doi.org/10.1038/s41593-019-0419-y

Guo, M., Bao, E.L., Wagner, M., Whitsett, J.A., Xu, Y., 2017a. SLICE: determining cell differentiation and lineage based on single cell entropy. Nucleic Acids Res. 45, e54. https://doi.org/10.1093/nar/gkw1278

Guo, M., Bao, E.L., Wagner, M., Whitsett, J.A., Xu, Y., 2017b. SLICE: determining cell differentiation and lineage based on single cell entropy. Nucleic Acids Res. 45, e54. https://doi.org/10.1093/nar/gkw1278

Hadjiolova, K.V., Hadjiolov, A.A., Bachellerie, J.-P., 1995. Actinomycin D Stimulates the Transcription of rRNA Minigenes Transfected into Mouse Cells. Eur. J. Biochem. 228, 605–615. https://doi.org/10.1111/j.1432-1033.1995.0605m.x

Hagemeyer, N., Hanft, K.-M., Akriditou, M.-A., Unger, N., Park, E.S., Stanley, E.R., Staszewski, O., Dimou, L., Prinz, M., 2017. Microglia contribute to normal myelinogenesis and to oligodendrocyte progenitor maintenance during adulthood. Acta Neuropathol. (Berl.) 134, 441–458. https://doi.org/10.1007/s00401-017-1747-1

Hagemeyer, N., Prinz, M., 2014. Burning down the house: IRF7 makes the difference for microglia. EMBO J. 33, 2885–2886. https://doi.org/10.15252/embj.201490345

Hahn, O., Foltz, A.G., Atkins, M., Kedir, B., Moran-Losada, P., Guldner, I.H., Munson, C., Kern, F., Pálovics, R., Lu, N., Kaur, A., Hull, J., Huguenard, J.R., Keller, A., Lehallier, B., Wyss-Coray, T., 2022. A spatiotemporal map of the aging mouse brain reveals white matter tracts as vulnerable foci. https://doi.org/10.1101/2022.09.18.508419

Haida, O., Al Sagheer, T., Balbous, A., Francheteau, M., Matas, E., Soria, F., Fernagut, P.O., Jaber, M., 2019. Sex-dependent behavioral deficits and neuropathology in a maternal immune activation model of autism. Transl. Psychiatry 9, 1–12. https://doi.org/10.1038/s41398-019-0457-y

Haimon, Z., Volaski, A., Orthgiess, J., Boura-Halfon, S., Varol, D., Shemer, A., Yona, S., Zuckerman, B., David, E., Chappell-Maor, L., Bechmann, I., Gericke, M., Ulitsky, I., Jung, S., 2018. Re-evaluating microglia expression profiles using RiboTag and cell isolation strategies. Nat. Immunol. 19, 636–644. https://doi.org/10.1038/s41590-018-0110-6

Hamilton, K.A., Wang, Y., Raefsky, S.M., Berkowitz, S., Spangler, R., Suire, C.N., Camandola, S., Lipsky, R.H., Mattson, M.P., 2018. Mice lacking the transcriptional regulator Bhlhe40 have enhanced neuronal excitability and impaired synaptic plasticity in the hippocampus. PLoS ONE 13, e0196223. https://doi.org/10.1371/journal.pone.0196223

Hammond, T.R., Dufort, C., Dissing-Olesen, L., Giera, S., Young, A., Wysoker, A., Walker, A.J., Gergits, F., Segel, M., Nemesh, J., Marsh, S.E., Saunders, A., Macosko, E., Ginhoux, F., Chen, J., Franklin, R.J.M., Piao, X., McCarroll, S.A., Stevens, B., 2019a. Single-Cell RNA Sequencing of Microglia throughout the Mouse Lifespan and in the Injured Brain Reveals Complex Cell-State Changes. Immunity 50, 253-271.e6. https://doi.org/10.1016/j.immuni.2018.11.004

Hammond, T.R., Dufort, C., Dissing-Olesen, L., Giera, S., Young, A., Wysoker, A., Walker, A.J., Gergits, F., Segel, M., Nemesh, J., Marsh, S.E., Saunders, A., Macosko, E., Ginhoux, F., Chen, J., Franklin, R.J.M., Piao, X., McCarroll, S.A., Stevens, B., 2019b. Single-Cell RNA Sequencing of Microglia throughout the Mouse Lifespan and in the Injured Brain Reveals Complex Cell-State Changes. Immunity 50, 253-271.e6. https://doi.org/10.1016/j.immuni.2018.11.004

Han, X., Wang, R., Zhou, Y., Fei, L., Sun, H., Lai, S., Saadatpour, A., Zhou, Z., Chen, H., Ye, F., Huang, D., Xu, Y., Huang, W., Jiang, M., Jiang, X., Mao, J., Chen, Y., Lu, C., Xie, J., Fang, Q., Wang, Y., Yue, R., Li, T., Huang, H., Orkin, S.H., Yuan, G.-C., Chen, M., Guo, G., 2018. Mapping the Mouse Cell Atlas by Microwell-Seq. Cell 172, 1091-1107.e17. https://doi.org/10.1016/j.cell.2018.02.001

Hanamsagar, R., Alter, M.D., Block, C.S., Sullivan, H., Bolton, J.L., Bilbo, S.D., 2017a. Generation of a microglial developmental index in mice and in humans reveals a sex difference in maturation and immune reactivity. Glia 65, 1504–1520. https://doi.org/10.1002/glia.23176

Hanamsagar, R., Alter, M.D., Block, C.S., Sullivan, H., Bolton, J.L., Bilbo, S.D., 2017b. Generation of a microglial developmental index in mice and in humans reveals a sex difference in maturation and immune reactivity. Glia 65, 1504–1520. https://doi.org/10.1002/glia.23176

Hao, Y., Hao, S., Andersen-Nissen, E., Mauck, W.M., Zheng, S., Butler, A., Lee, M.J., Wilk, A.J., Darby, C., Zager, M., Hoffman, P., Stoeckius, M., Papalexi, E., Mimitou, E.P., Jain, J., Srivastava, A., Stuart, T., Fleming, L.M., Yeung, B., Rogers, A.J., McElrath, J.M., Blish, C.A., Gottardo, R., Smibert, P., Satija, R., 2021. Integrated analysis of multimodal single-cell data. Cell 184, 3573-3587.e29. https://doi.org/10.1016/j.cell.2021.04.048

Hart, A.D., Wyttenbach, A., Hugh Perry, V., Teeling, J.L., 2012. Age related changes in microglial phenotype vary between CNS regions: Grey versus white matter differences. Brain. Behav. Immun., Aging, Brain, Behavior, and Immunity 26, 754–765. https://doi.org/10.1016/j.bbi.2011.11.006

Hashimoto, D., Chow, A., Noizat, C., Teo, P., Beasley, M.B., Leboeuf, M., Becker, C.D., See, P., Price, J., Lucas, D., Greter, M., Mortha, A., Boyer, S.W., Forsberg, E.C., Tanaka, M., van Rooijen, N., García-Sastre, A., Stanley, E.R., Ginhoux, F., Frenette, P.S., Merad, M., 2013. Tissue resident macrophages self-maintain locally throughout adult life with minimal contribution from circulating monocytes. Immunity 38. https://doi.org/10.1016/j.immuni.2013.04.004

Hashimshony, T., Senderovich, N., Avital, G., Klochendler, A., de Leeuw, Y., Anavy, L., Gennert, D., Li, S., Livak, K.J., Rozenblatt-Rosen, O., Dor, Y., Regev, A., Yanai, I., 2016. CEL-Seq2: sensitive highly-multiplexed single-cell RNA-Seq. Genome Biol. 17, 77. https://doi.org/10.1186/s13059-016-0938-8

Hasselmann, J., Coburn, M.A., England, W., Figueroa Velez, D.X., Kiani Shabestari, S., Tu, C.H., McQuade, A., Kolahdouzan, M., Echeverria, K., Claes, C., Nakayama, T., Azevedo, R., Coufal, N.G., Han, C.Z., Cummings, B.J., Davtyan, H., Glass, C.K., Healy, L.M., Gandhi, S.P., Spitale, R.C., Blurton-Jones, M., 2019. Development of a Chimeric Model to Study and

Manipulate Human Microglia In Vivo. Neuron. https://doi.org/10.1016/j.neuron.2019.07.002

Heider, J., Vogel, S., Volkmer, H., Breitmeyer, R., 2021. Human iPSC-Derived Glia as a Tool for Neuropsychiatric Research and Drug Development. Int. J. Mol. Sci. 22, 10254. https://doi.org/10.3390/ijms221910254

Hertzano, R., Gwilliam, K., Rose, K., Milon, B., Matern, M.S., 2021. Cell Type–Specific Expression Analysis of the Inner Ear: A Technical Report. The Laryngoscope 131, S1–S16. https://doi.org/10.1002/lary.28765

Hickman, S.E., Kingery, N.D., Ohsumi, T.K., Borowsky, M.L., Wang, L., Means, T.K., El Khoury, J., 2013. The microglial sensome revealed by direct RNA sequencing. Nat. Neurosci. 16, 1896–1905. https://doi.org/10.1038/nn.3554

Hirbec, H., Déglon, N., Foo, L.C., Goshen, I., Grutzendler, J., Hangen, E., Kreisel, T., Linck, N., Muffat, J., Regio, S., Rion, S., Escartin, C., 2020. Emerging technologies to study glial cells. Glia. https://doi.org/10.1002/glia.23780

Hoeffel, G., Chen, J., Lavin, Y., Low, D., Almeida, F.F., See, P., Beaudin, A.E., Lum, J., Low, I., Forsberg, E.C., Poidinger, M., Zolezzi, F., Larbi, A., Ng, L.G., Chan, J.K.Y., Greter, M., Becher, B., Samokhvalov, I.M., Merad, M., Ginhoux, F., 2015. C-Myb+ Erythro-Myeloid Progenitor-Derived Fetal Monocytes Give Rise to Adult Tissue-Resident Macrophages. Immunity 42, 665–678. https://doi.org/10.1016/j.immuni.2015.03.011

Horvath, S., Raj, K., 2018. DNA methylation-based biomarkers and the epigenetic clock theory of ageing. Nat. Rev. Genet. 19, 371–384. https://doi.org/10.1038/s41576-018-0004-3

Hou, Y., Guo, H., Cao, C., Li, X., Hu, B., Zhu, P., Wu, X., Wen, L., Tang, F., Huang, Y., Peng, J., 2016. Single-cell triple omics sequencing reveals genetic, epigenetic, and transcriptomic heterogeneity in hepatocellular carcinomas. Cell Res. 26, 304–319. https://doi.org/10.1038/cr.2016.23

Hrvatin, S., Hochbaum, D.R., Nagy, M.A., Cicconet, M., Robertson, K., Cheadle, L., Zilionis, R., Ratner, A., Borges-Monroy, R., Klein, A.M., Sabatini, B.L., Greenberg, M.E., 2018. Single-cell analysis of experience-dependent transcriptomic states in the mouse visual cortex. Nat. Neurosci. 21, 120–129. https://doi.org/10.1038/s41593-017-0029-5

Hu, Y., Fryatt, G.L., Ghorbani, M., Obst, J., Menassa, D.A., Martin-Estebane, M., Muntslag, T.A.O., Olmos-Alonso, A., Guerrero-Carrasco, M., Thomas, D., Cragg, M.S., Gomez-Nicola, D., 2021. Replicative senescence dictates the emergence of disease-associated microglia and contributes to Aβ pathology. Cell Rep. 35, 109228. https://doi.org/10.1016/j.celrep.2021.109228

Hu, Y., Huang, K., An, Q., Du, G., Hu, G., Xue, J., Zhu, X., Wang, C.-Y., Xue, Z., Fan, G., 2016. Simultaneous profiling of transcriptome and DNA methylome from a single cell. Genome Biol. 17, 88. https://doi.org/10.1186/s13059-016-0950-z

Huang, G., Zhang, P., Hirai, H., Elf, S., Yan, X., Chen, Z., Koschmieder, S., Okuno, Y., Dayaram, T., Growney, J.D., Shivdasani, R.A., Gilliland, D.G., Speck, N.A., Nimer, S.D., Tenen, D.G., 2008. PU.1 is a major downstream target of AML1 (RUNX1) in adult mouse hematopoiesis. Nat. Genet. 40, 51–60. https://doi.org/10.1038/ng.2007.7

Huang, Y., Xu, Z., Xiong, S., Sun, F., Qin, G., Hu, G., Wang, J., Zhao, L., Liang, Y.-X., Wu, T., Lu, Z., Humayun, M.S., So, K.-F., Pan, Y., Li, N., Yuan, T.-F., Rao, Y., Peng, B., 2018. Repopulated microglia are solely derived from the proliferation of residual microglia after acute depletion. Nat. Neurosci. 21, 530–540. https://doi.org/10.1038/s41593-018-0090-8

Islam, S., Zeisel, A., Joost, S., La Manno, G., Zajac, P., Kasper, M., Lönnerberg, P., Linnarsson, S., 2014. Quantitative single-cell RNA-seq with unique molecular identifiers. Nat. Methods 11, 163–166. https://doi.org/10.1038/nmeth.2772

Ivashkiv, L.B., Donlin, L.T., 2014. Regulation of type I interferon responses. Nat. Rev. Immunol. 14, 36–49. https://doi.org/10.1038/nri3581

Jackson, C.A., Castro, D.M., Saldi, G.-A., Bonneau, R., Gresham, D., 2020. Gene regulatory network reconstruction using single-cell RNA sequencing of barcoded genotypes in diverse environments. eLife 9, e51254. https://doi.org/10.7554/eLife.51254

Jaitin, D.A., Adlung, L., Thaiss, C.A., Weiner, A., Li, B., Descamps, H., Lundgren, P., Bleriot, C., Liu, Z., Deczkowska, A., Keren-Shaul, H., David, E., Zmora, N., Eldar, S.M., Lubezky, N., Shibolet, O., Hill, D.A., Lazar, M.A., Colonna, M., Ginhoux, F., Shapiro, H., Elinav, E., Amit, I., 2019. Lipid-Associated Macrophages Control Metabolic Homeostasis in a Trem2-Dependent Manner. Cell 178, 686-698.e14. https://doi.org/10.1016/j.cell.2019.05.054

Jamur, M.C., Oliver, C., 2010. Permeabilization of Cell Membranes, in: Oliver, C., Jamur, M.C. (Eds.), Immunocytochemical Methods and Protocols, Methods in Molecular Biology. Humana Press, Totowa, NJ, pp. 63–66. https://doi.org/10.1007/978-1-59745-324-0_9

Janes, K.A., 2016. Single-cell states versus single-cell atlases—two classes of heterogeneity that differ in meaning and method. Curr. Opin. Biotechnol. 39, 120–125. https://doi.org/10.1016/j.copbio.2016.03.015

Jarjour, N.N., Schwarzkopf, E.A., Bradstreet, T.R., Shchukina, I., Lin, C.-C., Huang, S.C.-C., Lai, C.-W., Cook, M.E., Taneja, R., Stappenbeck, T.S., Randolph, G.J., Artyomov, M.N., Urban, J.F., Edelson, B.T., 2019. Bhlhe40 mediates tissue-specific control of macrophage proliferation in homeostasis and type 2 immunity. Nat. Immunol. 20, 687–700. https://doi.org/10.1038/s41590-019-0382-5

Jeong, S.-J., Kim, S., Park, J.-G., Jung, I., Lee, M.-N., Jeon, S., Kweon, H.Y., Yu, D.-Y., Lee, S.-H., Jang, Y., Kang, S.W., Han, K.-H., Miller, Y.I., Park, Y.M., Cheong, C., Choi, J.-H., Oh, G.T., 2018. Prdx1 (peroxiredoxin 1) deficiency reduces cholesterol efflux via impaired macrophage lipophagic flux. Autophagy 14, 120–133. https://doi.org/10.1080/15548627.2017.1327942

Jiang, H.-Y., Wek, S.A., McGrath, B.C., Lu, D., Hai, T., Harding, H.P., Wang, X., Ron, D., Cavener, D.R., Wek, R.C., 2004. Activating Transcription Factor 3 Is Integral to the Eukaryotic Initiation Factor 2 Kinase Stress Response. Mol. Cell. Biol. 24, 1365–1377. https://doi.org/10.1128/MCB.24.3.1365-1377.2004

Jin, C., Shao, Y., Zhang, X., Xiang, J., Zhang, R., Sun, Z., Mei, S., Zhou, J., Zhang, J., Shi, L., 2021. A Unique Type of Highly-Activated Microglia Evoking Brain Inflammation via Mif/Cd74 Signaling Axis in Aged Mice. Aging Dis. 12, 2125–2139. https://doi.org/10.14336/AD.2021.0520

Jin, S., Guerrero-Juarez, C.F., Zhang, L., Chang, I., Ramos, R., Kuan, C.-H., Myung, P., Plikus, M.V., Nie, Q., 2021. Inference and analysis of cell-cell communication using CellChat. Nat. Commun. 12, 1088. https://doi.org/10.1038/s41467-021-21246-9

Jin, X.-R., Chen, X.-S., Xiao, L., 2017. MeCP2 Deficiency in Neuroglia: New Progress in the Pathogenesis of Rett Syndrome. Front. Mol. Neurosci. 10.

Jin, Z., Wei, W., Yang, M., Du, Y., Wan, Y., 2014. Mitochondrial Complex I Activity Suppresses Inflammation and Enhances Bone Resorption by Tipping the Balance of Macrophage-Osteoclast Polarization. Cell Metab. 20, 483–498. https://doi.org/10.1016/j.cmet.2014.07.011

Jordão, M.J.C., Sankowski, R., Brendecke, S.M., Sagar, Locatelli, G., Tai, Y.-H., Tay, T.L., Schramm, E., Armbruster, S., Hagemeyer, N., Groß, O., Mai, D., Çiçek, Ö., Falk, T., Kerschensteiner, M., Grün, D., Prinz, M., 2019. Single-cell profiling identifies myeloid cell subsets with distinct fates during neuroinflammation. Science 363. https://doi.org/10.1126/science.aat7554

Jung, S., Aliberti, J., Graemmel, P., Sunshine, M.J., Kreutzberg, G.W., Sher, A., Littman, D.R., 2000. Analysis of Fractalkine Receptor CX3CR1 Function by Targeted Deletion and Green Fluorescent Protein Reporter Gene Insertion. Mol. Cell. Biol. 20, 4106–4114. https://doi.org/10.1128/MCB.20.11.4106-4114.2000

Kamphuis, W., Kooijman, L., Schetters, S., Orre, M., Hol, E.M., 2016a. Transcriptional profiling of CD11c-positive microglia accumulating around amyloid plaques in a mouse model for Alzheimer's disease. Biochim. Biophys. Acta BBA - Mol. Basis Dis. 1862, 1847–1860. https://doi.org/10.1016/j.bbadis.2016.07.007

Kamphuis, W., Kooijman, L., Schetters, S., Orre, M., Hol, E.M., 2016b. Transcriptional profiling of CD11c-positive microglia accumulating around amyloid plaques in a mouse model for Alzheimer's disease. Biochim. Biophys. Acta BBA - Mol. Basis Dis. 1862, 1847–1860. https://doi.org/10.1016/j.bbadis.2016.07.007

Kana, V., Desland, F.A., Casanova-Acebes, M., Ayata, P., Badimon, A., Nabel, E., Yamamuro, K., Sneeboer, M., Tan, I.-L., Flanigan, M.E., Rose, S.A., Chang, C., Leader, A., Bourhis, H.L., Sweet, E.S., Tung, N., Wroblewska, A., Lavin, Y., See, P., Baccarini, A., Ginhoux, F., Chitu, V., Stanley, E.R., Russo, S.J., Yue, Z., Brown, B.D., Joyner, A.L., Witte, L.D.D., Morishita, H., Schaefer, A., Merad, M., 2019. CSF-1 controls cerebellar microglia and is required for motor function and social interaction. J. Exp. Med. jem.20182037. https://doi.org/10.1084/jem.20182037

Keren-Shaul, H., Kenigsberg, E., Jaitin, D.A., David, E., Paul, F., Tanay, A., Amit, I., 2019. MARS-seq2.0: an experimental and analytical pipeline for indexed sorting combined with single-cell RNA sequencing. Nat. Protoc. 14, 1841–1862. https://doi.org/10.1038/s41596-019-0164-4

Keren-Shaul, H., Spinrad, A., Weiner, A., Matcovitch-Natan, O., Dvir-Szternfeld, R., Ulland, T.K., David, E., Baruch, K., Lara-Astaiso, D., Toth, B., Itzkovitz, S., Colonna, M., Schwartz, M., Amit, I., 2017a. A Unique Microglia Type Associated with Restricting Development of Alzheimer's Disease. Cell 169, 1276-1290.e17. https://doi.org/10.1016/j.cell.2017.05.018

Keren-Shaul, H., Spinrad, A., Weiner, A., Matcovitch-Natan, O., Dvir-Szternfeld, R., Ulland, T.K., David, E., Baruch, K., Lara-Astaiso, D., Toth, B., Itzkovitz, S., Colonna, M., Schwartz, M., Amit, I., 2017b. A Unique Microglia Type Associated with Restricting Development of Alzheimer's Disease. Cell 169, 1276-1290.e17. https://doi.org/10.1016/j.cell.2017.05.018

Keren-Shaul, H., Spinrad, A., Weiner, A., Matcovitch-Natan, O., Dvir-Szternfeld, R., Ulland, T.K., David, E., Baruch, K., Lara-Astaiso, D., Toth, B., Itzkovitz, S., Colonna, M., Schwartz, M., Amit, I., 2017c. A Unique Microglia Type Associated with Restricting Development of Alzheimer's Disease. Cell 169, 1276-1290.e17. https://doi.org/10.1016/j.cell.2017.05.018

Kernfeld, E.M., Genga, R.M.J., Neherin, K., Magaletta, M.E., Xu, P., Maehr, R., 2018. A Single-Cell Transcriptomic Atlas of Thymus Organogenesis Resolves Cell Types and Developmental Maturation. Immunity 48, 1258-1270.e6. https://doi.org/10.1016/j.immuni.2018.04.015

Kierdorf, K., Erny, D., Goldmann, T., Sander, V., Schulz, C., Perdiguero, E.G., Wieghofer, P., Heinrich, A., Riemke, P., Hölscher, C., Müller, D.N., Luckow, B., Brocker, T., Debowski, K., Fritz, G., Opdenakker, G., Diefenbach, A., Biber, K., Heikenwalder, M., Geissmann, F., Rosenbauer, F., Prinz, M., 2013a. Microglia emerge from erythromyeloid precursors via

Pu.1- and Irf8-dependent pathways. Nat. Neurosci. 16, 273–280. https://doi.org/10.1038/nn.3318

Kierdorf, K., Erny, D., Goldmann, T., Sander, V., Schulz, C., Perdiguero, E.G., Wieghofer, P., Heinrich, A., Riemke, P., Hölscher, C., Müller, D.N., Luckow, B., Brocker, T., Debowski, K., Fritz, G., Opdenakker, G., Diefenbach, A., Biber, K., Heikenwalder, M., Geissmann, F., Rosenbauer, F., Prinz, M., 2013b. Microglia emerge from erythromyeloid precursors via Pu.1- and Irf8-dependent pathways. Nat. Neurosci. 16, 273–280. https://doi.org/10.1038/nn.3318

Kierdorf, K., Masuda, T., Jordão, M.J.C., Prinz, M., 2019. Macrophages at CNS interfaces: ontogeny and function in health and disease. Nat. Rev. Neurosci. 20, 547–562. https://doi.org/10.1038/s41583-019-0201-x

Kim, M., Franke, V., Brandt, B., Lowenstein, E.D., Schöwel, V., Spuler, S., Akalin, A., Birchmeier, C., 2020. Single-nucleus transcriptomics reveals functional compartmentalization in syncytial skeletal muscle cells. Nat. Commun. 11, 6375. https://doi.org/10.1038/s41467-020-20064-9

Kocur, M., Schneider, R., Pulm, A.-K., Bauer, J., Kropp, S., Gliem, M., Ingwersen, J., Goebels, N., Alferink, J., Prozorovski, T., Aktas, O., Scheu, S., 2015. IFNβ secreted by microglia mediates clearance of myelin debris in CNS autoimmunity. Acta Neuropathol. Commun. 3, 20. https://doi.org/10.1186/s40478-015-0192-4

Köhler, C., 2007. Allograft inflammatory factor-1/Ionized calcium-binding adapter molecule 1 is specifically expressed by most subpopulations of macrophages and spermatids in testis. Cell Tissue Res. 330, 291–302. https://doi.org/10.1007/s00441-007-0474-7

Korsunsky, I., Millard, N., Fan, J., Slowikowski, K., Zhang, F., Wei, K., Baglaenko, Y., Brenner, M., Loh, P., Raychaudhuri, S., 2019. Fast, sensitive and accurate integration of single-cell data with Harmony. Nat. Methods 16, 1289–1296. https://doi.org/10.1038/s41592-019-0619-0

Kracht, L., Borggrewe, M., Eskandar, S., Brouwer, N., Lopes, S.M.C. de S., Laman, J.D., Scherjon, S.A., Prins, J.R., Kooistra, S.M., Eggen, B.J.L., 2020. Human fetal microglia acquire homeostatic immune-sensing properties early in development. Science 369, 530–537. https://doi.org/10.1126/science.aba5906

Krasemann, S., Madore, C., Cialic, R., Baufeld, C., Calcagno, N., El Fatimy, R., Beckers, L., O'Loughlin, E., Xu, Y., Fanek, Z., Greco, D.J., Smith, S.T., Tweet, G., Humulock, Z., Zrzavy, T., Conde-Sanroman, P., Gacias, M., Weng, Z., Chen, H., Tjon, E., Mazaheri, F., Hartmann, K., Madi, A., Ulrich, J.D., Glatzel, M., Worthmann, A., Heeren, J., Budnik, B., Lemere, C., Ikezu, T., Heppner, F.L., Litvak, V., Holtzman, D.M., Lassmann, H., Weiner, H.L., Ochando, J., Haass, C., Butovsky, O., 2017a. The TREM2-APOE Pathway Drives the Transcriptional Phenotype of Dysfunctional Microglia in Neurodegenerative Diseases. Immunity 47, 566-581.e9. https://doi.org/10.1016/j.immuni.2017.08.008

Krasemann, S., Madore, C., Cialic, R., Baufeld, C., Calcagno, N., El Fatimy, R., Beckers, L., O'Loughlin, E., Xu, Y., Fanek, Z., Greco, D.J., Smith, S.T., Tweet, G., Humulock, Z., Zrzavy, T., Conde-Sanroman, P., Gacias, M., Weng, Z., Chen, H., Tjon, E., Mazaheri, F., Hartmann, K., Madi, A., Ulrich, J.D., Glatzel, M., Worthmann, A., Heeren, J., Budnik, B., Lemere, C., Ikezu, T., Heppner, F.L., Litvak, V., Holtzman, D.M., Lassmann, H., Weiner, H.L., Ochando, J., Haass, C., Butovsky, O., 2017b. The TREM2-APOE Pathway Drives the Transcriptional Phenotype of Dysfunctional Microglia in Neurodegenerative Diseases. Immunity 47, 566-581.e9. https://doi.org/10.1016/j.immuni.2017.08.008

Kretzschmar, K., Watt, F.M., 2012. Lineage Tracing. Cell 148, 33–45. https://doi.org/10.1016/j.cell.2012.01.002

Lacar, B., Linker, S.B., Jaeger, B.N., Krishnaswami, S., Barron, J., Kelder, M., Parylak, S., Paquola, A., Venepally, P., Novotny, M., O'Connor, C., Fitzpatrick, C., Erwin, J., Hsu, J.Y., Husband, D., McConnell, M.J., Lasken, R., Gage, F.H., 2016. Nuclear RNA-seq of single neurons reveals molecular signatures of activation. Nat. Commun. 7. https://doi.org/10.1038/ncomms11022

Lai, W.S., Arvola, R.M., Goldstrohm, A.C., Blackshear, P.J., 2019. Inhibiting transcription in cultured metazoan cells with actinomycin D to monitor mRNA turnover. Methods, Biochemical and Next Generation Sequencing Approaches to Study RNA Regulation 155, 77–87. https://doi.org/10.1016/j.ymeth.2019.01.003

Laks, E., McPherson, A., Zahn, H., Lai, D., Steif, A., Brimhall, J., Biele, J., Wang, B., Masud, T., Ting, J., Grewal, D., Nielsen, C., Leung, S., Bojilova, V., Smith, M., Golovko, O., Poon, S., Eirew, P., Kabeer, F., Algara, T.R. de, Lee, S.R., Taghiyar, M.J., Huebner, C., Ngo, J., Chan, T., Vatrt-Watts, S., Walters, P., Abrar, N., Chan, S., Wiens, M., Martin, L., Scott, R.W., Underhill, T.M., Chavez, E., Steidl, C., Costa, D.D., Ma, Y., Coope, R.J.N., Corbett, R., Pleasance, S., Moore, R., Mungall, A.J., Mar, C., Cafferty, F., Gelmon, K., Chia, S., Hannon, G.J., Battistoni, G., Bressan, D., Cannell, I., Casbolt, H., Jauset, C., Kovačević, T., Mulvey, C., Nugent, F., Ribes, M.P., Pearsall, I., Qosaj, F., Sawicka, K., Wild, S., Williams, E., Aparicio, S., Laks, E., Li, Y., O'Flanagan, C., Smith, A., Ruiz, T., Balasubramanian, S., Lee, M., Bodenmiller, B., Burger, M., Kuett, L., Tietscher, S., Windager, J., Boyden, E., Alon, S., Cui, Y., Emenari, A., Goodwin, D., Karagiannis, E., Sinha, A., Wassie, A.T., Caldas, C., Bruna, A., Callari, M., Greenwood, W., Lerda, G., Lubling, Y., Marti, A., Rueda, O., Shea, A., Harris, O., Becker, R., Grimaldi, F., Harris, S., Vogl, S., Joyce, J.A., Hausser, J., Watson, S., Shah, S., McPherson, A., Vázquez-García, I., Tavaré, S., Dinh, K., Fisher, E., Kunes, R., Walton, N.A., Sa'd, M.A., Chornay, N., Dariush, A., Solares, E.G., Gonzalez-Fernandez, C., Yoldas, A.K., Millar, N., Zhuang, X., Fan, J., Lee, H., Duran, L.S., Xia, C., Zheng, P., Marra, M.A., Hansen, C., Shah, S.P., Aparicio, S., 2019. Clonal Decomposition and DNA Replication States Defined by Scaled Single-Cell Genome Sequencing. Cell 179, 1207-1221.e22. https://doi.org/10.1016/j.cell.2019.10.026

Lara-Astiaso, D., Weiner, A., Lorenzo-Vivas, E., Zaretsky, I., Jaitin, D.A., David, E., Keren-Shaul, H., Mildner, A., Winter, D., Jung, S., Friedman, N., Amit, I., 2014. Chromatin state dynamics during blood formation. Science 345, 943–949. https://doi.org/10.1126/science.1256271

Lau, S.-F., Chen, C., Fu, W.-Y., Qu, J.Y., Cheung, T.H., Fu, A.K.Y., Ip, N.Y., 2020. IL-33-PU.1 Transcriptome Reprogramming Drives Functional State Transition and Clearance Activity of Microglia in Alzheimer's Disease. Cell Rep. 31, 107530. https://doi.org/10.1016/j.celrep.2020.107530

Lauridsen, F.K.B., Jensen, T.L., Rapin, N., Aslan, D., Wilhelmson, A.S., Pundhir, S., Rehn, M., Paul, F., Giladi, A., Hasemann, M.S., Serup, P., Amit, I., Porse, B.T., 2018. Differences in Cell Cycle Status Underlie Transcriptional Heterogeneity in the HSC Compartment. Cell Rep. 24, 766–780. https://doi.org/10.1016/j.celrep.2018.06.057

Lavin, Y., Winter, D., Blecher-Gonen, R., David, E., Keren-Shaul, H., Merad, M., Jung, S., Amit, I., 2014. Tissue-Resident Macrophage Enhancer Landscapes Are Shaped by the Local Microenvironment. Cell 159, 1312–1326. https://doi.org/10.1016/j.cell.2014.11.018

Lawson, L.J., Perry, V.H., Dri, P., Gordon, S., 1990. Heterogeneity in the distribution and morphology of microglia in the normal adult mouse brain. Neuroscience 39, 151–170. https://doi.org/10.1016/0306-4522(90)90229-W

Lee, C.Z.W., Kozaki, T., Ginhoux, F., 2018. Studying tissue macrophages in vitro: are iPSC-derived cells the answer? Nat. Rev. Immunol. 18, 716–725. https://doi.org/10.1038/s41577-018-0054-y

Lee, H.-T., Oh, S., Ro, D.H., Yoo, H., Kwon, Y.-W., 2020. The Key Role of DNA Methylation and Histone Acetylation in Epigenetics of Atherosclerosis. J. Lipid Atheroscler. 9, 419–434. https://doi.org/10.12997/jla.2020.9.3.419

Lee, J., Hyeon, D.Y., Hwang, D., 2020. Single-cell multiomics: technologies and data analysis methods. Exp. Mol. Med. 52, 1428–1442. https://doi.org/10.1038/s12276-020-0420-2

Lee, J.-K., Tansey, M.G., 2013. Microglia Isolation from Adult Mouse Brain, in: Joseph, B., Venero, J.L. (Eds.), Microglia: Methods and Protocols, Methods in Molecular Biology. Humana Press, Totowa, NJ, pp. 17–23. https://doi.org/10.1007/978-1-62703-520-0_3

Lee, M., Lee, Y., Song, J., Lee, J., Chang, S.-Y., 2018. Tissue-specific Role of CX3CR1 Expressing Immune Cells and Their Relationships with Human Disease. Immune Netw. 18, e5. https://doi.org/10.4110/in.2018.18.e5

Lee, S., Varvel, N.H., Konerth, M.E., Xu, G., Cardona, A.E., Ransohoff, R.M., Lamb, B.T., 2010. CX3CR1 Deficiency Alters Microglial Activation and Reduces Beta-Amyloid Deposition in Two Alzheimer's Disease Mouse Models. Am. J. Pathol. 177, 2549–2562. https://doi.org/10.2353/ajpath.2010.100265

Lee, Y., Bogdanoff, D., Wang, Y., Hartoularos, G.C., Woo, J.M., Mowery, C.T., Nisonoff, H.M., Lee, D.S., Sun, Y., Lee, J., Mehdizadeh, S., Cantlon, J., Shifrut, E., Ngyuen, D.N., Roth, T.L., Song, Y.S., Marson, A., Chow, E.D., Ye, C.J., 2021. XYZeq: Spatially resolved single-cell RNA sequencing reveals expression heterogeneity in the tumor microenvironment. Sci. Adv. https://doi.org/10.1126/sciadv.abg4755

Lemche, E., 2018. Early Life Stress and Epigenetics in Late-onset Alzheimer's Dementia: A Systematic Review. Curr. Genomics 19, 522–602. https://doi.org/10.2174/1389202919666171229145156

Lent, J.V., Breukers, J., Ven, K., Ampofo, L., Horta, S., Pollet, F., Imbrechts, M., Geukens, N., Vanhoorelbeke, K., Declerck, P., Lammertyn, J., 2021. Miniaturized single-cell technologies for monoclonal antibody discovery. Lab. Chip 21, 3627–3654. https://doi.org/10.1039/D1LC00243K

Lenz, K.M., Nugent, B.M., Haliyur, R., McCarthy, M.M., 2013. Microglia Are Essential to Masculinization of Brain and Behavior. J. Neurosci. 33, 2761–2772. https://doi.org/10.1523/JNEUROSCI.1268-12.2013

Leppä, S., Bohmann, D., 1999. Diverse functions of JNK signaling and c-Jun in stress response and apoptosis. Oncogene 18, 6158–6162. https://doi.org/10.1038/sj.onc.1203173

Li, L., Garden, R.W., Sweedler, J.V., Li, L., Garden, R.W., Sweedler, J.V., 2000. Single-cell MALDI: a new tool for direct peptide profiling. Trends Biotechnol. 18, 151–160. https://doi.org/10.1016/S0167-7799(00)01427-X

Li, Q., Cheng, Z., Zhou, L., Darmanis, S., Neff, N.F., Okamoto, J., Gulati, G., Bennett, M.L., Sun, L.O., Clarke, L.E., Marschallinger, J., Yu, G., Quake, S.R., Wyss-Coray, T., Barres, B.A., 2019a. Developmental Heterogeneity of Microglia and Brain Myeloid Cells Revealed by Deep Single-Cell RNA Sequencing. Neuron 101, 207-223.e10. https://doi.org/10.1016/j.neuron.2018.12.006

Li, Q., Cheng, Z., Zhou, L., Darmanis, S., Neff, N.F., Okamoto, J., Gulati, G., Bennett, M.L., Sun, L.O., Clarke, L.E., Marschallinger, J., Yu, G., Quake, S.R., Wyss-Coray, T., Barres, B.A., 2019b. Developmental Heterogeneity of Microglia and Brain Myeloid Cells Revealed by Deep Single-Cell RNA Sequencing. Neuron 101, 207-223.e10. https://doi.org/10.1016/j.neuron.2018.12.006

Li, Z., Ju, X., Silveira, P.A., Abadir, E., Hsu, W.-H., Hart, D.N.J., Clark, G.J., 2019. CD83: Activation Marker for Antigen Presenting Cells and Its Therapeutic Potential. Front. Immunol. 10.

Lichanska, A.M., Hume, D.A., 2000. Origins and functions of phagocytes in the embryo. Exp. Hematol. 28, 601–611. https://doi.org/10.1016/S0301-472X(00)00157-0

Lin, C.-C., Bradstreet, T.R., Schwarzkopf, E.A., Sim, J., Carrero, J.A., Chou, C., Cook, L.E., Egawa, T., Taneja, R., Murphy, T.L., Russell, J.H., Edelson, B.T., 2014. Bhlhe40 controls cytokine production by T cells and is essential for pathogenicity in autoimmune neuroinflammation. Nat. Commun. 5, 3551. https://doi.org/10.1038/ncomms4551

Lituma, P.J., Woo, E., O'Hara, B.F., Castillo, P.E., Sibinga, N.E.S., Nandi, S., 2021. Altered synaptic connectivity and brain function in mice lacking microglial adapter protein Iba1. Proc. Natl. Acad. Sci. 118. https://doi.org/10.1073/pnas.2115539118

Liu, L., Liu, C., Quintero, A., Wu, L., Yuan, Y., Wang, M., Cheng, M., Leng, L., Xu, L., Dong, G., Li, R., Liu, Y., Wei, X., Xu, J., Chen, X., Lu, H., Chen, D., Wang, Quanlei, Zhou, Q., Lin, X., Li, G., Liu, S., Wang, Qi, Wang, H., Fink, J.L., Gao, Z., Liu, X., Hou, Y., Zhu, S., Yang, H., Ye, Y., Lin, G., Chen, F., Herrmann, C., Eils, R., Shang, Z., Xu, X., 2019. Deconvolution of single-cell multi-omics layers reveals regulatory heterogeneity. Nat. Commun. 10, 470. https://doi.org/10.1038/s41467-018-08205-7

Liu, X.F., Xiang, L., Zhou, Q., Carralot, J.-P., Prunotto, M., Niederfellner, G., Pastan, I., 2016. Actinomycin D enhances killing of cancer cells by immunotoxin RG7787 through activation of the extrinsic pathway of apoptosis. Proc. Natl. Acad. Sci. 113, 10666–10671.

Loomes, R., Hull, L., Mandy, W.P.L., 2017. What Is the Male-to-Female Ratio in Autism Spectrum Disorder? A Systematic Review and Meta-Analysis. J. Am. Acad. Child Adolesc. Psychiatry 56, 466–474. https://doi.org/10.1016/j.jaac.2017.03.013

Lopes, K. de P., Snijders, G.J.L., Humphrey, J., Allan, A., Sneeboer, M.A.M., Navarro, E., Schilder, B.M., Vialle, R.A., Parks, M., Missall, R., van Zuiden, W., Gigase, F.A.J., Kübler, R., van Berlekom, A.B., Hicks, E.M., Böttcher, C., Priller, J., Kahn, R.S., de Witte, L.D., Raj, T., 2022. Genetic analysis of the human microglial transcriptome across brain regions, aging and disease pathologies. Nat. Genet. 1–14. https://doi.org/10.1038/s41588-021-00976-y

Lun, A.T.L., Riesenfeld, S., Andrews, T., Dao, T.P., Gomes, T., Marioni, J.C., participants in the 1st Human Cell Atlas Jamboree, 2019. EmptyDrops: distinguishing cells from empty droplets in droplet-based single-cell RNA sequencing data. Genome Biol. 20, 63. https://doi.org/10.1186/s13059-019-1662-y

Luo, C., Keown, C.L., Kurihara, L., Zhou, J., He, Y., Li, J., Castanon, R., Lucero, J., Nery, J.R., Sandoval, J.P., Bui, B., Sejnowski, T.J., Harkins, T.T., Mukamel, E.A., Behrens, M.M., Ecker, J.R., 2017. Single-cell methylomes identify neuronal subtypes and regulatory elements in mammalian cortex. Science.

Ma, S., Zhang, B., LaFave, L.M., Earl, A.S., Chiang, Z., Hu, Y., Ding, J., Brack, A., Kartha, V.K., Tay, T., Law, T., Lareau, C., Hsu, Y.-C., Regev, A., Buenrostro, J.D., 2020. Chromatin Potential Identified by Shared Single-Cell Profiling of RNA and Chromatin. Cell 183, 1103-1116.e20. https://doi.org/10.1016/j.cell.2020.09.056

Macaulay, I.C., Haerty, W., Kumar, P., Li, Y.I., Hu, T.X., Teng, M.J., Goolam, M., Saurat, N., Coupland, P., Shirley, L.M., Smith, M., Van der Aa, N., Banerjee, R., Ellis, P.D., Quail, M.A., Swerdlow, H.P., Zernicka-Goetz, M., Livesey, F.J., Ponting, C.P., Voet, T., 2015. G&T-seq: parallel sequencing of single-cell genomes and transcriptomes. Nat. Methods 12, 519–522. https://doi.org/10.1038/nmeth.3370

Machado, L., Esteves de Lima, J., Fabre, O., Proux, C., Legendre, R., Szegedi, A., Varet, H., Ingerslev, L.R., Barrès, R., Relaix, F., Mourikis, P., 2017. In Situ Fixation Redefines Quiescence and Early Activation of Skeletal Muscle Stem Cells. Cell Rep. 21, 1982–1993. https://doi.org/10.1016/j.celrep.2017.10.080

Machado, L., Geara, P., Camps, J., Santos, M.D., Teixeira-Clerc, F., Herck, J.V., Varet, H., Legendre, R., Pawlotsky, J.-M., Sampaolesi, M., Voet, T., Maire, P., Relaix, F., Mourikis, P., 2021a. Tissue damage induces a conserved stress response that initiates quiescent muscle stem cell activation. Cell Stem Cell 28, 1125-1135.e7. https://doi.org/10.1016/j.stem.2021.01.017

Machado, L., Relaix, F., Mourikis, P., 2021b. Stress relief: emerging methods to mitigate dissociation-induced artefacts. Trends Cell Biol. 31, 888–897. https://doi.org/10.1016/j.tcb.2021.05.004

Machado, L., Relaix, F., Mourikis, P., 2021c. Stress relief: emerging methods to mitigate dissociation-induced artefacts. Trends Cell Biol. 0. https://doi.org/10.1016/j.tcb.2021.05.004

MacManus, D.B., Pierrat, B., Murphy, J.G., Gilchrist, M.D., 2017. Region and species dependent mechanical properties of adolescent and young adult brain tissue. Sci. Rep. 7, 13729. https://doi.org/10.1038/s41598-017-13727-z

Macosko, E., Goldman, M., 2018. Drop-Seq Laboratory Protocol [WWW Document]. protocols.io. URL https://www.protocols.io/view/drop-seq-laboratory-protocol-mkbc4sn (accessed 1.27.22).

Macosko, E.Z., Basu, A., Satija, R., Nemesh, J., Shekhar, K., Goldman, M., Tirosh, I., Bialas, A.R., Kamitaki, N., Martersteck, E.M., Trombetta, J.J., Weitz, D.A., Sanes, J.R., Shalek, A.K., Regev, A., McCarroll, S.A., 2015. Highly parallel genome-wide expression profiling of individual cells using nanoliter droplets. Cell 161, 1202–1214. https://doi.org/10.1016/j.cell.2015.05.002

Mak, I.W., Evaniew, N., Ghert, M., 2014. Lost in translation: animal models and clinical trials in cancer treatment. Am. J. Transl. Res. 6, 114–118.

Malkki, H., 2014. Effects of the APOE ε4 allele on brain development. Nat. Rev. Neurol. 10, 4–4. https://doi.org/10.1038/nrneurol.2013.258

Mancuso, R., Daele, J.V.D., Fattorelli, N., Wolfs, L., Balusu, S., Burton, O., Liston, A., Sierksma, A., Fourne, Y., Poovathingal, S., Arranz-Mendiguren, A., Frigerio, C.S., Claes, C., Serneels, L., Theys, T., Perry, V.H., Verfaillie, C., Fiers, M., Strooper, B.D., 2019. Stem-cell-derived human microglia transplanted in mouse brain to study human disease. Nat. Neurosci. 1–6. https://doi.org/10.1038/s41593-019-0525-x

Manno, G.L., Soldatov, R., Hochgerner, H., Zeisel, A., Petukhov, V., Kastriti, M.E., Lönnerberg, P., Furlan, A., Fan, J., Liu, Z., Bruggen, D. van, Guo, J., Sundström, E., Castelo-Branco, G., Adameyko, I., Linnarsson, S., Kharchenko, P.V., 2017. RNA velocity in single cells. bioRxiv 206052. https://doi.org/10.1101/206052

March-Diaz, R., Lara-Ureña, N., Romero-Molina, C., Heras-Garvin, A., Ortega-de San Luis, C., Alvarez-Vergara, M.I., Sanchez-Garcia, M.A., Sanchez-Mejias, E., Davila, J.C., Rosales-Nieves, A.E., Forja, C., Navarro, V., Gomez-Arboledas, A., Sanchez-Mico, M.V., Viehweger, A., Gerpe, A., Hodson, E.J., Vizuete, M., Bishop, T., Serrano-Pozo, A., Lopez-Barneo, J., Berra, E., Gutierrez, A., Vitorica, J., Pascual, A., 2021. Hypoxia compromises the mitochondrial metabolism of Alzheimer's disease microglia via HIF1. Nat. Aging 1, 385–399. https://doi.org/10.1038/s43587-021-00054-2

Marschallinger, J., Iram, T., Zardeneta, M., Lee, S.E., Lehallier, B., Haney, M.S., Pluvinage, J.V., Mathur, V., Hahn, O., Morgens, D.W., Kim, J., Tevini, J., Felder, T.K., Wolinski, H., Bertozzi, C.R., Bassik, M.C., Aigner, L., Wyss-Coray, T., 2020. Lipid-droplet-accumulating microglia represent a dysfunctional and proinflammatory state in the aging brain. Nat. Neurosci. 23, 194–208. https://doi.org/10.1038/s41593-019-0566-1

Marsh, S.E., Walker, A.J., Kamath, T., Dissing-Olesen, L., Hammond, T.R., de Soysa, T.Y., Young, A.M.H., Murphy, S., Abdulraouf, A., Nadaf, N., Dufort, C., Walker, A.C., Lucca, L.E., Kozareva, V., Vanderburg, C., Hong, S., Bulstrode, H., Hutchinson, P.J., Gaffney, D.J., Hafler, D.A., Franklin, R.J.M., Macosko, E.Z., Stevens, B., 2022. Dissection of artifactual and confounding glial signatures by single-cell sequencing of mouse and human brain. Nat. Neurosci. 25, 306–316. https://doi.org/10.1038/s41593-022-01022-8

Martinez, F.O., Gordon, S., 2014. The M1 and M2 paradigm of macrophage activation: time for reassessment. F1000Prime Rep. 6. https://doi.org/10.12703/P6-13

Mass, E., Ballesteros, I., Farlik, M., Halbritter, F., Günther, P., Crozet, L., Jacome-Galarza, C.E., Händler, K., Klughammer, J., Kobayashi, Y., Gomez-Perdiguero, E., Schultze, J.L., Beyer, M., Bock, C., Geissmann, F., 2016a. Specification of tissue-resident macrophages during organogenesis. Science 353. https://doi.org/10.1126/science.aaf4238

Mass, E., Ballesteros, I., Farlik, M., Halbritter, F., Günther, P., Crozet, L., Jacome-Galarza, C.E., Händler, K., Klughammer, J., Kobayashi, Y., Gomez-Perdiguero, E., Schultze, J.L., Beyer, M., Bock, C., Geissmann, F., 2016b. Specification of tissue-resident macrophages during organogenesis. Science 353, aaf4238. https://doi.org/10.1126/science.aaf4238

Masuda, T., Amann, L., Sankowski, R., Staszewski, O., Lenz, M., d´Errico, P., Snaidero, N., Costa Jordão, M.J., Böttcher, C., Kierdorf, K., Jung, S., Priller, J., Misgeld, T., Vlachos, A., Luehmann, M.M., Knobeloch, K.-P., Prinz, M., 2020a. Novel Hexb-based tools for studying microglia in the CNS. Nat. Immunol. 21, 802–815. https://doi.org/10.1038/s41590-020-0707-4

Masuda, T., Sankowski, R., Staszewski, O., Böttcher, C., Amann, L., Sagar, Scheiwe, C., Nessler, S., Kunz, P., van Loo, G., Coenen, V.A., Reinacher, P.C., Michel, A., Sure, U., Gold, R., Grün, D., Priller, J., Stadelmann, C., Prinz, M., 2019. Spatial and temporal heterogeneity of mouse and human microglia at single-cell resolution. Nature 566, 388–392. https://doi.org/10.1038/s41586-019-0924-x

Masuda, T., Sankowski, R., Staszewski, O., Prinz, M., 2020b. Microglia Heterogeneity in the Single-Cell Era. Cell Rep. 30, 1271–1281. https://doi.org/10.1016/j.celrep.2020.01.010

Masuda, T., Tsuda, M., Yoshinaga, R., Tozaki-Saitoh, H., Ozato, K., Tamura, T., Inoue, K., 2012. IRF8 Is a Critical Transcription Factor for Transforming Microglia into a Reactive Phenotype. Cell Rep. 1, 334–340. https://doi.org/10.1016/j.celrep.2012.02.014

Matcovitch-Natan, O., Winter, D.R., Giladi, A., Aguilar, S.V., Spinrad, A., Sarrazin, S., Ben-Yehuda, H., David, E., González, F.Z., Perrin, P., Keren-Shaul, H., Gury, M., Lara-Astaiso, D., Thaiss, C.A., Cohen, M., Halpern, K.B., Baruch, K., Deczkowska, A., Lorenzo-Vivas, E., Itzkovitz, S., Elinav, E., Sieweke, M.H., Schwartz, M., Amit, I., 2016. Microglia development follows a stepwise program to regulate brain homeostasis. Science 353, aad8670. https://doi.org/10.1126/science.aad8670

Matejuk, A., Ransohoff, R.M., 2020. Crosstalk Between Astrocytes and Microglia: An Overview. Front. Immunol. 11.

Mathys, H., Adaikkan, C., Gao, F., Young, J.Z., Manet, E., Hemberg, M., De Jager, P.L., Ransohoff, R.M., Regev, A., Tsai, L.-H., 2017. Temporal Tracking of Microglia Activation in

Neurodegeneration at Single-Cell Resolution. Cell Rep. 21, 366–380. https://doi.org/10.1016/j.celrep.2017.09.039

Mattei, D., Ivanov, A., van Oostrum, M., Pantelyushin, S., Richetto, J., Mueller, F., Beffinger, M., Schellhammer, L., vom Berg, J., Wollscheid, B., Beule, D., Paolicelli, R.C., Meyer, U., 2020. Enzymatic Dissociation Induces Transcriptional and Proteotype Bias in Brain Cell Populations. Int. J. Mol. Sci. 21, 7944. https://doi.org/10.3390/ijms21217944

Mazutis, L., Gilbert, J., Ung, W.L., Weitz, D.A., Griffiths, A.D., Heyman, J.A., 2013. Single-cell analysis and sorting using droplet-based microfluidics. Nat. Protoc. 8, 870. https://doi.org/10.1038/nprot.2013.046

McDonough, A., Lee, R.V., Weinstein, J.R., 2017. Microglial Interferon Signaling and White Matter. Neurochem. Res. 42, 2625–2638. https://doi.org/10.1007/s11064-017-2307-8

McQuade, A., Kang, Y.J., Hasselmann, J., Jairaman, A., Sotelo, A., Coburn, M., Shabestari, S.K., Chadarevian, J.P., Fote, G., Tu, C.H., Danhash, E., Silva, J., Martinez, E., Cotman, C., Prieto, G.A., Thompson, L.M., Steffan, J.S., Smith, I., Davtyan, H., Cahalan, M., Cho, H., Blurton-Jones, M., 2020. Gene expression and functional deficits underlie TREM2-knockout microglia responses in human models of Alzheimer's disease. Nat. Commun. 11, 5370. https://doi.org/10.1038/s41467-020-19227-5

Mecca, C., Giambanco, I., Donato, R., Arcuri, C., 2018. Microglia and Aging: The Role of the TREM2–DAP12 and CX3CL1-CX3CR1 Axes. Int. J. Mol. Sci. 19. https://doi.org/10.3390/ijms19010318

Menassa, D.A., Muntslag, T.A.O., Martin-Estebané, M., Barry-Carroll, L., Chapman, M.A., Adorjan, I., Tyler, T., Turnbull, B., Rose-Zerilli, M.J.J., Nicoll, J.A.R., Krsnik, Z., Kostovic, I., Gomez-Nicola, D., 2022. The spatiotemporal dynamics of microglia across the human lifespan. Dev. Cell 57, 2127-2139.e6. https://doi.org/10.1016/j.devcel.2022.07.015

Menassa, D.A., Muntslag, T.A.O., Martin-Estebane, M., Barry-Carroll, L., Chapman, M.A., Adorjan, I., Tyler, T., Turnbull, B., Rose-Zerilli, M.J.J., Nicoll, J.A.R., Krsnik, Z., Kostovic, I., Gomez-Nicola, D., 2021. Spatiotemporal Dynamics of Human Microglia are Linked with Brain Developmental Processes Across the Lifespan (SSRN Scholarly Paper No. ID 3932600). Social Science Research Network, Rochester, NY. https://doi.org/10.2139/ssrn.3932600

Mendiola, A.S., Ryu, J.K., Bardehle, S., Meyer-Franke, A., Ang, K.K.-H., Wilson, C., Baeten, K.M., Hanspers, K., Merlini, M., Thomas, S., Petersen, M.A., Williams, A., Thomas, R., Rafalski, V.A., Meza-Acevedo, R., Tognatta, R., Yan, Z., Pfaff, S.J., Machado, M.R., Bedard, C., Rios Coronado, P.E., Jiang, X., Wang, J., Pleiss, M.A., Green, A.J., Zamvil, S.S., Pico, A.R., Bruneau, B.G., Arkin, M.R., Akassoglou, K., 2020. Transcriptional profiling and therapeutic targeting of oxidative stress in neuroinflammation. Nat. Immunol. 21, 513–524. https://doi.org/10.1038/s41590-020-0654-0

Mogilenko, D.A., Shchukina, I., Artyomov, M.N., 2022. Immune ageing at single-cell resolution. Nat. Rev. Immunol. 22, 484–498. https://doi.org/10.1038/s41577-021-00646-4

Mrdjen, D., Pavlovic, A., Hartmann, F.J., Schreiner, B., Utz, S.G., Leung, B.P., Lelios, I., Heppner, F.L., Kipnis, J., Merkler, D., Greter, M., Becher, B., 2018. High-Dimensional Single-Cell Mapping of Central Nervous System Immune Cells Reveals Distinct Myeloid Subsets in Health, Aging, and Disease. Immunity 48, 380-395.e6. https://doi.org/10.1016/j.immuni.2018.01.011

Mueller-Steiner, S., Zhou, Y., Arai, H., Roberson, E.D., Sun, B., Chen, J., Wang, X., Yu, G., Esposito, L., Mucke, L., Gan, L., 2006. Antiamyloidogenic and Neuroprotective Functions of Cathepsin B: Implications for Alzheimer's Disease. Neuron 51, 703–714. https://doi.org/10.1016/j.neuron.2006.07.027

Mussil, B., Suspène, R., Caval, V., Durandy, A., Wain-Hobson, S., Vartanian, J.-P., 2019. Genotoxic stress increases cytoplasmic mitochondrial DNA editing by human APOBEC3 mutator enzymes at a single cell level. Sci. Rep. 9, 1–11. https://doi.org/10.1038/s41598-019-39245-8

Nagle, M.P., Tam, G.S., Maltz, E., Hemminger, Z., Wollman, R., 2021. Bridging scales: From cell biology to physiology using in situ single-cell technologies. Cell Syst. 12, 388–400. https://doi.org/10.1016/j.cels.2021.03.002

Nesterenko, P.A., McLaughlin, J., Cheng, D., Bangayan, N.J., Sojo, G.B., Seet, C.S., Qin, Y., Mao, Z., Obusan, M.B., Phillips, J.W., Witte, O.N., 2021. Droplet-based mRNA sequencing of fixed and permeabilized cells by CLInt-seq allows for antigen-specific TCR cloning. Proc. Natl. Acad. Sci. 118. https://doi.org/10.1073/pnas.2021190118

Nikodemova, M., Kimyon, R.S., De, I., Small, A.L., Collier, L.S., Watters, J.J., 2015. Microglial numbers attain adult levels after undergoing a rapid decrease in cell number in the third postnatal week. J. Neuroimmunol. 0, 280–288. https://doi.org/10.1016/j.jneuroim.2014.11.018

Nimmerjahn, A., Kirchhoff, F., Helmchen, F., 2005. Resting Microglial Cells Are Highly Dynamic Surveillants of Brain Parenchyma in Vivo. Science 308, 1314–1318. https://doi.org/10.1126/science.1110647

Nott, A., Holtman, I.R., Coufal, N.G., Schlachetzki, J.C.M., Yu, M., Hu, R., Han, C.Z., Pena, M., Xiao, J., Wu, Y., Keulen, Z., Pasillas, M.P., O'Connor, C., Nickl, C.K., Schafer, S.T., Shen, Z., Rissman, R.A., Brewer, J.B., Gosselin, D., Gonda, D.D., Levy, M.L., Rosenfeld, M.G., McVicker, G., Gage, F.H., Ren, B., Glass, C.K., 2019. Brain cell type–specific enhancer-promoter interactome maps and disease risk association. Science. https://doi.org/10.1126/science.aay0793

Nugent, A.A., Lin, K., van Lengerich, B., Lianoglou, S., Przybyla, L., Davis, S.S., Llapashtica, C., Wang, J., Kim, D.J., Xia, D., Lucas, A., Baskaran, S., Haddick, P.C.G., Lenser, M., Earr, T.K., Shi, J., Dugas, J.C., Andreone, B.J., Logan, T., Solanoy, H.O., Chen, H., Srivastava, A., Poda, S.B., Sanchez, P.E., Watts, R.J., Sandmann, T., Astarita, G., Lewcock, J.W., Monroe, K.M., Di Paolo, G., 2020. TREM2 Regulates Microglial Cholesterol Metabolism upon Chronic Phagocytic Challenge. Neuron 105, 837-854.e9. https://doi.org/10.1016/j.neuron.2019.12.007

Nugent, B.M., Wright, C.L., Shetty, A.C., Hodes, G.E., Lenz, K.M., Mahurkar, A., Russo, S.J., Devine, S.E., McCarthy, M.M., 2015. Brain feminization requires active repression of masculinization via DNA methylation. Nat. Neurosci. 18, 690–697. https://doi.org/10.1038/nn.3988

Oakley, H., Cole, S.L., Logan, S., Maus, E., Shao, P., Craft, J., Guillozet-Bongaarts, A., Ohno, M., Disterhoft, J., Eldik, L.V., Berry, R., Vassar, R., 2006. Intraneuronal β-Amyloid Aggregates, Neurodegeneration, and Neuron Loss in Transgenic Mice with Five Familial Alzheimer's Disease Mutations: Potential Factors in Amyloid Plaque Formation. J. Neurosci. 26, 10129–10140. https://doi.org/10.1523/JNEUROSCI.1202-06.2006

Obst, J., Simon, E., Mancuso, R., Gomez-Nicola, D., 2017. The Role of Microglia in Prion Diseases: A Paradigm of Functional Diversity. Front. Aging Neurosci. 9. https://doi.org/10.3389/fnagi.2017.00207

Obst, J., Simon, E., Martin-Estebane, M., Pipi, E., Barkwill, L.M., Gonzalez-Rivera, I., Buchanan, F., Prescott, A.R., Faust, D., Fox, S., Brownlees, J., Taylor, D., Perry, V.H., Nuthall, H., Atkinson, P.J., Karran, E., Routledge, C., Gomez-Nicola, D., 2020. Inhibition of IL-34 Unveils Tissue-Selectivity and Is Sufficient to Reduce Microglial Proliferation in a Model of Chronic

Neurodegeneration. Front. Immunol. 11, 2360. https://doi.org/10.3389/fimmu.2020.579000

O'Flanagan, C.H., Campbell, K.R., Zhang, A.W., Kabeer, F., Lim, J.L.P., Biele, J., Eirew, P., Lai, D., McPherson, A., Kong, E., Bates, C., Borkowski, K., Wiens, M., Hewitson, B., Hopkins, J., Pham, J., Ceglia, N., Moore, R., Mungall, A.J., McAlpine, J.N., Shah, S.P., Aparicio, S., The CRUK IMAXT Grand Challenge Team, 2019. Dissociation of solid tumor tissues with cold active protease for single-cell RNA-seq minimizes conserved collagenase-associated stress responses. Genome Biol. 20, 210. https://doi.org/10.1186/s13059-019-1830-0

Olah, M., Menon, V., Habib, N., Taga, M.F., Ma, Y., Yung, C.J., Cimpean, M., Khairallah, A., Coronas-Samano, G., Sankowski, R., Grün, D., Kroshilina, A.A., Dionne, D., Sarkis, R.A., Cosgrove, G.R., Helgager, J., Golden, J.A., Pennell, P.B., Prinz, M., Vonsattel, J.P.G., Teich, A.F., Schneider, J.A., Bennett, D.A., Regev, A., Elyaman, W., Bradshaw, E.M., De Jager, P.L., 2020. Single cell RNA sequencing of human microglia uncovers a subset associated with Alzheimer's disease. Nat. Commun. 11, 6129. https://doi.org/10.1038/s41467-020-19737-2

Olah, M., Patrick, E., Villani, A.-C., Xu, J., White, C.C., Ryan, K.J., Piehowski, P., Kapasi, A., Nejad, P., Cimpean, M., Connor, S., Yung, C.J., Frangieh, M., McHenry, A., Elyaman, W., Petyuk, V., Schneider, J.A., Bennett, D.A., De Jager, P.L., Bradshaw, E.M., 2018. A transcriptomic atlas of aged human microglia. Nat. Commun. 9. https://doi.org/10.1038/s41467-018-02926-5

Olmos-Alonso, A., Schetters, S.T.T., Sri, S., Askew, K., Mancuso, R., Vargas-Caballero, M., Holscher, C., Perry, V.H., Gomez-Nicola, D., 2016. Pharmacological targeting of CSF1R inhibits microglial proliferation and prevents the progression of Alzheimer's-like pathology. Brain 139, 891–907. https://doi.org/10.1093/brain/awv379

Orihuela, R., McPherson, C.A., Harry, G.J., 2016. Microglial M1/M2 polarization and metabolic states. Br. J. Pharmacol. 173, 649–665. https://doi.org/10.1111/bph.13139

Orkin, S.H., Zon, L.I., 2008. Hematopoiesis: An Evolving Paradigm for Stem Cell Biology. Cell 132, 631–644. https://doi.org/10.1016/j.cell.2008.01.025

Ormel, P.R., Sá, R.V. de, Bodegraven, E.J. van, Karst, H., Harschnitz, O., Sneeboer, M.A.M., Johansen, L.E., Dijk, R.E. van, Scheefhals, N., Berlekom, A.B. van, Martínez, E.R., Kling, S., MacGillavry, H.D., Berg, L.H. van den, Kahn, R.S., Hol, E.M., Witte, L.D. de, Pasterkamp, R.J., 2018. Microglia innately develop within cerebral organoids. Nat. Commun. 9, 4167. https://doi.org/10.1038/s41467-018-06684-2

Osorio, D., Cai, J.J., 2020. Systematic determination of the mitochondrial proportion in human and mice tissues for single-cell RNA sequencing data quality control. Bioinforma. Oxf. Engl. https://doi.org/10.1093/bioinformatics/btaa751

Pakos-Zebrucka, K., Koryga, I., Mnich, K., Ljujic, M., Samali, A., Gorman, A.M., 2016. The integrated stress response. EMBO Rep. 17, 1374–1395. https://doi.org/10.15252/embr.201642195

Pan, Y., Cao, W., Mu, Y., Zhu, Q., 2022. Microfluidics Facilitates the Development of Single-Cell RNA Sequencing. Biosensors 12, 450. https://doi.org/10.3390/bios12070450

Pandey, A.K., Williams, R.W., 2014. Chapter Eight - Genetics of Gene Expression in CNS, in: Hitzemann, R., Mcweeney, S. (Eds.), International Review of Neurobiology, Brain Transcriptome. Academic Press, pp. 195–231. https://doi.org/10.1016/B978-0-12-801105-8.00008-4

Paolicelli, R.C., Bolasco, G., Pagani, F., Maggi, L., Scianni, M., Panzanelli, P., Giustetto, M., Ferreira, T.A., Guiducci, E., Dumas, L., Ragozzino, D., Gross, C.T., 2011. Synaptic Pruning by

Microglia Is Necessary for Normal Brain Development. Science 333, 1456–1458. https://doi.org/10.1126/science.1202529

Pareek, V., Tian, H., Winograd, N., Benkovic, S.J., 2020. Metabolomics and mass spectrometry imaging reveal channeled de novo purine synthesis in cells. Science. https://doi.org/10.1126/science.aaz6465

Pavel, A., Sandra, L., Jaroslav, T., Mikael, K., Radek, S., 2019. Preparation of single-cell suspension from mouse breast cancer focusing on preservation of original cell state information and cell type composition. bioRxiv 824714. https://doi.org/10.1101/824714

Percin, G.I., Eitler, J., Kranz, A., Fu, J., Pollard, J.W., Naumann, R., Waskow, C., 2018. CSF1R regulates the dendritic cell pool size in adult mice via embryo-derived tissue-resident macrophages. Nat. Commun. 9, 5279. https://doi.org/10.1038/s41467-018-07685-x

Petrany, M.J., Swoboda, C.O., Sun, C., Chetal, K., Chen, X., Weirauch, M.T., Salomonis, N., Millay, D.P., 2020. Single-nucleus RNA-seq identifies transcriptional heterogeneity in multinucleated skeletal myofibers. Nat. Commun. 11, 6374. https://doi.org/10.1038/s41467-020-20063-w

Picelli, S., Björklund, Å.K., Faridani, O.R., Sagasser, S., Winberg, G., Sandberg, R., 2013. Smart-seq2 for sensitive full-length transcriptome profiling in single cells. Nat. Methods 10, 1096–1098. https://doi.org/10.1038/nmeth.2639

Pinares-Garcia, P., Stratikopoulos, M., Zagato, A., Loke, H., Lee, J., 2018. Sex: A Significant Risk Factor for Neurodevelopmental and Neurodegenerative Disorders. Brain Sci. 8, 154. https://doi.org/10.3390/brainsci8080154

Podcasy, J.L., Epperson, C.N., 2016. Considering sex and gender in Alzheimer disease and other dementias. Dialogues Clin. Neurosci. 18, 437–446. https://doi.org/10.31887/DCNS.2016.18.4/cepperson

Qin, Y., Garrison, B.S., Ma, W., Wang, R., Jiang, A., Li, J., Mistry, M., Bronson, R.T., Santoro, D., Franco, C., Robinton, D.A., Stevens, B., Rossi, D.J., Lu, C., Springer, T.A., 2018. A Milieu Molecule for TGF-β Required for Microglia Function in the Nervous System. Cell 174, 156-171.e16. https://doi.org/10.1016/j.cell.2018.05.027

Qiu, L.-Q., Abey, S., Harris, S., Shah, R., Gerrish, K.E., Blackshear, P.J., 2015. Global Analysis of Posttranscriptional Gene Expression in Response to Sodium Arsenite. Environ. Health Perspect. 123, 324–330. https://doi.org/10.1289/ehp.1408626

Qiu, M., Xu, E., Zhan, L., 2021. Epigenetic Regulations of Microglia/Macrophage Polarization in Ischemic Stroke. Front. Mol. Neurosci. 14.

Quality Control [WWW Document], n.d. . Single RNA-Seq Data Anal. R. URL https://nbisweden.github.io/excelerate-scRNAseq/session-qc/Quality_control.html (accessed 3.5.22).

Raj, A., van den Bogaard, P., Rifkin, S.A., van Oudenaarden, A., Tyagi, S., 2008. Imaging individual mRNA molecules using multiple singly labeled probes. Nat. Methods 5, 877–879. https://doi.org/10.1038/nmeth.1253

Ramos-Cejudo, J., Wisniewski, T., Marmar, C., Zetterberg, H., Blennow, K., de Leon, M.J., Fossati, S., 2018. Traumatic Brain Injury and Alzheimer's Disease: The Cerebrovascular Link. EBioMedicine 28, 21–30. https://doi.org/10.1016/j.ebiom.2018.01.021

Ransohoff, R.M., 2016. A polarizing question: do M1 and M2 microglia exist? Nat. Neurosci. 19, 987–991. https://doi.org/10.1038/nn.4338

Rappez, L., Stadler, M., Triana, S., Gathungu, R.M., Ovchinnikova, K., Phapale, P., Heikenwalder, M., Alexandrov, T., 2021. SpaceM reveals metabolic states of single cells. Nat. Methods 18, 799–805. https://doi.org/10.1038/s41592-021-01198-0

Rauschmeier, R., Gustafsson, C., Reinhardt, A., A-Gonzalez, N., Tortola, L., Cansever, D., Subramanian, S., Taneja, R., Rossner, M.J., Sieweke, M.H., Greter, M., Månsson, R., Busslinger, M., Kreslavsky, T., 2019. Bhlhe40 and Bhlhe41 transcription factors regulate alveolar macrophage self-renewal and identity. EMBO J. 38, e101233. https://doi.org/10.15252/embj.2018101233

Ravindran, T.S., Teerawattananon, Y., Tannenbaum, C., Vijayasingham, L., 2020. Making pharmaceutical research and regulation work for women. BMJ 371, m3808. https://doi.org/10.1136/bmj.m3808

Regev, A., Teichmann, S.A., Lander, E.S., Amit, I., Benoist, C., Birney, E., Bodenmiller, B., Campbell, P., Carninci, P., Clatworthy, M., Clevers, H., Deplancke, B., Dunham, I., Eberwine, J., Eils, R., Enard, W., Farmer, A., Fugger, L., Göttgens, B., Hacohen, N., Haniffa, M., Hemberg, M., Kim, S., Klenerman, P., Kriegstein, A., Lein, E., Linnarsson, S., Lundberg, E., Lundeberg, J., Majumder, P., Marioni, J.C., Merad, M., Mhlanga, M., Nawijn, M., Netea, M., Nolan, G., Pe'er, D., Phillipakis, A., Ponting, C.P., Quake, S., Reik, W., Rozenblatt-Rosen, O., Sanes, J., Satija, R., Schumacher, T.N., Shalek, A., Shapiro, E., Sharma, P., Shin, J.W., Stegle, O., Stratton, M., Stubbington, M.J.T., Theis, F.J., Uhlen, M., van Oudenaarden, A., Wagner, A., Watt, F., Weissman, J., Wold, B., Xavier, R., Yosef, N., Human Cell Atlas Meeting Participants, 2017. The Human Cell Atlas. eLife 6, e27041. https://doi.org/10.7554/eLife.27041

Reik, W., 2007. Stability and flexibility of epigenetic gene regulation in mammalian development. Nature 447, 425–432. https://doi.org/10.1038/nature05918

Réu, P., Khosravi, A., Bernard, S., Mold, J.E., Salehpour, M., Alkass, K., Perl, S., Tisdale, J., Possnert, G., Druid, H., Frisén, J., 2017. The Lifespan and Turnover of Microglia in the Human Brain. Cell Rep. 20, 779–784. https://doi.org/10.1016/j.celrep.2017.07.004

Rosenberg, L.E., Rosenberg, D.D., 2012. Chapter 7 - Expression of Genes and Genomes, in: Rosenberg, L.E., Rosenberg, D.D. (Eds.), Human Genes and Genomes. Academic Press, San Diego, pp. 97–116. https://doi.org/10.1016/B978-0-12-385212-0.00007-X

Roy, E.R., Wang, B., Wan, Y., Chiu, G., Cole, A., Yin, Z., Propson, N.E., Xu, Y., Jankowsky, J.L., Liu, Z., Lee, V.M.-Y., Trojanowski, J.Q., Ginsberg, S.D., Butovsky, O., Zheng, H., Cao, W., 2020. Type I interferon response drives neuroinflammation and synapse loss in Alzheimer disease. J. Clin. Invest. 130, 1912–1930. https://doi.org/10.1172/JCI133737

Rubino, S.J., Mayo, L., Wimmer, I., Siedler, V., Brunner, F., Hametner, S., Madi, A., Lanser, A., Moreira, T., Donnelly, D., Cox, L., Rezende, R.M., Butovsky, O., Lassmann, H., Weiner, H.L., 2018. Acute microglia ablation induces neurodegeneration in the somatosensory system. Nat. Commun. 9. https://doi.org/10.1038/s41467-018-05929-4

Rustenhoven, J., Smith, A.M., Smyth, L.C., Jansson, D., Scotter, E.L., Swanson, M.E.V., Aalderink, M., Coppieters, N., Narayan, P., Handley, R., Overall, C., Park, T.I.H., Schweder, P., Heppner, P., Curtis, M.A., Faull, R.L.M., Dragunow, M., 2018. PU.1 regulates Alzheimer's disease-associated genes in primary human microglia. Mol. Neurodegener. 13, 44. https://doi.org/10.1186/s13024-018-0277-1

Saelens, W., Cannoodt, R., Todorov, H., Saeys, Y., 2019. A comparison of single-cell trajectory inference methods. Nat. Biotechnol. 37, 547. https://doi.org/10.1038/s41587-019-0071-9

Safaiyan, S., Besson-Girard, S., Kaya, T., Cantuti-Castelvetri, L., Liu, L., Ji, H., Schifferer, M., Gouna, G., Usifo, F., Kannaiyan, N., Fitzner, D., Xiang, X., Rossner, M.J., Brendel, M., Gokce, O.,

Simons, M., 2021a. White matter aging drives microglial diversity. Neuron 109, 1100-1117.e10. https://doi.org/10.1016/j.neuron.2021.01.027

Safaiyan, S., Besson-Girard, S., Kaya, T., Cantuti-Castelvetri, L., Liu, L., Ji, H., Schifferer, M., Gouna, G., Usifo, F., Kannaiyan, N., Fitzner, D., Xiang, X., Rossner, M.J., Brendel, M., Gokce, O., Simons, M., 2021b. White matter aging drives microglial diversity. Neuron. https://doi.org/10.1016/j.neuron.2021.01.027

Safaiyan, S., Kannaiyan, N., Snaidero, N., Brioschi, S., Biber, K., Yona, S., Edinger, A.L., Jung, S., Rossner, M.J., Simons, M., 2016. Age-related myelin degradation burdens the clearance function of microglia during aging. Nat. Neurosci. 19, nn.4325. https://doi.org/10.1038/nn.4325

Saito, T., Matsuba, Y., Mihira, N., Takano, J., Nilsson, P., Itohara, S., Iwata, N., Saido, T.C., 2014. Single App knock-in mouse models of Alzheimer's disease. Nat. Neurosci. 17, 661–663. https://doi.org/10.1038/nn.3697

Sala Frigerio, C., Wolfs, L., Fattorelli, N., Thrupp, N., Voytyuk, I., Schmidt, I., Mancuso, R., Chen, W.-T., Woodbury, M.E., Srivastava, G., Möller, T., Hudry, E., Das, S., Saido, T., Karran, E., Hyman, B., Perry, V.H., Fiers, M., De Strooper, B., 2019. The Major Risk Factors for Alzheimer's Disease: Age, Sex, and Genes Modulate the Microglia Response to Aβ Plaques. Cell Rep. 27, 1293-1306.e6. https://doi.org/10.1016/j.celrep.2019.03.099

Sandberg, R., 2014. Entering the era of single-cell transcriptomics in biology and medicine. Nat. Methods 11, 22–24. https://doi.org/10.1038/nmeth.2764

Sankowski, R., Monaco, G., Prinz, M., 2021. Evaluating microglial phenotypes using single-cell technologies. Trends Neurosci. https://doi.org/10.1016/j.tins.2021.11.001

Sanz, E., Yang, L., Su, T., Morris, D.R., McKnight, G.S., Amieux, P.S., 2009. Cell-type-specific isolation of ribosome-associated mRNA from complex tissues. Proc. Natl. Acad. Sci. 106, 13939–13944. https://doi.org/10.1073/pnas.0907143106

Sasmono, R.T., Williams, E., 2012a. Generation and Characterization of MacGreen Mice, the Cfs1r-EGFP Transgenic Mice, in: Leucocytes, Methods in Molecular Biology. Humana Press, pp. 157–176. https://doi.org/10.1007/978-1-61779-527-5_11

Sasmono, R.T., Williams, E., 2012b. Generation and Characterization of MacGreen Mice, the Cfs1r-EGFP Transgenic Mice, in: Ashman, R.B. (Ed.), Leucocytes: Methods and Protocols, Methods in Molecular Biology. Humana Press, Totowa, NJ, pp. 157–176. https://doi.org/10.1007/978-1-61779-527-5_11

Sasmono, R.T., Williams, E., 2012c. Generation and Characterization of <Emphasis Type="Italic">MacGreen</Emphasis> Mice, the <Emphasis Type="Italic">Cfs1r</Emphasis>-EGFP Transgenic Mice, in: Leucocytes, Methods in Molecular Biology. Humana Press, pp. 157–176. https://doi.org/10.1007/978-1-61779-527-5_11

Satija, R., Farrell, J.A., Gennert, D., Schier, A.F., Regev, A., 2015a. Spatial reconstruction of single-cell gene expression data. Nat. Biotechnol. 33, 495–502. https://doi.org/10.1038/nbt.3192

Satija, R., Farrell, J.A., Gennert, D., Schier, A.F., Regev, A., 2015b. Spatial reconstruction of single-cell gene expression. Nat. Biotechnol. 33, 495–502. https://doi.org/10.1038/nbt.3192

Schaum, N., Karkanias, J., Neff, N.F., May, A.P., Quake, S.R., Wyss-Coray, T., Darmanis, S., Batson, J., Botvinnik, O., Chen, M.B., Chen, S., Green, F., Jones, R.C., Maynard, A., Penland, L., Pisco, A.O., Sit, R.V., Stanley, G.M., Webber, J.T., Zanini, F., Baghel, A.S., Bakerman, I., Bansal, I., Berdnik, D., Bilen, B., Brownfield, D., Cain, C., Chen, M.B., Chen, S., Cho, M.,

Cirolia, G., Conley, S.D., Darmanis, S., Demers, A., Demir, K., de Morree, A., Divita, T., du Bois, H., Dulgeroff, L.B.T., Ebadi, H., Espinoza, F.H., Fish, M., Gan, Q., George, B.M., Gillich, A., Green, F., Genetiano, G., Gu, X., Gulati, G.S., Hang, Y., Hosseinzadeh, S., Huang, A., Iram, T., Isobe, T., Ives, F., Jones, R.C., Kao, K.S., Karnam, G., Kershner, A.M., Kiss, B.M., Kong, W., Kumar, M.E., Lam, J.Y., Lee, D.P., Lee, S.E., Li, G., Li, Q., Liu, L., Lo, A., Lu, W.-J., Manjunath, A., May, A.P., May, K.L., May, O.L., Maynard, A., McKay, M., Metzger, R.J., Mignardi, M., Min, D., Nabhan, A.N., Neff, N.F., Ng, K.M., Noh, J., Patkar, R., Peng, W.C., Penland, L., Puccinelli, R., Rulifson, E.J., Schaum, N., Sikandar, S.S., Sinha, R., Sit, R.V., Szade, K., Tan, W., Tato, C., Tellez, K., Travaglini, K.J., Tropini, C., Waldburger, L., van Weele, L.J., Wosczyna, M.N., Xiang, J., Xue, S., Youngyunpipatkul, J., Zanini, F., Zardeneta, M.E., Zhang, F., Zhou, L., Bansal, I., Chen, S., Cho, M., Cirolia, G., Darmanis, S., Demers, A., Divita, T., Ebadi, H., Genetiano, G., Green, F., Hosseinzadeh, S., Ives, F., Lo, A., May, A.P., Maynard, A., McKay, M., Neff, N.F., Penland, L., Sit, R.V., Tan, W., Waldburger, L., Youngyunpipatkul, J., Batson, J., Botvinnik, O., Castro, P., Croote, D., Darmanis, S., DeRisi, J.L., Karkanias, J., Pisco, A.O., Stanley, G.M., Webber, J.T., Zanini, F., Baghel, A.S., Bakerman, I., Batson, J., Bilen, B., Botvinnik, O., Brownfield, D., Chen, M.B., Darmanis, S., Demir, K., de Morree, A., Ebadi, H., Espinoza, F.H., Fish, M., Gan, Q., George, B.M., Gillich, A., Gu, X., Gulati, G.S., Hang, Y., Huang, A., Iram, T., Isobe, T., Karnam, G., Kershner, A.M., Kiss, B.M., Kong, W., Kuo, C.S., Lam, J.Y., Lehallier, B., Li, G., Li, Q., Liu, L., Lu, W.-J., Min, D., Nabhan, A.N., Ng, K.M., Nguyen, P.K., Patkar, R., Peng, W.C., Penland, L., Rulifson, E.J., Schaum, N., Sikandar, S.S., Sinha, R., Szade, K., Tan, S.Y., Tellez, K., Travaglini, K.J., Tropini, C., van Weele, L.J., Wang, B.M., Wosczyna, M.N., Xiang, J., Yousef, H., Zhou, L., Batson, J., Botvinnik, O., Chen, S., Darmanis, S., Green, F., May, A.P., Maynard, A., Pisco, A.O., Quake, S.R., Schaum, N., Stanley, G.M., Webber, J.T., Wyss-Coray, T., Zanini, F., Beachy, P.A., Chan, C.K.F., de Morree, A., George, B.M., Gulati, G.S., Hang, Y., Huang, K.C., Iram, T., Isobe, T., Kershner, A.M., Kiss, B.M., Kong, W., Li, G., Li, Q., Liu, L., Lu, W.-J., Nabhan, A.N., Ng, K.M., Nguyen, P.K., Peng, W.C., Rulifson, E.J., Schaum, N., Sikandar, S.S., Sinha, R., Szade, K., Travaglini, K.J., Tropini, C., Wang, B.M., Weinberg, K., Wosczyna, M.N., Wu, S.M., Yousef, H., Barres, B.A., Beachy, P.A., Chan, C.K.F., Clarke, M.F., Darmanis, S., Huang, K.C., Karkanias, J., Kim, S.K., Krasnow, M.A., Kumar, M.E., Kuo, C.S., May, A.P., Metzger, R.J., Neff, N.F., Nusse, R., Nguyen, P.K., Rando, T.A., Sonnenburg, J., Wang, B.M., Weinberg, K., Weissman, I.L., Wu, S.M., Quake, S.R., Wyss-Coray, T., The Tabula Muris Consortium, Overall coordination, Logistical coordination, Organ collection and processing, Library preparation and sequencing, Computational data analysis, Cell type annotation, Writing group, Supplemental text writing group, Principal investigators, 2018. Single-cell transcriptomics of 20 mouse organs creates a Tabula Muris. Nature 562, 367–372. https://doi.org/10.1038/s41586-018-0590-4

Schaum, N., Lehallier, B., Hahn, O., Pálovics, R., Hosseinzadeh, S., Lee, S.E., Sit, R., Lee, D.P., Losada, P.M., Zardeneta, M.E., Fehlmann, T., Webber, J.T., McGeever, A., Calcuttawala, K., Zhang, H., Berdnik, D., Mathur, V., Tan, W., Zee, A., Tan, M., Pisco, A.O., Karkanias, J., Neff, N.F., Keller, A., Darmanis, S., Quake, S.R., Wyss-Coray, T., 2020. Ageing hallmarks exhibit organ-specific temporal signatures. Nature 583, 596–602. https://doi.org/10.1038/s41586-020-2499-y

Schluederberg, A., Hendel, R.C., Chavanich, S., 1971. Actinomycin D: Renewed RNA Synthesis after Removal from Mammalian Cells. Science 172, 577–579. https://doi.org/10.1126/science.172.3983.577

Schubert, W., Bonnekoh, B., Pommer, A.J., Philipsen, L., Böckelmann, R., Malykh, Y., Gollnick, H., Friedenberger, M., Bode, M., Dress, A.W.M., 2006. Analyzing proteome topology and function by automated multidimensional fluorescence microscopy. Nat. Biotechnol. 24, 1270–1278. https://doi.org/10.1038/nbt1250

Schwabenland, M., Brück, W., Priller, J., Stadelmann, C., Lassmann, H., Prinz, M., 2021. Analyzing microglial phenotypes across neuropathologies: a practical guide. Acta Neuropathol. (Berl.). https://doi.org/10.1007/s00401-021-02370-8

Schwabenland, M., Mossad, O., Peres, A.G., Kessler, F., Maron, F.J.M., Harsan, L.-A., Bienert, T., von Elverfeldt, D., Knobeloch, K.-P., Staszewski, O., Heppner, F.L., Meuwissen, M.E.C., Mancini, G.M.S., Prinz, M., Blank, T., 2019. Loss of USP18 in microglia induces white matter pathology. Acta Neuropathol. Commun. 7, 106. https://doi.org/10.1186/s40478-019-0757-8

Schwarz, J.M., Bilbo, S.D., 2012. Sex, Glia, and Development: interactions in health and disease. Horm. Behav. 62, 243–253. https://doi.org/10.1016/j.yhbeh.2012.02.018

Schwarz, J.M., McCarthy, M.M., 2008. Steroid-induced sexual differentiation of the developing brain: multiple pathways, one goal. J. Neurochem. 105, 1561–1572. https://doi.org/10.1111/j.1471-4159.2008.05384.x

Seeker, L.A., Bestard-Cuche, N., Jäkel, S., Kazakou, N.-L., Bøstrand, S.M.K., Kilpatrick, A.M., Bruggen, D.V., Kabbe, M., Pohl, F.B., Moslehi, Z., Henderson, N.C., Vallejos, C.A., Manno, G.L., Castelo-Branco, G., Williams, A., 2022. Marked regional glial heterogeneity in the human white matter of the central nervous system. https://doi.org/10.1101/2022.03.22.485367

Seydel, C., 2021. Single-cell metabolomics hits its stride. Nat. Methods 18, 1452–1456. https://doi.org/10.1038/s41592-021-01333-x

Shapiro, E., Biezuner, T., Linnarsson, S., 2013. Single-cell sequencing-based technologies will revolutionize whole-organism science. Nat. Rev. Genet. 14, 618–630. https://doi.org/10.1038/nrg3542

Shemer, A., Grozovski, J., Tay, T.L., Tao, J., Volaski, A., Süß, P., Ardura-Fabregat, A., Gross-Vered, M., Kim, J.-S., David, E., Chappell-Maor, L., Thielecke, L., Glass, C.K., Cornils, K., Prinz, M., Jung, S., 2018. Engrafted parenchymal brain macrophages differ from microglia in transcriptome, chromatin landscape and response to challenge. Nat. Commun. 9, 5206. https://doi.org/10.1038/s41467-018-07548-5

Sheng, J., Ruedl, C., Karjalainen, K., 2015. Most Tissue-Resident Macrophages Except Microglia Are Derived from Fetal Hematopoietic Stem Cells. Immunity 43, 382–393. https://doi.org/10.1016/j.immuni.2015.07.016

Shepherd, G.M.G., 2013. Corticostriatal connectivity and its role in disease. Nat. Rev. Neurosci. 14, 278–291. https://doi.org/10.1038/nrn3469

Sierra, A., Encinas, J.M., Deudero, J.J., Chancey, J.H., Enikolopov, G., Overstreet-Wadiche, L.S., Tsirka, S.E., Maletic-Savatic, M., 2010. Microglia shape adult hippocampal neurogenesis through apoptosis-coupled phagocytosis. Cell Stem Cell 7, 483–495. https://doi.org/10.1016/j.stem.2010.08.014

Silva, N.J., Dorman, L.C., Vainchtein, I.D., Horneck, N.C., Molofsky, A.V., 2021. In situ and transcriptomic identification of microglia in synapse-rich regions of the developing zebrafish brain. Nat. Commun. 12, 5916. https://doi.org/10.1038/s41467-021-26206-x

Single Cell ATAC [WWW Document], n.d. . 10x Genomics. URL https://www.10xgenomics.com/products/single-cell-atac (accessed 1.5.22).

Single Cell CNV [WWW Document], n.d. . 10x Genomics. URL https://www.10xgenomics.com/products/single-cell-cnv (accessed 1.5.22).

Single Cell Gene Expression [WWW Document], n.d. . 10x Genomics. URL https://www.10xgenomics.com/products/single-cell-gene-expression (accessed 1.5.22).

Single Cell Multiome ATAC + Gene Expression [WWW Document], n.d. . 10x Genomics. URL https://www.10xgenomics.com/products/single-cell-multiome-atac-plus-gene-expression (accessed 4.18.22).

Slyper, M., Porter, C.B.M., Ashenberg, O., Waldman, J., Drokhlyansky, E., Wakiro, I., Smillie, C., Smith-Rosario, G., Wu, J., Dionne, D., Vigneau, S., Jané-Valbuena, J., Tickle, T.L., Napolitano, S., Su, M.-J., Patel, A.G., Karlstrom, A., Gritsch, S., Nomura, M., Waghray, A., Gohil, S.H., Tsankov, A.M., Jerby-Arnon, L., Cohen, O., Klughammer, J., Rosen, Y., Gould, J., Nguyen, L., Hofree, M., Tramontozzi, P.J., Li, B., Wu, C.J., Izar, B., Haq, R., Hodi, F.S., Yoon, C.H., Hata, A.N., Baker, S.J., Suvà, M.L., Bueno, R., Stover, E.H., Clay, M.R., Dyer, M.A., Collins, N.B., Matulonis, U.A., Wagle, N., Johnson, B.E., Rotem, A., Rozenblatt-Rosen, O., Regev, A., 2020. A single-cell and single-nucleus RNA-Seq toolbox for fresh and frozen human tumors. Nat. Med. 26, 792–802. https://doi.org/10.1038/s41591-020-0844-1

Snaidero, N., Simons, M., 2014. Myelination at a glance. J Cell Sci 127, 2999–3004. https://doi.org/10.1242/jcs.151043

Song, Q., Su, J., 2021. DSTG: deconvoluting spatial transcriptomics data through graph-based artificial intelligence. Brief. Bioinform. 22, bbaa414. https://doi.org/10.1093/bib/bbaa414

Soufi, A., Dalton, S., 2016. Cycling through developmental decisions: how cell cycle dynamics control pluripotency, differentiation and reprogramming. Dev. Camb. Engl. 143, 4301–4311. https://doi.org/10.1242/dev.142075

Sousa, C., 2018. Single-cell transcriptomics reveals distinct inflammation-induced microglia signatures. EMBO Rep. 19, e46171. https://doi.org/10.15252/embr.201846171

Stoeckius, M., Hafemeister, C., Stephenson, W., Houck-Loomis, B., Chattopadhyay, P.K., Swerdlow, H., Satija, R., Smibert, P., 2017. Simultaneous epitope and transcriptome measurement in single cells. Nat. Methods 14, 865–868. https://doi.org/10.1038/nmeth.4380

Streit, W.J., Sammons, N.W., Kuhns, A.J., Sparks, D.L., 2004. Dystrophic microglia in the aging human brain. Glia 45, 208–212. https://doi.org/10.1002/glia.10319

Stuart, T., Butler, A., Hoffman, P., Hafemeister, C., Papalexi, E., Mauck, W.M., Hao, Y., Stoeckius, M., Smibert, P., Satija, R., 2019. Comprehensive Integration of Single-Cell Data. Cell 177, 1888-1902.e21. https://doi.org/10.1016/j.cell.2019.05.031

Subramanian, A., Alperovich, M., Yang, Y., Li, B., 2021. Biology-inspired data-driven quality control for scientific discovery in single-cell transcriptomics. https://doi.org/10.1101/2021.10.27.466176

Svensson, V., da Veiga Beltrame, E., Pachter, L., 2020. A curated database reveals trends in single-cell transcriptomics. Database J. Biol. Databases Curation 2020, baaa073. https://doi.org/10.1093/database/baaa073

Svensson, V., Natarajan, K.N., Ly, L.-H., Miragaia, R.J., Labalette, C., Macaulay, I.C., Cvejic, A., Teichmann, S.A., 2017. Power analysis of single-cell RNA-sequencing experiments. Nat. Methods 14, 381–387. https://doi.org/10.1038/nmeth.4220

Svoboda, D.S., Barrasa, M.I., Shu, J., Rietjens, R., Zhang, S., Mitalipova, M., Berube, P., Fu, D., Shultz, L.D., Bell, G.W., Jaenisch, R., 2019. Human iPSC-derived microglia assume a primary microglia-like state after transplantation into the neonatal mouse brain. Proc. Natl. Acad. Sci. 116, 25293–25303. https://doi.org/10.1073/pnas.1913541116

Swinnen, N., Smolders, S., Avila, A., Notelaers, K., Paesen, R., Ameloot, M., Brône, B., Legendre, P., Rigo, J.-M., 2013. Complex invasion pattern of the cerebral cortex bymicroglial cells during development of the mouse embryo. Glia 61, 150–163. https://doi.org/10.1002/glia.22421

Szepesi, Z., Manouchehrian, O., Bachiller, S., Deierborg, T., 2018. Bidirectional Microglia–Neuron Communication in Health and Disease. Front. Cell. Neurosci. 12.

Tan, J.C., Bouriakov, V.D., Feng, L., Richmond, T.A., Burgess, D., 2016. Targeted LncRNA Sequencing with the SeqCap RNA Enrichment System, in: Feng, Y., Zhang, L. (Eds.), Long Non-Coding RNAs: Methods and Protocols, Methods in Molecular Biology. Springer New York, New York, NY, pp. 73–100. https://doi.org/10.1007/978-1-4939-3378-5_8

Tansley, S., Uttam, S., Ureña Guzmán, A., Yaqubi, M., Pacis, A., Parisien, M., Deamond, H., Wong, C., Rabau, O., Brown, N., Haglund, L., Ouellet, J., Santaguida, C., Ribeiro-da-Silva, A., Tahmasebi, S., Prager-Khoutorsky, M., Ragoussis, J., Zhang, J., Salter, M.W., Diatchenko, L., Healy, L.M., Mogil, J.S., Khoutorsky, A., 2022. Single-cell RNA sequencing reveals time- and sex-specific responses of mouse spinal cord microglia to peripheral nerve injury and links ApoE to chronic pain. Nat. Commun. 13, 843. https://doi.org/10.1038/s41467-022-28473-8

Tay, T.L., Sagar, Dautzenberg, J., Grün, D., Prinz, M., 2018a. Unique microglia recovery population revealed by single-cell RNAseq following neurodegeneration. Acta Neuropathol. Commun. 6. https://doi.org/10.1186/s40478-018-0584-3

Tay, T.L., Sagar, Dautzenberg, J., Grün, D., Prinz, M., 2018b. Unique microglia recovery population revealed by single-cell RNAseq following neurodegeneration. Acta Neuropathol. Commun. 6, 87. https://doi.org/10.1186/s40478-018-0584-3

Teschendorff, A.E., Enver, T., 2017. Single-cell entropy for accurate estimation of differentiation potency from a cell's transcriptome. Nat. Commun. 8, 15599. https://doi.org/10.1038/ncomms15599

Thion, M.S., Low, D., Silvin, A., Chen, J., Grisel, P., Schulte-Schrepping, J., Blecher, R., Ulas, T., Squarzoni, P., Hoeffel, G., Coulpier, F., Siopi, E., David, F.S., Scholz, C., Shihui, F., Lum, J., Amoyo, A.A., Larbi, A., Poidinger, M., Buttgereit, A., Lledo, P.-M., Greter, M., Chan, J.K.Y., Amit, I., Beyer, M., Schultze, J.L., Schlitzer, A., Pettersson, S., Ginhoux, F., Garel, S., 2018a. Microbiome Influences Prenatal and Adult Microglia in a Sex-Specific Manner. Cell 172, 500-516.e16. https://doi.org/10.1016/j.cell.2017.11.042

Thion, M.S., Low, D., Silvin, A., Chen, J., Grisel, P., Schulte-Schrepping, J., Blecher, R., Ulas, T., Squarzoni, P., Hoeffel, G., Coulpier, F., Siopi, E., David, F.S., Scholz, C., Shihui, F., Lum, J., Amoyo, A.A., Larbi, A., Poidinger, M., Buttgereit, A., Lledo, P.-M., Greter, M., Chan, J.K.Y., Amit, I., Beyer, M., Schultze, J.L., Schlitzer, A., Pettersson, S., Ginhoux, F., Garel, S., 2018b. Microbiome Influences Prenatal and Adult Microglia in a Sex-Specific Manner. Cell 172, 500-516.e16. https://doi.org/10.1016/j.cell.2017.11.042

Thomsen, E.R., Mich, J.K., Yao, Z., Hodge, R.D., Doyle, A.M., Jang, S., Shehata, S.I., Nelson, A.M., Shapovalova, N.V., Levi, B.P., Ramanathan, S., 2016. Fixed single-cell transcriptomic characterization of human radial glial diversity. Nat. Methods 13, 87–93. https://doi.org/10.1038/nmeth.3629

Thrupp, N., Sala Frigerio, C., Wolfs, L., Skene, N.G., Fattorelli, N., Poovathingal, S., Fourne, Y., Matthews, P.M., Theys, T., Mancuso, R., de Strooper, B., Fiers, M., 2020. Single-Nucleus RNA-Seq Is Not Suitable for Detection of Microglial Activation Genes in Humans. Cell Rep. 32, 108189. https://doi.org/10.1016/j.celrep.2020.108189

Tran, H.T.N., Ang, K.S., Chevrier, M., Zhang, X., Lee, N.Y.S., Goh, M., Chen, J., 2020. A benchmark of batch-effect correction methods for single-cell RNA sequencing data. Genome Biol. 21, 12. https://doi.org/10.1186/s13059-019-1850-9

Tränkner, D., Boulet, A., Peden, E., Focht, R., Van Deren, D., Capecchi, M., 2019. A Microglia Sublineage Protects from Sex-Linked Anxiety Symptoms and Obsessive Compulsion. Cell Rep. 29, 791-799.e3. https://doi.org/10.1016/j.celrep.2019.09.045

Trapnell, C., Cacchiarelli, D., Grimsby, J., Pokharel, P., Li, S., Morse, M., Lennon, N.J., Livak, K.J., Mikkelsen, T.S., Rinn, J.L., 2014. The dynamics and regulators of cell fate decisions are revealed by pseudotemporal ordering of single cells. Nat. Biotechnol. 32, 381–386. https://doi.org/10.1038/nbt.2859

Travaglini, K.J., Nabhan, A.N., Penland, L., Sinha, R., Gillich, A., Sit, R.V., Chang, S., Conley, S.D., Mori, Y., Seita, J., Berry, G.J., Shrager, J.B., Metzger, R.J., Kuo, C.S., Neff, N., Weissman, I.L., Quake, S.R., Krasnow, M.A., 2020. A molecular cell atlas of the human lung from single-cell RNA sequencing. Nature 587, 619–625. https://doi.org/10.1038/s41586-020-2922-4

Tung, P.-Y., Blischak, J.D., Hsiao, C.J., Knowles, D.A., Burnett, J.E., Pritchard, J.K., Gilad, Y., 2017. Batch effects and the effective design of single-cell gene expression studies. Sci. Rep. 7, 39921. https://doi.org/10.1038/srep39921

Ulland, T.K., Song, W.M., Huang, S.C.-C., Ulrich, J.D., Sergushichev, A., Beatty, W.L., Loboda, A.A., Zhou, Y., Cairns, N.J., Kambal, A., Loginicheva, E., Gilfillan, S., Cella, M., Virgin, H.W., Unanue, E.R., Wang, Y., Artyomov, M.N., Holtzman, D.M., Colonna, M., 2017. TREM2 Maintains Microglial Metabolic Fitness in Alzheimer's Disease. Cell 170, 649-663.e13. https://doi.org/10.1016/j.cell.2017.07.023

Utz, S.G., See, P., Mildenberger, W., Thion, M.S., Silvin, A., Lutz, M., Ingelfinger, F., Rayan, N.A., Lelios, I., Buttgereit, A., Asano, K., Prabhakar, S., Garel, S., Becher, B., Ginhoux, F., Greter, M., 2020. Early Fate Defines Microglia and Non-parenchymal Brain Macrophage Development. Cell 181, 557-573.e18. https://doi.org/10.1016/j.cell.2020.03.021

Van Hove, H., Martens, L., Scheyltjens, I., De Vlaminck, K., Pombo Antunes, A.R., De Prijck, S., Vandamme, N., De Schepper, S., Van Isterdael, G., Scott, C.L., Aerts, J., Berx, G., Boeckxstaens, G.E., Vandenbroucke, R.E., Vereecke, L., Moechars, D., Guilliams, M., Van Ginderachter, J.A., Saeys, Y., Movahedi, K., 2019. A single-cell atlas of mouse brain macrophages reveals unique transcriptional identities shaped by ontogeny and tissue environment. Nat. Neurosci. 22, 1021–1035. https://doi.org/10.1038/s41593-019-0393-4

van Velthoven, C.T.J., de Morree, A., Egner, I.M., Brett, J.O., Rando, T.A., 2017. Transcriptional Profiling of Quiescent Muscle Stem Cells In Vivo. Cell Rep. 21, 1994–2004. https://doi.org/10.1016/j.celrep.2017.10.037

van de Laar, L., Saelens, W., De Prijck, S., Martens, L., Scott, C.L., Van Isterdael, G., Hoffmann, E., Beyaert, R., Saeys, Y., Lambrecht, B.N., Guilliams, M., 2016. Yolk Sac Macrophages, Fetal Liver, and Adult Monocytes Can Colonize an Empty Niche and Develop into Functional Tissue-Resident Macrophages. Immunity 44, 755–768. https://doi.org/10.1016/j.immuni.2016.02.017

VanRyzin, J.W., Marquardt, A.E., Pickett, L.A., McCarthy, M.M., 2020. Microglia and sexual differentiation of the developing brain: A focus on extrinsic factors. Glia 68, 1100–1113. https://doi.org/10.1002/glia.23740

Villa, A., Gelosa, P., Castiglioni, L., Cimino, M., Rizzi, N., Pepe, G., Lolli, F., Marcello, E., Sironi, L., Vegeto, E., Maggi, A., 2018a. Sex-Specific Features of Microglia from Adult Mice. Cell Rep. 23, 3501–3511. https://doi.org/10.1016/j.celrep.2018.05.048

Villa, A., Gelosa, P., Castiglioni, L., Cimino, M., Rizzi, N., Pepe, G., Lolli, F., Marcello, E., Sironi, L., Vegeto, E., Maggi, A., 2018b. Sex-Specific Features of Microglia from Adult Mice. Cell Rep. 23, 3501. https://doi.org/10.1016/j.celrep.2018.05.048

Villani, A.-C., Satija, R., Reynolds, G., Sarkizova, S., Shekhar, K., Fletcher, J., Griesbeck, M., Butler, A., Zheng, S., Lazo, S., Jardine, L., Dixon, D., Stephenson, E., Nilsson, E., Grundberg, I., McDonald, D., Filby, A., Li, W., Jager, P.L.D., Rozenblatt-Rosen, O., Lane, A.A., Haniffa, M., Regev, A., Hacohen, N., 2017. Single-cell RNA-seq reveals new types of human blood dendritic cells, monocytes, and progenitors. Science 356, eaah4573. https://doi.org/10.1126/science.aah4573

Vitak, S.A., Torkenczy, K.A., Rosenkrantz, J.L., Fields, A.J., Christiansen, L., Wong, M.H., Carbone, L., Steemers, F.J., Adey, A., 2017. Sequencing thousands of single-cell genomes with combinatorial indexing. Nat. Methods 14, 302–308. https://doi.org/10.1038/nmeth.4154

Von Bernhardi, R., Eugenin-von Bernhardi, L., Eugenin, J., 2015. Microglial cell dysregulation in Brain Aging and Neurodegeneration. Front. Aging Neurosci. 7.

Waddington, C.H., Kacser, H., 1957. The Strategy of the Genes: A Discussion of Some Aspects of Theoretical Biology. Allen & Unwin.

Wagner, A., Regev, A., Yosef, N., 2016. Revealing the vectors of cellular identity with single-cell genomics. Nat. Biotechnol. 34, nbt.3711. https://doi.org/10.1038/nbt.3711

Waise, S., Parker, R., Rose-Zerilli, M.J.J., Layfield, D.M., Wood, O., West, J., Ottensmeier, C.H., Thomas, G.J., Hanley, C.J., 2019. An optimised tissue disaggregation and data processing pipeline for characterising fibroblast phenotypes using single-cell RNA sequencing. Sci. Rep. 9, 9580. https://doi.org/10.1038/s41598-019-45842-4

Wang, J., Huang, M., Torre, E., Dueck, H., Shaffer, S., Murray, J., Raj, A., Li, M., Zhang, N.R., 2018. Gene expression distribution deconvolution in single-cell RNA sequencing. Proc. Natl. Acad. Sci. 201721085. https://doi.org/10.1073/pnas.1721085115

Wang, S., Mustafa, M., Yuede, C.M., Salazar, S.V., Kong, P., Long, H., Ward, M., Siddiqui, O., Paul, R., Gilfillan, S., Ibrahim, A., Rhinn, H., Tassi, I., Rosenthal, A., Schwabe, T., Colonna, M., 2020. Anti-human TREM2 induces microglia proliferation and reduces pathology in an Alzheimer's disease model. J. Exp. Med. 217. https://doi.org/10.1084/jem.20200785

Wang, X., Park, J., Susztak, K., Zhang, N.R., Li, M., 2019. Bulk tissue cell type deconvolution with multi-subject single-cell expression reference. Nat. Commun. 10, 380. https://doi.org/10.1038/s41467-018-08023-x

Wang, Z.-Y., Qin, W., Yi, F., 2015. Targeting histone deacetylases: perspectives for epigenetic-based therapy in cardio-cerebrovascular disease. J. Geriatr. Cardiol. JGC 12, 153–164. https://doi.org/10.11909/j.issn.1671-5411.2015.02.010

Wehrspaun, C.C., Haerty, W., Ponting, C.P., 2015. Microglia recapitulate a hematopoietic master regulator network in the aging human frontal cortex. Neurobiol. Aging 36, 2443.e9-2443.e20. https://doi.org/10.1016/j.neurobiolaging.2015.04.008

Wendeln, A.-C., Degenhardt, K., Kaurani, L., Gertig, M., Ulas, T., Jain, G., Wagner, J., Häsler, L.M., Wild, K., Skodras, A., Blank, T., Staszewski, O., Datta, M., Centeno, T.P., Capece, V., Islam, M.R., Kerimoglu, C., Staufenbiel, M., Schultze, J.L., Beyer, M., Prinz, M., Jucker, M., Fischer, A., Neher, J.J., 2018a. Innate immune memory in the brain shapes neurological disease hallmarks. Nature 1. https://doi.org/10.1038/s41586-018-0023-4

Wendeln, A.-C., Degenhardt, K., Kaurani, L., Gertig, M., Ulas, T., Jain, G., Wagner, J., Häsler, L.M., Wild, K., Skodras, A., Blank, T., Staszewski, O., Datta, M., Centeno, T.P., Capece, V., Islam, M.R., Kerimoglu, C., Staufenbiel, M., Schultze, J.L., Beyer, M., Prinz, M., Jucker, M.,

Fischer, A., Neher, J.J., 2018b. Innate immune memory in the brain shapes neurological disease hallmarks. Nature 556, 332–338. https://doi.org/10.1038/s41586-018-0023-4

Wirth, M., Pichet Binette, A., Brunecker, P., Köbe, T., Witte, A.V., Flöel, A., 2017. Divergent regional patterns of cerebral hypoperfusion and gray matter atrophy in mild cognitive impairment patients. J. Cereb. Blood Flow Metab. 37, 814–824. https://doi.org/10.1177/0271678X16641128

Wlodarczyk, A., Holtman, I.R., Krueger, M., Yogev, N., Bruttger, J., Khorooshi, R., Benmamar-Badel, A., Boer-Bergsma, J.J. de, Martin, N.A., Karram, K., Kramer, I., Boddeke, E.W., Waisman, A., Eggen, B.J., Owens, T., 2017a. A novel microglial subset plays a key role in myelinogenesis in developing brain. EMBO J. 36, 3292–3308. https://doi.org/10.15252/embj.201696056

Wlodarczyk, A., Holtman, I.R., Krueger, M., Yogev, N., Bruttger, J., Khorooshi, R., Benmamar-Badel, A., de Boer-Bergsma, J.J., Martin, N.A., Karram, K., Kramer, I., Boddeke, E.W., Waisman, A., Eggen, B.J., Owens, T., 2017b. A novel microglial subset plays a key role in myelinogenesis in developing brain. EMBO J. 36, 3292–3308. https://doi.org/10.15252/embj.201696056

Wolf, S.A., Boddeke, H.W.G.M., Kettenmann, H., 2017. Microglia in Physiology and Disease. Annu. Rev. Physiol. 79, 619–643. https://doi.org/10.1146/annurev-physiol-022516-034406

Wolf, Y., Yona, S., Kim, K.-W., Jung, S., 2013. Microglia, seen from the CX3CR1 angle. Front. Cell. Neurosci. 7.

Wooten, G.F., Currie, L.J., Bovbjerg, V.E., Lee, J.K., Patrie, J., 2004. Are men at greater risk for Parkinson's disease than women? J. Neurol. Neurosurg. Psychiatry 75, 637–639. https://doi.org/10.1136/jnnp.2003.020982

Wu, S.-Y., Chen, Y.-W., Tsai, S.-F., Wu, S.-N., Shih, Y.-H., Jiang-Shieh, Y.-F., Yang, T.-T., Kuo, Y.-M., 2016. Estrogen ameliorates microglial activation by inhibiting the Kir2.1 inward-rectifier K+ channel. Sci. Rep. 6, 22864. https://doi.org/10.1038/srep22864

Wu, Y.E., Pan, L., Zuo, Y., Li, X., Hong, W., 2017. Detecting Activated Cell Populations Using Single-Cell RNA-Seq. Neuron 96, 313-329.e6. https://doi.org/10.1016/j.neuron.2017.09.026

Xiang, R., Wang, W., Yang, L., Wang, S., Xu, C., Chen, X., 2021. A Comparison for Dimensionality Reduction Methods of Single-Cell RNA-seq Data. Front. Genet. 12.

Xie, X., Shi, Q., Wu, P., Zhang, X., Kambara, H., Su, J., Yu, H., Park, S.-Y., Guo, R., Ren, Q., Zhang, S., Xu, Y., Silberstein, L.E., Cheng, T., Ma, F., Li, C., Luo, H.R., 2020. Single-cell transcriptome profiling reveals neutrophil heterogeneity in homeostasis and infection. Nat. Immunol. 21, 1119–1133. https://doi.org/10.1038/s41590-020-0736-z

Xu, J., Zhu, L., He, S., Wu, Y., Jin, W., Yu, T., Qu, J.Y., Wen, Z., 2015. Temporal-Spatial Resolution Fate Mapping Reveals Distinct Origins for Embryonic and Adult Microglia in Zebrafish. Dev. Cell 34, 632–641. https://doi.org/10.1016/j.devcel.2015.08.018

Xu, S., Mei, S., Lu, J., Wu, H., Dong, X., Shi, L., Zhou, J., Zhang, J., 2021. Transcriptome Analysis of Microglia Reveals That the TLR2/IRF7 Signaling Axis Mediates Neuroinflammation After Subarachnoid Hemorrhage. Front. Aging Neurosci. 13.

Yang, T.-T., Lin, C., Hsu, C.-T., Wang, T.-F., Ke, F.-Y., Kuo, Y.-M., 2013. Differential distribution and activation of microglia in the brain of male C57BL/6J mice. Brain Struct. Funct. 218, 1051–1060. https://doi.org/10.1007/s00429-012-0446-x

Yung, A., 2019. The Role of Human APOE Variants on Microglia Modulation After Early-life Stress and Predisposition to Earlier Onset of Alzheimer's Disease. Digit. Access Scholarsh. Harv. 48.

Yuzwa, S.A., Borrett, M.J., Innes, B.T., Voronova, A., Ketela, T., Kaplan, D.R., Bader, G.D., Miller, F.D., 2017. Developmental Emergence of Adult Neural Stem Cells as Revealed by Single-Cell Transcriptional Profiling. Cell Rep. 21, 3970–3986. https://doi.org/10.1016/j.celrep.2017.12.017

Zhang, S.-Q., Ma, K.-Y., Schonnesen, A.A., Zhang, M., He, C., Sun, E., Williams, C.M., Jia, W., Jiang, N., 2018. High-throughput determination of the antigen specificities of T cell receptors in single cells. Nat. Biotechnol. 36, 1156–1159. https://doi.org/10.1038/nbt.4282

Zhang, X., Li, T., Liu, F., Chen, Y., Yao, J., Li, Z., Huang, Y., Wang, J., 2019. Comparative Analysis of Droplet-Based Ultra-High-Throughput Single-Cell RNA-Seq Systems. Mol. Cell 73, 130-142.e5. https://doi.org/10.1016/j.molcel.2018.10.020

Zheng, J., Ru, W., Adolacion, J.R., Spurgat, M.S., Liu, X., Yuan, S., Liang, R.X., Dong, J., Potter, A.S., Potter, S.S., Chen, K., Chen, R., Varadarajan, N., Tang, S.-J., 2021. Single-cell RNA-seq analysis reveals compartment-specific heterogeneity and plasticity of microglia. iScience 24, 102186. https://doi.org/10.1016/j.isci.2021.102186

Zhou, L., Li, Q., 2019. Isolation of Region-specific Microglia from One Adult Mouse Brain Hemisphere for Deep Single-cell RNA Sequencing. JoVE J. Vis. Exp. e60347. https://doi.org/10.3791/60347

Zhou, Y., Zhou, B., Pache, L., Chang, M., Khodabakhshi, A.H., Tanaseichuk, O., Benner, C., Chanda, S.K., 2019. Metascape provides a biologist-oriented resource for the analysis of systems-level datasets. Nat. Commun. 10, 1523. https://doi.org/10.1038/s41467-019-09234-6

Zhu, C., Yu, M., Huang, H., Juric, I., Abnousi, A., Hu, R., Lucero, J., Behrens, M.M., Hu, M., Ren, B., 2019. An ultra high-throughput method for single-cell joint analysis of open chromatin and transcriptome. Nat. Struct. Mol. Biol. 26, 1063–1070. https://doi.org/10.1038/s41594-019-0323-x

Zhu, H., Li, Q., Liao, T., Yin, X., Chen, Q., Wang, Z., Dai, M., Yi, L., Ge, S., Miao, C., Zeng, W., Qu, L., Ju, Z., Huang, G., Cang, C., Xiong, W., 2021. Metabolomic profiling of single enlarged lysosomes. Nat. Methods 18, 788–798. https://doi.org/10.1038/s41592-021-01182-8

Ziegenhain, C., Vieth, B., Parekh, S., Reinius, B., Guillaumet-Adkins, A., Smets, M., Leonhardt, H., Heyn, H., Hellmann, I., Enard, W., 2017. Comparative Analysis of Single-Cell RNA Sequencing Methods. Mol. Cell 65, 631-643.e4. https://doi.org/10.1016/j.molcel.2017.01.023

Zucker, I., Beery, A.K., 2010. Males still dominate animal studies. Nature 465, 690–690. https://doi.org/10.1038/465690a